MOLECULAR SIEVES

7 *Science and Technology*

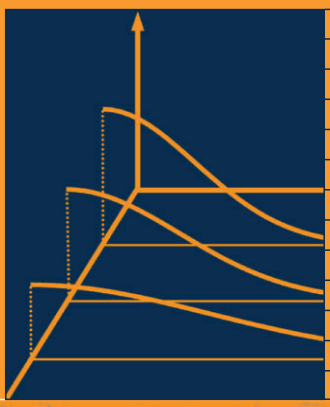

ADSORPTION AND DIFFUSION

H.G. Karge
J. Weitkamp (Eds.)

Springer

7
Molecular Sieves
Science and Technology

Editors: H. G. Karge · J. Weitkamp

Molecular Sieves

Editors: H. G. Karge · J. Weitkamp

Recently Published and Forthcoming Volumes

Adsorption and Diffusion
Editors: Karge, H. G., Weitkamp J.
Vol. 7, 2008

Acidity and Basicity
Vol. 6, 2008

Characterization II
Editors: Karge, H. G., Weitkamp J.
Vol. 5, 2006

Characterization I
Editors: Karge, H. G., Weitkamp J.
Vol. 4, 2004

Post-Synthesis Modification I
Editors: Karge, H. G., Weitkamp J.
Vol. 3, 2003

Structures and Structure Determination
Editors: Karge, H. G., Weitkamp J.
Vol. 2, 1999

Synthesis
Editors: Karge, H. G., Weitkamp J.
Vol. 1, 1998

Adsorption and Diffusion

Editors: Hellmut G. Karge · Jens Weitkamp

With contributions by
S. Brandani · M. Eic · E. J. M. Hensen · H. Jobic · A. M. de Jong
H. G. Karge · J. Kärger · L. V. C. Rees · D. M. Ruthven
R. A. van Santen · L. Song

Springer

Molecular Sieves – Science and Technology will be devoted to all kinds of microporous crystalline solids with emphasis on zeolites. Classical alumosilicate zeolites as well as microporous silica will typically be covered; titaniumsilicate, alumophosphates, gallophosphates, silicoalumophosphates, and metalloalumophosphates are also within the scope of the series. It will address such important items as hydrothermal synthesis, structures and structure determination, post-synthesis modifications such as ion exchange or dealumination, characterization by all kinds of chemical and physico-chemical methods including spectroscopic techniques, acidity and basicity, hydrophilic vs. hydrophobic surface properties, theory and modelling, sorption and diffusion, host-guest interactions, zeolites as detergent builders, as catalysts in petroleum refining and petrochemical processes, and in the manufacture of organic intermediates, separation and purification processes, zeolites in environmental protection.
As a rule, contributions are specially commissioned. The editors and publishers will, however, always be pleased to receive suggestions and supplementary information. Papers for *Molecular Sieves* are accepted in English. In references *Molecular Sieves* is abbreviated *Mol Sieves* and is cited as a journal.
Springer WWW home page: springer.com
Visit the Molecular Sieves home page at springerlink.com

ISBN 978-3-540-73965-4 e-ISBN 978-3-540-73966-1
DOI 10.1007/978-3-540-73966-1

Molecular Sieves ISSN 1436-8269

Library of Congress Control Number: 2008921483

© 2008 Springer-Verlag Berlin Heidelberg

This work is subject to copyright. All rights are reserved, whether the whole or part of the material is concerned, specifically the rights of translation, reprinting, reuse of illustrations, recitation, broadcasting, reproduction on microfilm or in any other way, and storage in data banks. Duplication of this publication or parts thereof is permitted only under the provisions of the German Copyright Law of September 9, 1965, in its current version, and permission for use must always be obtained from Springer. Violations are liable to prosecution under the German Copyright Law.

The use of general descriptive names, registered names, trademarks, etc. in this publication does not imply, even in the absence of a specific statement, that such names are exempt from the relevant protective laws and regulations and therefore free for general use.

Cover design: WMXDesign GmbH, Heidelberg
Typesetting and Production: le-tex publishing services oHG, Leipzig

Printed on acid-free paper

9 8 7 6 5 4 3 2 1 0

springer.com

Editors

Dr. Hellmut G. Karge
Fritz Haber Institute
of the Max Planck Society
Faradayweg 4–6
14195 Berlin
Germany

Professor Dr.-Ing. Jens Weitkamp
Institute of Technical Chemistry
University of Stuttgart
70550 Stuttgart
Germany

Molecular Sieves
Also Available Electronically

For all customers who have a standing order to Molecular Sieves, we offer the electronic version via SpringerLink free of charge. Please contact your librarian who can receive a password or free access to the full articles by registering at:

springerlink.com

If you do not have a subscription, you can still view the tables of contents of the volumes and the abstract of each article by going to the SpringerLink Homepage, clicking on "Browse by Online Libraries", then "Chemical Sciences", and finally choose Molecular Sieves.

You will find information about the

- Editorial Board
- Aims and Scope
- Instructions for Authors
- Sample Contribution

at springer.com using the search function.

Color figures are published in full color within the electronic version on SpringerLink.

Preface to the Series

Following Springer's successful series *Catalysis – Science and Technology*, this series of monographs has been entitled *Molecular Sieves – Science and Technology*. It will cover, in a comprehensive manner, all aspects of the science and application of zeolites and related microporous and mesoporous materials.

After about 50 years of prosperous research, molecular sieves have gained a firm and important position in modern materials science, and we are witnessing an ever increasing number of industrial applications. In addition to the more traditional and still prevailing applications of zeolites as water softeners in laundry detergents, as adsorbents for drying, purification and separation purposes, and as catalysts in the petroleum refining, petrochemical and chemical industries, novel uses of molecular sieves are being sought in numerous laboratories.

By the beginning of 1999, the Structure Commission of the International Zeolite Association had approved approximately 120 different zeolite structures which, altogether, cover the span of pore diameters from about 0.3 nm to 2 nm. The dimensions of virtually all molecules (except macromolecules) chemists are concerned with fall into this same range. It is this coincidence of molecular dimensions and pore widths which makes zeolites so unique in adsorption and catalysis and enables molecular sieving and shape-selective catalysis. Bearing in mind that each zeolite structure can be modified by a plethora of post-synthesis techniques, an almost infinite variety of molecular sieve materials are nowadays at the researcher's and engineer's disposal. In many instances this will allow the properties of a zeolite to be tailored to a desired application. Likewise, remarkable progress has been made in the characterization of molecular sieve materials by spectroscopic and other physico-chemical techniques, and this is particularly true for structure determination. During the last decade, we have seen impressive progress in the application of quantum mechanical ab initio and other theoretical methods to zeolite science. The results enable us to obtain a deeper understanding of physical and chemical properties of zeolites and may render possible reliable predictions of their behavior. All in all, the science and application of zeolites is a flourishing and exciting field of interdisciplinary research which has reached a high level of sophistication and a certain degree of maturity.

The editors believe that, at the turn of the century, the time has come to collect and present the huge knowledge on zeolite molecular sieves. *Molecular Sieves – Science and Technology* is meant as a handbook of zeolites, and the term "zeolites" is to be understood in the broadest sense of the word. While, throughout the handbook, some emphasis will be placed on the more traditional alumosilicate zeolites with eight-, ten- and twelve-membered ring pore openings, materials with other chemical compositions and narrower and larger pores (such as sodalite, clathrasils, $AlPO_4$–8, VPI-5 or cloverite) will be covered as well. Also included are microporous forms of silica (e.g., silicalite-1 or -2), alumophosphates, gallophosphates, silicoalumophosphates and titaniumsilicalites etc. Finally, zeolite-like amorphous mesoporous materials with ordered pore systems, especially those belonging to the M41S series, will be covered. Among other topics related to the science and application of molecular sieves, the book series will put emphasis on such important items as: the preparation of zeolites by hydrothermal synthesis; zeolite structures and methods for structure determination; post-synthesis modification by, e.g., ion exchange, dealumination or chemical vapor deposition; the characterization by all kinds of physico-chemical and chemical techniques; the acidic and basic properties of molecular sieves; their hydrophilic or hydrophobic surface properties; theory and modelling; sorption and diffusion in microporous and mesoporous materials; host/guest interactions; zeolites as detergent builders; separation and purification processes using molecular sieve adsorbents; zeolites as catalysts in petroleum refining, in petrochemical processes and in the manufacture of organic chemicals; zeolites in environmental protection; novel applications of molecular sieve materials.

The handbook will appear over several years with a total of ten to fifteen volumes. Each volume of the series will be devoted to a specific sub-field of the fundamentals or application of molecular sieve materials and contain five to ten articles authored by renowned experts upon invitation by the editors. These articles are meant to present the state of the art from a scientific and, where applicable, from an industrial point of view, to discuss critical pivotal issues and to outline future directions of research and development in this sub-field. To this end, the series is intended as an up-to-date highly sophisticated collection of information for those who have already been dealing with zeolites in industry or at academic institutions. Moreover, by emphasizing the description and critical assessment of experimental techniques which have been used in molecular sieve science, the series is also meant as a guide for newcomers, enabling them to collect reliable and relevant experimental data.

The editors would like to take this opportunity to express their sincere gratitude to the authors who spent much time and great effort on their chapters. It is our hope that *Molecular Sieves – Science and Technology* turns out to be

both a valuable handbook the advanced researcher will regularly consult and a useful guide for newcomers to the fascinating world of microporous and mesoporous materials.

Hellmut G. Karge
Jens Weitkamp

Preface to Volume 7

Sorption into, release from and diffusion inside microporous and mesoporous materials are of paramount interest in view of separation processes and catalysis by zeolites and related structures. Thus, volume 7 of the handbook-like series "Molecular Sieves – Science and Technology" is exclusively devoted to the phenomena of adsorption into, desorption out of and diffusion in the pores of zeolite crystallites.

Fundamentals of sorption and sorption kinetics by zeolites are described and analyzed in the first Chapter which was written by D. M. Ruthven. It includes the treatment of the sorption equilibrium in microporous solids as described by basic laws as well as the discussion of appropriate models such as the Ideal Langmuir Model for mono- and multi-component systems, the Dual-Site Langmuir Model, the Unilan and Toth Model, and the Simplified Statistical Model. Similarly, the Gibbs Adsorption Isotherm, the Dubinin–Polanyi Theory, and the Ideal Adsorbed Solution Theory are discussed. With respect to sorption kinetics, the cases of self-diffusion and transport diffusion are discriminated, their relationship is analyzed and, in this context, the Maxwell–Stefan Model discussed. Finally, basic aspects of measurements of micropore diffusion both under equilibrium and non-equilibrium conditions are elucidated. The important role of micropore diffusion in separation and catalytic processes is illustrated.

The discussion of experimental techniques for diffusion measurements especially under non-equilibrium conditions is continued in Chapter 2 which is co-authored by D. M. Ruthven, St. Brandani, and M. Eic. Results obtained by uptake rate measurements using evaluation of, for example, piezometric (pressure change), chromatographic, frequency response (FR), zero-length column (ZLC), membrane permeation, and effectiveness factor experiments or employing temporal analysis of products (TAP) are critically analyzed. A review of experimental diffusivity data for selected systems presents examples of both consistencies and discrepancies between "microscopic" measurements, for example, pulsed-field gradient NMR (PFG NMR) or quasi-elastic neutron scattering (QENS) on the one side and "macroscopic" determination of diffusivities by uptake techniques as listed above on the other. Possible origins of discrepancies are addressed. This chapter closes with a brief treatment of diffusion in bi-porous structures such as mesoporous silica materials.

Diffusion measurements by NMR spectrometry represent the most prominent methods for determining the rate of migration of molecules in the framework of zeolites under equilibrium conditions. The fundamentals of the pulsed-field gradient (PFG) NMR method, i.e. the measuring principle, the range of applicability, and its limitations are described in Chapter 3, which was contributed by J. Kärger. The PFG NMR method belongs to the category of "microscopic" methods, in that it operates on a sub-crystal scale (cf. Chapter 1). The non-invasive NMR technique is able to yield valuable information about the elementary steps of diffusion, especially about mean jump and reorientation times. Furthermore, PFG NMR allows, as shown in this chapter, studying particular phenomena of diffusion in zeolites such as long-range diffusion, additional diffusion resistances (surface barriers), structure-related diffusion, and diffusion under transient conditions. Complementarily to Chapter 2, the last section of Chapter 3 provides a detailed comparison of PFG NMR results with those of other techniques, which is particularly important in view of the two broad classes of diffusion measurements in zeolites, viz. experiments under macroscopic equilibrium ("self-diffusion") by "microscopic" techniques and under non-equilibrium conditions, i.e. under concentration differences ("transport diffusion") via "macroscopic" methods.

In Chapter 4, H. G. Karge and J. Kärger describe diffusion measurements by means of macro-infrared Fourier transform spectroscopy (Macro-FTIR), micro-infrared Fourier transform spectroscopy (Micro-FTIR, employing a so-called IR microscope), and interference microscopy (diffusion interference microscopy, DIFM). The FTIR methods enables studies of mono- and multi-component diffusion, especially in the case of slowly migrating species ($D < 10^{-3}$ m^2 s^{-1}). In the case of bi-component diffusion with chemically different diffusants such as, for example, benzene and ethylbenzene, for the first time diffusivities were determined upon co- and counter-diffusion. The novel diffusion interference microscopy (DIFM) has proven to be a most powerful tool for studying phenomena of adsorption on and diffusion in zeolites, especially when combined with "FTIR microscopy." In single crystals of zeolites, it enables the determination of concentration profiles with a very good local resolution and provides, inter alia, structural data, for example, information about the role of boundaries and intergrowth effects. From the analysis of transient concentration profiles occurring during uptake or release of sorbate molecules, diffusivity data and their concentration dependence as well as information about surface resistances, permeabilities, and sticking probabilities may be obtained.

Similar to the PFG NMR method, neutron scattering techniques are successfully employed for the determination of diffusivities under equilibrium conditions. These techniques and their application are discussed in Chapter 5 by H. Jobic. Particularly efficient is a novel combination of quasi-elastic neutron scattering (QENS) and a neutron spin-echo technique (NSE), which considerably expands the range of accessible diffusivities, viz. down to 10^{-14} m^2 s^{-1}, so

that the range is now the same as that of PFG NMR (cf. Chapter 3). Although hydrogen has the largest neutron cross section, the neutron scattering technique is no longer restricted to the study of hydrogen-containing molecules. For instance, the self-diffusivities of hydrocarbons may be measured with the hydrogen-containing and the transport diffusivity with the deuterated molecules.

An ingenious method for measurements of adsorption on and diffusion in zeolites was available on the advent of the so-called frequency response spectroscopy (FR). L. Song and L. V. C. Rees have contributed Chapter 6 of this volume, which is exclusively devoted to the FR method. With great regret we have to announce that L.V.C. Rees, who pioneered the application of this technique in zeolite science and technology, passed away in 2006. Theory, experimental principles, and applications of FR with respect to the investigation of diffusivities in micropores and bi-dispersed porous solids are reviewed. The diffusive behavior of hydrocarbons and other sorbates in microporous crystallites and related pellets is analyzed. The high potential of the FR method for elucidating multi-kinetic mechanisms is demonstrated when surface resistances, surface barriers, or subtle differences in molecular shape and size of the diffusing species play a role.

E. J. M. Hensen, A. M. de Jong, and R. A. van Santen have written Chapter 7, which introduces the tracer exchange positron emission profiling (TEX-PEP) as an attractive technique for in-situ investigations, for example, in a stainless steel reactor, of the adsorption and diffusive properties of hydrocarbons in zeolites under chemical steady-state conditions. Self-diffusion coefficients of hydrocarbons, labeled by proton-emitting ^{11}C at finite loadings and even in the presence of another unlabeled alkane, may be extracted. The method is illustrated by adsorption and diffusion measurements of linear (n-hexane) and branched (2-methylpentane) alkanes in H-ZSM-5 and silicalite-1.

The closing Chapter 8 is authored by J. Kärger and deals with the so-called single-file diffusion. Single-file diffusion occurs when a mutual passage of diffusants in zeolites with one-dimensional channels is excluded. The chapter provides a thorough analytical treatment and informative discussion of experimental studies by PFG NMR, QENS, ZLC, FR, and permeation methods. Monte-Carlo simulations and analytical approaches reveal striking peculiarities in single-file systems of finite length.

Thus, Volume 7 of the series "Molecular Sieves – Science and Technology" presents descriptions, critical analyses, and illustrative examples of applications of the most important methods for investigations of sorption and sorption kinetics in zeolite systems and related materials. The editors hope that the volume will be helpful for researchers as well as technologists who are confronted with the important phenomena of adsorption and diffusion in microporous materials as they occur, for instance, in separation processes and catalysis.

January 2008

Hellmut G. Karge
Jens Weitkamp

Contents

Mol Sieves (2008) 7: 1–43
DOI 10.1007/3829_007
© Springer-Verlag Berlin Heidelberg
Published online: 13 January 2006

Fundamentals of Adsorption Equilibrium and Kinetics in Microporous Solids

Douglas M. Ruthven

Department of Chemical and Biological Engineering, University of Maine, Orono, ME USA
druthven@umche.maine.edu

Abstract This chapter is intended to provide a general introduction to the basic principles of adsorption equilibrium and kinetics, which is the focus of the present volume. The discussion of adsorption equilibrium (Sect. 2) includes a brief review of the many different expressions that are commonly used for correlation and prediction of equilibrium isotherms, with a short discussion of the underlying assumptions and approximations. Section 3 provides a short summary of diffusion in microporous adsorbents with emphasis on the phenomenological behavior and the generalized Maxwell–Stefan theory. Representative examples of the practical importance of micropore diffusion in zeolite-based adsorption separation and catalytic processes are presented in Sect. 4.

Abbreviations

A	Surface area per molecule (Eq. 16)
$A_1, A_2, \ldots$	Parameters in Eqs. 12 or 19
b, b_1	Langmuir equilibrium constant (Eq. 5)
B	Mobility (Eq. 34)
c	Gas-phase concentration
c_0	Molar density or total concentration in gas phase
D	Diffusivity
D_0	Corrected diffusivity
$\mathcal{D}$	Self-diffusivity
$Đ_{ij}$	Mutual diffusivity in Maxwell–Stefan model (Eq. 38)
$Đ_{Az}$	$D_{0A}(1 - \theta_A - \theta_B)$ Eq. 39
k	Reaction rate constant
K, K^1	Henry's law equilibrium constant (Eq. 1)
N_i	Molar flux of component i
p, p^0	Sorbate pressure or partial pressure
p_s	Saturation vapor pressure of pure liquid sorbate (Eq. 20)
q, q^0	Adsorbed-phase concentration
q_s	Saturation limit (Eq. 5)
$\boldsymbol{r}$	Position vector
R	Gas constant; particle radius (Eq. 14)
s	Parameter in Eq. 8; number of molecules per cage (Eq. 11)
t	Time; parameter in Eq. 9
T	Temperature (absolute)
U	Internal energy
V_m	Molar volume of sorbate
W	Volume of sorbate per unit mass of sorbent
W_0	Specific micropore volume of sorbent
X_i	Mole fraction in adsorbed phase
Y_i	Mole fraction in vapor phase
z	Distance coordinate
α	Separation factor (Eq. 23)
β	Molecular volume (or area of a molecule in Eq. 16)
$-\Delta H$	Heat of adsorption
ε	Adsorption potential (Eq. 20)
θ	Fractional loading (q/q_s)
π	Spreading pressure (Eq. 15)
κ	Constant
μ	Chemical potential
η	Effectiveness factor (Eq. 47)
Φ	Thiele modulus (Eq. 47)
ζ	Defined by Eq. 13
ψ_i	π/RT (Eq. 24)
$C_2^=$	Ethylene
$C_3^=$	Propylene
CHA	Chabazite*
CMS	Carbon molecular sieve
DAB	Differential-adsorption bed

DME	Dimethyl ether
EB	Ethylbenzene
ETS-4	Engelhard titanosilicalite structure 4
FTIR	Fourier-transform infrared
IAST	Ideal adsorbed solution theory
MeOH	Methanol
MTO	Methanol to olefins process
MX	*m*-Xylene
OX	*o*-Xylene
PFG NMR	Pulsed field gradient nuclear magnetic resonance
PX	*p*-Xylene
QENS	Quasi-elastic neutron scattering
SSTM	Simplified statistical model
Si-CHA	Silicon analog of chabazite*
SAPO-34	Zeolite analog widely used as the active ingredient of MTO catalysts*
TZLC	Tracer ZLC
X	Zeolite of faujasite structure with $1.0 < Si/Al < 1.5$*
Y	Zeolite of faujasite structure with Si/Al ratio greater than 1.5*
ZLC	Zero-length column
ZSM-5	Zeolite with MFI structure*

* see Baerlocher C, Meier WM, Olson DH (2001) Atlas of zeolite framework types, 5th edn. Elsevier, Amsterdam

1 Introduction

The main focus of this volume is on understanding the transport of molecules in microporous solids such as zeolites and carbon molecular sieves, and the kinetics of adsorption/desorption. This subject is of both practical and theoretical interest, since the performance of zeolite-based catalysts and adsorbents is strongly influenced by resistances to mass transfer and intracrystalline diffusion. However, at an even more basic level, the performance of microporous catalysts and adsorbents depends on favorable adsorption equilibria for the relevant species, so a general understanding of the fundamentals of adsorption equilibrium is a necessary prerequisite for understanding kinetic behavior. This chapter is intended to provide a concise summary of the general principles of adsorption equilibrium and of the main features of sorption kinetics in microporous solids, which generally depend on a combination of both equilibrium and kinetic properties.

2
Sorption Equilibrium in Microporous Solids

2.1
Physical Adsorption and Chemisorption

Adsorption depends on the existence of a force field at the surface of a solid, which reduces the potential energy of an adsorbed molecule below that of the ambient fluid phase. It is useful to distinguish two broad classes of adsorption (physical adsorption and chemisorption) depending on the nature of the surface forces. The forces of physical adsorption consist of the ubiquitous dispersion–repulsion forces (van der Waals forces), which are a fundamental property of all matter, supplemented by various electrostatic contributions (polarization, field–dipole and field gradient–quadrupole interactions), which can be important or even dominant for polar adsorbents. The forces involved in chemisorption are much stronger and involve a substantial degree of electron transfer or electron sharing, as in the formation of a chemical bond. As a result, chemisorption is highly specific and the adsorption energies are generally substantially greater than those for physical adsorption (see Table 1).

Chemisorption is by its very nature limited to less than monolayer coverage of the surface whereas, in physical adsorption, multilayer adsorption is common. In a microporous solid the ultimate capacity for physical adsorption corresponds to the specific micropore volume, which is generally much larger than the monolayer coverage. The economic viability of an adsorption

Table 1 Physical adsorption and chemisorption

Physical adsorption	Chemisorption
Low heat of adsorption (1.0 to 1.5 times latent heat of evaporation)	High heat of adsorption (> 1.5 times latent heat of evaporation)
Nonspecific	Highly specific
Monolayer or multilayer	Monolayer only
No dissociation of adsorbed species	May involve dissociation
Only significant at relatively low temperatures	Possible over a wide range of temperatures
Rapid, nonactivated, reversible	Activated, may be slow and irreversible.
No electron transfer, although polarization of sorbate may occur	Electron transfer leading to bond formation between sorbate and surface

separation process depends on both the selectivity and the capacity of the adsorbent. Because of their high selectivity and low capacity chemisorption systems are generally viable only for trace impurity removal; bulk separation processes almost always depend on physical adsorption. In catalytic processes both physical adsorption and chemisorption can be important.

The surfaces of adsorbents such as activated carbon and high-silica zeolites are essentially nonpolar although, in the case of carbon adsorbents, oxidation can impart a degree of surface polarity. With nonpolar adsorbents van der Waals forces are dominant, and relative affinity is determined largely by the size and polarizability of the sorbate molecules and the dimensions of the pores. The influence of the nature of the surface is then secondary so the affinities (for a given sorbate) of a carbonaceous adsorbent or a high-silica zeolite adsorbent of similar pore size are similar. Since nonpolar adsorbents have a relatively low affinity for water and a higher affinity for most organics, such materials are often described as hydrophobic.

By contrast, in the aluminum-rich zeolites, there are strong intracrystalline electric fields, so that electrostatic forces of adsorption are very important, particularly for polar or quadrupolar sorbate molecules. Such adsorbents are classified as hydrophilic because they adsorb polar molecules such as water very strongly. Control of the Si/Al ratio in a zeolite adsorbent thus provides a useful means of adjusting the selectivity of an adsorbent for a particular separation.

2.2 Henry's Law

Basic thermodynamic considerations require that, at sufficiently low adsorbed-phase concentrations on a homogeneous surface, the equilibrium isotherm for physical adsorption should always approach linearity (Henry's law). The limiting slope of the isotherm is called the Henry constant:

$$\lim_{c\to 0}(\partial q/\partial c)_T = K\,; \qquad \lim_{p\to 0}(\partial q/\partial p)_T = K^1\,. \tag{1}$$

It is evident that the Henry constant is simply the thermodynamic equilibrium constant for adsorption, and the temperature dependence should therefore follow a van't Hoff expression:

$$K = K_\infty\, \mathrm{e}^{-\Delta U/RT}\,; \qquad K^1 = K^1_\infty\, \mathrm{e}^{-\Delta H/RT}\,, \tag{2}$$

where ΔU and ΔH are respectively the internal energy change and the enthalpy change for adsorption from the ambient fluid (gas) phase. Since adsorption is generally exothermic, the Henry constant decreases with temperature. The relationship between K and K^1 is simply:

$$K = K^1 RT\,. \tag{3}$$

Henry's law corresponds physically to the situation where the adsorbed phase is so dilute that there is neither competition for adsorption sites nor interaction between adsorbed molecules. At higher loadings both these effects become significant, leading to curvature of the equilibrium isotherm and variation of the heat of adsorption with loading.

If the potential field within the micropores is known as a function of position $[U(\boldsymbol{r})]$ the dimensionless Henry constant can be calculated by integration over the accessible pore volume:

$$K = \int_V \mathrm{e}^{-U(\boldsymbol{r})/RT}\,\mathrm{d}\boldsymbol{r}\,. \tag{4}$$

Computer software that allows the calculation of $U(\boldsymbol{r})$ for any known structural framework is now widely available, thus enabling the a priori prediction of Henry constants—see, for example, Nicholson and Parsonage [1]. This approach works well for zeolites (and other similar materials) where the structure is regular and the positions of all atoms in the framework are well defined. It is less useful for amorphous adsorbents.

2.3 Ideal Langmuir Model

At higher loadings (beyond the Henry's law region) the equilibrium isotherms for microporous adsorbents are generally of Type I form in Brunauer's classification [2]. Several different models have been suggested to represent such isotherms, the simplest being the ideal Langmuir expression [3]:

$$\theta = \frac{q}{q_\mathrm{s}} = \frac{bc}{1+bc} = \frac{b^1 p}{1+b^1 p}\,; \qquad b^1 p = \frac{\theta}{1-\theta}\,, \tag{5}$$

where q_s is the saturation capacity and b (or b^1) is an equilibrium constant which is directly related to the Henry constant ($bq_\mathrm{s} = K$; $b^1 q_\mathrm{s} = K^1$). Although originally developed to represent chemisorption on an ideal surface, Eq. 5 has the correct asymptotic form at both low and high loadings, and it has therefore been widely used to correlate both chemisorption isotherms and physical adsorption isotherms of Type I form. When the product bp is large, Eq. 5 reduces to the rectangular form typical of highly favorable or irreversible adsorption. In the low concentration limit when $bp \ll 1$ the isotherm approaches Henry's law.

Although the simple Langmuir expression provides a useful qualitative representation of the equilibrium behavior of many systems it is generally not quantitatively reliable, especially at higher loadings. There have therefore been numerous attempts to develop more accurate models, a few of which are noted here.

2.4 Dual-Site Langmuir Model

For energetically heterogeneous adsorbents one may choose to represent the isotherm as the sum of the contributions from two independent sets of Langmuir sites:

$$q = \frac{b_1 q_{s1} p}{1 + b_1 p} + \frac{b_2 q_{s2} p}{1 + b_2 p} . \tag{6}$$

Such an expression contains four independent constants, so it will obviously provide a better fit to experimental data than the simple two-constant Langmuir expression. However, such a model makes physical sense for systems such as the adsorption of polar (or quadrupolar) molecules on a cationic zeolite, where the most favorable sites are those associated with the exchangeable cations and the less favorable sites correspond to adsorption elsewhere on the framework or simply within the micropores. For example, it has been shown that the analysis of equilibrium isotherms for CO_2 on various different forms of zeolite A yields site densities that are consistent with structural information [4].

2.5 Unilan

Integration of the simple Langmuir expression assuming a uniform distribution of site energies yields the three-parameter Unilan expression [5]:

$$\frac{q}{q_s} = \frac{1}{2s} \ln \left[\frac{1 + \kappa p \, e^{s}}{1 + \kappa p \, e^{-s}} \right] . \tag{7}$$

This expression reduces to Henry's law at low loadings with the dimensionless Henry constant given by:

$$K = \kappa \sinh s/s . \tag{8}$$

2.6 Toth

Another three-parameter expression which has been widely used to represent equilibrium data for activated carbon adsorbents is the Toth model [6]:

$$\frac{q}{q_s} = \frac{p}{\left(b + p^t\right)^{1/t}} \tag{9}$$

for which the dimensionless Henry constant is given by:

$$K = \frac{q_s RT}{b^{1/t}} . \tag{10}$$

2.7 Simplified Statistical Model

The simplified statistical model (SSTM) is based on the assumption that the sorbate–sorbent interaction is characterized by the Henry constant, and the saturation limit is determined by the quotient of the specific micropore volume and the molecular volume of the sorbate [7]. Sorbate–sorbate interactions are characterized by reduction in the accessible pore volume. For zeolites such as those of type A, in which the pore system consists of discrete cages interconnected by windows, most of the occluded molecules are held within the cages and the saturation limit corresponds to the maximum number of sorbate molecules that can fit within a cage. This is given approximately by the ratio of the free volume of the cage (v) to the effective volume of the sorbate molecule (β). For a mobile adsorbed phase the configuration integral (and hence the Henry constant) is directly proportional to the accessible pore volume so it is assumed that, in a multiply occupied cage, the configuration integral should be reduced by the factor $A_s = [(1 - s\beta/v)/(1 - \beta/v)]$, where s is the number of molecules of effective volume β in a cage of free volume v. This leads to an isotherm expression of the form [8]:

$$\overline{q} = \frac{K^1 p + A_2 \left(K^1 p\right)^2 + \ldots + A_s \left(K^1 p\right)^s / (s-1)!}{1 + K^1 p + \ldots + A_s \left(K^1 p\right)^s / s!}, \qquad (11)$$

(molecules/cage)

where the maximum value of s is given by $q_s = s_{max}$ (integer) $\leq v/\beta$. For $s_{max} = 1$, Eq. 11 reduces to the simple Langmuir form with $q_s = 1$ molecule/cage, while for large values of s_{max} it approaches the Volmer form (Eq. 17). This is physically reasonable since the Volmer model assumes free molecular mobility within the available micropore volume. The variation in the shape of the isotherm with s_{max} is shown in Fig. 1. This model has been shown to provide a good representation of the experimental isotherms for light alkanes in 5A [9] and for benzene in 13X zeolite (see Fig. 2) [8].

Since the assumptions from which Eq. 11 is derived are obviously only rough approximations, which may be expected to become increasingly inaccurate at high loadings, an alternative approach has been suggested for correlation of the isotherm data for strongly adsorbed species. The parameters A_s characterizing the reduction in the configuration integral for multiply occupied cages are retained as empirical constants in the isotherm equation. Thus for $s_{max} = 3$ the isotherm becomes:

$$q = \frac{K^1 p + A_2 \left(K^1 p\right)^2 + A_3 \left(K^1 p\right)^3 / 2!}{1 + K^1 p + A_2 \left(K^1 p\right)^2 / 2 + A_3 \left(K^1 p\right)^3 / 3!}, \qquad (12)$$

which is a three-parameter model (K^1, A_2, A_3).

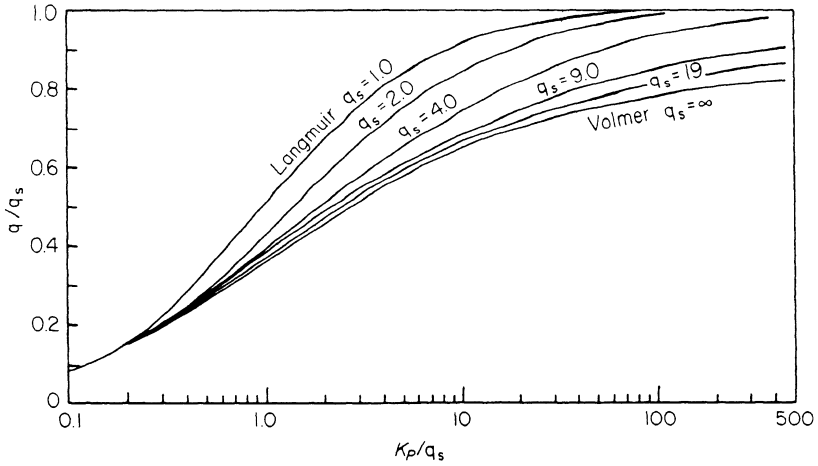

Fig. 1 Theoretical isotherms calculated according to Eq. 11 showing the transition from Langmuir to Volmer form with increasing s_{max}. From Ruthven [8]

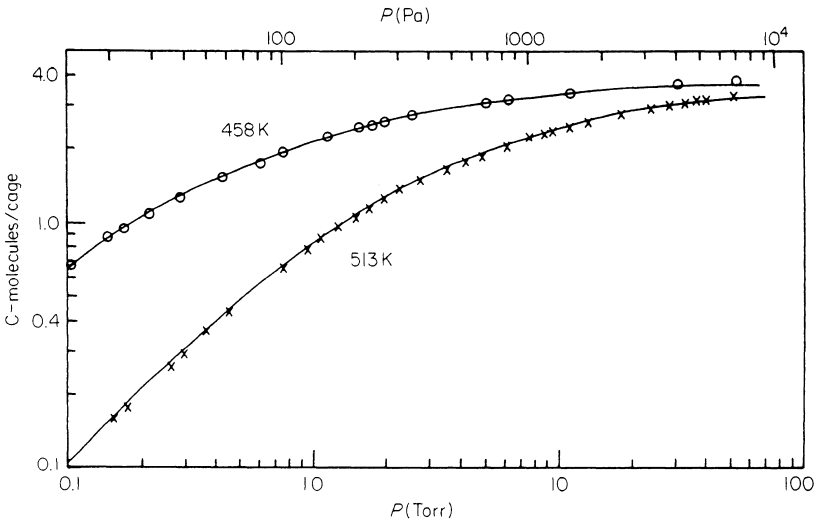

Fig. 2 Experimental equilibrium isotherm for benzene in 13X zeolite at 458 and 513 K showing conformity with the SSTM isotherm (Eq. 11) with $m \leq \nu/\beta = 5.0$ and $K^1 = 8.8$ molecules/cage Torr at 458 K and 1.25 molecules/cage Torr at 513 K. From Ruthven [8]

Integration of Eq. 12 in accordance with the Gibbs isotherm (Eq. 15) yields:

$$\int_0^{p^0} q\frac{\mathrm{d}p}{p} = \frac{\pi}{RT} = \ln\zeta = \ln\left[1 + K^1 p^0 + \frac{A_2(K^1 p^0)^2}{2} + \frac{A_3(K^1 p^0)^3}{3!}\right]. \qquad (13)$$

It follows that

$$\frac{\zeta - 1 - K^1 p^0}{(K^1 p^0)^2} = \frac{A_2}{2} + \frac{A_3 K^1 p^0}{6}. \tag{14}$$

A plot of this function against $K^1 p^0$ thus provides a convenient test for the model and a simple way to extract the parameters A_2 and A_3. Examples of

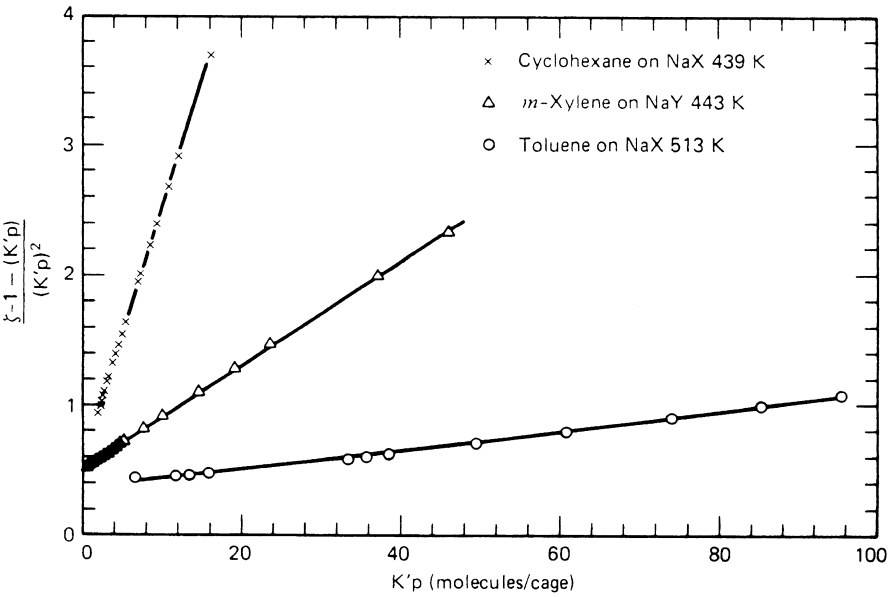

Fig. 3 Experimental equilibrium isotherm for hydrocarbons on NaX and NaY showing conformity with Eqs. 12–14. From Ruthven and Goddard [10]

Table 2 Correlation of equilibrium isotherms for hydrocarbons on zeolite NaX and NaY according to Eq. 14

Sorbent	Sorbate	T (K)	$K\left(\frac{\text{Molecules}}{\text{cage Torr}}\right)$	A_2	A_3
NaX	Cyclohexane	439	0.38	0.99	1.45
NaX	Toluene	513	4.95	0.81	0.001
NaY	*o*-Xylene	477	8.7	1.04	1.01
NaY	*m*-Xylene	477	5.9	0.98	2.3
NaY	*p*-Xylene	477	5.7	1.16	4.8
NaY	Ethylbenzene	477	15.9	0.97	0.007

Affinity sequence (C_8 aromatics—NaY)
Low concentration (K): EB > OX > MX ~ PX
High concentration (KA $(1/3)^3$): PX > OX > MX > EB

such plots showing excellent linearity with a common intercept corresponding to $A_2 \approx 1.0$ are shown in Fig. 3.

The results of an experimental study of the sorption of several aromatic and cyclic hydrocarbons in X and Y zeolites, for which $s_{max} \cong 3$, are summarized in Table 2 [10]. Equation 12 was found to provide an excellent fit of all the isotherms, as may be seen from Fig. 3. Values of the parameter A_2 were in all cases very close to unity but the parameter A_3 varied widely. This suggests that, for these systems, when a cage contains only two molecules sorbate–sorbate interactions are minor, but for three molecules per cage such effects become important and may be either repulsive ($A_3 < 1.0$) or attractive ($A_3 > 1.0$). This provides a simple explanation for the strong variation in selectivity which is often observed at higher loadings in binary and multicomponent systems [11].

2.8 Spreading Pressure and the Gibbs Adsorption Isotherm

The isotherm equations discussed so far are based on simplified mechanistic models for the adsorbed phase. In an alternative approach, pioneered by Willard Gibbs [12], the adsorbed phase is regarded simply as a fluid held within the force field of the adsorbent and characterized by an equation of state. The Gibbs adsorption isotherm, which is derived in a manner similar to the derivation of the Gibbs–Duhem equation, may be written:

$$\frac{\pi}{p} = \left(\frac{\partial \pi}{\partial p}\right)_T , \tag{15}$$

where π is the "spreading pressure". Integration of this expression with the appropriate equation of state for the adsorbed phase [$\pi = f(q, T)$] yields the expression for the equilibrium isotherm. For example, if the adsorbed phase obeys the analog of the ideal gas law ($\pi A = RT$, where $A \propto 1/q$), the isotherm corresponds to Henry's law ($q = Kc$). If the equation of state for the adsorbed phase has the form:

$$\pi(A - \beta) = RT , \tag{16}$$

where A ($\propto 1/q$) is the surface area per molecule and β is the actual area occupied by a molecule, then for $\beta \ll A$ (low loading) the isotherm assumes the Langmuir form (Eq. 5), whereas at higher loadings it will approach the Volmer form [13]:

$$bp = \frac{\theta}{1-\theta} \exp\left(\frac{\theta}{1-\theta}\right) , \tag{17}$$

where $\theta = \beta/A$. If the equation of state for the adsorbed phase is a virial form:

$$\frac{\pi}{RT} = q + A_1 q^2 + A_2 q^3 + \ldots \tag{18}$$

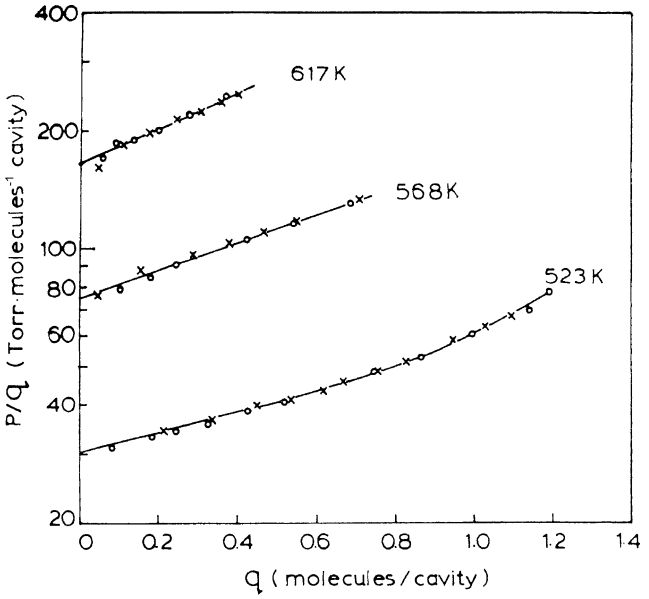

Fig. 4 Plot of $\log(p/q)$ vs q for pentane in 5A zeolite showing conformity with the virial isotherm and the linear extrapolation to determine the Henry constant. From Vavlitis et al. [14]

the corresponding expression for the isotherm becomes:

$$\frac{Kc}{q} = \exp\left(2A_1 q + \frac{3}{2}A_2 q^2 + \ldots\right) . \tag{19}$$

This form is particularly useful as it provides the basis for a convenient way to extract the Henry constant from data at higher loadings (beyond the Henry region). A plot of $\ln(p/q)$ vs q should yield a linear asymptote with slope $2A_1$ and intercept $-\ln K$ (see Fig. 4) [14].

2.9 Dubinin–Polanyi Theory

A third general approach to the correlation of adsorption equilibria for microporous adsorbents was developed by Dubinin [15, 16] from ideas originally suggested by Polanyi [17] and Berenyi [18, 19]. The adsorbed phase within the micropores is assumed to behave as a liquid but, as a result of the force field of the adsorbent, the properties differ from those of the bulk liquid sorbate. The difference in free energy between the adsorbed fluid and the saturated liquid sorbate at the same temperature is referred to as the adsorption potential (ε) which, assuming an ideal vapor phase, may be calculated from

the equilibrium vapor pressure (p) and the saturation vapor pressure (p_s):

$$\varepsilon = -RT \ln(p/p_s) . \tag{20}$$

For a given adsorbent–adsorbate system the relationship between ε and the fractional occupation of the micropore volume is defined by the "characteristic curve", which is assumed to be independent of temperature (see Fig. 5). Such an assumption should be valid for systems dominated by dispersion–repulsion forces (which are temperature independent), but cannot be expected to hold when electrostatic forces (which are temperature dependent) are important. The characteristic curve generally has a Gaussian form leading to an isotherm of the form:

$$\ln(q/q_s) = -\kappa[\ln(p/p_s)]^2 . \tag{21}$$

This expression, known as the Dubinin–Raduschkevich equation [20], has been widely used to correlate the equilibrium data for hydrocarbons and other organics on activated carbon adsorbents.

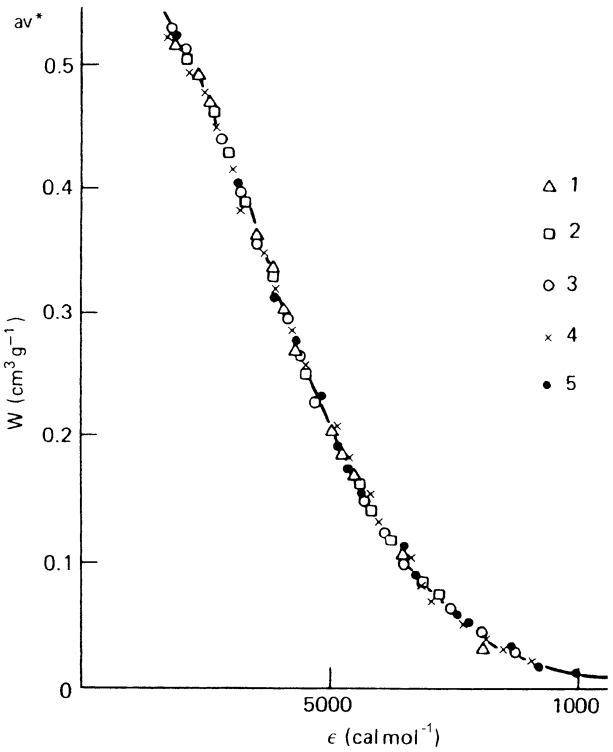

Fig. 5 Characteristic curve for benzene on activated carbon at five different temperatures (1 = 20 °C, 2 = 50 °C, 3 = 80 °C, 4 = 110 °C, 5 = 140 °C) showing conformity with the Dubinin–Polanyi theory. From Kiselev [21] with permission

This approach has the advantage that the characteristic curve, which can be determined from a single isotherm (provided that it spans the entire range of loadings), provides a concise correlation of the equilibrium data at all temperatures. However, it has two serious disadvantages. To convert the fractional loading (q/q_s) to the absolute loading requires knowledge of q_s ($= W_0/V_m$). The specific micropore volume (W_0) can be found from the extrapolation of the characteristic curve to zero adsorption potential, but the molecular volume of the adsorbed fluid (V_m) is not known. It has been suggested that V_m may be estimated by linear interpolation or extrapolation between the molecular volume of the saturated liquid sorbate at its normal boiling point and the van der Waals covolume (b) at the critical temperature, but such methods obviously provide only a rough approximation. A further difficulty concerns the asymptotic behavior of Eq. 21, which does not reduce to Henry's law in the low-pressure limit. In summary, although the Dubinin–Raduschkevich equation provides a useful semi-empirical correlation of equilibrium data it is of only limited value for fundamental studies.

2.10 Adsorption of Mixtures

A major advantage of the Langmuir model is that it allows a straightforward extension to binary and multicomponent systems:

$$\frac{q_A}{q_s} = \frac{b_A p_A}{1 + b_A p_A + b_B p_B}; \qquad \frac{q_B}{q_s} = \frac{b_B p_B}{1 + b_A p_A + b_B p_B}. \tag{22}$$

Thermodynamic consistency requires that the saturation limit (q_s) must be the same for all components [22, 23], so the model is clearly inappropriate for mixtures of molecules of very different sizes, even if the pure component isotherms conform to the Langmuir expression.

It follows from Eq. 22 that the separation factor (α) should correspond to the ratio of the Henry constants and should be independent of loading:

$$\alpha_{AB} \equiv \frac{q_A/p_A}{q_B/p_B} = \frac{K_A}{K_B}. \tag{23}$$

This justifies the use of Henry constants for preliminary screening of selective adsorbents, but in practice a significant loading dependence of the separation factor is generally observed as a result of deviations from the binary (or multicomponent) Langmuir model.

The SSTM also yields a direct extension to binary and multicomponent systems [24] allowing multicomponent equilibria to be predicted directly from the Henry constants and saturation capacities for the pure components. This approach has been shown to work well for some systems such as propane–cyclopropane in 5A zeolite. For CH_4–CO_2 in 5A and 13X zeolites it provides a good prediction of the binary isotherm at elevated pres-

sures [25]. The observed increase in separation factor with loading for *p*-xylene/*m*-xylene and *p*-xylene/*o*-xylene in zeolite Y is also correctly predicted by a simple extension of the generalized statistical model, but this approach is not universally applicable.

2.11 Ideal Adsorbed Solution Theory

Perhaps the most useful general approach is still the ideal adsorbed solution theory (IAST) developed many years ago by Myers and Prausnitz [26]. The spreading pressure for the pure components may be calculated as a function of equilibrium pressure (p_i) by integration of the Gibbs isotherm:

$$\psi_i\left(p^0\right) = \frac{\pi}{RT} = \int_{p=0}^{p^0} \frac{q_i \mathrm{d}p_i}{p_i} . \tag{24}$$

Note that for an ideal Langmuir isotherm this yields:

$$\psi_i = q_s \ln\left(1 + b_i^1 p_i\right) \tag{25}$$

and for the SSTM isotherm:

$$\psi_i = \ln\left[1 + K^1 p + \ldots + A_s (K^1 p)^s / s!\right] . \tag{26}$$

For a binary system which is ideal in the sense required by IAST (no interactions in the binary other than those present in the conjugate single-component systems) the equilibrium partial pressures are given by:

$$p_A = p_A^0(\pi) X_A = Y_A\, P ; \qquad p_B = p_B^0(\pi)(1 - X_A) = (1 - Y_A) P . \tag{27}$$

Mixing is assumed to occur at constant spreading pressure so p_A^0 and p_B^0 are the values for the single-component systems at the relevant value of π, calculated from Eq. 24. The procedure for calculating the equilibrium partial pressures and the composition of the adsorbed phase in the binary is as follows:

1. Choose a value of π
2. Calculate p_A^0 and p_B^0 according to Eq. 24
3. Substitute p_A^0 and p_B^0 in Eq. 24

Since p is fixed this yields a pair of equations from which X_A and Y_A can be found directly. The total loading is then found from:

$$\frac{1}{q_A + q_B} = \frac{X_A}{q_A^0} + \frac{(1 - X_A)}{q_B^0} , \tag{28}$$

where q_A^0, q_B^0 are the loadings for the pure components at the same spreading pressure (π).

In contrast to the binary Langmuir or SSTM models, the ideal adsorbed solution theory does not lead to a simple explicit relation for the adsorbed-phase composition and loading in terms of the partial pressures. Calculation of the equilibrium for a particular gas-phase composition therefore requires a trial and error procedure.

2.12 Heats or Energies of Adsorption

The temperature dependence of the equilibrium vapor pressure is governed by the Clausius–Clapeyron equation:

$$\left(\frac{\partial \ln p}{\partial T}\right)_q = \frac{\Delta H}{RT^2}. \tag{29}$$

Integration, on the assumption that the heat of adsorption is independent of temperature, yields:

$$\ln p = -\frac{\Delta H}{RT} + \text{constant} \tag{30}$$

showing that, subject to this approximation, the isostere should be linear when plotted as $\ln p$ vs $1/T$ (see Fig. 6). This provides a convenient way of measuring the heat of adsorption as well as a straightforward way to extrapolate and interpolate between equilibrium isotherms. At low loadings the heat

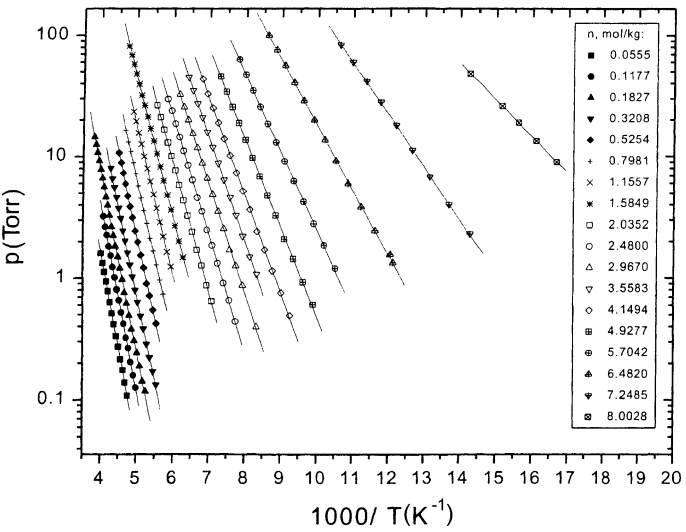

Fig. 6 Experimental isosteres for the system N_2–CaA zeolite showing linearity over a wide temperature range. The variation in slope corresponds to the variation in heat of adsorption with loading. From Shen et al. [27] with permission

of adsorption derived from the slope of the isosteres should correspond with the value derived from the temperature dependence of the Henry constant (Eq. 2). For a Langmuirian system the heat of adsorption should be independent of loading, but for most real systems a significant loading dependence is observed.

Several different effects are important. Small molecules generally show a monotonic decrease in heat of adsorption with loading (see Fig. 7a). For nonpolar species such as methane this is probably due to energetic heterogeneity arising from the presence of structural defects. On polar adsorbents the magnitude of the decline is greater for quadrupolar and polar sorbates,

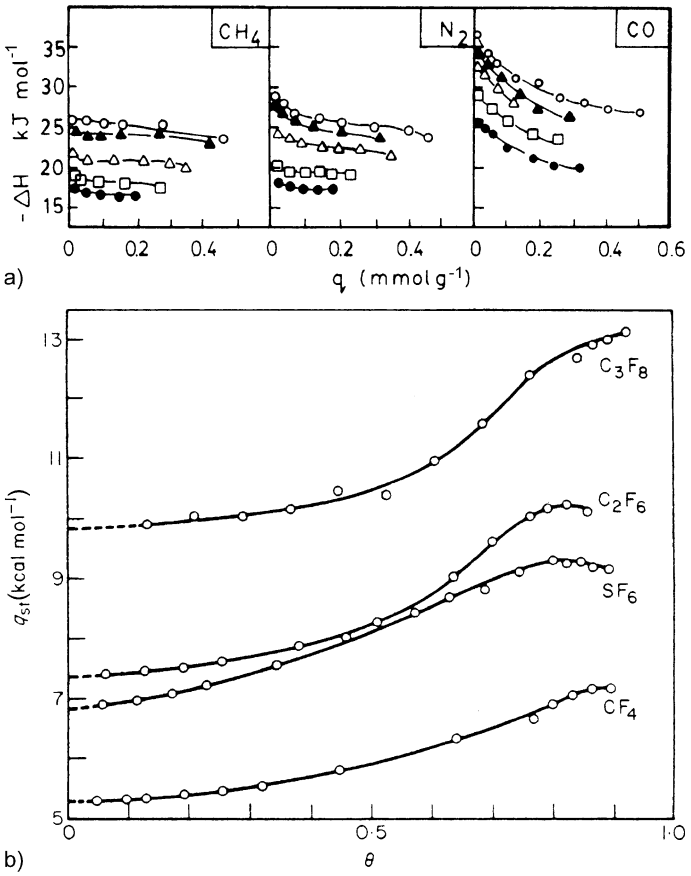

Fig. 7 **a** Variation of heat of adsorption with loading for CH_4, N_2, and CO on NaCaA zeolites (•, NaA; □, 30% Ca exchange; △, 46% Ca exchange; ▲, 85% Ca exchange; and ○, CaA). From Masuda et al. [28] with permission. **b** Variation of heat of adsorption with loading for nonpolar molecules on NaX zeolite. From Barrer and Reucroft [29] with permission

since the effect of structural defects is then supplemented by preferential filling of the sites associated with the strongest electrical field or field gradient. For larger nonpolar molecules the effect of defect sites becomes less pronounced as a result of spatial averaging of energies over a larger region, and a modest increase in heat of adsorption with loading is then observed (see Fig. 7b). This has often been attributed to sorbate–sorbate interaction but it may be noted that such an effect is predicted by the simplified statistical model as a consequence of the increase in molecular volume with temperature. In some cases the effects of energetic heterogeneity and sorbate–sorbate interactions compensate, leading to an essentially constant heat of adsorption and fortuitous conformity with the ideal Langmuir model (see Fig. 8) [30, 31].

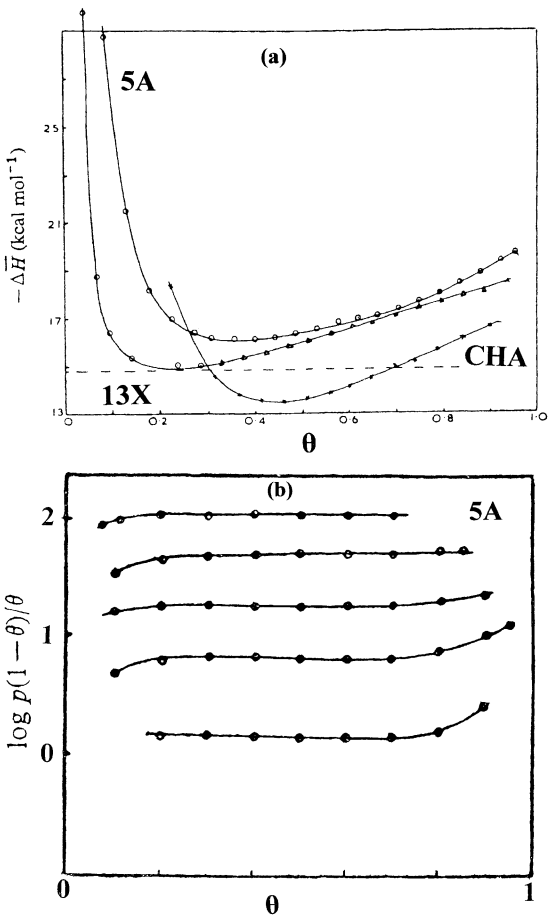

Fig. 8 **a** Variation of heat of adsorption with fractional loading for I_2 on 5A, 13X, and CHA zeolites. **b** Equilibrium isotherms for I_2–5A at 573, 538, 503, 468, and 393 K (*top down*) showing conformity with Eq. 5. From Barrer and Wasilewski [30, 31] with permission

2.13
Measurement of Adsorption Equilibrium

Single-component equilibrium isotherms are commonly measured by gravimetric or piezometric methods (see Fig. 9). An alternative technique based

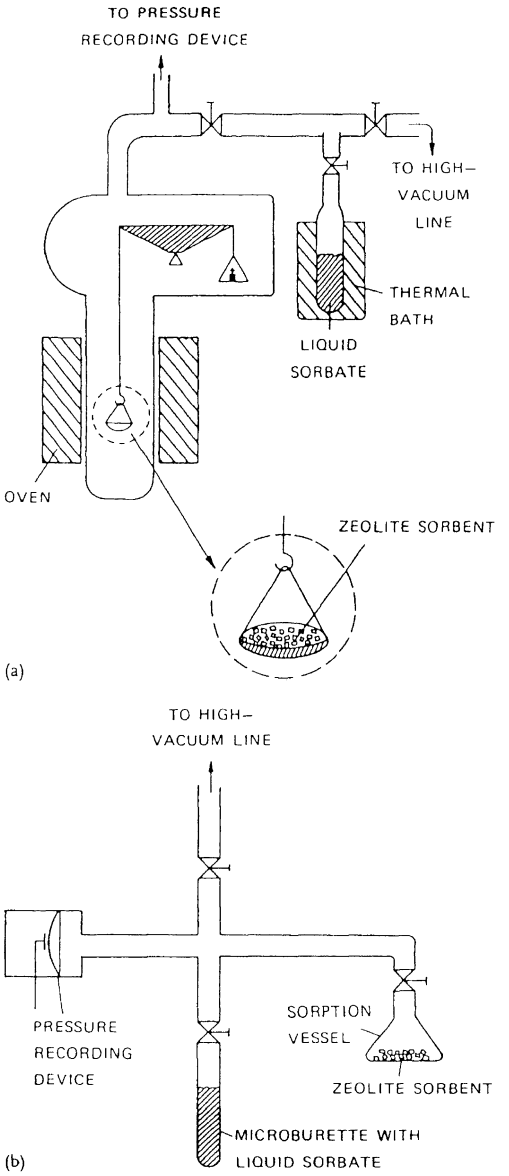

Fig. 9 Experimental system for **a** gravimetric and **b** piezometric methods

on linearity of the isosteres has also been widely used [32]. If the gas space within a piezometric system is kept small and the quantity of adsorbent is relatively large, then virtually all the sorbate molecules will be held within the adsorbed phase regardless of the equilibrium sorbate pressure. Measurement of the pressure as a function of temperature for a series of different sorbate loadings thus yields a family of isosteres from which the isotherms can be constructed. If only the Henry's law constant is required the chromatographic method [33, 34] provides a useful alternative since it is generally faster.

A variant of the zero-length column (ZLC) method has also been developed to permit rapid measurement of both Henry constants and complete isotherms [4]. This method works well provided the curvature of the isotherm is moderate but it breaks down for highly favorable (rectangular) isotherms.

Measurement of binary isotherms by traditional methods is tedious and time-consuming. For systems in which the two components are adsorbed with comparable strength the ZLC approach has been shown to provide a relatively rapid and straightforward measurement of the separation factor, but determination of the complete isotherm by this method is still somewhat labor intensive.

3 Sorption Kinetics

The intrinsic rate of physical adsorption is very rapid so the overall sorption rate is generally controlled by the diffusional resistances associated with mass transfer to the adsorption site. Commercial zeolite-based catalysts and adsorbents consist of small (micron-sized) zeolite crystals formed into macroporous (millimeter-sized) particles, generally with the aid of a clay binder. Such materials offer at least three and in some cases four distinct mass transfer resistances (see Fig. 10) [35]:

1. External fluid film diffusion
2. Diffusion through the macropores of the formed particles
3. Diffusion through the intracrystalline micropores

As a result of the imbalance of the interatomic forces, the micropores are often constricted at the crystal surface, leading to an additional transport resistance associated with penetration of this surface barrier.

Macropore and film diffusion are relatively well understood and are therefore not discussed in any detail in this volume. In contrast, despite intensive study over the last 30 years, our understanding of micropore diffusion is still far from complete. At the micropore scale diffusive transport is largely controlled by steric interactions which are dominated by repulsive forces. The relative diameter of the micropore and the diffusing molecule is clearly a critical variable. For small spherical or spheroidal molecules there is a clear

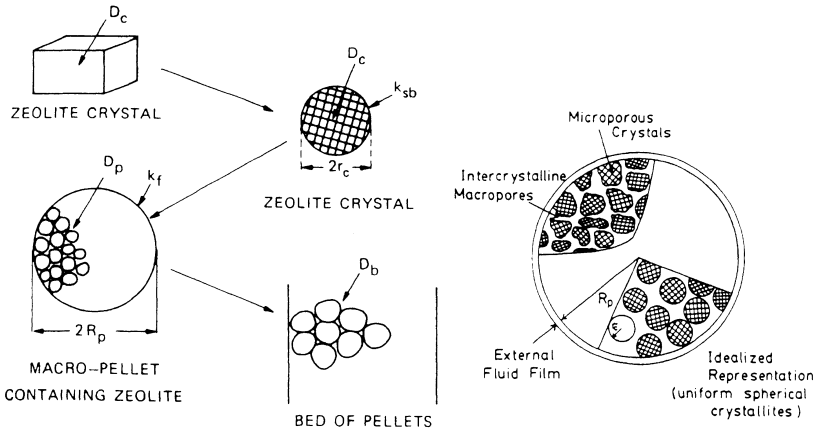

Fig. 10 Schematic representation showing the formation of a composite zeolite adsorbent and the various resistances to mass transfer. From Ruthven and Post [35]

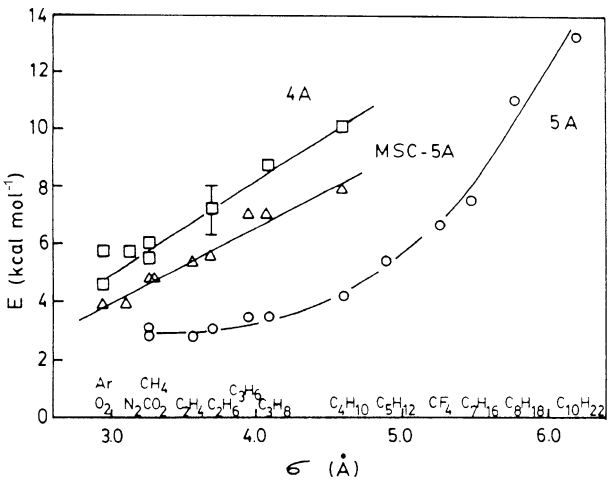

Fig. 11 Variation of diffusional activation energy with van der Waals diameter for diffusion in 4A and 5A zeolites and molecular sieve carbon [36]

correlation between the diffusional activation energy and the kinetic diameter of the sorbate, as shown in Fig. 11 [36]. However, for larger molecules which can adjust their conformation such correlations are less clear.

3.1 Self-Diffusion and Diffusive Transport

Diffusion depends on the random (Brownian) motion of molecules. Because the motion is random, in a nonuniform mixture of different molecular species

there will be a net flux down the concentration gradient. The diffusion coefficient or (transport) diffusivity is defined in accordance with Fick's first equation (or law):

$$J = - D\frac{\partial q}{\partial z} . \tag{31}$$

The diffusivity (D) defined in this way is not necessarily independent of concentration. It should be noted that for diffusion in a binary fluid phase the flux (J) is defined relative to the plane of no net volumetric flow and the coefficient D is called the mutual diffusivity. The same expression can be used to characterize migration within a porous (or microporous) solid, but in that case the flux is defined relative to the fixed frame of reference provided by the pore walls. The diffusivity is then more correctly termed the transport diffusivity. Note that the existence of a gradient of concentration (or chemical potential) is implicit in this definition.

In the case of self-diffusion the physical situation is different since there is now no gradient of species concentration. We may define the tracer diffusivity ($\mathcal{D}$) characterizing the migration of marked molecules in a fluid of uniform total concentration in a manner similar to Eq. 31:

$$J^* = - \mathcal{D}\frac{\partial q^*}{\partial z}\Big|_q . \tag{32}$$

The distinction between these two definitions is illustrated in Fig. 12.

One may also define a self-diffusivity by reference to the Einstein equation:

$$\mathcal{D} = \frac{1}{2}\frac{\langle z^2\rangle}{t} \text{ (one dimension) or } \mathcal{D} = \frac{1}{6}\frac{\langle r^2\rangle}{t} \text{ (three dimensions)} . \tag{33}$$

By considering the solution of the transient diffusion equation for a point source, it may be shown that the definitions of Eqs. 32 and 33 are equivalent [37].

The Fickian definition (Eq. 31) suggests that the driving force for molecular transport is the gradient of concentration. However, thermodynamic consistency considerations suggest that the true driving force must be the gradient of chemical potential:

$$J = - Bq\frac{\partial \mu}{\partial z} . \tag{34}$$

Assuming an ideal vapor phase the chemical potential is given by:

$$\mu = \mu^0 + RT \ln p . \tag{35}$$

Combining these equations and comparing with Eq. 31 yields, for the Fickian diffusivity:

$$D = BRT\frac{\mathrm{d}\ln p}{\mathrm{d}\ln q} = D_0\frac{\mathrm{d}\ln p}{\mathrm{d}\ln q} \tag{36}$$

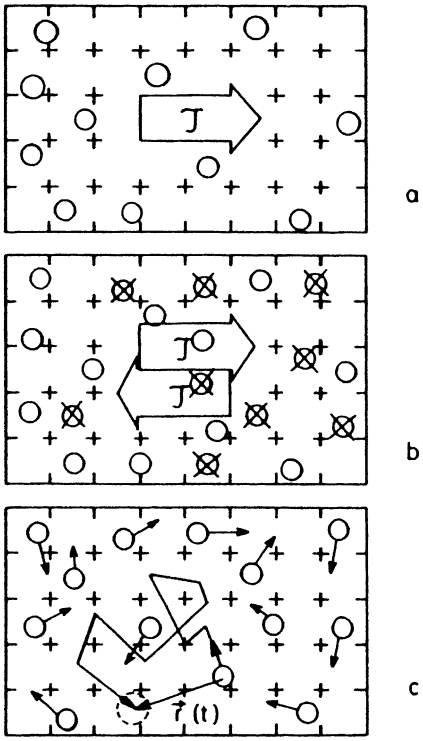

Fig. 12 Schematic diagram showing **a** self-diffusion, **b** tracer diffusion, and **c** self-diffusion (Brownian motion). From Kärger and Ruthven [37]

where $\mathrm{d}\ln p/\mathrm{d}\ln q$ represents the slope of the equilibrium isotherm plotted in logarithmic coordinates. The parameter D_0 is commonly referred to as the "limiting" or "corrected" diffusivity. This expression is often called the Darken equation since it was used by Darken in 1946 to interpret experimental data for the interdiffusion of two metals [38]. However, it was first suggested much earlier in the works of Maxwell [39] and Stefan [40].

Within the Henry's law region $\mathrm{d}\ln p/\mathrm{d}\ln q = 1.0$ and $D = D_0$. Thus one can expect that at sufficiently low loadings transport diffusion can be accurately represented by the simple Fickian model with a constant diffusivity, but at higher loadings the diffusivity may be expected to be concentration dependent. For a system obeying the Langmuir isotherm (Eq. 5), Eq. 36 implies:

$$D = \frac{D_0}{1-\theta} \tag{37}$$

suggesting that the Fickian diffusivity will increase rapidly as the saturation limit is approached, since in this region $\mathrm{d}\ln p/\mathrm{d}\ln q \to \infty$.

There is no fundamental reason why the corrected diffusivity should be independent of concentration, but experimental evidence shows that for many systems this is approximately true [41–43] (see, for example, Fig. 13). From molecular simulations of intracrystalline diffusion Krishna has identified two limiting cases depending on the degree to which the sorbate molecules are confined: strong confinement [$D_0 \propto (1 - \theta)$] and weak confinement [$D_0 \approx$ constant] [44].

A completely different situation arises in one-dimensional channels when the molecules are too large to pass each other. The transport can no longer be characterized by a Fickian model. Such behavior is discussed in this volume in the chapter Single-File Diffusion in Zeolites by Jörg Kärger.

The relationship between the corrected transport diffusivity and the self-diffusivity is more complex. Darken assumed that these quantities should be

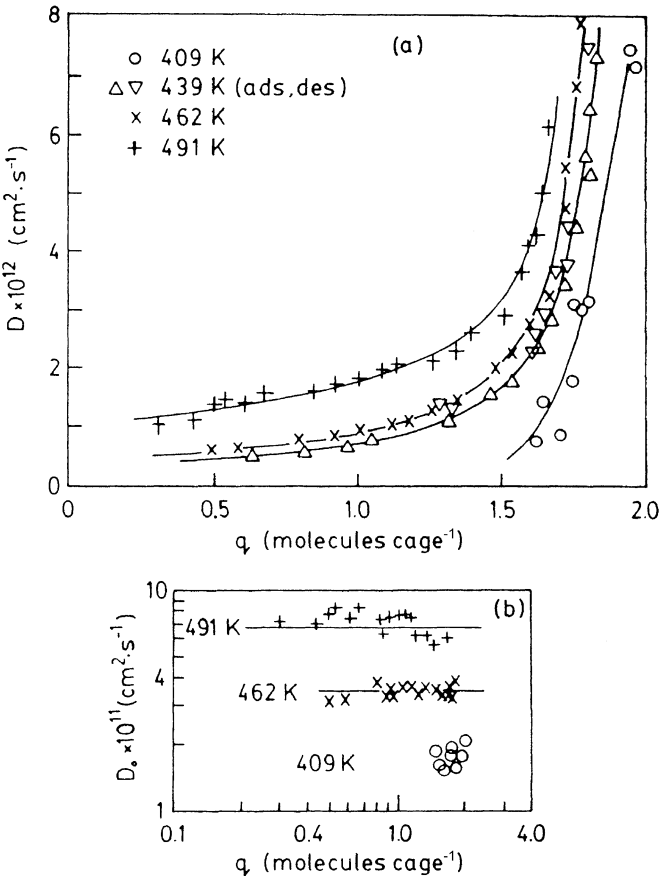

Fig. 13 Variation of **a** diffusivity and **b** corrected diffusivity with loading for *n*-heptane in 5A zeolite crystals. From Doetsch et al. [41]

the same. This should be true at low loadings (within the Henry's law region) since the basic mechanisms of self-diffusion and diffusive transport are the same and, at sufficiently low concentrations, there is no interference between diffusing molecules. However, at higher loadings this simple equivalence no longer holds.

3.2 The Maxwell–Stefan Model

To establish the relationship between self- and transport diffusion it is necessary first to consider diffusion in a binary adsorbed phase within a micropore. This can be conveniently modeled using the generalized Maxwell–Stefan approach [45, 46], in which the driving force is assumed to be the gradient of chemical potential with transport resistance arising from the combined effects of molecular friction with the pore walls and collisions between the diffusing molecules. Starting from the basic form of the Maxwell–Stefan equation:

$$\sum_{\substack{j=1 \\ i\neq j}}^{n} \frac{X_j N_i - X_i N_j}{c_0 Đ_{ij}} = -X_i \frac{\nabla \mu_i}{RT} . \tag{38}$$

To describe the diffusion of two species (A and B) in a microporous zeolite we write this equation in the form:

$$\frac{\theta_B N_A - \theta_A N_B}{Đ_{AB}} + \frac{(1-\theta_A-\theta_B)N_A}{Đ_{Az}} = -q_A \frac{\nabla \mu_A}{RT} , \tag{39}$$

where $\theta_i = q_i/q_s$. To maintain consistency with Eq. 36 we incorporate the fraction of unoccupied micropore space $(1-\theta_A-\theta_B)$ into the definition of D_{0A}:

$$\frac{\theta_B N_A - \theta_A N_B}{Đ_{AB}} + \frac{N_A}{D_{0A}} = -q_A \frac{\nabla \mu_A}{RT} . \tag{40}$$

This expression contains two different diffusion coefficients: D_{0A} which characterizes the frictional resistance with the pore walls and $Đ_{AB}$ which characterizes the interaction between the two differing species (the mutual diffusivity). For self-diffusion $N_B = -N_A$ and $\theta = \theta_A + \theta_B$ (the total fractional loading), so that for diffusion in the z direction:

$$N_A \left(\frac{\theta}{D_{AB}} + \frac{1}{D_{0A}} \right) = -\frac{q_A}{RT} \frac{\partial \mu_A}{\partial z} = -\frac{\partial q_A}{\partial z} . \tag{41}$$

Comparison with Eq. 32 shows that the self-diffusivity is given by:

$$\frac{1}{Đ_A} = \frac{1}{D_{0A}} + \frac{\theta}{Đ_{AA}} . \tag{42}$$

This result, first obtained by Krishna and Paschek [47], suggests that at low loadings the self-diffusivity should approach the corrected diffusivity, while at higher loadings the self-diffusivity should be smaller than the corrected diffusivity. However, if the mutual diffusivity $Đ_{AA}$ is large then the self-diffusivity and transport diffusivity will be almost equal even at high loadings. Such behavior has been observed for diffusion of benzene in silicalite [48]. Equation 42 may also be written in the form:

$$\frac{\mathcal{D}_A}{D_{0A}} = \frac{1}{1 + \theta D_{0A}/Đ_{AA}} \approx 1 - \theta \frac{D_{0A}}{Đ_{AA}} . \tag{43}$$

Expressions of similar general form are obtained from irreversible thermodynamics as well as from a simple kinetic model [49].

The generalized Maxwell–Stefan equation provides a rational basis for the analysis of sorption rate measurements and membrane permeation in multicomponent systems. For a binary Langmuir system:

$$\frac{N_A}{q_s} = \frac{-D_{0A}}{1 - \theta_A - \theta_B} \frac{[(1 - \theta_B) + \theta_A D_{0B}/Đ_{AB}]\,\nabla\theta_A + \theta_A\,[1 + D_{0B}/Đ_{AB}]\,\nabla\theta_B}{1 + \theta_B D_{0A}/Đ_{AB} + \theta_A D_{0B}/Đ_{AB}} \tag{44}$$

with a similar expression for N_B. If there is no interference between diffusing species ($Đ_{AB} \to \infty$) this reduces to the simpler expression:

$$\frac{N_A}{q_s} = \frac{-D_{0A}}{1 - \theta_A - \theta_B} [(1 - \theta_B)\nabla\theta_A + \theta_A \nabla\theta_B] \tag{45}$$

as originally derived by Habgood [50, 51].

The corrected diffusivities (D_{0A}, D_{0B}) can be obtained from single-component measurements but the mutual diffusivity is not amenable to direct measurement. Krishna has suggested that it may be estimated from the Vignes correlation [52], which was originally suggested for diffusion in liquid systems:

$$Đ_{AB} = D_{0A}^{\frac{\theta_A}{\theta_A+\theta_B}} D_{0B}^{\frac{\theta_B}{\theta_A+\theta_B}} . \tag{46}$$

Representative comparisons between experimental permeance and selectivity data for methane/ethane mixtures permeating through a silicalite membrane and the predictions derived from the generalized Maxwell–Stefan model (Eq. 44) are shown in Fig. 14 [53]. Also shown are the predictions derived from the corresponding Habgood model, in which mutual diffusion is ignored. For the slower diffusing species the predictions from both models are almost identical and fit the experimental data well. However, for the faster diffusing species (CH_4) the flux predicted from the Habgood model is much too high. The full model provides an excellent fit of the data for both components, and provides a logical explanation for the observed selectivity being substantially larger than that predicted from the simpler Habgood model.

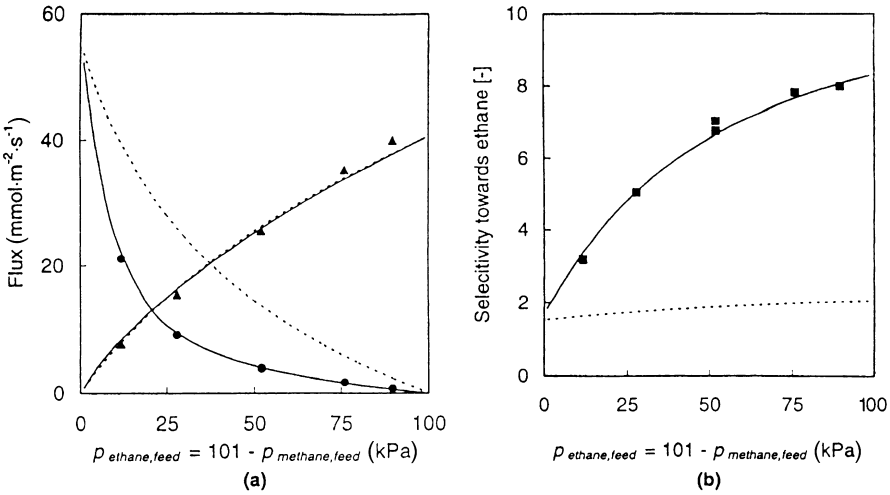

Fig. 14 Separation of C_2H_6/CH_4 mixtures by permeation through a silicalite membrane. **a** Flux; **b** selectivity. *Continuous lines* show the predictions of the Maxwell–Stefan model (Eq. 44) based on single-component diffusivities (D_{0A}, D_{0B}) with $Đ_{AB}$ from the Vignes correlation (Eq. 46). *Dotted lines* show predictions from the simplified Habgood model in which mutual diffusion effects are ignored (Eq. 45). From van de Graaf et al. [53] with permission

A detailed analysis of the influence of mutual diffusion in such systems has been carried out by Karimi and Farooq [54]. They show that the effect is generally small at low loadings but becomes important at high loadings, especially when the difference in the mobilities of the diffusing species is large.

3.3 Measurement of Micropore Diffusion

A wide range of different experimental techniques have been applied to the measurement of micropore diffusion. A chronological summary is given in Table 3. It is convenient to distinguish between equilibrium techniques in which the self-diffusivity is measured and nonequilibrium techniques which measure transport diffusion. True equilibrium measurements are made on a scale smaller than the dimensions of an individual crystal by following the mean square displacement of the molecules in a known time interval by either nuclear magnetic resonance (PFG NMR) or by neutron scattering (QENS). Most of the other methods for measuring transport diffusion are "macroscopic" in that they depend on measuring the flux under a well-defined gradient of concentration. Two exceptions are the neutron spin-echo technique developed by Jobic [96] and effectiveness factor measurements which depend on measuring the rate of a catalytic reaction under diffusion-controlled conditions. Representative references are included in Table 3. Single crystal

Table 3 Measurements of diffusion in zeolite crystals: historical development

Method	Author
Direct monitoring of transient conc. profile (H_2O–heulandite)	Tiselius (1943) [55, 56]
Transient sorption rate	
– Volumetric/gravimetric	Barrer (1940) [57, 58]
– Piezometric	Bülow (1970) [59, 60]; Do [61, 62]
NMR relaxation	Resing (1967) [63, 64]
PFG NMR	Pfeifer, Kärger, Lechert (1970s) [65–68]
Chromatography (gas)	Haynes, Ma, Ruthven (mid 1970s) [69–71]
Membrane permeation	Hayhurst, Wernick (1983) [72, 73]
Effectiveness factor	Haag, Post (early 1980s) [74, 75]
ZLC	Eic and Ruthven (mid 1980s) [76, 77]
Frequency response	Yasuda, Rees (late 1980s) [78–80]
QENS	Cohen de Lara, Jobic (late 1980s) [81, 82]
Chromatography (liquid)	Awum (1988) [83]
Fourier-transform infrared absorption (FTIR)	Niessen and Karge (1991) [84–86]
Differential adsorption bed	Do (1991) [87]
IR and IR/freq. response	Grenier, Meunier, Bourdin (1994) [88, 89]
Tracer ZLC	Hufton (1994) [90, 91]
TAP reactor	Baerns and Keipert [92]; Nijhuis (1997) [93]
Interference microscopy	Kärger et al. (1999) [94, 95]
Neutron spin-echo	Jobic (2000) [96]

membrane permeation, together with FTIR and the recently developed interference microscopy technique, both of which are applied at the scale of the individual crystal, may be classified as mesoscopic methods (see Table 4).

Many of the macroscopic techniques can be applied to the measurement of self-diffusion by using isotopically labeled tracers. Such methods, first introduced by Barrer and Fender [97], have been widely applied in order to obtain data which should be directly comparable with microscopic self-diffusion measurements. Such comparisons are presented in several of the chapters within the present volume.

For several reasons the reliable measurement of micropore diffusion has proved to be far more difficult than expected. We now know that when the diameter of the diffusing molecule is even slightly smaller than the pore diameter, diffusion within an ideal micropore is surprisingly fast and difficult to measure by macroscopic methods, since the size of available zeolite crystals is limited. Such fast processes can, however, be measured relatively easily by PFG NMR and QENS. As the molecular diameter of the sorbate approaches (or even exceeds) the minimum diameter of the pore, the diffusional activa-

Table 4 Classification of methods for measuring intracrystalline diffusion in zeolites

Microscopic methods (sub-crystal scale)	QENS	
	NMR – Relaxation	
	– PFG	
	Neutron spin-echo	
Mesoscopic methods (single-crystal scale)	Single crystal permeation	
	FTIR	
	Interference microscopy	
Macroscopic methods (many crystals)	Transient	Sorption rate
		Flow – ZLC/TZLC
		Batch – DAB
		– Gravimetric
		– Piezometric
		– FTIR
		– Temp. response
		Chromatographic
		Gas phase
		Liquid phase
		Wall-coated column
		Frequency Response
		Pressure
		Pressure/temperature
	Quasi-steady state	Membrane
		Wicke Kallenbach
		Single crystal
		Zeolite membrane
		Catalyst effectiveness factor

tion energy increases and the diffusivity drops by orders of magnitude. Slow transport diffusion (for example ethane, propane, etc. in CHA zeolites; see Fig. 15) is easily measured macroscopically but is inaccessible to microscopic techniques. The range of systems and experimental conditions where reliable measurements can be made by both macroscopic and microscopic methods is therefore quite restricted.

Transient uptake rate measurements are subject to intrusion of heat transfer limitations, especially in batch measurements at low pressures. Membrane permeation, frequency response, and ZLC measurements should not be subject to serious heat transfer limitations but, especially in frequency response and ZLC, there is always a danger of intrusion of extracrystalline resistances to mass transfer, although in principle these can be eliminated by reducing the sample size and ensuring that the crystals within the sample are dis-

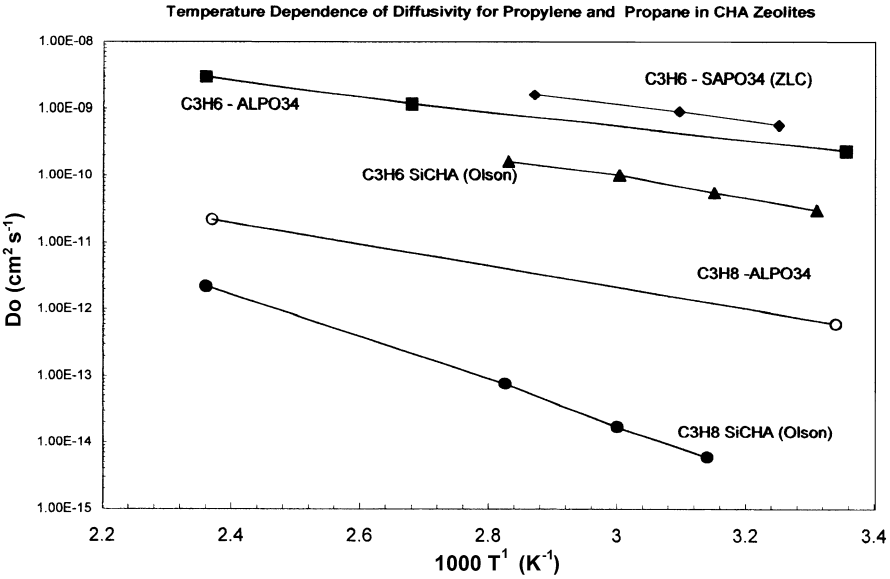

Fig. 15 Arrhenius plot showing the temperature dependence of intracrystalline diffusivity for C_3 hydrocarbons in various CHA zeolites. Data are from [108–110]. ZLC data for C_3H_6–SAPO34 have not been previously reported

persed rather than aggregated together. Recent measurements have, however, shown that for many systems significant discrepancies between microscopic and macroscopic diffusion measurements remain even when the intrusion of extracrystalline resistances is carefully minimized. Similarly, the diffusivities measured by quasi-steady-state membrane permeation tend to be larger than the values determined by transient macroscopic methods, although still substantially smaller than the microscopic values derived from PFG NMR, QENS, and molecular dynamic simulation (see Fig. 16) [96, 99].

A major advantage of the recently developed interference microscopy technique [94, 95] is that in addition to allowing a direct measurement of sorption/desorption rates on the single-crystal scale it provides, from the form of the transient concentration profiles, direct experimental evidence concerning the nature of the rate-controlling resistances to mass transfer. Recent studies by this technique have shown that the influence of structural defects and surface resistance to mass transfer are far more important than has been generally assumed [100–104]. For some systems it appears that sorption rates are controlled by surface resistance, while in other cases the profiles suggest a combination of surface and internal diffusional resistance control—see, for example, Fig. 17 [103]. Sometimes portions of the intracrystalline pore volume are completely inaccessible due to barriers associated with the crystal growth planes. In the case of ferrierite it appears that transport occurs entirely through

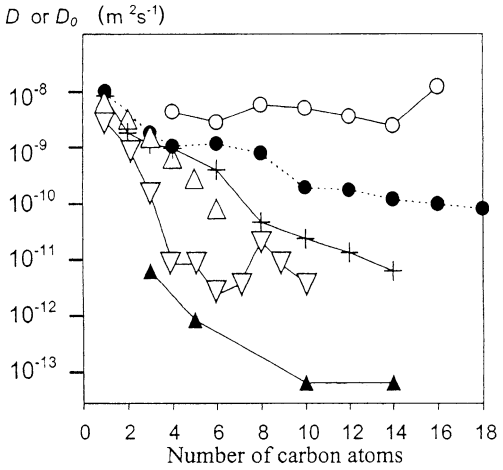

Fig. 16 Comparison of diffusivities for *n*-alkanes in silicalite measured by different experimental methods: ○,●, MD simulations; +, QENS; ▽, single crystal membrane; △, PFG NMR; ▲, ZLC. Data are from various sources. From Jobic [96] with permission

the eight-ring channels, while the large ten-ring channels provide no access, presumably as a result of a surface barrier [105]. Less pronounced internal barriers, most likely resulting from fault planes within the crystal, have also been observed [101, 102].

It thus appears that in real zeolite crystals diffusion over long distances reflects the influence of surface and internal barriers rather than the pore structure of the idealized framework. As a result the apparent intracrystalline diffusivities often show a strong dependence on the length scale of the measurement. Measurements by QENS and neutron spin-echo methods over distances corresponding to a few unit cells often approach the theoretical values derived by MD calculations for an ideal lattice. Similar values are often obtained by PFG NMR when the measurement is made over short distances. Measurements by most macroscopic methods are on the length scale of the crystals, and these tend to yield lower apparent diffusivities as a consequence of the intrusion of surface barriers and internal resistances due to structural defects.

Measurements by interference microscopy are, under favorable conditions, capable of yielding both internal diffusivities and apparent diffusivities based on overall sorption rates. The former tend to approach the values obtained from microscopic measurements while the latter yield values similar to those obtained by other macroscopic methods. Of necessity these studies have been carried out in large zeolite crystals. One may expect that smaller crystals may be less defective, although the influence of surface resistance may be expected to be greater. The extent to which these conclusions are applicable to the small zeolite crystals generally used in commercial zeolite catalysts and adsorbents remains an open question.

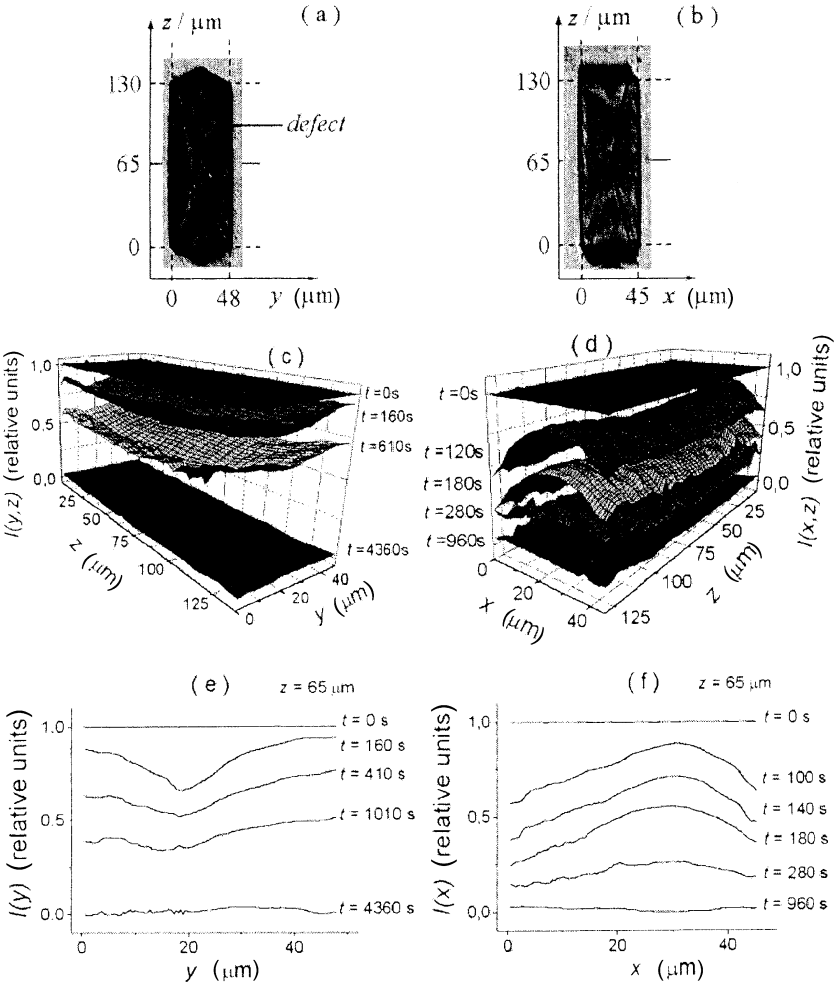

Fig. 17 Transient profile for desorption of isobutane from a surface-etched silicalite. The observation direction was perpendicular to the *x*–*y* plane in (**a**) and (**c**) and perpendicular to the *z*–*x* plane in (**b**), (**d**) , and (**f**). The form of the profiles suggests that the desorption rate is controlled by the combined effects of internal diffusion and surface resistance. The effect of a crack in the crystal is evident in (**c**) and (**e**). From Kortunov et al. [103]

4
Impact of Micropore Diffusion in Zeolite-Based Processes

Most adsorption separation processes depend on differences in adsorption equilibrium. In such processes the impact of mass transfer resistance is negative, so the design engineer seeks to minimize the effect by reducing particle size and crystal size and by appropriate choice of the operating condi-

tions. However, there are several important catalytic and separation processes which depend on differences in sorption kinetics. Two representative examples of such processes are given below. Significant kinetic selectivity is achieved only when the sorption kinetics are controlled by micropore (intracrystalline) diffusion so, for these processes, the operating conditions must be selected to maximize the intrusion of this resistance. Zeolite membranes provide another important class of systems for which intracrystalline diffusion is dominant.

4.1 Olefin/Paraffin Separations

The separation of light olefins (C_2H_4 and C_3H_6) from the corresponding paraffins (C_2H_6 and C_3H_8) has traditionally been carried out by cryogenic distillation [106], but the difference in boiling points is small, so the process is energy intensive and therefore costly. The earliest such processes took advantage of the fact that, on cationic zeolites, olefins are adsorbed more strongly than the corresponding paraffins [107]. However, the equilibrium selectivity is relatively modest ($K_A/K_B \sim 10$) and not sufficiently high to achieve a high-purity olefin product at high recovery. The possibility of developing an efficient kinetic separation has therefore attracted much recent attention [108–110].

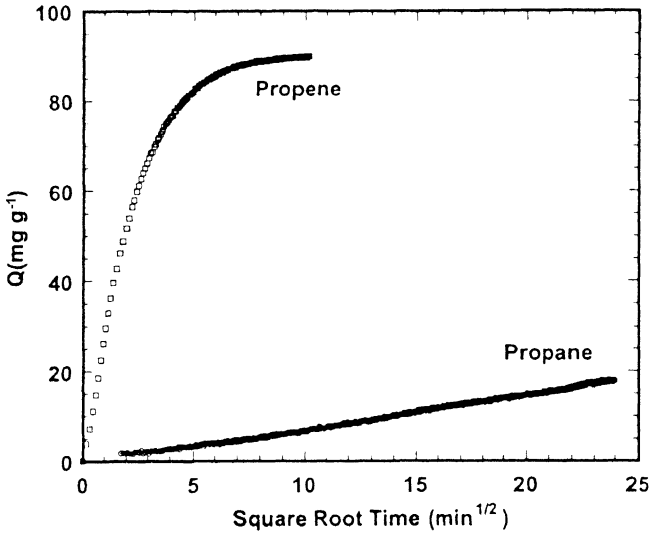

Fig. 18 Comparative (integral) uptake curves for C_3H_6 and C_3H_8 in Si-CHA at 80 °C and 600 Torr. From Olson et al. [36]. Note that the curves show linearity in $\sqrt{t}$ in the initial region, as expected for diffusion control. From Olson et al. [109] with permission

Figure 15 shows diffusivity data for the C_3 olefins and paraffins in several different CHA zeolites. In 5A zeolite diffusion of the C_2 species is not significantly constrained by steric hindrance, so the diffusional activation energy is low ($\sim$ 1.5 kcal/mol) with little difference in diffusivity between C_2H_4 and C_2H_6. Steric hindrance is substantially greater in 4A zeolite, resulting in higher diffusional activation energies and significantly faster diffusion of C_2H_4, which is the slightly smaller molecule. However, in zeolites of the CHA family, the pores of which are controlled by distorted eight-membered rings, the differences in diffusivity between olefins and paraffins are much greater (3 to 4 orders of magnitude for C_3H_6/C_3H_8 in high-silicon chabazite). Comparative uptake curves for this system are shown in Fig. 18.

The window dimensions and hence the diffusivity and the diffusivity ratio are correlated with the unit cell size. Silicon chabazite, which has the smallest cell size, has the highest kinetic selectivity but the diffusion of propylene is rather slow, thus restricting the cycle time. The choice between a high selectivity with slow uptake of propylene and a lower selectivity with faster uptake thus represents an interesting optimization problem.

4.2 N_2/CH_4 Separation over ETS-4

Titanosilicalites such as ETS-4 represent a new class of crystalline microporous molecular sieves, similar to zeolites in their general structure but significantly different in their composition. Like the small-pore zeolites, ETS-4 has a three-dimensional channel structure controlled by eight-membered oxygen rings, but the dimensions of the unit cell and hence both the size and shape of the eight-membered ring windows change dramatically with the dehydration temperature [111]. Provided that the thermal stability limit ($\sim$ 200 °C for Na form, 330 °C for Sr form) is not exceeded this effect is reversible. This flexibility endows these adsorbents with a unique "tunability" that allows the dimensions of the molecular sieve to be optimized to achieve a particular separation (see Fig. 19). So far the most important industrial application of these materials is in the purification of nitrogen-rich natural gas (CH_4).

To meet the calorific value specification for pipeline-grade gas the nitrogen content must not exceed about 4%. Many deposits of natural gas, however, contain much larger concentrations of nitrogen. Cryogenic distillation is uneconomic and on both zeolite and CMS adsorbents N_2 and CH_4 are similarly adsorbed with respect to both equilibrium and kinetics, so the search for an economically viable process for nitrogen removal presented the gas industry with an important challenge. The use of ETS-4 dehydrated at 270 °C appears to be a promising solution, since this material shows a high kinetic selectivity for N_2 over CH_4 (see Fig. 20), thus allowing an effective kinetic separation to be achieved [112]. Following successful pilot plant trials a full-scale unit has

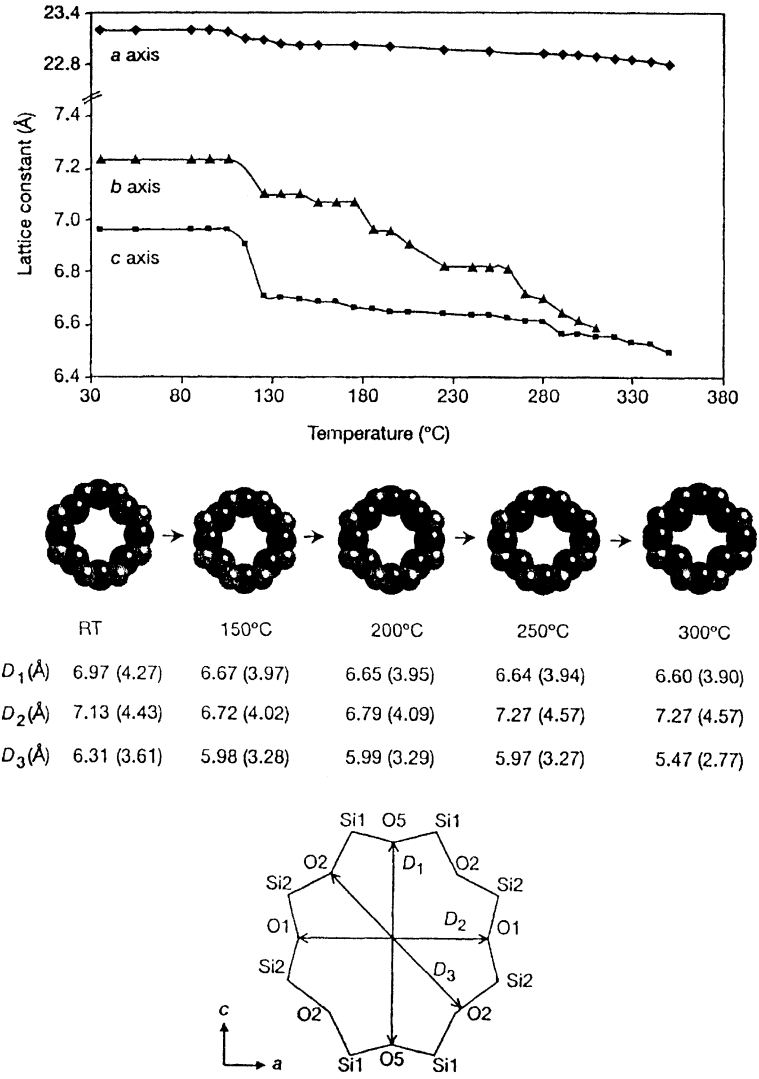

Fig. 19 Variation of lattice parameters and pore dimensions of Sr-ETS-4 with dehydration temperature. Modified from Kuznicki et al. [111] with permission

been developed using a relatively fast cycle (timescale of minutes) pressure-swing adsorption process. About 75% of the N_2 is removed with 95% recovery of CH_4 [113]. However, the process is not without its problems:

1. The capacity of the adsorbent is relatively low so a large volume of adsorbent is needed.
2. It is essential to dry the feed gas to very low humidity levels.

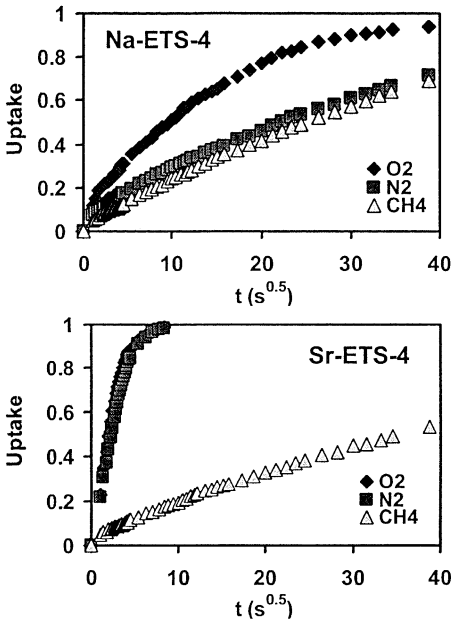

Fig. 20 Comparative uptake curves for O_2, N_2, and CH_4 in Na-ETS-4 and Sr-ETS-4, dehydrated at 270 °C. From Farooq et al. [112] with permission

3. Methane diffuses into the structure, albeit slowly, necessitating periodic thermal regeneration of the adsorber beds. This adds significantly to the process cost.

4.3 Catalytic Reactions

Diffusion plays a major role in influencing both the activity and selectivity of many catalysts. For a first-order reaction in a spherical catalyst particle the intrinsic rate constant (k) is reduced by a factor η (the effectiveness factor):

$$k_e = k\eta \tag{47}$$

$$\eta = \frac{3}{\Phi}\left[1 - \frac{1}{\tanh \Phi}\right]$$

$$\Phi = R\sqrt{k/D}\,.$$

This basic analysis is commonly attributed to Thiele (1939) [114] and the dimensionless parameter Φ is commonly called the Thiele modulus, although essentially the same analysis was published many years earlier, in 1909, by Jüttner [115].

In a zeolite catalyst diffusional limitations may occur at either the particle scale or the crystal scale. In the latter case the basic analysis remains the same, but since the rate constant is defined with respect to the concentration of reactant in the vapor phase while the intracrystalline diffusivity is defined with respect to the adsorbed phase concentration, the Thiele modulus must be redefined to introduce the dimensionless adsorption equilibrium constant (K):

$$\Phi_s = R\sqrt{k/KD} = \left(\frac{R^2}{D}\frac{k}{K}\right)^{1/2} . \tag{48}$$

Both the intrinsic rate constant and the effective diffusivity (KD) can be extracted from measurements of the reaction rate with different size fractions of the zeolite crystals. This approach has been demonstrated by Haag et al. [116] for cracking of n-hexane on HZSM5 and by Post et al. [117] for isomerization of 2,2-dimethylbutane over HZSM-5. It is worth commenting that in Haag's analysis the equilibrium constant (or distribution coefficient K) was omitted, leading to erroneously large apparent diffusivity values.

The methanol to olefins (MTO) reaction offers a more modern example of a catalytic reaction controlled by intracrystalline diffusion. Stimulated by the escalating demand for light olefins, this reaction has attracted much recent attention. The reaction of methanol at 350–450 °C over HZSM-5 yields a wide spectrum of products including light alkanes, light olefins, and single-ring aromatics [118–120]. The yield of $C_2^= + C_3^=$ (the desirable products for polyolefin feedstock) amounts to only 30–40%. The introduction of SAPO-34 (a structural analog of chabazite) as the catalyst [121] gave a dramatic improvement in both selectivity and conversion, making the process much more attractive. Under properly selected conditions light olefin yields ($C_2^= + C_3^=$) approaching 80% can be achieved with only small amounts of higher olefins and paraffins and essentially no aromatics [122].

The absence of aromatic products appears to be related to the size of the chabazite cage which is too small to allow the formation of a benzene ring. The reaction mechanism has been established in broad outline [123–125], although many important details are still not fully understood:

$$\begin{aligned} &1. \quad 2CH_3OH \longrightarrow CH_3 - O - CH_3 + H_2O \\ &2. \quad CH_3 - O - CH_3 \longrightarrow C_2H_4 + H_2O \\ &3. \quad 1.5C_2H_4 \longleftrightarrow C_3H_6 \end{aligned} \tag{49}$$

Slow polymerization to higher molecular weight species (coke) also occurs. Reaction 3 is reversible and exothermic; this probably accounts for the observed increase in $C_2^= + C_3^=$ yield with temperature.

Detailed studies of the kinetics of this reaction over different size fractions of SAPO-34 crystals, together with measurements of the sorption rate and the equilibrium isotherm, have been reported by Chen et al. [127–132]. These data are summarized in Fig. 21. The dominance of intracrystalline

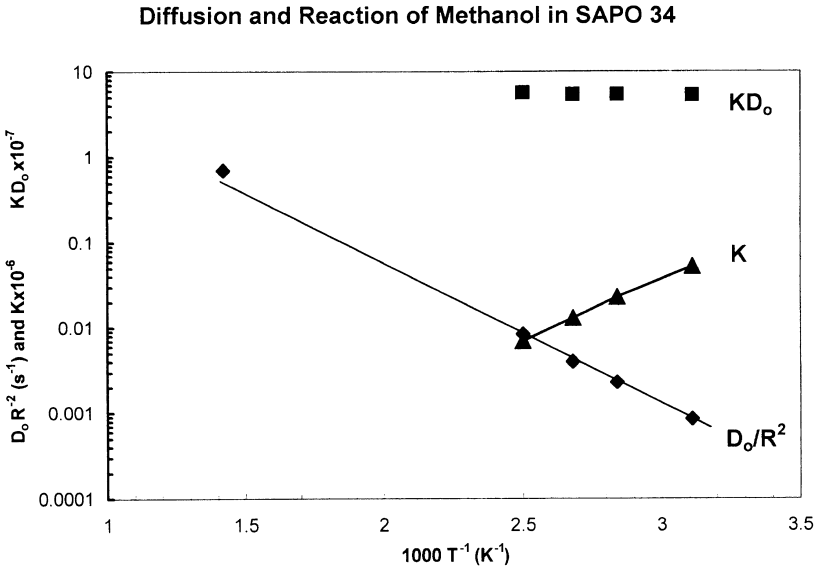

Fig. 21 Variation of diffusional time constant (D_0/R^2), dimensionless Henry constant (K), and the product KD_0 with temperature. (From data of Chen et al. [127].) The value of D_0/R^2 calculated from reaction rate measurements at 698 K is also shown. Corrected diffusivities are calculated from the reported integral diffusivities according to the analysis of Garg and Ruthven [126]. From Ruthven [98]

diffusion in controlling the sorption rate was shown by varying the crystal size. Values of the diffusional time constant (R^2/D_0) derived from reaction rate measurements at 698 K are close to the value extrapolated from sorption rate measurements at lower temperatures with the same batch of SAPO-34 crystals [127, 128]. The temperature dependence of the dimensionless Henry constant, also shown in Fig. 21, yields an adsorption energy of $\Delta U \approx -31$ kJ/mol, which is almost the same as the diffusional activation energy derived from the temperature dependence of the (corrected) diffusivity ($E = 30.5$ kJ/mol). Consequently the product KD_0, referred to by Chen as the "steady-state diffusivity", is almost independent of temperature. A similar situation was noted by Garcia and Weisz [133, 134] in their study of the reaction of various aromatics over HZSM-5.

As the catalyst ages, the light olefin yield and the selectivity both increase [127, 129]. This appears to be related to the buildup of coke within the intracrystalline pores, which reduces both the intrinsic rate constant and the intracrystalline diffusivity [128, 129]. Detailed measurements with different crystal sizes show that with increasing coke levels the diffusivity declines more rapidly than the rate constant, so that diffusional limitations become more pronounced as the catalyst ages. A high yield of light olefins requires that the dimethyl ether formed in the first step of the reaction be retained

within the crystal long enough for it to be essentially fully converted by reaction 2. This requires that the ratio of the Thiele moduli should be large:

$$\frac{\Phi_2}{\Phi_1} = \left(\frac{k_2}{k_1}\frac{D_{\mathrm{MeOH}}}{D_{\mathrm{DME}}}\right)^{\frac{1}{2}} \gg 1\,. \tag{50}$$

This ratio is independent of crystal size, so varying the crystal size has no effect on the yield, in accordance with experimental observations [122].

Since $k_2 < k_1$ a high ratio of $D_{\mathrm{MeOH}}/D_{\mathrm{DME}}$ is necessary to achieve a high ratio Φ_2/Φ_1 and thus a high olefin yield. As the dimethyl ether molecule is larger than the methanol molecule it is reasonable to assume that, under sterically restricted conditions, the diffusivity ratio $D_{\mathrm{MeOH}}/D_{\mathrm{DME}}$ will increase as the effective pore size decreases. The observations that the olefin yield increases as the catalyst cokes and that an improvement in yield is obtained by increasing the Si/Al ratio (which decreases the unit cell size and therefore the effective window size) are consistent with this hypothesis. However, varying the Si/Al ratio also changes the strength of the acid sites so such evidence is not entirely conclusive.

5 Concluding Remarks

Since the groundbreaking work of Professor Barrer in the 1940s, the study of adsorption and diffusion in microporous solids, particularly zeolites, has made much progress. Many of the topics mentioned in this introductory chapter have been explored in considerable detail. Reviews of some of these areas are presented in subsequent chapters of this volume. However, numerous challenges still remain in both our understanding of the fundamentals of guest–host interactions and the technological application of these systems. Despite the undoubted progress that has been achieved, this remains a promising and rewarding field for future research.

Acknowledgements The author is grateful to the Alexander von Humboldt Foundation for financial support and to Professor Jörg Kärger for arranging and hosting a sabbatical leave at the University of Leipzig (2003–2004), during which part of this review was prepared.

References

1. Nicholson D, Parsonage NG (1982) Computer simulation and the statistical mechanics of adsorption. Academic, London
2. Brunauer S, Deming LS, Deming WE, Teller EJ (1940) J Am Chem Soc 62:1723
3. Langmuir I (1918) J Chem Soc 40:1361

4. Brandani F, Ruthven DM, Coe CG (2003) Ind Eng Chem Res 42:1451
5. Jarionec M (1975) J Colloid Interface Sci 53:422
6. Toth J (1971) Acta Chim Acad Sci Hung 69:311
7. Ruthven DM (1971) Nature Phys Sci 232:70
8. Ruthven DM (1982) Zeolites 2:242
9. Ruthven DM, Loughlin KF (1972) J Chem Soc Faraday Trans I 68:696
10. Ruthven DM, Goddard M (1983) In: Myers AL, Belfort G (eds) Proceedings of the 1st international conference on fundamentals of adsorption, Schloss Elmau, Bavaria, Germany, May 1983. Engineering Foundation, New York, p 533
11. Ruthven DM (1984) Principles of adsorption and adsorption processes. Wiley, New York, pp 96–98
12. Gibbs JW (1928) Collected works. Yale University Press, New Haven, CT
13. Volmer M (1925) Z Phys Chem 115:253
14. Vavlitis A, Ruthven DM, Loughlin KF (1981) J Colloid Interface Sci 84:526
15. Dubinin MM (1960) Chem Rev 60:235
16. Dubinin MM (1965) Pure Appl Chem 10:309
17. Polanyi M (1932) Trans Faraday Soc 28:316
18. Berenyi L (1920) Z Phys Chem Leipzig 94:628
19. Berenyi L (1923) Z Phys Chem Leipzig 105:55
20. Dubinin MM, Radushkevich LV (1947) Dokl Akad Nauk SSSR 55:327
21. Kiselev AV (1977) In: Flanigan EM, Sand LB (eds) Molecular sieve zeolites. Proceedings of the 2nd international zeolite conference, 8–11 September 1970, Worcester, MA, vol II. Adv Chem Ser 102, American Chemical Society, Washington, DC, pp 37–68, especially p 66
22. Kemball C, Rideal EK, Guggenheim EA (1948) Trans Faraday Soc 44:952
23. Broughton DB (1948) Ind Eng Chem 40:1506
24. Ruthven DM, Loughlin KF, Holborrow KA (1973) Chem Eng Sci 28:701
25. Rolniak PD, Kobayashi R (1980) AIChE J 26:616
26. Myers AL, Prausnitz JM (1965) AIChE J 11:121
27. Shen D, Bülow M, Siperstein F, Engelhard M, Myers AL (2000) Adsorption 6:275
28. Masuda T, Tsutsumi K, Takahashi H (1980) In: Rees LVC (ed) Proceedings of the 5th international zeolite conference, Naples, Italy, 2–6 June 1980. Heyden, London, p 483
29. Barrer RM, Reucroft PJ (1960) Proc R Soc Lond A 258:449
30. Barrer RM, Wasilewski S (1961) Trans Faraday Soc 57:1141
31. Barrer RM, Wasilewski S (1961) Trans Faraday Soc 57:1153
32. Bülow M, Lorenz P (1986) In: Liapis AI (ed) Proceedings of the 2nd international conference on fundamentals of adsorption, Santa Barbara, CA, May 1986. Engineering Foundation, New York, p 119
33. Kubin M (1965) Collect Czech Chem Commun 30:1104
34. Kubin M (1965) Collect Czech Chem Commun 30:2900
35. Ruthven DM, Post M (2001) In: van Bekkum H, Flanigan EH, Jacobs PA, Jansen JC (eds) Introduction to zeolite science and practice, 2nd edn. Elsevier, Amsterdam, p 525
36. Ruthven DM (1984) Principles of adsorption and adsorption processes. Wiley, New York, p 148
37. Kärger J, Ruthven DM (1992) Diffusion in zeolites and other microporous solids. Wiley, New York, p 6
38. Darken LS (1948) Trans AIME 175:184
39. Maxwell JC (1867) Philos Trans R Soc Lond 157:49
40. Stefan J (1872) Wien Ber 65:323

41. Doetsch IH, Ruthven DM, Loughlin KF (1974) Can J Chem 52:2717
42. Yucel H, Ruthven DM (1980) J Chem Soc Faraday Trans I 76:71
43. Yucel H, Ruthven DM (1980) J Colloid Interface Sci 74:186
44. Krishna R, Baur R (2004) Chem Eng J 97:37
45. Krishna J, Wesselingh JA (1997) Chem Eng Sci 52:861
46. Keil F, Krishna R, Coppens M-O (2000) Rev Chem Eng 16:71
47. Krishna R, Paschek D (2000) Sep Purif Technol 21:111
48. Brandani S, Jama M, Ruthven DM (2000) Microporous Mesoporous Mater 35:283
49. Kärger J, Ruthven DM (1992) Diffusion in zeolites and other microporous solids. Wiley, New York, p 76, 110
50. Habgood HW (1958) Can J Chem 36:1384
51. Round GF, Habgood HW, Newton R (1956) Sep Sci 1:219
52. Vignes A (1966) Ind Eng Chem Fund 5:189
53. van de Graaf JM, Kapteijn F, Moulijn JA (1999) AIChE J 45:497
54. Karimi IA, Farooq S (2000) Chem Eng Sci 55:3529
55. Tiselius A (1934) Z Phys Chem A169:425
56. Tiselius A (1935) Z Phys Chem A174:401
57. Barrer RM (1941) Trans Faraday Soc 37:590
58. Barrer RM (1978) Zeolites and clay minerals. Academic, London
59. Bülow M, Kärger J, van Phat N, Schirmer W (1976) Z Phys Chem (Leipzig) 257:1205
60. Bülow M, Mietk W, Struve P, Schirmer W, Kočirik M, Kärger J (1983) In: Olson D, Bisio A (eds) Proceedings of the 6th international zeolite conference, Reno, NV, 10–15 July 1983. Butterworths, Guildford, UK, p 242
61. Do DD (1995) Chem Eng Sci 50:549
62. Do DD (1998) Chem Eng Sci 53:3459
63. Resing HA, Thompson JK (1967) J Chem Phys 46:2876
64. Resing HA, Murday JS (1973) In: Meier WM, Uytterhoeven JB (eds) Molecular sieves. Proceedings of the 3rd international zeolite conference, Zurich, Switzerland, 3–7 September 1973. Adv Chem Ser 121, American Chemical Society, Washington, DC, p 414
65. Kärger J (1971) Z Phys Chem (Leipzig) 248:27
66. Pfeifer H (1972) NMR and relaxation of molecules adsorbed on solids. In: NMR—Basic principles & progress, Vol 7. Springer, Berlin Heidelberg New York, p 53
67. Lechert H, Wittern K-P, Schweitzer W (1978) In: Fejes P (ed) Proceedings of the symposium on zeolites, Szeged, Hungary, 11–14 September 1978. Acta Universitas Szegediensis, p 201
68. Lechert H, Wittern K-P, Schweitzer W (1978) Acta Phys Chem 24:201
69. Ma YA, Mancel C (1973) In: Meier WM, Uytterhoeven JB (eds) Molecular sieves. Proceedings of the 3rd international zeolite conference, Zurich, Switzerland, 3–7 September 1973. Adv Chem Ser 121, American Chemical Society, Washington, DC, p 392
70. Haynes HW, Sarma PN (1974) Adv Chem Ser 133, American Chemical Society, Washington, DC, p 205
71. Shah DB, Ruthven DM (1977) AIChE J 23:804
72. Paravar A, Hayhurst DT (1983) In: Olson D, Bisio A (eds) Proceedings of the 6th international zeolite conference, Reno, 10–15 July 1983. Butterworths, Guildford, UK, p 217
73. Wernick DL, Osterhuber EJ (1983) In: Olson D, Bisio A (eds) Proceedings of the 6th international zeolite conference, Reno, 10–15 July 1983. Butterworths, Guildford, UK, p 122

74. Haag WO, Lago RM, Weisz PB (1982) Faraday Discuss 72:317
75. Post MFM, van Amstel J, Kouwenhoeven HW (1983) In: Olson D, Bisio A (eds) Proceedings of the 6th international zeolite conference, Reno, 10–15 July 1983. Butterworths, Guildford, UK, p 517
76. Eic M, Ruthven DM (1988) Zeolites 8:40
77. Ruthven DM, Eic M (1988) Am Chem Soc Symp Ser 368:362
78. Yasuda Y (1976) J Phys Chem 80:1867
79. van-den-Begin NG, Rees LVC (1989) In: Jacobs PA, van Santen RA (eds) Zeolites: facts, figures, future. Proceedings of the 8th international zeolite conference, Amsterdam, 10–14 July 1989. Elsevier, Amsterdam, p 915
80. van-den-Begin NG, Rees LVC (1989) Stud Surf Sci Catal 49:915
81. Jobic H, Bee M, Kearley GJ (1989) Zeolites 9:312
82. Cohen de Lara E, Jahn R, Mezei F (1983) J Chem Soc Faraday Trans 79:1911
83. Awum F, Narayan S, Ruthven DM (1988) Ind Eng Chem Res 27:1510
84. Niessen W, Karge HG (1990) In: Inui T, Namba S, Tatsumi T (eds) Proceedings of the international symposium on chemistry of microporous crystals, 26–29 June 1990. Kodansha, Tokyo/Elsevier, Amsterdam, p 213
85. Niessen W, Karge HG (1990) Stud Surf Sci Catal 60:213
86. Niessen W, Karge HG (1993) Microporous Mater 1:1
87. Do DD, Xu X, Mayfield PLJ (1991) Gas Sep Purif 5:35
88. Grenier Ph, Meunier F, Gray PG, Kärger J, Xu Z, Ruthven DM (1994) Zeolites 14:242
89. Bourdin V (1996) PhD thesis, University of Paris XI
90. Hufton JR, Brandani S, Ruthven DM (1994) In: Weitkamp J, Karge HG, Pfeifer H, Hölderich W (eds) Zeolites and related microporous materials: state of the art 1994. Proceedings of the 10th international zeolite conference, Garmisch-Partenkirchen, Germany, 17–22 July 1994. Elsevier, Amsterdam, p 1323
91. Hufton JR, Brandani S, Ruthven DM (1994) Stud Surf Sci Catal 84:1323
92. Baerns M, Keipert O (1998) Chem Eng Sci 53:3623
93. Nijhuis TA, van den Broeke LJP (1997) Chem Eng Sci 52:3401
94. Schemmert U, Kärger J, Weitkamp J (1999) Microporous Mesoporous Mater 32:101
95. Kärger J, Schemmert U (2000) In: Do DD (ed) Adsorption science and technology. Proceedings of the 2nd Pacific conference on adsorption, Brisbane, 14–18 May 2000. World Scientific, Singapore, p 324
96. Jobic H (2000) In: Kanellopoulos NK (ed) Recent advances in gas separation by microporous ceramic membranes. Elsevier, Amsterdam, p 109
97. Barrer RM, Fender BEF (1961) J Phys Chem Solids 21:12
98. Ruthven DM (2005) In: Kärger J, Grinberg F, Heitjans P (eds) Diffusion fundamentals. Leipziger Universitätsverlag, Leipzig, Germany, p 366
99. Kärger J, Ruthven DM (2002) In: Schüth F, Sing KSW, Weitkamp J (eds) Handbook of porous solids, vol 4. Mass transfer in porous solids. Wiley, Weinheim, p 2089
100. Geier O, Vasenkov S, Lehmann E, Kärger J, Schemmert U, Rakoczy RA, Weitkamp J (2001) J Phys Chem 105:10217
101. Vasenkov S, Kärger J (2002) Microporous Mesoporous Mater 55:139
102. Wloch J (2003) Microporous Mesoporous Mater 62:81
103. Kortunov P, Vasenkov S, Chmelik C, Kärger J, Ruthven DM, Wloch J (2004) Chem Mater 16:3552
104. Lehmann E, Chmelik C, Scheidt H, Vasenkov S, Staudte B, Kärger J, Kremer F, Zadrozna G, Kornakowski J (2002) J Am Chem Soc 124:8690
105. Kortunov P, Chmelik C, Kärger J, Racoczy RA, Ruthven DM, Traa Y, Vasenkov S, Weitkamp J, Adsorption (in press)

106. Eldridge RB (1993) Ind Eng Chem Res 32:2208
107. Peterson DL, Helfferich F, Griep RK (1967) In: Molecular sieves. Proceedings of the 1st international zeolite conference, London, 4–6 April 1967. Society of the Chemical Industry, London, p 217
108. Olson D (2002) US Patent 6,488,741 B2, 3 December 2002
109. Olson D, Camblor MA, Villaescusa LA, Kühl GH (2004) Microporous Mesoporous Mater 67:27
110. Reyes SC et al. (2004) US Patent 6,730,142 B2, 4 May 2004
111. Kuznicki SM, Bell VA, Nair S, Hillhouse HW, Jacubinas RM, Braunbath C-M, Toby BH, Tsapatsis M (2001) Nature 412:720
112. Marathe RP, Mantri K, Srinivasan MP, Farooq S (2004) Ind Eng Chem Res 43:5281
113. Mitariten M (2001) Am Oil Gas Rep, March 2001, p 103
114. Thiele EW (1939) Ind Eng Chem 31:916
115. Jüttner F (1909) Z Phys Chem 65:595
116. Haag WO, Lago RM, Weisz PB (1982) Discuss Faraday Soc 72:317
117. Post MFM, van Amstel J, Kouwenhoven HW (1983) In: Olson D, Bisio A (eds) Proceedings of the 6th international zeolite conference, Reno, NV, 10–15 July 1983. Butterworths, Guildford, UK, p 517
118. Chang CD, Chu CTW, Socha RF (1984) J Catal 86:289
119. Chen NY, Garwood WE, Dwyer FG (1989) Shape selective catalysis in industrial operations. Marcel Dekker, New York, p 233
120. Chang CD (1983) Hydrocarbons from Methanol, Catal Rev - Sci Eng 25:1
121. Kaiser SW (1985) US Patent 4,499,327
122. Wilson S, Barger P (1999) Microporous Mesoporous Mater 29:117
123. Froment GF, Dehertog WJH, Marchi AJ (1992) In: Spivey JJ (ed) Catalysis, vol 9, Chap. 1. Royal Society of Chemistry, London, p 1
124. Dahl IM, Kolkoe S (1994) J Catal 149:458
125. Dahl IM, Kolkoe S (1996) J Catal 161:304
126. Garg DR, Ruthven DM (1972) Chem Eng Sci 27:417
127. Chen D, Rebo HP, Moljord K, Holman A (1999) Ind Eng Chem Res 38:4241
128. Chen D, Rebo HP, Holman A (1999) Chem Eng Sci 54:3465
129. Chen D, Rebo HP, Moljord K, Holman A (1997) Ind Eng Chem Res 36:3473
130. Chen D, Rebo HP, Moljord K, Holman A (1996) Chem Eng Sci 51:2687
131. Chen D, Rebo HP, Moljord K, Holman A (1998) In: Dabrowski A (ed) Adsorption and its applications in industry and environmental protection. Elsevier, Amsterdam, p 521
132. Chen D, Rebo HP, Moljord K, Holman A (1998) Stud Surf Sci Catal 119:521
133. Garcia SF, Weisz PB (1990) J Catal 121:294
134. Garcia SF, Weisz PB (1993) J Catal 142:691

Mol Sieves (2008) 7: 45–84
DOI 10.1007/3829_009
© Springer-Verlag Berlin Heidelberg
Published online: 20 December 2005

Measurement of Diffusion in Microporous Solids by Macroscopic Methods

Douglas M. Ruthven[1] (✉) · Stefano Brandani[2] · Mladen Eic[3]

[1]Department of Chemical and Biological Engineering, University of Maine, Orono, ME USA
druthven@umche.maine.edu

[2]Department of Chemical Engineering, University College London, Torrington Place, London WC1E 7JE, UK
s.brandani@ucl.ac.uk

[3]Department of Chemical Engineering, University of New Brunswick, Fredericton, NB E3B 5A3, Canada
meic@unb.ca

Abstract In this chapter the main macroscopic experimental methods for measuring diffusion in microporous solids are reviewed and the advantages and disadvantages of the various techniques are discussed. For several systems experimental measurements have been made by more than one technique, and in Part 3 the results of such comparative studies are reviewed. While in some cases the results show satisfactory consistency, there are also many systems for which the apparent intracrystalline diffusivities derived from macroscopic measurements are substantially smaller than the values from microscopic measurements such as PFG NMR. Recent measurements of the transient intracrystalline concentration profiles show that surface resistance and intracrystalline barriers are both

more common and more important than has been generally recognized. This may explain such discrepancies. Part 4 comprises a brief review of recent experimental studies of diffusion in mesoporous silica structures, which, in contrast to zeolites, have a well-defined bimodal distribution of pore size.

Abbreviations

a	External surface area/volume ratio for adsorbent particle
c	Sorbate concentration in fluid phase
c_0	Initial steady value of c
C_p	Heat capacity of adsorbent
D	Diffusivity
D_c	Intracrystalline diffusivity
D_e	Effective diffusivity for macroporous pellet (see Eq. 21)
D_L	Axial dispersion coefficient
D_p	Macropore or mesopore diffusivity
F	Fluid flow rate
h	Overall heat transfer coefficient
k	Solid "film" mass transfer coefficient
k_f	External fluid film mass transfer coefficient
K	Dimensionless Henry constant
K_o	Pre-exponential factor in temperature dependence of K
l	Half width of zeolite crystal
L	Column length; parameter defined by Eq. 11
M_t/M_∞	Fractional approach to equilibrium in an uptake experiment
p	Partial pressure
P	Total pressure
q	Sorbate concentration in adsorbed phase
q_o	Value of q at equilibrium with c_0
r_c	Zeolite crystal radius (Eq. 14)
R	Particle or crystal radius
R_g	Gas constant (e.g., Eq. 10)
t	Time
T	Temperature (K)
V	Column volume
V_d	Volume of dosing chamber
V_f	Volume of fluid
V_s	Volume of solid
V_u	Volume of uptake chamber
v	Interstitial fluid velocity
w	Volume fraction of zeolite in adsorbent pellet
z_i	Parameter defined in Eq. 10
α	Heat transfer parameter $(ha/\rho C_p)/(D_c/r_c^2)$
β	$(\Delta H/\rho C_p)(\partial q^*/\partial T)$—nonisothermal equilibrium parameter
β_i	Roots of Eq. 9 or Eq. 16
γ	Parameter defined in Eq. 10
δ	Parameter defined in Eq. 10
ε	Voidage of adsorbent bed
ε_p	Porosity of adsorbent particle
$-\Delta H$	Heat of adsorption

$-\Delta U$	Internal energy of adsorption
μ	Mean retention time
ρ	Particle (or sample) density
ρ_d, ρ_u	Dimensionless pressure changes defined in Eq. 10
σ^2	Variance of chromatographic response
η	Effectiveness factor
ϕ	Thiele modulus
$\overline{\chi}$	Valve constant (Eq. 10)
FR	Frequency response
IR	Infrared
MCM-41	Mesoporous silica
MD	Molecular dynamics
NMR	Nuclear magnetic resonance
PFG NMR	Pulse field gradient nuclear magnetic resonance
TZLC	Tracer zero length column
ZLC	Zero length column
ZSM-5	Zeolite of MFI structure

1 Introduction

Because of the practical importance of microporous materials, notably zeolites and carbon molecular sieves, as catalysts and selective adsorbents, the problem of measuring micropore diffusivities has attracted considerable attention [1–4]. This task has proved more difficult than might have been anticipated largely because these materials are generally available only as rather small particles (or crystals). A wide range of different experimental techniques have been applied including both microscopic and macroscopic methods and transient and steady-state measurements. A historical summary including references is given in Chap. 1. In this chapter we consider only macroscopic methods in which the diffusive flux is measured under well-defined experimental conditions; the microscopic approach in which the movement of the molecules is tracked directly is discussed in Chap. 3 of this volume [5].

A simple classification of the main macroscopic techniques is shown in Table 1, and this provides a useful framework for our review. Macroscopic measurements generally yield "transport" diffusivities, although variants of the techniques, using isotopically tagged tracers, can be devised to measure self-diffusivities. The large majority of the macroscopic techniques involve transient measurements. Steady-state or quasi-steady-state methods, notably membrane permeation and catalyst effectiveness measurements, have been demonstrated, but their application has been limited to a few systems.

Since most microscopic techniques measure self-diffusion, whereas the macroscopic techniques generally measure transport diffusion, direct comparisons between the measured diffusivities are not meaningful, except in the

Table 1 Classification of macroscopic methods for measuring diffusion in microporous solids

Transient				Quasi-steady state	
Uptake rate		Chromatography	Frequency response	Zeolite membrane	Effectiveness factor
[1, 4, 6, 7]		[38–42]	[29, 30]	[62–66]	[67, 68]
Batch	Flow				
Gravimetric [8–14]	ZLC [48–57]	Gas/liquid [44, 45]	Pressure [30–33]	Single crystal	
Piezometric [15–23]	TZLC [28, 51, 54]	Packed/wall-coated column [46, 47]	Pressure/temp. [35–37]	Multicrystal	
FTIR [25, 26]					
Temp. Response [27]					

low concentration limit. At higher loadings the microscopic self-diffusivity may be compared with the "corrected" transport diffusivity (D_o), defined by Eq. 1 (cf. [1], p 11):

$$D_o = D(\mathrm{d}\ln q/\mathrm{d}\ln p)\,, \tag{1}$$

where $(\mathrm{d}\ln q/\mathrm{d}\ln p)$ represents the gradient of the equilibrium isotherm in logarithmic coordinates. The corrected diffusivity calculated in this way represents the transport coefficient based on the chemical potential gradient as the driving force.

2
Survey of Macroscopic Methods for Measuring Micropore Diffusion

2.1
Uptake Rate Measurements

Perhaps the most obvious experimental approach to the determination of micropore diffusivities is to measure directly the sorption/desorption rate for an adsorbent particle subjected to a well-defined change in the ambient concentration of sorbate. For an isothermal spherical particle subjected to a step change in sorbate concentration at the external surface at time zero, the ap-

proach to equilibrium, under conditions of diffusion control, is given by [1]:

$$\frac{M_t}{M_\infty} = 1 - \frac{6}{\pi^2}\sum_{n=1}^{\infty}\frac{1}{n^2}\exp\left(-n^2\pi^2 Dt/R^2\right) . \tag{2}$$

The short and long time asymptotes are given by:

$$\text{Short Time:} \quad \frac{M_t}{M_\infty} = \frac{6}{R}\sqrt{\frac{Dt}{\pi}} \tag{3a}$$

$$\text{Long Time:} \quad \frac{M_t}{M_\infty} = 1 - \frac{6}{\pi^2}\exp\left(-\pi^2 Dt/R^2\right) . \tag{3b}$$

The form of the response curves is shown in Fig. 1. The corresponding expressions for other particle shapes are easily derived but there is little numerical difference from the response for a spherical particle of the same external area to volume ratio (i.e., based on an equivalent radius).

In contrast, for the same situation, a particle with surface resistance control follows a simple exponential approach to equilibrium:

$$\frac{M_t}{M_\infty} = 1 - \exp\left(-3kt/R\right) . \tag{4}$$

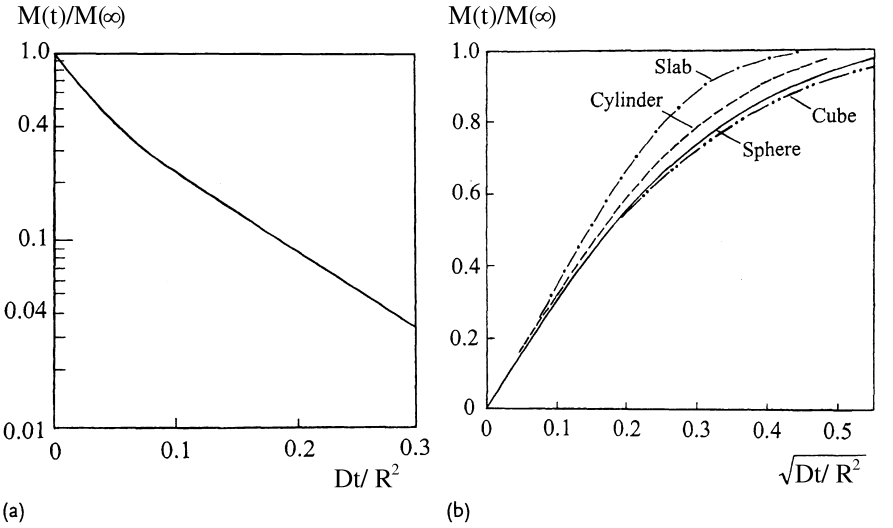

Fig. 1 Theoretical uptake curves for isothermal diffusion-controlled system showing **a** long time asymptote according to Eq. 2 or 3b and **b** form of short time response plotted in accordance with Eq. 3a. Note that the initial slope is quite insensitive to the particle shape (the equivalent radius r is defined as the radius of a sphere with the same surface-to-volume ratio as the actual particles)

When mass transfer is rapid and the approach to equilibrium is controlled entirely by heat transfer, the uptake curve for a differential pressure step obeys [8, 9]:

$$\frac{M_t}{M_\infty} = 1 - \left(\frac{\beta}{1+\beta}\right) \exp\left[\frac{-3ht}{\rho C_p R} \cdot \frac{1}{(1+\beta)}\right], \tag{5}$$

where $\beta = \left(\Delta H/\rho C_p\right)\left(\partial q^*/\partial T\right)_p$. A plot of $\log\left(1 - M_t/M_\infty\right)$ vs. t thus provides clear evidence concerning the nature of the rate limiting resistance and a convenient way to extract the time constant (R^2/D, $R/3k$, or $\rho C_p R/3h$).

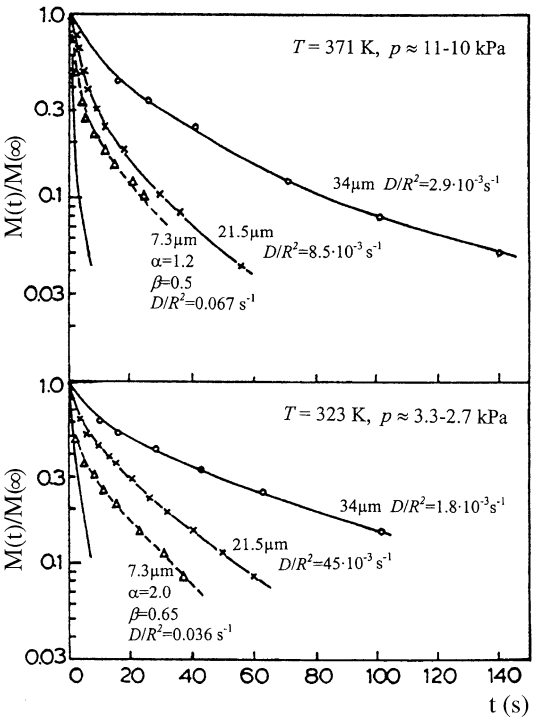

Fig. 2 Experimental uptake curves for CO_2 in 4A zeolite crystals showing near isothermal behavior in large (34 and 21.5 μm) crystals ($D \approx 9 \times 10^{-9}$ cm^2 s^{-1} at 371 K and 5.2×10^{-9} cm^2 s^{-1} at 323 K). The *solid lines* are the theoretical curves for isothermal diffusion from Eq. 2 with the appropriate value of D_c/r_c^2. The uptake curves for the small (7.3 μm) crystals show considerable deviation from the isothermal curves but conform well to the theoretical nonisothermal curves with the values of D_c estimated from the data for the large crystals, the value of β calculated from the equilibrium data, and the value of α estimated using heat transfer parameters estimated from uptake rate measurements with a similar system under conditions of complete heat-transfer control. The limiting isothermal curve is also shown by a *continuous line* with no points. From Ruthven et al. [8]

The apparent simplicity of this approach is, however, deceptive. For measurement of intracrystalline diffusion the method works well when diffusion is relatively slow (large crystals and/or low diffusivity), but when sorption rates are rapid the uptake rate may be controlled by extracrystalline diffusion (through the interstices of the adsorbent bed) and/or by heat transfer. The intrusion of such effects is not always obvious from the shape of the uptake curve, but it may generally be detected by changing the sample quantity and/or the sample configuration. It is in principle possible to allow for such effects in the mathematical model used to interpret the uptake curves (Fig. 2), and indeed the modeling of nonisothermal systems has been studied in considerable detail [8–12]. However, any such intrusion will obviously diminish the accuracy and confidence with which the intracrystalline diffusivities can be determined.

This technique may also be used to measure effective macropore diffusivities in biporous adsorbent pellets [13, 14]. For such a system with a linear equilibrium isotherm and assuming rapid intracrystalline diffusion, the governing diffusion equation is of the same form as for micropore control. The solution is identical to Eq. 1 except that R now refers to the particle radius and the diffusivity D is replaced by the effective diffusivity $D_e = D_p\varepsilon_p/\big(\varepsilon_p + (1 - \varepsilon_p)K\big)$. Since the equilibrium constant (K) is generally large and varies with temperature according to the van't Hoff equation ($K = K_o\, e^{-\Delta U/R_g T}$), it is clear that a macropore-controlled system will generally yield an effective diffusivity that is much smaller than the pore diffusivity and shows a strong (Arrhenius) form of temperature dependence but with an apparent activation energy that approximates the energy of adsorption. This may lead the unwary investigator to conclude that the rate is controlled by an activated (micropore) diffusion process, whereas in fact the effect results from the temperature dependence of the capacity of the microparticles. However, a change in the gross particle size can often be used to provide an unequivocal diagnosis of the nature of the controlling resistance.

With vapor phase gravimetric systems it is generally possible to achieve a good approximation to a step change in sorbate pressure, although for strongly adsorbed species this requires a large system volume and a very small adsorbent sample. For piezometric measurements and for liquid phase systems, however, the external concentration (or pressure) is the measured quantity, and to achieve accuracy it is therefore necessary to minimize the external system volume. In solving the diffusion equation, the time dependence of the boundary condition at the particle surface must then be considered, and this leads to a slightly more complex expression for the uptake curve. The piezometric method has been widely applied [15–23], but a detailed analysis of this technique (Sect. 2.2) reveals that the restrictions on the conditions required to obtain reliable diffusivity data by this method are in fact more severe than had been generally appreciated in the earlier studies.

In both gravimetric and piezometric experiments it is generally desirable to make the measurement over a small differential concentration change in order to ensure that the assumption of system linearity is fulfilled. Under these conditions the transient sorption curve (expressed as fractional approach to equilibrium) should be independent of either the step size or direction (adsorption or desorption). Varying the step size and direction thus provides a simple and sensitive experimental test for system linearity.

Uptake rate measurements with large oriented crystals have been used by Caro [24] to demonstrate the nonisotropy of silicalite. Diffusion coefficients for the longitudinal and transverse directions differed by a factor of about three.

An ingenious alternative to the gravimetric method has been developed by Karge and coworkers [25, 26], who tracked the progress of sorption by monitoring the intensity of an IR band characteristic of the adsorbed species. With a modern high sensitivity spectrometer this approach may be used to follow sorption rates in a single zeolite crystal. Furthermore, this method offers the important advantage that, by a judicious choice of the IR wavelength, it may be applied to follow sorption of one (or more) components in a multicomponent system (cf. Vol. 7, Chap. 4 of this series).

Regardless of the way in which progress of the sorption is followed, all uptake rate measurements are subject to the intrusion of heat transfer resistance, and such effects are more severe for strongly adsorbed and rapidly diffusing species. To circumvent this problem Grenier et al. [27] introduced

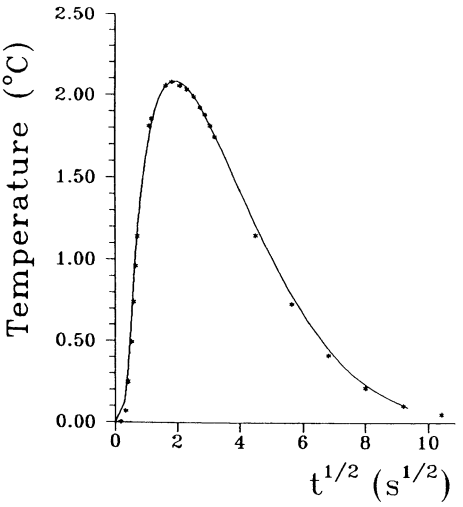

Fig. 3 Transient temperature response for CH_3OH – NaX, pressure step 48–80 Pa (step A, run 13) showing conformity between experimentally observed temperature and theoretical curve, calculated from diffusion model with $D_o = 2.6 \times 10^{-12}$ m^2 s^{-1}; $h = 2.3$ Wm^{-2} K^{-1}. From Grenier et al. [27]

a novel approach in which progress of the uptake is followed indirectly by monitoring the temperature of the adsorbent sample using a sensitive IR detector. A representative response curve is shown in Fig. 3. A nonisothermal model containing time constants for both heat transfer and diffusion is needed to interpret the experimental data. However, detailed analysis shows that the initial rising portion of the response curve is determined primarily by diffusion, while the long time region is determined mainly by heat transfer. Both the diffusion and heat-transfer parameters can therefore be determined with confidence, even from a single experimental response curve.

2.2 The Piezometric Method

The piezometric method involves following the pressure response in a dosing cell connected to an uptake cell containing a sample of the adsorbent. According to the results reported in the literature, the piezometric method can be used to accurately measure intracrystalline diffusivities for fast diffusing and strongly adsorbed species such as benzene on NaX [15, 16]. Furthermore, it is also claimed to provide the required accuracy needed to study combined intracrystalline processes such as diffusion and first-order reaction [17].

The analysis of the response curves is not as direct as for other methods, since we have to consider the flow through the valve connecting the two chambers. Furthermore, the time required to fully open the valve is typically 0.5–0.7 s. Qualitatively it is evident that the initial part of the response will be influenced by the flow through the valve, the opening of the valve, and the mass transfer to the solid, and it is therefore obvious that the initial portion of the response cannot be used to obtain reliable diffusional time constants. The final stages of the response are not affected by the initial opening of the valve, and the pressure difference across the valve becomes very small. Qualitatively it can be argued that useful diffusion information can be obtained from the long time region of the response curve. However, it has been clearly shown that this portion of the response curve is strongly affected by heat effects [8–12]. It follows from this observation that the ability of the piezometric method to yield reliable intracrystalline diffusivity values is constrained, especially for fast diffusing and strongly adsorbed species. Such considerations have been ignored by Bülow and Micke [18], who simply suggest a total curve fitting procedure using a numerical solution of the isothermal model equations.

Even if isothermal behavior is assumed, there are still serious restrictions on the range of applicability of the method. Considering an instantaneous opening of the valve and linearizing the model equations it is possible to derive a simple analytic solution for the dimensionless pressure in the dosing

and uptake cells [23].

$$\frac{\rho_d}{\rho_d^o} = \frac{3\delta}{1+3\delta+3\gamma} + \sum_{i=1}^{\infty} a_i \exp\left(-\beta_i^2 \tau\right) , \tag{6}$$

$$\frac{\rho_u}{\rho_d^o} = \frac{3\delta}{1+3\delta+3\gamma} + \sum_{i=1}^{\infty} a_i \left(1-\beta_i^2/w\right) \exp\left(-\beta_1^2 \tau\right) , \tag{7}$$

where:

$$a_i = \frac{2w^2\delta\beta_i^2}{2w^2\delta\beta_i^2 + \left(w-\beta_i^2\right)^2\left(\beta_i^2 + z_i^2 - z_i + 2\gamma\beta_i^2\right)} \tag{8}$$

and β_i are the positive nonzero roots of

$$\beta_i \cot \beta_i - z_i = 0 . \tag{9}$$

The dimensionless variables are defined as follows:

$$z_i = 1 + \gamma\beta_i^2 + \frac{w\delta\beta_i^2}{w-\beta_i^2}; \quad y = \frac{1}{3}\frac{V_u}{KV_s}; \quad \delta = \frac{1}{3}\frac{V_d}{KV_s}; \quad w = \frac{RgT\,\overline{\chi}D}{V_d R^2}; \tag{10}$$

$$\overline{\chi} = \text{Valve Constant}, \quad \rho_d = \frac{P_d - P_u^o}{P_\infty - P_u^o}, \quad \rho_u = \frac{P_u - P_u^o}{P_\infty - P_u^o} .$$

The subscripts u and d refer to the uptake and dosing volumes (V_u and V_d), respectively.

The dimensionless parameters defined in Eq. 10 clearly show that the response is influenced by the ratios of the accumulation in the fluid and solid phase, γ and δ, and the ratio of the time constants for the valve and for the diffusion process, w. The ratio δ/γ depends on the geometric configuration of the system and has a typical value of 1.5 [16].

Representative response curves for the dosing and uptake cells, calculated from Eqs. 6–10, are shown in Fig. 4. The system response depends strongly on both the adsorption equilibrium and the time constant of the valve. If the value of w is large, the pressure in the two cells equilibrates rapidly followed by a slow decay to the final equilibrium level. The rate of this process is controlled by diffusion into the adsorbent. If w is small, the system is close to equilibrium control; the rate controlling process is then the flow through the valve, and no useful kinetic data can be derived from the response. Under both equilibrium and kinetic control the pressure in the dosing cell shows a monotonic decline to the equilibrium value. However, the pressure response in the uptake cell is much more sensitive to the nature of the rate controlling process. Under conditions approaching equilibrium control the pressure increases monotonically, whereas under kinetic control the pressure passes through a maximum before declining to the equilibrium level.

Unfortunately, in many of the earlier reported applications of this technique, only the pressure in the dosing cell was measured. This greatly reduces

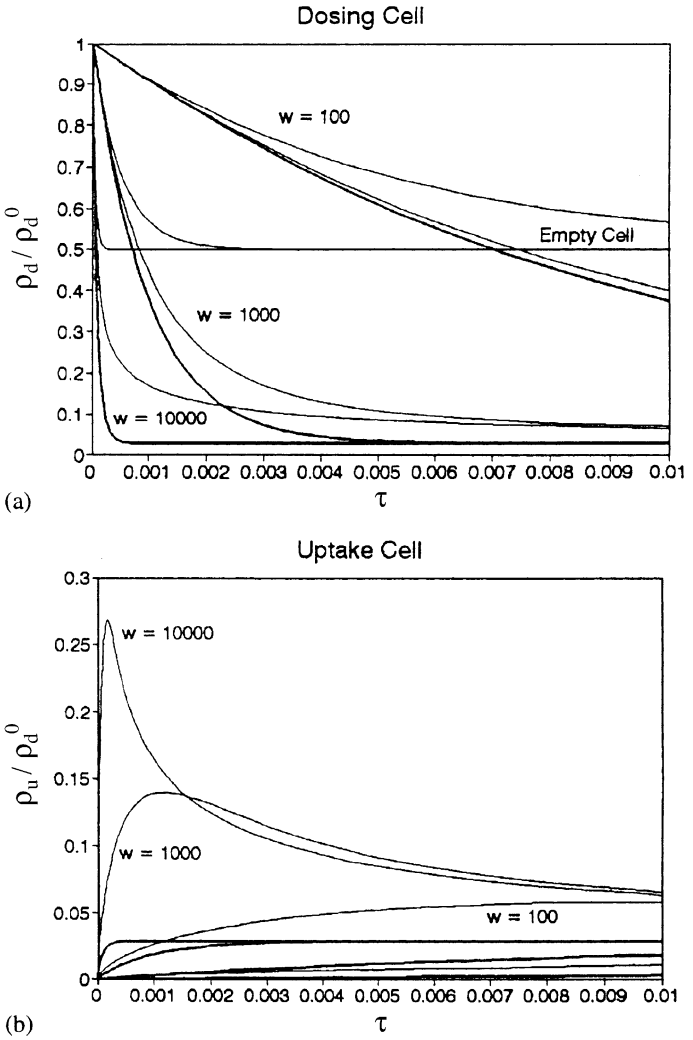

Fig. 4 Theoretical piezometric response curves for **a** the dosing cell and **b** the uptake cell, calculated from Eqs. 6–9 with $\gamma = \delta = 0.01$ and various values of parameter w. The curves corresponding to equilibrium control are shown by *heavier lines*. From Brandani [23] with permission

the sensitivity of the technique and the reliability of the derived diffusivities. For example, Bülow et al. studied in detail the adsorption of benzene in large (120 μm) crystals of NaX [16] and reported intracrystalline diffusivities close to the self-diffusivities obtained from PFG NMR measurements. However, detailed analysis shows that, under the experimental conditions, the system must have been very close to equilibrium control so, regardless of the method of data analysis, no reliable diffusivity data could have been obtained.

A very similar analysis of the piezometric method has been reported by Schumacher et al. [19], who also concluded that, for the reliable application of this technique, it is essential to monitor the sorbate pressure in the uptake cell rather than in the dosing cell. Schumacher and Karge [20–22] have used this approach to study the sorption of the monoalkyl benzenes and diethyl benzene in ZSM-5. For all systems the measured differential diffusivities (D) increased regularly with loading up to near the saturation limit, followed by a sharp decline as saturation was reached. The thermodynamically corrected diffusivities (D_o) calculated from Eq. 1 are essentially constant over a wide range of loading. Representative data for ethyl benzene at several temperatures are shown in Fig. 5 [20]. These results are consistent with recent tracer ZLC measurements that, for p-xylene and benzene in silicalite, show essentially constant self-diffusivities over a wide range of loading [28].

We conclude that the piezometric technique is capable of yielding reliable diffusivity data provided that the pressures are monitored in the uptake cell and the limitations imposed by the time constant of the valve and finite heat dissipation rates are respected. For strongly adsorbed species theses restrictions limit the applicability to relatively slow processes (half times of at least several seconds). For weakly adsorbed species somewhat faster diffusion processes can be measured. A detailed assessment of the range of validity of this method, as a function of the system variables, has been presented by Schumacher and Karge [19]. In reviewing earlier reported piezometric diffusivity data, the values derived from measuring only the pressure in the dosing cell should not be accepted without further detailed analysis.

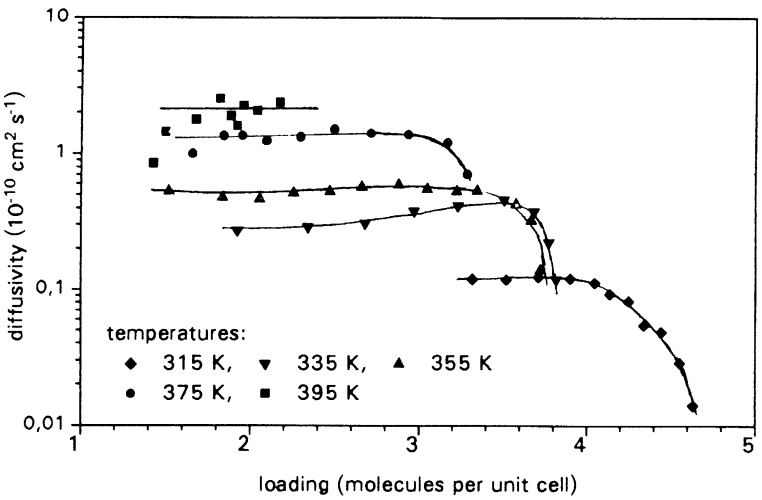

Fig. 5 Loading dependence of corrected diffusivities (D_o) for ethylbenzene in H-ZSM-5 at various temperatures, measured by piezometric technique. From Schumacher et al. [20] with permission

2.3 Frequency Response

In the frequency response method, first applied to the study of zeolitic diffusion by Yasuda [29] and further developed by Rees and coworkers [2, 30–33], the volume of a system containing a widely dispersed sample of adsorbent, under a known pressure of sorbate, is subjected to a periodic (usually sinusoidal) perturbation. If there is no mass transfer or if mass transfer is infinitely rapid so that gas–solid mass-transfer equilibrium is always maintained, the pressure in the system should follow the volume perturbation with no phase difference. The effect of a finite resistance to mass transfer is to cause a phase shift so that the pressure response lags behind the volume perturbation. Measuring the "in-phase" and "out-of-phase" responses over a range of frequencies yields the characteristic frequency response spectrum, which may be matched to the spectrum derived from the theoretical model in order to determine the time constant of the mass-transfer process. As with other methods the response may be influenced by heat-transfer resistance, so to obtain reliable results, it is essential to carry out sufficient experimental checks to eliminate such effects or to allow for them in the theoretical model. The form of the frequency response spectrum depends on the nature of the dominant mass-transfer resistance and can therefore be helpful in distinguishing between diffusion-controlled and surface-resistance-controlled processes.

However, the argument that the cyclic nature of the perturbation eliminates the intrusion of heat effects must be treated with caution. For both p-xylene and 2-butyne in silicalite Shen and Rees [31, 32] observed a bimodal response spectrum and they interpreted the two peaks as indicative of two different transport processes corresponding to diffusion through the straight and sinusoidal channels. There is some NMR evidence to support the view that such molecules cannot easily reorient themselves at the channel intersections, and for silicalite-2, which contains only straight channels of similar dimensions, only a single response peak is observed; so this hypothesis is certainly plausible. However, Sun and Bourdin [34] have shown that an alternative explanation is also possible. If the heat balance equations are included in the theoretical model, the predicted response assumes a bimodal form and the heat-transfer parameter required to match the experimental data appears to be quite reasonable.

In a recent development of the frequency response technique Bourdin et al. applied the frequency response approach to their IR temperature measurement system [35–37]. In this experiment the volume of the system is perturbed sinusoidally and both the pressure and temperature responses are measured. It was found that the phase differences between the pressure and temperature were more reliable and reproducible than the phase differences between the pressure and the volume. The explanation seems to be that since the quantity of adsorbent is quite small, a small amount of superficial adsorp-

tion on the walls of the apparatus can distort the phase relationship between the pressure and the volume but will not affect the temperature–pressure phase relationship. In light of this observation there may be a need to reexamine some of the earlier FR results that were derived from measurements of the phase difference between the driver piston and the pressure response (cf. also Chap. 6 of this volume).

2.4 Chromatographic Measurements

For fast diffusing systems the limitations imposed by extracrystalline resistances to mass and heat transfer make it impossible to derive reliable intracrystalline diffusivity values from direct sorption rate measurements, regardless of the technique used to follow the uptake. Since both heat and mass transfer are enhanced in a flow system, the possibility of deriving reliable diffusion values from measurements of the dynamic response of a packed adsorption column has attracted considerable attention. The early models for mass-transfer resistance in a chromatographic column were based on the equilibrium stage concept. The Kubin–Kucera model [38, 39], by showing the relationship between the height equivalent to a theoretical plate (HETP) and the diffusional time constant, provided the essential theoretical basis for the chromatographic approach to the measurement of intraparticle diffusivities. The generalization to biporous particles was provided by Sarma and Haynes [40].

The chromatographic response is conveniently analyzed in terms of the first and second moments of the pulse response:

$$\mu \equiv \frac{\int_0^\infty ct\,\mathrm{d}t}{\int_0^\infty c\,\mathrm{d}t} = \frac{L}{V}\left[1 + \left(\frac{1-\varepsilon}{\varepsilon}\right)K\right], \tag{11}$$

where, for a composite particle:

$$K = \varepsilon_\mathrm{p} + \left(1-\varepsilon_\mathrm{p}\right) wK_\mathrm{C}\,, \tag{12}$$

$$\sigma^2 = \frac{\int_0^\infty \left(t-\mu\right)^2\,\mathrm{d}t}{\int_0^\infty c\,\mathrm{d}t}\,, \tag{13}$$

$$\mathrm{HETP} \equiv \frac{\sigma^2}{\mu^2}L \tag{14}$$

$$= 2\frac{D_\mathrm{L}}{v} + \frac{2\varepsilon v}{(1-\varepsilon)}\left[\frac{R}{3k_\mathrm{f}} + \frac{R^2}{15\varepsilon_\mathrm{p}D_\mathrm{p}} + \frac{r_\mathrm{c}^2}{15KD_\mathrm{c}}\right]\left[1 + \frac{\varepsilon}{(1-\varepsilon)K}\right]^{-2}.$$

It is evident that the HETP measures only the overall resistance to mass transfer and cannot provide evidence concerning the nature of this resistance. The chromatographic response is indeed remarkably insensitive to differences in

the nature of the mass-transfer resistance, so regardless of the way in which the data are analyzed, it is not possible to obtain any such information except by varying critical parameters such as the particle size.

The major difficulty in the analysis of chromatographic data is separating the axial dispersion and mass-transfer contributions since, except for gaseous systems at very low flow rates, the axial dispersion coefficient (D_L) is velocity dependent. For liquid systems D_L varies essentially linearly with velocity so a plot of HETP vs. superficial velocity (εv) should be linear with the mass-transfer resistance directly related to the slope (Fig. 6). For gaseous systems at a high Reynolds number this same plot can be used, but in the low Reynolds number region a plot of H/v vs. $1/v^2$ may be more convenient since in this region D_L is essentially constant and the intercept thus yields the mass-transfer resistance [43–45].

In the application of the chromatographic method to the measurement of intracrystalline diffusivity it is preferable to pack the column directly with unaggregated crystals rather than with composite (pelleted) material since this eliminates the possible intrusion of macropore resistance. The small crystal size of commercial zeolite samples presents a significant practical problem. Early attempts to utilize a column packed directly with such crys-

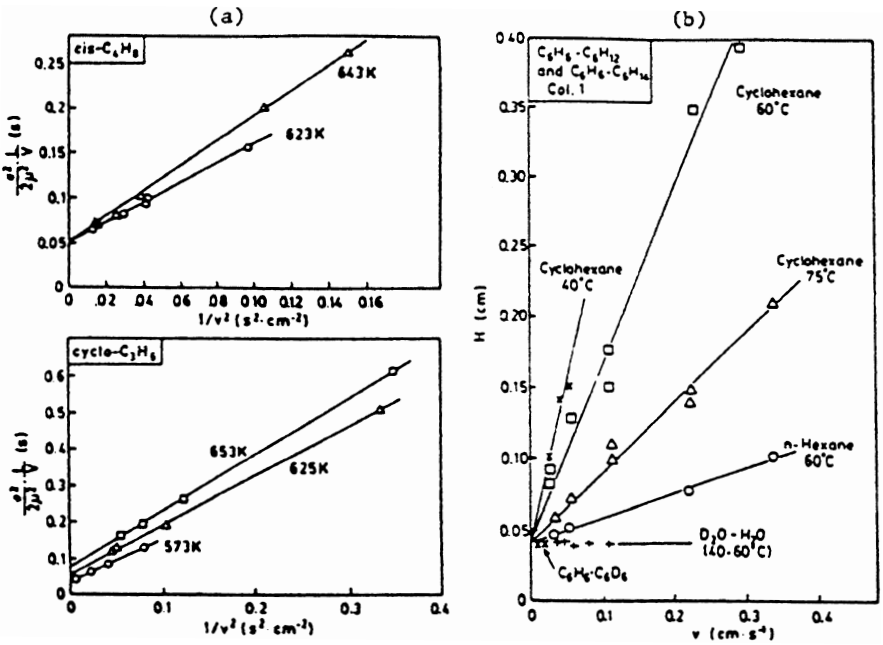

Fig. 6 Chromatographic HETP data. **a** Plots of $H/2v$ vs. $1/v^2$ for *cis*-butene and cyclopropane in 5A zeolite. From Haq and Ruthven [47]. **b** Plots of H vs. v for benzene/*n*-hexane in NaX (40 μm crystals). Note that the axial dispersion term ($2D_L/v \approx 0.04$ cm) is essentially the same for $C_6H_6 - C_6D_6$ and for $H_2O - D_2O$. From Awum et al. [44]

tals were not very successful. Erroneously small apparent diffusivities were obtained, probably reflecting the anomalously high axial dispersion that is observed in beds of very small particles due to the tendency of such particles to form agglomerates. Columns packed with large synthetic crystals work well [46], and this approach has the advantage that the use of large crystals increases the relative importance of the diffusional resistance (the second term on the right-hand side of Eq. 14), thus minimizing the impact of any errors in the estimation of the axial dispersion. However, this approach obviously precludes the use of small commercial crystallites. Small commercial crystallites have, however, been successfully applied in the form of a wall-coated column [47], and this may be the best approach when larger crystals are not available.

2.5
Zero Length Column (ZLC) Method

The zero length column (ZLC) technique may be regarded either as a flow variant of an uptake rate measurement or as a variant of the chromatographic method using an infinitesimal column. This has the important advantage that the intrusion of axial dispersion is eliminated. The technique depends on following the desorption of sorbate from a previously equilibrated (small) sample of adsorbent into an inert carrier stream. This approach was introduced, for gas phase adsorption systems, in the late 1980s by Eic and Ruthven [48, 49], and since then it has found widespread application as a simple and relatively inexpensive way of measuring limiting diffusivities for hydrocarbons and other simple molecules in zeolites and other microporous adsorbents [1]. The method has been extended to the measurement of counterdiffusion in liquid phase adsorption systems by Ruthven and Stapleton [50]. A variant of the technique, tracer ZLC or TZLC, has also been developed to allow the measurement of self-diffusivities over the entire range of sorbate loadings [51]. These developments have been summarized in a recent review [52].

An experimental setup for gaseous systems is shown in Fig. 7. The actual ZLC column consists of a thin layer of adsorbent material placed between two porous sinter discs. The individual particles (or crystals) are dispersed approximately as a monolayer across the area of the sinter. This minimizes the external resistances to heat and mass transfer, so that the adsorption cell can be considered as a perfectly mixed isothermal, continuous-flow cell. The validity of this assumption has been examined in detail [52]. The isothermal approximation is generally valid for studies of diffusion in zeolite crystals, but it can break down for strongly adsorbed species in large composite particles under conditions of macropore diffusion control.

Brandani and Ruthven [53] have derived the solution for the general model that accounts for the capacity of the fluid phase as well as that of the

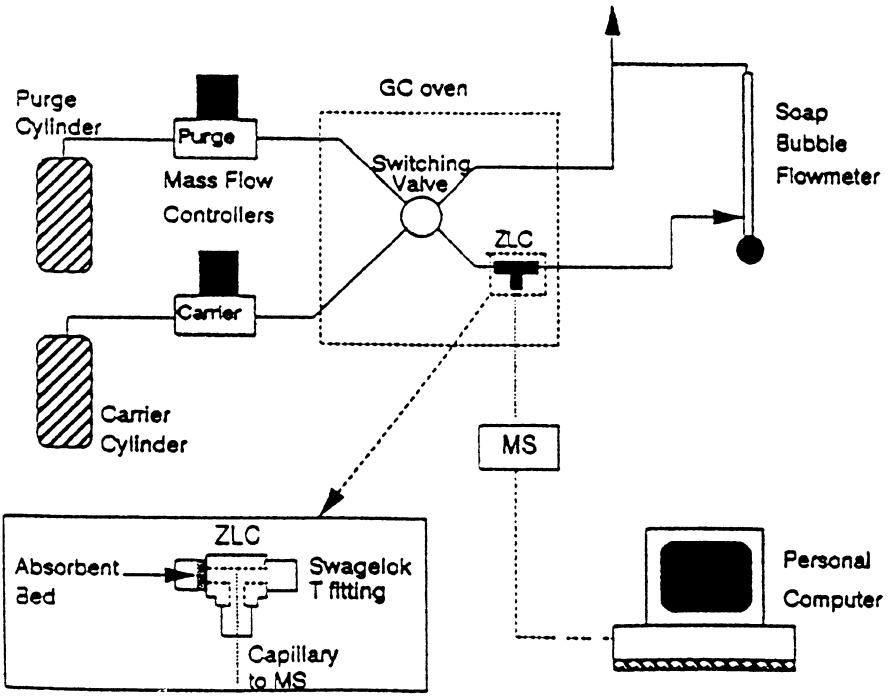

Fig. 7 Experimental system for vapor phase ZLC or TZLC measurements

adsorbent:

$$\frac{c(t)}{c_0} = \sum \frac{2L}{\beta_n^2 + (1 - L + \gamma\beta_n^2)^2 + L - 1 + \gamma\beta_n^2} \exp\left(-\beta_n^2 \frac{D}{R^2} t\right), \tag{15}$$

where the β_n are the positive roots of:

$$\beta_n \cot \beta_n + L - 1 - \gamma\beta_n^2 = 0, \tag{16}$$

with

$$L = \frac{1}{3} \frac{F}{KV_s} \frac{R^2}{D}; \quad \gamma = \frac{1}{3} \frac{V_f}{KV_s}. \tag{17}$$

Clearly, the parameter γ is of the order of $1/K$. Therefore, the limiting case $\gamma = 0$ provides a very useful approximation for gaseous systems where the holdup in the fluid phase can generally be neglected in comparison with the adsorbed phase accumulation. In this situation, Eq. 15 reduces to:

$$\frac{c}{c_0} = 2L \sum \frac{\exp\left(-\beta_n^2 \frac{D}{R^2} t\right)}{\beta_n^2 + L(L-1)}, \tag{18}$$

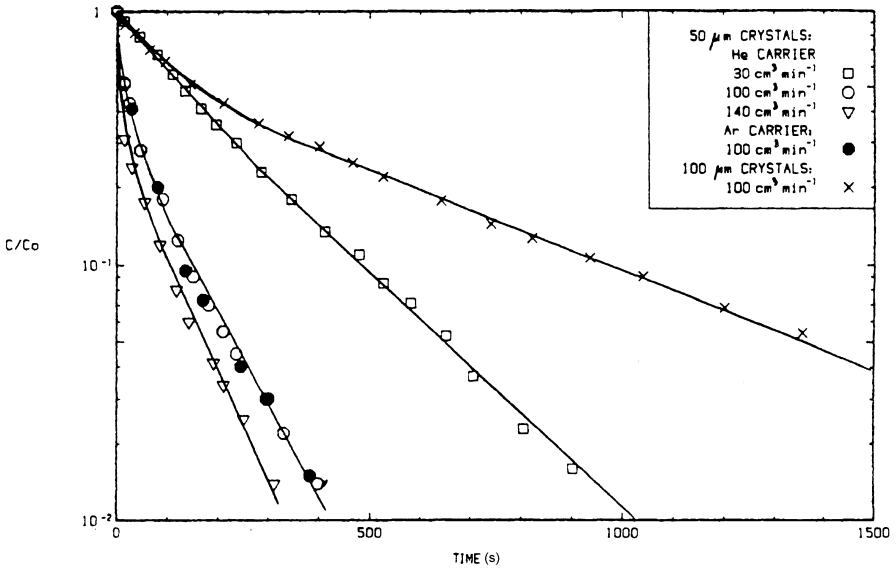

Fig. 8 Experimental ZLC response curves for *o*-xylene on NaX zeolite crystals (50 μm and 100 μm) showing effects of purge flow rate and composition (He or Ar) and zeolite crystal size. From Ruthven and Eic [49]

which is the form obtained from the original ZLC model [48, 49]. It has been shown that Eq. 18 can be used with confidence for $\gamma < 0.1$. This model for gas phase adsorption systems has been studied in detail by Brandani and Ruthven [54]. Representative experimental ZLC response curves showing the effects of changes in flow rate, crystal size, and purge composition are shown in Fig. 8.

Most of the experimental applications of the ZLC technique have been with gaseous systems, and for these systems the technique may now be regarded as a standard method. Based on our experience it is possible to suggest some guidelines as to how the experiments should be carried out. The key parameter is L, which from its definition (Eq. 17) can be considered the ratio of the diffusional and washout time constants: R^2/D and KV_s/F. This parameter is also equal to the dimensionless adsorbed phase concentration gradient at the surface of the solid at time zero.[1] From either of these definitions it is evident that L gives an indication of how far removed the system is from equilibrium control. This parameter is proportional to the flow rate, so it can be easily varied, and to extract a reliable time constant, it is necessary to run the experiment at at least two different flow rates.

[1] From the column mass balance $\frac{KV_s}{\bar{q}_0}\frac{d\bar{q}}{dt} = -F\frac{c}{c_0}$ it is possible to obtain $\frac{3KV_sD}{R^2}\left(\frac{\partial Q}{\partial \xi}\right)_{\xi=1} = -F\frac{c}{c_0}$ and $\left(\frac{\partial Q}{\partial \xi}\right)_{\xi=1}^{t=0} = -L$.

A major advantage of the ZLC method is that, for any particular system, the validity of the basic assumptions under the experimental conditions can be verified directly by a series of simple experimental tests. To establish the validity of the zero length limit, measurements are repeated with columns containing different amounts of adsorbent (Fig. 9). To exclude external mass-transfer resistances, experiments may be run with two different carrier gases, typically argon and helium (Figs. 8 and 9). Heat effects can be minimized using high flow rates and system linearity can be checked varying the inlet composition.

If $L > 10$, the time constant can be easily extracted from the long time asymptote where Eq. 18 reduces to:

$$\frac{c}{c_0} = 2L\frac{\exp\left(-\beta_1^2\frac{D}{R^2}t\right)}{\beta_1^2 + L(L-1)}. \tag{19}$$

A semilog plot of the dimensionless concentration yields L and D/R^2 from the intercept and slope. For $L > 10$ the slope should remain constant. Problems can be encountered if the accuracy of the measuring device is limited or if the experimental conditions are beyond the range of the Henry law limit. For hydrocarbons a FI detector is typically used and ensures high accuracy. It can be argued qualitatively that, even if the initial concentration is in the nonlinear part of the equilibrium curve, the concentration in the solid will eventually fall to a value at which the linearity assumption is valid and the long time asymptote should therefore still yield reliable information on the diffusional time constant. If this asymptote can be measured, the slope should always increase with the flow rate. Since the ZLC response is determined primarily by the limiting behavior at low concentration, the method is not well suited for determining the concentration dependence of diffusivity from integral measurements.

Although the ZLC technique was originally developed for the measurement of intracrystalline diffusion, it may also be applied to measure macropore diffusion in composite adsorbent particles [56].

There remains the question of whether the desorption rate is controlled by intracrystalline diffusion or by surface resistance. It is possible to distinguish between these two situations through a partial loading experiment. The preconditioned adsorbent is exposed to the carrier stream containing the sorbate for a short period, but allowing sufficient time to approach equilibrium in the adsorbed phase, before the flow is switched to the pure purge stream. The resulting ZLC response curve is compared with the curve obtained, under the same conditions, for a fully equilibrated sample. For a surface-resistance-controlled system the transient concentration profile through the crystal is flat, even under partial loading conditions, so the response curve, plotted as c/c_0 vs. $\ln t$ should remain the same under partial loading conditions as for a fully equilibrated sample. In contrast,

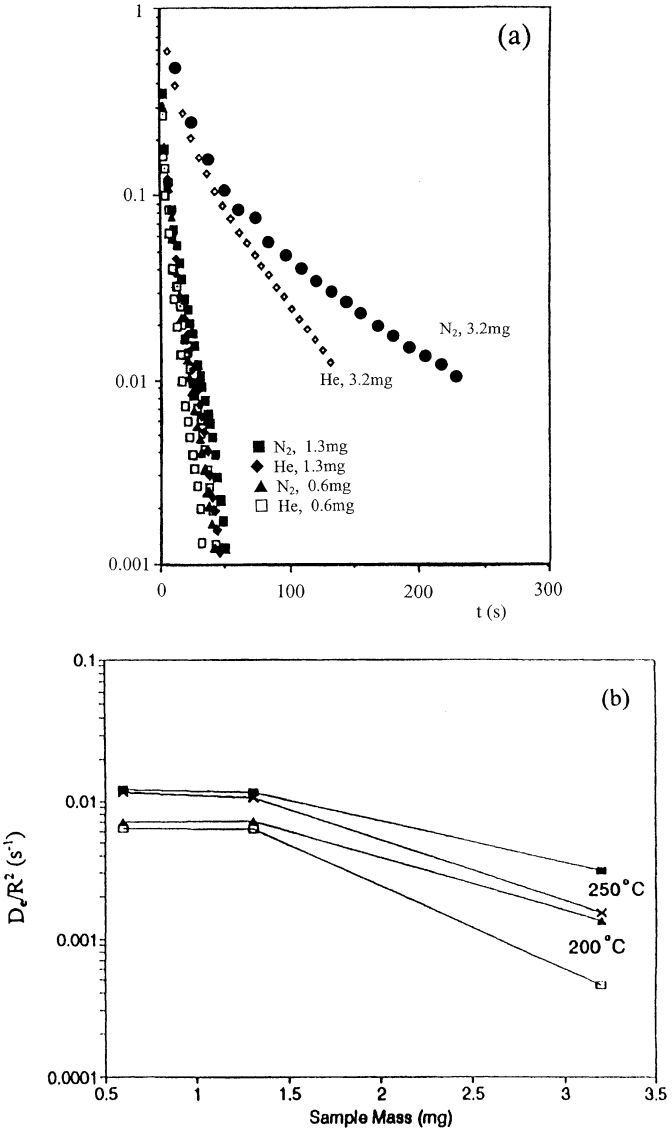

Fig. 9 Effect of sample quantity and nature of purge gas on ZLC response curves for benzene in 50-μm crystals of NaX zeolite at 250 °C. **a** Desorption curves. Note that when the sample is sufficiently small, desorption is rapid and the curves for He and N_2 purge coincide, but for a larger sample we see slower desorption with a significant difference between the curves for He and N_2, indicating the intrusion of external diffusional resistance. **b** Apparent diffusional time constants showing the variation with sample mass. *Filled symbols* denote He purge, *open symbols* denote N_2 purge. Note that when the sample mass is sufficiently small, the time constants for He and N_2 become coincident and independent of sample mass, showing the absence of external diffusional resistance. From Brandani et al. [55]

for a diffusion-controlled system, as a result of the nonuniform initial profile the ZLC response will show a larger intercept under partial loading conditions. The theory has been discussed by Brandani and Ruthven [54] in relation to a detailed study of the desorption of propane from large (100 μm) crystals of NaX that showed clear evidence of intracrystalline diffusion control.

A further issue concerns the possible intrusion of heat effects. This issue has been addressed both theoretically and experimentally [52, 57], and a simple criterion for the validity of the isothermal approximation was developed. The isothermal assumption is normally valid for measurements with zeolite crystals (< 150 μm), but for large macroporous particles some intrusion of heat-transfer effects can be anticipated when the heat of adsorption is large.

In tracer ZLC (TZLC) [28, 51, 58] the experiment is similar to the standard method, but the monitored species is the deuterated form of the sorbate. This introduces an additional cost for the material and the requirement for an online mass spectrometer. The advantages are the elimination of all possible heat effects, strict linearity of the equilibrium between the fluid phase and the adsorbed phase, and the possibility of measuring directly the tracer diffusivities (which should be the same as the microscopically measured self-diffusivity) over a wide range of loading. To reduce the costs the carrier is prepared with a mixture of pure and deuterated hydrocarbons. It has been shown that small imbalances in the concentration of the carrier and the purge streams do not affect the desorption dynamics [58].

2.6 Temporal Analysis of Products (TAP)

The TAP reactor system was originally developed to allow the rapid analysis of products from a fast catalytic reaction [59]. A small pulse of the reactant gas is injected at the inlet of a fixed bed of zeolite crystals through which it is drawn by pulling a vacuum at the bed outlet where the reaction products are detected by an online mass spectrometer. The time dependence of the pulse response is a function of *inter alia* the rate of diffusion within the zeolite crystals. However, the sensitivity of the response to intracrystalline diffusion depends critically on the relative magnitudes of the other mass-transfer processes involved. Recent applications of this technique to study the diffusion of linear alkanes in MFI zeolites have led to conflicting results. Keipert and Baerns [60] concluded that, for *n*-butane and *n*-hexane in silicalite, reliable measurements of intracrystalline diffusion could not be made because, for these sorbates, the intracrystalline resistance is smaller than the extracrystalline resistances. Diffusion of *n*-butane in silicalite was also studied by Nijhuis et al. [61], who under similar conditions reported diffusivities of order 10^{-9} m^2 s^{-1}. However, a detailed review of these data shows that the response times scale directly with the Henry's Law constants, suggest-

ing that the sorption kinetics must have been controlled by extracrystalline diffusion [62]. Therefore, in conformity with the conclusion of Keipert and Baerns, it would not have been possible to make reliable measurements of intracrystalline diffusion under these conditions.

2.7 Membrane Measurements

Measurement of the flux through a zeolite crystal membrane under well-defined conditions of sorbate pressure on the high- and low-pressure faces provides an intrinsically attractive approach to the measurement of intracrystalline diffusion. However, in practice this approach is not at all straightforward. The earliest attempts were by Wernick and Osterhuber [63] and Paravar and Hayhurst [64]. Both these groups made their membrane from a single large zeolite crystal held in a small hole and sealed with epoxy. Wernick and Osterhuber studied diffusion of butane in NaX while Paravar and Hayhurst studied light paraffins in silicalite. Both used the quasi-steady-state mode of operation in which a relatively high sorbate pressure is maintained on one side of the crystal with a vacuum on the other side. The flux is then deter-

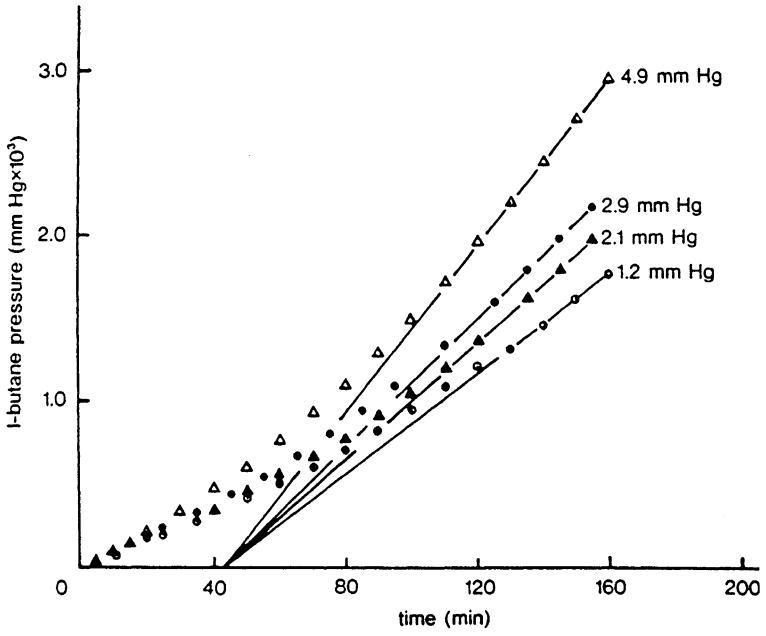

Fig. 10 Permeability measurement through a single (100 μm) crystal of silicalite (*i*-butane at 334 K). Note asymptotic approach to same intercept regardless of pressure. This implies that the diffusivity is independent of concentration over the relevant range. From Paravar and Hayhurst [64]

mined from the rate of pressure increase on the low-pressure side. The form of the pressure response is shown in Fig. 10. The initial transient leads to a time delay, while in the long time region a linear asymptote of pressure vs. time is approached. Values for the diffusivity can be derived from both the slope and intercept of such plots, and the consistency of these two values provides a check on the validity of the measurements. The main problem with this approach is associated with the difficulty of properly mounting the small crystal and ensuring that the active faces are not blocked by stray epoxy. More recent measurements of this kind have been reported by Talu et al. [65], while similar measurements with a composite silicalite crystal membrane grown on a stainless-steel support have been reported by Kapteijn et al. [66].

2.8 Effectiveness Factor

For a first-order reaction in spherical catalyst particles the effectiveness factor (and hence the observed reaction rate constant) depends on the Thiele Modulus ($\phi \equiv R\sqrt{k/D}$), which is in essence the square root of the ratio of the time constants for reaction and diffusion. Then, the effectiveness factor is:

$$\eta = \frac{3}{\phi}\left[\frac{1}{\tan h\phi} - \frac{1}{\phi}\right]. \tag{20}$$

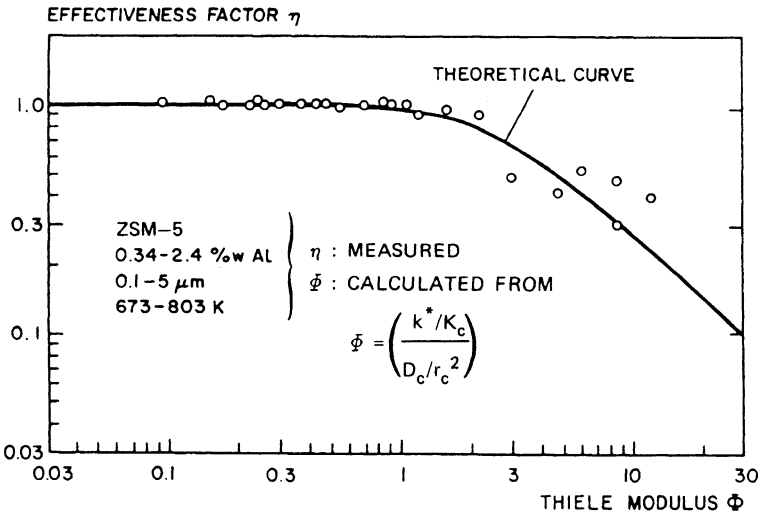

Fig. 11 Experimental verification of Thiele analysis as applied to intracrystalline diffusion control of catalytic reaction of 2,2-dimethylbutane in H-ZSM-5 catalysts. *Open symbols* are from Post et al. [68], *filled symbols* are from Haag et al. [67], duly corrected to adsorbed phase basis. From Post et al. [68]

For sufficiently small particles $\phi \to 0$ and $\eta \to 1$, so the measured rate constant approaches the intrinsic rate constant (k). By making replicate measurements under similar conditions, with different particle size fractions it is possible to determine both the intrinsic rate constant and the effective interparticle diffusivity. Haag [67] suggested that this approach could be used to determine intracrystalline diffusivities in zeolite crystals. A more complete experimental study in which the diffusivity of 2,2-dimethyl butane in HZSM-5 was determined both chromatographically and from measurements of the cracking rate under diffusion-limited conditions was reported by Post et al. [68] – see Fig. 11. This approach has the advantage that it makes steady-state rather than transient measurements, but it is limited to sorbates for which a suitable catalytic reaction occurs.

3
Review of Experimental Diffusivity Data for Selected Systems

The techniques outlined above have been used to study diffusion in a wide range of zeolite systems. In general we find that there is reasonable agreement between the different macroscopic methods and also between the microscopic methods (QENS, and PFG NMR). However, although for several systems the macroscopic and microscopic measurements are also consistent, there are many systems for which we see significant discrepancies between the two classes of measurements.

3.1
Systems Showing Consistent Behavior

Benzene–Silicalite [69]
Diffusion of benzene in silicalite has been studied by several different macroscopic techniques with broadly consistent results (Fig. 12). However, diffusion in this system is too slow to allow reliable PFG NMR measurements so no comparison between micro and macro techniques is possible.

Xe, $CO_2C_3H_8$, nC_4H_{10}-5A
The consistency between sorption rate measurements and PFG NMR measurements in large crystals of 5A zeolite was noted many years ago. In more recent studies a similar pattern of consistency between sorption rate, ZLC, and PFG NMR data has been observed for Xe, CO_2, and C_3H_8 in 5A zeolite (Fig. 13).

CH_3OH-NaX [71]
This system has been studied by ZLC, tracer ZLC, and infrared temperature-rise measurements as well as by PFG NMR, with striking consistency between

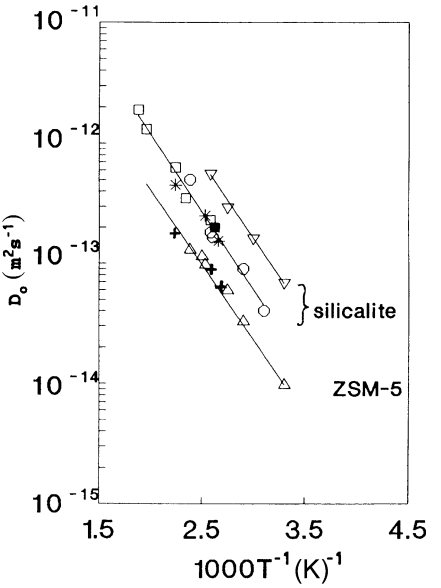

Fig. 12 Comparison of corrected diffusivity of benzene in silicalite-1 and H-ZSM-5 at low sorbate concentrations. □ Van Den-Begin et al., square wave; ○ Eic and Ruthven, ZLC; △, ▽ Zikanova et al., piezometric; ∗ silicalite-1, + H-ZSM-5, SSFR; ■ NMR tracer exchange. From Shen and Rees [69]

the reported results (Fig. 14). It is notable that diffusion rates in this system are as fast as or even faster than in most of the systems for which discrepancies are found.

3.2 Systems Showing Discrepancies Between Micro and Macro Measurements

Propane, Propene – NaX [58]

The recently reported tracer ZLC data for propane and propene in NaX show a similar discrepancy and for these systems there is evidently a clear difference in the trend of diffusivity with sorbate loading, as well as in the order of magnitude of the diffusivity values (Fig. 15a).

Aromatics – NaX

The striking discrepancy between the results of sorption rate measurements with large (100 μm, 250 μm) crystals, and the PFG NMR data for the xylenes in NaX was pointed out in 1989 [72]. The behavior of benzene in NaX is similar [55]. Diffusion of benzene is about an order of magnitude faster than the xylenes, and direct derivation of diffusivities from uptake rate measurements is therefore possible only over a very limited range of conditions. This system

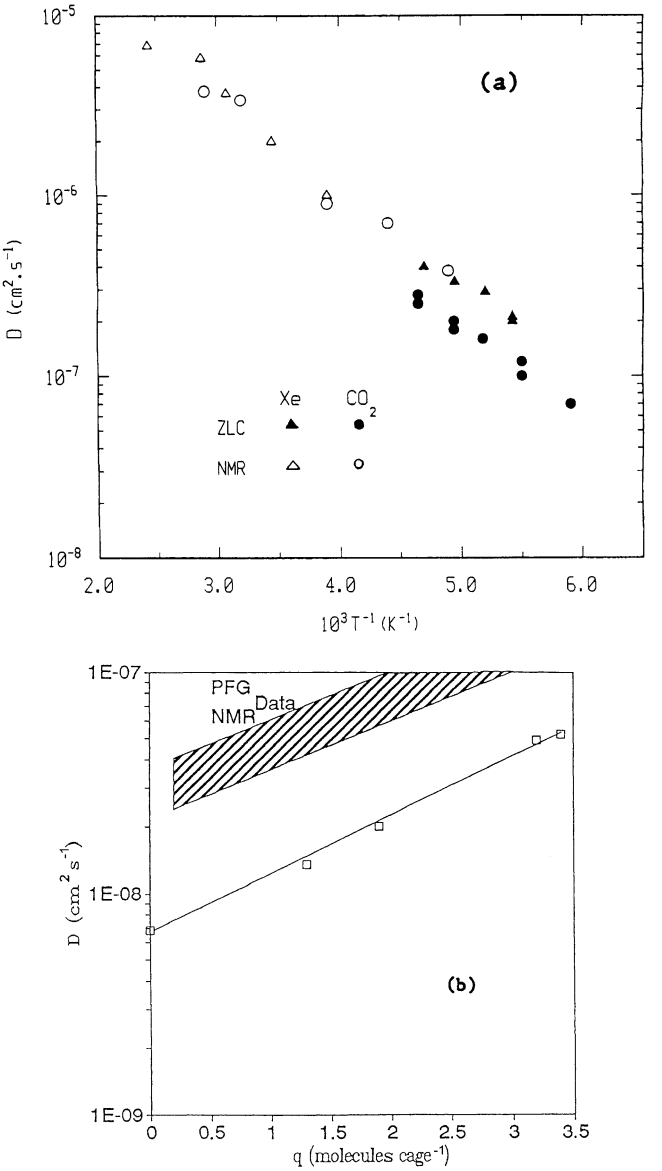

Fig. 13 Comparison of PFG NMR and ZLC diffusivities for **a** Xe and CO_2 in 5A zeolite [70]; **b** Propane in 5A zeolite [51]

has, however, been studied in great detail by FR and by the ZLC and tracer ZLC methods, all of which yield diffusivities that are quite consistent with lower-temperature sorption rate measurements but substantially smaller than the PFG NMR values (Fig. 15b).

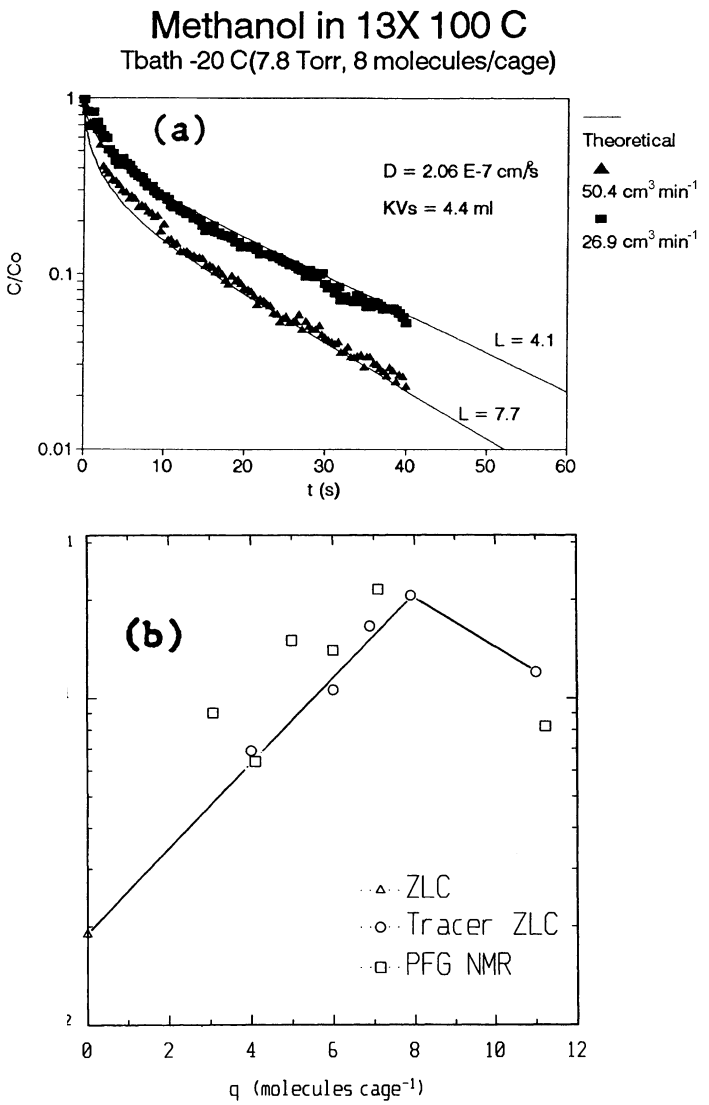

Fig. 14 Diffusion of methanol in NaX zeolite crystals at 100 °C. **a** Tracer ZLC response curves. **b** Variation of self-diffusivity with loading showing comparison of ZLC and PFG NMR data. From Brandani et al. [71]

Propane – $AlPO_4$-5 [73]

There has recently been much interest in the phenomenon of single file diffusion, which occurs in a unidimensional pane system when the diffusing molecules are too large to pass one another. In this situation the mean square displacement increases in proportion to the square root of elapsed

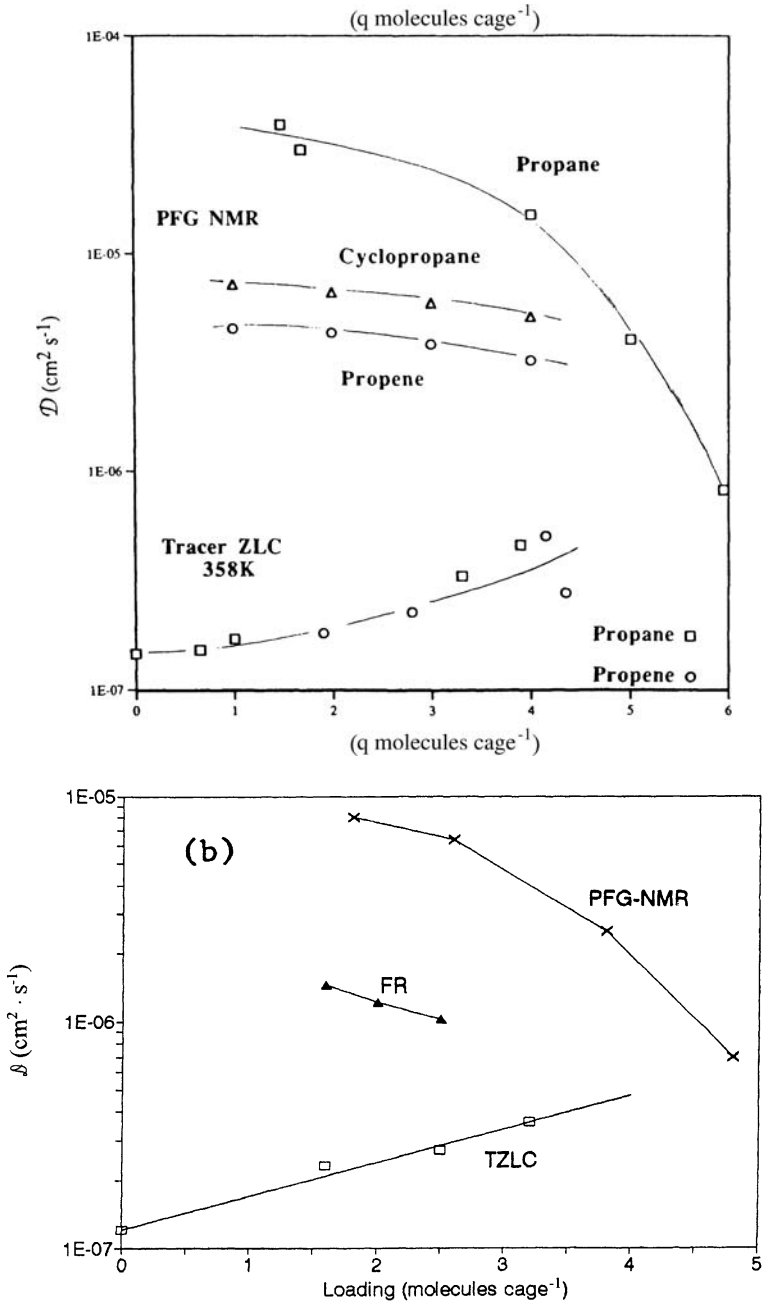

Fig. 15 **a** Comparison of PFG NMR diffusivity data (325 K) and tracer ZLC data (358 K) for propane and propene in NaX zeolite crystals. From Brandani et al. [58]. **b** Comparison of PFG NMR, frequency response (FR), and tracer ZLC diffusivity data for benzene–NaX at 468 K. From Brandani et al. [55]

Table 2 Diffusion in $AlPO_4$-5 (300 K) [73]

Sorbate	Technique	Time scale (s)	Mechanism	D ($cm^2\ s^{-1}$)
CH_4	PFG NMR	0.01–0.1	Single file [$D \propto 1\sqrt{t}$]	5×10^{-9}–5×10^{-8}
C_3H_8	TZLC	1–10	Fickian [D const]	10^{-6}–5×10^{-5}

Unidimensional pore system diameter $\sim$ 7.3 Å

time, rather than linearly with time, as in a Fickian system. Such behavior was observed in an experimental PFG NMR study of diffusion of methane in large crystals of $AlPO_4$-5. However, when diffusion in the same crystals was studied by the tracer ZLC method, the results were entirely consistent with normal one-dimensional Fickian diffusion. Remarkably, in this case the macroscopically observed diffusivities were larger than the values estimated (via the Einstein equation) from the PFG NMR data. This appears to be the first reported instance in which the micro measurements suggest slower diffusion than the macroscopic measurement. The time scales of the two sets of measurements are, however, quite different (Table 2). This raises the possibility that the difference in the observed pattern of behavior may reflect a lack of long-range coherence in the channel system, which could give rise to single file behavior over a short range (of distance and time) but, over distances of the order of the crystal length, the behavior may be dominated by the passing places arising from the defects in the structure.

Light Alkanes in Silicalite

The diffusion of light alkanes in silicalite has been studied by several different experimental methods, including both macroscopic and microscopic techniques. Representative results are summarized in Fig. 16. A similar general pattern has also been observed for other systems for which the experimental data are less complete.

The comparison is based on self-diffusivities for the microscopic measurements (PFG NMR and QENS) and corrected transport diffusivities (D_o) for the macroscopic measurements. There is generally good agreement between the PFG NMR and QENS values, and at low carbon numbers these values approach the values derived from molecular dynamic (MD) simulations. However, the MD values decline only slightly with carbon number while the experimental (QENS and PFG NMR) values decline more strongly, leading to discrepancies of more than an order of magnitude for the higher homologs. The macroscopic values (single crystal membrane and ZLC) are about two orders of magnitude smaller than the microscopic values.

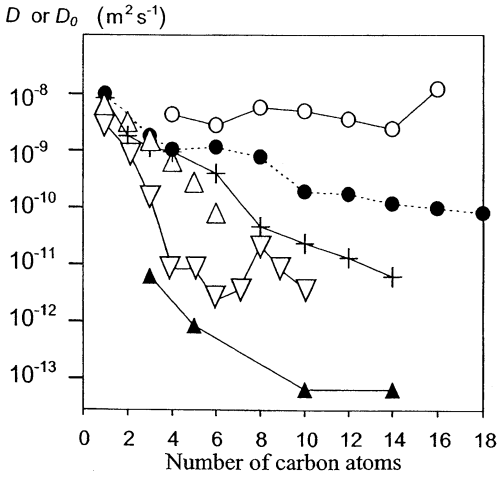

Fig. 16 Variation of diffusivity with carbon number for linear alkanes in silicalite at 300 K showing comparison between self-diffusivities and corrected transport diffusivities obtained by different techniques. ○ MD simulation [74]; ● hierarchical simulation [75]; + QENS [78]; △ PFG NMR [76]; ▽ single crystal membrane [65]; ▲ ZLC [77]. The ZLC values were calculated based on the assumption of isotropic diffusion in an equivalent spherical particle. The present figure has been modified by the addition of further experimental data from a figure originally presented by Jobic [78]

3.3 Origin of Discrepancies

In the studies noted here the more obvious possible sources of discrepancies between microscopic and macroscopic measurement (heat effects, intrusion of extracrystalline resistances to mass transfer, errors in data analysis) have generally been eliminated, and in some cases the lower macroscopic diffusivity values have been confirmed by more than one experimental technique. While the origin of these discrepancies has still not been unequivocally confirmed, recent experimental studies by "mesoscopic" techniques such as interference microscopy and IR absorption, which allow direct measurement of the transient concentration profiles through a single zeolite crystal during adsorption or desorption, provide a plausible explanation. These measurements show, very clearly, that the effects of surface barriers and internal barriers arising from growth planes or faults within the crystal are much more important than has been generally assumed [79–83]. For example, in ferrierite, transport occurs only through the 8-membered oxygen rings: the larger 10-ring channels are evidently closed by a barrier at or near the crystal surface [79]. In both silicalite and ferrierite the transient intracrystalline profiles show clear evidence of surface resistance, in addition to internal diffusional resistance (Fig. 17), and in some crystals the surface resistance

is completely dominant. In such cases the intracrystalline diffusivities derived from microscopic measurements, even at length scales approaching the crystal dimensions, will be much larger than the diffusivities derived from sorption rate measurements. Although the situations corresponding to surface resistance control and intracrystalline diffusion control are, in principle, distinguishable from the form of the uptake curves, in real systems where thermal effects are significant and there is usually a distribution of crystal size, this distinction may not be obvious from the experimental data. It is also worth noting that a few high-energy internal barriers (3 or 4) will lead to an isothermal uptake curve that closely mimics the form of a diffusion-controlled response [84].

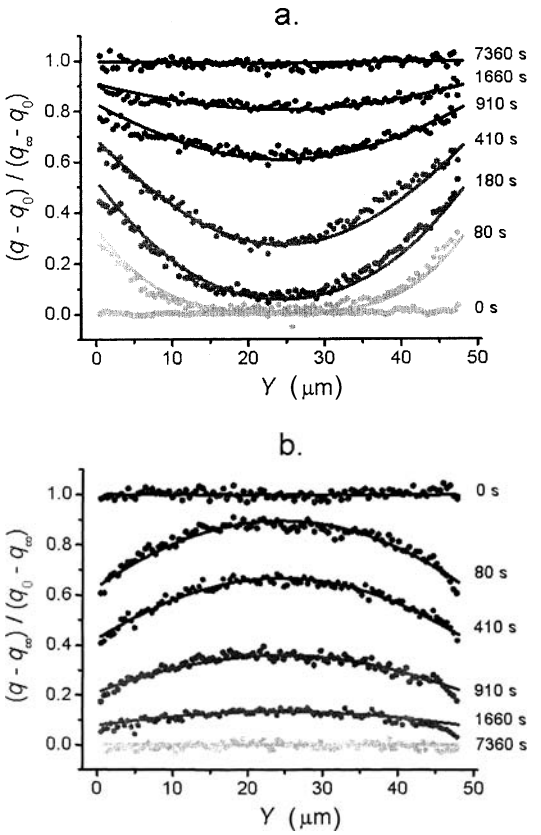

Fig. 17 Transient concentration profiles in y-direction (i.e., along 8-ring channels) measured by interference microscopy for **a** adsorption and **b** desorption of methanol in a large crystal of ferrierite for pressure steps $5 \rightarrow 10$ and $10 \rightarrow 5$ mbar. The form of the profiles shows that both surface resistance and internal diffusion (along the 8-ring channels) contribute to the mass-transfer resistance ($k/l \approx 1.7 \times 10^{-3}$ s^{-1}; $D/l^2 \approx 1.3 \times 10^{-3}$ s^{-1}; $l = 25$ μm). From Kortunov et al. [79]

These results demand a reassessment of our basic ideas on sorption kinetics and the role of intracrystalline diffusion in zeolite-based processes. It seems clear that intracrystalline diffusion can be reliably measured only by microscopic or "mesoscopic" techniques. In "ideal" crystals these values should correspond with the values derived from macroscopic measurements of sorption rates, but, since the majority of crystals that have been studied appear to be far from ideal, such a correspondence should not be assumed a priori. Conversely, the role of true intracrystalline diffusion in determining the rates of sorption and catalytic processes may be minimal and we may be forced to conclude that the rates of most large-scale processes are in fact largely influenced or even controlled by surface and internal barriers unrelated to the ideal zeolite structure.

At the present state of development the mesoscopic techniques are applicable only to relatively large zeolite crystals ($> 100\ \mu m$), so the extent to which surface and internal transport barriers are important in small commercial crystals is still uncertain.

4
Diffusion in Biporous Structures

Since the discovery of MCM-41 in the early 1990s mesoporous silicas and other similar materials, notably SBA-15, have attracted a great deal of attention. These materials combine a high surface area with relatively large access pores (2–30 nm), making them potentially attractive as both adsorbents and catalysts [85–87]. However, in contrast to microporous materials such as zeolites, the transport properties of mesoporous materials have attracted only limited experimental study [88–96]. Although many different mesoporous structures have been developed, most have limited hydrothermal stability and relatively low acidity, making them unattractive as potential adsorbents and catalysts. During the last few years substantial efforts have been made to overcome these structural problems, resulting in the development of materials such as zeolite/MCM-41 composites [97, 98], UL zeolites [99, 100] and the promising series of SBA-15-based materials [86, 101, 102]. We present here a short summary of the results of recent ZLC measurements of diffusion in such materials.

4.1
Diffusion in SBA-15

Recent studies of SBA-15 materials have shown the existence of micropores within the pore walls of their mesoporous structure, thus confirming the biporous nature of these materials [102–105]. Figure 18 shows a schematic representation of a typical SBA-15 pore structure. According to the diagram these materials have an array of hexagonally ordered primary mesopores, but

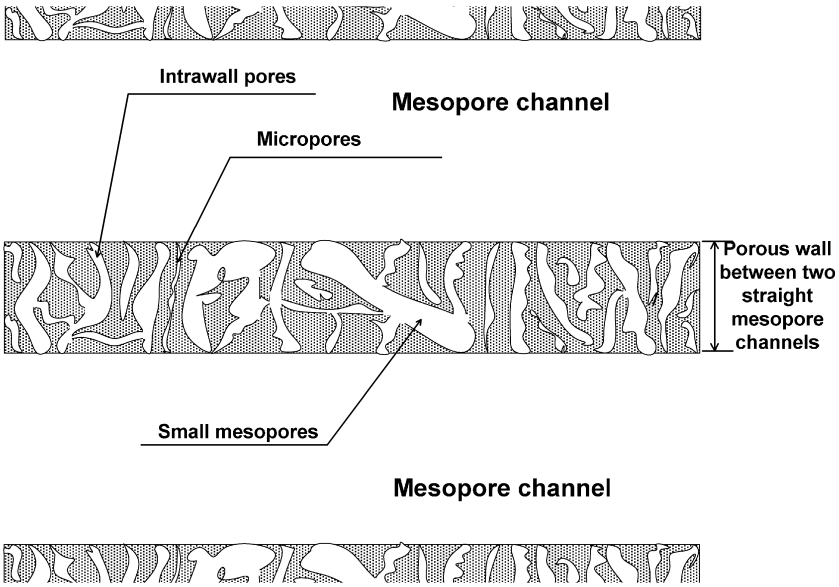

Fig. 18 Schematic representation of pore structure of SBA-15 material

the mesopore walls are also porous. These intrawall pores include micropores ranging from ultra- to supermicropores as well as small (secondary) mesopores, which may either be open at both ends (thus providing a connection between adjacent mesopore channels) or closed at one end and therefore providing no connection between channels.

In a recent study, Hoang et al. [105] showed that the microporosity of the SBA-15 materials can be effectively controlled by careful selection of the synthesis conditions. The influence of the biporous structure on the diffusion characteristics has been investigated using three probe molecules of different sizes: *n*-heptane, cumene, and mesitylene with kinetic diameters of 0.43, 0.67, and 0.87 nm, respectively [106]. A summary of the effective diffusivity data obtained by the ZLC technique on a series of SBA-15 materials designated as MMS samples is shown in Table 3. As can be seen from the table, the lowest diffusivity value at 30 °C and the highest activation energies for all probe molecules are for the MMS-1 and 2 samples, which have the highest microporosity, i.e., 64.7 and 54.1%, respectively. Under experimental conditions corresponding to low partial pressures, as required by the ZLC method, only the micropores and the smaller (secondary) mesopores can be filled with sorbates. These pores constitute the intrawall pore structure of the SBA-15 or MMS samples and are considered to play a central role in the diffusion process, particularly for small molecules, such as *n*-heptane, which can easily penetrate these pores. Therefore, *n*-heptane diffusion in the samples with the highest microporosities appears similar to diffusion in microporous solids

Table 3 Diffusivity data of *n*-heptane, cumene, and mesitylene for SBA-15 samples at 30 °C

Sample	Microporosity (%)	Sorbate	D_{eff} ($m^2\ s^{-1}$)	E ($kJ\ mol^{-1}$)
MMS-1	64.7	*n*-heptane	3.40×10^{-14}	22.2
		Cumene	1.23×10^{-14}	17.2
		Mesitylene	0.73×10^{-14}	15.8
MMS-2	54.1	*n*-heptane	3.97×10^{-14}	20.2
		Cumene	1.42×10^{-14}	14.8
		Mesitylene	0.86×10^{-14}	13.9
MMS-3	31.6	*n*-heptane	7.73×10^{-14}	12.8
		Cumene	2.92×10^{-14}	12.2
		Mesitylene	1.70×10^{-14}	11.4
MMS-4	18.6	*n*-heptane	9.33×10^{-14}	6.5
		Cumene	3.98×10^{-14}	7.5
		Mesitylene	2.17×10^{-14}	8.9

such as small-pore zeolites, although, in contrast to the highly ordered and uniform micropores typical of zeolites, the micropores in the walls of SBA-15 materials are nonuniform and highly disordered. For saturated hydrocarbons such as the C-5 to C-10 linear alkanes in silicalite/ZSM-5, the diffusional activation energies reported in the literature are in the range 17–24 kJ/mol [1]. These values are in general agreement with the activation energies of 22.2 and 20.2 kJ/mol obtained for *n*-heptane diffusion in the MMS-1 and MMS-2 samples, respectively, thus suggesting a micropore-controlled diffusion mechanism in these materials. However, significantly lower activation energies of 12.8 and 6.5 kJ/mol are found for *n*-heptane in the MMS-3 and MMS-4 samples, respectively (Table 3). These samples have significantly lower proportions of micropores in their intrachannel walls (31.6 and 18.6%, respectively). The predominant pores in these materials are the larger and more orderly secondary mesopores, and this leads to a diffusion process governed by either a combination of micro- and mesopore diffusion (MMS-3) or almost entirely by diffusion in the secondary mesopores (MMS-4). For the mesopore-controlled process the effective diffusivity is given by [1]:

$$D_{eff} = \frac{\varepsilon_p D_p}{\varepsilon_p + (1 - \varepsilon_p)K}, \tag{21}$$

where ε_p is mesoporosity, D_p is pore diffusivity, and K is the Henry's Law constant. The pore diffusivity (D_p) obtained from Eq. 21 was found to be about three orders of magnitude smaller than Knudsen diffusivity calculated for the secondary mesopores [105]. This result suggests that Knudsen diffusion

is replaced by surface diffusion as the dominant transport process in these mesopores. It is assumed that sorbate molecules effectively slide along the surface of the mesopores, rather than executing long trajectories [107, 108].

The larger probe molecules (cumene, 0.67 nm and mesitylene, 0.87 nm) have generally lower diffusivities, as shown in Table 3. However, the difference in diffusivities between the smaller probe molecule (*n*-heptane, 0.43 nm) and the larger ones (cumene and mesitylene) are relatively small, as can be seen from the same table. While the effective diffusivities for *n*-heptane in SBA-15 samples are comparable to the diffusivities of that sorbate in silica or silica-rich zeolites, e.g., silicalite and ZSM-5 [1], the effective diffusivities for cumene and mesitylene in the SBA-15 materials are several orders of magnitude higher in comparison with zeolite ZSM-5 [109–111]. The variation of effective diffusivity (at 30 °C) for *n*-heptane, cumene, and mesitylene with respect to the percentage microporosity of the SBA-15 samples is summarized in Fig. 19. As can be seen from that figure, the effective diffusivities decrease more substantially, particularly for *n*-heptane, as the percentage microporosity increases from 18.6 to 31.6%, while they only decrease marginally as the percentage microporosity increases from 54.1 to 64.7%. This clearly suggests that, at least for *n*-heptane, the diffusion process in the MMS-1 and MMS-2 samples is controlled by the micropores in the intrawall structures. Another interesting observation is related to the activation energies that, for all samples except MMS-4, are lower for the larger cumene and mesitylene probe molecules than for *n*-heptane (which has the smallest kinetic diameter). The reported activation energies for diffusion of cumene and mesitylene in ZSM-5 (40–66.5 kJ/mol [111, 112]) are much higher than the values obtained for the SBA-15 samples (7.5–17.2 kJ/mol), as shown in Table 3. This interesting observation provides further evidence of the specific impact of the SBA-15

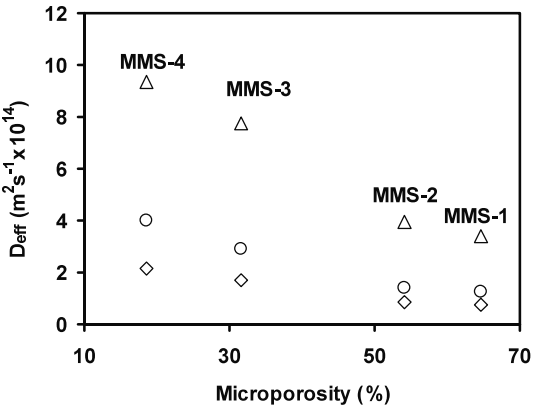

Fig. 19 Dependence of effective diffusivity (D_{eff}) at 30 °C on percentage of microporosity for: △ *n*-heptane; ○ cumene; and ◇ mesitylene

structures in governing the diffusion processes. The MMS-1 to MMS-3 samples have micropore sizes ranging from ca. 0.4 to 0.7 nm [105, 106]. This provides a simple explanation for the observation that *n*-heptane (0.43 nm) and, to a lesser extent, cumene (0.67 nm) can penetrate the microporous channels within the mesoporous walls of these materials. On the other hand, mesitylene having a kinetic diameter of 0.87 nm is probably excluded from these micropores, thus making the diffusivity of this sorbate only marginally dependent on the percentage of micropores, as shown in Fig. 19.

In the case of the MMS-4 sample it was shown that, as a result of the synthesis conditions, all the micropores collapsed with only supermicropores and small (secondary) mesopores having pore sizes greater than 1 nm remained in the mesoporous walls [105]. Consequently, in this material, all the probe molecules can be transported through the intrawall pores, and diffusion is generally controlled by resistance within the larger pores. This is confirmed by the low values of the activation energies for this sample (Table 3). Moreover, the activation energies for *n*-heptane, cumene, and mesitylene increase in that order, which is the sequence of their respective kinetic diameters. However, the differences in the activation energies are probably not significant, since the kinetic diameters for all three probe molecules are small relative to the pore diameters of the supermicropores and secondary mesopores (1–3 nm) [106].

It is clear that comparative ZLC measurements can provide useful information concerning the transport properties of even such structurally complex materials as the mesoporous silicas.

References

1. Kärger J, Ruthven DM (1992) Diffusion in zeolites and other microporous solids. Wiley, New York
2. Rees LVC (1994) Exciting new advances in diffusion of sorbates in zeolites and microporous solids. In: J Weitkamp, Karge HG, Pfeifer H, Hölderich W (eds) Zeolites and related microporous materials: state of the art 1994. Proc 10th Int Zeolite Conf, Garmisch-Partenkirchen, Germany, 17–22 July 1994. Elsevier, Amsterdam, p 1133; Stud Surf Sci Catal 84:1133
3. Kanellopoulos NK (2000) Recent advances in gas separation by microporous ceramic membranes. Membrane Science and Technology Series 6. Elsevier, Amsterdam
4. Kärger J, Ruthven DM (2002) In: Schüth F, Sing KSW, Weitkamp J (eds) Handbook of porous solids, Vol 4. Wiley, Weinheim, Germany, p 2087
5. Kärger J (2006) In: Karge HG, Weitkamp J (eds) Molecular sieves – science and technology, Vol 7, Chap 3. Diffusion coefficients by NMR techniques. Springer, Berlin Heidelberg New York
6. Barrer RM (1941) Trans Faraday Soc 37:590
7. Barrer RM (1978) Zeolites and clay minerals. Academic, London
8. Ruthven DM, Lee L-K, Yucel H (1980) AIChE J 26:16
9. Ruthven DM, Lee L-K (1981) AIChE J 27:654

10. Lee L-K, Ruthven DM (1979) J Chem Soc Faraday Trans I 75:2406
11. Haul R, Stremming H (1984) J Colloid Interface Sci 97:348
12. Sun LM, Meunier F (1987) Chem Eng Sci 42:1585
13. Youngquist GR, Allen JL, Eisenberg J (1971) Ind Eng Chem Prod Res Develop 10:308
14. Ruthven DM, Derrah RI (1972) Can J Chem Eng 50:743
15. Bülow M, Mietk W, Struve P, Schirmer W, Kocirik M, Kärger J (1984) In: Olson D, Bisio A (eds) Proc 6th Int Zeolite Conf, Reno, NV, USA, 10–15 July 1983. Butterworths, Guildford, Surrey, UK, p 242
16. Bülow M, Mietk W, Struve P, Lorenz P (1983) J Chem Soc Faraday Trans I 79:2457
17. Micke A, Bülow M (1994) Micropor Mater 3:185
18. Bülow M, Micke A (1995) Adsorption 1:29
19. Schumacher R, Erhardt K, Karge HG (1999) Langmuir 11:3965
20. Schumacher R, Lorenz P, Karge HG (1997) In: Chon H, Ihm S-K, Uh YS (eds) Progress in zeolite and microporous materials. In: Proc 11th Int Zeolite Conf, Seoul, Korea, 12–17 August 1996. Elsevier, Amsterdam, p 1747; Stud Surf Sci Catal 105:1747
21. Schumacher R, Karge HG (1999) J Phys Chem B 103:1477
22. Schumacher R, Karge HG (1999) Micropor Mesopor Mater 30:307
23. Brandani S (1998) Adsorption 4:17
24. Caro J, Noack M, Marlow F, Griepentrog D, Kornatowski K (1993) J Phys Chem 97:13,68
25. Niessen W, Karge HG (1991) In: Inui T, Namba S, Tatsumi T (eds) Proc Int Symp Chemistry of Microporous Crystals, Tokyo, 26–29 June 1990. Kodansha, Tokyo, Elsevier, Amsterdam, p 213; Stud Surf Sci Catal 60:213
26. Niessen W, Karge HG (1993) Micropor Mater 1:1
27. Grenier Ph, Meunier F, Gray PG, Kärger J, Xu Z, Ruthven DM (1994) Zeolites 14:242
28. Brandani S, Jama M, Ruthven DM (2000) Micropor Mesopor Mater 35–36:283
29. Yasuda Y (1976) J Phys Chem 80:1867
30. van den Begin NG, Rees LVC (1989) In: Jacobs PA, van Santen RA (eds) (1989) Zeolites: facts, figures, future. Proc 8th Int Zeolite Conf, Amsterdam, 10–14 July 1989. Elsevier, Amsterdam, p 915; Stud Surf Sci Catal 49:915
31. Shen DM, Rees LVC (1991) Zeolites 11:684
32. Shen DM, Rees LVC (1993) J Chem Soc Faraday Trans 89:1063
33. Rees LVC, Song L (2000) In: Kanellopoulos NK (ed) Recent advances in gas separation by microporous ceramic membranes. Membrane Science and Technology Series 6. Elsevier, Amsterdam, p 139
34. Sun LM, Bourdin V(1993) Chem Eng Sci 48:3783
35. Bourdin V, Grenier Ph, Meunier F, Sun LM (1996) AIChE J 42:700
36. Bourdin V, Germanus A, Grenier Ph, Kärger J (1996) Adsorption 2:205
37. Grenier Ph, Malka-Edery A, Bourdin V (1999) Adsorption 5:135
38. Kubin M (1965) Coll Czech Chem Commun 30:1104, 30:2900
39. Kucera EJ (1965) J Chromatog 19:237
40. Haynes HW, Sarma PN (1974) Adv Chem Series 133:205
41. Ma YH, Mancel C (1973) In: Meier WM, Uytterhoeven JB (eds) Molecular sieves. Proc 3rd Int Zeolite Conf, Zurich, Switzerland, 3–7 September 1973, p 392; Adv Chem Series 121:392
42. Shah DB, Ruthven DM (1977) AIChE J 23:804
43. Haq N, Ruthven DM (1986) J Colloid Interface Sci 112:164
44. Awum F, Narayan S, Ruthven DM (1988) I EC Res 27:1510
45. Ching CB, Ruthven DM (1988) Zeolites 8:68
46. Hufton JR, Ruthven DM, Danner RP (1995) Micropor Mater 5:39

47. Delmas M, Cornu C, Ruthven DM (1995) Zeolites 15:45
48. Eic M, Ruthven DM (1988) Zeolites 8:40
49. Ruthven DM, Eic M (1988) In: Flank WH, Whyte Jr TE (eds) Perspectives in molecular sieve science. Am Chem Soc Symp Ser 368:362
50. Ruthven DM, Stapleton P (1993) Chem Eng Sci 48:89
51. Hufton JR, Brandani S, Ruthven DM (1994) Measurement of intracrystalline diffusion by zero length column tracer exchange. In: J Weitkamp, Karge HG, Pfeifer H, Hölderich W (eds) Zeolites and related microporous materials: state of the art 1994. Proc 10th Int Zeolite Conf, Garmisch-Partenkirchen, Germany, 17–22 July 1994. Elsevier, Amsterdam, p 1323; Stud Surf Sci Catal 84:1323
52. Ruthven DM, Brandani S (2000) In: Kanellopoulos NK (ed) Recent advances in gas separation by microporous ceramic membranes. Membrane Science and Technology Series 6. Elsevier, Amsterdam, p 187
53. Brandani S, Ruthven DM (1995) Chem Eng Sci 50:2055
54. Brandani S, Ruthven DM (1996) Adsorption 2:133
55. Brandani S, Xu Z, Ruthven DM (1996) Micropor Mater 7:323
56. Ruthven DM, Xu Z (1993) Chem Eng Sci 48:3307
57. Brandani S, Cavalcante C, Guimoares A, Ruthven DM (1998) Adsorption 4:275
58. Brandani S, Hufton JR, Ruthven DM (1995) Zeolites 15:624
59. Gleaves JT, Ebner JR, Kuechler TC (1988) Catal Rev Sci Eng 30:49
60. Keipert OP, Baerns M (1998) Chem Eng Sci 53:3623
61. Nijhuis TA, van der Broeke LJP, van de Graaf JM, Kapteijn F, Makkee M, Moulijn JA (1997) Chem Eng Sci 52:3401
62. Brandani S, Ruthven DM (2000) Chem Eng Sci 55:1935
63. Wernick DL, Osterhuber EJ (1984) In: Olson D, Bisio A (eds) Proc 6th Int Zeolite Conf, Reno, NV, USA, 10–15 July 1983. Butterworths, Guildford, Surrey, UK, p 122
64. Paravar A, Hayhurst DT (1984) Direct measurement of diffusivity for butane across a single large silicalite crystal. In: Olson D, Bisio A (eds) Proc 6th Int Zeolite Conf, Reno, NV, USA, 10–15 July 1983. Butterworths, Guildford, Surrey, UK, p 217
65. Talu O, Sun MS, Shah DB (1998) AIChE J 44:681
66. Kapteijn F, Bakker WJW, Zheng G, Pappe J, Moulijn JA (1995) Chem Eng J 57:145
67. Haag WO, Lago RM, Weisz PB (1982) Faraday Discussions Chem Soc Lond 72:317
68. Post MFM, van Amstel J, Kouwenhoeven HW (1984) In: Olson D, Bisio A (eds) Proc 6th Int Zeolite Conf, Reno, NV, USA, 10–15 July 1983. Butterworths, Guildford, Surrey, UK, p 517
69. Shen D, Rees LVC (1991) Zeolites 11:666
70. Ruthven DM (1993) Zeolites 13:594
71. Brandani S, Ruthven DM, Kärger J (1995) Zeolites 15:494
72. Kärger J, Ruthven DM (1989) Zeolites 9:267
73. Brandani S, Ruthven DM, Kärger J (1997) Micropor Mater 8:193
74. Runnebaum RC, Maginn EJ (1997) J Phys Chem B 101:6394
75. Maginn EJ, Theodorou DN (1996) J Phys Chem B 100:7155
76. Heink W, Kärger J, Pfeifer H, Datema KP, Nowak AK (1992) J Chem Soc Faraday Trans I 88:3505
77. Eic M, Ruthven DM (1989) In: Jacobs PA, van Santen RA (eds) Zeolites: Facts, Figures, Future Proc 8th Int Zeolite Conf, Amsterdam, 10–14 July 1989. Elsevier, Amsterdam, p 897; Stud Surf Sci Catal 49B:897
78. Jobic H (2000) In: Kanellopoulos NK (ed) Recent advances in gas separation by microporous ceramic membranes. Membrane Science and Technology Series 6. Elsevier, Amsterdam, p 109

79. Kortunov P, Chmelik C, Kärger J, Rakoczy RA, Ruthven DM, Traa Y, Vasenkov S, Weitkamp J (2005) Adsorption (in press)
80. Geier O, Vasenkov S, Lehmann E, Kärger J, Schemmert U, Rakoczy RA, Weitkamp J (2001) J Phys Chem B 105:10217
81. Kortunov P, Vasenkov S, Chmelik C, Kärger J, Ruthven DM, Wloch J (2004) Chem Mater 16:3552
82. Vasenkov S, Kärger J (2002) Micropor Mesopor Mater 55:139
83. Vasenkov S, Böhlmann W, Galvasas P, Geier O, Liu H, Kärger J (2001) J Phys Chem B 105:5922
84. Ruthven DM (1995) In: Bonneviot L, Kaliaguine S (eds) A refined tool for designing catalytic sites. Proc Int Symp, Québec, Canada, 15–20 October 1995. Elsevier, Amsterdam, p 223; Stud Surf Sci Catal 97:223
85. Kresge CT, Leonowitz ME, Roth WJ, Vartuli JC, Beck JS (1992) Nature 359:710
86. Zhao D, Feng J, Huo Q, Melosh N, Frederickson GH, Chmelka BF, Stucky GD (1998) Science 279:548
87. Trong-On D, Desplantier-Giscard D, Danumah D, Kaliaguine S (2001) Appl Catal A 222:299
88. Hansen EW, Courivaud F, Karlsson A, Kolboe S, Stöcker M (1998) Micropor Mesopor Mater 22:309
89. Gjerdaker L, Aksnes DW, Sorland GH, Stöcker M (2001) Micropor Mesopor Mater 42:89
90. Stallmach F, Kärger J, Krause C, Jeschke M, Oberhagemann U (2000) J Am Chem Soc 122:9237
91. Seebacher C, Hellriegel C, Deeg FW, Brauchie C, Altmaier S, Behrens P, Mullen K (2002) J Phys Chem B 106:5591
92. Newalkar B, Choudhary NV, Kumar P, Komarneni S, Bhat TSG (2002) Chem Mater 14:304
93. Newalkar B, Choudhary NV, Turaga UT, Vijayalakshmi RP, Kumar P, Komarneni S, Bhat TSG (2003) Chem Mater 15:1474
94. Vinh-Thang H, Malekian A, Eić M, Trong-On D, Kaliaguine S (2003) In: Park S-E, Ryoo R, Ahn W-S, Lee CW, Chang (eds) Nanotechnology in mesostructured materials. Proc 3rd Int Mesostructured Materials Symp, Jeju, Korea, 8–11 July 2002. Elsevier, Amsterdam, p 235; Stud Surf Sci Catal 146:235
95. Campos DS, Eić M, Occelli M (2000) In: Sayari A, Jaroniec M, Pinnavaia TJ (eds) Proc 2nd Conf Access in Nanoporous Materials, Banff, Alberta, Canada, May 25–30, 2000, Elsevier, Amsterdam, p 639; Stud Surf Sci Catal 129:639
96. Krause C, Stallmach F, Honicke D, Spange S, Kärger J (2003) Adsorption 9:235
97. Han YJ, Xiao FS, Wu S, Sun Y, Meng X, Li D, Lin S, Deng F, Ai X (2001) J Phys Chem B 105:7963
98. Liu Y, Zhang W, Pinnavaia TJ (2001) Angew Chem Int Ed 40:1255
99. Trong-On D, Kaliaguine S (2001) Micropor Mesopor Mater 44/45:435
100. Trong-On D, Kaliaguine S (2001) Angew Chem Int Ed 9:3248
101. Zhao D, Huo Q, Feng J, Chmelka BF, Stucky GD (1998) J Am Chem Soc 120:6024
102. Vinh-Thang H, Huang Q, Eić M, Trong-On D, Kaliaguine S (2005) Langmuir 21:5094
103. Kruk M, Jaroniec M, Ko CH, Ryoo R (2000) Chem Mater 12:1961
104. Ravikovitch PI, Neimark AV (2001) J Phys Chem B 105:6817
105. Vinh-Thang H, Huang Q, Eić M, Trong-On D, Kaliaguine S (2005) Langmuir 21:2051
106. Vinh-Thang H, Huang Q, Eić M, Trong-On D, Kaliaguine S (2005) In: Fraissard J, Conner C (eds) Proc NATO-ASI Meeting on Fluid Transport in Nanoporous Materials (2003) Springer-Verlag, Berlin, Heidelberg (in press)

107. Bhatia SK, Nicholson D (2003) J Chem Phys 119:1719
108. Jepps OG, Bhatia SK, Searles D (2003) J Phys Rev Lett 91:126102
109. Choudhary VR, Nayak VS, Choudhary TV (1997) Ind Eng Chem Res 36:1812
110. Choudhary VR, Singh AP (1986) Zeolites 6:206
111. Choudhary VR, Mamman AS, Nayak VS (1989) Ind Eng Chem Res 28:1241
112. Satterfield CN, Katzer JR, Vieth WR (1971) Ind Eng Chem Fundamentals 10:478

Mol Sieves (2008) 7: 85–133
DOI 10.1007/3829_2007_019
© Springer-Verlag Berlin Heidelberg
Published online: 5 February 2008

Diffusion Measurements by NMR Techniques

Jörg Kärger

Fakultät für Physik und Geowissenschaften, Universität Leipzig, Linnéstraße 5, 04103 Leipzig, Germany
kaerger@physik.uni-leipzig.de

Abstract As a non-invasive technique, NMR spectroscopy allows the observation of molecular transport in porous media without any disturbance of their intrinsic molecular dynamics. The space scale of the diffusion phenomena accessible by NMR ranges from the elementary steps (as studied, e.g., by line-shape analysis or relaxometry) up to macroscopic dimensions. Being able to follow molecular diffusion paths from ca. 100 nm up to ca. 100 μm, PFG NMR has proven to be a particularly versatile tool for diffusion studies in heterogeneous systems. With respect to zeolites, PFG NMR is able to provide direct information about the rate of molecular migration in the intracrystalline space and through assemblages of zeolite crystallites as well as about possible transport resistances on the outer surface of the crystallites (surface barriers).

The potentials of PFG NMR have been substantially improved by recent methodical developments ensuring a significant enhancement in the sensitivity of signal detection. In this way, diffusion measurements with nuclei different from protons were enabled. Similarly, high-resolution studies allowing the simultaneous observation of the diffusivities of various molecular species under the conditions of multicomponent adsorption have become possible. The most attractive fields of current research include the in-situ application of PFG NMR during catalytic processes, the clarification of the relation between molecular transport under equilibrium and under non-equilibrium conditions, and the study of structure-related diffusion. The latter topic addresses such fundamental questions as the occurrence of single-file diffusion and the relation between crystal structure and diffusion anisotropy. The wealth of challenging tasks is continuously augmented by

both the increasing number of absorbents with new structural features and the increasing demand of the industry for the clarification of their transport properties. Thus, PFG NMR is most likely to continue to prosper in an ever growing field of application to both zeolite science and technology.

Keywords Diffusion tensor · In-situ measurement · Intracrystalline diffusion · Molecular dynamics · Propagator · Random walk · Surface barriers

Abbreviations

LTA	Three-letter code of the International Zeolite Association for zeolite A
La-X	Lanthanum-exchanged zeolite X
MD	Molecular dynamics
MFI	Three-letter code of the International Zeolite Association for zeolites ZSM-5/silicalite-1
Na-A	Sodium-form of zeolite A
Na,Ca-A	Zeolite A containing sodium and calcium cations
Na,Ca-X	Zeolite X containing sodium and calcium cations
Na-X	Sodium-form of zeolite X
Na-Y	Sodium-form of zeolite Y
NMR	Nuclear magnetic resonance
NSE	Neutron spin echo (in QENS)
PFG NMR	Pulsed-field gradient NMR
rf	Radio frequency
QENS	Quasielastic neutron scattering
ZLC	Zero length column chromatography
5A	Zeolite Na,Ca-A, with about 67% of Na^+ exchanged by Ca^{2+}

Symbols

A	Quantity defined by Eq. 18
a, b, c	Unit cell dimensions
B	Intensity of magnetic field
B_{add}	Added inhomogeneous field (=gz)
B_o	Constant magnetic field
$c(p)$	Sorbate concentration at sorbate pressure p
D	Coefficient of self-diffusion, (self-)diffusivity
D_{app}	Apparent diffusivity
D_c	Corrected transport diffusivity
D_{eff}	Effective diffusivity
$D_{l.r.}$	Coefficient of long-range self-diffusion (= $p_{inter}D_{inter}$)
D_{inter}	Coefficient of self-diffusion in the intercrystalline space
D_{intra}	Coefficient of intracrystalline self-diffusion
D_o	Diffusivity with "open" windows
D_t	Transport diffusivity
D_x, D_y, D_z	Principal elements of the diffusion tensor
D_{xy}	Principal element of a diffusion tensor of rotational symmetry in the plane perpendicular to the symmetry axis
f	Ratio of transition rates through blocked and open windows
g	Magnetic field gradient intensity
M_1	First statistical moment of an adsorption/desorption curve ($\equiv \tau_{intra}$)

p	Pressure; probability to find an unblocked window
p_{inter}	Relative number of molecules in the intercrystalline space
$P(\Delta z, t)$	Probability density that during time t a molecule is shifted over a distance Δz (=propagator)
R	Crystallite radius
r	Space vector
r_{c}	Crystal radius
r_{p}	Pellet radius
t	Time
v	Mean thermal velocity
x	Space coordinate
y	Space coordinate
z	Space coordinate in the direction of the magnetic field gradient; coordination number
γ	Gyromagnetic ratio
$\gamma(t)$	Fraction of molecules leaving their original crystallite during time interval t
δ	Duration of the magnetic field gradient pulses
$\langle \Delta r \rangle^2$	Mean square displacement
$\langle \Delta z \rangle^2$	Mean square displacement in z direction
$\Delta\varphi$	Phase shift
σ	Lennard–Jones distance
λ_{eff}	Effective mean free path in the intercrystalline space
τ_{tort}	Tortuosity factor
τ_{intra}	Intracrystalline mean life time
$\tau_{\text{intra}}^{\text{Diff}}$	Theoretical value of τ_{intra} in the case of diffusion control
ϕ	Phase of the precessional motion
ψ	Attenuation of the spin echo in PFG NMR experiments
ω	Larmor frequency

1 Introduction

As a non-invasive method, NMR spectroscopy allows the investigation of sample structure and sample dynamics without any interference with the internal processes within the sample. Since the phenomenon of nuclear magnetic resonance is controlled by the local environment of the nuclei under study, any change in the position of a molecule and hence of the nuclei belonging to it may appear in the NMR signal. In this way, NMR spectroscopy is able to yield valuable information about the elementary steps of diffusion, in particular about mean jump times and reorientation times. Information of this type is contained in the magnetic relaxation times ("relaxation analysis" [1]), which may be determined even for individual groups within the molecules [2]. Examples of the application of proton nuclear magnetic relaxation time measurements for the determination of hopping rates are presented in the literature for methane in zeolite Na-A [3, 4] and for different fluoromethanes in Na-Y [5, 6]. Information about the elementary processes of

diffusion may also be deduced from the NMR line shape, in particular for nuclei with spin I >1/2 (e.g., ^{2}H [7–9]) and from chemical shift anisotropy (e.g., ^{13}C and ^{31}P [10, 11]). On the basis of a model of activated jumps, the molecular reorientation times as determined, e.g., from the ^{2}H NMR spectra may be transferred into intracrystalline diffusivities [12–18].

For nuclei with large electron clouds like ^{129}Xe, the chemical shift (i.e. the position of the resonance line) may dramatically depend on the surroundings. On the basis of this interrelation, J. Fraissard and coworkers [19, 20] have developed a powerful technique for probing structural properties of zeolites by ^{129}Xe NMR. This possibility has been applied to the study of diffusion fluxes in both the intracrystalline [21] and intercrystalline [22–24] spaces by using ^{129}Xe as a probe [25]. By applying 2D ^{129}Xe exchange NMR, it has even become possible to determine the hopping rates of the xenon atoms between supercages of different occupancy in zeolite Na-A [17, 26–30]. Similarly, ^{129}Xe NMR line shape analysis has also been applied to explore molecular dynamics in nanochannels [31]. 2D ^{2}H and ^{13}C exchange NMR has been also applied to record reorientational and translational dynamics of benzene in zeolite Na-Y [32].

In parallel with the thus-provided information about the elementary steps of diffusion, NMR spectroscopy is also able to follow molecular transportation over macroscopic dimensions. Measurements of this type are based on the ability of NMR to monitor molecular distributions within the sample. Since the nuclear magnetic resonance frequency (Larmor frequency), $\omega = \gamma B$, is proportional to the intensity B of the applied magnetic field (with the magnetogyric ratio γ as a factor of proportionality), under the influence of a space-dependent magnetic field, $B = B_0 + gz$, the distribution of the resonance frequencies coincides with the spatial distribution of the nuclear spins with respect to the direction of the gradient of the magnetic field (which is usually assumed to be given by the z coordinate). Two- and three-dimensional images may be produced, e.g., by combining projections taken for different field gradient orientations. Owing to the spectacular progress of its application to anatomical imaging in medicine, this measuring principle has become popular under the name NMR tomography or NMR spin mapping [33–36]. It has repeatedly been applied to the determination of concentration profiles in beds of adsorbents [37–44]. The space resolution depends on the rate of profile propagation and is typically of the order of hundreds of micrometers.

NMR spectroscopy shares its ability to provide information about the elementary steps of diffusion and the resulting concentration profiles with other spectroscopic techniques like IR [45, 46], neutron [47–49] and dielectric [50, 51] spectroscopy. With respect to its ability to follow molecular diffusion paths between hundreds of nanometers up to hundreds of micrometers, however, it is unique. Measurements of this type are based on the application of an inhomogeneous magnetic field. In the technique, being so far the most

effective one, the inhomogeneous magnetic field is applied as "field gradient pulses" over short time intervals. The present contribution is intended to provide a survey of the ample field of application of the pulsed-field gradient (PFG) NMR method to studying molecular diffusion in zeolites, with particular emphasis on novel results and developments, which have not yet been included in previous reviews on this topic [52–56].

2
Fundamentals of Pulsed-Field Gradient NMR

2.1
The Measuring Principle

Superimposing the constant magnetic field B_o with an inhomogeneous magnetic field $B_{add} = gz$, the precessional ("Larmor") frequency ($\omega = \gamma B$) of a spin about the direction of the magnetic field (B) becomes space dependent:

$$\omega = \omega(z) = \gamma B = \gamma \left(B_0 + gz\right) = \omega_0 + \gamma gz \,. \tag{1}$$

γ denotes the gyromagnetic ratio of the nucleus under study (e.g., 2.67×10^8 T^{-1} s^{-1} for ^1H; 0.67×10^8 T^{-1} s^{-1} for ^{13}C; 0.27×10^8 T^{-1} s^{-1} for ^{15}N; 2.52×10^8 T^{-1} s^{-1} for ^{19}F, and 0.75×10^8 T^{-1} s^{-1} for ^{129}Xe) and the z coordinate is assumed to be aligned along the direction of the applied field gradient. By combining a suitably chosen sequence of rf pulses with two field gradient pulses, differences Δz in the positions of a particular spin at the instants of the two field gradient pulses lead to a phase shift

$$\Delta\varphi = \gamma g \Delta z \delta \,, \tag{2}$$

in their precessional motion. Since the intensity of the NMR signal (the "spin echo") is proportional to the total magnetization, i.e., to the vector sum of the contributions of the individual spins, the application of field gradient pulses thus leads to a signal attenuation

$$\psi = \int P(\Delta z, t) \cos(\gamma \delta g \Delta z) \, \mathrm{d}(\Delta z) \,, \tag{3}$$

where $P(\Delta z, t)$ denotes the probability (density) that an arbitrarily selected spin within the sample has been shifted over a distance Δz with respect to the z coordinate in the time interval t between the two field gradient pulses. $P(\Delta z, t)$ has been termed the (average) propagator [34, 57, 58] and represents the probability distribution of molecular displacements. The cosine term on the right hand side of Eq. 3 takes into account that the spins contribute to the total magnetization only by their projection on the direction of the total

magnetization. Fourier inversion of Eq. 3 yields

$$P(\Delta z, t) = \frac{1}{2\pi} \int \psi(\delta g, t) \cos(\gamma \delta g \Delta z)\, \mathrm{d}(\gamma \delta g)\,. \tag{4}$$

Equation 4 shows that the PFG NMR signal attenuation directly yields the average propagator.

As an example, Fig. 1 shows the propagator representation of molecular self-diffusion of ethane in beds of zeolite Na,Ca-A with two different crystallite sizes. Being symmetric in z, for simplicity the propagator is only represented

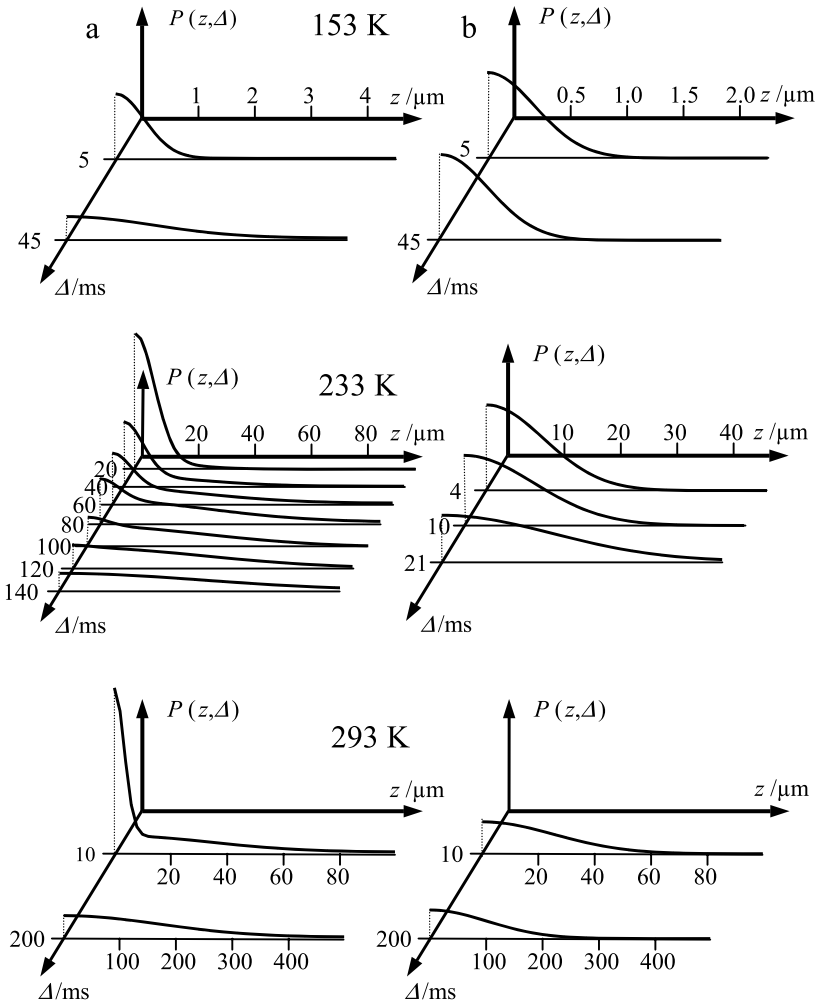

Fig. 1 Propagator representation of the self-diffusion of ethane in zeolite Na,Ca-A with mean crystallite radii of $R = 8\ \mu m$ (**a**) and $0.4\ \mu m$ (**b**). From [57] with permission

for $z > 0$. For the lowest temperature (153 K), the distribution widths of molecular displacement during the considered time intervals (5 ... 45 ms) are found to be small in comparison with the mean radius of the larger crystallites (8 μm). In this case, PFG NMR is able to monitor genuine intracrystalline self-diffusion. In the smaller crystallites, the probability distribution of molecular displacement is found to remain unaffected by the observation time. Moreover, the mean width is of the order of the crystallite radii. One has to conclude, therefore, that at the given temperature over the considered time intervals the ethane molecules are essentially confined by the individual crystallites. Their thermal energy is not high enough to allow them to surpass the step in the potential energy from the intracrystalline space into the surrounding gas phase (intercrystalline space). Since in a crystallite of sufficiently large size the ethane molecules have been shown to be able to cover much larger diffusion paths (Fig. 1a), molecular displacement in the small crystallites becomes a measure of the crystal size. This way of tracing the extension of microscopic regions has become popular under the name "dynamic imaging" [34, 59]. Eventually, with increasing temperature, a substantial fraction of the ethane molecules are able to leave the crystallites. This leads to distribution widths of molecular propagation which are much larger than the crystallite radii. Under these conditions (T = 233 and 293 K), PFG NMR is able to monitor the rate of molecular propagation through the bed of crystallites ("long-range" diffusion). In the case of the larger crystallites (Fig. 1a) one is, at these temperatures, able to distinguish between a narrow distribution (corresponding to those molecules which remain in the interior of the individual crystallites) and a broader constituent which corresponds to those molecules which have passed several crystallites. With increasing observation time, the contribution of the broader constituent increases at the expense of the narrower one, since more and more molecules will leave the individual crystallites.

A plot of the relative intensity of the broad constituent versus the observation time (i.e. the separation between the two field gradient pulses) contains information which is analogous to that of a tracer exchange experiment between a particular crystallite containing e.g. labelled molecules and the unlabelled surroundings. Therefore, this way of analysis of PFG NMR data of zeolitic diffusion has been termed the NMR tracer desorption technique [60]. The first statistical moment ("time constant") of the NMR tracer desorption curve represents the intracrystalline mean lifetime τ_{intra} of the molecules under study.

In the limiting cases of intracrystalline and long-range diffusion, the propagator is given by a Gaussian

$$P(\Delta z, t) = \left(2\pi \left\langle (\Delta z)^2 \right\rangle\right)^{-1/2} \exp\left[-(\Delta z)^2 / 2\left\langle (\Delta z)^2 \right\rangle\right], \tag{5}$$

with a half mean square width (mean square displacement), $\langle(\Delta z)^2\rangle$, increasing linearly with the observation time. This is an immediate consequence

of the central limit theorem of statistics. It applies as soon as the system under study may be considered as quasi-homogeneous, i.e. if the considered molecular displacements may be partitioned in a sequence of smaller displacements ("steps") with equal probability distributions. The self-diffusivity D of the process under study may be introduced by the Einstein relation

$$\left\langle (\Delta z)^2 \right\rangle = 2Dt \,. \tag{6}$$

The definition of D via Eq. 6 is equivalent to Fick's first law, where the self-diffusivity is introduced as a factor of proportionality between the concentration gradient of labelled molecules and their flux density. In isotropic systems one has $\langle(\Delta x)^2\rangle = \langle(\Delta y)^2\rangle = \langle(\Delta z)^2\rangle = \langle(\Delta r)^2\rangle/3$, and Eq. 6 may be transferred into

$$\left\langle (\Delta r)^2 \right\rangle = 6Dt \,. \tag{7}$$

Figure 2 summarizes the three main parameters of molecular transport accessible by PFG NMR and illustrates the conditions under which they may be obtained. Sections 3 and 4 provide examples of the message provided by the study of long-range diffusion ($D_{\text{l.r.}}$) and intercrystalline exchange rates (τ_{intra}^{-1}). Since the scientific interest in molecular propagation is primarily focussed on intracrystalline diffusion, the main part of this contribution (Sect. 5) will be devoted to the measurement of D_{intra}.

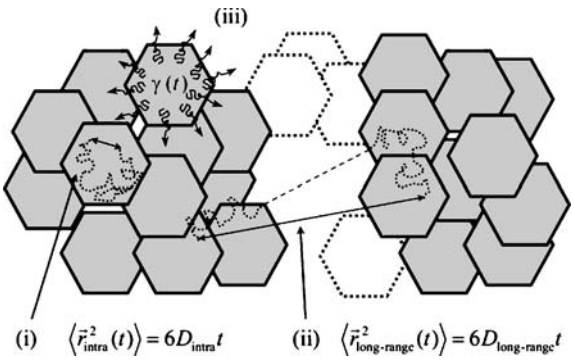

Fig. 2 Parameters of molecular transport in beds of zeolite crystallites as accessible by PFG NMR measurements

2.2 Range of Applicability and Limitations

By inserting Eq. 5 into Eq. 3, the PFG NMR signal attenuation may be simplified to

$$\psi = \exp\left[-\gamma^2\delta^2 g^2 \left\langle (\Delta z)^2 \right\rangle /2\right] \,, \tag{8}$$

or, with Eq. 6, to

$$\psi = \exp\left(-\gamma^2\delta^2 g^2 D t\right) . \tag{9}$$

Eqs. 8 and 9 are the standard relations for the application of PFG NMR to "normal" diffusion, i.e. to mass transfer phenomena characterized by Eqs. 5 and 6. Plotting the signal attenuation in a logarithmic representation versus the square of the pulse width, δ, or gradient amplitude, g, yields a straight line. The mean square displacement $\langle(z^2)\rangle$ in the direction of the applied field gradient and/or the self-diffusivity D in this direction follow immediately from the slope of this line. Vice versa, if the PFG NMR signal attenuation is found to be given by an exponential of the type of Eq. 8 or Eq. 9, the molecular propagator is well approximated by a Gaussian. One may easily determine the mean square displacement on the basis of Eq. 8 by comparison with the attenuation for a standard liquid with known diffusivity (e. g., water with $D = 2.04 \times 10^{-9}$ m^2 s^{-1} at 293 K [61]) by applying the same pulse programme and by calculating $\langle(\Delta z)^2\rangle$ on the basis of Eq. 6 from the known diffusivity. The diffusivity of the sample under study follows either by the analogous procedure from Eq. 9 or from the mean square displacement via Eq. 6. In the limiting cases of the root mean square displacements either much smaller or much larger than the mean crystallite diameters, the thus-obtained diffusivities are the coefficients of intracrystalline or long-range diffusion.

On deriving Eq. 3, it has been assumed that during the field gradient pulses the spins assume well-defined positions. Such an assumption is clearly only acceptable if molecular displacements during the field gradient pulses are negligibly small in comparison with those in the time interval between the gradient pulses. In the case of normal diffusion it may be shown that the PFG NMR signal attenuation under the influence of field gradient pulses of finite duration becomes [52, 62–64]

$$\psi = \exp\left[-\gamma^2\delta^2 g^2 D(t - \delta/3)\right] . \tag{10}$$

Eq. 8 may be used for an estimate of the lower limit of molecular displacements accessible by PFG NMR. Under the assumption that a reliable measurement of $\langle(z^2)\rangle$ is only possible if the field gradient pulses lead to a signal attenuation of $\psi = e^{-1}$, with typical maximum values for the field gradient amplitude ($g = 25$ T m^{-1}) and the pulse width ($\delta = 2$ ms), for hydrogen-containing molecules one obtains $\langle(\Delta z)^2\rangle_{\min}^{1/2} \approx 100$ nm. With Eq. 6, the lower limit of the diffusivity accessible by NMR is thus found to be $\langle(\Delta z)^2\rangle_{\min}/(2t_{\max})$ where $t_{\max}$ denotes the maximum possible observation time. If the NMR signal is generated by a $\pi/2$-π-(primary) echo sequence, $t_{\max}$ is determined by the transverse nuclear magnetic relaxation time T_2, which is typically of the order of a few milliseconds. However, the range of observation times may be significantly enhanced by applying the $\pi/2$-$\pi/2$-$\pi/2$-(stimulated) echo sequence. In this case, $t_{\max}$ is determined by the longitudinal relaxation time T_1, which attains seconds. Thus, $D_{\min}$ may be as small as 10^{-14} m^2 s^{-1}. In reality, however,

these limiting values are only attained in exceptional cases [65, 66], and realistic lower limits are of the order of 300 nm and 10^{-13} m^2 s^{-1}, respectively. It may easily be deduced from Eqs. 8 and 9 that the measuring conditions deteriorate with decreasing gyromagnetic ratio. Thus, for ^{13}C and ^{129}Xe, the lower limits of molecular displacement are by a factor of about 4, and in the case of ^{15}N even by one order of magnitude larger. The measurement of intracrystalline diffusion necessitates the application of crystallites with diameters distinctly exceeding the observed molecular displacements. Hence, PFG NMR measurements of intracrystalline diffusion with nuclei different from hydrogen are additionally complicated and necessitate the application of particularly large crystallites.

Because the amplitude, g, of the magnetic field gradient pulses is limited by the specification of the given amplifier for the gradient pulses, sensitivity enhancement towards smaller displacements has to be based on an enhancement of the total time, δ, of gradient application. Long magnetic field gradient pulses, in turn, imply correspondingly long periods of time within the PFG NMR pulse sequences, during which nuclear magnetization is oriented in the plane perpendicular to the direction of the magnetic field. The application of magnetic field gradient pulses of long duration, δ, is limited, therefore, by the rate of the decay of transverse magnetizations. Even if applying very strong field gradients and thus reducing δ, the induction of eddy currents necessitates a delay between applications of gradient pulses and detection or subsequent r.f. pulses. Hence, the rapid decay of transverse magnetization strongly hampers the applications of PFG NMR experiments. Most recently it was shown that these disturbing influences are notably reduced by Magic Angle Spinning (MAS) PFG NMR, with the directions of the spinning axis and the field gradients parallel to each other [67, 68].

Under the assumption that the shape of the zeolite crystallites may be approximated by spheres of mean radius R, [69] presents a detailed study of the influence of intracrystalline confinement of molecular diffusion on the PFG NMR measurements. Following the classical paper by Murday and Cotts [70], it is shown that also under the influence of confinement the PFG NMR signal attenuation may be approached by a relation of the type of Eq. 9 with D replaced by an apparent diffusivity D_{app}. Figure 3 shows the ratio between the apparent diffusivity D_{app} and the true intrinsic one as a function of a suitably chosen, normalized observation time as determined in [69]. Both diffusivities clearly coincide for short observation times, while with increasing observation times, as an effect of the confinement, the apparent diffusivity is more and more reduced. In the case of a moderate influence of the confinement, the representation of Fig. 3 may be used to determine the true intracrystalline diffusivity from the measured (apparent) diffusivity and the normalized observation time. In this type of measurement it is supposed that the molecules are in fact confined within the intracrystalline space. Figure 1b demonstrates that this may generally be ensured by choosing sufficiently low

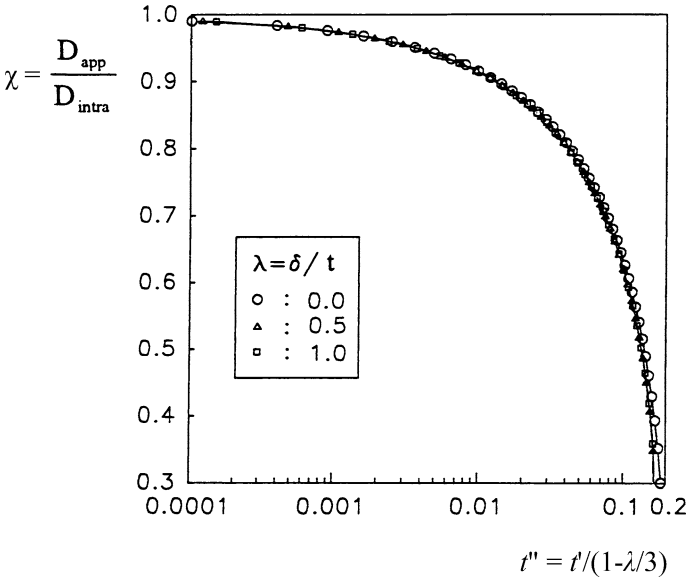

Fig. 3 The ratio D_{app}/D_{intra} between the apparent and the intracrystalline diffusivity in PFG NMR experiments with zeolite crystallites of radius R as a function of the normalized observation time $t' = D_{app}t/R^2$. From [69] with permission

temperatures. A more detailed discussion of the influence of the finite size of the zeolite crystallites on the obtained diffusivities, including the limiting cases of both "reflecting" and "absorbing" boundaries on the crystal surface shall be presented in Sect. 4.

The PFG NMR method works under the supposition that the field gradient pulses acting on the NMR sample are identical. Any difference between the values of δg for the first and second field gradient pulses lead to a signal attenuation which erroneously may be interpreted as being caused by diffusion. Hence, the correct application of PFG NMR necessitates extremely stable gradient currents (which generate the field gradient pulses within suitably structured field gradient coils [34, 63, 64]) as well as a high mechanical stability of both the field gradient coils and the sample, since any movement of the sample with respect to the coils would also lead to differences in the local field at the instants of the first and second field gradient pulses. In order to ensure that the observed signal attenuation with increasing values of g or δ is genuinely due to diffusion (and not due to differences in the values of δg within a pair of field gradient pulses), it is, therefore, useful to apply the identical PFG NMR pulse programme to a sample with a sufficiently low diffusivity (e.g., cross-linked polybutadiene with a diffusivity smaller than 10^{-15} m^2 s^{-1} and a T_2 in the ms range [71]). In this case the field gradient pulse programme must not lead to a signal attenuation. With powder samples like in the case of beds of zeolite crystallites one must be aware of another pit-

fall [72]. Even within completely fixed sample tubes the sample particles may move under the influence of the mechanical pulses generated by the forces acting on the field gradient coils during the current pulses. This influence is particularly stringent for short observation times (i.e. separations between the field gradient pulses) and may be reduced by avoiding any mechanical contact between the sample tube and the probe and/or by compacting the sample material below a contraction in the sample tube.

Methodical development in PFG NMR is focussed on the generation of extremely large field gradient pulses [65, 66, 73–77]. The difficulties arising from the requirement of perfect matching between the two field gradient pulses may be circumvented by applying the stimulated spin echo method under the influence of a strong constant field gradient [78, 79], which is provided by the stray field of the superconducting magnet ("stray field gradient" NMR). It may be shown that the intensity of the stimulated echo is only influenced by the field gradient applied between the two first $\pi/2$ pulses and between the third $\pi/2$ pulse and the echo. Therefore, signal attenuation due to diffusion is also determined by Eqs. Eq. 4, 8 or 9 with an effective pulse width which is identical to the spacing between the first two $\pi/2$ pulses (which is also the spacing between the third $\pi/2$ pulse and the maximum of the stimulated echo). With this technique, presently the largest field gradient "amplitudes" (up to 150 T/m) may be achieved [80]. In comparison with PFG NMR, however, the signal-to-noise ratio in this technique is dramatically reduced, so that much larger acquisition times are inevitable. Moreover, the constant magnetic field excludes the application of Fourier Transform PFG NMR for diffusion studies of multicomponent systems. The measurements are additionally complicated by the fact that by varying the "width" of the field gradient "pulses" (i.e. by changing the spacing between the first two rf pulses) the signal is affected by both diffusion and transverse nuclear magnetic relaxation.

With the advent of superconducting magnets and the option of magnetic field strengths up to 20 T corresponding to NMR frequencies close to the GHz range, the heterogeneity in the susceptibility of typical zeolite samples leads to significant internal field gradients which, in general, are not negligibly small anymore, in comparison with the pulsed-field gradient amplitudes as considered, e.g., in [81]. To circumvent the disturbing influences resulting from interference effects between the constant and pulsed-field gradients, the so-called 13-interval pulse sequence [82] may be applied. It is a modification of the conventional stimulated-echo technique where—by applying pairs of alternating field gradient pulses with a π pulse in between, rather than mere field gradient pulses—the disturbing influence of the internal field gradients brought about by the sample heterogeneity may be extinguished. As a prerequisite for a successful application of the 13-interval pulse sequence, the local magnetic field gradient experienced by each individual diffusant has to be assumed to remain the same over the whole trajectory during the observation

time. By use of the so-called magic pulsed-field gradient ratios [76, 77, 83], even this constraint may be released.

3 Long-Range Diffusion

If the mean molecular displacements in the interval between the two field-gradient pulses are much larger than the crystallite diameters, the diffusivity resulting from PFG NMR measurements reflects the rate of molecular propagation through the bed of crystallites. This coefficient of long-range diffusion may be shown to be determined by [84]

$$D_{\text{l.r.}} = p_{\text{inter}} D_{\text{inter}} , \tag{11}$$

with p_{inter} and D_{inter} denoting respectively the relative amount of diffusants in the intercrystalline space and their diffusivity. Equation 11 may be rationalized by realizing that at any instant only the fraction p_{inter} of the total amount of molecules within the sample effectively contributes to "long-range" transportation. As an example, Fig. 4 shows the long-range diffusivities of cyclohexane in a loose bed of crystallites of zeolite Na-X [85] both in the pure adsorbent–adsorbate system and under the influence of an argon atmosphere. The obtained results may be rationalized on the basis of the simple microdynamic approach

$$D_{\text{inter}} \approx \frac{1}{3} \lambda_{\text{eff}} \nu / \tau_{\text{tort}} , \tag{12}$$

with λ_{eff}, ν and τ_{tort} denoting, respectively, the effective mean free path, the mean thermal velocity and the tortuosity factor, which takes account of the enhancement of the diffusion paths in the gas phase due to the presence of the crystallites. Typical values of the tortuosity factor are of the order of 2 to 4. For sufficiently low temperatures, the gas-phase concentration within the closed NMR sample tube is so small that the mean free path is determined by the collisions of the molecules in the intercrystalline space with the outer surface of the crystallites. Since λ_{eff} hence remains unaffected by temperature variation and ν varies only with the square root of the temperature, the temperature dependence of $D_{\text{l.r.}}$ is essentially determined by p_{inter}. For sufficiently small gas-phase concentrations, p_{inter} is proportional to the gas-phase pressure, so that the activation energy of long-range diffusion must be expected to be of the order of the isosteric heat of adsorption (which determines the pressure with increasing temperature in a closed sample). The experimental data (58 ± 6 kJ mol^{-1} for the activation energy of $D_{\text{l.r.}}$ and 55 kJ mol^{-1} for the heat of adsorption [86]) are in satisfactory agreement with the expected behavior.

The deviation from the Arrhenius dependence as observed with further increasing temperature is caused by the onset of mutual collisions between

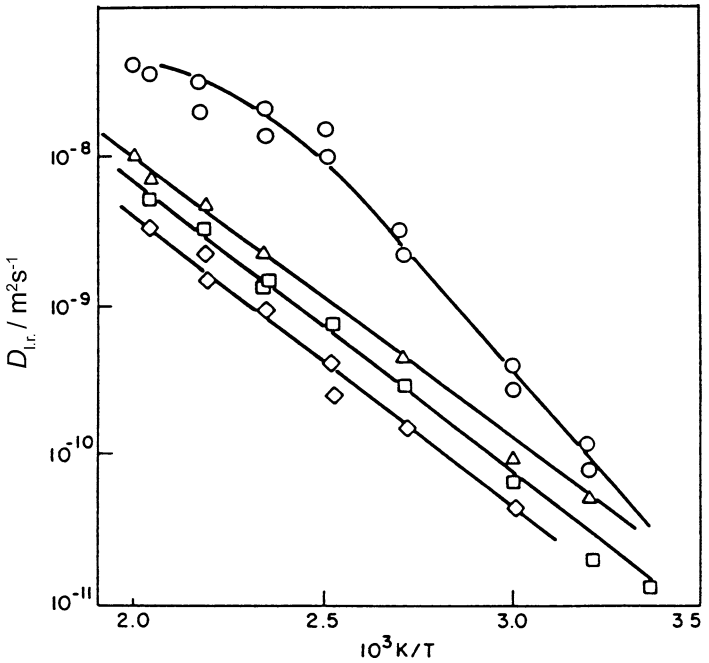

Fig. 4 Coefficients of long-range diffusion of cyclohexane in zeolite Na-X at a sorbate concentration of 1.9 molecules per cavity in the pure adsorbent–adsorbate system (○), and under the influence of an argon atmosphere of ≤ 0.06 MPa (△), 0.13 MPa (□), and 0.2 MPa (◇). From [85] with permission

the molecules in the intercrystalline space. Now the increase of $D_{l.r.}$ due to the increase of p_{inter} with increasing temperature is partially compensated by the reduction of λ_{eff} (and, hence, of D_{inter}). Under the influence of an argon atmosphere, the mean free path of the cyclohexane molecules is determined by the collisions with the argon atoms. The activation energy of long-range diffusion should therefore coincide with the difference between the heats of adsorption of cyclohexane (controlling the increase of p_{inter} with increasing temperature) and argon (controlling the decrease of λ_{eff} and hence of D_{inter} through the increase of the argon concentration in the gas phase). With an adsorption heat of 12 kJ mol^{-1} for argon on Na-X [87] one obtains a theoretical value of 43 kJ mol^{-1}, which is in satisfactory agreement with the experimental result (39$\pm$5 kJ mol^{-1}).

Figure 5 shows the long-range diffusivity of nitrogen adsorbed on a commercial 5A-type zeolite (Na,Ca-A, with about 67% of Na^+ exchanged by Ca^{2+}) in comparison with a theoretical estimate on the basis of Eq. 12 with p_{inter} determined from the adsorption isotherm and the packing density of the bed of crystallites [88]. For simplicity, the limiting value of the mean free path for sufficiently low temperatures has been set equal to the crystallite radius, and

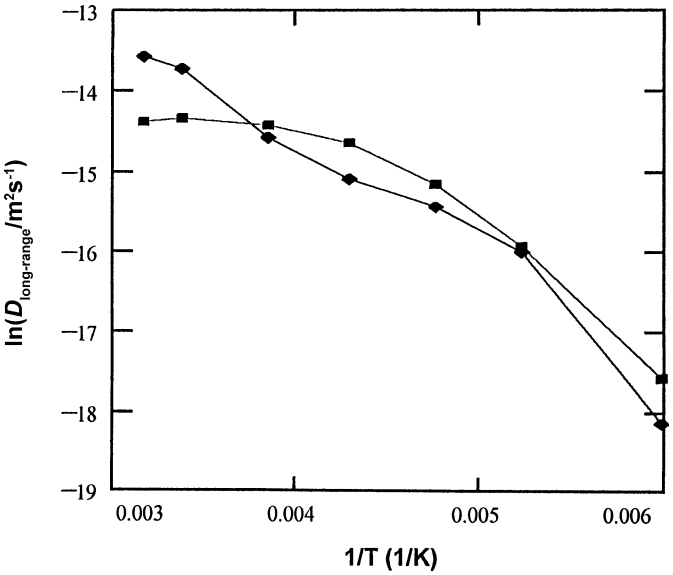

Fig. 5 Comparison between the experimentally (*diamonds*) and theoretically (*squares*) determined long-range diffusivities for nitrogen in zeolite Na,Ca-A. From [88] with permission

the tortuosity factor has been chosen to yield best agreement in the absolute values. Irrespective of the rough model, the theoretical data satisfactorily reflect the temperature dependence. In this way it is quantitatively confirmed that the decreasing slope of the Arrhenius plot with increasing temperature is a consequence of the decreasing mean free path.

As discussed in Sect. 2.2, the spatial resolution of ^{15}N PFG NMR diffusion measurements is by about one order of magnitude poorer than in the case of ^{1}H PFG NMR, as a consequence of the corresponding difference in the gyromagnetic ratios. This deficiency is crucial for measuring intracrystalline diffusion, since in this case the resolution of intracrystalline diffusion paths has to be ensured. However, this limitation does not concern long-range diffusion, since in this case the molecular displacements have to exceed the crystalline diameters rather than remain below it. Not unexpectedly, ^{15}N PFG NMR has, therefore, been routinely applied to the measurement of long-range diffusion in beds of zeolites [89–91]. In fact, using alternately ^{1}H, ^{13}C and ^{15}N PFG NMR, in [89] for the first time simultaneously the long-range diffusivities of methane, carbon monoxide and nitrogen adsorbed in beds of zeolite Na-X and Na,Ca-A have been measured. In all these studies, the tortuosities have been introduced as fitting parameters following Eq. 12, where the mean free path was assumed to be of the order of the diameters of the zeolite crystallites.

Having the highest value of the gyromagnetic ratio and, hence, the largest signal intensity, ^{1}H PFG NMR studies offer the best options for a better than just qualitative comparison of experimental long-range diffusivity data with gas kinetic concepts. As an example, Fig. 6 displays the long-range diffusivity of ethane in a bed of crystallites of zeolite Na-X. The insets illustrate the two limiting situations of Knudsen diffusion (at low temperatures) and bulk diffusion (at high temperatures) in the gas phase between the crystallites. A quantitative analysis [92], based on the adsorption isotherms and the intercrystalline porosity, yielded the remarkable result that a satisfactory fit between the experimental data and the estimates of $D_{\mathrm{l.r.}} = p_{\mathrm{inter}} D_{\mathrm{inter}}$ following Eqs. 11 and 12 did only lead to coinciding results if the tortuosity factors τ are assumed to differ under the conditions of Knudsen and bulk diffusion by at least a factor of 3. Similar results have been obtained by dynamic Monte Carlo (MC) simulations [93–96]. In [97] it is shown that the increase in the tortuosity factor under the conditions of Knudsen diffusion may be attributed to the fact that with increasing tortuosity subsequent jumps are more and more anti-correlated, i.e. that any jump tends to counteract the displacement by the preceding one.

It should be mentioned that—if zeolites are technically applied as formed pellets—transport limitation may be due to both intracrystalline zeolitic diffusion and long-range diffusion as just considered. Denoting the mean radii of the crystallites and of the pellets by r_{C} and r_{P}, respectively, the respec-

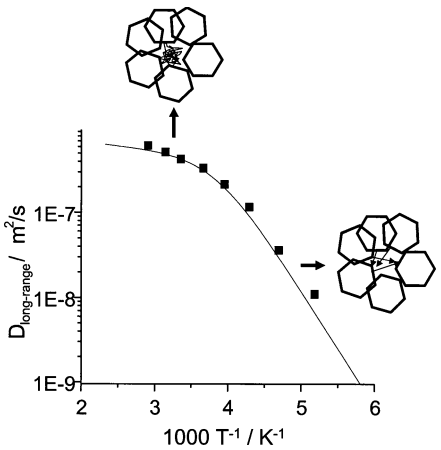

Fig. 6 Temperature dependence of the coefficient of long-range self-diffusion of ethane measured by PFG NMR in a bed of crystallites of zeolite Na-X (*points*) and comparison with the theoretical estimate (*line*). The theoretical estimate is based on the sketched models of prevailing Knudsen diffusion (low temperatures, molecular trajectories consist of straight lines connecting the points of surface encounters) and gas-phase diffusion (high temperatures, mutual collisions of the molecules lead to Brownian-type trajectories in the intercrystalline space). From [92] with permission

tive time constants are $\tau_C = r_C^2/(15D_{intra})$ and $\tau_P = r_P^2/(15D_{l.r.})$ [52, 98, 99]. Hence, being able to directly determine both D_{intra} and $D_{l.r.}$, PFG NMR provides a straightforward means to explore the governing transport mechanism under technical application. In the case of FCC (fluid catalytic cracking) catalysts, among the commercially most attractive zeolite catalysts [100], it could be in this way shown that—at least for the investigated, industrially used catalysts—the intracrystalline transport resistance was of no influence on the overall process, in contrast to long-range ("intra-pellet") diffusion [101, 102].

4 Surface Barriers

The quantitative information provided by PFG NMR about the existence of additional transport resistances on the external surface of the zeolite crystallites (surface barriers) results from a comparison of the values for the intracrystalline mean life time determined directly (viz. τ_{intra}) by an analysis of the time dependence of the spin-echo attenuation (and, hence, of the propagator), and determined indirectly (viz. τ_{intra}^{Diff}) from the intracrystalline diffusivity on the assumption that molecular exchange between different crystallites is controlled by intracrystalline diffusion. On the additional assumption that the shape of the crystallites may be approximated by spheres with a mean square radius $\langle R^2 \rangle$ one has in the latter case [87, 103]

$$\tau_{intra}^{Diff} = \frac{\langle R^2 \rangle}{15D} . \tag{13}$$

A representation of the values for the intracrystalline mean life time in parallelepipeds with varying edge lengths may be found in [104].

Figure 7 illustrates how the PFG NMR data are analyzed to yield the intracrystalline mean lifetime. The spin echo attenuation (Fig. 7a) is supposed to be represented by the superposition of two exponentials corresponding according to Eq. 4 to two Gaussian propagators. Denoting the relative amount of molecules, which have exchanged between different crystallites by $\gamma(t)$, the quantity $1 - \gamma(t)$ follows directly from the relative intensity of the slowly decaying part of the spin echo attenuation (Fig. 7b), which corresponds to the narrower constituent of the propagator representation. The intracrystalline mean life time follows as the first statistical moment of the "NMR tracer desorption" curve $\gamma(t)$ (Fig. 7c):

$$M_1 \equiv \tau_{intra} = \int_0^\infty [1 - \gamma(t)] \, dt . \tag{14}$$

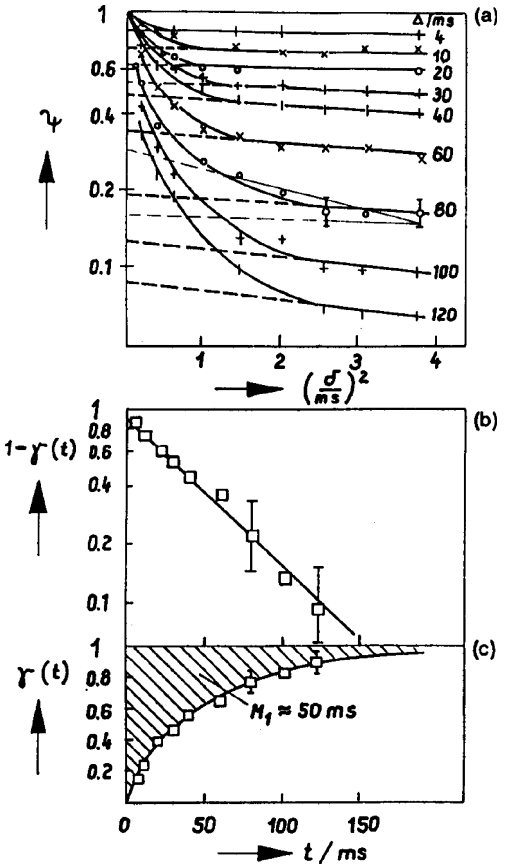

Fig. 7 Analysis of PFG NMR data for NMR tracer desorption studies (butane/Na-X, 165 mg g^{-1}, $R = 25$ μm, 353 K). From [60] with permission

Figure 8 provides an example of the information resulting from a comparison between $\tau_{\text{intra}}^{\text{Diff.}}$ and τ_{intra}. Using methane as a probe molecule, in the as-synthesized ZSM-5 crystallite the values for τ_{intra} and $\tau_{\text{intra}}^{\text{Diff.}}$ are essentially found to coincide. Molecular exchange between different crystallites must, therefore, be concluded to be in fact controlled by intracrystalline diffusion. The transport properties of the zeolite crystallites are significantly changed by subjecting them to a coking procedure [105]. Using mesitylene as a coking compound, the intracrystalline mobility of methane and, hence, $\tau_{\text{intra}}^{\text{Diff.}}$ remain essentially unaffected, while the intracrystalline mean lifetime increases. Such a behavior can only be explained by a preferential coke deposition on the crystallite surface. The thus-formed surface barriers reduce the rate of intercrystalline exchange, while the intracrystalline mobility remains unaffected. With *n*-hexane as a coking compound, the intercrystalline exchange rate is reduced in the same way as the rate of intracrystalline diffusion. In this case, the

carbonaceous compounds must be distributed homogeneously over the crystallites. Only for larger coking times, the diverging patterns of τ_{intra} and $\tau_{intra}^{Diff.}$ indicate that in this second stage the carbonaceous compounds form a surface barrier.

Deviations from normal diffusion, i.e. from molecular propagation within a quasi-homogeneous, essentially infinitely extended medium, may be taken into account by introducing an effective diffusivity D_{eff}. It is defined in the same way as the self-diffusivity, i.e. via Eqs. 6 and 7, however, without the requirement of the validity of Fick's laws 1 and 2. Therefore, D_{eff} may become a function of the (observation) time. In the considered case of zeolitic diffusion and for intracrystalline diffusion paths being sufficiently small in comparison with the crystallite radii, the effective diffusivity may be shown to be represented by a power series [106–108], leading to

$$D_{eff}(t)/D = 1 - \frac{4}{3\sqrt{\pi}}\frac{1}{R}\sqrt{Dt} - \frac{1}{2R^2}(Dt)\,, \tag{15a}$$

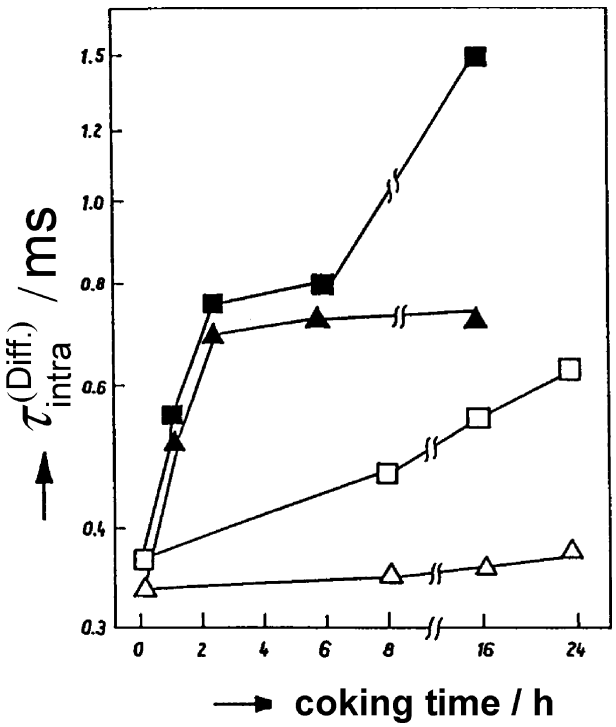

Fig. 8 Values for the intracrystalline mean life time τ_{intra} (□,■) and the quantity τ_{intra}^{Diff} (△,▲) for methane in H-ZSM5 which has been coked by *n*-hexane (*filled symbols*) and mesitylene (*open symbols*) as a function of the coking time (methane concentration: 12 molecules per unit cell; measuring temperature: 296 K). From [116] with permission

and

$$D_{\mathrm{eff}}(t)/D = 1 - \frac{2}{3\sqrt{\pi}}\frac{1}{R}\sqrt{Dt} - \frac{1}{R^2}(Dt)\,, \tag{15b}$$

where D stands for the genuine intracrystalline diffusivity. As to be expected, the experimentally accessible quantity D_{eff} coincides with the true intracrystalline diffusivity in the limiting case of negligible displacements, i.e. for $(Dt)^{1/2} \to 0$. Equation Eq. 15a describes the situation of ideal confinement to intracrystalline space (top of Fig. 1). In this case, the crystallite surface acts as an (ideally) reflecting boundary for the molecules in the intracrystalline space. Equation Eq. 15b has been derived for absorbing boundaries [106–108]. PFG NMR diffusion measurements with beds of zeolites do in fact comply with this limiting case, when the long-range diffusivity is much larger than the intracrystalline diffusivity (Fig. 1, bottom left) and one is only analyzing the intracrystalline constituent of the propagator (viz. the narrow one).

The influence of confining boundaries on the effective diffusivity as reflected by Eqs. 15a,b has been repeatedly applied to determine the pore surface in rocks or beds of sand grains [106–115]. In [116], this concept has been for the first time successfully applied to beds of zeolites. Figure 9 shows the results of these studies, which have been performed with two different samples of Na-X, one loaded with *n*-hexane (two molecules per supercage), the other with *n*-hexane and hexafluoromethane (one molecule per supercage for either). In both samples, for the *n*-hexane measurements a temperature of 298 K was chosen, where the *n*-hexane molecules were found to be totally confined so that the data analysis could be based on Eq. 15a. The measure-

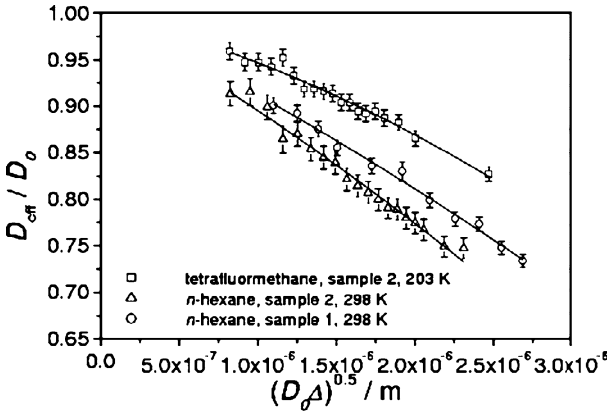

Fig. 9 Relative effective diffusivities for *n*-hexane (△, sample 2) and tetrafluoromethane (□, sample 2) under two-component adsorption and for *n*-hexane under single-component adsorption (○, sample 1). The *lines* represent the appropriate fits of Eqs. 15a,b, respectively. From [116] with permission

ment of the sample containing two different diffusants provided the option to operate with one and the same sample under the conditions of reflecting boundaries [(Eq. 15a), ^{1}H PFG NMR with *n*-hexane] and absorbing boundaries [(Eq. 15b), ^{19}F PFG NMR with CF_4]. The latter type of measurements had to be carried out at 203 K, since only at these low temperatures were the diffusivities small enough to allow molecular displacements sufficiently small in comparison with the crystallite radii (as a supposition for the series expansion). Even at this low temperature the long-range diffusivity was found to be large enough to permit the limiting case of absorbing boundaries, i.e. of Eq. 15b. It is noteworthy that the good fit between the experimental data and the theoretical curves was only possible by involving the second-order terms in $(Dt)^{1/2}$. It is worth noting that, within a range of 20%, five different ways to analyze the crystallite size have led to coinciding results on the size of the crystallites under study [116], viz. (1) microscopic inspection, (2) restricted diffusion in the limit of large observation times (situation shown by Fig. 1, top right), (3) application of Eq. 13 to the results of the PFG NMR tracer desorption technique, and, finally, consideration of the limit of short observation times for (4) reflecting boundaries (Eq. 15a) and (5) absorbing boundaries (Eq. 15b).

5
Intracrystalline Diffusion

5.1
Structure-Related Diffusion

Intracrystalline molecular diffusion is governed by the mutual interaction of the diffusants as well as by their interaction with the pore system. Depending on the importance and on the nature of these two influences, the intracrystalline diffusivity may yield quite different patterns of variation with sorbate concentration. Figure 10 provides a few examples of the patterns of concentration dependence observed so far. The mutual interaction between the diffusants obviously effects a decrease with increasing concentration (patterns I and II), while molecular confinement either by strong adsorption sites or by contractions ("windows" between adjacent cavities) gives rise to an increase of the diffusivities with increasing concentration (patterns III and V). Pattern IV results as a combination of both tendencies.

The microkinetic interpretation of the origin of these different patterns may be confirmed by molecular dynamics (MD) simulations. As an example, Fig. 11 presents the result of an MD study with methane in a cation-free zeolite of type LTA [117, 118]. By increasing the Lennard–Jones distance σ between the methane molecules and the oxygen of the zeolite lattice one is able to simulate the influence of a reduction of the window diameter on the dif-

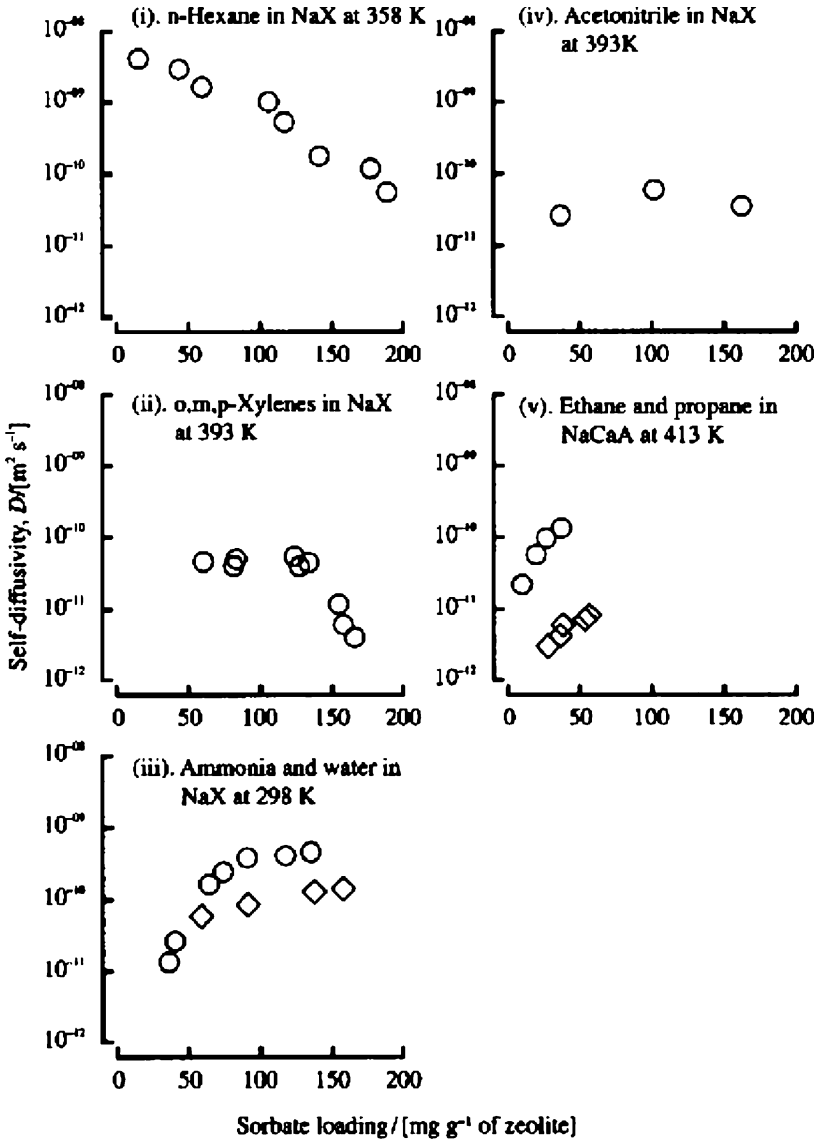

Fig. 10 The different patterns of concentration dependence of intracrystalline self-diffusivities as determined from PFG NMR measurements. From Keil et al. [232], based on experimental data from Kärger and Pfeifer [202]

fusion behavior. As to be expected, the translational mobility is found to be reduced with decreasing window diameter. In addition, for sufficiently small window diameters (corresponding to sufficiently large values for σ) an inversion in the concentration dependence is observed. As a consequence of

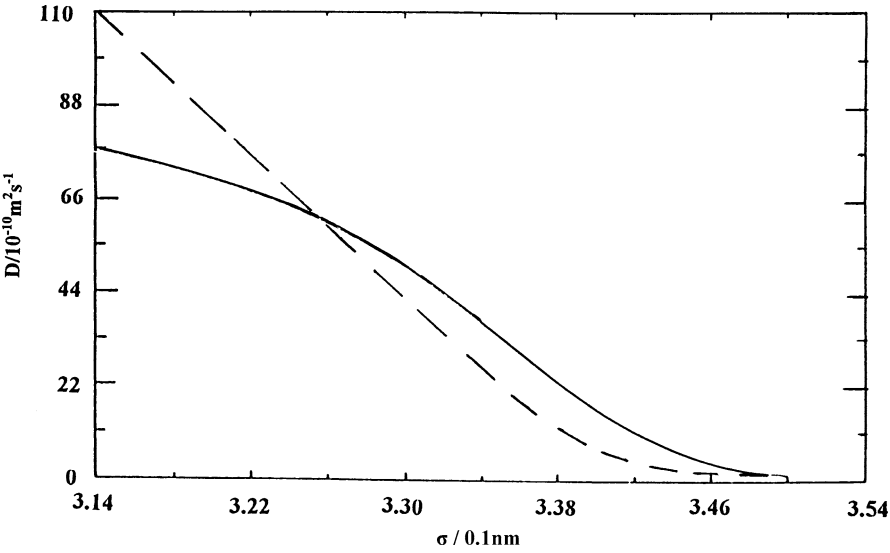

Fig. 11 Result of MD simulations of the intracrystalline diffusion of methane in a cation-free zeolite LTA at 300 K as a function of the Lennard–Jones distance between methane and the oxygen of the zeolite lattice for a concentration of 1 (*broken line*) and 6 (*full line*) molecules per cavity. From [117, 118] with permission

molecular confinement by small window diameters, the diffusivity is found to increase with increasing concentration.

In contrast to the X and A type zeolites, the framework of ZSM-5 is of non-cubic structure. Hence, as a consequence of the interrelation between zeolite structure and molecular mobility, molecular diffusion in different crystallographic directions has to proceed at different rates so that, strictly speaking, molecular diffusion must be described by a diffusion tensor rather than by the diffusion coefficient, i.e. a scalar quantity.

The investigation of diffusion anisotropy in synthetic zeolites is complicated by the small size of the crystallites, which excludes the possibility of measurements with one particular single crystal. However, by introducing large zeolite crystals of type ZSM-5 into an array of parallel capillaries [119, 120], it was possible to align a sufficiently large amount of crystallites with respect to the crystallographic z axis (Fig. 12). With the pulsed-field gradients directed either perpendicular or parallel to the capillaries, the effective diffusivities provided by PFG NMR predominantly reflect molecular propagation in the xy plane or in the z direction, respectively. Figure 13 shows the diffusivities of methane in a sample with oriented ZSM-5 crystallites for the two different gradient directions [120]. The two channel types, the sinusoidal and the straight one, mark the directions of the x and y axes. Since there is no channel system directed along the z axis, molecular diffusion in this di-

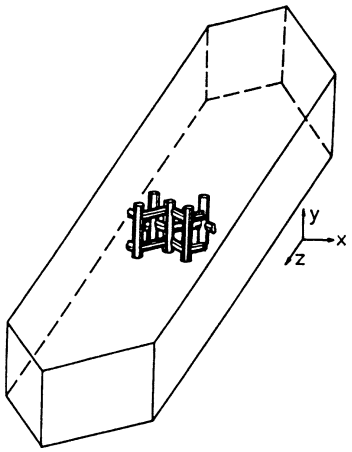

Fig. 12 Schematic representation of the orientation of the internal channel system within zeolite crystallites of type ZSM-5. From [119] with permission

rection can only proceed by interchanging periods of migration along the segments of the straight and sinusoidal channels. As therefore to be expected, the diffusivities in PFG NMR measurements with field gradients oriented perpendicular to the capillaries of the "container" are larger than in the case with field gradients parallel to the capillaries. Since the crystal alignment within the capillaries is not perfect, the measured effective diffusivities clearly cannot coincide with the diffusivities in the z direction, D_z, and with the mean value $1/2(D_x + D_y)$ of the diffusivities in the xy plane. Estimating the influence of the deviation from a perfect alignment on the effective diffusivities, one can determine the possible range of values for D_z and $1/2(D_x + D_y)$. These values are also presented in Fig. 13. Since molecular alignment is only possible with respect to the z axis, a separate determination of D_x and D_y in the proposed way is impossible.

As an alternative way to study diffusion anisotropy in zeolite crystallites, it is possible to analyze the shape of the NMR signal attenuation with increasing field gradient intensity. Since in a powder sample all orientations of the zeolite crystals with respect to the field gradient direction are possible, the signal attenuation results as a superposition of exponentials of the type of Eq. 9 with diffusivities determined by the orientation of any individual crystallite. All information about the diffusion tensor must be contained, therefore, in the shape of the echo attenuation.

It would probably be rather difficult if not even impossible to deduce three different parameters from a single, monotonically decaying, noisy curve. In the present case, however, the situation is not as bad. Taking into consideration that the rate of molecular transition between adjacent unit cells is determined by only two parameters, viz. the transition rate through segments

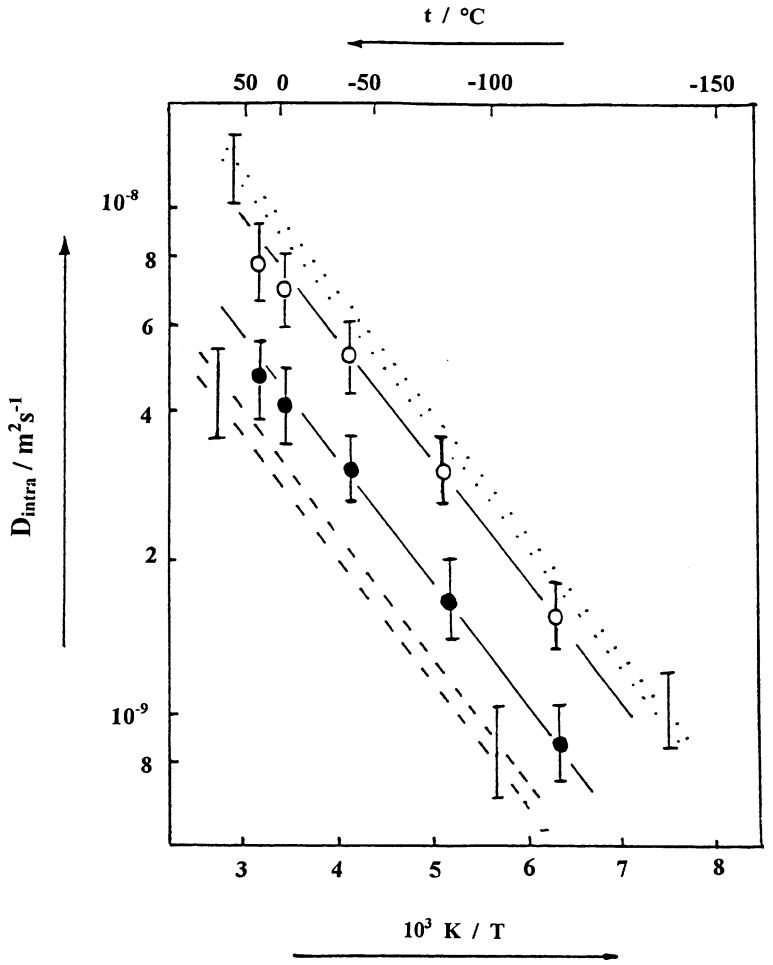

Fig. 13 Arrhenius plot of the diffusivities of methane in ZSM-5 at a sorbate concentration of 12 molecules per unit cell with field gradients applied parallel (•) and perpendicular (○) to the capillaries of the container system. The broken (*dotted*) lines indicate the expected range of D_z and $1/2(D_x + D_y)$. From [120] with permission

of the straight and sinusoidal channels, one may conclude that the three principal elements of the diffusion tensor cannot be independent from each other. By simple statistic arguments [121–123], the correlation rule between the diffusivities in ZSM-5 may be derived to be

$$c^2/D_z = a^2/D_x + b^2/D_y\,, \tag{16}$$

where $a \approx b \approx 2$ nm and $c \approx 1.34$ nm denote the unit cell dimensions in the x, y and z direction. As a necessary and sufficient supposition of Eq. 16, it must be required that the correlation time of molecular migration is much smaller

than the mean passage time between adjacent channel intersections, i.e. that the molecules arriving at a particular channel intersection have "forgotten" where they came from. MD simulations [124–127] indicate that Eq. 16 may in fact be considered as a reasonable first-order approximation for the interrelation of the main elements of the diffusion tensor of MFI-type zeolites. Approaches to higher-order correlations are presented and discussed in [128–130].

Using Eq. 16, the spin-echo attenuation curves for PFG NMR diffusion measurements with powder samples of ZSM-5 have been calculated numerically for different values of D_y/D_x [119]. Figure 14 shows these results in a dimensionless representation. The included experimental data are in best agreement with the theoretical plots for $D_y/D_x \approx 2.5$, independent of the measuring temperature. The activation energy of self-diffusion must, therefore, be expected to be identical for all directions. Figure 15 provides a comparison between the thus-determined diffusivities, the measurements with oriented crystallites and MD simulations by different authors. All data are found to be in reasonably good agreement. It should be clearly pointed out that, as a consequence of the fitting procedure, the accuracy of the PFG NMR

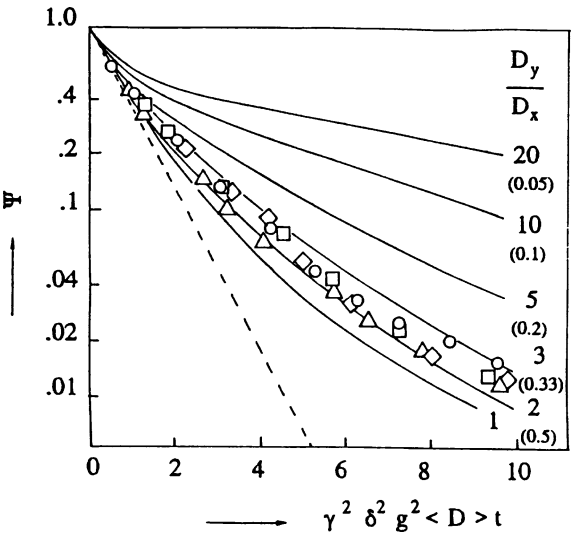

Fig. 14 Theoretical dependence of the signal decay in PFG NMR experiments for different values of the ratio D_y/D_x, calculated by means of Eq. 16, and comparison with the data experimentally determined at 193 (○), 223 (□), 273 (◇) and 298 (△) K for methane adsorbed in ZSM-5 at a sorbate concentration of 12 molecules per unit cell. The broken line represents the signal decay in the case of isotropic diffusion. The calculated dependences are symmetric in D_x and D_y. In view of the geometrical conditions and the MD results, for the experimental data the possibility $D_y/D_x < 1$ may be excluded. From [119] with permission

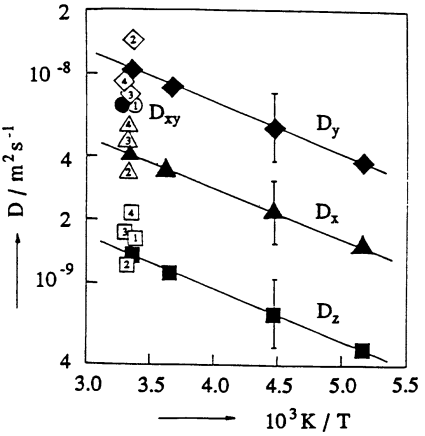

Fig. 15 Arrhenius plot of the principal values of the diffusion tensor for methane adsorbed in ZSM-5, as determined on the basis of Fig. 14 (*full symbols*), and comparison with the results of the measurement with oriented samples (1) and of MD simulations presented in Refs. [233] (2), [234] (3) and [235] (4) (*open symbols* with inserted numbers). From [119] with permission

data as indicated by the error bars in Fig. 15 is only modest. It cannot be excluded, therefore, that the ratio between D_y and D_x is in reality shifted to smaller values, which might be a consequence of internal intergrowths of the ZSM-5 crystals under study [127]. In uptake measurements with oriented crystals [131], this effect has been considered as an explanation of the fact that the resulting anisotropy factor was smaller than expected on the basis of Eq. 16. The extent up to which such an effect may be relevant for PFG NMR diffusion measurements depends on the relation between the diffusion paths covered in the PFG NMR experiments and the extension of the regions of perfect crystallinity.

Like with MFI-type zeolites, structure-related diffusion anisotropy might as well be anticipated for chabazites [132]. The chabazite pore system consists of an arrangement of large cavities of the shape of prolate ellipsoids. Each cavity is connected to six adjacent ones, with the centers of three of them above and with the other three below the center of this cavity. As a consequence, molecular propagation from cavity to cavity implies correlated shifts into the direction of the longitudinal extension of the cavities (z coordinate) and within the plane perpendicular to it (xy plane). Incorporating the relevant crystal geometry yields the correlation rule [133, 134]

$$D_z/D_{xy} = 0.8\,, \tag{17}$$

which, in the case of chabazite, assumes the role which Eq. 16 had for MFI-type zeolites. Most interestingly, experimental measurements of the diffusion anisotropy of water with both natural single crystals and polycrystalline sam-

ples yield a value of $D_z/D_{xy} = 0.4 \pm 0.1$ [133]. Obviously, experimental evidence indicates that the rate of molecular propagation in the direction of the longitudinal extension of the cavities is smaller than expected on the basis of the simple correlation rule.

Deviations of this type may clearly be brought about by deviations of the structure of the zeolites under study from the ideal structure as implied for the deviation of Eq. 17. It would be most remarkable, however, if for two completely different chabazite species, viz. the big single crystals and polycrystalline samples, identical deviations from the ideal structure would occur, as suggested by the experimental data.

For deriving Eq. 17, one has additionally to imply that molecular propagation within one cavity has to proceed much faster than the transfer to the adjacent cavities. However, it has been evidenced by MD simulations [134] that there are two maxima in the population density of the water molecules within the large cavity, separated from each other in the longitudinal (i.e. z) direction. Assuming that the exchange between these two sites is not infinitely fast in comparison with the exchange between adjacent cavities, propagation in the z direction is retarded in comparison with propagation in the xy plane. It is, in fact, this behavior which is nicely reflected by the experimental data of [133].

In contrast to ZSM-5, where an array of channels pointing in one direction is interconnected by another array of channels pointing in another direction, there are a substantial number of zeolites containing only one system of channels. In this case, the principal elements of the diffusion tensor in the direction perpendicular to the channel axes degenerate to zero. Depending on the relation between the diameters of the channels and of the molecules under study, molecular diffusion along the channel axis may proceed by two completely different mechanisms. As soon as the molecules are small enough so that they are able to pass each other, molecular propagation obeys the laws of normal diffusion. Results of this type are described in [135]. However, if molecular confinement within the channels is so stringent that a mutual passage of the molecules is excluded, the time dependence of molecular propagation is completely different from normal diffusion, yielding proportionality of the mean square displacement with the square root of the observation time rather than with the observation time itself [136]. This type of molecular propagation has been termed single-file diffusion [136, 137]. Indications of single-file diffusion in zeolites have in fact been observed by PFG NMR [138–142]. Details of these investigations may be found in [144], which is exclusively devoted to single-file systems.

The diffusion properties of zeolites may be significantly influenced by their content of exchangeable cations. As an example, by both nuclear magnetic relaxation [1, 143] and PFG NMR [145] measurements, the molecular mobility of aromatics in zeolite Na-X was found to be larger than in Na-Y. Since the adsorbate–adsorbent interaction of unsaturated hydrocarbons is dominated by the interaction between the π electrons of the double bonds and

the sodium ions [146], this experimental finding was explained by the higher cation concentration in Na-X leading to an overlap of the wells in the potential energy of the molecules. The increase in the mobility of alkanes in Na,Ca-A with increasing amounts of Ca^{2+}, as observed in both uptake [147] and PFG NMR [148] diffusion measurements, has been attributed to the increasing amount of open "windows" between adjacent cavities as a consequence of the decreasing total amount of cations. Zeolitic diffusion under such conditions may be adequately described by a random walk on percolation networks [149, 150]. In [147] and [148], the increase in molecular mobility with increasing calcium content could nearly quantitatively be explained in this way. Such an explanation implies, however, that the influence of the cation–adsorbate interaction is negligibly small in comparison with the transport resistances exerted by the "windows".

Unlike the mobility of unsaturated hydrocarbons, the mobility of saturated hydrocarbons in Na-X is, in fact, essentially unaffected by the presence of sodium cations. This has been confirmed by PFG NMR diffusion studies with benzene and *n*-heptane in zeolite Na-X and La-X [103, 151]. Since the trivalent lanthanum ions are predominantly localized at positions in the hexagonal prisms and sodalite units, the molecules adsorbed in lanthanum-exchanged zeolites are essentially without contact to the cations. As a consequence of the specific interaction between the cations and the unsaturated hydrocarbon, the benzene mobility in Na-X was found to be two orders of magnitude smaller than in La-X, while the *n*-heptane diffusivities were the same.

In view of their higher electrostatic field, calcium ions must be expected to give rise to a much stronger interaction with the saturated hydrocarbons than sodium ions. Since in zeolite Na,Ca-A any replacement of Na^+ by Ca^{2+} may simultaneously change both the sorbate–sorbent interaction and the number of "open" and "closed" windows, the more open framework of X-type zeolites provides better prospects for such studies. Figure 16 gives a comparison of the diffusivities of methane in zeolite Na-X and in zeolite Na,Ca-X with 30% and 75% of Na^+ replaced by Ca^{2+} [152]. Since the first calcium cations are known to assume positions outside the large cavities [153], they cannot come into contact with the methane molecules. Methane diffusion in Na-X and Na(30),Ca-X is therefore found to be the same, following the type I concentration dependence as classified by Fig. 10. With a higher content of calcium, however, a significant change in the diffusion properties is effected: Now the diffusivities follow pattern V of the concentration dependence, and at small concentrations they are up to two orders of magnitude smaller than in zeolite Na-X. Obviously, the interaction with the calcium ions has led to a dramatic reduction in the mobility of methane. It is interesting to note that in the limit of large concentrations the methane diffusivities in Na-X and Na(75),Ca-X approach each other.

Similarly, also the *n*-hexane diffusivity in Na(75),Ca-X is found to be much smaller than in Na-X at small concentrations [152]. In this case, however,

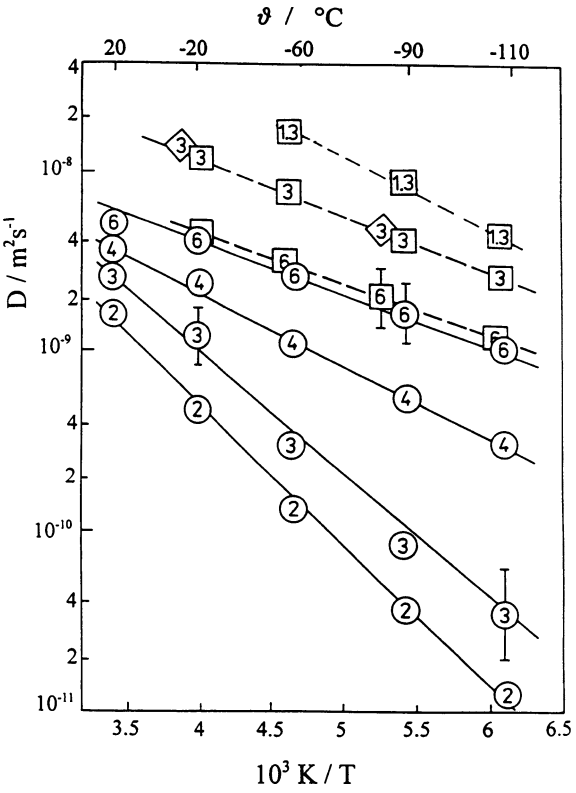

Fig. 16 Coefficient of intracrystalline self-diffusion of methane in zeolite (○) Na75,Ca-X, (◇) Na30,Ca-X, and (□) Na-X determined by PFG NMR. The numbers inserted in the symbols indicate the concentration in molecules per supercage. From [152] with permission

the diffusivities approach each other already at medium concentrations, so that the *n*-hexane diffusivity in Na(75),Ca-X passes a maximum, following the type III concentration pattern.

Comparison of the diffusivities in Na,Ca-X and Na,Ca-A at comparable calcium exchange show [152] that the methane diffusivities are of the same order, while the *n*-hexane diffusivity in Na,Ca-A is much smaller than in Na,Ca-X. One has to conclude, therefore, that for the diffusion of the longer *n*-alkanes in Na,Ca-A it is justified to consider the passage through the windows as the rate-limiting step. For methane and ethane, however, the transport properties are dominated by the interaction with the cations. MD simulations of methane in Na,Ca-A are in satisfactory agreement with the NMR data and confirm this conclusion [154].

As a consequence of the much smaller window diameters, window blocking in zeolite A is easier to be achieved than in zeolite X. However, there are examples, where the co-adsorption of a second molecular species (e.g., water

in addition to C_2 or C_4 hydrocarbons [155]) leads to a dramatic reduction in the molecular mobility which can only be explained by the formation of adsorption complexes in the windows between adjacent supercages.

An analytical description of the diffusivity of molecules in pore systems with open and obstructed windows may be based on the effective medium approximation of percolation systems [156, 157]. Lowest-order effective medium approximation yields for the diffusivity [149, 156, 158, 159]

$$D = \frac{D_0}{2}\left\{A + \left[A^2 + 4f/(z/2-1)\right]^{1/2}\right\}, \tag{18}$$

with

$$A = 1 - p + fp - (f + p - fp)/(z/2-1), \tag{19}$$

where D_0 is the diffusivity in the open pore lattice, p is the fraction of the obstructed windows ("bonds") and z is the coordination number of the pore lattice. In the special cases of A and X type zeolites, one thus has $z = 6$ and 4, respectively. f represents the ratio of the transition rates through "obstructed" and "open" windows. Hence, the diffusivity in the pore lattice with all windows obstructed would be fD_0.

Figure 17 illustrates the use of this concept for the interpretation of the influence of co-adsorbed, less mobile molecules (benzene, ethylene) on the mobility of a highly mobile species (methane) in zeolite Na-Y. It turns out that the reduction in the methane mobility with an increasing amount of co-adsorbed molecules [159] may be satisfactorily explained by the assumption that any co-adsorbed molecule reduces the transition rate through a particu-

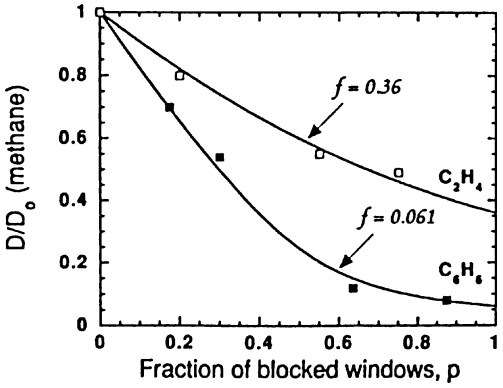

Fig. 17 Intracrystalline self-diffusivity of methane (≈2 molecules per supercage, at 25 °C) as a function of the amount of co-adsorbed molecules per "window". The *solid lines* are predictions based on the effective medium approximation of percolation theory with f denoting the ratio of the transition rates through "blocked" and "open" windows. From [158] with permission

lar window to the fraction f of its original value [158]. As to be expected, the blocking efficiency of the larger benzene molecule ($f = 0.061$) is found to be much larger than that of ethylene ($f = 0.36$). Similarly, in ZSM-5 the methane mobility was found to be much more effectively reduced by co-adsorbed pyridinium ions than by ammonium ions [160, 161].

5.2 Monitoring Self-Diffusion under Transient Conditions

PFG NMR measurements are generally performed with closed samples containing the adsorbate in equilibrium with the adsorbent. In general, the measurements are carried out hours or even days after the introduction of the adsorbate into the activated sample. Moreover, the process of equilibration may be accelerated by keeping the sample at an elevated temperature. Once equilibrium is established, the measurements may be repeated as often as desired. There are examples [162], where more than 20 years after the first measurement, PFG NMR measurement of an adsorbate–adsorbent system within a closed sample tube yielded identical diffusivities.

As a non-invasive method, however, PFG NMR also provides excellent conditions for the measurement of molecular diffusivities under transient conditions. As an example, Fig. 18 shows the results of space- and time-resolved self-diffusion measurements over a bed of activated zeolite Na-X during the uptake of *n*-hexane [163]. Taking into account that, due to the finite size of

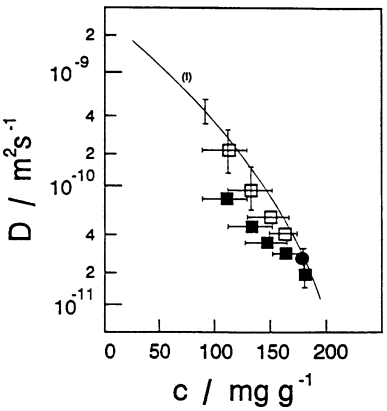

Fig. 18 Apparent coefficients of intracrystalline self-diffusion of *n*-hexane as observed by time- and space-resolved ^{1}H PFG NMR in a bed of zeolite Na-X with restricted (■) and unrestricted (●) sorbate supply in dependence on the sorbate concentration. The real diffusivities (*open symbols*) were calculated from these values by using the correspondence presented by Fig. 3. The full line with the indicated error bars represents the range of intracrystalline diffusivities as observed in previous PFG NMR studies with closed sample tubes. From [163] with permission

the crystallites, the measured apparent diffusivities had to be transferred into the true intracrystalline diffusivities by the procedure described in Sect. 2.2, the diffusivities measured immediately after the advent of the adsorption front were identical with those observed for the same sorbate concentration in closed sample tubes, i.e. after the final establishment of equilibrium. This result does especially exclude the possibility that differences in uptake and self-diffusion measurements (see Sect. 5.3) may be explained by assuming that molecular mobility at the instant of adsorption is different from the mobility under equilibrium conditions.

The ability of PFG NMR, to monitor simultaneously the mobility of different components [159, 164] makes it a very effective tool for studying the mobility of the reactant and product molecules during chemical reaction. Figure 19 shows the results of in-situ PFG NMR measurement during the conversion of cyclopropane to propene in zeolite Na-X [165]. In addition to the diffusivity of the reactant molecule (cyclopropane) and the product molecule (propene), also the time dependence of the relative amounts of the involved molecular species is presented. Since the conversion times are much larger than the intercrystalline exchange times as following from the diffusivities, the considered reaction may clearly be assumed to be reaction controlled.

The application of ^{1}H PFG NMR to studying multicomponent diffusion in adsorbate–adsorbent systems is limited by the fact that the chemical shifts are of the order of the line width. The separation between the diffusivities of different compounds is, therefore, only possible in exceptional cases like the rather simple reaction shown in Fig. 19. Owing to the larger chemical shifts, ^{13}C PFG NMR provides much better conditions for such studies. On the other hand, measurements of this type are much more expensive due to the need for ^{13}C-enriched chemical compounds. However, even with the application of ^{13}C-enriched compounds accumulation times up to hours are sometimes inevitable, so that in-situ measurements are only possible with rather slow processes. Presently, it is difficult to decide whether in addition to the ample information provided by in-situ MAS NMR on chemical reactions [166–169], PFG NMR is able to provide substantial news about molecular transportation which is not available by equilibrium measurements.

Figure 20 shows the diffusivities of isopropanol, acetone and propene under the conditions of single-component adsorption on zeolite Na-X [170]. All three compounds are involved in a well-established test reaction to discriminate between acid and basic zeolites [171, 172]: Isopropanol is dehydrated to propene on acid catalysts, while it is dehydrogenated to acetone on basic catalysts. Figure 20 shows that the diffusivity of propene, i.e. of the product of the acid-catalyzed reaction is more than one order of magnitude larger than the diffusivities of the reactant (isopropanol) and of the product (acetone) of the base-catalyzed reaction. Hence, if the acid- and base-catalyzed reactions both were to occur in parallel, the difference in

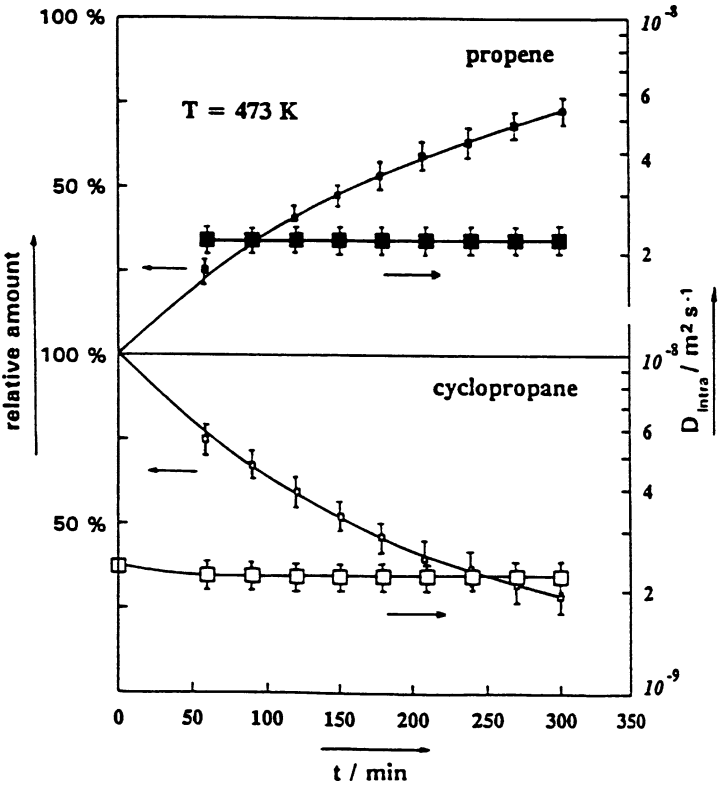

Fig. 19 Time dependence of the relative amount of cyclopropane and propene during the conversion of cyclopropane to propene in Na-X and their self-diffusion coefficients (□, cyclopropane; ■, propene) at 473 K. From [165] with permission

the product diffusivities could lead to a transport-promoted output of the acid-catalyzed product, propene, if the process is diffusion limited and if the relation between the diffusivities of the individual compounds in the mixture are comparable with the relations observed at single-component adsorption.

Figure 21 presents the results of the first in-situ ^{13}C PFG NMR diffusion measurements carried out during the conversion of isopropanol in Na-X [173, 174]. In complete agreement with the single-component measurements presented in Fig. 20, also in the multicomponent system evolving under reaction conditions, the propene diffusivities are found to be much larger than the diffusivity of isopropanol. The increase in the propene diffusivity with increasing reaction time may be easily understood by realizing that the transport inhibition of propene effected by the less mobile isopropanol molecules becomes less significant with the decrease in the total content of isopropanol.

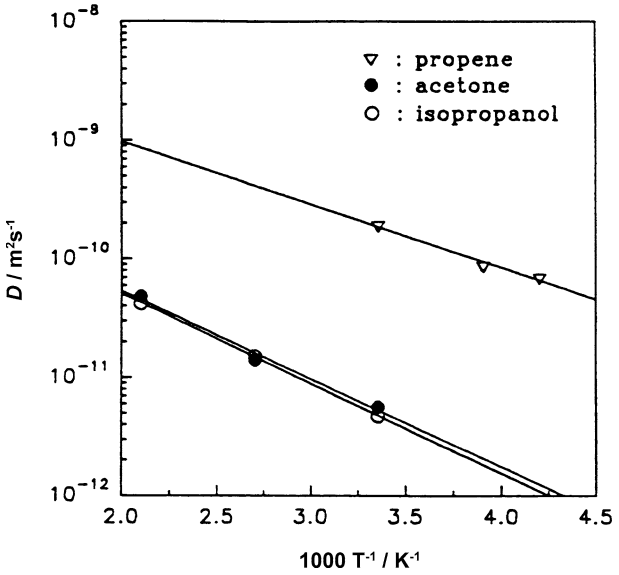

Fig. 20 Intracrystalline diffusivities of isopropanol, acetone and propene in Na-X. From [170] with permission

The application of PFG NMR to chemical reactions in zeolite catalysts is not necessarily confined to the observation of the reactant and product molecules. By monitoring the diffusivity of an inert molecule it is also possible directly to trace any changes in the transport properties of the catalyst during the reaction. As an example of this procedure, in [236] tetrafluoromethane is used to follow the transport inhibition within ZSM-5 during ethene conversion. In these studies, an H-ZSM-5 zeolite was loaded with 4 CF_4 and 12 ethene molecules per unit cell and kept at a temperature of 343 K. The representation of the results in Fig. 22 shows that the mobility of the probe species drops by a factor of 6 during the first 3 hours of reaction and then remains relatively constant. Obviously, ethene conversion leads to the formation of larger compounds, which more effectively reduce the mobility of the probe molecules than is the case with the ethene molecules.

In looking at ethene conversion on H-ZSM-5 [177, 178], one has to distinguish between low-temperature products and high-temperature products. The low-temperature products are formed below about 500 K and mainly consist of alkyl chains, while the high-temperature products are comprised largely of aromatics [180]. For comparing the influence of these different types of reaction products on the diffusivity of CF_4, after exposing the closed sample tubes for 3.5 h to a temperature of either 370 K or 575 K, the ^{19}F PFG NMR measurements have been carried out in both cases at 300 K. The resulting diffusivities after high-temperature treatment ($D \sim 2 \times 10^{-12}$ m^2 s^{-1}) were found to be much smaller than the

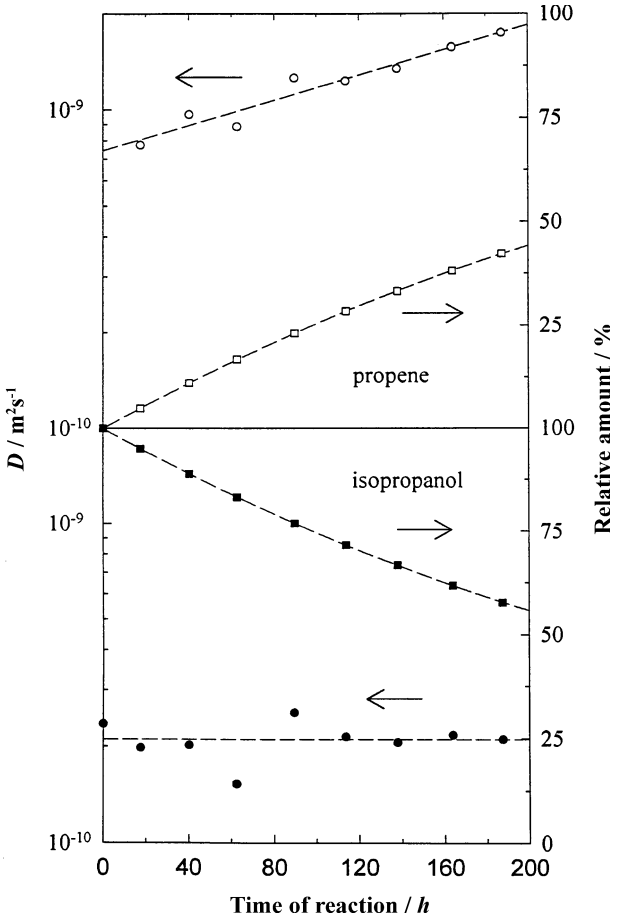

Fig. 21 Time dependence of the relative amount of isopropanol and propene during the conversion of isopropanol in Na-X and their self-diffusivities at 473 K. From [174] with permission

diffusivity after low-temperature treatment ($D \sim 10^{-10}$ m^2 s^{-1}). This finding is in agreement with the results of self-diffusion measurements of CF_4 with co-adsorbed benzene and *n*-hexane, where the diffusivity of the probe molecules is much more significantly reduced by benzene than by *n*-hexane [236]. This large effect may be explained by the differences in the preferred adsorption siting: Both experimental evidence and MD simulations suggest that the *n*-alkanes prefer the channel segments [179], while aromatics adsorb preferentially in the channel intersections [181, 182].

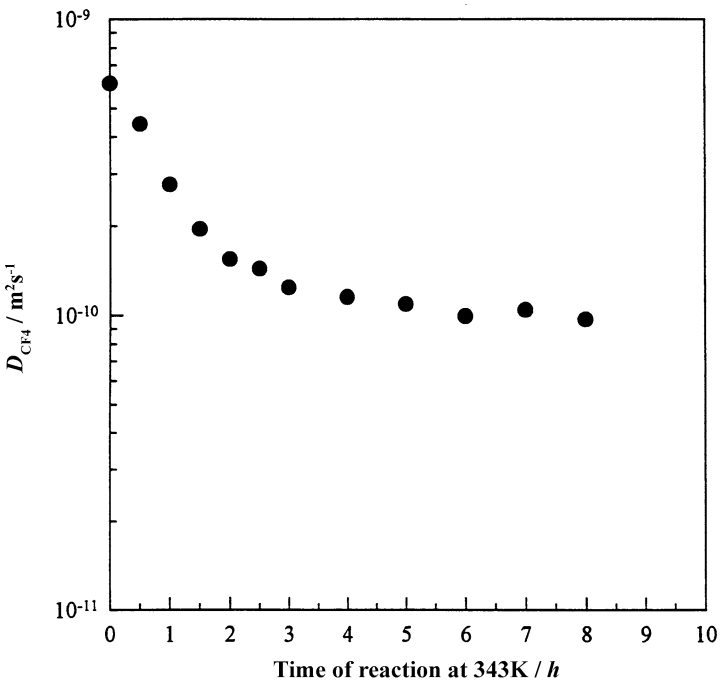

Fig. 22 Self-diffusivities of the inert CF_4 probe during ethene conversion in H-ZSM-5 at 343 K resulting from in-situ ^{19}F PFG NMR measurements during the chemical reaction. From [236] with permission

5.3 Comparison with Other Techniques

Diffusion measurements fall into two broad classes. Under macroscopic equilibrium, i.e. if the overall concentration within the sample remains constant, molecular diffusion can only be studied by following the diffusion path of the individual molecules ("microscopic" measurement by quasielastic neutron scattering (QENS) [48, 183, 184], nuclear magnetic relaxation and line-shape analysis, PFG NMR) or by introducing differently labelled (but otherwise identical) molecules into the sample and monitoring their equilibration over the sample ("macroscopic" measurements by "tracer" techniques) [185, 186]. The process of molecular movement studied under such conditions is called self-diffusion.

Molecular movement under non-equilibrium conditions (i.e. under the influence of differences in the overall concentration) is associated with a macroscopic particle transfer and is generally referred to as transport diffusion. Transport diffusion may be measured under both steady-state conditions (e.g., by studying the permeation rates through zeolite membranes [187–

189]) and transient conditions, as for example, by measuring the rate of molecular adsorption or desorption, in the frequency response technique [162, 190–193] or in chromatographic measurements [194, 195]. Among the chromatographic techniques, the zero length column (ZLC) method [186, 196–198] has attained particular relevance since it allows the observation of transport diffusion and—by applying isotopes—of self-diffusion with rather fast response times [199].

Since transport diffusion and self-diffusion refer to different physical situations, the corresponding diffusion coefficients cannot be expected to be identical. However, since both transport and self-diffusion are controlled by the same elementary steps, viz. irregular molecular movement, both processes cannot be expected to be independent of each other. In particular, for sufficiently small concentrations, i.e. in the limiting case of negligibly small mutual interaction of the adsorbed molecules, the coefficients of transport and self-diffusion must be expected to coincide. It was therefore a rather intriguing result that with the introduction of PFG NMR, intracrystalline diffusivities in zeolites have been found to be up to five orders of magnitude larger than assumed so far on the basis of conventional uptake measurements [54, 55, 200–205]. It is now well established that many of the earlier uptake rate measurements were corrupted by the intrusion of processes other than intracrystalline diffusion (external mass transfer resistance, heat transfer etc. [206–208]). However, together with a series of systems exhibiting reasonably good agreement between PFG NMR and uptake data on molecular diffusion, there are also well-documented experimental studies, where the transport diffusivities are found to be much smaller than expected on the basis of the PFG NMR investigations.

As an example, Figs. 23 and 24 provide a comparison between the diffusivity data obtained for *n*-alkanes of varying chain lengths in zeolites

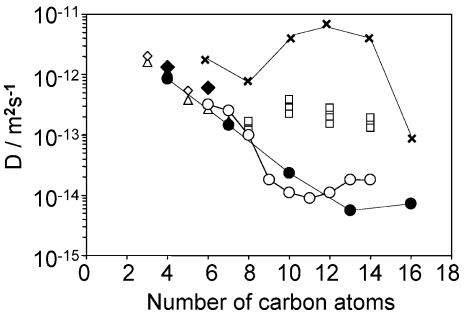

Fig. 23 Variation of the diffusivity of *n*-alkanes in zeolite Na,Ca-A with the carbon number at 473 K as observed with different techniques [QENS spin-echo technique (NSE), 12 carbon atoms per cavity: ×; PFG NMR, 1 molecule per cavity: Δ, □ (more recent data), 2 molecules per cavity: ♦; ZLC, limit of vanishing concentration: ●, ○ (more recent data)]. From [176], with permission

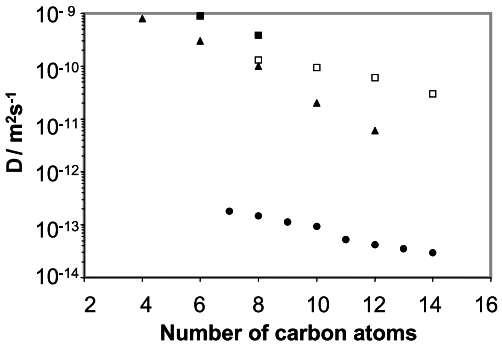

Fig. 24 Variation of the diffusivity of *n*-alkanes in MFI-type zeolites with the carbon number at 473 K as observed with different techniques (QENS, 6 carbon atoms per channel intersection: □ ZSM-5, [239]), ■ (silicalite-1, more recent data); PFG NMR, 1 molecule per cavity: ▲; ZLC, limit of vanishing concentration: ●. From [240, 241], with permission

Na,Ca-A and ZSM-5/silicalite-1 by PFG NMR, quasi-elastic neutron scattering (QENS) and the ZLC technique. Strictly speaking, in the case of ZSM-5/silicalite-1—as a consequence of the non-cubic zeolite structure—the indicated data have to be considered as mean diffusivities, which in the case of the microscopic techniques (QENS, PFG NMR) coincide with one third of the trace of the diffusion tensor, viz. $1/3(D_x + D_y + D_z)$. As a concerted activity within an international research group, all measurements have been performed with essentially identical zeolite material. In all cases the absolute values of the diffusivities reveal the same tendency: they are smallest in the measurements by the (macroscopic) ZLC technique and largest for the QENS measurements. Since the displacements monitored by QENS are of the order of tens of nanometers maximum and, hence, much smaller than the displacements followed by PFG NMR, this sequence in the diffusivities supports an explanation of the observed differences, which has been repeatedly suggested in the literature (see, for example [209]): In general, zeolite particles cannot be assumed to represent ideal, homogeneous nanoporous crystals following the given textbook structure. Rather, their internal dynamics and their exchange properties are also affected by the presence of additional transport resistances, possibly occurring both on the external surface and in the intracrystalline space. With such a model in mind, one may easily rationalize that the effect of molecular retardation by these barriers, i.e. a diminution of the measured diffusivities in comparison with the values to be expected for the genuine zeolite structure, increases with increasing molecular displacements. One may thus expect that the genuine intracrystalline diffusivities are observed by QENS, since the molecular displacements recorded by this technique are sufficiently small in comparison with the spacing of the intracrystalline transport resistances. The diffusivities obtained by PFG NMR with typical displacements of the order of micrometers, i.e. of thousands of unit

lengths of the elementary cells, are recorded over distances, for which deviations from the ideal structure and hence the formation of additional transport resistances, cannot be excluded. Since such deviations are difficult to observe by other techniques, PFG NMR represents a valuable tool for elucidating such structural peculiarities by simply recording their influence on the translational mobility. Finally, the macroscopic techniques, like the ZLC method in the representations shown in Figs. 23 and 24, may be additionally influenced by transport resistances occurring on the outer surface of the zeolite crystallites, the so-called surface barriers.

Irrespective of the differences in the absolute values, the trends in the *n*-alkane diffusivities with increasing chain lengths are remarkably similar in all three types of measurements: Similarly as with zeolite Na-X [210], in the MFI-type zeolites the diffusivities decay monotonically with increasing chain lengths, representing the dependency as observed with the free liquid. Most interestingly, in the Na,Ca-A zeolites all techniques reveal deviations from this trend. They are most pronounced for the QENS measurements (in this case by the neutron spin-echo technique yielding the transport diffusivities on a microscopic scale), where the diffusivities are observed to pass a clear maximum for chain lengths around carbon numbers of 10 to 12 [49]. In a very simplistic picture, such a behavior may be rationalized by realizing that, starting from these chain lengths, the *n*-alkane molecules become too large to be easily accommodated by one cavity. Being accommodated by two cavities implies that at any time a part of the chain will be situated in the window, so that the retarding effect of the entropic and/or energetic barrier in the windows between adjacent cavities upon molecular propagation is notably reduced. In parallel with this effect, clearly, the drag exerted by the pore wall on the n-alkane molecule is continuously increasing with increasing chain lengths. Combination of these opposing tendencies, obviously, leads to the formation of a maximum of mobility with increasing chain length. With these measurements, for the first time reliable experimental evidence about a phenomenon has been provided, which has initiated numerous theoretical approaches [211–213], but the experimental basis of which [214] has been shown to be rather questionable [215, 237, 238].

The existence of intracrystalline transport resistances has been confirmed by PFG NMR self-diffusion measurements of short-chain length alkanes in MFI-type zeolites [216, 217] with varying observation time. Figure 25 presents the relevant data obtained with n-butane as a probe molecule. Here, the diffusivities are plotted in a way, which is made possible by the special features of PFG NMR, viz. as a function of the displacements over which the molecular diffusion paths (giving rise to the plotted diffusivities) have been measured. This is achieved on the basis of Eq. 7 by which the measured diffusivities may be transferred into the mean square displacements covered by the molecules during the observation time. Obviously, in the case of ordinary diffusion, i.e. in the original notion of Eq. 7, the diffusivity depends on neither

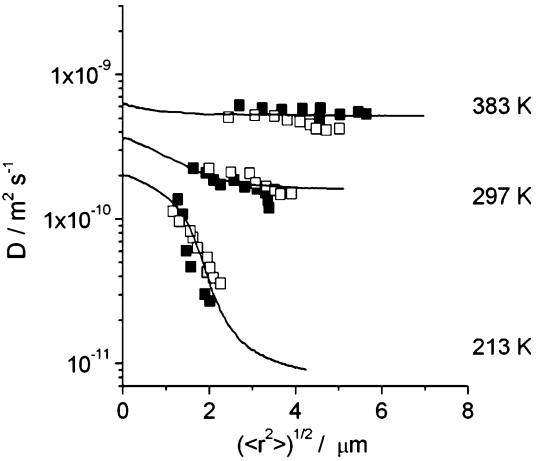

Fig. 25 Dependencies of the diffusion coefficients of *n*-butane in silicalite-1 on the root of mean square displacements at different temperatures and comparison with the results of dynamic MC simulations for a barrier separation of 3 μm with the assumption that jumps across the barriers occur with an activation energy exceeding that of intracrystalline diffusion by 21.5 kJ mol^{-1}. *Filled* and *open symbols* correspond to measurements performed with two different samples of silicalite-1. From [216, 217], with permission

the observation time nor the displacements. However, Eq. 7 has turned out to be a reasonable relation for introducing "effective" diffusivities, reflecting the transport properties also under conditions deviating from those for normal diffusion.

In the Mitra formalism [106–108] mentioned in Sect. 4 and in its application to zeolites [116], such deviations may be referred to the size of the individual crystallites. In the studies of [216, 217], however, crystallites of such large extension ($100\times25\times20\ \mu m^3$) have been applied, so that only for displacements notably larger than 10 μm the crystallite surfaces might have given rise to such a steep decay as observed at the lowest temperatures.

To the best of our knowledge, the only explanation of this behavior implies the existence of extended intracrystalline transport resistances (i.e. of internal barriers as postulated on comparing the diffusivities obtained by different measuring techniques), giving rise to the observed dependence of the effective diffusivities on the covered displacements. Obviously, at the highest temperature the thermal energy of the diffusing molecules is high enough to overcome these barriers, so that their influence becomes negligibly small in comparison with the transport resistance due to the genuine pore system. The solid lines in Fig. 25 show the results of dynamic Monte Carlo simulations. They have been performed with the assumption that, in addition to the energetic barrier characterizing diffusion in the genuine intracrystalline pore system, at a distance of 3 μm the diffusing molecules have to overcome additional potential barriers of 21.5 kJ/mol [217]. It is remarkable that the

anomaly of the PFG NMR data may be satisfactorily explained already by such a rather simplistic model. Also, for other zeolitic adsorbate–adsorbent systems meanwhile PFG NMR studies have been published [218–221], possibly reflecting the occurrence of such internal barriers.

The occurrence of such barriers is not unexpected, judging from both the concepts of crystal formation [222, 223] and the existence of distorted terraces on the surface of such crystallites [224]. Moreover, the novel options of interference and IR microscopy [225–230] provide plenty of evidence for notable differences between the real structure of zeolite crystallites and their ideal (text book) structure [231]. The direct structural demonstration of these barriers, however, has to remain a task for the future.

6 Conclusions

As a non-invasive technique, NMR spectroscopy allows the observation of molecular transport in porous media without any disturbance of their intrinsic molecular dynamics. The space scale of the diffusion phenomena accessible by NMR ranges from the elementary steps (as studied, e.g., by line-shape analysis or relaxometry) up to macroscopic dimensions. Being able to follow molecular diffusion paths from ca. 100 nm up to ca. 100 μm, PFG NMR has proven to be a particularly versatile tool for diffusion studies in heterogeneous systems. With respect to zeolites, PFG NMR is able to provide direct information about the rate of molecular migration in the intracrystalline space and through assemblages of zeolite crystallites as well as about possible transport resistances on the outer surface of the crystallites (surface barriers).

The potentials of PFG NMR have been substantially improved by recent methodical developments ensuring a significant enhancement in the sensitivity of signal detection. In this way, diffusion measurements with nuclei different from protons were enabled. Similarly, high-resolution studies allowing the simultaneous observation of the diffusivities of various molecular species under the conditions of multicomponent adsorption have become possible. The most attractive fields of current research include the in-situ application of PFG NMR during catalytic processes, the clarification of the relation between molecular transport under equilibrium and under non-equilibrium conditions, and the study of structure-related diffusion. The latter topic addresses such fundamental questions as the occurrence of single-file diffusion (see [144]) and the relation between crystal structure and diffusion anisotropy. The wealth of challenging tasks is continuously augmented by both the increasing number of absorbents with new structural features and the increasing demand of the industry for the clarification of their transport properties. Thus, PFG NMR is most likely to continue to prosper in an ever growing field of application to both zeolite science and technology.

References

1. Pfeifer H (1976) Phys Reports 26:293
2. Schwerk U, Michel D (1996) J Phys Chem 100:352
3. Freude D (1986) Zeolites 6:12
4. Allonneau JM, Volino F (1986) Zeolites 6:431
5. Murata MY, Ishiwata M, Yoshida T (2003) Adsorpt J Int Adsorption Soc 9:153
6. Ishiwata M, Murata AY, Yoshida T (2004) J Phys Soc Jpn 73:1036
7. Zibrowius B, Caro J, Pfeifer H (1988) J Chem Soc, Faraday Trans I 84:2347
8. Spiess HW (1983) Colloid Polym Sci 261:193
9. Rigby SP (2002) Langmuir 18:1613
10. Spiess HW (1974) Chem Phys 6:217
11. Zibrowius B, Bülow M, Pfeifer H (1985) Chem Phys Lett 120:420
12. Boddenberg B, Burmeister R (1988) Zeolites 8:480
13. Boddenberg B, Burmeister R, Spaeth G (1989) In: Karge HG, Weitkamp J (eds) Zeolites as catalysts, sorbents and detergent builders. Proc Int Symp, Würzburg, Germany, September 4–8, 1988. Elsevier, Amsterdam, p 533
14. Boddenberg B, Burmeister R, Spaeth G (1989) Stud Surf Sci Catal 46:533
15. Turro NJ, Lei XG, Li W, Liu ZQ, Ottaviani MF (2000) J Am Chem Soc 122:12571
16. Stepanov AG, Shubin AA, Luzgin MV, Shegai TO, Jobic H (2003) J Phys Chem B 107:7095
17. Stepanov AG, Alkaev MM, Shubin AA, Luzgin MV, Shegai TO, Jobic H (2002) J Phys Chem B 106:10114
18. Docquir F, Norberg V, Su BL (2004) Chem Phys Lett 387:188
19. Bonardel J-L, Gedeon A, Springuel-Huet M-A, Fraissard J (2006) Mol Sieves 5:155
20. Fraissard J, Ito T (1988) Zeolites 8:350
21. Kärger J, Pfeifer H, Wutscherk T, Ernst S, Weitkamp J, Fraissard J (1992) J Phys Chem 96:5059
22. Bansal N, Dybowski CJ (1990) J Magn Res 89:21
23. Chmelka B, Gilles JV, Petersen EE, Radke CJ (1988) AIChe J 36:1562
24. Springuel-Huet MA, Nosov A, Kärger J, Fraissard J (1996) J Phys Chem 100:7200
25. N'Gokoli-Kekele P, Springuel-Huet M-A, Fraissard J (2002) Adsorption 8:35
26. Larsen RG, Shore J, Schmidt-Rohr K, Emsley L, Long H, Pines A, Janicks M, Chmelka BF (1993) Chem Phys Lett 214:220
27. Janicke M, Chmelka B, Larsen RG, Shore J, Schmidt-Rohr K, Emsley L, Long H, Pines A (1994) In: Weitkamp J, Karge HG, Pfeifer H, Hölderich W (eds) Zeolite and related materials: state of the art 1994, Proc 10th Int Zeolite Conf, Garmisch-Partenkirchen, Germany, July 17–22, 1994. Elsevier, Amsterdam, p 519
28. Janicke M, Chmelka B, Larsen RG, Shore J, Schmidt-Rohr K, Emsley L, Long H, Pines A (1994) Stud Surf Sci Catal 84:519
29. Jameson AK, Jameson CJ, Gerald RE (1994) J Chem Phys 101:1775
30. Jameson CJ, Jameson AK, Lim HM (1996) J Chem Phys 104:1709
31. Jameson CJ, de Dios AC (2002) J Chem Phys 116:3805
32. Geil B, Isfort O, Boddenberg B, Favre DE, Chmelka BF, Fujara F (2002) J Chem Phys 116:2184
33. Mansfield P, Morris PG (1982) NMR imaging in biomedicine. Academic Press, New York
34. Callaghan PT (1991) Principles of NMR microscopy. Clarendon Press, Oxford, p 492
35. Blümich B (2000) NMR Imaging of materials. Clarendon Press, Oxford, p 541

36. Kimmich R (1997) NMR Tomography, diffusometry, relaxometry. Springer, Berlin Heidelberg New York, p 526
37. Heink W, Kärger J, Pfeifer H (1978) Chem Eng Sci 33:1019
38. Guillot G, Kassab G, Hulin JP, Rigord P (1991) J Phys D Appl Phys 24:763
39. Guillot G, Trokiner A, Darrasse L, Saintjalmes H (1989) J Phys D Appl Phys 22:1646
40. Hughes PDM, McDonald PJ, Halse MR, Leone B, Smith EG (1995) Phys Rev B 51:11332
41. Gladden LF (2003) AIChe J 49:2
42. Sederman AJ, Gladden LF (2001) Chem Eng Sci 56:2615
43. Yuen EHL, Sederman AJ, Gladden LF (2002) Appl Cat 232:29
44. Fraissard J (2005) In: Kärger J, Grinberg F, Heitjans P (eds) Diffusion fundamentals. Leipziger Universitätsverlag, Leipzig, p 413
45. Karge HG, Niessen W (1991) Catal Today 8:451
46. Karge HG, Geidel E (2004) In: Karge HG, Weitkamp J (eds) Molecular Sieves—Science and Technology, Vol. 4, Characterization I. Springer, Berlin Heidelberg New York, p 1
47. Stockmeyer R (1993) Microporous Mater 1:373
48. Jobic H (1994) In: Imelik B, Vedrine JC (eds) Catalyst Characterization: Physical techniques for solid materials. Plenum Press, New York, p 347
49. Jobic H, Methivier A, Ehlers G, Farago B, Haeussler W (2004) Angew Chem Int Edn 43:364
50. Kirst KU, Kremer F, Litvinov VM (1993) Macromolecules 26:975
51. Kremer F, Schönhals A (2002) Broadband dielectric spectroscopy. Springer, Berlin Heidelberg New York
52. Kärger J, Ruthven DM (1992) Diffusion in zeolites and other microporous Solids. Wiley, New York
53. Kärger J, Pfeifer H (1994) In: Pines A, Bell A (eds) NMR techniques in catalysis. Marcel Dekker, New York, p 69
54. Rees LVC (1994) In: Weitkamp J, Karge HG, Pfeifer H, Hölderich W (eds) Zeolites and related microporous materials: State of the art 1994, Proc 10th Int Zeolite Conf, Garmisch-Partenkirchen, Germany, July 17–22, 1994. Elsevier, Amsterdam, p 1133
55. Rees LVC (1994) Stud Surf Sci Catal 84:1133
56. Stallmach F, Kärger J (1999) Adsorption 5:117
57. Kärger J, Heink W (1983) J Magn Reson 51:1
58. Cotts RM (1991) Nature 351:443
59. Callaghan PT, Macgowan D, Packer KJ, Zelaya FO (1990) J Magn Reson 90:177
60. Kärger J (1982) AIChe J 28:417
61. Weingartner H (1982) Z Phys Chem Wiesbaden 132:129
62. Stejskal EO, Tanner JE (1965) J Chem Phys 42:288
63. Kärger J, Pfeifer H, Heink W (1988) Adv Magn Reson 12:2
64. Stilbs P (1987) Prog Nucl Magn Reson Spectrosc 19:1
65. Komlosh ME, Callaghan PT (1998) J Chem Phys 109:10053
66. Galvosas P, Stallmach F, Seiffert G, Kärger J, Kaess U, Majer G (2001) J Magn Reson 151:260
67. Pampel A, Kärger J, Michel D (2003) Chem Phys Lett 379:555
68. Pampel A, Fernandez M, Freude D, Kärger J (2005) Chem Phys Lett 407:53
69. Bär NK, Ernst S, Kärger J, Schwarz HB, Weitkamp J (1996) Microporous Mater 6:355
70. Murday JS, Cotts RM (1968) J Chem Phys 48:4938
71. Skirda VD, Doroginizkij MM, Sundukov VI, Maklakov AI, Fleischer G, Hausler KG, Straube E (1988) Makromolek Chem Rapid Commun 9:603

72. Bär NK, Kärger J, Krause C, Schmitz W, Seiffert G (1995) J Magn Reson Ser A 113:278
73. Callaghan PT, Coy A (1992) Phys Rev Lett 68:3176
74. Callaghan PT (1990) J Magn Reson 88:493
75. Heink W, Kärger J, Seiffert G, Fleischer G, Rauchfuss J (1995) J Magn Reson A 114:101
76. Galvosas P, Stallmach F, Kärger J (2004) J Magn Reson 166:164
77. Stallmach F, Galvosas P (2007) Ann Rep NMR Spectrosc 52:131
78. Kimmich R, Unrath W, Schnur G, Rommel E (1991) J Magn Reson 91:136
79. Fujara F, Geil B, Sillescu H, Fleischer G (1992) Z Phys B 88:195
80. Chang IY, Fujara F, Geil B, Hinze G, Sillescu H, Tolle A (1994) J Non Cryst Solids 172:674
81. Kärger J, Pfeifer H, Rudtsch S (1989) J Magn Reson 85:381
82. Cotts RM, Hoch MJR, Sun T, Markert JT (1989) J Magn Reson 83:252
83. Sun PZ, Seland JG, Cory D (2003) J Magn Reson 161:168
84. Kärger J, Kocirik M, Zikanova A (1981) J Colloid Interface Sci 84:240
85. Kärger J, Zikanova A, Kocirik M (1984) Z Phys Chem 265:587 (Leipzig)
86. Thamm H (1975) PhD Thesis, Academy of Sciences, Berlin
87. Barrer RM (1978) Zeolites and clay minerals as sorbents and molecular sieves. Academic Press, London, p 497
88. McDaniel PL, Coe CG, Kärger J, Moyer JD (1996) J Phys Chem 100:16263
89. Rittig F, Coe CG, Zielinski JM (2003) J Phys Chem B 107:4560
90. Rittig F, Farris TS, Zielinski JM (2004) AIChe J 50:589
91. Rittig F, Coe CG, Zielinski JM (2002) J Am Chem Soc 124:5264
92. Geier O, Vasenkov S, Kärger J (2002) J Chem Phys 117:1935
93. Burganos VN (1998) J Chem Phys 109:6772
94. Malek K, Coppens MO (2001) Phys Rev Lett 8712:125505
95. Malek K, Coppens MO (2002) Colloid Surf A Physicochem Eng Asp 206:335
96. Malek K, Coppens MO (2003) J Chem Phys 119:2801
97. Zalc JM, Reyes SC, Iglesia E (2004) Chem Eng Sci 59:2947
98. Chen NY, Degnan TF, Smith CM (1994) Molecular transport and reaction in zeolites. VCH, New York, p 309
99. Keil F (1999) Diffusion und Chemische Reaktion in der Gas/Feststoff-Katalyse. Springer, Berlin Heidelberg New York, p 340
100. Weitkamp J, Puppe L (1999) Catalysis and zeolites. Springer, Berlin Heidelberg New York, p 564
101. Kärger J, Vasenkov S (2005) Micropor Mesopor Mater 85:195
102. Kortunov P, Vasenkov S, Kärger J, Elia MF, Perez M, Stöcker M, Papadopoulos GK, Theodorou D, Drescher B, McElhiney G, Bernauer B, Krystl V, Kocirik M, Zikanova A, Jirglova H, Berger C, Glaser R, Weitkamp J, Hansen EW (2005) Magn Reson Imaging 23:233
103. Kärger J (2005) Diffusion Fundamentals 1:5.1
104. Förste C, Kärger J, Pfeifer H, Riekert L, Bülow M, Zikanova A (1990) J Chem Soc, Faraday Trans I 86:881
105. Kärger J, Pfeifer H, Caro J, Bülow M, Schlodder H, Mostowicz R, Völter J (1987) Appl Catal 29:21
106. Mitra PP, Sen PN (1992) Phys Rev B 45:143
107. Mitra PP, Sen PN, Schwartz LM (1993) Phys Rev B 47:8565
108. Mitra PP, Sen PN, Schwartz LM, Ledoussal P (1992) Phys Rev Lett 68:3555
109. Mair RW, Rosen MS, Wang R, Cory DG, Walsworth RL (2002) Magn Reson Chem 40:S29

110. Mair RW, Sen MN, Hurlimann MD, Patz S, Cory DG, Walsworth RL (2002) J Magn Reson 156:202
111. Mair RW, Walsworth RL (2002) Appl Magn Reson 22:159
112. Mair RW, Wang R, Rosen MS, Candela D, Cory DG, Walsworth RL (2003) Magn Reson Imaging 21:287
113. Latour LL, Mitra PP, Kleinberg RL, Sotak CH (1993) J Magn Reson A 101:342
114. Stallmach F, Vogt C, Kärger J, Helbig K, Jacobs F (2002) Phys Rev Lett 88:105505
115. Stallmach F, Kärger J (2003) Phys Rev Lett 90:039602
116. Geier O, Snurr RQ, Stallmach F, Kärger J (2004) J Chem Phys 120:1
117. Fritzsche S, Haberlandt R, Kärger J, Pfeifer H, Waldherr-Teschner M (1994) In: Weitkamp J, Karge HG, Pfeifer H, Hölderich W (eds) Zeolites and related microporous materials: state of the art 1994, Proc 10 th Int Zeolite Conf, Garmisch-Partenkirchen, Germany, July 17–22, 1994. Elsevier, Amsterdam, p 2139
118. Fritzsche S, Haberlandt R, Kärger J, Pfeifer H, Waldherr-Teschner M (1994) Stud Surf Sci Catal 84:2139
119. Hong U, Kärger J, Pfeifer H, Müller U, Unger KK (1991) Z Phys Chem 173:225
120. Hong U, Kärger J, Kramer R, Pfeifer H, Seiffert G, Müller U, Unger KK, Lück HB, Ito T (1991) Zeolites 11:816
121. Kärger J (1991) J Phys Chem 95:5558
122. Kärger J, Pfeifer H (1992) Zeolites 12:872
123. Fenzke D, Kärger J (1993) Z Phys D 25:345
124. Snurr RQ, Bell AT, Theodorou DN (1994) J Phys Chem 98:11948
125. Maginn EJ, Bell AT, Theodorou DN (1996) J Phys Chem 100:7155
126. Dumont D, Bougeard D (1995) Zeolites 15:650
127. Price GD, Pluth JJ, Smith JV, Bennett JM, Patton RL (1982) J Am Chem Soc 104:5971
128. Kärger J, Demontis P, Suffritti GB, Tilocca A (1999) J Chem Phys 110:1163
129. Demontis P, Karger J, Suffritti GB, Tilocca A (2000) Phys Chem Chem Phys 2:1455
130. Schüring A, Fritzsche S, Haberlandt R, Vasenkov S, Kärger J (2004) Phys Chem Chem Phys 6:3676
131. Caro J, Noack M, Marlow F, Peterson D, Griepenstrog M, Kornatowksi JJ (1993) J Phys Chem 97:13685
132. Baerlocher C, Meier WM, Olson DH (2001) Atlas of zeolite framework types. Elsevier, Amsterdam
133. Bär NK, Kärger J, Pfeifer H, Schäfer H, Schmitz W (1998) Micropor Mesopor Mater 22:289
134. Jost S, Fritzsche S, Haberlandt R (2002) In: Aiello R, Giordano G, Testa F (eds) Studies in Surface and Catalysis. Elsevier Science, Amsterdam, p 1947
135. Nivarthi SS, McCormick AV, Davis HT (1994) Chem Phys Lett 229:297
136. Kärger J, Petzold M, Pfeifer H, Ernst S, Weitkamp J (1992) J Catal 136:283
137. Riekert L (1970) Adv Catal 21:281
138. Kukla V, Hahn K, Kärger J, Kornatowksi JJ, Pfeifer H (1995) In: Rozwadowski M (ed) Proc 2nd Polish-German Zeolite Colloquium Torun. Nicholas Copernicus Univ Press, Torun, Poland, p 110
139. Gupta V, Nivarthi SS, McCormick AV, Davis HT (1995) Chem Phys Lett 247:596
140. Keffer D, McCormick AV, Davis HT (1996) Molec Phys 87:367
141. Hahn K, Kärger J, Kukla V (1996) Phys Rev Lett 76:2762
142. Kukla V, Kornatowski J, Demuth D, Gimus I, Pfeifer H, Rees LVC, Schunk S, Unger KK, Kärger J (1996) Science 272:702
143. Nagel H, Pfeifer H, Winkler H (1974) Z Phys Chem 255:283 (Leipzig)

144. Kärger J (2008) Single-File Diffusion in Zeolites, in this volume
145. Germanus A, Kärger J, Pfeifer H, Samulevich NN, Zhdanov SP (1985) Zeolites 5:91
146. Hoffmann WD (1976) Z Phys Chem 257:315 (Leipzig)
147. Ruthven DM (1974) Can J Chem 52:3523
148. Caro J, Kärger J, Finger G, Pfeifer H, Schöllner R (1976) Z Phys Chem 257:903 (Leipzig)
149. Keffer D, McCormick AV, Davis HT (1996) J Phys Chem 100:967
150. Vasenkov S, Kärger J, Freude D, Rakoczy RA, Weitkamp J (2000) J Mol Catal A Chem 158:373
151. Lorenz P, Bülow M, Kärger J (1980) Izv Akad Nauk SSSR, Ser Khim:1741
152. Heink W, Kärger J, Ernst S, Weitkamp J (1994) Zeolites 14:320
153. Breck DW (1974) Zeolite molecular sieves. Wiley, New York, p 636
154. Fritzsche S, Haberlandt R, Kärger J, Pfeifer H, Heinzinger K, Wolfsberg M (1995) Chem Phys Lett 242:361
155. Germanus A, Kärger J, Pfeifer H (1984) Zeolites 4:188
156. Kirkpatr S (1971) Phys Rev Lett 27:1722
157. Sabini M (1995) Flow and transport in porous media and fractured rook. VCH, Weinheim, p 169
158. Nivarthi SS, Davis HT, McCormick AV (1995) Chem Eng Sci 50:3217
159. Nirvarthi SS, McCormick AV (1995) J Phys Chem 99:4661
160. Caro J, Bulow M, Kärger J, Pfeifer H (1988) J Catal 114:186
161. Geier O, Vasenkov S, Freude D, Kärger J (2003) J Catal 213:321
162. Bourdin V, Germanus A, Grenier P, Kärger J (1996) Adsorption 2:205
163. Stallmach F, Kärger J, Pfeife H (1993) J Magn Res 102:270
164. Hong U, Kärger J, Pfeifer H (1991) J Am Chem Soc 113:4812
165. Hong U, Kärger J, Hunger B, Feoktistova NN, Zhdanov SP (1992) J Catal 137:243
166. Ferguson DB, Haw JF (1995) Anal Chem 67:3342
167. Ernst H, Freude D, Mildner T, Wolf I (1995) Z Phys Chem 189:221
168. Hunger M, Brunner E (2004) In: Karge HG, Weitkamp J (eds) Molecular Sieves—Science and Technology, Vol. 4, Characterization I. Springer, Berlin Heidelberg New York, p 201
169. Hunger M, Weitkamp J (2001) Angew Chem Int Ed 40:2954
170. Schwarz HB, Ernst H, Ernst S, Kärger J, Roser T, Snurr RQ, Weitkamp J (1995) Appl Catal A 130:227
171. Yashima T, Suzuki H, Hara N (1974) J Catal 33:486
172. Hathaway PE, Davis ME (1989) J Catal 116:263
173. Kärger J, Ernst H, Freude D, Mildner T, Schwarz HB, Snurr RQ, Weitkamp J (1996) In: Weitkamp J, Lücke B (eds) DGMK-Conference Catalysis on Solid Acids and Bases, Berlin. German Society for Petroleum and Coal Science and Technology, Hamburg, p 87
174. Schwarz HB, Ernst S, Kärger J, Knorr B, Seiffert G, Snurr RQ, Staudte B, Weitkamp J (1997) J Catal 167:248
175. Brandani S, Caro J, Jobic H, Krause C, Kärger J, Möller A, Ruthven D, Staudt R, Yang X (2005) In: Kärger J, Grinberg F, Heitjans P (eds) Diffusion Fundamentals. Leipziger Universitätsverlag, Leipzig, p 432
176. Brandani S et al. (2005) Diffusion Fundamentals 2:84 (online Journal)
177. Karge HG, Darmstadt H, Gutsze A, Vieth HM, Bunkowsky G (1994) Stud Surf Sci Catal 84:1465
178. Karge HG (1991) Stud Surf Sci Catal 58:531

179. June RL, Bell AT, Theodorou DN (1990) J Phys Chem 94:1508
180. Bauer F, Karge HG (2006) Mol Sieves 5:249
181. Snurr RQ, Bell AT, Theodorou DN (1993) J Phys Chem 97:13742
182. Forste C, Germanus A, Kärger J, Pfeifer H, Caro J, Pilz W, Zikanova A (1987) J Chem Soc, Faraday Trans I 83:2301
183. Jobic H, Theodorou DN (2007) Micropor Mesopor Mater 21:50
184. Jobic H (2000) In: Kanellopoulos NK (ed) Recent Advances in Gas Separation by Microporous Ceramic Membranes. Elsevier, Amsterdam, p 109
185. Goddard M, Ruthven DM (1986) Zeolites 6:445
186. Ruthven DM, Brandani S (2000) In: Kanellopoulos NK (ed) Recent Advances in Gas Separation by Microporous Ceramic Membranes. Elsevier, Amsterdam, p 187
187. Wernick DL, Osterhuber EJ (1984) In: Olson D, Bisio A (eds) 6th Int Zeolite Conf, Remo, USA, 10–15 July, 1993. Butterworths, Guildford, p 122
188. Paravar A, Hayhurst DT (1994) In: Olson D, Bisio A (eds) 6th Int Zeolite Conf. Butterworths, Guildford, p 217
189. Caro J, Noack M, Kölsch P, Schäfer R (2000) Micropor Mesopor Mater 38:3
190. Yasuda Y (1994) Heterogen Chem Rev 1:103
191. Shen D, Rees LVC (1991) Zeolites 11:666
192. Rees LVC, Song L (2000) In: Kanellopoulos NK (ed) Recent advances in gas separation by microporous ceramic membranes. Elsevier, Amsterdam, p 139
193. Onyestyak G, Valyon J, Rees LVC (2001) Solid State Ion 141:93
194. Haynes HW (1988) Catal Rev Sci Eng 30:563
195. Boniface H, Ruthven DM (1985) Chem Eng Sci 60:1401
196. Eic M, Ruthven DM (1988) Zeolites 8:40
197. Eic M, Ruthven DM (1989) In: Jacobs PA, van Santen RA (eds) Zeolites: Facts, Figures, Future Proc 8th Int Zeolite Conf, Amsterdam, The Netherlands, July 10–14, 1989. Elsevier, Amsterdam, p 897
198. Eic M, Ruthven DM (1989) Stud Surf Sci Catal 49:897
199. Brandani S, Hufton J, Ruthven D (1995) Zeolites 15:624
200. Kärger J, Caro J (1977) J Chem Soc, Faraday Trans I 73:1363
201. Kärger J, Ruthven DM (1981) J Chem Soc, Faraday Trans I 77:1485
202. Kärger J, Pfeifer H (1987) Zeolites 7:90
203. Kärger J (1999) In: Treacy MMJ, Marcus BK, Bisher ME, Higgins JB (eds) 12th Int Zeolite Conf, Maryland, USA, July 5–10, 1998, Baltimore. Material Research Society, Warrendale, p 35
204. Kärger J (2002) Indust Eng Chem Res 41:3335
205. Ruthven DM, Post MFM (2001) In: van Bekkum H, Flanigen EM, Jacobs PA, Jansen JC (eds) Introduction to zeolite science and practice, 2nd Edn. Elsevier, Amsterdam, p 525
206. Ruthven DM, Lee LK, Yucel H (1980) AIChe J 26:16
207. Prinz D, Riekert L (1986) Ber Bunsenges Phys Chem 90:413
208. Bülow M, Struve P, Mietk W, Kocirik M (1984) J Chem Soc, Faraday Trans I 80:813
209. Kärger J, Ruthven DM (1989) Zeolites 9:267
210. Kärger J, Pfeifer H, Rauscher M, Walter A (1980) J Chem Soc, Faraday Trans I 76: 717
211. Ghorai PK, Yashonath S, Demontis P, Suffritti GB (2003) J Am Chem Soc 125:7116
212. Runnebaum RC, Maginn EJ (1997) J Phys Chem B 101:6394
213. Dubbeldam D, Smit B (2003) J Phys Chem B 107:12138
214. Gorring RL (1973) J Catal 31:13

215. Cavalcante CL, Eic M, Ruthven DM, Occelli ML (1995) Zeolites 15:293
216. Vasenkov S, Böhlmann W, Galvosas P, Geier O, Liu H, Kärger J (2001) J Phys Chem B 105:5922
217. Vasenkov S, Kärger J (2002) Micropor Mesopor Mater 55:139
218. Takaba H, Yamamoto A, Hayamizu K, Nakao SI (2005) In: Kärger J, Grinberg F, Heitjans P (eds) Diffusion Fundamentals. Leipziger Universitätsverlag, Leipzig, p 476
219. Takaba H, Yamamoto A, Hayamizu K, Nakao SI (2005) Diffusion Fundamentals 2:106 (online Journal)
220. Adem Z, Guenneau F, Springuel-Huet MA, Gedeon A (2005) In: Kärger J, Grinberg F, Heitjans P (eds) Diffusion Fundamentals. Leipziger Universitätsverlag, Leipzig, p 424
221. Adem Z, Guenneau F, Springuel-Huet MA, Gedeon A (2005) Diffusion Fundamentals 2:80 (online Journal)
222. Kirschhock CEA, Ravishankar R, Van Looveren L, Jacobs PA, Martens JA (1999) J Phys Chem B 103:4972
223. Kirschhock CEA, Ravishankar R, Verspeurt F, Grobet PJ, Jacobs PA, Martens JA (1999) J Phys Chem B 103:4965
224. Agger JR, Hanif N, Cundy CS, Wade AP, Dennison S, Rawlinson PA, Anderson MW (2003) J Am Chem Soc 125:830
225. Kortunov P, Chmelik C, Kärger J, Rakoczy RA, Ruthven DM, Traa Y, Vasenkov S, Weitkamp J (2005) Adsorpt J Int Adsorption Soc 11:235
226. Kortunov P, Vasenkov S, Chmelik C, Kärger J, Ruthven DM, Wloch J (2004) Chem Mater 16:3552
227. Lehmann E, Vasenkov S, Kärger J, Zadrozna G, Kornatowski J (2003) J Chem Phys 118:6129
228. Lehmann E, Vasenkov S, Kärger J, Zadrozna G, Kornatowski J, Weiss Ö, Schüth F (2003) J Phys Chem B 107:4685
229. Kärger J, Vasenkov S (2003) In: Laeri F, Schüth F, Simon U, Wark M (eds) Host-Guest systems based on nanoporous crystals. Wiley-VCH, Weinheim, p 255
230. Kärger J, Valiullin R, Vasenkov S (2005) New J Phys 7:1
231. Karge HG, Kärger J (2008) Application of IR Spectroscopy, IR Microscopy and Optical Interference Microscopy on Diffusion in Zeolites, in this volume
232. Keil FJ, Krishna R, Coppens MO (2000) Rev Chem Engin 16:71
233. Demontis P, Fois ES, Suffritti G, Quartieri S (1990) J Phys Chem 94:4329
234. Goodbody SJ, Watanabe K, MacGowan D, Walton JPB, Quirke N (1991) J Chem Soc, Faraday Trans 87:1951
235. June RL, Bell AT, Theodorou DN (1990) J Phys Chem 94:8232
236. Snurr RQ, Hagen A, Ernst H, Schwarz HB, Ernst S, Weitkamp J, Kärger J (1996) J Catal 163:130
237. Ruthven DM (2004) J Phys Chem B 108:16328–16329
238. Ruthven DM (2006) Micropor Mesopor Mater 96:262–269
239. Jobic H (2000) J Mol Catal A Chem 158:135
240. Bourdin V, Brandani S, Gunadi A, Jobic H, Krause C, Kärger J, Schmidt W (2005) In: Kärger J, Grinberg F, Heitjans P (eds) Diffusion Fundamentals. Leipziger Universitätsverlag, Leipzig, p 430
241. Bourdin V, Brandani S, Gunadi A, Jobic H, Krause C, Kärger J, Schmidt W (2005) Diffusion Fundamentals 2:83 (online Journal)
242. Kärger J (2005) In: Kärger J, Grinberg F, Heitjans P (eds) Diffusion Fundamentals. Leipziger Universitätsverlag, Leipzig, p 389
243. Kärger J (2005) Diffusion Fundamentals 2:78 (online Journal)

Mol Sieves (2008) 7: 135–206
DOI 10.1007/3829_2008_020
© Springer-Verlag Berlin Heidelberg
Published online: 14 May 2008

Application of IR Spectroscopy, IR Microscopy, and Optical Interference Microscopy to Diffusion in Zeolites

Hellmut G. Karge[1] (✉) · Jörg Kärger[2] (✉)

[1]Fritz Haber Institute of the Max Planck Society, Faradayweg 4–6, 14195 Berlin, Germany
karge@fhi-berlin.mpg.de

[2]University of Leipzig, Linnéstraße 5, 04103 Leipzig, Germany
kaerger@physik.uni-leipzig.de

Abstract Infrared spectroscopic methodsfor the measurement of adsorption and adsorption kinetics of some aromatics (benzene, ethylbenzene, *p*-xylene), pyridine, and paraffins in solid microporous materials such as zeolites (MOR, ZSM-5, silicalite-1) are described as well as the evaluation of the spectroscopically obtained data. The adsorption isotherms are of the Langmuir–Freundlich type. Isosteric heats of adsorption, transport diffusivities, and activation energies of diffusion as deduced from the spectroscopic measurements are compared with literature data as far as available, and they are found to be in reasonable agreement with results provided by independent techniques. Special attention is paid to sorption and sorption kinetics of binary mixtures, especially the problems of co- and counter-diffusion .

The design and application of a very promising novel technique for the measurement of sorbate transport in porous materials, viz. diffusion interference microscopy, is presented and pertinent results obtained by this technique are reported.

Keywords Diffusion · Co- and Counterdiffusion · Adsorption · IR techniques · Interference microscopy

Abbreviations

A	Area
AFI	Zeolite framework type ([1])
AlPOs	Microporous aluminophosphates ([1])
B	Benzene
b_i	Constant, specific of the adsorbate component i (Eq. 2)
C	Concentration
C_{eq}	Equilibrium concentration
C_0	Concentration on the external surface of a zeolite crystal
CrAPO	Chromium-containing AlPO-5, member of the AFI family
C_{surf}	Actual surface concentration
D	Transport diffusion coefficient
D_0	"Corrected" diffusion coefficient
$D_{x(y,z)}$	Principal tensor elements
DIFM	Diffusion interference microscopy
E_A	Activation energy of diffusion, [kJ mol^{-1}]
EB	Ethylbenzene
Ferrierite	Particular zeolite (structure type FER, see [1])
FR	Frequency response (technique)
FTIR	Fourier transform infrared (spectroscopy)
H-MOR	(Acid) proton-exchanged form of MOR ([1])
H-SSZ-24	Particular microporous materials ([111])
H-ZSM-5	(Acid) proton-exchanged form of ZSM-5 ([1])
H-ZSM-11	(Acid) proton-exchanged form of ZSM-11 ([1])
^{1}H NMR	Proton nuclear magnetic resonance (spectroscopy)
HgCdTe	Mercury cadmium telluride
IFM	(Optical) interference microscopy
IR	Infrared
j	Particle flux
j_{in}	Particle flux into crystal
j_{os}	Flux of particles colliding with outer crystal surface
j_{out}	Particle flux out of crystal

L	Ratio between time constants, defined by Eq. 22
l	Half length of crystal extension
Li-ZSM-5	Lithium-exchanged ZSM-5 ([1])
M	Molecular weight
m	Specific constant in the Freundlich–Langmuir equation
$m(t)$	Uptake (at time t)
"Macro"-FTIR	Conventional FTIR using pressed wafers
MCT	Mercury cadmium telluride (detector)
MFI	Particular zeolite structure ([1])
m_i	Constant, specific of adsorbate component i (Eq. 2)
"Micro"-FTIR	FTIR using a microscope and (large) single crystals
MOF	Metal–organic framework
MOR	Mordenite, particular zeolite structure ([1])
n	Coverage, [mmol g^{-1}]
N_A	Avogadro constant
Na-LSX	Particular microporous materials ([117])
Na-X	Sodium-exchanged X zeolite ([1])
Na-ZSM-5	Sodium-exchanged ZSM-5 ([1])
NEOP	Neopentane
n_i	Coverage with adsorbate component i
n_o	Maximum coverage, [mmol g^{-1}]
n_{oi}	Maximum coverage with adsorbate component i
NMR	Nuclear magnetic resonance
p	Equilibrium partial pressure, [Pa] or [mbar]
p_i	Equilibrium partial pressure of adsorbate component i
p-X	*Para*-xylene
PFG	Pulsed field gradient
Py	Pyridine
PyB	Pyridine bound to Brønsted sites
PyL	Pyridine attached to Lewis sites
Q_{ad}	Heat of adsorption (from microcalorimetric measurements)
QENS	Quasi-elastic neutron scattering
Q_{iso}	Isosteric heat of adsorption, [kJ mol^{-1}]
R	Gas constant
r	Radius coordinate
SAPOs	Microporous silico-aluminophosphates ([1])
SEM	Scanning electron microscopy
Silicalite-1	Microporous material, MFI structure, $n_{Si}/n_{Al} \rightarrow \infty$ ([1])
STA-7	Particular zeolite (see [2, 3])
STIR	Surface temperature infrared (spectroscopy)
t	Time, [s]
T	Temperature, [K]
T	Toluene
T_{ad}	Temperature of adsorption
T_{diff}	Temperature of diffusion
w	Ordinate intercept of C_{surf}–m plots
x	Coordinate
X	Particular zeolite structure, cubic, faujasite-type ([1]) or
X	Xylene
y	Coordinate

z	Coordinate
ZLC	Zero-length column
ZSM-5	Particular zeolite structure ([1])
2-D	Two-dimensional

Symbols, Greek Letters

α	Surface permeability
$\alpha_{z,(z)}$	Surface permeability through the crystal faces perpendicular to y- (z-) direction
β	Time constant characterizing the time lag in diffusion in experiments, [s^{-1}]
β_n	n-th root of Eq. 22
η	Variable defined by $y/\sqrt{t}$
ΔT	Temperature difference between sample and black box in STIR
Δx, Δy	Spatial resolution
λ	Integration variable
σ	Standard deviation
τ_{diff}	Time constant of diffusion-limited uptake
τ_{surf}	Time constant of barrier-limited uptake
$\phi(t)$	Function accounting for the time lag

1 Introduction

Zeolites, i.e., crystalline microporous aluminosilicates and related materials (AlPOs, SAPOs, etc.), play an important role as adsorbents, e.g., in gas separation processes, and as constituents of catalysts, e.g., for hydrocarbon conversions. In both gas separation and catalysis, adsorption, diffusion, and desorption of adsorbates or reactants are fundamental intermediate steps. Classical methods for studying adsorption–desorption and diffusion in zeolites are gravimetry, barometry, zero-length-column (ZLC) techniques, frequency response (FR) spectroscopy, pulsed field gradient NMR spectroscopy (PFG NMR), and quasi-elastic neutron scattering (QENS). Generally, these techniques are inappropriate for investigating the adsorption and adsorption kinetics of bi- or multicomponent adsorbates in zeolites. However, NMR investigations provided data in cases of self-diffusion in binary adsorbed phases in zeolites [4], e.g., in the system heptane/benzene in Na-X zeolite (see also [5]). An exception with respect to counter-diffusion in zeolites is the experiment by Förste et al. [6], who studied via tracer exchange ^{1}H NMR experiments the counter-diffusion of C_6H_6 and C_6D_6 under equilibrium conditions.

However, the adsorption and adsorption kinetics of binary or even more complex adsorbate mixtures are of paramount importance in gas separation and catalysis. Thus, even in the simplest case of the conversion of a reactant A into a product A′ inside the pore system of a zeolite catalyst, the

in-going A molecules must pass the out-going A′ molecules, and the phenomenon of counter-diffusion comes into play. Without any experimental basis, only speculations were possible on the effect of the presence of the second component, A′, on, e.g., the diffusivity of the first, A, and vice versa. Some estimates suggested that the diffusion coefficients in the case of counter-diffusion may be smaller by several orders of magnitude compared to the single-component case (see Choudary et al. [7, 8]).

A way out of the difficulties of investigating co- and counter-diffusion seemed to be possible with the aid of IR spectroscopy. In a few cases, IR spectroscopy had been successfully employed to investigate quantitatively the adsorption into zeolites. In such cases of adsorption the IR method used IR bands, which were typical of the respective species of a *single* adsorbate inside the pore system. An early example of an adsorption isotherm obtained via IR spectroscopy is that of ethene on zeolite Y reported by Liengme and Hall [9]. Here, the absorbance of an IR band of the adsorbate was monitored by IR as a measure of the coverage of the solid. A more systematic utilization of monitoring the uptake of an adsorbent via sets of IR spectra as a function of time was attempted by Karge and Klose in 1975 [10]. These authors studied the kinetics of adsorption of pyridine into Na- and H-mordenite. Thus, the method was expected to be also capable of discriminating between *different* species in cases of adsorption of mixtures, and of monitoring co- and counter-diffusion of *different* molecules. A qualitative experiment on the counter-diffusion of pyridine molecules (indicated through their bands at 1542 and 1452 cm^{-1}) versus benzene molecules (indicated through their band at 1478 cm^{-1}), or benzene molecules (band at 1478 cm^{-1}) versus ethylbenzene molecules (bands at 1495 and 1453 cm^{-1}) in H-mordenite was carried out by Karge and Weitkamp [11] (see Fig. 1).

These experiments confirmed that IR spectroscopy indeed provides a promising means for the investigation of the uptake of binary mixtures into microporous materials and its kinetics. This successful experiment prompted us to start a systematic study on the adsorption and adsorption kinetics of some aromatics in zeolites by Fourier transform IR spectroscopy (FTIR) and FTIR microscopy or, more precisely, IR "micro"-spectroscopy. This topic is dealt with in Sect. 2, where the generally employed apparatuses and procedures are also described. In this context, it should be mentioned that micro-FTIR spectroscopy was also applied by Schüth and coworkers in studying the adsorption of guest molecules in microporous solids [12–14].

Moreover, the "macro"- and "micro"-FTIR techniques enable us to obtain spectra in situ from a working catalyst, since the cells used (see Sect. 2.1.1) may be operated as flow-through reactors. Thus, coking of zeolite catalysts upon reaction of ethane or ethylbenzene was investigated in situ, and the decrease of diffusivities (e.g., of benzene) in the coking samples was measured as a function of the amount of coke deposited [15]. Similarly, the sorption of *para*-, *meta*-, and *ortho*-diethylbenzene from the gas phase into H-ZSM-5

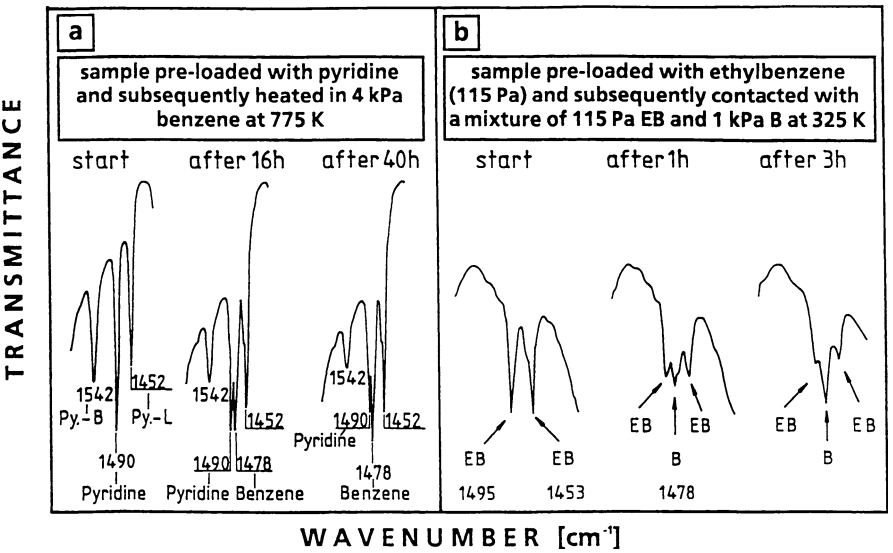

Fig. 1 Counter-diffusion of **a** benzene (B) vs pyridine (Py) and **b** vs ethylbenzene (EB) in hydrogen mordenite (H-MOR) [11]

was studied by means of in situ macro-FTIR spectroscopy with respect to the selectivity of diethylbenzene disproportionation. Thus, it was found that the *para* selectivity reflects the interplay of catalytic reaction and mass transfer phenomena [16].

Another but quite different approach to investigation of diffusion in zeolites by means of IR measurements should be mentioned here. Grenier et al. [17] employed IR spectroscopy in order to monitor the changes of the sorbent temperature upon interaction of the adsorbate with the surface of the adsorbent as a function of time (see Figure 2a). The IR emission due to the temperature change during the uptake is measured by an HgCdTe detector. A chopper and a lock-in amplifier are employed to obtain a signal, which is proportional to the temperature difference, ΔT, between the sample and a thermostatted black body. ΔT is directly related to the amount adsorbed or desorbed. A response curve for the example of CH_3OH sorbed into Na-X is displayed in Fig. 2b.

Evaluation of the data requires time constants for both the heat transfer and diffusion under nonisothermal conditions. It turns out that the initial part of the response curve is mainly determined by the mass transport (transport diffusion), whereas the descending part is mainly governed by the heat transfer. The STIR technique avoids intrusion by the evolution of heat, in that it measures the transient temperature, and has a rapid response (time constant about 10^{-8} s). Results obtained for the diffusion of CH_3OH into Na-X were essentially consistent with those derived from the ZLC and PFG NMR

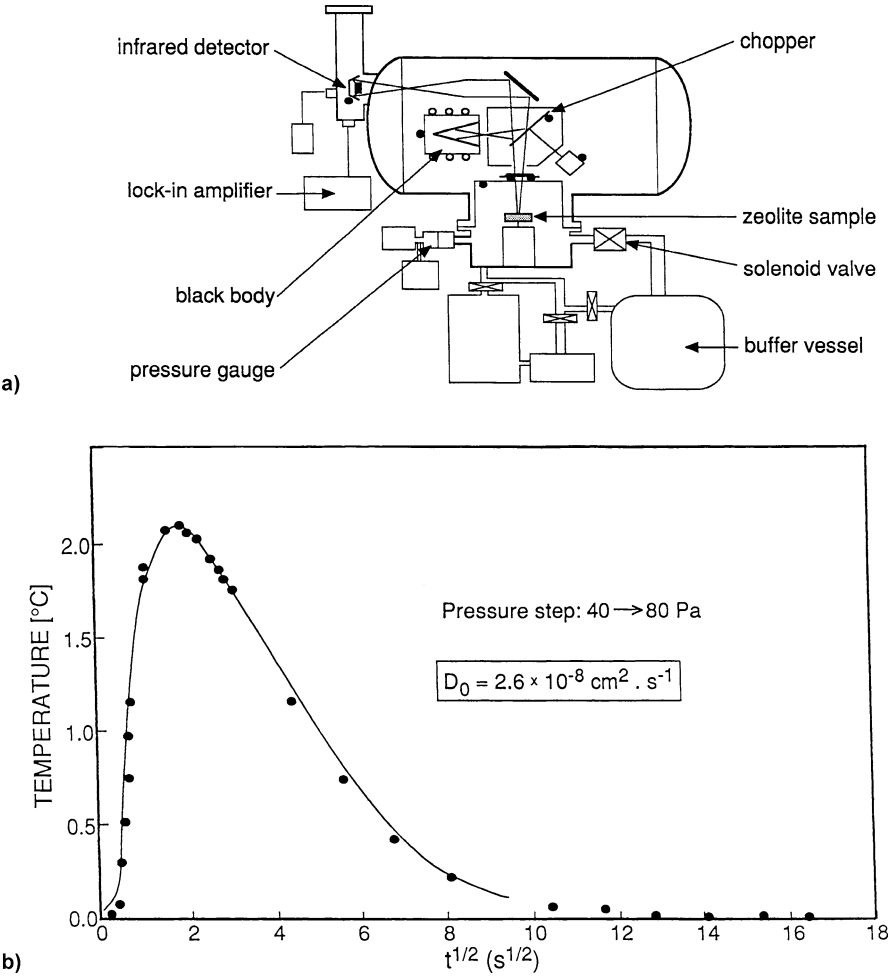

Fig. 2 **a** System for surface temperature infrared (STIR) measurements. **b** Transient temperature response upon methanol sorption into Na-X zeolite as a function of the square root of time [17]

techniques. Furthermore, the technique was successfully combined with the FR method such that both the pressure and temperature responses were monitored. Even though, in view of diffusion studies in zeolites, the STIR approach seems very attractive, Grenier's method will not be discussed in more detail in the context of this chapter, since it does not directly relate to the spectroscopic and/or microscopic study of sorbate transport in porous materials.

A very promising novel technique for studying various features of sorption into zeolites and the related sorption kinetics was first suggested by

Kärger et al. [18, 19] and later on developed by Schemmert [20] and Kärger et al. [21] to a very sophisticated method, when employing optical interference microscopy (IFM) . The design of the experiments using interference microscopy for diffusion studies (DIFM), the data acquisition through this type of experiment, and the evaluation of selected data obtained by DIFM are described in Sect. 3.

2
Infrared "Macro"- and "Micro"-Spectroscopic Investigations of Adsorption, Desorption, Diffusion, and Co- and Counter-Diffusion in Zeolites

2.1
Experimental

2.1.1
Apparatuses and Procedures

Since the investigation of diffusion phenomena in zeolites by macro-FTIR and micro-FTIR spectroscopy is still not a routine technique, the experimental aspects will be described in more detail.

The apparatus and procedure generally used for macro-FTIR diffusion experiments are described in detail by Niessen [22], Karge and Niessen [23, 24], Karge [25], and Bludau et al. [26]. The central parts are an up to 575 K heatable flow-through IR cell (see [22, 23, 26] and Vol. 4, Chap. 1 of this series, p. 42) and an arrangement of a number of sensitive and very fast responding flow controllers (vide infra, Fig. 5). This enabled us to purge the cell and self-supporting zeolite wafers in the upper quartz glass part of the cell in a fast flow (800 ml min^{-1}) of helium for activation and, if necessary, dehydroxylation at temperatures up to 1100 K. The lower metal compartment of the cell with sealed-on IR transparent CaF_2 windows, which was penetrated by the IR beam coming from an FTIR spectrometer, could be purged in the same helium stream at a chosen temperature of adsorption/desorption. A main flow of helium was passed through the cell with a high flow rate (800 ml min^{-1}). This high flow rate guaranteed a rapid dissipation of the heat of adsorption and, thus, isothermic conditions and a steady maintenance of the constant sorbate concentration in the intercrystalline space. Thus, two pitfalls of macroscopic, nonequilibrium uptake methods for investigation of diffusion in zeolites were avoided: the lack of isothermic conditions due to the adsorption heat evolved and the lack of constant intercrystalline sorbate concentration. These have been identified by Doelle and Riekert as main sources of error in macroscopic uptake experiments ([27, 28]; cf. also [29]).

It was confirmed that the presence of the carrier gas (helium) did not affect the diffusion measurements. When helium was replaced by neon, argon, or krypton, no change in the results was observed; only xenon caused some deviation of the results (Niessen W, private communication). The main flow could be very rapidly connected with streams of the adsorbates in helium (8 ml min^{-1}) in such a way that the total flow and pressure remained constant. The adsorbate partial pressures could be varied, i.e., increased or decreased, almost instantaneously by small jumps. The experiment was started by scanning the spectrum of the pure, activated adsorbent. After a first pressure jump, e.g., from zero to 115 Pa, at a chosen adsorption temperature, the spectrum of the adsorbate/adsorbent was monitored in short intervals. An FTIR spectrometer of Perkin–Elmer type 1800 was employed. An example with sets of spectra of ethylbenzene adsorbed into H-ZSM-5 is shown in Fig. 3.

For the FTIR microscopic diffusion measurements (micro-FTIR spectroscopy) [30–32] the same Perkin–Elmer 1800 spectrometer was used, but a so-called IR microscope (Spectra Tech model IR-Plan) and an appropriate flow-through micro-cell were attached (see Figures 4a,b).

The microscope enables focusing by Cassegrainian mirrors. Optical and IR beam paths are collinear and switched by tilting mirrors. Thus, samples may be characterized and selected visually before recording the spectra. Strictly speaking, the IR microscope is operated as a microscope only in the optical mode, thereby creating a magnified image of the sample. In the IR mode, the image is created at a 1 : 1 scale on a narrow band MCT detector with a sensitive area of about 250 $\mu m \times 25\ \mu m$. The focal diameter of the IR beam is about

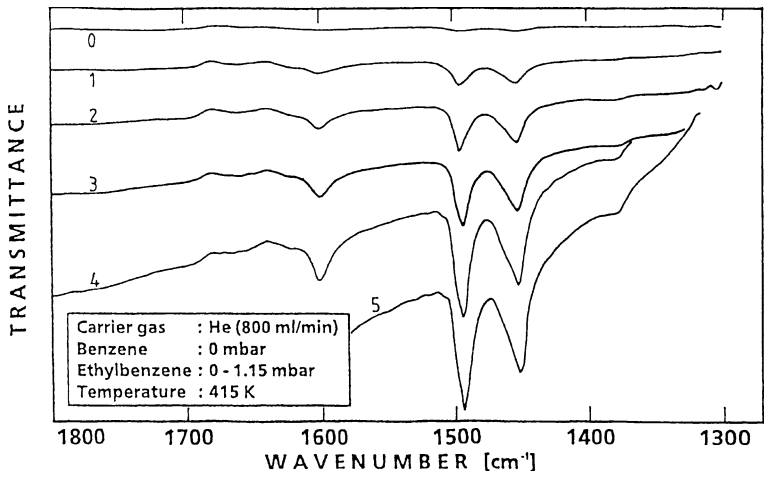

Fig. 3 Set of FTIR spectra indicating successive states of sorption of ethylbenzene into H-ZSM-5 at 415 K (0, 1, 2, 3, 4, 5: after 0, 11.1, 33.3, 55.6, 103.7, and 348 s, respectively). Pressure jump: from 0 to 1.15 mbar partial pressure of ethylbenzene in helium stream; "thickness" of the sample wafer: 10 mg cm^{-2} (corresponding to about 0.1 mm)

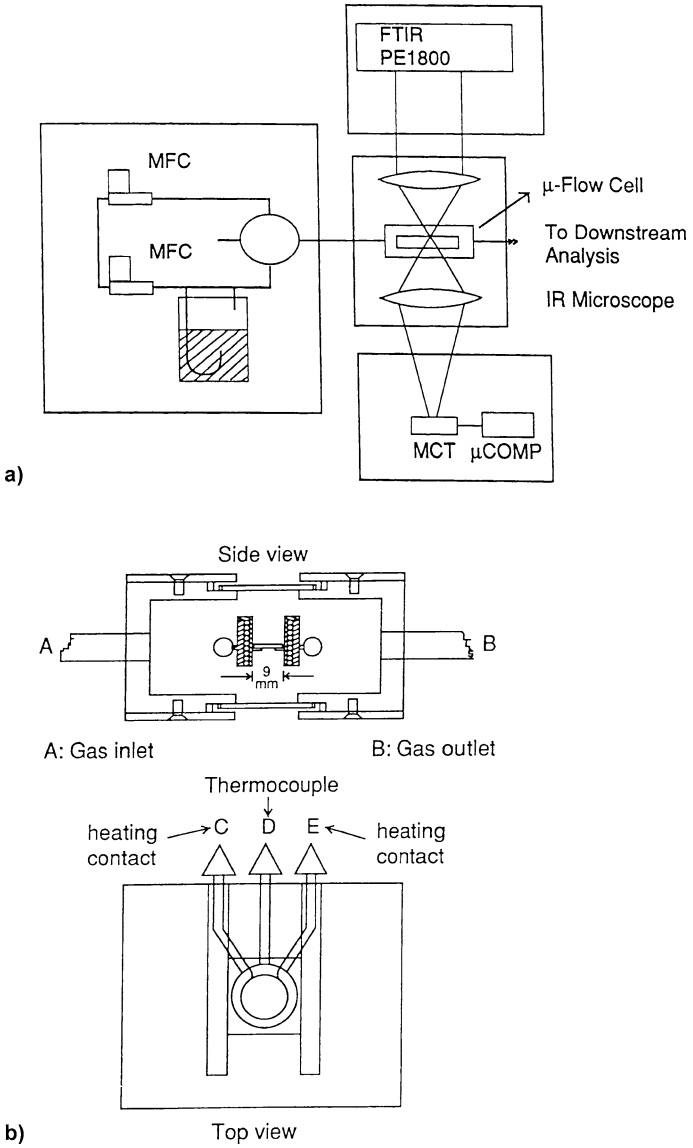

Fig. 4 **a** Schematic setup for experimental studies of sorption and sorption kinetics by "micro"-FTIR spectroscopy (so-called FTIR microscopy). **b** Flow cell for micro-FTIR investigations of sorption and sorption kinetics in zeolites [30, 31]

0.5 mm; the beam may be confined further by adjustable rectangular apertures. The minimum spatial resolution is given by the diffraction limit. In the IR spectral range, approximately 10 μm may be reached. However, the minimum sample size is rather limited by the signal-to-noise ratio, and typical

areas are 40 μm×40 μm. Besides the possibility to study sorption kinetics in single crystals, conventionally pressed wafers (as, e.g., in the macro-FTIR experiments reported in Sect. 2.1.2.1) or zeolite powder particles may also be investigated. In the latter case, IR microscopy requires only tiny amounts of powder crystallites, i.e., ca. 10 mg. The micro-flow cell (Fig. 4b) attached to the microscope by means of an *xy* stage is manufactured of stainless steel. Sample observation is performed through CaF_2 windows sealed with Teflon rings. The cell accommodates a micro-oven, the diameter of which is about 10 mm. The adsorbate supply is achieved with the same type of equipment as used for the macro-FTIR spectroscopic measurements (vide supra, and see Fig. 5).

To deduce from the spectra the absolute amounts adsorbed or desorbed, calibrations were carried out. This was achieved by measuring the absorbances of the typical IR adsorbate bands as a function of the barometrically determined (admitted or removed) amounts of adsorbate. The thus-obtained calibration curves were almost linear in the range of coverage of interest (see, e.g., Vol. 4, Chap. 1 of this series, p. 37). Uptake of the adsor-

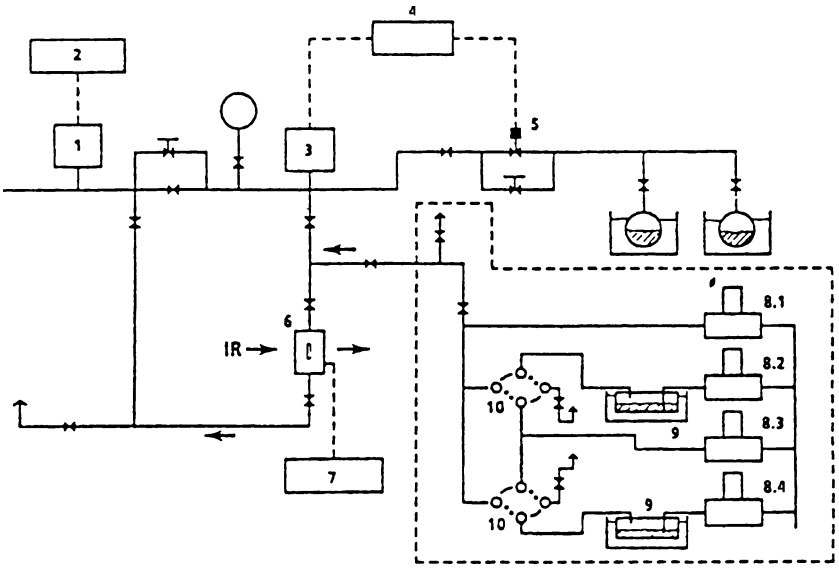

Fig. 5 Experimental setup for diffusion measurements in zeolites. Schematic arrangement around the IR flow-through cell (6), which for macro-FTIR measurements may be that described in Vol. 4, Chap. 1, p 42 of this series (see also [23]) or for micro-FTIR measurements the cell represented in Fig. 4b. Detailed explanation of main parts: (1) ionization gauge; (2) ionization gauge controller; (3) baratron; (4) pressure controller; (5) magnetic valve; (6) IR flow cell with sample; (7) temperature controller; (8) mass flow controllers; (9) thermostatted saturators; (10) four-way valves

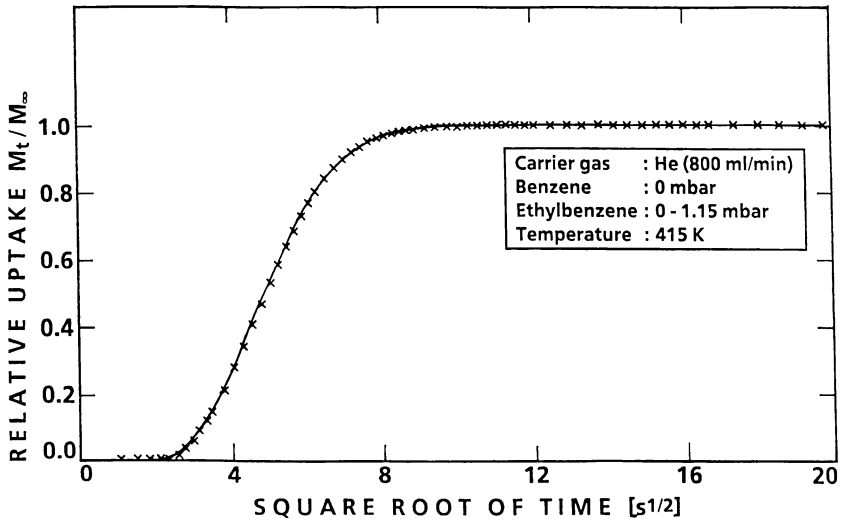

Fig. 6 Uptake curve of ethylbenzene diffusing at 415 K into an activated (at 675 K) H-ZSM-5 sample (wafer) upon a pressure jump from 0 to 1.15 mbar; experimental data: × × × ×

bate ethylbenzene for a partial pressure jump from 0 to 1.15 mbar at 415 K is illustrated in Fig. 6.

2.1.2 Materials

The adsorbents used in the experiments described in the following paragraphs were H-ZSM-5, Na-ZSM-5, Li-ZSM-5, silicalite-1, and H-MOR, the compositions of which are listed in Table 1. Samples No. 5, Li-ZSM-5, and No. 6, Na-ZSM-5, were produced via a fivefold conventional ion exchange in 0.1 N solutions of NaOH and LiOH from the starting material No. 3. The starting material No. 3 and the silicalite-1 sample were prepared and kindly provided by Dr. H.K. Beyer, Institute of Chemistry, Hungarian Academy of Sciences (Budapest, Hungary). Relatively large single crystals of H-ZSM-5 (sample No. 7, ca. 120 μm × 20 μm × 20 μm) for investigations by FTIR microscopy (micro-FTIR spectroscopy) were kindly provided by Prof. J. Weitkamp, University of Stuttgart. According to X-ray checks, all samples exhibited good crystallinity. The size and the shape (spheres or slabs) of the samples were determined by optical microscopy and SEM and were taken into account for data evaluation (see Sect. 2.2.3). In polarized light, the crystals of sample No. 7 exhibited inside hourglass-like structures (see Fig. 7).

This observation might indicate intracrystal interfaces as discussed by Geus et al. [33], which may affect the diffusion pathways and thus the sorption behavior (see also Sect. 3, Fig. 35). The activation of zeolite samples for

Table 1 Properties of the zeolite sorbents used

No.	Zeolite	Formula	n_{Si}/n_{Al}	Particle size [μm][a]
1	H-ZSM-5	$H_{2.5}Na_{0.1}Fe_{0.3}Al_{2.8}Si_{93.2}O_{192}$	33.2	$8.8 \times 5.2 \times 3.2$
2	H-mordenite	$H_{5.5}Na_{0.5}Fe_{0.1}Al_{6.2}Si_{41.8}O_{96}$	6.7[a]	0.8
3	H-Na-ZSM-5	$H_{1.7}Na_{0.9}Al_{2.6}Si_{91.5}O_{192}$	35.2	2.0
4	Silicalite-1	$Na_{0.1}Al_{0.1}Si_{95.9}O_{192}$	> 800	4.0
5	Li-ZSM-5	$Li_{2.6}Al_{2.6}Si_{91.5}O_{192}$	35.2	2.0
6	Na-ZSM-5	$Na_{2.6}Al_{2.6}Si_{91.5}O_{192}$	35.2	2.0
7	H-ZSM-5	$H\,Al_{3.0}Si_{91.1}O_{192}$	30.4	$120 \times 20 \times 20$

[a] Samples No. 2–6 were almost spherically shaped. The formulae of samples No. 1 and 2 are idealized, i.e., both samples possess significant amounts of Al-containing extra-framework species ("true" Lewis sites)

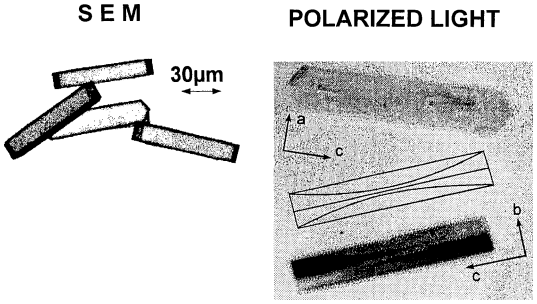

Fig. 7 Specimen of large single crystals of H-ZSM-5 ($n_{Si}/n_{Al} = 30.4$) provided by Prof. J. Weitkamp, Stuttgart; size: 100 μm × 20 μm × 20 μm; *left*: imaged by scanning electron microscopy; *right*: imaged by an optical microscope in polarized light

sorption and diffusion measurements is usually performed in dynamic high vacuum (10^{-5} Pa for at least 2 h) or in a stream of extremely dry helium or hydrogen (in particular in micro-FTIR experiments); the activation temperature is usually 675 K and reached by slow heating (5 K min^{-1}). Subsequently, the temperature is slowly lowered (10 K min^{-1}) to the required sorption temperature. During performing this temperature program, the high vacuum or a carrier gas stream (helium) of 10 ml min^{-1} is maintained.

As usual, spectral grade adsorbates (benzene, ethylbenzene, *p*-xylene, and pyridine) were employed (e.g., from Merck, Darmstadt, Germany). They must be further purified via distillation, passage through an alumina column to remove, particularly from ethylbenzene, contaminating oxygenates, subjected to three freeze–pump–thaw cycles and, finally, stored over highly (at 525 K under 10^{-4} Pa) activated 4A molecular sieves. These previously activated zeolite A samples were employed to remove even traces of water: ampoules with

activated zeolite 4A were sealed after activation under high vacuum and were broken in the bulb containing the highly purified adsorbate.

Chromatography grade gases (99.996% He, Ar, Kr, Xe) were purchased from Messer-Griesheim, sorbate paraffins (spectroscopic grade *n*-hexane, *n*-heptane, *n*-octane, and neopentane) from Fluka; these were used without additional purification.

2.2 Selected Examples

2.2.1 Adsorption and Desorption of Single-Component Adsorbates by "Macro"-FTIR

Generally, the adsorption and desorption experiments described in this section as well as those reported in Sect. 2.2.2 (vide infra) were carried out using macro-infrared spectroscopy as described in the first part of Sect. 2.1.1.

2.2.1.1 Benzene, Ethylbenzene, and *p*-Xylene in H-ZSM-5

The following IR bands being indicative of the adsorbates benzene , ethylbenzene, and *p*-xylene were monitored: at 1478, 1496/1453, and 1516 cm^{-1}, respectively. Sets of spectra of benzene or *p*-xylene on H-ZSM-5 analogous to that shown for ethylbenzene (Fig. 3) were monitored and, using the appropriate calibration curves, the corresponding adsorption and desorption curves of the type displayed for ethylbenzene in Figs. 8a,b obtained (see also discussion of Fig. 29 below).

From the plateaux appearing for the various coverages at chosen temperatures, adsorption isotherms could be derived. They were of the Freundlich–Langmuir type, i.e., describable by an equation of the type shown in Eq. 1:

$$n = n_o \cdot b \cdot p^m (1 + p^m) , \tag{1}$$

where n = coverage, n_o = maximum coverage, p = equilibrium partial pressure of the adsorbate; m, b = specific constants.

A set of such isotherms is shown in Fig. 9 for the system ethylbenzene/H-ZSM-5. From such sets, in turn, isosteres were constructed and isosteric heats of adsorption, Q_{iso}, determined via the Clausius–Clapeyron equation. This is illustrated in Fig. 10 using the system ethylbenzene/H-ZSM-5 as an example.

The results for the above-indicated three adsorbates are summarized in Table 2 and compared with data provided by independent techniques and reported in the literature (see [24, 25, 34–37]). The agreement is quite satisfactory. This also holds for the diffusion coefficients, D_0, the evaluation of which will be discussed in Sect. 2.2.3.

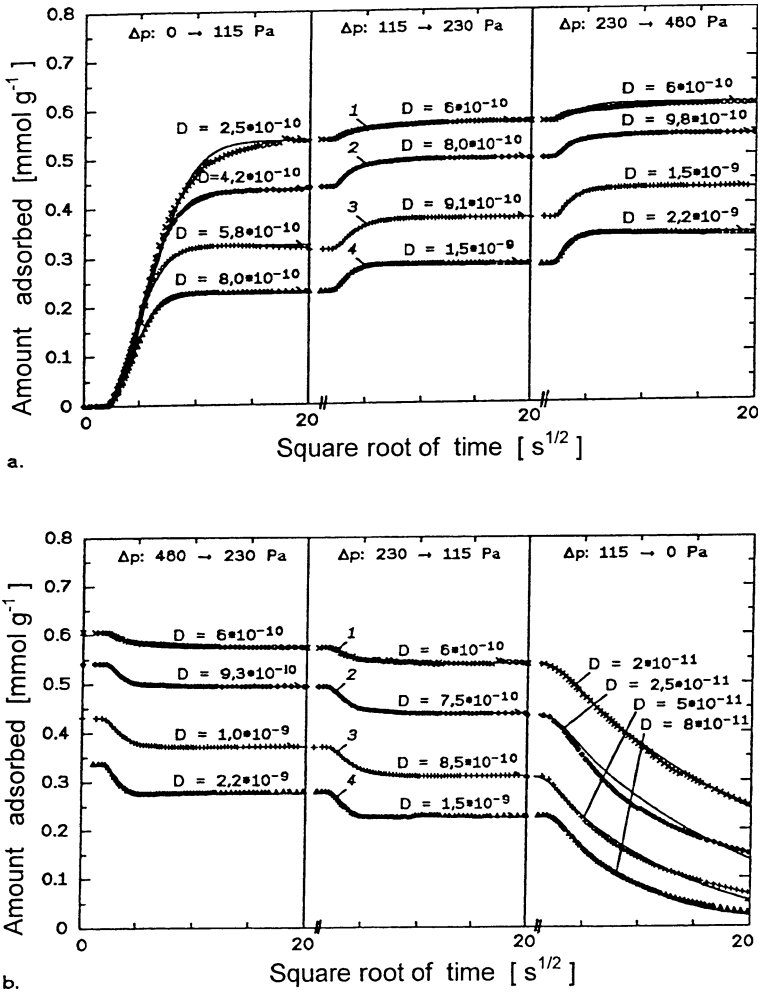

Fig. 8 Effect of temperature on the amounts (**a**, *upper part*) adsorbed and (**b**, *lower part*) desorbed of ethylbenzene in ZSM-5 for different pressure jumps and three final partial pressures (115, 230, and 460 Pa) and effect on the (corrected) diffusivities (vide infra). The uptake curves 1, 2, 3, and 4 were determined at 355, 375, 395, and 415 K, respectively

2.2.1.2 Pyridine in H-MOR, H-ZSM-5, Li-ZSM-5, Na-ZSM-5, and Silicalite-1

Measurements of adsorption of pyridine into acid zeolites were severely impeded by the strong interaction of the adsorbate molecules with the adsorption sites, that is, centers of Brønsted and/or Lewis acid types, i.e., acidic OH groups and only threefold coordinated framework Al or Al-containing extra-framework species, respectively ("true" Lewis sites; see Vol. 4, Chap. 1,

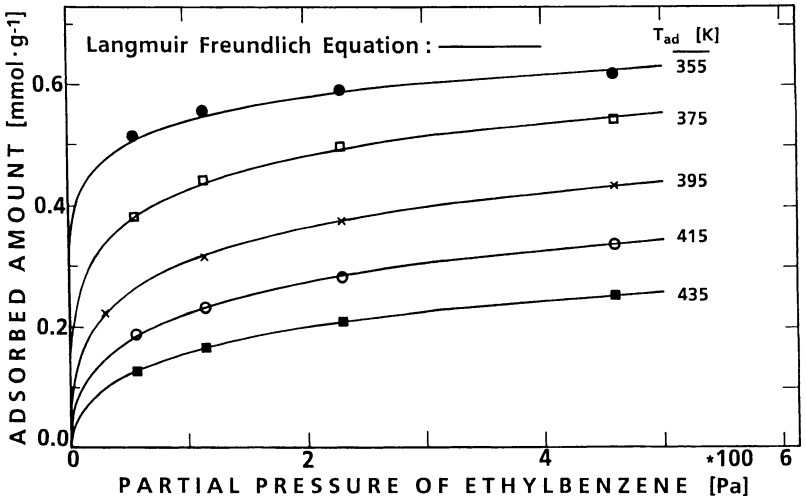

Fig. 9 Isotherms of ethylbenzene adsorption on H-ZSM-5 for various adsorption temperatures: amounts adsorbed (mmol g^{-1}) as a function of the ethylbenzene partial pressure (Pa)

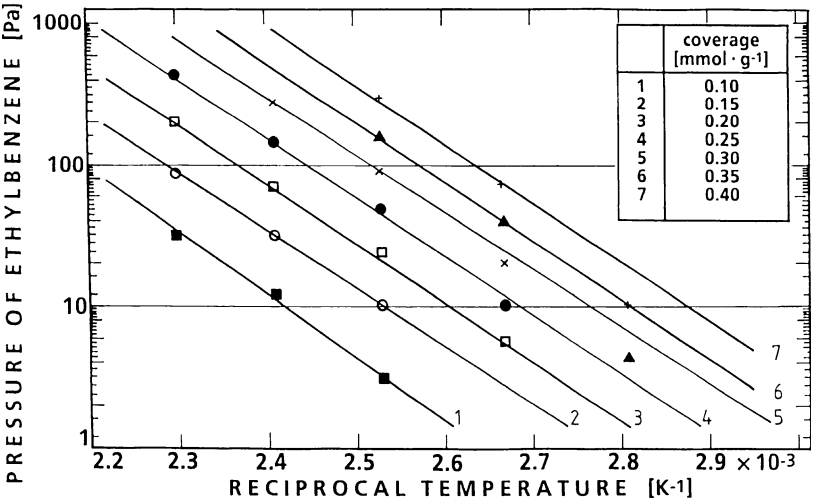

Fig. 10 Isosteres of ethylbenzene adsorption on H-ZSM-5 for various coverages

Sect. 5.5.2.6). As a consequence of this strong interaction, the hopping rate of the adsorbate molecules, moving from one site to another, was found to be rather low, and one has to accept correspondingly long times for equilibration. However, it turned out that the uptake was in no case reversible, i.e., it could not be reversed through desorption at decreased adsorbate pressures, even at the highest temperatures (575 K) which were experimen-

Table 2 Isosteric heat, Q_{iso}, and microcalorimetrically measured heat of adsorption, Q_{ad}, of benzene, ethylbenzene, and *p*-xylene in H-ZSM-5

Sorbate	Coverage [mmol/g]	Q_{iso} [kJ/mol]	Refs.	Q_{ad} [kJ/mol]	Refs.
Benzene	0.35	64 ± 5	[33]	64.5 ± 5	[33]
	0.35	60	[34]		
Ethylbenzene	0.35	82 ± 5	[33]	86.5 ± 5	[33]
p-Xylene	0.35	79 ± 5	[24]	78 ± 2	[35]
		80	[36]		

tally available (see Sect. 2.1.1 and [22–26]). Therefore, adsorption isotherms for the systems pyridine/H-MOR or pyridine/H-ZSM-5 could not be obtained [26]. This is a serious problem, since the adsorption of pyridine into acid zeolites is a very popular procedure to indicate qualitatively through the positions of the typical bands the *Brønsted acid* sites (pyridinium ion band at 1545 cm^{-1}) as well as the *"true" Lewis acid centers* (band of pyridine coordinatively bound to extra-framework, aluminum-containing, and electron-pair accepting species at 1450 cm^{-1}) and, finally, the *cations* (bands of pyridine attached to cations at 1441–1450 cm^{-1}), as was discussed in Vol. 4,

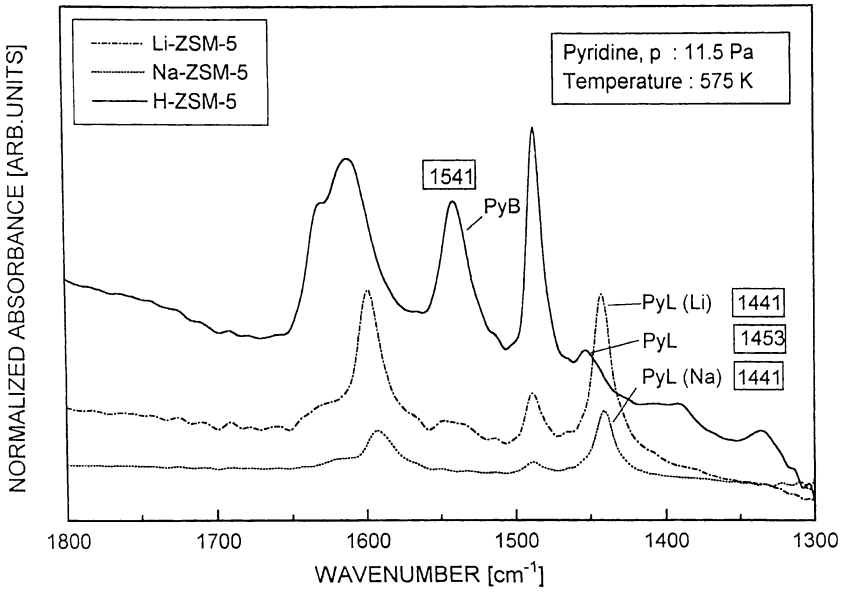

Fig. 11 FTIR spectra of the ring deformation region after pyridine sorption into H-ZSM-5 (sample No. 3), Li-ZSM-5 (sample No. 5), and Na-ZSM-5 (sample No. 6) monitored through the changes in the absorbance of the band at 1443 cm^{-1}

Chap. 1 of the present series (see also Fig. 11). Similarly, the amounts of Brønsted and Lewis centers are often measured via pyridine adsorption, and the strength of such acid sites in zeolites is frequently determined by temperature-programmed desorption of previously adsorbed pyridine (see, e.g., [38]).

The assumption that the strong interaction between the strongly acidic adsorbent and the strongly basic adsorbate under our experimental conditions was the reason for the failure to achieve reversibility was confirmed when adsorbents with the same structure but lower (Li-ZSM-5 or Na-ZSM-5) or zero acidity (silicalite-1) were employed [26]. Figure 12 demonstrates the perfect reversibility of pyridine sorption into the slightly acidic Li-ZSM-5 zeolite.

Also, pyridine was reversibly adsorbed into the essentially nonacidic silicalite-1 (sample No. 4), which has the same MFI structure as H-ZSM-5, but no acid centers. A set of spectra of pyridine uptake into silicalite-1 was scanned in short intervals and is displayed in Fig. 13.

The bands at 1595 and 1443 cm^{-1} are very close to those observed with the slightly acidic samples Nos. 5 and 6 (see Table 1). They were easily removed by short purging with helium or evacuation. From sets of spectra analogous to those of Fig. 12 (reversible) uptake curves were obtained similar to those of Fig. 8, and likewise isotherms (see, e.g., Fig. 14) and isosteres (Fig. 15) were constructed therefrom.

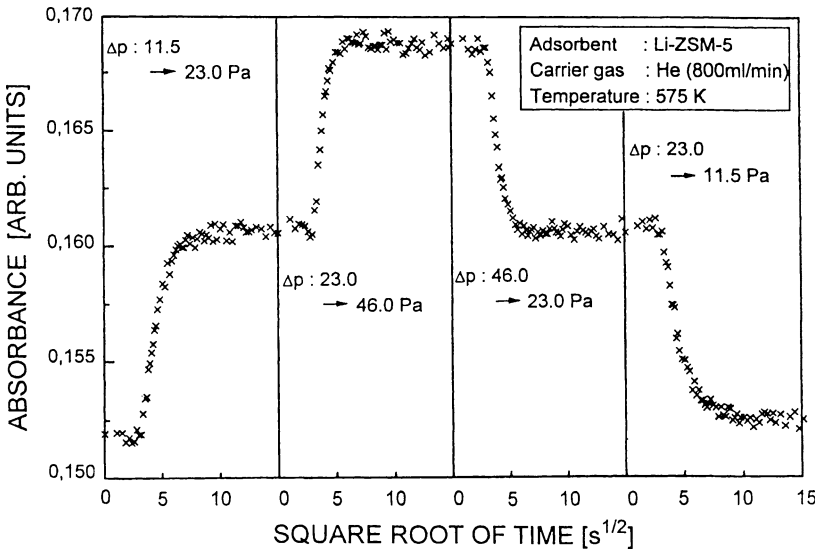

Fig. 12 Curves obtained upon *reversible* uptake sorption (*left side*) and desorption (*right side*) of pyridine into and out of Li-ZSM-5

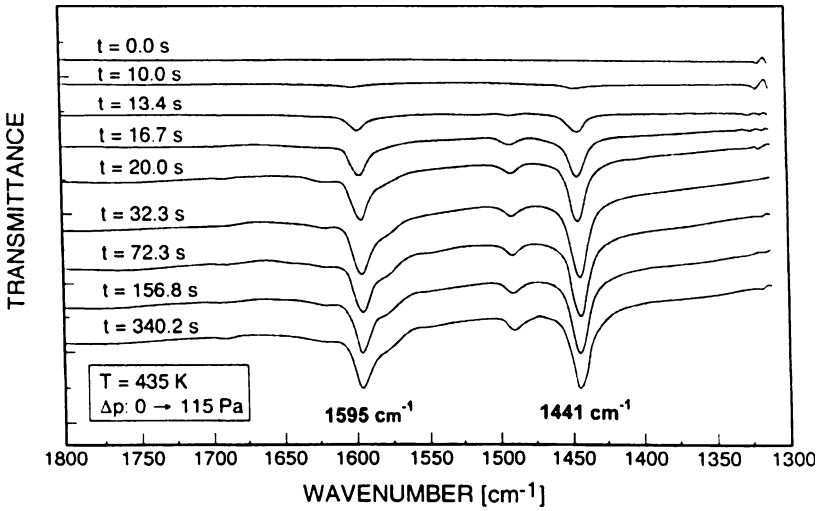

Fig. 13 Set of FTIR spectra of successive states of uptake of pyridine into silicalite-1 (sample No. 4)

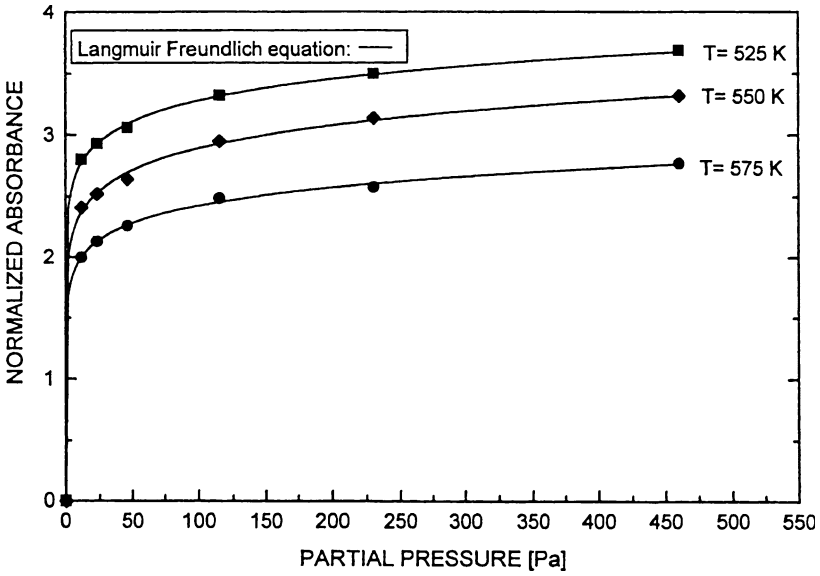

Fig. 14 Isotherms of pyridine adsorption on Li-ZSM-5 (sample No. 5) at various temperatures T, and described by a Langmuir–Freundlich equation (*solid lines*)

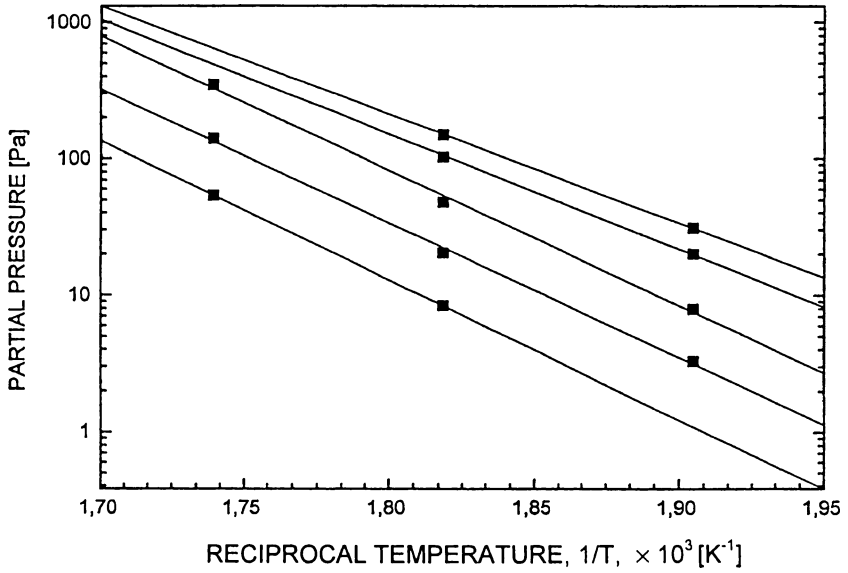

Fig. 15 Isosteres of pyridine adsorption on Li-ZSM-5 (sample No. 5) for various coverages. From the slopes isosteric heats of adsorption, Q_{iso}, of 195–155 kJ mol^{-1} were derived, depending on the coverage

2.2.2 Adsorption of Binary Mixtures by "Macro"-FTIR

2.2.2.1 Benzene/Ethylbenzene

The IR technique also enables us to determine the adsorption and desorption of binary mixtures, provided the IR spectra of the two components were sufficiently different so that the spectra of the mixtures could be reliably decomposed. This was, e.g., the case for the pairs benzene/ethylbenzene, benzene/*p*-xylene, and ethylbenzene/*p*-xylene (compare, e.g., Figs. 3 and 16).

An example of isotherms for the mixture of benzene and ethylbenzene is provided by Fig. 17. Also in this case, the isotherms were well described by a Langmuir–Freundlich equation of the type shown in Eq. 2:

$$n_i = n_{oi} \times b_i \times p_i^{m_i} / (1 + \sum_j b_j \times p_j^{m_j}) \,, \tag{2}$$

where p_i = equilibrium partial pressure of adsorbate, n_i = coverage with adsorbate, n_{oi} = maximum coverage with adsorbate, b_i, m_i = constants specific to the adsorbate, and j = number of adsorbate (see [22]).

The adsorption isosteres for ethylbenzene (see Figure 18), adsorbed from a benzene/ethylbenzene mixture into H-ZSM-5, provided isosteric heats of

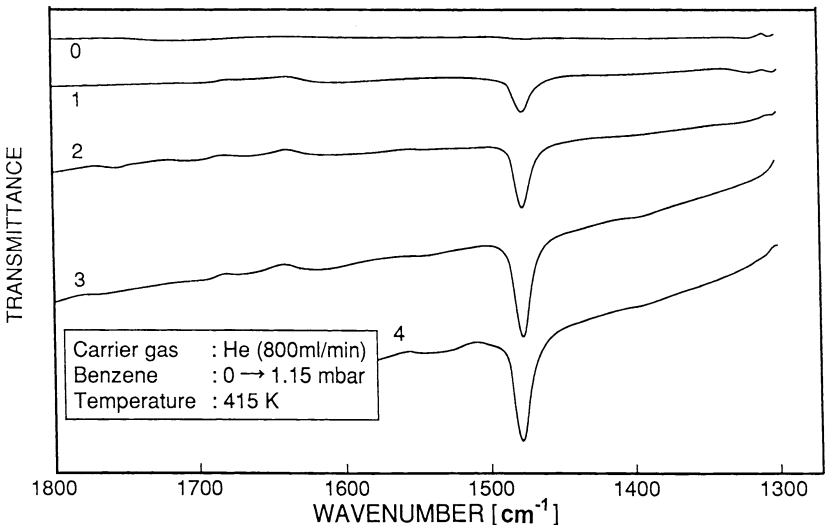

Fig. 16 Set of FTIR spectra indicating successive states of sorption of benzene into H-ZSM-5 at 415 K (0, 1, 2, 3, 4: after 0, 18.5, 48.1, 64.8, and 871.5 s, respectively). Pressure jump: from 0 to 1.15 mbar partial pressure of ethylbenzene in helium stream; "thickness" of the sample wafer: 10 mg cm^{-2} (corresponding to about 0.1 mm)

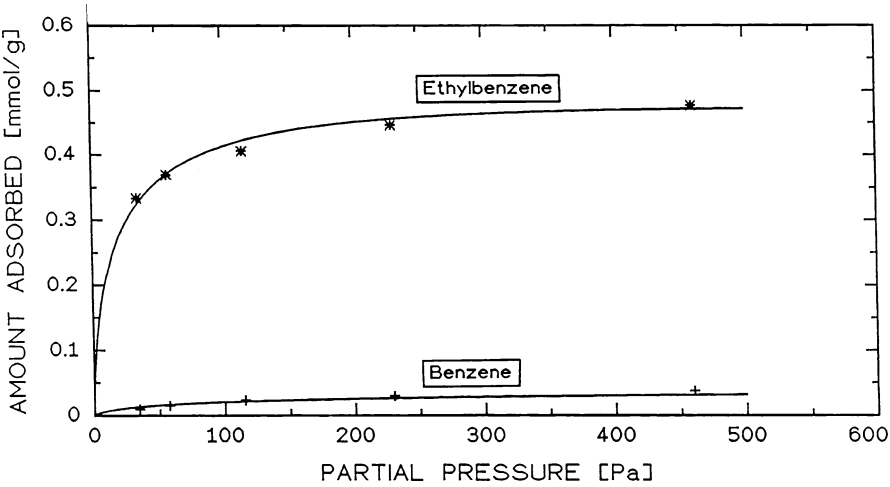

Fig. 17 Isotherms for the mixed adsorption at 415 K of benzene and ethylbenzene on simultaneous changes of the partial pressures of the components

adsorption of about 63–70 kJ mol^{-1}, which were definitely lower than that of pure ethylbenzene (82 kJ mol^{-1}) due to the effect of the simultaneously adsorbed benzene (see Table 2).

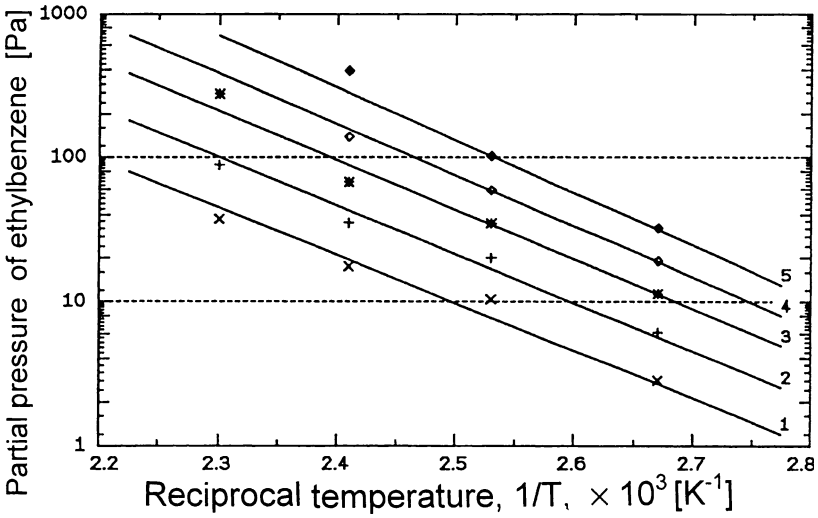

Fig. 18 Sorption isosteres of the sorbate ethylbenzene from simultaneous sorption of the binary mixture of ethylbenzene and benzene; pressure as a function of the reciprocal temperature at constant loading (in mmol g^{-1}): (1) 0.10; (2) 0.15; (3) 0.20; (4) 0.25; (5) 0.30

2.2.3
Adsorption and Desorption Kinetics of Single-Component Adsorbates

2.2.3.1
Diffusion of Benzene, Ethylbenzene, and *p*-Xylene in H-ZSM-5 by "Macro"-FTIR

From sets of spectra such as those shown in Fig. 3 and uptake curves displayed by Fig. 8 not only isotherms and isosteres could be derived, using the respective plateaux for the temperatures and pressures indicated, but also from the ascending branches (measured via FTIR after an upward pressure jump) or the descending branches (determined after a downward pressure jump) the kinetics of adsorption and desorption into zeolitic pores could be derived. These processes were assumed to be diffusion controlled. Their evaluation required a fit of the appropriate solution of Fick's second law as provided by Crank [39] to the experimentally measured uptake (or removal) points, which are indicated in Fig. 6 by filled crosses for the case of ethylbenzene uptake.

The solid curve in Fig. 6 represents the solution of Fick's second law adopted for the present experiments (Eq. 3, cf. [22, 23]):

$$C = -\frac{2D}{ra}\sum_{n=0}^{\infty}(-1)^n \mathrm{e}^{-\frac{Dn^2\pi^2 t}{a^2}} n\pi^* \sin\frac{n\pi r}{a}\int_0^t \mathrm{e}^{\frac{Dn^2\pi^2\lambda}{a^2}}\phi(\lambda)\,\mathrm{d}\lambda\,, \qquad (3)$$

where C, D, t, r, a, and $\phi(\lambda)$ denote concentration, diffusion coefficient, time, radius coordinate, radius of the crystallite, and a function accounting for the time lag, respectively (see above, Fig. 6). D is first assumed to be independent of coverage. The time lag was best described by an exponential function, Eq. 4:

$$\phi(t) = C_0(1 - e^{-\beta t}) , \tag{4}$$

where C_0 and β stand for the surface concentration and a time constant, respectively.

In the case of the FTIR microscopic experiments, where a relatively small cell was employed (see Sect. 2.1.1), the time constant could be reproducibly determined as $\beta \approx 0.6\ s^{-1}$. The evaluation proceeds analogously in the case of desorption upon downward pressure jumps. More details concerning the data evaluation are provided by Niessen [22] and Karge and Niessen [23, 24].

Thus, from the procedure of fitting the experimental data, two parameters were obtained, viz. β (typical of the time lag, vide supra) and D, the unmodified (vide infra) transport diffusion coefficient. The time lag, characterized by β, is due to the fact that after increasing or decreasing the partial pressure of the adsorbate in the gas stream, the corresponding surface concentration on the adsorbent surface is not instantaneously established but only after a finite (measurable) time (cf., e.g., Figs. 3 and 6). The transport diffusion coefficient D is frequently transferred by Eq. 5 (see [40]) into a modified, i.e., so-called corrected, diffusivity D_0. Equation 5 is called the Darken equation even though, in fact, its origin goes back to Maxwell, Stefan, and Einstein. The aim is to eliminate a possible dependence on the coverage and obtain the so-called intrinsic diffusion coefficients, D_0, which should allow a comparison with diffusivities obtained under equilibrium conditions, e.g., by PFG NMR or QENS, i.e., the self-diffusion constants. In fact, the thus-modified diffusivity is found in many cases, but not always, to approach the self-diffusivity. Equation 5 is given as:

$$D = D_0(\Delta \ln p)/(\Delta \ln C) , \tag{5}$$

where D_0 is the "corrected" diffusion coefficient, p the partial pressure of the adsorbate in the gas phase, and C the adsorbate concentration in the sample. For such corrections, the IR-determined adsorption isotherms may be used.

In Fig. 8, a set of uptake curves for ethylbenzene adsorbed and desorbed at various temperatures after various partial pressure changes has already been shown. The diffusivities of benzene and *p*-xylene derived from IR measurements in the same way as described for ethylbenzene are collected in Tables 3 and 4. Table 3 includes data for single-component diffusion as well as for co- and counter-diffusion (see Sect. 2.2.4.1)

Similar to the conclusions drawn from Table 2 (vide supra) with respect to the caloric effects, we now find in view of Table 4 that the good agreement between the diffusivities obtained for benzene in MFI structures through

Table 3 Diffusivities of benzene (B), ethylbenzene (EB), and *p*-xylene (*p*-X) upon pressure jumps of $\Delta p[B] = \Delta p[EB] = \Delta p[p\text{-X}]$: $0 \rightarrow 115$ Pa, H-ZSM-5 (sample No. 1) at 395 K (for more data and experimental details, see [22–24, 34])

Type	n (B) [mmol g^{-1}]	D_0 (B) [cm^2 s^{-1}]	n (EB) [mmol g^{-1}]	D_0 (EB) [cm^2 s^{-1}]	n (*p*-X) [mmol g^{-1}]	D_0 (*p*-X) [cm^2 s^{-1}]
[a]	0.16	6.8×10^{-10}	0.32	5.8×10^{-10}	0.33	1.5×10^{-9}
[b]	0.03	–	0.30	3.5×10^{-10}	0.29	1.3×10^{-9}
[c]	0.02	2.0×10^{-10}	0.30	2.0×10^{-10}		
	0.05	8.0×10^{-10}			0.30	8.0×10^{-10}

[a] Single-component diffusion
[b] Co-diffusion (B + EB or B + *p*-X)
[c] Counter-diffusion (B vs EB or B vs *p*-X, i.e., B preadsorbed under $p[B] = 115$ Pa)
n Coverage

Table 4 Diffusivities of benzene in H-ZSM-5 or silicalite-1 and comparison with literature data

Authors	Karge, Niessen [22, 23]	Bülow et al. [41, 42]	Zikánová et al. [35]	Förste et al. [6]	Ruthven et al. [43]	Shen et al. [37] Van-Den-Begin et al. [44]
Method	FTIR	V = const. p = variable	Grav., piezo.	NMR tracer	ZLC[a]	FR
D_0 [cm^2 s^{-1}]	5.3×10^{-10}	6×10^{-10}	6×10^{-10}	(5–9) $\times 10^{-10}$	2×10^{-9}	1.4×10^{-9}
$T_{Diff.}$ [K]	375	363	363	386	373	375
n [molec./ u.c.]	1.4	2.0	1.4	4	–	1.4

[a] Silicalite-1

the IR technique described on the one hand, and those determined by various independent methods (see [6, 22, 23, 35, 37, 41–44]) on the other, suggests a high reliability of the IR spectroscopic method. This also gives confidence in the reliability of the diffusion coefficients of ethylbenzene, D_0 (EB), and *p*-xylene, D_0 (*p*-X), determined via IR measurements (see Table 3) and, furthermore, in the diffusion coefficients obtained for the cases of co- and counter-diffusion, i.e., for the kinetics of simultaneous adsorption or desorption of the mixtures benzene/ethylbenzene or benzene/*p*-xylene (see Sect. 2.2.4.1). For example, it should be mentioned here that Schumacher and Karge [45] obtained with the same adsorbent and adsorbate as used in the FTIR study, but through a rather sophisticated barometric measurement, an only slightly lower diffusion coefficient for ethylbenzene than

that listed in Table 3, viz. $(1.3 \pm 0.2) \times 10^{-10}$ cm^2 s^{-1} ($E_A = 34 \pm 3$ kJ mol^{-1}). Mirth and Lercher [46] and Gründling et al. [47, 48] extracted from time-resolved FTIR spectroscopic measurements diffusion coefficients of toluene (T) and xylenes (X) in H-ZSM-5. With toluene taken up at 320 K into single crystals of H-ZSM-5, these authors found $D(\mathrm{T}) \approx (3.9\text{–}11) \times 10^{-10}$ cm^2 s^{-1}, in reasonable agreement with literature data obtained by different techniques. The diffusivities of *p*-xylene reported in [46–48] were in the order of 10^{-11}–10^{-12} cm^2 s^{-1} and seemed to be too low. However, in later measurements [49] and under similar conditions, Lercher and coworkers arrived at $D(p\text{-X}) \approx 1.5 \times 10^{-9}$ cm^2 s^{-1}, which is very close to the value given in Table 3.

Since there are, in uptake curves like that of Fig. 8, ascending and descending branches appearing at various experimental temperatures, the diffusion coefficients could also be obtained for a variety of temperatures. From an Arrhenius plot, D_0 vs $1/T$, the activation energies of diffusion, E_A, were derived and collected in Table 5. Again, these data are in excellent agreement with results reported from measurements by completely independent techniques.

As mentioned in Sect. 1, the FTIR spectroscopic technique enables us to study mass transport phenomena as well as chemical conversions in situ, i.e., at or close to reaction conditions at which the IR cells may be operated as (micro-) flow-through reactors. An example is the study of coke formation during ethene or ethylbenzene conversion on H-ZSM-5 and the simultaneous measurement of the decrease of reactant diffusivities [15]. The EB conversion was monitored at 475 and 575 K, resulting in two types of coke distinguished by their IR spectra. The amount of coke was measured through the absorbance of the so-called coke band at 1610 cm^{-1} (Fig. 19). The diffusivities of ethylbenzene in the weakly coking catalyst, H-ZSM-5, decreased with increasing time of coking (see Figure 20 and Table 6) and, in fact, linearly with the amount of coke deposited.

Table 5 Activation energies for diffusion of benzene, ethylbenzene, and *p*-xylene in H-ZSM-5

Sorbate	E_A [kJ mol^{-1}]	Refs.	E_A [kJ mol^{-1}]	Refs.
Benzene	23	[22, 34]	26	[34]
			27	[41]
			27	[43]
Ethylbenzene	31	[22, 34]	30	[43]
p-Xylene	30	[24]	30	[43]

Table 6 Correlation between coke formation, diffusivity, and sorption capacity after coking via ethylbenzene conversion at 575 K

Expt. no.	t_{coking} [h]	A[1490] $\times 10^3$	A[1610] $\times 10^3$	n_∞ [EB] [mmol g^{-1}]	$\Delta n/n$ [%]	D_0 [EB] $\times 10^{-10}$ [cm^2 s^{-1}]
1	–	–	–	0.31	–	5.5
2	3.0	1.2	0.1	0.29	6	5.5
3	13.0	2.7	0.5	0.27	13	5.5
4	25.5	3.7	0.7	0.27	13	5.5
5	42.5	4.8	0.8	0.25	20	5.3
6	70.0	6.0	1.0	0.24	23	4.3
7	104.0	7.8	1.2	0.22	29	2.7

(1) Freshly activated sample; (2)–(7) coked samples. t_{coking}: time on stream during coking; D_0 [EB]: Fickian diffusivity of ethylbenzene; n: sorption capacity for ethylbenzene at $T_{diff} = 395$ K under Δp [EB] $= 0 \rightarrow 115$ Pa; $\Delta n/n$: percentage of loss of sorption capacity; A[1490], A[1610]: maximum absorbance of typical coke bands at 1490 and 1610 cm^{-1}, respectively, as a measure of coke deposited. The error of the diffusivity values is about $\pm 0.5 \times 10^{-1}$ cm^2 s^{-1}

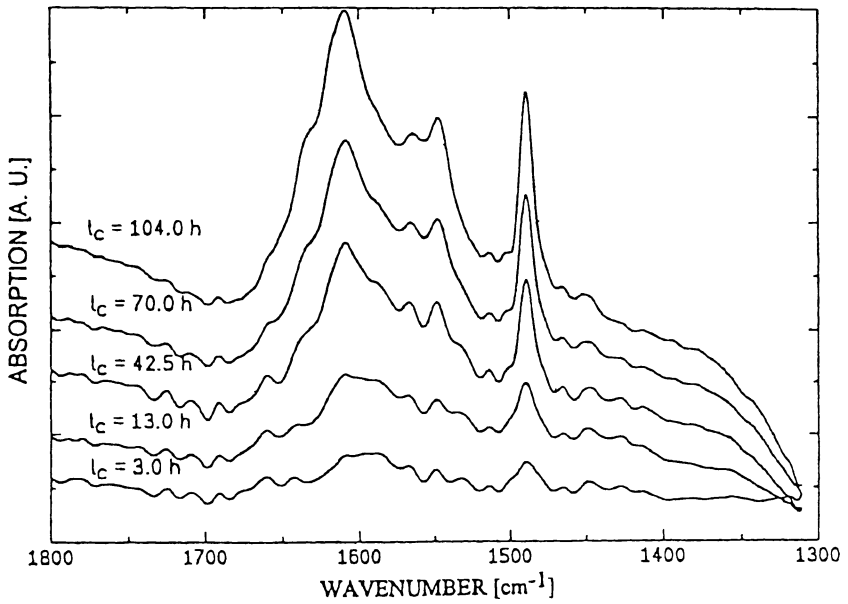

Fig. 19 Set of spectra obtained after coking due to ethylbenzene conversion at 575 K over H-ZSM-5 (sample No. 3). The spectra obtained after activation and after 25.5 h of time on stream (see Table 6) are omitted for the sake of clarity

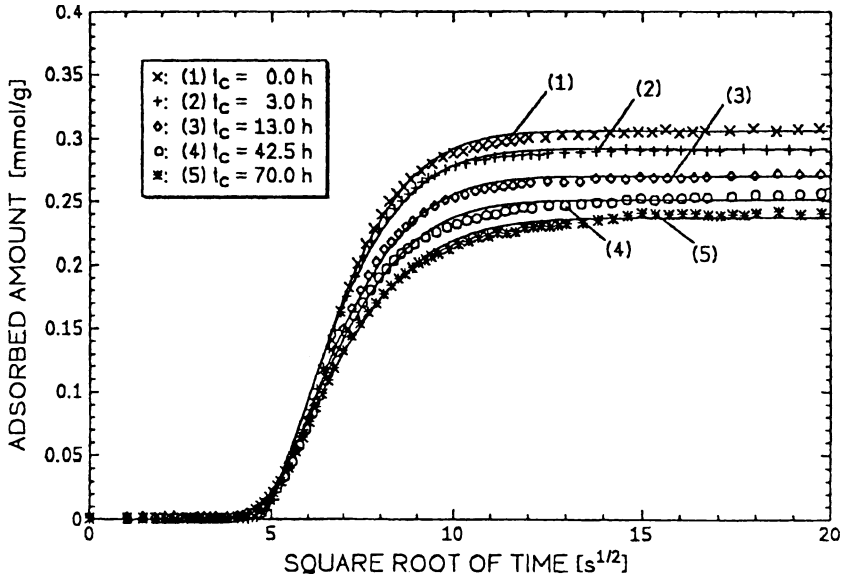

Fig. 20 Uptake curves for ethylbenzene in freshly activated and coked H-ZSM-5 (sample No. 3). The curves obtained after 25.5 and 104 h of time on stream (see Table 6) are omitted for the sake of clarity

2.2.3.2
Diffusion of Pyridine in H-ZSM-5, H-MOR, Na-ZSM-5, Li-ZSM-5, and Silicalite-1 by "Macro"-FTIR

As mentioned earlier, the lack of reversibility is a severe hindrance in obtaining reliable adsorption isotherms of pyridine in acid zeolites such as H-MOR or H-ZSM-5. The same problem arises with the kinetics investigation of adsorption of pyridine into and desorption out of acid zeolites. However, compared to earlier attempts [10], considerable progress was achieved when, upon a modification of the IR flow cell, the application of a higher experimental temperature became possible [26]. An example of pyridine uptake into H-ZSM-5 at 575 K is demonstrated by Fig. 21. Compared to the earlier study [10], the higher adsorption temperature (575 K instead of 395–475 K) enabled a description of the kinetics of the pyridine uptake using only *one*, i.e., a *unique* "noncorrected" transport diffusion coefficient D, for the whole process. This holds both for the pyridine uptake via Brønsted (B) and Lewis (L) acid centers (PyB) and (PyL), respectively. Note, however, that the process of uptake of pyridine, even though described by a solution of Fick's law, is not reversible, i.e., pyridine was not desorbable at the same temperature at which it had been sorbed. A tentative explanation is given below.

The diffusion coefficients were found to be of the order of 5×10^{-11} cm^2 s^{-1}, which seems reasonable when compared with the diffusivities obtained for

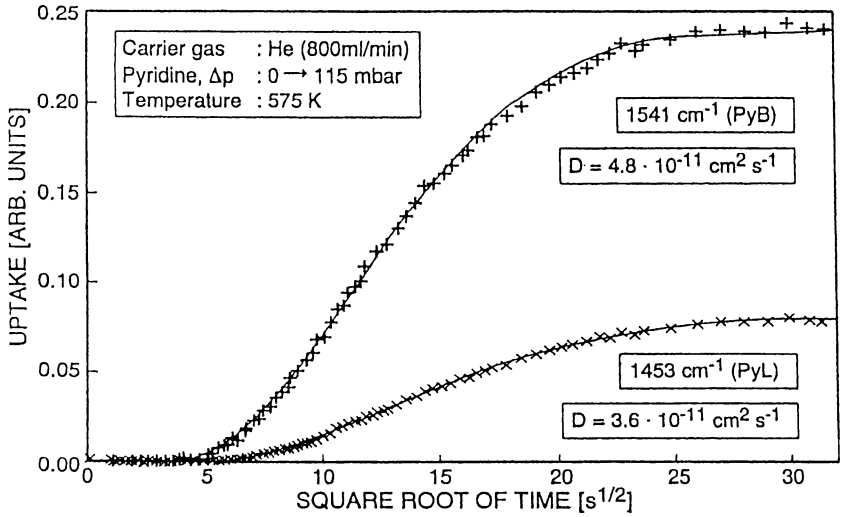

Fig. 21 Uptake of pyridine into H-ZSM-5 as a function of the square root of time monitored by the increase of the absorbance of the typical bands at 1541 cm^{-1} (pyridine reacted with Brønsted sites to give pyridinium ions, PyB, *crosses* ++++) and 1453 cm^{-1} (pyridinium attached to Lewis sites, PyL, *crosses* $\times \times \times \times$) described by a solution of Fick's second law (*solid line*)

benzene, ethylbenzene, or *p*-xylene (see Table 3). In the case of pyridine taken up by H-mordenite at 525 K a diffusion coefficient of 1×10^{-12} cm^2 s^{-1} was determined, almost coincident with a very early result by Klose and Karge [10]. However, this agreement might be fortuitous, since the uptake was, even at 575 K, still not reversible, and the amount adsorbed could not be removed by a corresponding decrease of the partial pressure (vide supra). In other words, in the case of pyridine in acid zeolites the diffusion model of "random walk" seems to be not applicable at the temperatures attainable so far. The fact, however, that the adsorption step was quantitatively reproduced and described by the solution of Fick's second law (Eq. 3) might be explained in the following way. The observed behavior is possibly indicative of a mechanism where a rather slow migration of the adsorbate is followed by a very rapid (and irreversible) reaction with strongly acidic Brønsted and/or Lewis centers. In this sense, the *diffusion* of pyridine may be the rate-determining step in the overall *uptake* process of pyridine into H-mordenite and H-ZSM-5.

When the strong acidity of the MFI zeolite (H-ZSM-5) was removed via ion exchange, as in the case of Li-ZSM-5 or Na-ZSM-5, or was intrinsically absent, as in the case of silicalite-1, adsorption of pyridine was entirely reversible, and reasonable ("corrected") diffusion coefficients were obtained. As an example, Fig. 12 illustrates the reversible pyridine adsorption into and desorption out of Li-ZSM-5. The diffusion coefficient of pyridine transport in

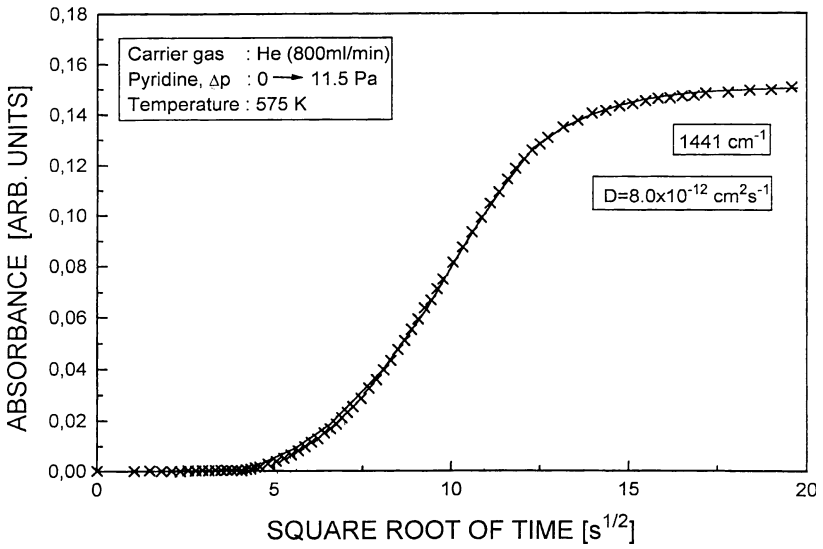

Fig. 22 Uptake of pyridine into Li-ZSM-5 (sample No. 5) as a function of the square root of time monitored through the increase of the absorbance of Py → Li band (× × × × ×) at 1441 cm^{-1} and fitted (*solid lines*) by a solution of Fick's second law according to Eqs. 3 and 4

Table 7 Diffusivities of pyridine in various zeolites

Sample no.	Zeolite	Temperature [K]	Diffusivity [$cm^2\ s^{-1}$]	Uptake
1	H-ZSM-5	575	4×10^{-11}	irreversible
2	H-mordenite	525	1×10^{-12}	irreversible
4	Silicalite-1	525	2×10^{-9}	reversible
5	Li-ZSM-5	575	8×10^{-12}	reversible
6	Na-ZSM-5	575	2×10^{-11}	reversible

Li-ZSM-5 was determined as 8.0×10^{-12} $cm^2\ s^{-1}$ (Fig. 22). The diffusivities of pyridine in all adsorbents investigated are listed in Table 7.

2.2.3.3 Diffusion of Paraffins in H-ZSM-5 by "Micro"-FTIR

The diffusion of paraffins was investigated by micro-FTIR spectroscopy. In Fig. 23, spectra of the freshly activated, unloaded zeolite sample No. 7, as well as of the otherwise unchanged sample after admitting a partial pressure of 3.1 mbar of *n*-hexane, are presented. The experimental resolution was 2 cm^{-1}.

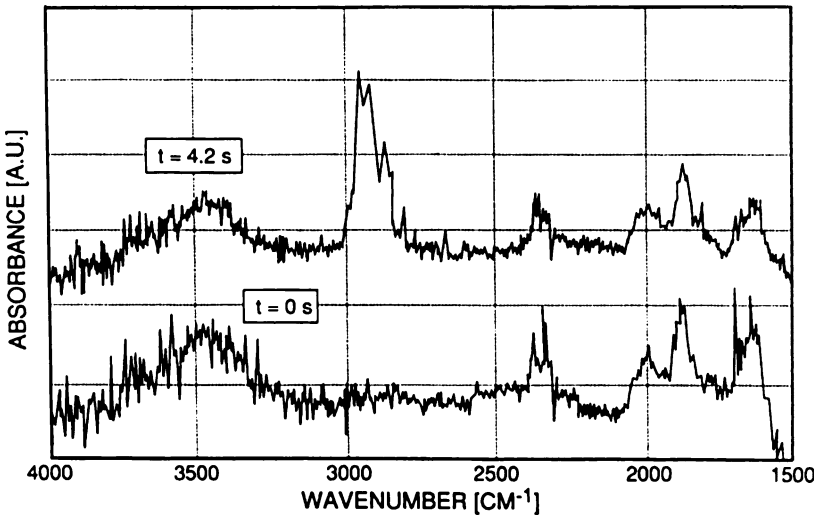

Fig. 23 Monitoring the absorbance of an H-ZSM-5 sample during uptake of *n*-hexane at 398 K via micro-FTIR spectroscopy; 3.1 mbar partial pressure of *n*-hexane in a helium flow (100 ml min^{-1})

Although 25 spectra were accumulated, the signal-to-noise ratio is, due to the small sample area of about 20 μm×20 μm, rather low.

The band at 2350 cm^{-1} is attributed to CO_2 present in the beam path within the IR microscope. The spectrum of the freshly activated sample exhibits IR bands at 2007, 1882, and 1644 cm^{-1}, which may be attributed to overtones of zeolite framework vibrations [52, 53]. The broad feature at 3500 cm^{-1} is due to Si(OH) groups of lattice defects [44]. After equilibration of the sample with 3.1 mbar of *n*-hexane, the positions and relative intensities of the IR bands mentioned remain essentially unchanged. Additionally, the spectrum shows the IR bands characteristic of *n*-hexane, i.e., the asymmetric vibrations of the CH_3 and CH_2 groups at ν = 2960 and 2930 cm^{-1}, respectively, and the symmetric counterparts at ν = 2890 and 2870 cm^{-1} (see Vol. 4, Chap. 1 of the present series).

Thus, by referencing the absorbances of the unloaded sample to those of the unloaded one, any influence of the adsorbent on the IR absorbances is eliminated, and the amount of sorbate may be deduced simply from the intensity of the characteristic IR bands. In the case of the single component *n*-hexane, the asymmetric vibration of the methyl group, ν_{as}^{CH3}, was evaluated.

To illustrate the quality of the data, no accumulation and/or averaging of the absorbances were carried out. For the sorbates *n*-heptane (see Fig. 24), *n*-octane, and *n*-nonane similarly well-fitted uptake curves were obtained [32]. In Fig. 25, the uptake curves for *n*-hexane into sample No. 7 at various sorption temperatures are presented. The symbols denote the

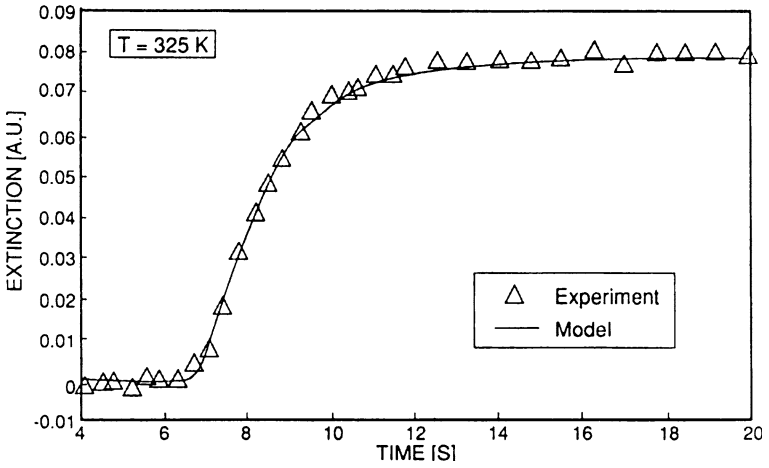

Fig. 24 Uptake curve of *n*-heptane into H-ZSM-5 at 325 K as measured via micro-FTIR spectroscopy. *Solid line*: calculated uptake curve; △: experiment

experimental data; the corresponding calculated uptake curves, the fitting of which provides the transport diffusivities , *D*, are plotted as solid lines.

Since the amount of sorbate decreases with increasing sorption temperature, the signal-to-noise ratio deteriorated. Also, crystals of lower quality caused increased scatter. In such cases repeated uptake runs may be performed to reduce the experimental error. Repetition of the uptake runs is easily performed if the sorbate can be completely removed by short purging with pure carrier gas. This holds, e.g., for *n*-hexane, *n*-heptane, and neopentane, whereas *n*-octane and *n*-nonane desorbed at lower temperatures only to about 70%, and raising the temperature to 475 K for a time of 5 min was necessary to recover the unloaded zeolite. Thus, only uptake of *n*-hexane and *n*-heptane is, in a strict sense, reversible in that at the temperature of adsorption by successive lowering of the sorbate partial pressure the uptake curve is exactly passed through by small steps but in a reverse direction. The above-mentioned reduction of the scatter of the experimental uptake curves could also be achieved by superimposing results obtained with more than one large crystal.

The results presented here were not subject to a Darken correction (vide supra, Eq. 4), which generally accounts for a nonlinearity of the adsorption isotherms . In previous experiments, it was established that for the partial pressures employed in the experiments described in this section, the adsorption isotherm may be considered as linear.

All sorbates exhibited transport diffusivities of the order 10^{-8} cm^2 s^{-1}, increasing with increasing temperature. The errors of the transport diffusion coefficients are estimated to be $\pm 0.75 \times 10^{-8}$ cm^2 s^{-1} in the case of *n*-hexane and *n*-heptane. Due to the lower absolute absorbance in the case of *n*-octane and *n*-nonane, the estimated error is higher, viz. $\pm 1.25 \times 10^{-8}$ cm^2 s^{-1}. The re-

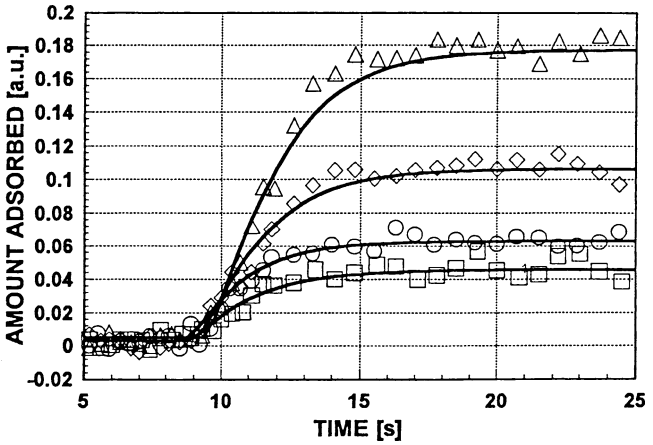

Fig. 25 Uptake of *n*-hexane under 3.1 mbar partial pressure with helium as carrier gas at various sorption temperatures monitored via micro-FTIR spectroscopy. *Solid lines*: calculated uptake curves; *symbols*: △ = 398 K, ◇ = 423 K, ○ = 448 K, □ = 473 K

sults obtained via the technique of micro-FTIR spectroscopy agree well with data obtained by other uptake techniques. Van-Den-Begin et al. [44] reported a (corrected) transport diffusion coefficient of 2×10^{-7} cm^2 s^{-1} for *n*-hexane in single crystals of silicalite-1 at a sorption temperature of 379 K, measured by the single-step frequency response technique. The application of the ZLC method by Eic and Ruthven [54, 55] resulted in an intracrystalline transport diffusivity of 10^{-8} cm^2 s^{-1} at a sorption temperature of 334 K. (Generally, the diffusivities in silicalite-1 are found to be a little higher than in H-ZSM-5.) The diffusivities determined for *n*-hexane, *n*-heptane, *n*-octane, and *n*-nonane at various temperatures are listed in Table 8. Jobic et al. [56] measured by QENS diffusivities which were about one order of magnitude higher; (cf. also discussion in Chapter 5 of this volume).

Table 8 Transport diffusivities of *n*-paraffins in single crystals of H-ZSM-5

N_{Carbon}[a]	6	7	8	9
T_{Diff} [K]	Transport diffusivities [10^{-8} cm^2 s^{-1}]			
398	4.5	3.0	2.7	1.5
423	6.2	3.5	3.0	2.3
448	8.0	4.1	3.0	2.6
473	9.5	6.0	5.0	3.3
E_A [kJ mol^{-1}][b]	15.6	14.6	16.9	16.4

[a] N_{Carbon}: number of carbon atoms in the paraffin chain
[b] E_A: activation energy of diffusion

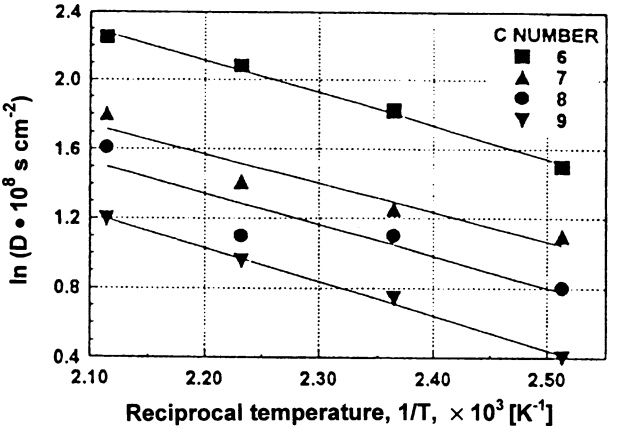

Fig. 26 Arrhenius plot of transport diffusivities of *n*-paraffins (*n*-hexane, *n*-heptane, *n*-octane, *n*-nonane) in H-ZSM-5 single crystals

From the uptake curves of the four *n*-paraffins (as shown, e.g., in Figs. 24 and 25 for diffusion of *n*-heptane and *n*-hexane, respectively) into H-ZSM-5 as a function of adsorption temperature, the corresponding Arrhenius plots were derived and are shown in Fig. 26.

Table 8 also summarizes the activation energies, E_A, which do not exhibit any apparent dependence on the chain length. This behavior was also stated by Eic and Ruthven [54, 55], who found an increasing activation energy for the diffusion of paraffins in silicalite-1 up to *n*-hexane and a leveling off for carbon numbers greater than six. For *n*-pentane, these authors determined $E_A = 19.3\ \text{kJ mol}^{-1}$.

2.2.4
Kinetics of Adsorption and Desorption of Adsorbate Mixtures

2.2.4.1
Co-diffusion of Benzene, Ethylbenzene, and *p*-Xylene by "Macro"-FTIR

In a co-diffusion experiment, first the spectrum of the pure, activated adsorbent wafer is scanned, and then the desired pressure jumps of both adsorbates are simultaneously realized, followed by monitoring the uptake of both components through their IR spectra. An example is provided in Fig. 27, where the co-diffusion of benzene (monitored by the development of the band at $1478\ \text{cm}^{-1}$) and *p*-xylene (monitored by the development of the band at $1516\ \text{cm}^{-1}$) is described.

In cases of co-diffusion such as that illustrated in Fig. 27, one frequently encounters the phenomenon of "overshooting" for the following reason. At higher coverages the more strongly interacting component, which is in the

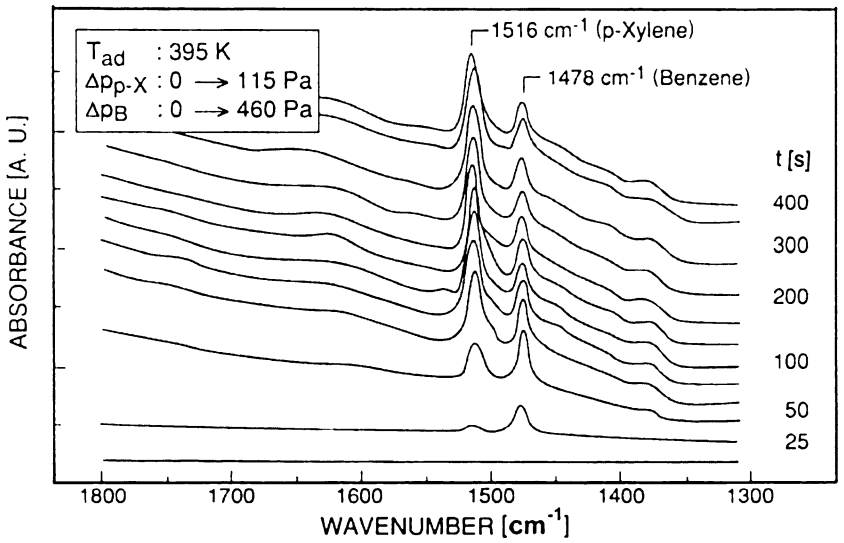

Fig. 27 Set of spectra monitored via macro-FTIR spectroscopy during co-diffusion of benzene (partial pressure: 460 Pa) and *p*-xylene (partial pressure: 115 Pa) from a gas stream (with helium as carrier gas) into H-ZSM-5. First, benzene is preferentially sorbed, then it is partially replaced by *p*-xylene, which is more strongly interacting with the adsorbent (see Fig. 28)

present case *p*-xylene exhibiting $Q_{iso} = 80\,kJ\,mol^{-1}$, starts to replace a fraction of the component with the weaker interaction, here benzene with $Q_{iso} = 64\,kJ\,mol^{-1}$. A similar behavior was observed when ethylbenzene and benzene were co-diffusing [22, 23]. Ethylbenzene interacted more strongly with the sorbent than benzene. Thus benzene, having the somewhat higher diffusion coefficient, migrates initially more rapidly into the H-ZSM-5 pore system, but is subsequently replaced to some extent by more strongly adsorbed EB molecules ($Q_{iso}(EB) > Q_{iso}(B)$). This effect was expected from theoretical considerations [57–59]. The evaluation of diffusion coefficients in cases of co-diffusion follows essentially the same procedure as in the treatment of single-component diffusion. Some results are incorporated into Table 3 (vide supra).

2.2.4.2
Counter-Diffusion of Benzene vs Ethylbenzene, Ethylbenzene vs Benzene, Benzene vs *p*-Xylene, and *p*-Xylene vs Benzene by "Macro"-FTIR

A counter-diffusion experiment is usually conducted as follows. First, the activated adsorbent wafer is loaded at a given experimental temperature with a certain amount of component 1 (e.g., benzene) according to a certain partial pressure jump of this component in the gas stream (vide supra).

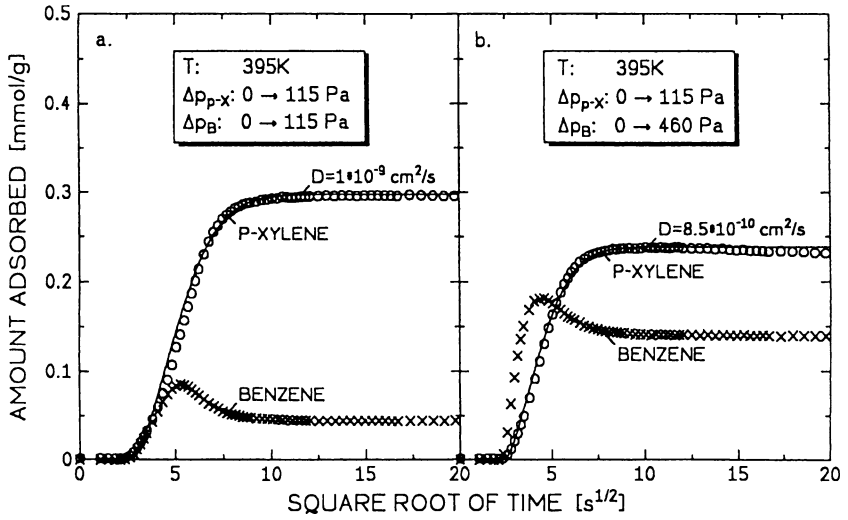

Fig. 28 Co-diffusion of *p*-xylene and benzene. Uptake from a mixture of benzene and *p*-xylene as a function of the square root of time at 395 K but for two different partial pressures of benzene in the mixture. The "overshooting" of benzene sorption is clearly demonstrated (see text)

Second, when a stationary state is reached, i.e., no further changes in the spectra observed, component 2 (e.g., *p*-xylene) is admitted to the main gas stream via injecting an appropriately prepared partial stream with component 2. Then, component 2 travels into the adsorbent and replaces part of the preadsorbed component 1. Thus, component 1 produces a descending branch (here, decreasing absorbance of the typical band at 1478 cm^{-1}), whereas the in-going component 2 gives rise to an ascending branch of the uptake curve (i.e., increasing absorbance of the typical band at 1516 cm^{-1}) as shown by Fig. 29 [24]. From both branches the respective diffusion coefficients can be evaluated in essentially the same manner as that described for the adsorption kinetics of single-component systems. Data for the systems investigated are incorporated into Table 3 (vide supra).

It is worth noting that the last desorption step (part b of Fig. 29) yielded significantly lower diffusivities than part a with the ascending branch for the first uptake step of *p*-xylene. Similar phenomena were observed with other systems (cf. similar features in, e.g., Fig. 8). Note, however, that these differences between the results obtained in adsorption and desorption decrease with respect to the subsequent pressure jumps. The observed effect is most likely due to a strong interaction of the adsorbate molecules with a small fraction of rather strong adsorption sites of the adsorbent, so that it is difficult to remove the very last molecules by desorption. Their slow hopping via these strong sites reduces the diffusion coefficient. This assumption is supported by the observation that the range of deviation of the data obtained

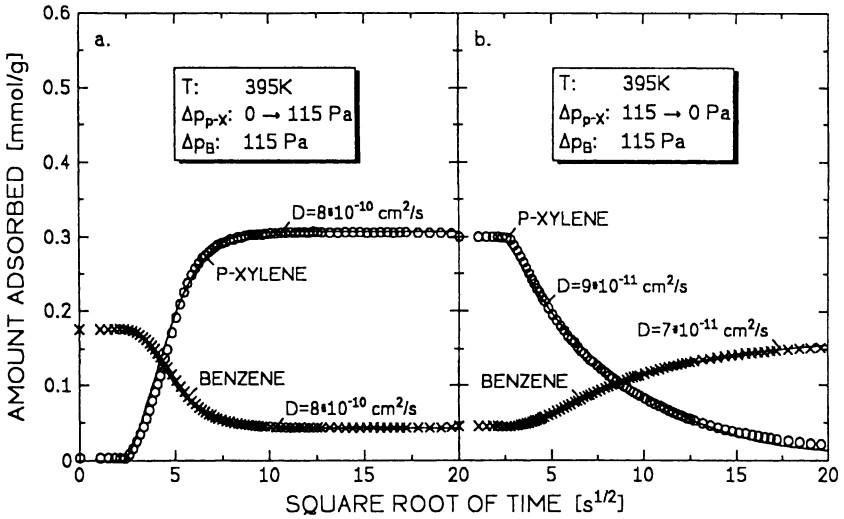

Fig. 29 Counter-diffusion of *p*-xylene versus benzene in H-ZSM-5. Amount adsorbed from a gas mixture in adsorption (**a**) and desorption (**b**) experiments with *p*-xylene as a function of the square root of time

by desorption could be very much reduced when smaller jumps of decreasing pressures were chosen, for instance 115 → 57.5 Pa, 57.5 → 28.5 Pa, and 28.5 → 0 Pa. Then, the reduced diffusivities were observed only for the very last jump, indicating that only a small fraction of strong sites were operative. Note that the differences in the data of the first adsorption and last desorption steps were almost absent when the sample was cleaned by purging with helium after a first run and the adsorption/desorption cycle was repeated in a second run. A similar effect was observed when the sample activated in a flow of pure helium was first contacted at the adsorption temperature, T_{ad}, with a helium stream containing a small sorbate partial pressure (e.g., upon a pressure jump Δp_i: 0 → 1.15 Pa for 0.5 min), which was followed by purging again with pure helium. In such cases, the very strong adsorption sites were already occupied prior to the first pressure jump to start the adsorption/desorption cycle.

Analogous counter-diffusion experiments were also performed with the sorbate pairs benzene vs ethylbenzene and ethylbenzene vs benzene (see [22, 23, 34]).

2.2.4.3 Counter-Diffusion of *n*-Hexane vs Neopentane and Neopentane vs *n*-Hexane by "Micro"-FTIR

Experiments devoted to the phenomena of co- and counter-diffusion using the micro-FTIR technique were basically performed in the same way as

described above for the macro-FTIR method. As a particularly interesting example we have selected the systems *n*-hexane vs neopentane and neopentane vs *n*-hexane, respectively, in H-ZSM-5 [60].

Figure 30 demonstrates that the IR features of *n*-hexane and neopentane are sufficiently different to monitor the changes in their absorbances when both components are present in the adsorbent. The respective bands were decomposed by an appropriate computer program. For the determination of the amounts of neopentane, the band of the asymmetric vibration of the methyl group, ν_{as}^{CH3}, at 2960 cm^{-1} and for that of *n*-hexane the band of the asymmetric vibrations of the CH_2 group at 2930 cm^{-1} were used.

As can be recognized from Fig. 31, the adsorbent single crystal was, after activation at 675 K, preloaded with neopentane (at 475 K and under a partial pressure of neopentane, $p_{NEOP} \approx 3.1$ mbar). Subsequently, a partial stream of helium loaded with *n*-hexane (3.1 mbar) was injected. The sorbate *n*-hexane replaced the preadsorbed neopentane almost completely; only a few percent neopentane was left inside the zeolite adsorbent.

The reverse experiment showed that neopentane was, under the given conditions, unable to replace any of the preloaded *n*-hexane. Admission of neopentane did not change the steady-state concentration of the preloaded *n*-hexane, but led to an additional uptake of neopentane (see Fig. 32).

It may be tentatively assumed that the interaction of *n*-hexane with the adsorbent H-ZSM-5 is considerably more intense than that of neopentane. Most probably, *n*-hexane possesses a distinctly higher number of centers of possible interaction with the adsorbent. Compared to *n*-hexane, neopentane

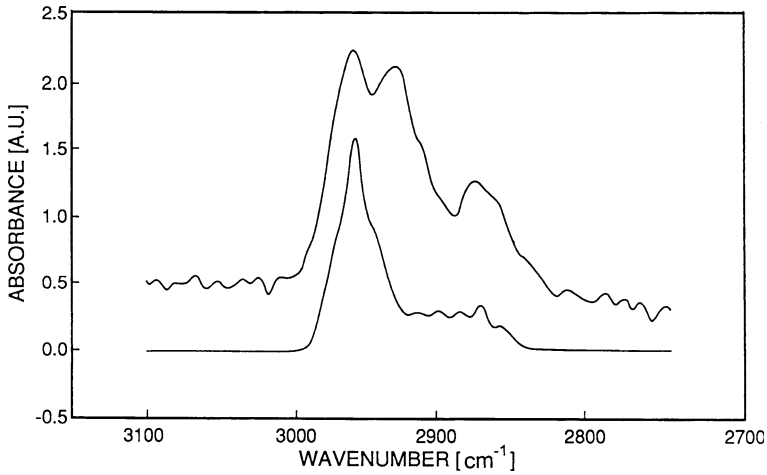

Fig. 30 Difference in the IR absorbance spectra of *n*-hexane (*upper spectrum*) and neopentane (*lower spectrum*) in H-ZSM-5

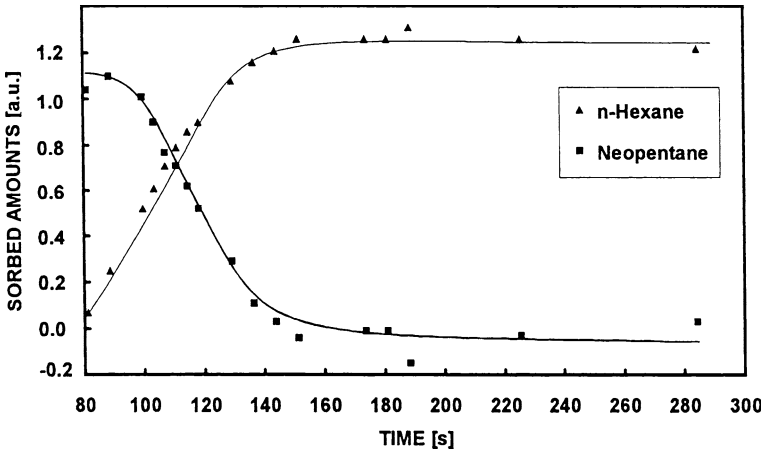

Fig. 31 Counter-diffusion of neopentane (preloaded) versus *n*-hexane (subsequently admitted) in H-ZSM-5

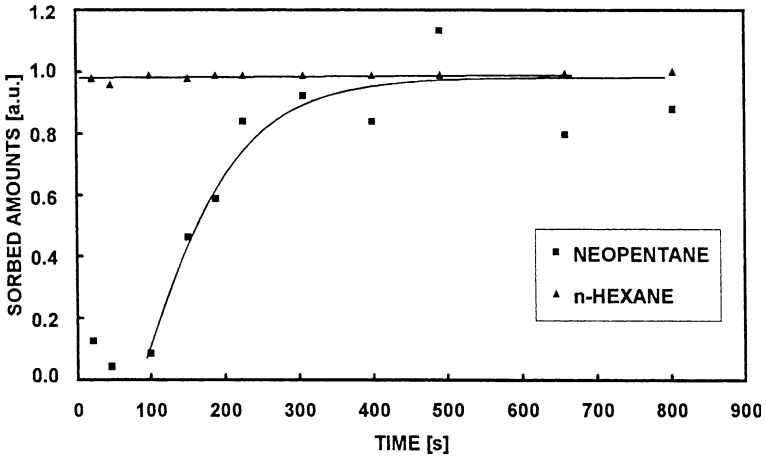

Fig. 32 Counter-diffusion of *n*-hexane (preloaded) versus neopentane (subsequently admitted)

is a spherelike molecule with CH_3 groups in its outer shell with only a few possible contact sites. On the contrary, the shape of a chain of two CH_3 groups and four CH_2 groups provides distinctly more centers for possible contact with sites of the adsorbent, i.e., the H-ZSM-5 zeolite. In this context, it would be certainly very interesting to determine and compare, for instance, the heats of adsorption of both components.

3
Unprecedented Insight by Interference Microscopy

3.1
Experimental

The application of interference techniques to diffusion measurements in liquids was established more than a century ago [61, 62], and first efforts to transfer this measuring principle to zeolites date back to the late 1970s [18, 19]. It was, however, not before the beginning of the new millennium that interference microscopy showed it is going to evolve into a most powerful technique for both diffusion measurement and structural characterization. This progress is in particular based on the synergism resulting from the joint application of interference and IR microscopy [63–65], which has become possible by exploiting the technical progress in interference microscopy [20, 66–68].

Figure 33 illustrates the application of interference microscopy to diffusion studies with nanoporous materials. The technique is based on the analysis of the interference pattern generated by the superposition of two light beams, one passing through the crystal and the other passing through the surrounding atmosphere. Since the optical density depends on the concentration

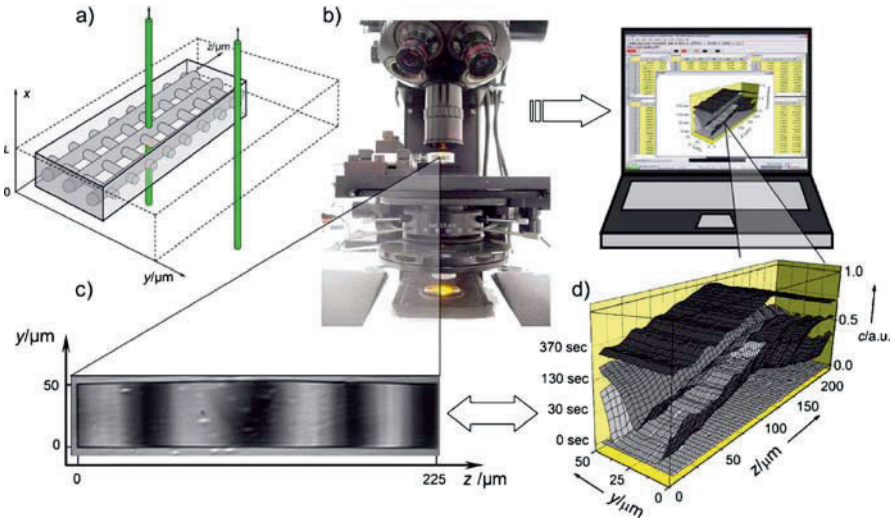

Fig. 33 Schematics of interference microscopy. **a** Two light beams, one passing through the crystal and the other through the surrounding atmosphere. **b** The interference microscope. **c** Interference patterns generated due to different optical properties of the media passed by the two beams. **d** Concentration profiles calculated from the changes in interference patterns with time

of the guest molecules, changes in local concentration appear directly as corresponding changes in the interference pattern (see Fig. 33b,c). It is therefore possible to deduce the concentration profiles (see Fig. 33d) from the measured changes in the interference pattern. The quantity directly accessible is the integral of the concentration through the crystal along the light path (this means the x direction in Fig. 33a) with a spatial resolution of $\Delta y \times \Delta z = 0.5 \times 0.5\ \mu m^2$. If, due to a corresponding blockage of the relevant crystal faces or because of the architecture of the pore system, diffusion in the x direction is prohibited, there will be no variation of concentration in this direction. In this case, interference microscopy yields directly the local concentrations $C(y,z)$. Such a situation occurs for materials with pore systems consisting of arrays of either parallel channels or two-dimensional channel networks (as assumed in Fig. 33a) if one is able to observe perpendicular to the channel axes.

For the measurements, about 100 crystals are placed in an optical vacuum cuvette connected to a vacuum system consisting mainly of a gas reservoir, a pressure sensor, and a turbo-molecular pump. The system allows the sorbate pressure in the cuvette to be changed rapidly (a step change initiating sorbate uptake or release) or to be maintained constant. The concentration integrals are measured of an individual crystal.

The optical cuvette has to be placed within the narrow space given by the optical device. This spatial confinement complicates temperature control. Hence, so far all measurements have been performed at room temperature. Another experimental limitation results from the extremely small size—and, hence, from the extremely small sorbate capacity—of the objects of investigations, namely the individual crystal. Thus, even spurious amounts of contamination within the sorbate supply or on the vessel surface may have a dramatic effect on the crystal under study. As an example, isobutane uptake on single crystals of silicalite-1 has been found to be dramatically retarded by spurious amounts of water molecules [69], which remained completely invisible for a larger assemblage of crystals, even if amounting to not more than a couple of milligrams. The problem is aggravated by the limited thermal stability of the optical cell, which allows in situ sample activation only under rather moderate conditions with temperatures of up to typically 200 °C maximum. It was in particular under these conditions where IR microscopy turned out to be essential for the development of interference microscopy. As extensively illustrated in the previous sections of this chapter, in contrast to interference microscopy, IR spectroscopy is sensitive to the different molecular species. Thus, application of IR spectroscopy under the same experimental conditions reveals the real nature of the guests on the crystal under study during the measurements. In this way, IR microscopy proves to be invaluable for elaborating those experimental conditions in which all corrupting effects by "unwanted" guest molecules may be excluded [63–65, 70–72].

Finally, one has to mention that interference microscopy is only able to record relative changes in sorbate concentration. Hence, the joint application of interference and IR microscopy turns out to be indispensable for the determination of the absolute loadings under which the experiments are performed.

3.2
Probing Zeolite Structures by Diffusion Measurements

3.2.1
Intergrowth Effects in MFI-Type Zeolites

Crystals of MFI-type zeolites are often found to reveal an internal hourglass structure as illustrated by the specimens shown in Fig. 34. By structure analysis, this peculiar behavior has been revealed to be caused by regular intergrowth effects [33, 73, 74]. As a consequence, the individual zeolite "crystals" turn out to be composed of several subunits. Figure 35 displays how these subunits ally to the well-shaped body which thus appears to be a perfect single crystal [73]. After subjecting such crystals to an iodine atmosphere, in [75] the interfaces between the subunits were found to be essentially immediately accommodated by iodine molecules. This most spectacular finding prompted the question whether molecular uptake by MFI-type zeolites may possibly proceed "the other way around", namely along gaplike interfaces directly into the very center of the particles, rather than through the particle's external surface. The particular explosiveness of this conception lies in the option that, like in metals by grain boundary diffusion [76], the rates of molecular uptake would be essentially useless for the exploration of the rate of intracrystalline diffusion. With the clarification of this issue [77], interference

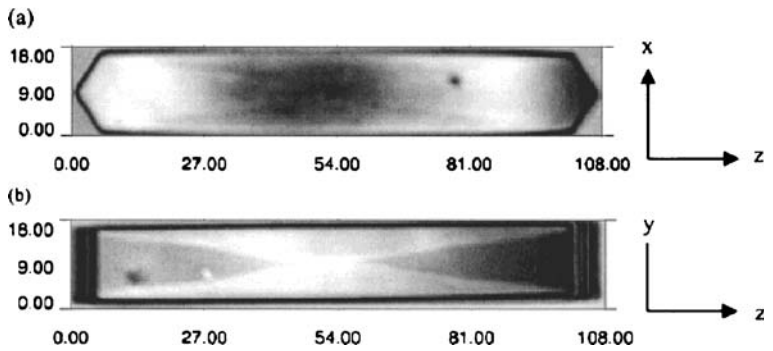

Fig. 34 Microscopic images of a typical silicalite-1 crystal in two different orientations. The hourglass structure is made visible by using the shearing mechanism of the microscope. The length scale in the *x*, *y*, and *z* directions is shown in micrometers

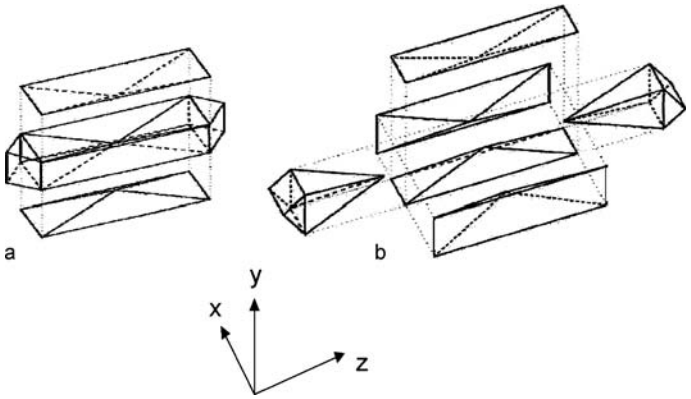

Fig. 35 Schematic representations of the internal structure of silicalite-1 crystals: **a** according to [73–75]; **b** according to [33]

microscopy—in combination with dynamic Monte Carlo simulations—gave a first example of its potential for structural elucidation.

Figure 36 compares the actual measurements of transient concentration profiles during molecular uptake by a silicalite-1 crystal as displayed in Fig. 34 with uptake simulations. The diagrams show the integrals of concentration in the x direction as a function of z (this is in longitudinal extension of the

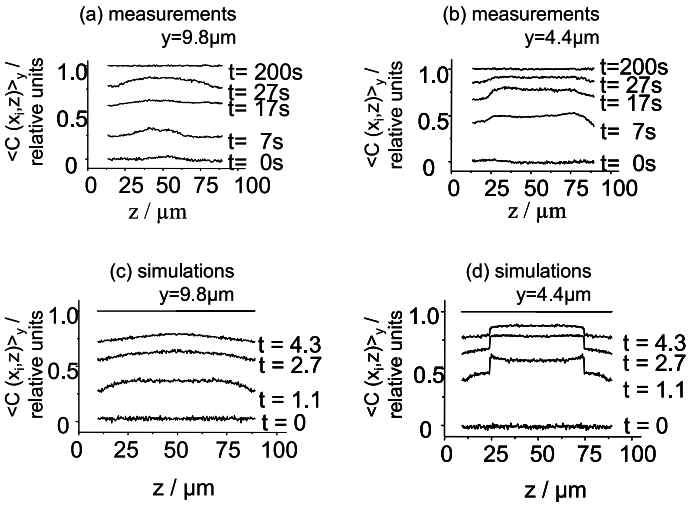

Fig. 36 Intracrystalline concentration profiles of isobutane in silicalite-1 along the z direction during adsorption: **a**,**b** profiles measured by interference microscopy; **c**,**d** simulated profiles, assuming that the internal interfaces serve only as transport barriers. For the simulated profiles the time unit is 10^3 elementary diffusion steps. The equilibrium values of $C(y, z)$ after the end of adsorption are equal to 1

crystal) along the central line ($y = 9.8\ \mu m$) and about half way to the surface plane ($y = 4.4\ \mu m$). The simulations have been performed by assuming either a moderate transport resistance along the interfaces or rapid diffusion so that the interfaces immediately equilibrate with the external gas phase [77]. Comparison with the experimental results (Fig. 36a,b) yields accordance with the behavior expected for moderate transport resistances (Fig. 36c,d), while the option of uptake accelerated by fast diffusion along the interfaces (which would result in internal maxima of concentration) may definitely be ruled out. In contrast to the small iodine atoms which, obviously, are able to slip along the plane of the interfaces, the diffusion of the considered alkane molecules is in no way promoted by the existence of the interfaces. For the specimens under study, these internal interfaces rather exhibit a slight transport resistance.

3.2.2
Intergrowth Effects in AFI-Type Zeolites

AFI-type zeolites consist of parallel channels with diameters of the order of 0.7 nm. Therefore, they have been considered as ideal host systems for the exploration of single-file diffusion (see Chap. 8 of this volume). By the application of interference microscopy, however, representatives of this structure type investigated so far turned out to be far away from a system which might be referred to as a microscopic bundle of "macaronis". As an example, Fig. 37 displays the intracrystalline guest profiles in a CrAPO-5 crystal established in a methanol atmosphere of 1 mbar at equilibrium. It turns out that, within the apparently perfect crystals, there are regions which remain completely inaccessible to the methanol molecules. The resulting model of accessible and inaccessible regions within the crystals is displayed in Fig. 38. It is only the space below the shown semi-pyramid (and, correspondingly, above a symmetric upper semi-pyramid which is omitted for clarity) to which the guest molecules may get. In view of these very puzzling results it was extremely important to support the evidence of interference microscopy by parallel studies using IR microscopy. Figure 39 illustrates the perfect agreement observed in these comparative studies.

Our perspective on the internal pore structure was notably qualified by comparative studies of the water distribution in the above considered CrAPO-5 crystals and in SAPO-5, as another representative of the AFI family [78]. Figure 40 displays the equilibrium distribution of water in crystals of CrAPO-5 (left) and SAPO-5 (right) in a water atmosphere of 1 mbar (top and bottom) and of 20 mbar (middle). The water distribution at 1 mbar has been considered after both adsorption from 0 mbar (top) and desorption from 20 mbar, i.e., from the situation shown in the middle of the figure (bottom). We note the following important results:

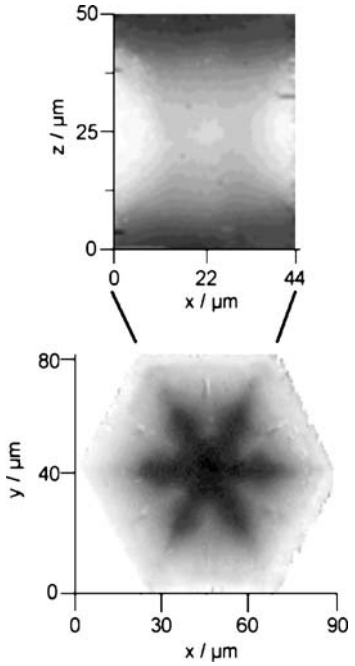

Fig. 37 profile of methanol inEquilibrium intracrystalline concentration profile of methanol in a CrAPO-5 crystal. The color intensity is proportional to the integrals of local concentration in the *y* direction (**a**) and *z* direction (**b**). *Darker regions* correspond to larger concentration integrals. *x*, *y*, and *z* are the crystallographic directions (the channel direction is *z*)

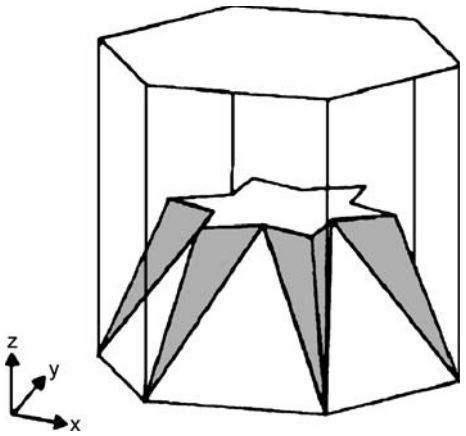

Fig. 38 Suggested internal structure of CrAPO-5 crystals (shown only for the lower part of the crystal). *x*, *y*, and *z* are the crystallographic directions

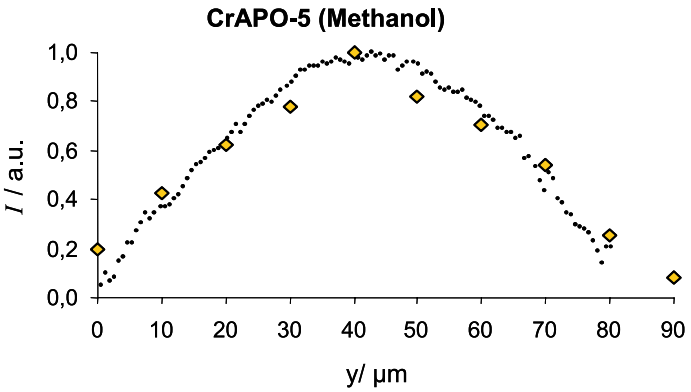

Fig. 39 The mean concentration integrals I recorded by FTIR (*diamonds*) and interference microscopy (*points*) along the y direction for x values between 35 and 55 µm; x, y, and z are the crystallographic directions

(i) Within the limits of accuracy, the representations on the top and bottom agree with each other. This indicates that there is no history dependence (hysteresis) in the sorption behavior.
(ii) The results obtained with CrAPO-5 at the smaller water pressure nicely reflect the behavior observed with methanol (Figs. 37–39). The water distribution is found to resemble the observed methanol distribution, namely with a reduction of guest concentration close to the external faces toward the central plane. The fact that these observations are not as distinct as the situation shown in Fig. 37, with the clear model suggestion given by Fig. 38, may be easily referred to the smaller size of the guest molecules.
(iii) This supposition is confirmed by the observation that, at a sufficiently high gas pressure, the water molecules are obviously "forced" to be accommodated in the total internal pore space.
(iv) SAPO-5 (right side of Fig. 40) reflects the exactly opposite behavior, i.e., a preferential population of the central part of the crystal, before—at sufficiently high gas-phase pressures—again the guest molecules are essentially homogeneously distributed over the crystal.

The evidence of interference microscopy nicely correlates with the models of crystallization, which in the case of SAPO-5 favor a pencil-like crystallization core [79, 80], while in CrAPO-5 crystallization proceeds via the formation of dumbbell-shaped structures [81, 82]. In no case could a nanoporous material with the desired structure of microscopic, ideal macaronis be identified. The appearing dramatic deviation from an ideal channel structure excludes the application of simple model assumptions for interpretation of the time evolution of the concentration profiles. In fact, in [83] the experimentally monitored concentration profiles during

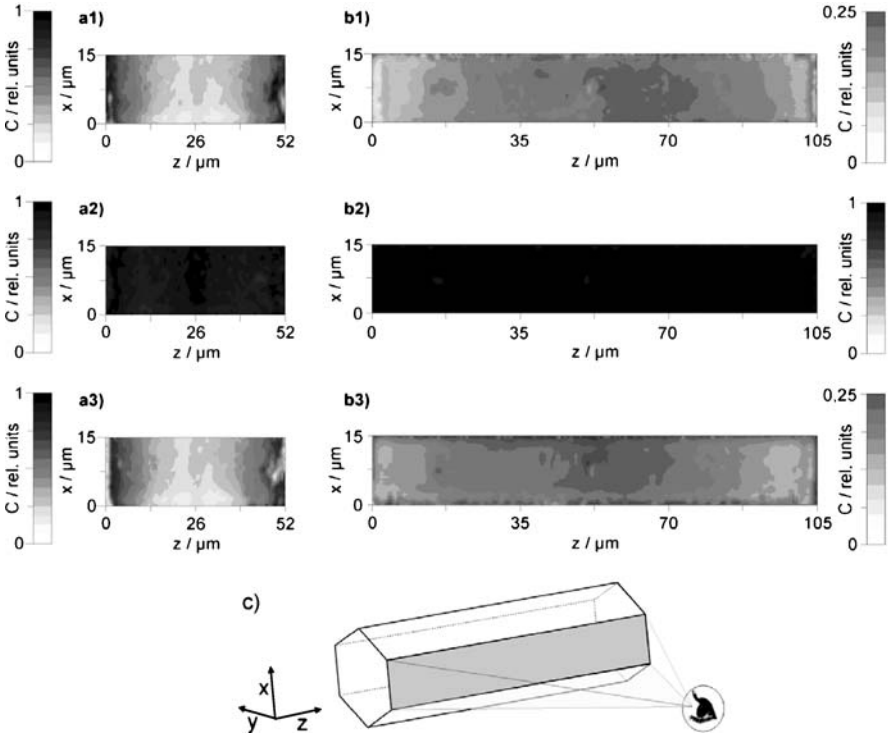

Fig. 40 Intracrystalline concentration profiles of water in CrAPO-5 (**a**1–3) and SAPO-5 (**b**1–3) crystals integrated along the *y* direction under equilibrium with water vapor at 1 mbar (**a**1, **b**1, **a**3, **b**3) and 20 mbar (**a**2, **b**2). The profiles under the pressure of 1 mbar were recorded after the change of the water pressure from 0 to 1 mbar (**a**1, **b**1) and from 20 to 1 mbar (**a**3, **b**3). The profiles are shown for only the crystal surface marked in **c**. The channels run along the *z* axis. *Darker regions* correspond to higher concentration integrals

molecular uptake of methanol on a CrAPO-5 crystal are shown to nicely follow the shape expected for diffusion-limited uptake by an ensemble of channels of varying length. However, the observation time in the experiment is found to progressively retard behind the simulation time. Though this tendency might be referred to an increasing mutual hindrance of the diffusants with increasing concentration, there is no further option for more detailed insights into the microdynamics of these systems. Considering further systems, it will be shown in the following that such insight has meanwhile also become accessible, in some cases even for zeolite specimens with apparently much more complicated pore structures.

3.3 Microscopic Measurement of Transport Diffusion and Permeation Through Transport Resistances on the Crystal Surface

The most appropriate conditions for observing mass transfer phenomena in nanoporous materials are provided for one-dimensional diffusion. Obviously, any deviation from one-dimensional diffusion complicates the handling of the associated equations. This concerns their rigorous analysis, numerical solutions, and dynamic simulations. It has already been mentioned (Sect. 3.1) that, from the experimental point of view, diffusion in one or two dimensions allows the direct measurement of the local concentration (rather than only of the concentration integral in observation direction). For one-dimensional diffusion, invariance of the concentration profiles in the direction perpendicular to diffusion facilitates analysis. Correspondingly, we are going to start our treatise in Sect. 3.3.1 by presenting diffusion results for a one-dimensional system, namely for manganese formate, a representative of the MOF family of nanoporous materials with a one-dimensional channel system. The second system under study, ferrierite, contains a two-dimensional channel network. It is found, however, that—due to a blockage of the entrances to one set of channels—molecular uptake and release proceeds essentially via one-dimensional diffusion (Sect. 3.3.2). Finally, Sect. 3.3.3 presents an algorithm which, under the conditions of three-dimensional diffusion, allows the transformation of the experimentally accessible integral concentrations $\int C(x,y,z)\mathrm{d}x$ into the genuine local concentration $C(x,y,z)$.

If we abandon the very unlikely case of anisotropic diffusion with principal tensor axes which are not perpendicular to the crystal faces normal, molecular fluxes may quite generally be assumed to be directed perpendicular to the crystal surfaces. Hence, molecular uptake and release may be considered to proceed via one-dimensional diffusion quite generally, as long as the fluxes stemming from different crystal faces do not superimpose upon each other. This includes in particular the initial phases of uptake and release. We shall see that due to this reason, by measuring surface permeabilities, interference microscopy is in general able to quantify the intensity of surface resistances.

3.3.1 Methanol in MOF Manganese Formate

Figure 41 illustrates the system under study and the coordinates of measurement, showing the SEM image of a typical $Mn(HCO_2)_2$ crystal (a) [84, 85], a scheme of the one-dimensional channel structure along the y direction (b), and the crystal under study with its extensions, the axes denomination, and the plane along which the concentration profiles have been recorded (c) (observation in z direction, plane extension in y direction, $x = 41\ \mu\mathrm{m}$). Figure 42a provides an impression of the transient concentration profiles measured dur-

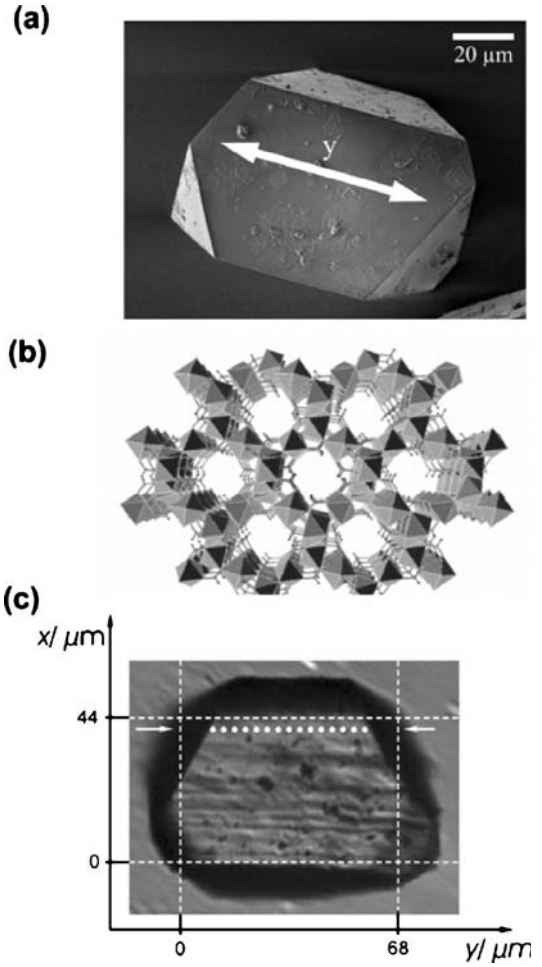

Fig. 41 SEM image of a typical $Mn(HCO_2)_2$ crystal with indicated y axis (**a**), scheme of the one-dimensional channel structure of $Mn(HCO_2)_2$ along the y axis [91] (**b**), and crystal part (*white dots* at $x = 41\ \mu m$) in which the profiles shown in Fig. 42b have been measured (**c**)

ing the uptake of methanol by an activated $Mn(HCO_2)_2$ crystal [86]. A detailed analysis has been performed along the plane $x = 41\ \mu m$. The corresponding profiles are shown in Fig. 42b. Knowledge of the evolution of the intracrystalline concentration profiles allows a microscopic application of Fick's second law [87]

$$\frac{\partial C}{\partial t} = \frac{\partial}{\partial y}\left(D\frac{\partial C}{\partial y}\right) = D\frac{\partial^2 C}{\partial y^2} + \frac{\partial D}{\partial C}\left(\frac{\partial C}{\partial y}\right)^2 . \tag{6}$$

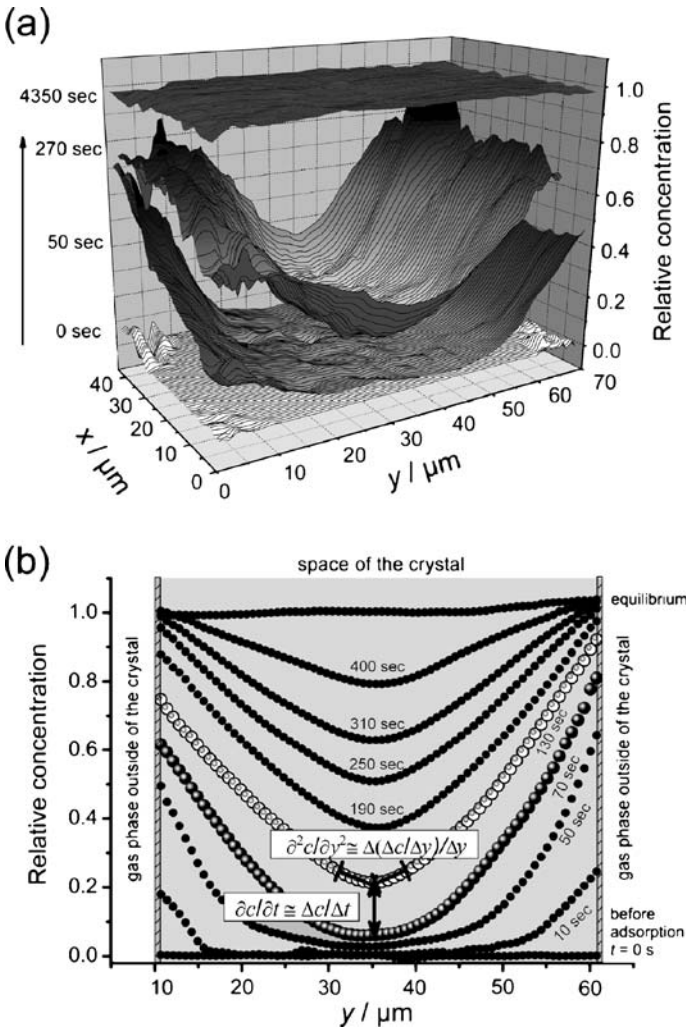

Fig. 42 Evolution of the two-dimensional concentration profiles (**a**) and of the one-dimensional concentration profiles in the y direction ($x = 41$ µm) (**b**) of methanol in the MOF crystal for a pressure step from 0 to 10 mbar. The method of evaluating the terms $\partial^2 C/\partial y^2$ and $\partial C/\partial t$ is also indicated

The present equations relate to nonequilibrium phenomena with the diffusivity D referred to as the coefficient of transport diffusion. Following Fick's first law, it is defined as the factor of proportionality between the particle flux, i.e., a phenomenon of genuine mass transport, and the concentration gradient. Note that this definition does not imply any assumption on the concentration dependence of D (which, as we still shall see, may most significantly depend on the concentration) [87]. This dependence has to be taken

into account by the second term on the right-hand side of Eq. 6. One may get rid of this second term by simply considering the evolution of the center of the concentration curves, since here $\partial C/\partial t$ is equal to zero. It is this range of the profiles which provides direct access to the transport diffusivity via the relation

$$D = \frac{\partial C/\partial t}{\partial^2 C/\partial y^2}\,, \tag{7}$$

with $\partial C/\partial t$ and $\partial^2 C/\partial y^2$ directly following from the experimental data, as illustrated by the inserts to Fig. 42b. Figure 43 displays the resulting diffusivities.

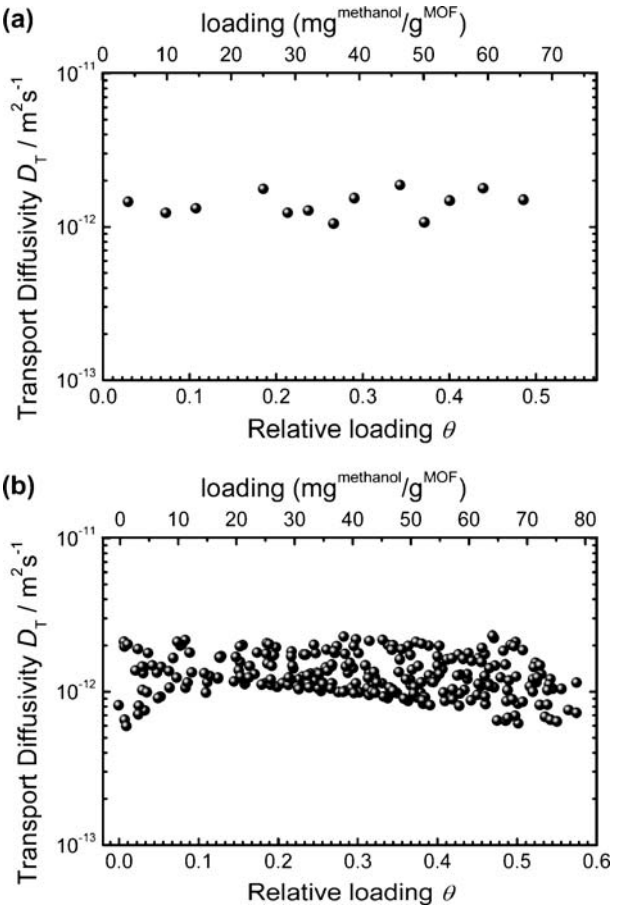

Fig. 43 Concentration dependence of the transport diffusivity as determined from the center (**a**) and from the entire profile (**b**)

The surface permeability α is defined as the factor of proportionality between the particle flux through the surface, j, and the difference $C_{eq} - C_{surf}(t)$ between the intracrystalline concentration established in equilibrium with the surrounding atmosphere and the actual concentration in the layer close to the crystal surface

$$j = \alpha \left(C_{eq} - C_{surf}(t) \right) \ . \tag{8}$$

The flux j results from the uptake per time following the relation

$$j = \frac{1}{2A}\frac{dm}{dt} = \frac{1}{2}\frac{d\left(\int_{-l}^{l} C(y)dy\right)}{dt} \tag{9}$$

where $m(t)$ denotes the total uptake by the entire crystal at time t, l is the half length of the crystal extension in the channel direction, and A stands for the area of the crystal fase perpendicular to the channels.

Combination of Eqs. 8 and 9 yields the permeability data plotted in Fig. 44. Figure 45 provides a comparison between the experimental data (those of Fig. 42b, without smoothing) and a numerical fit with $D = 1.5 \times 10^{-12}$ m^2 s^{-1} as resulting from Fig. 43a and a variable surface permeability α. The best agreement between the numerical solution and the experimental data as dis-

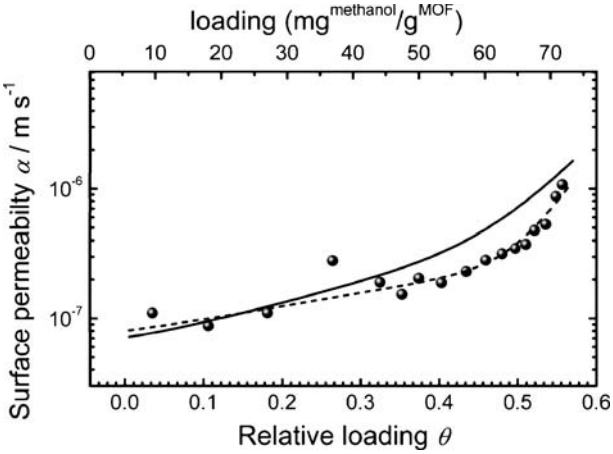

Fig. 44 Surface permeability of the MOF-type crystal under study during methanol uptake as a function of the boundary concentration (mean value during the considered time step) via Eqs. 7 and 8, with the boundary concentration $C_{surf}(t)$ taken from the margins of the measured concentrations. The polynomial fit to these data is given by the *broken line*. The *full line* shows the dependence of the permeability on concentration, which leads to the best fit of the recalculated concentration profiles to the experimental ones (Fig. 45)

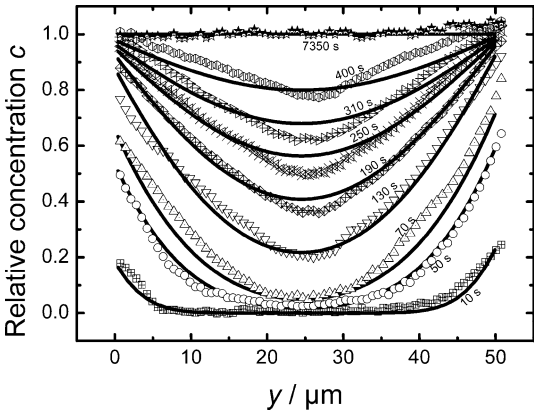

Fig. 45 Comparison of the transient concentration profiles during methanol uptake by the MOF-type crystal as recorded by interference microscopy (*symbols*) with the corresponding profiles recalculated from the measured diffusivities with surface permeabilities (*full line* in Fig. 44) which lead to the best fit to the experimental points

played in Fig. 45 is obtained with surface permeabilities given by the straight line in Fig. 44.

3.3.2 Methanol in Ferrierite

As schematically shown by Fig. 46a, ferrierite contains two mutually intersecting arrays of channels. In comparison with the strictly one-dimensional MOF crystals considered in the previous section, their analysis is additionally complicated by the existence of two rooflike parts on either side of the platelike main crystal body. It turned out, however, that these features did in no way complicate the method of analysis. Contrary to the MOFs, which required an additional activation step after each uptake experiment, methanol in ferrierite proved to be an ideal host–guest system, where one and the same crystal could alternately be subjected to adsorption and desorption without any perceptible change in the sorbate profiles. It were these special conditions under which interference microscopy could be developed to a technique of diffusion measurement in nanoporous materials of unprecedented power [63, 65, 70, 71, 88, 89].

Figure 46b and c provide an overview of the observed evolution of the molecular concentration (integrated in the x direction) during molecular uptake, namely the evolution over the total y–z plane (c) as well as, for clarity, selected profiles in the z direction (b) and y direction (d) [88, 90]. These latter two sets of profiles help us to understand that the time dependence of the observed integral concentrations may be easily explained by assuming a two-stage process, namely a first fast one during which the rooflike

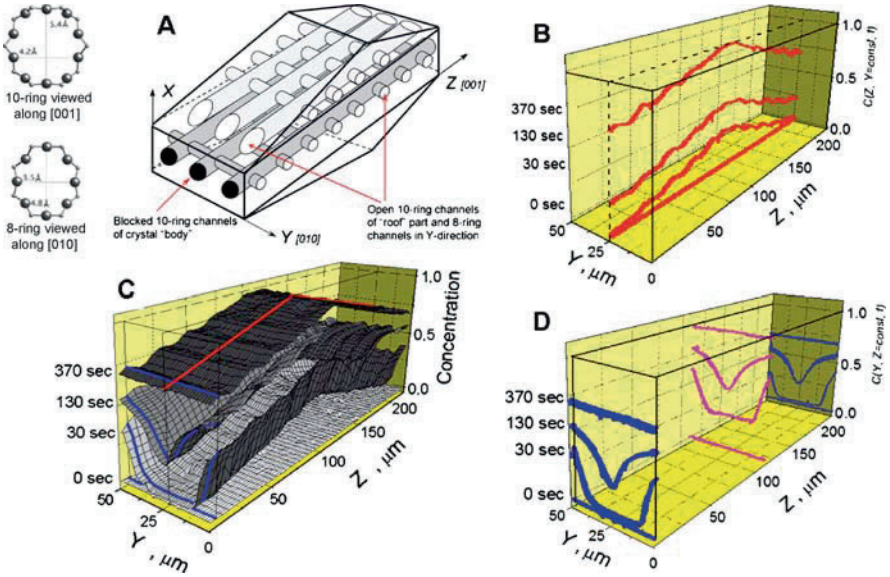

Fig. 46 Evolution of concentration profiles of methanol in a ferrierite crystal for a pressure step of $0 \rightarrow 80$ mbar. **a** Shape and 2-D pore structure of the ferrierite crystal; **b** concentration profiles in the z direction at $y = 25$ µm; **c** 2-D concentration profiles in the entire crystal; and **d** concentration profiles in the y direction at the center ($z = 120$ µm) and two locations close to the edges of the crystal. Relative concentration 1.0 corresponds to the ferrierite equilibrium loading by methanol at 80 mbar

parts on the top and bottom of the main crystal body essentially immediately accommodate the guest molecules, and a second one during which, eventually, the main body is filled. This course has to be referred to the different boundary conditions at the orifices of the larger ("ten-membered-ring") channels: while, obviously, in the rooflike parts they are easily accessible, molecular entrance along these channels is largely obstructed in the crystal main body. As a consequence, the observed profiles (Fig. 46d) essentially reflect the evolution of the guest concentration due to diffusion along the smaller ("eight-membered-ring") channels. The contribution provided by the (fast) uptake along the larger channels in the rooflike parts immediately appears in the short-time profiles displayed in Fig. 46b and may thus be easily subtracted from the overall value. The thus corrected concentration profiles have been analyzed [70, 88] following the procedure described in Sect. 3.3.1. Figure 47 displays the resulting transport diffusivity (in the small-channel direction, this means in the y direction) as a function of the loading [70]. Again we could benefit from a synergetic application of interference and IR microscopy, with the latter allowing us an estimate of the absolute intracrystalline concentrations. We note that now, in striking contrast to the behavior described in Sect. 3.3.2 for methanol in manganese formate, the transport

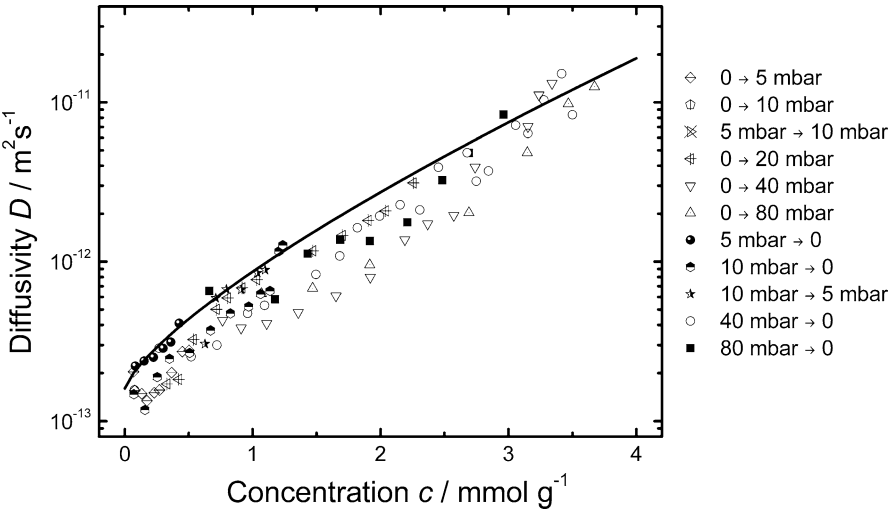

Fig. 47 Transport diffusivity in the *y* direction as a function of concentration obtained from the center of the crystal from different experiments. The *full line* represents the dependence used for calculating the concentration profiles in Fig. 48

diffusivity increases with increasing loading by almost two orders of magnitude. We take it as another example indicating that there is no general rule which, without reference to specific microdynamic models, might be able to predict the loading dependence of transport coefficients, including surface permeabilities and the self- and transport diffusivities. Close inspection of the concentration profiles resulting from the solution of Fick's law with the measured transport diffusivities and surface permeabilities revealed a systematic deviation from the data of measurement. This difference could be referred to the fact that, obviously, the access to the ten-ring channels in the *z* direction is not completely blocked. Allowing for appropriately chosen permeabilities and assuming a fast distribution of the entering molecules within these larger channels was shown to lead to good agreement with the measured data [69]. This is exemplified with the sets of transient concentration profiles during uptake (left) and release (right) in Fig. 48.

The height of the pressure step increases from top to bottom. Obviously, in this sequence the profiles during adsorption and desorption lose their

Fig. 48 Comparison of simulated and experimental profiles for pressure steps 0 to 5 mbar (**a**), 5 to 0 mbar (**b**), 0 to 10 mbar (**c**), 10 to 0 mbar (**d**), 0 to 40 mbar (**e**), 40 to 0 mbar (**f**), 0 to 80 mbar (**g**), and 80 to 0 mbar (**h**). The *points* refer to experimental measurements. The *lines* are simulated from the 2-D finite difference solution with the same concentration dependence of transport diffusivities as determined from Fig. 47 (*full line*) and the surface permeabilities determined from the use of Eqs. 7 and 8. For the simulations it is implied that $D_z \gg D_y$ ►

complementarity. This finding corresponds to the observed increase in diffusivity (and permeability) with increasing loading, which is also reflected by a progressive enhancement of the adsorption rates in comparison to the

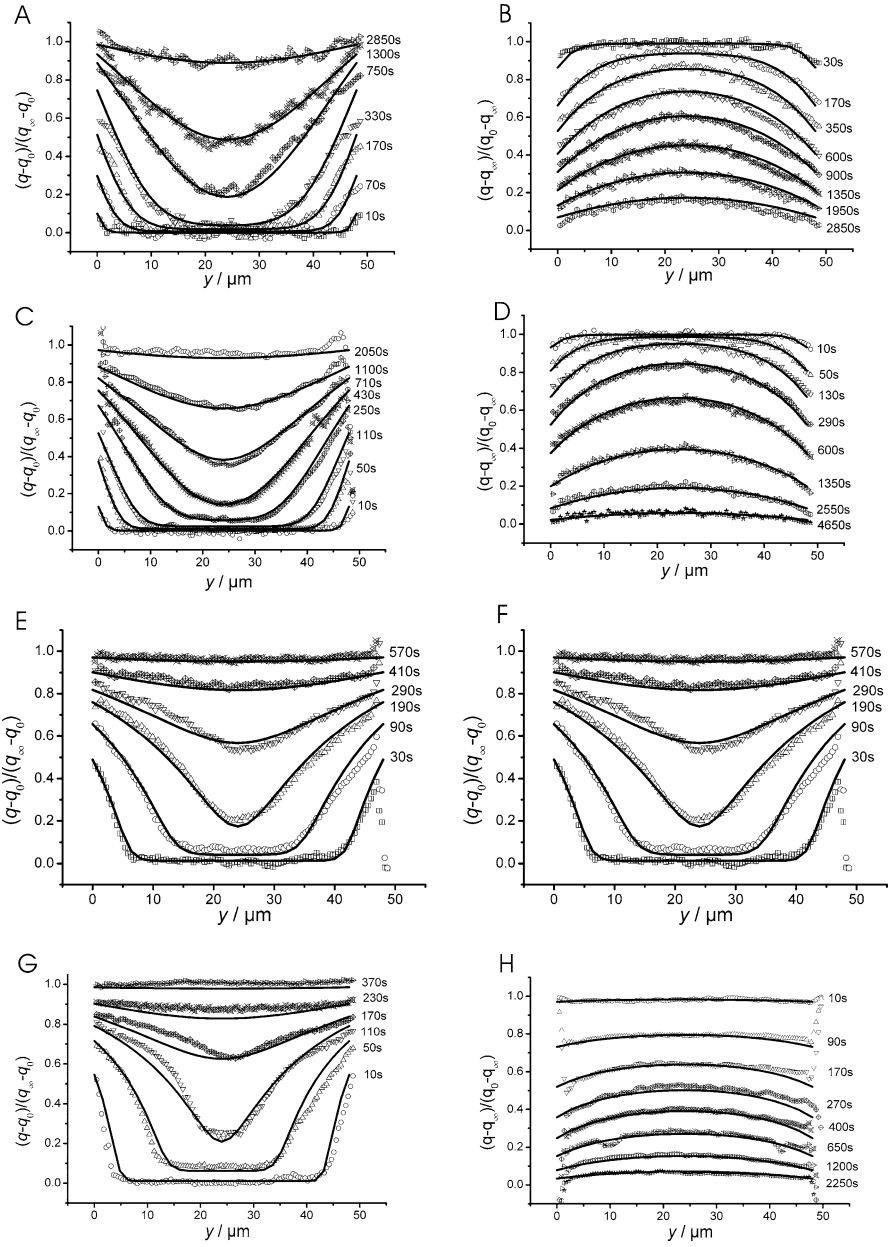

desorption rates. This behavior could again be nicely corroborated by IR monitoring of uptake and release by the individual crystals [63].

With the meaningful title "Sorption kinetics and intracrystalline diffusion of methanol in ferrierite: an example of disguised kinetics", [71] exemplifies the pitfalls which, in cases like the given one, will necessarily lead the researcher to completely wrong conclusions if he is only able to base his reasoning on the overall uptake and release rather than on the processes of intracrystalline mass transfer.

3.3.3 Three-Dimensional Diffusion in SAPO STA-7

The pore structure of SAPO STA-7 includes two types of cages, labeled A and B in Fig. 49 [3, 91]. The A and B cage types differ in shape and size with A being smaller than B. Connectivity along the crystallographic z direction in STA-7 is via two parallel paths, with the faster one between the B cages. Along x and y directions there is only one diffusion path, which is between the A and B cages. Intracrystalline diffusion has to be governed, therefore, by a diffusion tensor of rotational symmetry, with the symmetry axes in the z direction.

As an example of the primary data during methanol uptake, Fig. 50 displays a two-dimensional (a) and one-dimensional (b) presentation of the evolution of the integrals of concentration profiles over planes through the crystal center [92]. These presentations nicely reflect the expected symmetry with respect to the x and y axes. By softly knocking against the cuvette, the crystal under study may be turned around 90°, so that now the concentration profiles after integration in the x or y direction also become accessible to direct observation. Conventional techniques of X-ray computed tomography are able to convert such integrals into their "kernels", namely into the

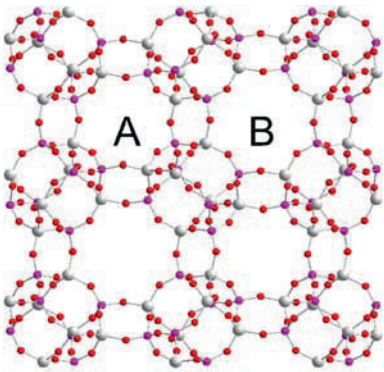

Fig. 49 STA-7 structure along the z direction with labeled cages A and B. The A–A window size is 0.32 nm and the B–B size is 0.41 nm. The window size between A and B is 0.35 nm

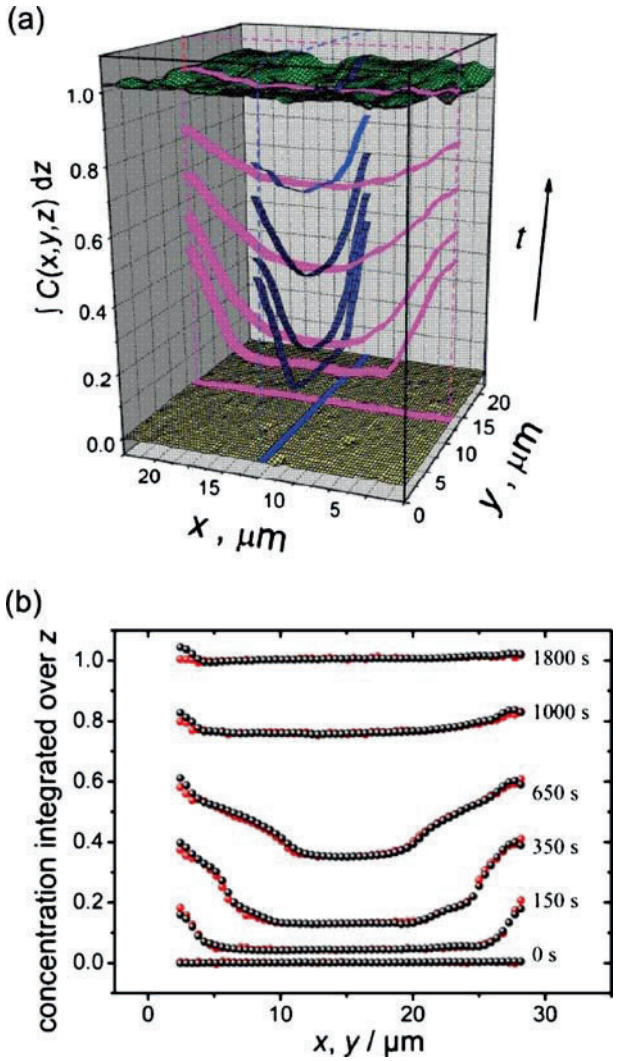

Fig. 50 Concentration profiles integrated over the z direction observed by interference microscopy during a methanol pressure step from 0 to 1 mbar. **a** Two-dimensional and **b** one-dimensional profiles in the crystal center along the x (*fair spheres*) and y (*black spheres*) directions. The times after onset of adsorption are indicated in **b**

desired concentrations, by considering a sufficiently large spectrum of orientations [93]. In the given case, the limitation in the directions of integration prohibits this access. The option of comparison with the expectation from Fick's second law, however, may be shown to provide a second, successful route for deducing the genuine intracrystalline concentrations from the

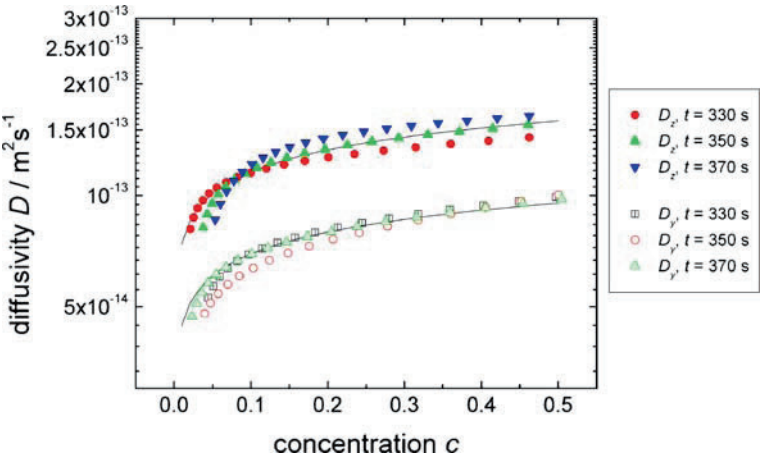

Fig. 51 Transport diffusivity calculated from the profiles in the y and z directions [92]. Analyzed concentration profiles are at 330, 350, and 370 s, where the concentration fronts propagating from opposite faces have not yet overlapped. The *thin lines* represent the analytical dependence of the diffusivities which yields excellent agreement with the measured concentration integrals (standard deviation $\sigma = 0.006$)

measured concentration integrals [92]. From an analysis of the thus attainable complete space and time dependence $C(x,y,z,t)$ of the intracrystalline concentration one is able to determine both the principal values $D_x = D_y$ and D_z of the diffusion tensor and the relevant surface permeabilities [92].

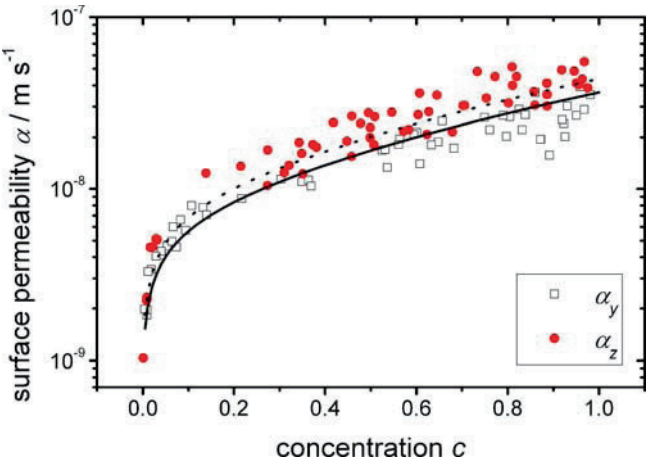

Fig. 52 Surface permeabilities determined from the calculated concentration profiles. The *solid line* (α_y) and the *dotted line* (α_z) represent the analytical dependence of the surface permeabilities which yields excellent agreement with the measured concentration integrals (standard deviation $\sigma = 0.006$)

These data are displayed in Figs. 51 and 52. The transport diffusivity in the z direction is approximately twice as large as that in the x or y direction. This correlates nicely with the difference in the critical sizes of the windows on the diffusion paths in the different directions. It is interesting to note that also the surface permeability in the z direction slightly (by about 20%) exceeds that in the x and y directions.

3.3.4
Textbook-like Sorption Behavior in Silicalite-1

In all the transient concentration profiles considered so far (Figs. 36, 42, 45, 46, 48, and 50), in no case did the boundary concentration immediately assume the equilibrium value. The consequences of this finding on the relation between the transport resistances exerted by the intracrystalline bulk phase and by the crystal surface on the overall uptake and release behavior will be

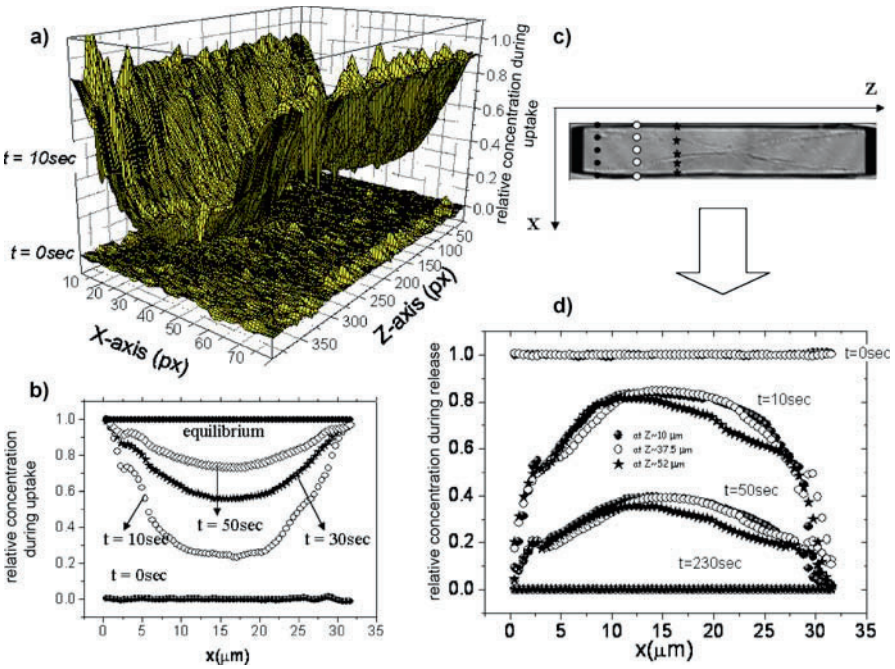

Fig. 53 Transient profiles of 2-methylpropane as a guest molecule in a nanoporous material (crystal of type silicalite-1). **a** Overview of the intracrystalline concentration profile 10 s after the onset of adsorption. **b** Evolution of the guest profiles along the x axis at $z \sim 10\,\mu m$ during uptake. **c** Host crystal with indication of the cross section to which the transient concentration profiles in **d** refer. **e** Evolution of the guest profiles along the x axis during release over different cross sections as indicated by **c**

discussed in Sect. 3.4.3. Here, we will provide an example where molecular uptake and release are in fact close to those patterns which one expects for diffusion-limited uptake [94].

The zeolite specimen of type silicalite-1 has been synthesized as specified in [95]. Prior to calcination, the silicalite-1 crystals used were exposed to fresh aqueous sodium hydroxide solution for one day.

Figure 53 displays, as an example, the transient intracrystalline concentration (integrated in the y direction) during the uptake of isobutane, showing the total profile in the x–z plane 10 s after the onset of the adsorption of isobutane (a) and the evolution of the profile at $z = 10$ μm at subsequent intervals of time (b), as well as the corresponding profiles during desorption (d), now comparing the evolution over different cross sections as indicated in (c). Both Fig. 53a and d indicate that, along the longitudinal extension of the crystal, there are no substantial differences in the sorption behavior. Most importantly, immediately after the onset of adsorption or desorption, the boundary concentrations are found to essentially coincide with the equilibrium data. With these measurements one has to abandon speculations about the ubiquity of surface barriers as a general feature of nanoporous materials.

3.4 The Novel Options of Data Analysis

The novel options of interference microscopy gave rise to the development and introduction of analytical tools which can be very helpful for a better understanding of the different phenomena of mass transfer in nanoporous materials. This will be illustrated by three examples. In Sect. 3.4.1 we will demonstrate that, owing to the potentials of interference microscopy, today also in diffusion studies with nanoporous host–guest systems we may benefit from Boltzmann's ingenious method to derive diffusivities from simply the shape of transient concentration profiles. This technique is particularly helpful for concentration-dependent diffusivities which exclude an analytical solution of the diffusion equation (Eq. 6). In Sect. 3.4.2 it will be shown that, simultaneously with the determination of surface resistances, interference microscopy also allows the direct measurement of the sticking factor, which means of the probability that a molecule encountering the external crystal surface will be able to continue its trajectory into the crystal interior. Finally, Sect. 3.4.3 will describe how the accessibility of transient intracrystalline concentration profiles allows a straightforward quantification of the relevance of transport resistances on the crystal surface for the overall rate of molecular uptake and release.

3.4.1 Analyzing Intracrystalline Concentration Profiles via Boltzmann's Integration Method

The application of Fick's second law (Eq. 6) to the assessment of molecular uptake or release becomes particularly simple if one may imply the following boundary and initial conditions:

$$C(0,t) = C_\infty \tag{10}$$

$$C(y,0) = C(\infty,t) = C_0\,. \tag{11}$$

Equation 6 together with Eqs. 10 and 11 describe a process of one-dimensional diffusion, initiated by a change in the surrounding atmosphere so that the corresponding equilibrium concentration varies from C_0 to C_∞. Equation 10 requires that immediately after the pressure step, the concentration at the boundary (namely for $y = 0$) assumes the new equilibrium value. This means that the existence of additional transport resistances at the surface of the system is excluded. The second term in Eq. 11 indicates that the process has to proceed as in a semi-infinite medium. This means in particular that the transient adsorption or desorption profiles originating from different crystal faces must not yet have met each other.

Under these conditions, by introducing the new variable $\eta = y/\sqrt{t}$, the partial differential equation, Eq. 6, may be transferred into

$$\frac{\mathrm{d}^2C}{\mathrm{d}\eta^2} + \frac{\eta}{2D}\frac{\mathrm{d}C}{\mathrm{d}\eta} + \frac{\mathrm{d}D/\mathrm{d}C}{D}\left(\frac{\mathrm{d}C}{\mathrm{d}\eta}\right)^2 = 0\,, \tag{12}$$

where the concentration now appears as a function of the sole variable $\eta = y/\sqrt{t}$. The initial and boundary conditions of Eq. 6, namely Eqs. 10 and 11, are now transferred into

$$C(\eta = 0) = C_\infty \tag{13}$$

$$C(\eta = \infty) = C_0\,. \tag{14}$$

Plotting the concentration profiles $C(y,t)$ as a function of this new parameter, i.e., as $C\left(\eta = y/\sqrt{t}\right)$, for different times t should therefore yield coinciding representations. Equation 12 cannot be integrated either. However, being interested only in the concentration dependence $D(C)$ of the diffusivity as the key quantity of our study, following Boltzmann [96, 97] we may rewrite Eq. 12 as

$$\frac{\mathrm{d}}{\mathrm{d}\eta}\left(D\frac{\mathrm{d}C}{\mathrm{d}\eta}\right) = -\frac{\eta}{2}\frac{\mathrm{d}C}{\mathrm{d}\eta}\,. \tag{15}$$

Integration over η from ∞ to $\eta(C)$, with $(\mathrm{d}C)/(\mathrm{d}\eta) = 0$ for $\eta = \infty$, yields

$$D(C) = -\frac{1}{2}\frac{\mathrm{d}\eta}{\mathrm{d}C}\int_{c=0}^{c}\eta \mathrm{d}c\,. \tag{16}$$

Figure 54 illustrates the way by which Eq. 16 allows the determination of the complete concentration dependence of the diffusivity from a single transient sorption profile [98].

The presented data refer to methanol uptake in ferrierite. We have described in Sect. 3.3.2 that the main uptake occurred along the small eight-ring channels, i.e., in the y direction. In addition, however, a small fraction of molecules was also able to enter through the margins of the ten-ring channels. Their contribution may be easily determined from the concentration increase in the middle of the eight-ring channels. Subtraction of this contribution leads to the plots shown in Fig. 54 [98]. In addition to the fact that the resulting boundary concentration remains invariant, it also appears that over the considered intervals of time, the sorption fronts from different sides are well separated from each other. Thus, the two main requirements for the application of Boltzmann's integration method, namely Eqs. 13 and 14, are fulfilled. It turns out that the sorbate profiles presented as a function of the sole variable $\eta = y/\sqrt{t}$ do not coincide for different times t, as is required for the rigorous application of Boltzmann's integration method. One has to have in mind, however, that the time invariance of the boundary condition in Fig. 54 was ensured by subtracting the influence of the uptake introduced by a second, perpendicular channel system, rather than by immediate equilibration with the surrounding atmosphere. It is demonstrated in [99] that the approximations

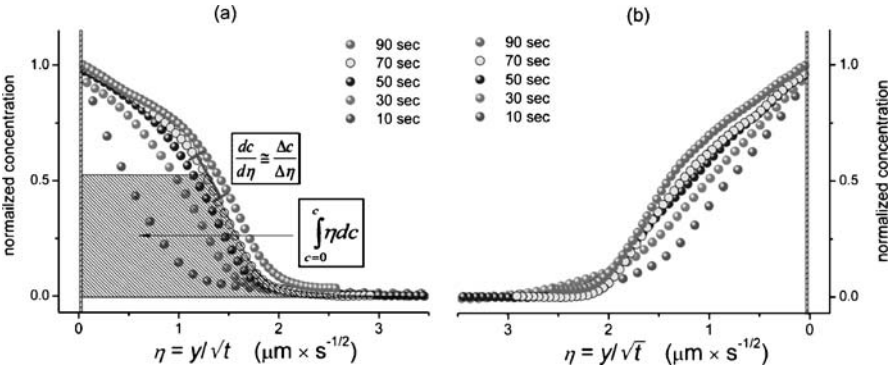

Fig. 54 Evolution of the concentration profiles in the y direction in the left (**a**) and right (**b**) sides of the ferrierite crystal as a function of the parameter $\eta = y/\sqrt{t}$; **a** also illustrates the way of determining $\int_{c=0}^{c} \eta\,\mathrm{d}c$ and $\frac{\mathrm{d}c}{\mathrm{d}\eta}$ yielding via Eq. 16 the diffusivity

leading to the data plots of Fig. 54 lead to an uncertainty in the diffusivities following the Boltzmann method of not more than a factor of 2. The Boltzmann method is thus found to be a powerful technique for the analysis of evolving adsorption and desorption fronts. The diffusivity data presented in Fig. 51 have been obtained by means of Boltzmann's integration method [37].

3.4.2 Sticking Probability

Let us now change our position and look at the surface of the nanoporous host system from the atmosphere [100]. Let us, in particular, follow the collision rate of the guest molecules with the external surface and the probability with which these molecules are able to propagate into the internal pore system. From elementary gas kinetics, the number of gas-phase molecules colliding with a plane surface is well known to be [101–103]

$$j_{os} = \frac{1}{\sqrt{2\pi}} N_A \frac{1}{\sqrt{RTM}} p \,, \tag{17}$$

with N_A, R, T, M, and p denoting, respectively, the Avogadro and gas constants, the absolute temperature, the molecular weight, and the gas pressure.

The flux density of molecules getting from the outer atmosphere into the pore space (j_{in}), on the other hand, may be easily noted on the basis of Eq. 8. The flux density j as considered in Eq. 8 results from the net effect of the fluxes entering and leaving the pore space, i.e.,

$$j = j_{in} - j_{out} \,. \tag{18}$$

The flux density out of the pore system, j_{out}, results from Eq. 8 for the case of total absence of an external atmosphere, i.e., for vanishing external pressure and hence for $C_{eq} = 0$, yielding

$$j_{out} = \alpha \cdot C_{surf} \,. \tag{19}$$

Since, under equilibrium conditions, $C_{surf} = C_{eq}$ and $j = 0$, combination of Eqs. 18 and 19 yields

$$j_{in} = \alpha \cdot C_{eq} \,. \tag{20}$$

Thus, with the ratio j_{in}/j_{os} directly following from Eqs. 17 and 20, the "sticking probability", i.e., the probability that a molecule, after having encountered the outer crystal surface, is going to continue its trajectory in the intracrystalline pore space, has become accessible by direct experimental determination. For the systems considered in Sects. 3.3.2 and 3.3.4 under the conditions of the reported experiments, i.e., for molecular uptake of isobutane by silicalite-1 at a pressure of 1 mbar and of methanol by ferrierite at a pressure of 10 mbar, it results to be 0.01 and 6×10^{-6}, respectively. Thus, it

turns out that for isobutane on silicalite-1 a notable fraction of at least 1% of the molecules colliding with the surface will continue their trajectory into the interior of the nanoporous material, while for ferrierite only a fraction of about 6×10^{-4}% of methanol molecules encountering the entrance plane to the ferrierite crystal in the *y* direction are allowed to enter [100].

Thus, direct experimental evidence is found to confirm the option that the sticking probabilities of guest molecules by nanoporous materials may cover several orders of magnitude between close to one and very small values, following the predictions of macroscopic analysis [102, 103].

3.4.3
Assessing Surface Resistances from Transient Concentration Profiles

The direct access to transient concentration profiles during molecular uptake and release, as displayed, e.g., in Fig. 48, may be used to plot the actual boundary concentration as a function of the relative uptake at the given instant of time. An example of such a correlation plot is provided by Fig. 55 [104]. It refers to molecular uptake of methanol on ferrierite for a pressure step from zero to 10 mbar as displayed in Fig. 48c. The values of relative uptake as indicated by the abscissa are determined from the total area below the transient concentration profiles. The actual boundary concentrations for each of these profiles are indicated by the associated values on the ordinate. Interestingly, toward its final point for total molecular uptake and equilibrium concentration, the correlation plot is found to approach a straight line. Backward prolongation of this straight line toward the ordinate marks a well-defined intercept which we are going to denoted by *w*.

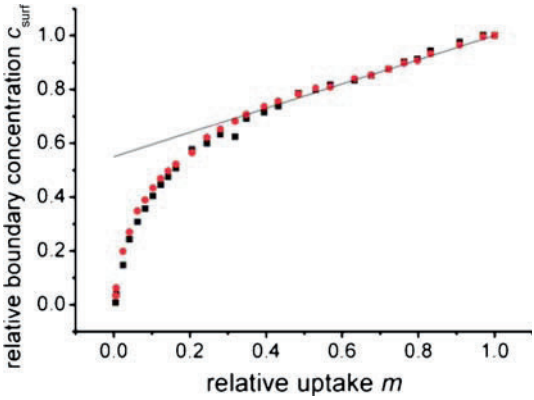

Fig. 55 Correlation between the actual boundary concentration (C_{surf}) and the relative uptake (m) at the corresponding instants of time for methanol uptake by ferrierite for a pressure step from 0 to 10 mbar

In fact, this behavior can be shown to hold quite generally. With the simplifying assumption of constant diffusivities and surface permeabilities, the normalized concentration profiles during molecular uptake by a plate of thickness $2l$ are given by the relation

$$C(y,t) = 1 - \sum_{n=1}^{\infty} \frac{2L\cos(\beta_n y/l)\exp(-\beta_n^2 Dt/l^2)}{(\beta_n^2 + L^2 + L)\cos\beta_n}\,, \tag{21}$$

where the β_n are the positive roots of

$$L = \frac{l\alpha}{D} = \beta_n \tan\beta_n\,. \tag{22}$$

Integration over the system from $-l$ to l yields

$$m(t) = 1 - \sum_{n=1}^{\infty} \frac{2L^2\exp(-\beta_n^2 Dt/l^2)}{(\beta_n^2 + L^2 + L)\beta_n^2}\,, \tag{23}$$

for the relative uptake at time t. In the long-time limit one may confine oneself to only considering the first terms in the sums in Eqs. 21 and 23, which then may be easily combined to give

$$C_{\mathrm{surf}}(t) = C(y = l, t) = 1 - \frac{\beta_1^2}{L} + \frac{\beta_1^2}{L}\cdot m(t)\,. \tag{24}$$

It is thus found that, with $m \to 1$, in fact any function $C_{\mathrm{surf}}(m)$ will approach a straight line, yielding an ordinate intercept

$$w = 1 - \frac{\beta_1^2}{L}\,. \tag{25}$$

Considering a large spectrum of quite different concentration dependences for both the diffusivities and surface permeabilities, such a dependence may be shown to hold quite generally, in excellent agreement with numerous examples of data analysis [105].

Let us discuss the significance of this finding in the context of the examples shown in Fig. 56. They represent the correlation plots calculated analytically for constant diffusivities and permeabilities for ratios $l\alpha/D = 100$, 1, and 0.01, respectively [104]. With the time constants $\tau_{\mathrm{diff}} = l^2/(3D)$ for diffusion-limited uptake and $\tau_{\mathrm{surf}} = l/\alpha$ for uptake limited by transport resistances on the crystal surface [106], the expression $l\alpha/D$ may be identified as a measure of the ratio $\tau_{\mathrm{diff}}/\tau_{\mathrm{surf}}$ between the time constants of uptake or release, brought about exclusively by either diffusion or surface permeation. One may easily rationalize that for prevailing surface resistances (i.e., for small values of $l\alpha/D$), the total amount adsorbed will increase essentially in parallel with the boundary concentration. On the contrary, large surface permeabilities will ensure that, essentially instantaneously with the beginning of molecular uptake, the boundary concentration will attain the

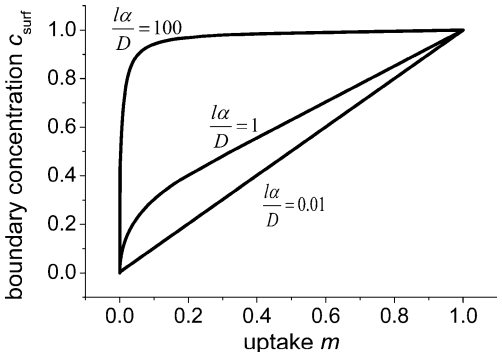

Fig. 56 Correlation between the actual boundary concentration (C_{surf}) and the relative uptake (m) at the corresponding instant of time. Three different cases are shown: the mass transport is essentially limited by intracrystalline diffusion ($l\alpha/D = 100$), by surface barriers ($l\alpha/D = 0.01$), and both by intracrystalline diffusion and surface resistance ($l\alpha/D = 1$)

equilibrium value. This is exactly the behavior reflected by Fig. 56. Moreover, quantitative analysis yields the reciprocal value of the ordinate intercept, w^{-1}, as an estimate of the ratio $\tau_{diff\,+\,surf}/\tau_{diff}$, i.e., the estimate of the factor by which the uptake time (or, quite generally, the time of equilibration) is enhanced by the existence of possibly existing surface barriers. Reference [105] provides numerous examples where this type of analysis is shown to nicely reproduce the results of the corresponding procedure based on a separate determination of intracrystalline diffusivites and surface permeabilities.

4 Concluding Remarks and Outlook

The FTIR technique has proven to be a powerful method for investigating adsorption, desorption, and diffusion of single components or binary mixtures in microporous solids such as zeolites. In the latter case of mixtures, the phenomena of codiffusion and counter-diffusion became accessible to measurement, which was not possible with methods of investigation based on changes of weight, volume, or pressure. Even with the powerful and most important NMR techniques (see Chap. 3 of the present volume), the study of multicomponent (e.g., H_2–D_2) self-diffusion rather than co- and counter-diffusion experiments is possible (see Sect. 1 and [6]). The only prerequisite for the IR method is that the IR spectra, which are contributed by the components of the mixture, can be sufficiently decomposed. This, however, was easily achieved for all systems studied so far, owing to appropriate computer programs nowadays available. Certainly, the computational methods

for decomposition of spectra of different components will be steadily improved. The potential of the method was demonstrated by the study of a number of systems. The good agreement of the results with literature data, as far as available, confirmed the reliability of the FTIR technique, which was also extended to so-called FTIR microscopy, or more precisely micro-FTIR spectroscopy, using a "microscope" (e.g., SpectraTech model IR plan). This enabled the study of sorption and sorption kinetics of light paraffins (*n*-hexane, neopentane, *n*-heptane, *n*-octane, and *n*-nonane) in large H-ZSM-5 crystals or into small powder samples (see Hermann et al. [30–32]). In those studies larger transport diffusivities were also shown to be measurable by the FTIR technique, e.g., 8×10^{-8} cm^2 s^{-1} for *n*-hexane in a $120\,\mu m \times 20\,\mu m \times 20\,\mu m$ crystal of H-ZSM-5, and the activation energy of diffusion was determined to be 15.6 kJ mol^{-1}. The new technique was even successfully employed in measuring the transport of cations into zeolite frameworks on solid-state ion exchange (see Vol. 3, Chap. 2 of the present series, [107]).

Even though the FTIR technique for adsorption and, particularly, diffusion is not a simple one, it is, little by little, being adopted and employed by other researchers as well. Thus, Zhobolenko and Dwyer [108] applied successfully the micro-FTIR technique to determine transport diffusivities of a number of hydrocarbons (benzene, toluene, *p*-xylene, cyclohexane) in large silicalite-1 crystals. The obtained diffusion coefficients were close to data arrived at by Niessen [22], Karge and Niessen [23], Niessen and Karge [24], and Niessen et al. [34].

Also, Roque-Malherbe et al. [109] and Wendelbo and Roque-Malherbe [110] employed FTIR methods like those described above for the investigation of diffusion and counter-diffusion in zeolites. Moreover, Roque-Malherbe and Ivanov [111] studied by FTIR the diffusion and counter-diffusion of xylenes in H-SSZ-24 and H-ZSM-11. These authors studied the kinetics of adsorption and desorption using benzene and *o*-xylene as adsorbates and H-MCM-22, H-ZSM-5, and H-Beta as sorbents.

Finally, the work by Jamis et al. [112, 113] should be mentioned. The FTIR technique was employed in studying the kinetics of uptake of hydrogen cyanide into synthetic zeolites Y, Beta, and mordenite as well as natural clinoptilolite, ferrierite, and stilbite. Tanaka et al. [114, 115] investigated the kinetic processes during adsorption and diffusion of aromatics in medium pore sized zeolites by time-resolved IR spectroscopy. Similarly, Makarova et al. [116] studied the diffusion of *tert*-butanol in zeolite Na,H-ZSM-5 by in situ FTIR kinetic measurements. More recently, Kazansky et al. [117] employed diffuse reflectance spectroscopy (DRIFT) for studying nitrogen sorption and nitrogen–oxygen transport codiffusion and counter-diffusion in, e.g., Na-ZSM-5 zeolites.

A particular advantage of the described FTIR technique for diffusion studies should not be forgotten. Different from most of the methods employed previously, the FTIR technique enables us to conduct measurements very

close to the conditions of catalytic experiments, i.e., a flow reactor cell is used and may be operated at pressures and temperatures applied in laboratory-designed catalytic experiments.

Certainly, the FTIR technique will experience improvement with respect to experimental device and procedure. Especially, it would be desirable to expand the experiment temperature to higher values to avoid immobilization effects such as those encountered with pyridine in H-ZSM-5 or pyridine in H-MOR. The applicability of higher temperatures depends in the first line on an appropriate sealing of the IR transparent windows. Also, the procedure of data evaluation to obtain diffusion coefficients was and still is open for refinement. It is, for instance, not optimum to determine the diffusion coefficients first as independent of coverage and only afterward "correct" them through the Darken equation, the more so as this correction does in fact not entirely eliminate the coverage dependence. Moreover, the fact that the diffusion must basically be described not by a single D value but a tensor of D values had to be considered in the evaluation methods. Here, the introduction of diffusion interference microscopy (DIFM) has brought about considerable progress (see Sect. 3.3.3 and [92]). With respect to the latter technique, application of conditions close to those of realistic processes, e.g., higher temperatures (as with FTIR experiments, vide supra) and application of flow reactor cells, are desirable. Thus, future theoretical and experimental developments will certainly improve the FTIR and DIFM techniques and foster their wider use.

References

1. Baerlocher C, Meier WM, Olson DH (2001) Atlas of framework types, 5th edn. Elsevier, Amsterdam, p 302
2. Castro M, Garcia R, Warrender SJ, Slawin AMZ, Wright PA, Cox PA, Fecant C, Mellot-Dranznieks C, Bats N (2007) Chem Commun 3470
3. Wright PA, Maple MJ, Slawin AMZ, Patinek V, Aitken RA, Welsh S, Cox PA (2000) J Chem Soc Dalton Trans 1243
4. Kärger J, Bülow M (1975) Chem Eng Sci 30:893
5. Kärger JA, Ruthven DM (1992) Diffusion in zeolites and other microporous solids. Wiley, New York, p 270
6. Förste C, Kärger J, Pfeifer H, Riekert L, Bülow M, Zikánová A (1990) J Chem Soc Faraday Trans I 86:881
7. Choudary NV, Jasra RV, Bhat SGT, Prasada Rao TSR (1989) In: Jacobs PA, van Santen RA (eds) Zeolites: facts, figures, future. Proceedings of the 8th international zeolite conference, Amsterdam, July 10–14 1989. Elsevier, Amsterdam, p 867
8. Choudary NV, Jasra RV, Bhat SGT, Prasada Rao TSR (1989) Stud Surf Sci Catal 49B:867
9. Liengme BV, Hall WK (1966) Trans Faraday Soc 3229
10. Karge HG, Klose K (1975) Ber Bunsenges Phys Chem 79:454
11. Karge HG, Weitkamp J (1986) Chem Ing Tech 58:946

12. Schüth F (1992) J Phys Chem 96:7493
13. Schüth F, Althoff R (1993) J Catal 143:338
14. Schüth F, Demuth D, Zibrowius B, Kornatowski J, Finger G (1994) J Am Chem Soc 116:1090
15. Karge HG, Niessen W, Bludau H (1996) Appl Catal A Gen 146:339
16. Arsenova-Härtel N, Bludau H, Schumacher R, Haag WO, Karge HG, Brunner E, Wild U (2000) J Catal 191:326
17. Grenier P, Meunier F, Gray PG (1994) Zeolites 14:242
18. Kärger J, Danz R, Caro J (1978) Feingerätetechnik 27:539
19. Kärger JA, Ruthven DM (1992) Diffusion in zeolites and other microporous solids. Wiley, New York, p 214
20. Schemmert U (2000) Ph.D. Thesis, University of Leipzig
21. Kärger J, Kortunov P, Vasenkov S, Heinke L, Shah DB, Rakoczy RA, Traa Y, Weitkamp J (2006) Angew Chem Int Edit 45:7846
22. Niessen W (1991) Ph.D. Thesis, University of Technology, Berlin
23. Karge HG, Niessen W (1991) Catal Today 8:4
24. Niessen W, Karge HG (1993) Micropor Mater 1:1
25. Karge HG (2005) CR Chim 8:303
26. Bludau H, Karge HG, Niessen W (1998) Micropor Mesopor Mater 22:297
27. Doelle H-J, Riekert L (1977) In: Katzer JR (ed) Proceedings of the 4th international zeolite conference, Chicago. Am Chem Soc, Washington, p 401
28. Doelle H-J, Riekert L (1977) ACS Symp Ser 40:401
29. Thamm H (1987) J Phys Chem 91:8
30. Hermann M, Niessen W, Karge HG (1995) In: Beyer HK, Karge HG, Kiricsi I, Nagy B-J (eds) Catalysis by Microporous Materials. Proceedings of ZEOCAT'95, Szombathely, Hungary, July 9–13 1995. Elsevier, Amsterdam, p 131
31. Hermann M, Niessen W, Karge HG (1995) Stud Surf Sci Catal 94:131
32. Hermann M, Niessen W, Karge HG (1996) In: Le Van MD (ed) Fundamentals of adsorption. Proceedings of the 5th international conference on fundamentals of adsorption, Asilomar, Pacific Grove, May 13–18 1995. Kluwer, Boston, p 377
33. Geus ER, Jansen JC, van Bekkum H (1994) Zeolites 14:82
34. Niessen W, Karge HG, Josefowicz L (1992) In: Suzuki M (ed) Fundamentals of adsorption. Proceedings of the 4th international conference on fundamentals of adsorption, Kyoto, May 17–22 1992. Kodansha, Tokyo, p 475
35. Zikánová A, Bülow M, Schlodder H (1987) Zeolites 7:115
36. Thamm H (1987) J Phys Chem 91:8
37. Shen D, Rees LVC (1992) In: von Ballmoos R, Higgins JB, Treacy MMJ (eds) Proceedings of the 12th International Zeolite Conference, Montreal, July 5–10 1992. Butterworth-Heinemann, Boston, p 45
38. Karge HG, Dondur V, Weitkamp J (1991) J Phys Chem 95:283
39. Crank J (1956) Mathematics of diffusion, chap 6. Oxford University Press, London, p 89
40. Darken LS (1948) Trans Metallurg Soc AIME 175:184
41. Bülow M, Caro J, Röhl-Kühn B, Zibrowius B (1988) In: Karge HG, Weitkamp J (eds) Zeolites as catalysts, sorbents and detergent builders—applications and innovations. Proceedings of the international symposium, Würzburg, 4–8 September 1988. Elsevier, Amsterdam, p 505
42. Bülow M, Caro J, Röhl-Kühn B, Zibrowius B (1988) Stud Surf Sci Catal 46:505
43. Ruthven DM, Eic M, Richard E (1991) Zeolites 11:647
44. Van-Den-Begin N, Rees LVC, Caro J, Bülow M (1989) Zeolites 9:287

45. Schumacher R, Karge HG (1999) J Phys Chem B 103:1479
46. Mirth G, Lercher J (1991) J Phys Chem 95:3736
47. Gründling C, Veefkind VA, Eder-Mirth G, Lercher J (1996) In: Chon H, Ihm S-K, Uh YS (eds) Progress in zeolite and microporous materials. Proceedings of the 11th international zeolite conference, Seoul, 12–17 August 1996. Elsevier, Amsterdam, p 591
48. Gründling C, Veefkind VA, Eder-Mirth G, Lercher J (1996) Stud Surf Sci Catal 105:591
49. Palomares AE, Eder-Mirth G, Rep M, Lercher JA (1998) J Catal 180:56
50. Niessen W, Karge HG (1994) In: Weitkamp J, Karge HG, Pfeifer H, Hölderich W (eds) Zeolites and related microporous materials: state of the art 1994. Garmisch-Partenkirchen, July 17–22 1994. Elsevier, Amsterdam, p 1191
51. Niessen W, Karge HG (1994) Stud Surf Sci Catal 84B:1191
52. Zecchina A, Bordiga S, Spoto G, Marchese L, Petrini G, Leofanti G, Padovan M (1992) J Phys Chem 96:4985
53. Zecchina A, Bordiga S, Spoto G, Marchese L, Petrini G, Leofanti G, Padovan M (1992) J Phys Chem 96:4991
54. Eic M, Ruthven DM (1994) In: Jacobs PA, van Santen RA (eds) Zeolites: facts, figures, future. Proceedings of the 8th international zeolite conference, Amsterdam, July 10–14 1989. Elsevier, Amsterdam, p 897
55. Eic M, Ruthven DM (1994) Stud Surf Sci Catal 49:897
56. Jobic H, Schmidt W, Krause CB, Kärger J (2006) Micropor Mesopor Mater 90:299
57. Timofejew DP (1967) Adsorptionskinetik. VEB Grundstoffindustrie, Leipzig, p 291
58. Kärger J, Bülow M (1975) Chem Eng Sci 30:893
59. Kärger J, Ruthven DM (1992) Diffusion in zeolites and other microporous solids. Wiley, New York, p 270
60. Karge HG (1998) In: Rozwadowski M (ed) Proceedings of the 3rd Polish–German zeolite colloquium, Torun, April 3–5 1997. Nicholas Copernicus University Press, Torun, p 11
61. Gouy GL (1880) Compt Rend 90:307
62. Tyrrell HJV, Harris RK (1984) Diffusion in liquids. Butterworth, London
63. Heinke L, Chmelik C, Kortunov P, Ruthven DM, Shah DB, Vasenkov S, Kärger J (2007) Chem Eng Technol 30:995
64. Lehmann E, Chmelik C, Scheidt H, Vasenkov S, Staudte B, Kärger J, Kremer F, Zadrozna G, Kornatowski J (2002) J Am Chem Soc 124:8690
65. Chmelik C, Kortunov P, Vasenkov S, Kärger J (2005) Adsorption 11:455
66. Beyer H, Schöppe G (1995) Theorie und Praxis der Interferenzmikroskopie. Akademie, Leipzig
67. Schemmert U, Kärger J, Krause C, Rakoczy RA, Weitkamp J (1999) J Europhys Lett 46:204
68. Schemmert U, Kärger J, Weitkamp J (1999) Micropor Mesopor Mater 32:101
69. Tzoulaki D, Schmidt W, Wilczok U, Kärger J (2008) Micropor Mesopor Mater 110:72
70. Kortunov P, Heinke L, Vasenkov S, Chmelik C, Shah DB, Kärger J, Rakoczy RA, Traa Y, Weitkamp J (2006) J Phys Chem B 110:23 821
71. Kortunov P, Chmelik C, Kärger J, Rakoczy RA, Ruthven DM, Traa Y, Vasenkov S, Weitkamp J (2005) Adsorption 11:235
72. Kortunov P, Vasenkov S, Chmelik C, Kärger J, Ruthven DM, Wloch J (2004) Chem Mater 16:3552
73. Caro J, Noack M, Richter-Mendau J, Marlow F, Peterson D, Griepenstrog M, Kornatowksi J (1993) J Phys Chem 97:13 685

74. Weidenthaler C, Fischer RX, Shannon RD, Medenbach O (1994) J Phys Chem 98:12 687
75. Kočirik M, Kornatowski J, Masarik V, Novak P, Zikanova A, Maixner J (1998) Micropor Mesopor Mater 23:295
76. Herzig C, Mishin Y (2005) Grain boundary diffusion in metals. In: Heitjans P, Kärger J (eds) Diffusion in condensed matter: methods, materials, models. Springer, Berlin, p 337
77. Geier O, Vasenkov S, Lehmann E, Kärger J, Schemmert U, Rakoczy RA, Weitkamp J (2001) J Phys Chem B 105:10 217
78. Lehmann E, Vasenkov S, Kärger J, Zadrozna G, Kornatowski J, Weiss Ö, Schüth F (2003) J Phys Chem B 107:4685
79. Jacobs W, Demuth DG, Schunk SA, Schüth F (1997) Micropor Mater 10:95
80. Schunk SA, Demuth DG, Schulz-Dobrick B, Unger KK, Schüth F (1996) Micropor Mater 6:273
81. Klap GJ, van Koningsveld H, Graafsma H, Schreurs AMM (2000) Micropor Mesopor Mater 38:403
82. Klap GJ, Wubbenhorst M, Jansen JC, van Koningsveld H, van Bekkum H, van Turnhout (1999) J Chem Mater 11:3497
83. Lehmann E, Vasenkov S, Kärger J, Zadrozna G, Kornatowski J (2003) J Chem Phys 118:6129
84. Dybtsev DN, Chun H, Yoon SH, Kim D, Kim K (2004) J Am Chem Soc 126:32
85. Arnold M, Kortunov P, Jones DJ, Nedellec Y, Kärger J, Caro J (2007) Eur J Inorg Chem 2007:60
86. Kortunov P, Heinke L, Arnold M, Nedellec Y, Jones DJ, Caro J, Kärger J (2007) J Am Chem Soc 129:8041
87. Kärger J (2007) Leipzig, Einstein, diffusion. Leipziger Universitätsverlag, Leipzig
88. Kärger J, Kortunov P, Vasenkov S, Heinke L, Shah DB, Rakoczy RA, Traa Y, Weitkamp J (2006) J Angew Chem Int Edit 45:7846
89. Heinke L, Kärger J (2008) New J Phys Chem 10:023 035
90. Rakoczy RA, Traa Y, Kortunov P, Vasenkov S, Kärger J, Weitkamp J (2007) Micropor Mesopor Mater 104:1195
91. Castro M, Garcia R, Warrender SJ, Slawin AMZ, Wright PA, Cox PA, Fecant A, Mellot-Dranznieks C, Bats N (2007) Chem Commun 3470
92. Heinke L, Kortunov P, Tzoulaki D, Castro M, Wright PA, Kärger J (2008) Europhys Lett 81:26 002
93. Hounsfield GN (1973) Br J Radiol 46:1016
94. Tzoulaki D, Heinke L, Schmidt W, Wilczok U, Kärger J (2008) Angew Chem Int Ed 47:19
95. Schmidt W, Wilczok U, Weidenthaler C, Medenbach O, Goddard R, Buth G, Cepak A (2007) J Phys Chem B 11:13 538
96. Boltzmann L (1894) Wiedemanns Ann 53:959
97. Jost W (1960) Diffusion in solids, liquids and gases. Academic, New York
98. Kortunov P, Heinke L, Kärger J (2007) Chem Mater 19:3917
99. Heinke L (2007) Diffus Fundam 4:9.1
100. Heinke L, Kortunov P, Tzoulaki D, Kärger J (2007) Phys Rev Lett 99:228 301
101. Evans JW, Abbasi MH, Sarin A (1980) J Chem Phys 72:2967
102. Jentys A, Mukti RR, Lercher JA (2006) J Phys Chem B 110:17 691
103. Simon J-M, Bellat J-B, Vasenkov S, Kärger J (2005) J Phys Chem B 109:13 523
104. Heinke L, Kortunov P, Tzoulaki D, Kärger J (2007) Adsorption 13:215
105. Heinke L (2007) Diffus Fundam 4:12.11

106. Barrer RM (1978) Zeolites and clay minerals as sorbents and molecular sieves. Academic, London
107. Karge HG, Beyer HK (2001) In: Karge HG, Weitkamp J (eds) Molecular sieves—science and technology, vol 3. Springer, Heidelberg, p 43
108. Zhobolenko VL, Dwyer J (1999) In: Treacy MMJ, Markus BK, Bisher ME, Higgins JB (eds) Proceedings of the 12th international zeolite conference, Baltimore, July 5–10 1998. Materials Research Society, Warrendale, p 183
109. Roque-Malherbe R, Wendelbo R, Mifsud A, Corma A (1995) J Phys Chem 99:14 064
110. Wendelbo R, Roque-Malherbe R (1997) Micropor Mater 10:231
111. Roque-Malherbe R, Ivanov V (2001) Micropor Mesopor Mater 47:25
112. Jamis J, Smith TD, Kwak TAP, Dyer A (1994) In: Weitkamp J, Karge HG, Pfeifer H, Hölderich W (eds) Zeolites and related microporous materials: state of the art 1994. Proceedings of the 10th international zeolite conference, Garmisch-Partenkirchen, July 17–22 1994. Elsevier, Amsterdam, p 1261
113. Jamis J, Smith TD, Kwak TAP, Dyer A (1994) Stud Surf Sci Catal 84:1261
114. Tanaka H, Zheng S, Jentys A, Lercher JA (2002) In: Aiello R, Testa F, Giordano G (eds) Impact of zeolites and other porous materials on the new technologies at the beginning of of the new millennium. Proceedings of the 2nd international FEZA (Federation of the European Zeolite Associations) conference, Taormina, Sept 1–5 2002. Elsevier, Amsterdam, p 1619
115. Tanaka H, Zheng S, Jentys A, Lercher JA (2002) Stud Surf Sci Catal 142:1619
116. Makarova MA, Paukstis E, Thomas JM, Williams C, Zamaraev KI (1991) Catal Today 9:61
117. Kazansky VB, Sokolova NA, Bülow M (2004) Micropor Mesopor Mater 67:283

Mol Sieves (2008) 7: 207–233
DOI 10.1007/3829_2007_012
© Springer-Verlag Berlin Heidelberg
Published online: 18 August 2007

Investigation of Diffusion in Molecular Sieves by Neutron Scattering Techniques

H. Jobic

Institut de Recherches sur la Catalyse et l'Environnement de LYON, CNRS, Université de Lyon, UMR5256, 2 avenue Albert Einstein, 69626 Villeurbanne, France
herve.jobic@ircelyon.univ-lyon1.fr

Abstract Neutron scattering was first used to derive the self-diffusivities of hydrocarbons in zeolites, but transport diffusivities of deuterated molecules and of molecules which do not contain hydrogen atoms can now be measured. The technique allows one to probe diffusion over space scales ranging from a few Å to hundreds of Å. The mechanism of diffusion can, thus, be followed from the elementary jumps between adsorption sites to Fickian diffusion. The neutron spin-echo technique pushes down the lower limit of diffusion coefficients, traditionally accessible by neutron methods, by two orders of magnitude. The neutron scattering results indicate that the corrected diffusivity is rarely constant and that it follows neither the Darken approximation nor the lattice gas model. The clear minimum and maximum in diffusivity observed by neutron spin-echo for *n*-alkanes in 5A zeolite is reminiscent of the controversial "window effect".

Keywords Corrected diffusivity · Neutron scattering · Self-diffusivity transport diffusivity · Zeolites

Abbreviations

$A_0(Q)$	Elastic incoherent structure factor, or EISF
$A_\ell(Q)$	Quasi-elastic incoherent structure factors
$AlPO_4$-5	Microporous aluminophosphate zeolite-like structure*
b	Scattering amplitude or scattering length
b_{coh}	Coherent scattering length

b_{inc}	Incoherent scattering length
$b_{\mathrm{inc}}^{\mathrm{H}}$	Incoherent scattering length for the hydrogen atom
barn	unit of the neutron cross-section, in 10^{-28} m^2 atom^{-1}
BS	Back-scattering
CBMC	configurational-bias Monte Carlo
CE	Chudley and Elliott jump diffusion model
d	Jump distance
d_0	Distance between two sites, (Eq. 30)
$\mathrm{d}\sigma/\mathrm{d}\Omega$	Differential scattering cross-section, (Eq. 3)
$\mathrm{d}^2\sigma/\mathrm{d}\Omega\,\mathrm{d}E$	Partial differential scattering cross-section, (Eq. 3)
D	Diffusion coefficient or diffusivity
D_{s}	self-diffusivity
D_{t}	Transport diffusivity
D_{o}	Corrected diffusivity
E_0	Energy of incident neutrons
E_1	Energy of scattered neutrons
EISF	Elastic incoherent structure factor
$G(\boldsymbol{r}, t)$	(Time-dependent) pair-correlation function
$G_{\mathrm{s}}(\boldsymbol{r}, t)$	Self-correlation function
$\hbar$	Planck's constant/2π
HR	Hall and Ross jump diffusion model
HWHM	Half-width at half-maximum
$I(\boldsymbol{Q}, t)$	Intermediate scattering function
j_ℓ	spherical Bessel function of order ℓ
$\boldsymbol{k}$	Neutron wave vector
k	Neutron wave number, or magnitude of $\boldsymbol{k}$
$\boldsymbol{k}_0$	Wave vector of incident neutrons
$\boldsymbol{k}_1$	Wave vector of scattered neutrons
MCM-41	Ordered mesoporous material
MD	Molecular dynamics
N	Number of atoms
Na-Y	Zeolite structure*
Na-X	Zeolite structure*
NEMD	Non-equilibrium molecular dynamics
NSE	Neutron spin-echo
P_ℓ	Legendre polynomial
$p(\boldsymbol{r}, t)$	Probability to find a particle at position $\boldsymbol{r}$ at time t
PFG NMR	Pulsed-field gradient nuclear magnetic resonance
$\boldsymbol{Q}$	scattering vector
QENS	Quasi-elastic neutron scattering
$\boldsymbol{r}$	General position vector of nucleus
r_0	Measure of the delocalization of a molecule on its site, (Eq. 30)
$\boldsymbol{r}_i(t)$	Position vector of the ith nucleus at time t
$\boldsymbol{r}_m$	Position vector of atom m relative to the center of mass
$\langle r^2 \rangle$	Mean-square jump length
$S(\boldsymbol{Q})$	Structure factor
$S(\boldsymbol{Q},\omega)$	Scattering function, or dynamical structure factor
$S_{\mathrm{coh}}(\boldsymbol{Q}, \omega)$	Coherent scattering function
$S_{\mathrm{inc}}(\boldsymbol{Q}, \omega)$	Incoherent scattering function
SS	Singwi and Sjölander jump diffusion model

T	Zeolite structure[1]
TOF	time-of-flight
5A	Zeolite structure[1]
ZSM-5	Zeolite structure[1]
Na-ZSM-5	Zeolite structure[1]

Greek symbols

$\delta(x)$	Dirac delta function
$\delta_{mm'}$	Kronecker delta function
δ_N	Fluctuation in the number of molecules N contained in a given volume
θ	Fractional occupancy
$\theta_{mm'}$	Angle between the Position vectors of atoms m and m'
λ	Neutron wavelength
ρ	Macroscopic number density
$\rho(r,t)$	Microscopic particle density operator
σ	Nucleus cross-section
σ_{coh}	Nucleus coherent cross-section
σ_{inc}	Nucleus incoherent cross-section
τ	Characteristic time of a dynamical process, residence time of a molecule on a given site
φ	Total precession angle
$\hbar\omega$	Neutron energy transfer
Γ	Thermodynamic correction factor
Γ_2	Intermediate component for propane in Na-Y, Fig. 4
$\Delta\omega$	Instrumental energy resolution
$\Delta\omega(Q)$	HWHM of the Lorentzian function for diffusion
Λ_{s}	Lorentzian profile in energy for the self-scattering function
Λ_{t}	Lorentzian profile for the coherent scattering function
$\Lambda_\ell^{\mathrm{rot}}$	Lorentzian functions for rotational diffusion
Ω	Solid angle
$\otimes$	Convolution

1 Introduction

Neutron scattering techniques are increasingly being used to study the structure and dynamics of molecules adsorbed in nanoporous materials. The most prominent example is neutron diffraction, which is complementary to X-ray diffraction to solve structural problems in zeolites and other microporous materials [1]. While the use of powder neutron diffraction is well established in the zeolite community, the spectroscopic applications of neutron scattering are less familiar. However, the constant amelioration of the neutron instrumentation and of the theoretical models provides unprecedented insights into the dynamics of the framework and of adsorbed molecules, at the atomic and

[1] cf. Baerlocher C, Meier WM, Olson DH (2001) Atlas of zeolite framework types, 5th edn, Elsevier Amsterdam, pp 302

molecular level. Using combined instruments, one can cover energy transfers ranging from a few neV to hundreds of meV, corresponding to time scales from about a microsecond to a femtosecond. For a molecular system, this allows one to probe the different motions of translation, rotation, and vibration.

The translational motion of molecules in porous media, i.e., diffusion, can be measured by a large variety of methods. This explains the large number of definitions of diffusion coefficients (or diffusivities) which can be found in the literature [2]. Pulsed-field gradient (PFG) NMR and incoherent quasi-elastic neutron scattering (QENS) measure the self-diffusivity, D_s, at thermodynamic equilibrium. Since hydrogen has the largest neutron incoherent cross-section, the first neutron measurements concerning diffusion in zeolites dealt with hydrogenated molecules. Diffusion in isotropic systems was mainly studied, although theoretical considerations were made on one-dimensional diffusion [3] long before the characteristic profiles could be measured with sufficient accuracy [4]. Until recently, the figure quoted in the literature for the lowest diffusivity accessible by QENS was 10^{-12} m^2 s^{-1}. The use of the neutron spin-echo (NSE) technique allows one to measure diffusivities down to 10^{-14} m^2 s^{-1}, so that the range of diffusivities is now exactly the same as with PFG NMR (in both techniques, there is no upper limit for the diffusivity). The space scale, which can be covered by neutron techniques with ideal zeolite samples, having a perfect crystallinity, can be of tens of nm. However, the available zeolite crystals have usually defects which give a strong intensity at small scattering angles; for this reason the maximum distance which can be probed is about 10 nm. On the other hand, this means that commercial samples, with crystallites of diameter 1 μm or less, can be studied with neutrons.

In separation or catalytic applications, it is the transport diffusivity, D_t, which matters (this quantity is also named Fickian or chemical diffusivity). Transport diffusivities are traditionally obtained under non-equilibrium conditions [2], but they can be measured at equilibrium by coherent QENS [5]. Coherent neutron scattering is in principle more complicated than incoherent scattering, but under certain conditions transport diffusivities can be extracted from the neutron data.

The derivation of D_t from coherent QENS is similar to a computation of D_t from the fluctuations in an equilibrium density distribution. This was accomplished by Tepper and co-workers for Ar in $AlPO_4$-5 [6]. Using the Green–Kubo formalism, they were able to extract this non-equilibrium quantity from just one equilibrium simulation. Moreover, the calculations being performed in reciprocal space, the variation of the diffusivity upon the wave vector was used to check when the system was in the linear regime [6]. The first application of non-equilibrium molecular dynamics (NEMD) to zeolites was performed by Maginn et al. on methane in silicalite [7]. Standard equilibrium MD techniques were later used by Sholl and co-workers to determine the concentration dependence of diffusivities [8].

The space and time scales accessible by the neutron scattering techniques are comparable to the ones covered by molecular simulations so that comparisons between experiment and predictions can be made not only for the diffusivities, but also for the jumps between adsorption sites and for the distribution of adsorbed molecules.

2 Theory

2.1 Scattering Theory, Neutron Cross-Sections

Neutrons interact with nuclei via very short range nuclear forces. A neutron has both particle-like and wave-like properties: it has zero charge, a spin $\frac{1}{2}$, a mass slightly larger than the mass of a proton, and a wavelength λ. Since λ is a scalar, one uses the wave vector $\boldsymbol{k}$ in scattering theory (the magnitude of $\boldsymbol{k}$ is $2\pi/\lambda$).

The wave vector transfer defines the scattering vector $\boldsymbol{Q}$

$$\boldsymbol{Q} = \boldsymbol{k}_0 - \boldsymbol{k}_1 \,, \tag{1}$$

where $\boldsymbol{k}_0$ and $\boldsymbol{k}_1$ are, respectively, the incident and final wave vectors. The momentum which is transferred to the sample is $\hbar\boldsymbol{Q}$. When there is an exchange of energy between the neutron and the sample, the energy transfer is defined as

$$\hbar\omega = E_0 - E_1 \,, \tag{2}$$

where E_0 and E_1 are, respectively, the incident and scattered neutron energies. In elastic scattering, only momentum changes are measured (like in X-ray diffraction). In inelastic scattering, energy transfers are also determined. Unquantified diffusive motions, such as translation, usually occur at small energy transfers, and since they yield a continuous spectrum centered around the elastic peak, this energy range is called quasi-elastic.

In QENS experiments, one measures the double-differential cross-section, $\mathrm{d}^2\sigma/\,\mathrm{d}\Omega\,\mathrm{d}E$, which represents the number of neutrons scattered into the solid angle $\mathrm{d}\Omega$ with energy in the range $\mathrm{d}E$. The amplitude of the scattered wave varies between nuclei (because of different isotopes or spins), so that averages have to be performed for each element. The total cross-section per scatterer is obtained by integrating over energies and solid angles

$$\sigma = \int \mathrm{d}\Omega \frac{\mathrm{d}\sigma}{\mathrm{d}\Omega} = \int \mathrm{d}E \int \mathrm{d}\Omega \frac{\mathrm{d}^2\sigma}{\mathrm{d}\Omega\,\mathrm{d}E} = 4\pi\langle b^2\rangle \,, \tag{3}$$

where b is the scattering length. The scattering cross-section can be split into coherent and incoherent contributions. The coherent elastic scattering has

a phase term in exp(i$\boldsymbol{Q}.\boldsymbol{r}$) and, thus, takes into account interference effects. The coherent scattering cross-section corresponds to an average over all isotopes and spin states

$$\sigma_{\mathrm{coh}} = 4\pi\,|b_{\mathrm{coh}}|^2 = 4\pi\,\langle b\rangle^2\,. \tag{4}$$

The incoherent part, which has no phase relationship, corresponds to the difference between the total and the coherent cross-sections

$$\sigma_{\mathrm{inc}} = 4\pi|b_{\mathrm{inc}}|^2 = 4\pi\left(\langle b^2\rangle - \langle b\rangle^2\right) \tag{5}$$

it, therefore, represents the mean square deviation from the mean potential, which can be due to isotopic or spin effects.

Instead of being scattered, the neutron can be absorbed. In this case, the neutron is captured by the nucleus, with the formation of a compound nucleus, which decays by emitting charged particles or γ-rays.

The relative incoherent and coherent cross-sections of some elements are shown in Fig. 1. The values are measured in barns (1 barn = 10^{-28} m^2), which indicates that the interaction of neutrons with matter is relatively weak. Hydrogen has the largest cross-section (82 barns). Further, this cross-section is essentially incoherent because the non-zero nuclear spin of ^{1}H $\left(\frac{1}{2}\right)$ gives rise to two scattering lengths of opposite sign with a weighted average close

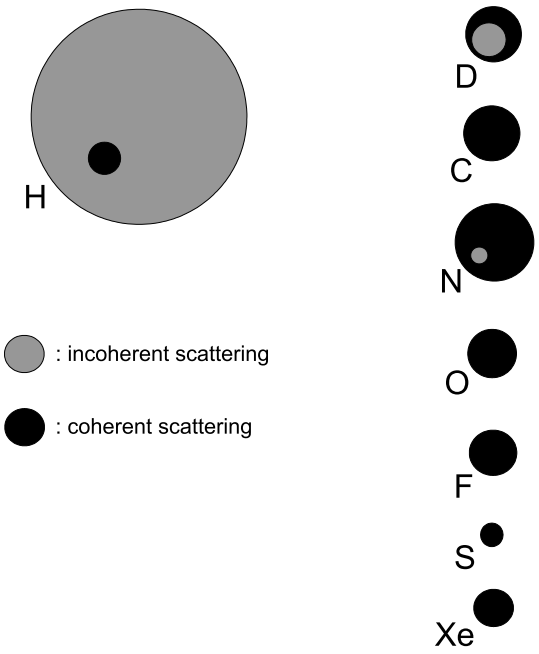

Fig. 1 Neutron scattering cross-sections for some elements and isotopes. The larger the area of the circle, the larger the cross-section

to zero. With incoherent scattering, the motions of individual protons or molecules inside a porous network can be investigated. From the early neutron experiments, self-diffusivities could be obtained and compared with PFG NMR data [9].

More recently, the diffusion of deuterated molecules and of molecules which do not contain hydrogen atoms has been studied. It appears from Fig. 1 that the cross-sections of these elements are about one order of magnitude smaller than hydrogen, which requires high neutron flux sources. At the Institut Laue-Langevin, Grenoble, France, it has been possible to determine the transport diffusivity of molecules such as CO_2, O_2, N_2, CF_4, SF_6, and deuterated alkanes or aromatics. The diffusion of rare gases has also been investigated: natural Ar has a very small cross-section, but ^{36}Ar has a very large coherent cross-section (77.9 barns). Natural Xe has a small coherent cross-section (2.96 barns) and a large absorption cross-section (13.28 barns for $\lambda = 1$ Å), which makes an experiment with a typical neutron wavelength of 6 Å difficult (the absorption cross-section would be ≈80 barns, since it is proportional to λ). However, it might be possible to use one of the various isotopes of Xe, having a coherent cross-section similar to natural Xe, but with a weaker absorption. Deuterium is special in the sense that its coherent and incoherent cross-sections are of the same order of magnitude.

Coherent and isotopic-incoherent scattering involve no spin-flip, whereas spin incoherent scattering (i.e., for hydrogenated molecules) inverts the neutron spin with a probability of 2/3. Since spin-polarized neutrons are used in the neutron spin-echo technique, the polarization of the neutron beam, after spin-incoherent scattering would be reversed and three times less intense.

The measured intensity can be split into coherent and incoherent contributions, as in the case of the scattering cross-sections

$$\frac{\mathrm{d}^2\sigma}{\mathrm{d}\Omega\,\mathrm{d}E} = \frac{k_1}{k_0}\frac{N}{4\pi\hbar}\Big[\sigma_{\mathrm{coh}}S_{\mathrm{coh}}(\boldsymbol{Q},\omega) + \sigma_{\mathrm{inc}}S_{\mathrm{inc}}(\boldsymbol{Q},\omega)\Big]\,, \tag{6}$$

where $S(\boldsymbol{Q},\omega)$ is called the scattering function, or dynamical structure factor. Integrating over energy yields the structure factor $S(\boldsymbol{Q})$. For incoherent scattering, the intensity is smoothly decaying with Q, but for coherent scattering one has a maximum related to the intermolecular distance [5] and the value at $Q = 0$ corresponds to the inverse of the thermodynamic factor (see Sect. 4.1).

For data fitting, it is easier to work with the scattering function than with the double-differential cross-section since there are no experimental parameters. During a normal QENS experiment, one measures in $\boldsymbol{Q}$–ω space motions, which occur in real space and in time. The scattering functions are the four-dimensional Fourier transforms of the van Hove correlation function $G(\boldsymbol{r},t)$ [10].

$$S(\boldsymbol{Q},\omega) = \frac{1}{2\pi}\int \mathrm{d}t\,\exp(-\,\mathrm{i}\omega t)\int \mathrm{d}\boldsymbol{r}\,\exp(\mathrm{i}\boldsymbol{Q}.\boldsymbol{r})G(\boldsymbol{r},t)\,. \tag{7}$$

The incoherent and coherent scattering functions are related to the self- and pair-correlation functions

$$S_{\mathrm{inc}}(\boldsymbol{Q},\omega) = \frac{1}{2\pi}\int \mathrm{d}t \exp(-\mathrm{i}\omega t)\int \mathrm{d}\boldsymbol{r}\exp(\mathrm{i}\boldsymbol{Q}.\boldsymbol{r})G_{\mathrm{s}}(\boldsymbol{r},t) \tag{8a}$$

$$S_{\mathrm{coh}}(\boldsymbol{Q},\omega) = \frac{1}{2\pi}\int \mathrm{d}t \exp(-\mathrm{i}\omega t)\int \mathrm{d}\boldsymbol{r}\exp(\mathrm{i}\boldsymbol{Q}.\boldsymbol{r})G(\boldsymbol{r},t)\,, \tag{8b}$$

where $G_S(\boldsymbol{r},t)$ corresponds to the probability of finding a particle at position $\boldsymbol{r}$ at time t if the *same* particle was at the origin at time zero, whereas $G(\boldsymbol{r},t)$ gives similarly the probability of finding *any* particle (including the same).

$\boldsymbol{Q}$ and ω are the Fourier-transformed variables of $\boldsymbol{r}$ and t. Q has the dimension of a reciprocal distance, and ω of an angular frequency. Therefore, macroscopic quantities will correspond to small Q, i.e., long wavelengths, involving averages over large distances. In analogy, slow diffusivities implying long times in $G(\boldsymbol{r},t)$ will correspond to small ω. Schematic representations of scattering functions are shown in Fig. 2a,b. When the characteristic time, τ, of the dynamical process to be measured is shorter than the inverse of the instrumental resolution, $\Delta\omega$, a broadening of the elastic peak will be observed (Fig. 2b), allowing one to derive a diffusion coefficient from the spectra obtained at various Q values. On the other hand, when τ is larger than $1/\Delta\omega$, the shape is given by the instrumental resolution (Fig. 2a). In this case, the diffusivity cannot be extracted from the measurements, and a higher energy resolution is required to probe longer times.

NSE is another neutron technique from which the Fourier transform of the scattering function, (Eq. 7), is obtained

$$I(\boldsymbol{Q},t) = \int \mathrm{d}\omega \exp(\mathrm{i}\omega t)S(\boldsymbol{Q},\omega)\,. \tag{9}$$

$I(\boldsymbol{Q},t)$ is called the intermediate scattering function since it is defined by

$$I(\boldsymbol{Q},t) = \int \mathrm{d}\boldsymbol{r}\exp(\mathrm{i}\boldsymbol{Q}.\boldsymbol{r})G(\boldsymbol{r},t) \tag{10}$$

so that the scattering function corresponds to

$$S(\boldsymbol{Q},\omega) = \frac{1}{2\pi}\int \mathrm{d}t \exp(-\mathrm{i}\omega t)I(\boldsymbol{Q},t)\,. \tag{11}$$

With the NSE method, data are not recorded as a function of energy transfer, but as a function of time. Elastic and quasi-elastic representations are shown in Fig. 2c,d, respectively. The normalization of $I(\boldsymbol{Q},t)$ is done using $I(\boldsymbol{Q},0)$, which corresponds to the structure factor, $S(\boldsymbol{Q})$

$$I(\boldsymbol{Q},0) = \int \mathrm{d}\omega S(\boldsymbol{Q},\omega) = S(\boldsymbol{Q})\,. \tag{12}$$

The integration over energy transfers in Eq. 12 is not straightforward in traditional QENS experiments, because the measurements are made at constant

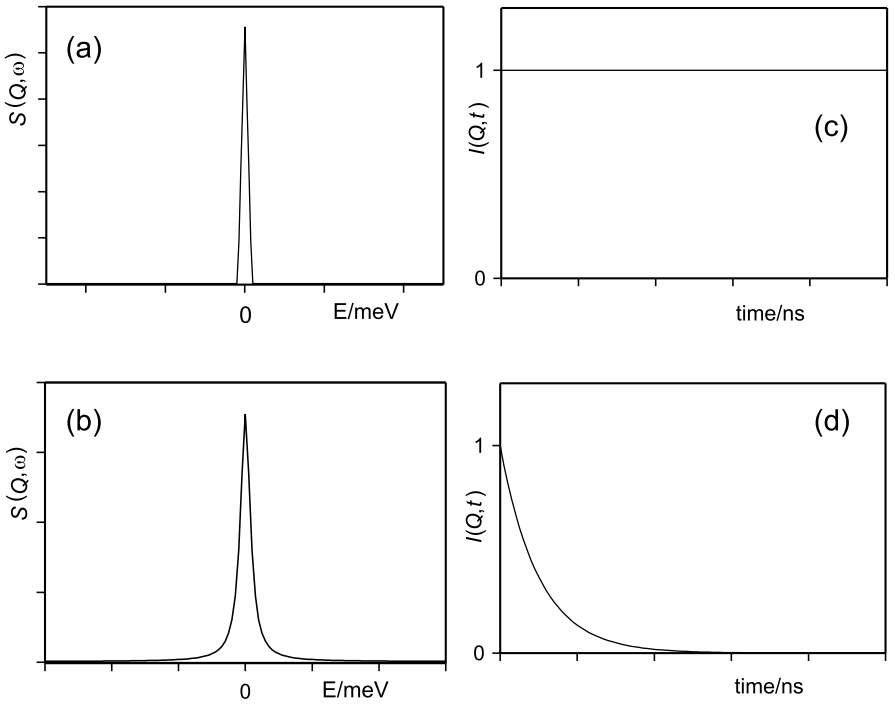

Fig. 2 Schematic representations, for one Q value, of the scattering function, $S(Q,\omega)$, and of the intermediate scattering function, $I(Q,t)$, in the case of **a** and **c**: elastic scattering; **b** and **d**: quasi-elastic scattering

scattering angles and not constant $\boldsymbol{Q}$. On the other hand, the structure factor is directly obtained from NSE experiments.

2.2 Derivation of Self- and Transport Diffusivities

In short, incoherent scattering allows one to determine the self-diffusivity, D_S, whereas coherent scattering gives access to the transport diffusivity, D_t, from experiments performed at equilibrium. When the scattering is both incoherent and coherent, then both diffusivities can in principle be determined simultaneously.

Let us examine first the **incoherent scattering**. For isotropic diffusion, the motion of a given atom (or single molecule) is represented by the diffusion equation (Fick's second law), for long enough times (and distances)

$$\frac{\partial p(\boldsymbol{r},t)}{\partial t} = D_s \nabla^2 p(\boldsymbol{r},t)\,. \tag{13}$$

The self-correlation function, $G_S(\boldsymbol{r}, t)$, is an appropriate solution for $p(\boldsymbol{r}, t)$, the probability to find the atom (or molecule) at position $\boldsymbol{r}$ at time t. If the atom is at the origin at time zero, $G_S(\boldsymbol{r}, 0) = \delta(\boldsymbol{r})$, the self-correlation function is given by the Gaussian expression

$$G_s(\boldsymbol{r}, t) = \frac{1}{(4\pi D_s t)^{3/2}} \exp\left(-\frac{r^2}{4D_s t}\right) . \tag{14}$$

The spectral profiles can then be calculated. As a first step, the spatial Fourier transform in Eq. 8a gives the intermediate self-scattering function

$$I_s(\boldsymbol{Q}, t) = \exp(-D_s Q^2 t) . \tag{15}$$

The incoherent scattering function, (Eq. 8a), is obtained from the time Fourier transform of the intermediate self-scattering function

$$S_{inc}(\boldsymbol{Q}, \omega) = \frac{1}{\pi} \frac{D_s Q^2}{\omega^2 + (D_s Q^2)^2} = \Lambda_s . \tag{16}$$

It is abbreviated by a capital lambda because it corresponds to a Lorentzian profile in energy. Equation 16 corresponds to an isotropic diffusion. Other analytical expressions can be derived for anisotropic diffusion (1-D, 2-D) or for single-file diffusion. The half-width at half-maximum (*HWHM*) of Λ_s is

$$\Delta\omega(Q)_{inc} = D_s Q^2 . \tag{17}$$

It should be noted that the above expressions are only valid at large distances, corresponding to small Q values. Analytical expressions for larger Q values (smaller distances) will be given in the Jump Diffusion Sect. 2.3.

For **coherent scattering**, the scattering function depends on the pair correlation function, $G(\boldsymbol{r}, t)$, as indicated in Eq. 8b. This correlation function can be expressed in terms of the microscopic particle density which specifies the position of a particle by a delta function

$$\rho(\boldsymbol{r}, t) = \sum_i \delta\left[\boldsymbol{r} - \boldsymbol{r}_i(t)\right] . \tag{18}$$

For molecules adsorbed at equilibrium in a zeolite, $G(\boldsymbol{r}, t)$ gives the correlation between the densities at two different positions and different times

$$G(\boldsymbol{r}, t) = \frac{1}{\rho}\left\langle \rho(0, 0)\rho(\boldsymbol{r}, t)\right\rangle , \tag{19}$$

where ρ is the macroscopic number density. This correlation function is, therefore, directly connected with the density fluctuations in the adsorbed phase. The transport diffusivity, D_t, can be obtained from QENS experiments, because one is following the evolution of local concentration gradients around equilibrium.

At low Q values, the coherent scattering function for an isotropic motion has the form [11]

$$S_{\mathrm{coh}}(\boldsymbol{Q},\omega) = \frac{S(Q)}{\pi}\frac{D_{\mathrm{t}}Q^2}{\omega^2 + (D_{\mathrm{t}}Q^2)^2} = S(Q)\Lambda_{\mathrm{t}}\,. \tag{20}$$

The first difference with incoherent scattering is that the intensity varies as $S(Q)$, leaving aside the influence of the Debye–Waller factor. One, therefore, expects a non-monotonic variation of the total intensity as a function of Q. In the small Q domain, the line-shape of the coherent scattering function is still Lorentzian, with a *HWHM*

$$\Delta\omega(Q)_{\mathrm{coh}} = D_{\mathrm{t}}Q^2\,. \tag{21}$$

The **scattering from a molecule** will be more complicated than for a single atom because the other molecular motions of rotation and vibration come into play. If there are no inelastic features in the measured energy transfer range studied, the vibrational term will only affect the measured intensities in the QENS domain through a Debye–Waller factor. On the other hand, the influence of the rotation on the observed profiles has to be treated in more detail. Sears has derived analytical expressions for the total differential cross-section of a molecular system, where the rotational motion is isotropic [12]. From his work, a simplified expression (Eq. 22) for the double-differential cross-section can be obtained; it is split into three terms:

$$\begin{aligned}
&\sum_{m=1}^{n} {b_{\mathrm{inc}}^{m}}^2\, j_0^2(Qr_m)\Lambda_{\mathrm{s}} \\
&+ \left|\sum_{m=1}^{n} b_{\mathrm{coh}}^{m} j_0(Qr_m)\right|^2 S(Q)\Lambda_{\mathrm{t}} \\
&+ \sum_{\ell=1}^{\infty}(2\ell+1)\sum_{m,m'=1}^{n}\left\{b_{\mathrm{coh}}^{m}b_{\mathrm{coh}}^{m'} + {b_{\mathrm{inc}}^{m}}^2\,\delta_{mm'}\right\} \\
&\times j_\ell(Qr_m)j_\ell(Qr_{m'})P_\ell(\cos\Theta_{mm'})\Lambda_{\mathrm{s}}\otimes\Lambda_\ell^{\mathrm{rot}}\,.
\end{aligned} \tag{22}$$

The first term is related to self-diffusion, the second to transport diffusion, and the third to a convolution (symbol $\otimes$) between self-diffusion and the rotational motion, which consists here of a rotational diffusion involving Lorentzian functions, $\Lambda_\ell^{\mathrm{rot}}$.

The symbol j_ℓ corresponds to the spherical Bessel function of order ℓ, $\boldsymbol{r}_m$ denotes the position of the atom m relative to the center of mass (there are n atoms within one molecule), P_ℓ is a Legendre polynomial, $\Theta_{mm'}$ is the angle between $\boldsymbol{r}_m$ and $\boldsymbol{r}_{m'}$, and $\delta_{mm'}$ the Kronecker delta.

If an incoherent scatterer like CH_4 is studied, the second term in Eq. 22 will be zero ($b_{coh} = 0$) and the measured intensity will be proportional to

$$\frac{d^2\sigma}{d\Omega\, dE} \propto 4{b_{inc}^H}^2 \Lambda_s \otimes \left[A_0(Q)\delta(\omega) + \sum_{\ell=1}^{\infty} A_\ell(Q) \Lambda_\ell^{rot} \right], \tag{23}$$

where $A_0(Q)$, the elastic incoherent structure factor (EISF) and $A_\ell(Q)$, the quasi-elastic incoherent structure factors are defined as

$$A_\ell(Q) = (2\ell + 1) j_\ell^2(QR)\,. \tag{24}$$

R is the C – H distance. The Legendre polynomials do not appear in Eq. 23 because $\Theta_{mm'}$ is equal to 0° and, thus, $P_\ell(\cos 0) = 1$.

The elastic ($\ell = 0$) and quasi-elastic incoherent structure factors for the isotropic rotation of methane are shown in Fig. 3. It appears from this figure that only the first three terms of the summation in expression 23 have to be considered in the Q range, which is usually covered by QENS instruments. The self-diffusivity will be obtained by first fitting the QENS spectra with expression 23 and then from the broadening of Λ_s with Q.

For a totally coherent scatterer like CF_4, the first term in expression 22 will be zero ($b_{inc} = 0$) and the number of contributions in the third term will depend on the symmetry of the molecule. The tetrahedral symmetry of CF_4 implies that the sum on the Legendre polynomials is zero for $\ell = 1$ and $\ell = 2$. The sum is non-zero only for $\ell = 3$. This means that in the Q range, which is the most important to extract diffusivities ($Q < 1$ Å^{-1}), the third term in ex-

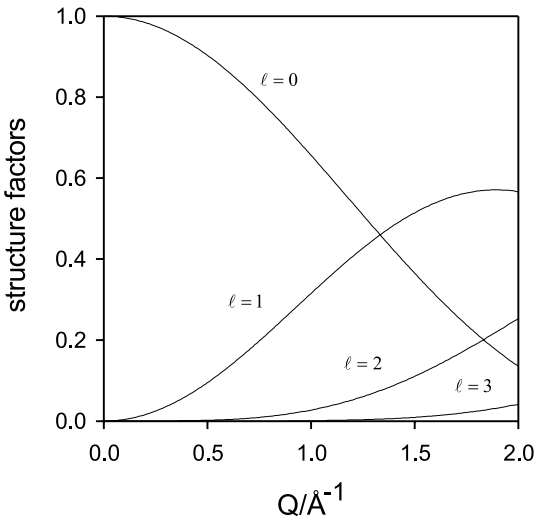

Fig. 3 Elastic ($\ell = 0$) and quasi-elastic ($\ell = 1, 2, 3$) incoherent structure factors for the rotational diffusion of methane ($R = 1.1$ Å)

pression 22 is negligible so that one has only to consider the first term, i.e., a single Lorentzian, in the data interpretation. The conclusion, which is somewhat surprising, is that for a symmetric molecule fitting is easier for a coherent scatterer than for an incoherent one (e.g., CF_4 compared with CH_4).

For a deuterated molecule, the scattering will be both incoherent and coherent, and the three terms in expression 22 may have to be taken into account. At low loadings, the structure factor is of the order of 1, so that the coherent term should dominate.

2.3 Jump Diffusion Models

The expressions derived above, in particular Eqs. 17 and 21, allow one to derive self- or transport diffusivities in a straightforward manner, since the width has a simple DQ^2 law. This Fickian diffusion is only observed at large distances, corresponding to small Q values. Typically, in a molecular liquid, Fickian diffusion is observed for distances larger than 10 Å. For a molecule diffusing in a zeolite, one has to probe translation over a few unit cells (≈ 60 Å). At smaller distances (larger Q values), there is usually a deviation from the linear relation between $\Delta\omega$ and Q^2. This sort of deviation is quite general and is due to the details of the elementary diffusive steps.

The models, which have been developed in the literature, concern essentially incoherent scattering, i.e., self-diffusion. Much less work has been performed on jump diffusion of coherent scatterers [5, 11]. If one considers only isotropic systems, the scattering function will always be a Lorentzian function, but the width (*HWHM*) of the energy spectra will differ from the simple DQ^2 behavior. For each spectrum measured at a given Q value, one can extract a diffusion coefficient D. One has to extrapolate $D(Q)$ to small Q values to obtain the Fickian diffusivity.

The models contain as parameters the characteristic lengths and times of the elementary steps. The available models were developed by the following researchers:

1. Chudley and Elliott (CE) [13]: in this model, the jump distance d is a constant and the *HWHM* is given by

$$\Delta\omega(Q) = \frac{1}{\tau}\left(1 - \frac{\sin(Qd)}{Qd}\right) , \tag{25}$$

   where τ is the residence time of the molecule on a given site.
2. Hall and Ross (HR) [14]: here, the jump distance is not fixed, but one has a jump length distribution of the form

$$\rho(r) = \frac{2r^2}{r_0^3(2\pi)^{1/2}} \exp\left(-\frac{r^2}{2r_0^2}\right) . \tag{26}$$

The broadening is given by

$$\Delta\omega(Q) = \frac{1}{\tau}\left(1 - \exp\left(-\frac{Q^2\langle r^2\rangle}{6}\right)\right) . \tag{27}$$

The diffusion coefficient is defined by $D = \langle r^2\rangle/6\tau$, where $\langle r^2\rangle$ is the mean-square jump length: $\langle r^2\rangle = \int_0^\infty r^2\rho(r)\,\mathrm{d}r = 3r_0^2$.

3. Singwi and Sjölander (SS) [15]: this is a model, where a jump length distribution different from the HR model is considered

$$\rho(r) = \frac{r}{r_0^2}\exp\left(-\frac{r}{r_0}\right) . \tag{28}$$

Assuming that the time taken for the jump can be neglected, one obtains for the broadening

$$\Delta\omega(Q) = \frac{1}{6\tau}\frac{Q^2\langle r^2\rangle}{1 + Q^2\langle r^2\rangle/6} . \tag{29}$$

In the SS model, one has $\langle r^2\rangle = 6r_0^2$.

4. Jobic: in this more recent model, the distance between two sites is defined by d_0, and r_0 is a measure of the delocalization of the molecule on its site [16]. The jump length distribution corresponds to

$$\rho(r) = \frac{r}{d_0 r_0 (2\pi)^{1/2}}\exp\left(-\frac{(r-d_0)^2}{2r_0^2}\right) . \tag{30}$$

Then, one obtains for the *HWHM*

$$\Delta\omega(Q) = \frac{1}{\tau}\left[1 - \frac{\sin(Qd_0)}{Qd_0}\exp\left(-\frac{Q^2r_0^2}{2}\right)\right] . \tag{31}$$

The mean-square jump length corresponding to this model is: $\langle r^2\rangle = d_0^2 + 3r_0^2$.

Experimentally, all these models have been found to be useful to describe molecular diffusion in zeolites. For example, in the case of *n*-pentane in Na-X [17], the broadenings (*HWHM*) derived from individual fits of the spectra showed a maximum at $Q^2 \approx 0.4$ Å^{-2}. This maximum is characteristic of a jump diffusion process with jumps of a fixed length occurring in random directions (the CE model). The jump length, 7 Å, is shorter than the distance between the centers of two adjacent supercages, ≈ 11 Å, which means that long-range diffusion does not simply corresponds to jumps from one cage to the adjacent one.

When the adsorption sites are randomly distributed in the framework, one has a distribution of jump lengths. This was found to be the case for ammonia in silicalite [18]. The broadenings of the spectra did not show a maximum, but converged progressively to an asymptotic value. All the spectra could be fitted simultaneously with the SS model, yielding a mean jump length of 5 Å.

In recent molecular dynamics (MD) studies of propane in Na-Y zeolite, the *HWHM* obtained from the simulations have been compared with jump diffusion models and with the experiment [19]. Figure 4 shows fits of different models to the MD data, at three temperatures. The error bars on the MD points is too large to select the "best" model. However, the oscillatory behavior expected for the CE model does not seem to be present either in the MD data or in the experimental QENS broadenings (Fig. 5).

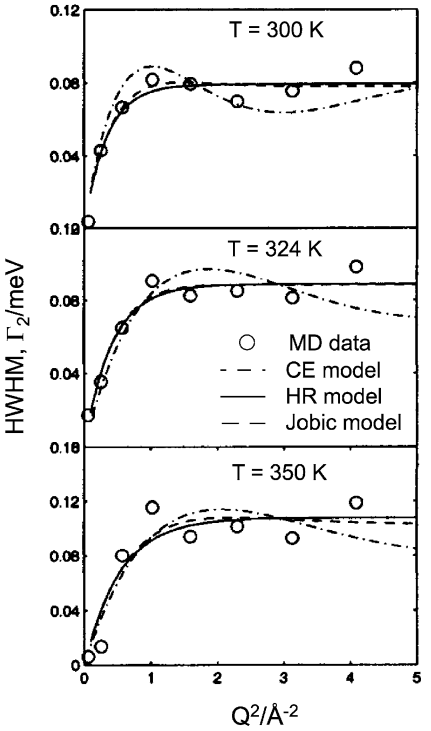

Fig. 4 The Q dependence of the intermediate component Γ_2, for propane in Na-Y showing a typical jump diffusion at three different temperatures. The *curves* are the fits of different models to the MD data. Adapted from [19]

Even if the jump parameters, obtained by fitting the different models to the data, can vary, the diffusion coefficient should stay constant if there are enough experimental points at small Q values, since all models share the same broadening behavior in this Q range of the form DQ^2.

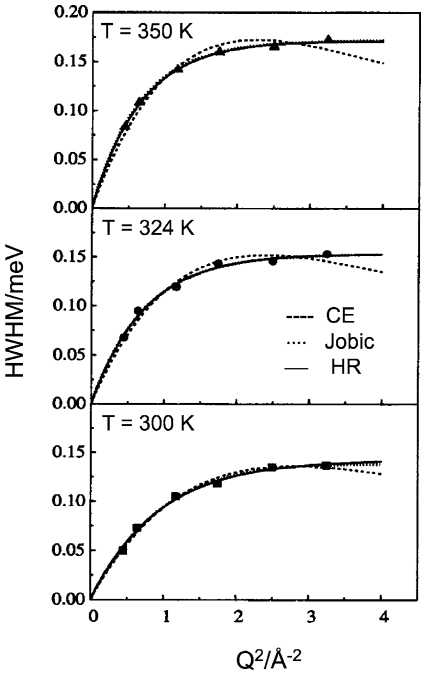

Fig. 5 The *Q* dependence of the *HWHM* of the Lorentzian function obtained from the experimental QENS data of propane in Na-Y, fitted with different model functions. Adapted from [19]

3 Experimental

The classical instruments to measure quasi-elastic neutron scattering are time-of-flight (TOF) and back-scattering (BS) spectrometers [20]. Depending upon the instrumental resolution, a broadening of the spectra will be observed if the molecules diffuse over a time scale ranging from 10^{-8} to 10^{-12} s. The typical energy resolution on a TOF instrument ranges between 10 and 100 μeV, while it is of the order of 1 μeV on a BS machine. Various TOF and BS spectrometers are found in neutron facilities around the world. The neutron spin-echo (NSE) method is of a more restricted access since there are only a few instruments. NSE has been shown recently to apply to zeolitic systems, extending the accessible time scale window to slower motions by two orders of magnitude [21]. The principle of the NSE technique is quite different from the traditional instrumentation [22]. On TOF and BS spectrometers, the incident energy has to be accurately defined, and a higher resolution can only be obtained at the expense of the incident neutron flux. A clear advantage of NSE is that monochromatization is decoupled from energy resolution and, thus, a broad wavelength distribution ($\Delta\lambda/\lambda \approx 15\%$) can be used. In NSE, the veloci-

ties of polarized neutrons are compared before and after the scattering event, using the Larmor precession of the neutron spin in a controlled magnetic field. One is able to detect very small relative velocity changes (of the order of 10^{-5}) despite the broad wavelength distribution. An echo group, as shown in Fig. 6, is obtained by varying the field integral around the symmetry point.

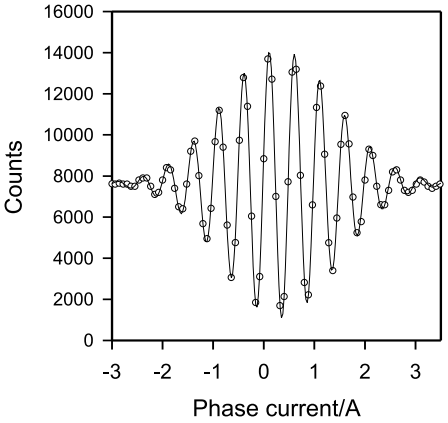

Fig. 6 Typical echo group obtained by varying the current in the phase coil. To save time during the experiment, only a limited number of points are measured near the maximum of the echo, to derive its phase and amplitude

In Fig. 6, the periodicity of the damped oscillation is determined by the average wavelength, and the envelope is the Fourier transform of the wavelength distribution. The amplitude of the echo indicates how much of the initial polarization is recovered. For an elastic scatterer, after correction from the instrumental resolution, the polarization is totally recovered (Fig. 2c). During the scattering event, the beam polarization can be reduced if the sample contains hydrogen atoms (see Sect. 2.1). This is the reason why deuterated molecules or coherent scatterers are preferably studied. With new NSE instruments under construction, increases in flux by one or two orders of magnitude will allow one to measure the diffusion of hydrogenated molecules as well.

In the case of quasi-elastic neutron scattering, the total precession angle, φ, is a function of the energy transfer ω: $\varphi = \omega t$. The detected intensity is the average of $\cos\varphi$, weighted by the scattering function of the sample $S(Q, \omega)$

$$\frac{\int S(Q,\omega)\cos(\omega t)\,\mathrm{d}\omega}{\int S(Q,\omega)\,\mathrm{d}\omega} = \frac{I(Q,t)}{I(Q,0)}\,. \tag{32}$$

Therefore, NSE directly measures the intermediate scattering function (see Eqs. 9–12). In the Fickian regime, one obtains the diffusivity in a straightfor-

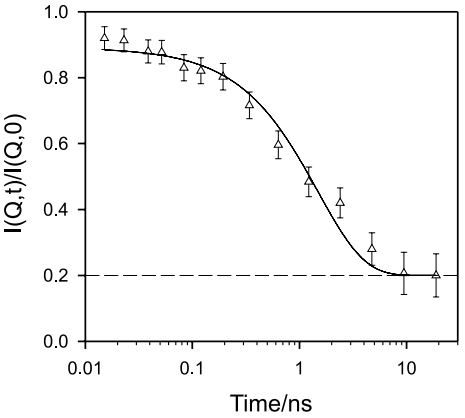

Fig. 7 Normalized intermediate scattering function obtained for benzene in Na-Y zeolite (1 molecule per supercage, on average, $T = 475$ K, $Q = 0.3$ Å^{-1}). The fraction of the intensity due to the zeolite is represented as a *dashed line*

ward manner from the normalized intermediate scattering function

$$\frac{I(\boldsymbol{Q}, t)}{I(\boldsymbol{Q}, 0)} = \exp\left(- D_t Q^2 t\right) \ . \tag{33}$$

For a given Q value, the decay of $I(\boldsymbol{Q}, t)$ can be followed for times up to several hundreds of ns (for the time being this is only possible at the Institut Laue-Langevin, in Grenoble, France). The equivalent energy resolution is then of a few neV.

Another characteristic of the NSE technique is that the dynamical range is very large (more than three orders of magnitude). This is larger than on TOF instruments, and much larger than on BS spectrometers. As an example, the intermediate scattering function obtained for benzene in Na-Y zeolite is shown in Fig. 7. The experimental data can be fitted with only one exponential function, whereas two decays would be expected from simulations, where two different time scales for intracage and intercage motion were considered [23]. The previous conclusion, derived from BS experiments, that both types of jumps occur on the same time scale is, thus, more clearly confirmed [24].

4 Applications

The QENS technique has been used to study the diffusion of hydrogen in metals, of molecules on flat surfaces, and of ions in oxides or solid electrolytes. Apart from zeolites, the method has been recently employed to characterize molecular diffusion in MCM-41 samples [25, 26], or in microp-

orous silica [27, 28]. In some papers, the time scale is sometimes too short to observe diffusion. Further, to derive a diffusion coefficient in zeolites, one must probe a length scale which is much larger than the cage-to-cage distance. This requires measuring data at small Q values, a range which may not be accessible on some instruments [29]. In that case, only local motions will be probed.

Despite extensive work in the last decade, large discrepancies still persist between the various experimental techniques which measure diffusion in zeolites. One of the difficulties is that one has to compare self-diffusivities, obtained by PFG NMR or QENS methods, with transport diffusivities derived from macroscopic experiments. The transport diffusivity is defined as the proportionality factor between the flux and a concentration gradient (Fick's first law)

$$J = - D_t \nabla c \,. \tag{34}$$

One expects that D_s and D_t will have a different concentration dependence. Comparisons between PFG NMR, QENS, and MD simulations could only be made in the past at the level of D_s. At equilibrium, one can now obtain experimentally D_t using coherent neutron scattering. From equilibrium MD simulations, one cannot derive D_t, but one can determine the corrected diffusivity D_o. These two diffusivities are linked by considering that the driving force for diffusion is the chemical potential gradient, and not the concentration gradient

$$D_t(c) = D_o(c) \left(\frac{\mathrm{d} \ln p}{\mathrm{d} \ln c} \right) = D_o(c) \Gamma \,, \tag{35}$$

where Γ is the thermodynamic correction factor (for a Langmuir isotherm, $\Gamma = (1 - \theta)^{-1}$, θ being the fractional occupancy). One approximation which can be found in the literature is to replace D_o by D_s. However, the self-, transport, and corrected diffusivities are only equal at zero concentration. All these diffusivities can have a different concentration dependence, and this is, indeed, what has been evidenced recently, both by experiments and by simulations.

4.1
Concentration Dependence of the Corrected Diffusivity

Coherent QENS measurements and MD simulations have been performed for N_2 and CO_2 in silicalite [30, 31]. It has been found that the self-diffusivities of the two gases decrease with increasing occupancy, while the transport diffusivities increase. For a comparison with other systems, it is appropriate to remove the influence of the thermodynamic correction factor and to discuss the collective mobility in terms of the corrected diffusivity (also called Maxwell–Stephan diffusivity). $D_o(c)$ is directly obtained from the simula-

tions; it is obtained experimentally by dividing the transport diffusivity by the thermodynamic correction factor calculated from the simulated adsorption isotherms. Significant differences for the loading dependence of D_o between the two gases were observed, both by experiment and simulation. The dependence on the loading of D_o was analyzed using the surface diffusion model of Reed and Ehrlich [32], as previously done by Krishna et al. [33]. The interaction parameters between sorbate molecules, extracted from the simulated adsorption isotherms, gave a good description of the loading dependence of D_o. The sorbate–sorbate interactions were found to be more attractive for CO_2 than for N_2, as expected on simple physical grounds.

CO_2 is more strongly adsorbed than CH_4 in silicalite, so that the QENS experiments could be performed at 300 K. On the other hand, N_2 is much more weakly adsorbed, and a temperature of 200 K was selected to reach an average concentration of 6.5 molecules per unit cell ($\theta = 0.35$), at atmospheric pressure [30, 31]. Larger pressures (or lower temperatures) would be needed to reach higher loadings. For CF_4 in silicalite, higher loadings (up to $\theta = 0.85$) could be reached at 200 K [34]. It has been shown in Sect. 2.2 that the scattering function for this coherent scatterer condensed to a single Lorentzian function. Its intensity is, however, governed by a structure factor, $S(Q)$, which is so small in liquids at small Q values that few coherent QENS experiments have been performed so far.

The experimental intensities, integrated over the quasi-elastic domain, are shown in Fig. 8a, at different CF_4 concentrations. A maximum for the scattered intensities is observed at the intermediate loading of seven molecules per u.c. After normalization with respect to the number of scattering molecules, one obtains a quantity which is related to the structure factor. The values for $S(Q)$ are reported in Fig. 8b; they show a continuous decreasing trend for increasing loadings. The extrapolation of $S(Q)$ at zero Q value is known to be a measure of the fluctuations of the number of particles contained in a given volume [35]

$$S(Q)_{Q\to 0} = \frac{\left\langle (\delta N)^2 \right\rangle}{\langle N \rangle} \,. \tag{36}$$

The thermodynamic correction factor has also been related to particle fluctuations (e.g. [32])

$$\Gamma = \frac{\langle N \rangle}{\left\langle (\delta N)^2 \right\rangle} \tag{37}$$

so that one has a simple relationship between $S(Q)$ at zero Q and Γ

$$S(Q)_{Q\to 0} = \Gamma^{-1} \,. \tag{38}$$

The kinetic theory of gases relates particle fluctuations to the isothermal compressibility. Therefore, at small Q values, one expects a larger scattering power, larger $S(Q)$, at small sorbate concentration (the sorbate phase is highly

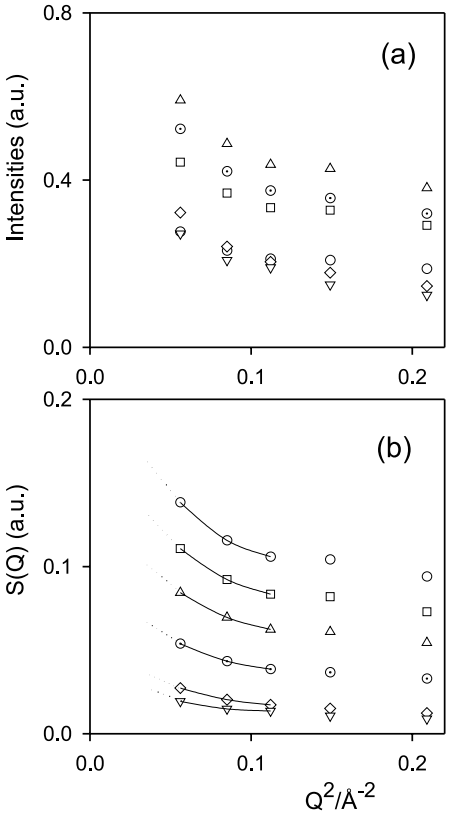

Fig. 8 **a** Neutron intensities derived for CF_4 in silicalite at 200 K, at different concentrations: (○) 2 CF_4/u.c., (□) 4 CF_4/u.c., (△) 7 CF_4/u.c., (⊙) 9.7 CF_4/u.c., (◇) 11.8 CF_4/u.c., (▽) 14 CF_4/u.c., **b** structure factors derived at the same loadings

compressible like a gas) than at saturation (a case similar to a liquid which is poorly compressible).

The value of $S(Q)$ at zero Q value cannot be determined experimentally on the same instrument that is used to measure diffusivities: there are not enough points at small Q in Fig. 8b. However, the $S(Q)$ scale, which is given in Fig. 8b in arbitrary units, can be renormalized. At infinite dilution, $S(0)$ should be equal to one (like in a gas), and sorption thermodynamics also imply that the thermodynamic correction factor should be equal to one, so that Eq. 38 will be fulfilled. On the other hand, at high concentrations, Γ increases while $S(0)$ goes down. In Fig. 8b, Γ is equal to 6.6 for a concentration of 14 CF_4 per u.c. so that $S(0)$ should go down to 0.15. A more quantitative analysis has been recently performed for *n*-hexane and *n*-heptane in silicalite [36] where the inverse of the thermodynamic factor, calculated from $S(Q)$ was found to be in good agreement with configurational-bias Monte Carlo (CBMC) simulations.

The transport and corrected diffusivities of CF_4 in silicalite at 200 K, as obtained from QENS and atomistic simulations, are reported in Fig. 9 [34]. They are found to be in excellent agreement, both in magnitude and loading dependence.

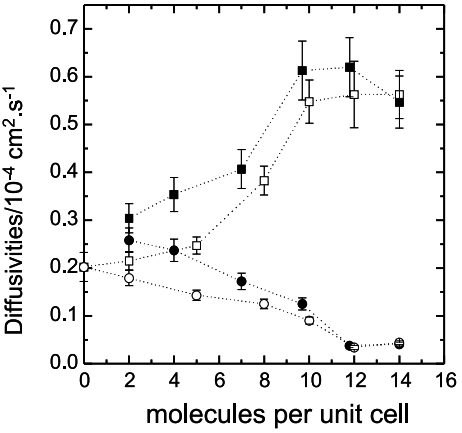

Fig. 9 Transport diffusivities (*squares*) and corrected diffusivities (*circles*) obtained for CF_4 in silicalite at 200 K, by QENS (*filled symbols*) and simulations (*open symbols*)

The experimental corrected diffusivities for CF_4 are replotted in Fig. 10 as a function of the fractional occupancy (the diffusivities were normalized by the corresponding $D_o(0)$ values). These data closely match the $(1 - \theta)$ de-

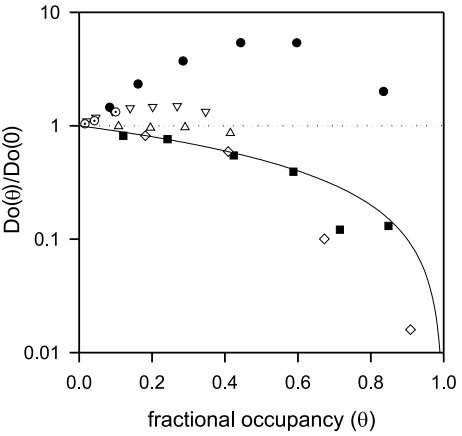

Fig. 10 Normalized corrected diffusivities obtained experimentally for several systems: (■) CF_4 in silicalite, (◇) benzene in Na-Y, (△) CO_2 in silicalite, (⊙) Ar in silicalite, (▽) N_2 in silicalite, (●) D_2 in Na-X. The *solid line* gives the $(1 - \theta)$ dependence, and the *dotted line* the "Darken approximation"

pendence expected for non-interacting particles hopping on a lattice, i.e., for a lattice gas model. In this case, the transport diffusivity does not depend on θ [37]. However, it can be seen in Fig. 10 that many other experimental systems do not follow this model. What is called sometimes in the literature as the Darken approximation is to assume that D_o is independent of θ. The data reported in Fig. 10 clearly show that this approximation is rarely valid. $D_o(\theta)$ displays a clear maximum for D_2 in Na-X [5] and a small one in the case of N_2 in silicalite [31]. Similar behaviors were observed from atomistic simulations performed for several gases adsorbed in silicalite [38]. The only quantitative analyses of the loading dependence of D_o have been made so far using the Reed–Ehrlich model. It is clear that this lattice model is an oversimplification of a sorbate–zeolite system and that more refined models will have to be developed.

4.2 Diffusion of Isobutane in Silicalite

Various experimental and theoretical methods have been used to determine the diffusivities of *n*-alkanes in silicalite or ZSM-5 zeolites. Branched alkanes are expected to be slower, but the ratio of the diffusivities between a normal alkane and a mono-methyl isomer may vary experimentally between a factor 5 to 1,000 [39, 40]. With a rigid framework, the value of this ratio obtained from simulations varies between two and six orders of magnitude [41–43]. The first QENS measurements on hydrogenated isobutane in ZSM-5 were performed on a back-scattering instrument [40]. The broadenings were small, only 10–20% of the instrumental resolution. The self-diffusivities, which were extracted, were $2–5 \times 10^{-12}$ m^2 s^{-1}, for temperatures ranging between 450 and 570 K [40].

As explained in the previous sections, slow motions are more easily detected on an NSE instrument, but coherent scatterers are preferably used, to obtain a better signal. The diffusion of deuterated isobutane in silicalite has been measured on a NSE spectrometer, at a low sorbate concentration: 2 molecules per u.c. [44]. The normalized intermediate scattering functions measured at 550 K, for two different Q values, are shown in Fig. 11. The lowest Q value, 0.08 Å^{-1}, allows one to probe diffusion over distances of $2\pi/Q \approx 80$ Å. The shift between the two Q values is partly due to the small-angle scattering due to the texture of the sample. Crystals of very high crystallinity would allow performing measurements at lower Q, so that diffusion could be followed over space scales of hundreds of Å.

From the NSE data obtained at various momentum transfers ranging from 0.08 to 0.3 Å^{-1}, transport diffusivities could be determined using a jump diffusion model to take into account the curvature of $D(Q)$. A value of 2×10^{-11} m^2 s^{-1} was derived at 490 K, which is sevenfold larger than the self-diffusivity previously obtained in Na-ZSM-5. Part of this difference is due

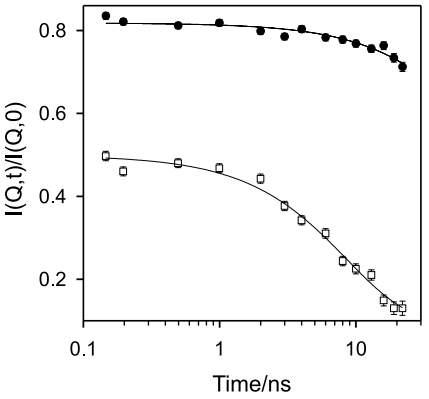

Fig. 11 Normalized intermediate scattering functions obtained for isobutane in silicalite at 550 K, for two different Q values: (●) 0.08 $Å^{-1}$, (□) 0.2 $Å^{-1}$

to the thermodynamic correction factor, but a blocking effect of the sodium cations is also probably observed.

By measuring diffusivities at several temperatures, an activation energy for diffusion of 22.6 kJ/mol was derived. Extrapolating the NSE diffusivities to 300 K, one obtains a value of 8×10^{-13} m^2 s^{-1}, which is in good agreement with an interference microscopy investigation performed on the same system which gave 1×10^{-12} m^2 s^{-1} [45]. This example shows the potential of the NSE technique to study the diffusion of more complex branched alkanes in silicalite.

4.3 Linear Alkanes in 5A Zeolite, the "Window Effect"

One of the most controversial issues in the field of diffusion in zeolites is the so-called "window effect". This term was coined by Gorring to interpret the anomalous transport results obtained for linear alkanes in zeolite T [46], but his experimental conditions have been criticized. More recent macroscopic studies could not reproduce the periodic variation in diffusivity, and a monotonic decline with carbon number was reported [47, 48]. However, a microscopic technique, such as neutron scattering, is better suited to probe anomalous diffusion mechanisms on a molecular scale, since it is much less sensitive to the influence of defects or internal transport barriers within the zeolite crystals.

Anomalous diffusion in zeolites is expected to happen only in structures which possess cages separated by windows, and the concept of the window effect depends both on the cage and window sizes. An unusual behavior may occur in systems where the sizes of the molecule and of the aperture between cavities are similar, and when the characteristic length scales of the molecule and of the cavity are comparable. If a molecule is too long to fit comfortably

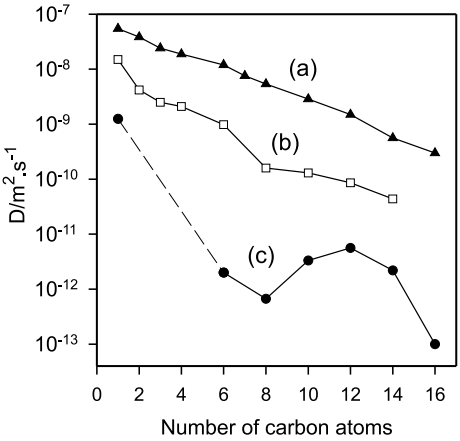

Fig. 12 Diffusivities of linear alkanes in different zeolites obtained at 475 K as a function of the carbon number **a** self-diffusivities derived from PFG NMR in Na-X zeolite, **b** self-diffusivities measured by QENS in ZSM-5, **c** transport diffusivities obtained by NSE in 5A [48]

in a cage and takes a configuration where at least one end of the molecule extends through a window, the energy barrier between adjacent cages is easier to cross, leading to a higher diffusivity.

As shown in Fig. 12, a monotonous decrease in the self-diffusion coefficient was measured by PFG NMR for a series of *n*-alkanes in Na-X [50]. A similar trend was observed in ZSM-5 by QENS. From the NSE experiments performed in 5A, one finds that D_t drops to a minimum at C_8 and has a clear maximum at C_{12}. A similar variation is obtained for D_o after correcting from the thermodynamic correction factor (the number of carbon atoms per cavity is the same). Recent PFG NMR results indicate also a small minimum for D_s at C_8 and a small maximum at C_{10} [51]. The NSE data obtained for longer *n*-alkanes in 5A are in contradiction with simulations which predict increasing diffusivities from C_{12} to C_{17} [52] whereas a decreasing trend is observed (Fig. 12). Finally, the activation energies derived from the NSE measurements show a minimum for C_{12}, in agreement with the explanation in terms of the window effect. These results are related to similar concepts such as resonant diffusion [53] or the levitation effect, which corresponds to a maximum in self-diffusivity when the size of the diffusant is comparable to the diameter of the void [54].

5 Conclusion

The combination of quasi-elastic neutron scattering (QENS) and neutron spin-echo (NSE) methods allows one to probe characteristic times ranging

from less than a picosecond to almost a microsecond. The space and time scales of the neutron scattering techniques are comparable with those explored by molecular simulation methods, so that direct comparisons can be made on the translational and rotational dynamics of adsorbed molecules.

Although hydrogen has the largest neutron cross-section, the neutron instrumentation is no more restricted to the study of hydrogenated molecules. One can now probe the diffusion of molecules which do not contain hydrogen atoms. At the time being, the self-diffusivity of hydrocarbons is measured with the hydrogenated molecule, and the transport diffusivity with the deuterated molecule. In future, it will be possible to derive simultaneously both diffusivities from measurements with a deuterated molecule, using polarization analysis to resolve the coherent and incoherent contributions.

References

1. Fitch AN, Jobic H (1999) In: Karge HG, Weitkamp J (eds) Molecular Sieves – Science and Technology, vol 2. Springer, Heidelberg, p 31
2. Kärger J, Ruthven DM (1992) Diffusion in Zeolites and Other Microporous Solids. Wiley, New York
3. Jobic H, Bée M, Renouprez A (1984) Surf Sci 140:307
4. Jobic H, Hahn K, Kärger J, Bée M, Tuel A, Noack M, Girnus I, Kearley GJ (1997) J Phys Chem B 101:5834
5. Jobic H, Kärger J, Bée M (1999) Phys Rev Lett 82:4260
6. Hoogenboom JP, Tepper HL, van der Vegt NFA, Briels WJ (2000) J Chem Phys 113:6875
7. Maginn EJ, Bell AT, Theodorou DN (1993) J Phys Chem 97:4173
8. Skoulidas AI, Sholl DS (2003) J Phys Chem A 107:10132
9. Jobic H, Bée M, Caro J, Bülow M, Kärger J (1989) J Chem Soc, Faraday Trans 1 85:4201
10. van Hove L (1954) Phys Rev 95:249
11. Cook JC, Richter D, Schärf O, Benham MJ, Ross DK, Hempelmann R, Anderson IS, Sinha SK (1990) J Phys: Condens Matter 2:79
12. Sears VF (1967) Can J Phys 45:237
13. Chudley CT, Elliott RJ (1961) Proc Phys Soc London 77:353
14. Hall PL, Ross DK (1981) Mol Phys 42:673
15. Singwi KS, Sjölander A (1960) Phys Rev 119:863
16. Jobic H (2000) In: Kanellopoulos NK (ed) Recent Advances in Gas Separation by Microporous Membranes, Membrane Science and Technology Series, 6. Elsevier, p 109
17. Jobic H (1999) Phys Chem Chem Phys 1:525
18. Jobic H, Ernst H, Heink W, Kärger J, Tuel A, Bée M (1998) Microporous Mesoporous Mater 26:67
19. Sayeed A, Mitra S, Avil Kumar AV, Mukhopadhyay R, Yashonath S, Chaplot SL (2003) J Phys Chem B 107:527
20. Bée M (1988) Quasielastic Neutron Scattering. Adam Hilger, Bristol
21. Jobic H, Méthivier A, Ehlers G (2002) Microporous Mesoporous Mater 56:27
22. Mezei F (ed) (1979) Neutron Spin Echo, Lectures Notes in Physics, vol 128. Springer, Berlin
23. Auerbach SM (2000) Int Rev Phys Chem 19:155

24. Jobic H (2002) Microporous Mesoporous Mater 55:159
25. Takahara S, Nakano M, Kittaka S, Kuroda Y, Mori T, Hamano H, Yamaguchi T (1999) J Phys Chem B 103:5814
26. Sahasrabudhe A, Mitra S, Tripathi AK, Mukhopadhyay R, Gupta NM (2002) J Phys Chem B 106:10923
27. Benes NE, Jobic H, Verweij H (2001) Microporous Mesoporous Mater 43:147
28. Benes NE, Jobic H, Réat V, Bouwmeester H, Verweij H (2003) Sep Purif Technol 32:9
29. Crupi V, Majolino D, Migliardo P, Venuti V, Wanderlingh U, Mizota T, Telling M (2004) J Phys Chem B 108:4314
30. Jobic H, Makrodimitris K, Papadopoulos GK, Schober H, Theodorou DN (2004) In: van Steen E et al. (ed) Proceedings of the 14th International Zeolite Conference. Cape Town, p 2056
31. Papadopoulos GK, Jobic H, Theodorou DN (2004) J Phys Chem B 108:12748
32. Reed DA, Ehrlich G (1981) Surf Sci 102:588
33. Paschek D, Krishna R (2001) Chem Phys Lett 342:148
34. Jobic H, Skoulidas AI, Sholl DS (2004) J Phys Chem B 108:10613
35. Guisnet A (1964) Théorie et technique de la radiocristallographie. Dunod, Paris
36. Jobic H, Laloué N, Laroche C, van Baten JM, Krishna R (2006) J Phys Chem B 110:2195
37. Kutner R (1981) Phys Lett 81A:239
38. Skoulidas AI, Sholl DS (2002) J Phys Chem B 106:5058
39. Xiao J, Wei J (1992) Chem Eng Sci 47:1143
40. Millot B, Méthivier A, Jobic H, Moueddeb H, Bée M (1999) J Phys Chem B 103:1096
41. Bouyermaouen A, Bellemans A (1998) J Chem Phys 108:2170
42. Schuring D, Jansen APJ, van Santen RA (2000) J Phys Chem B 104:941
43. Vlugt TJH, Dellago C, Smit B (2000) J Chem Phys 113:8791
44. Jobic H et al. (2005) Experimental Report at the FRJ-2 Reactor, Jülich
45. Geier O, Vasenkov S, Lehmann E, Kärger J, Schemmert U, Rakoczy RA, Weitkamp J (2001) J Phys Chem B 105:10217
46. Gorring RL (1973) J Catal 31:13
47. Cavalcante CL, Eic M, Ruthven DM, Occelli ML (1995) Zeolites 15:293
48. Magalhaes FD, Laurence RL, Conner WC (1996) AIChE J 42:68
49. Jobic H, Méthivier A, Ehlers G, Farago B, Haeussler W (2004) Angew Chem Int Ed 43:364
50. Kärger J, Pfeifer H, Rauscher M, Walter A (1980) J Chem Soc Faraday Trans 1 76:717
51. Jobic H, Kärger J, Krause C, Brandani S, Gunadi A, Méthivier A, Ehlers G, Farago B, Haeussler W, Ruthven DM (2005) Adsorption 11:403
52. Dubbeldam D, Calero S, Maesen TLM, Smit B (2003) Phys Rev Lett 90:245901/1
53. Runnebaum RC, Maginn EJ (1997) J Phys Chem B 101:6394
54. Yashonath S, Santikary P (1994) J Phys Chem 98:6368

Mol Sieves (2008) 7: 235–276
DOI 10.1007/3829_2007_013
© Springer-Verlag Berlin Heidelberg
Published online: 11 September 2007

Frequency Response Measurements of Diffusion in Microporous Materials

Lijuan Song[1,2] (✉) · Lovat V. C. Rees[1]

[1]School of Chemistry, The University of Edinburgh, King's Buildings, West Mains Road, Edinburgh EH9 3JJ, UK
lsong@lnpu.edu.cn

[2]Liaoning Key Laboratory of Petrochemical Engineering, Liaoning University of Petroleum & Chemical Technology, Fushun, 113001 Liaoning, China

Abstract Theoretical, experimental principles and the applications of the frequency response (FR) method for determining the diffusivities in microporous and bidispersed porous solid materials have been reviewed. Diffusivities of hydrocarbons and some other sorbates in microporous crystals and related pellets measured using the FR technique are presented, and the FR data are analysed to demonstrate the identification of the FR spectra. These results display the ability of the FR method to discriminate multi-kinetic mechanisms, including a surface resistance or surface barrier occurring simultaneously in the systems, which are difficult to be determined using other microscopic or macroscopic methods. The FR measurements also showed that the diffusivity of a system depends significantly on the subtle differences in molecular shape and size of sorbates in various

porous framework structures. Several FR techniques and future developments, including both theories and apparatus, have also been briefly described.

Keywords Diffusion · Frequency response · Hydrocarbons · Microporous materials

Abbreviations

4A, 5A	Linde Type Zeolite A*
$AlPO_4$-5	Aluminophosphate-five molecular sieve*
α	Ratio of the concentration of sorbate in the gas phase to the concentration in the sorbent at equilibrium
C_{Be}	Bulk sorbate concentration under equilibrium conditions, mmol g^{-1}
C_g	Concentration of diffusate in the gas phase, mmol g^{-1}
CH	Cyclohexane
CMS	Carbon molecular sieve
CP	Cyclopentane
C_s	Volumetric heat capacity of the sorbent, kJ m^{-3} K^{-1}
D	Transport diffusion coefficient in crystals, m^2 s^{-1}
D_0	Self-diffusion coefficient in crystals, m^2 s^{-1}
DMCH	Dimethylcyclohexane
D_p	Macropore diffusivity, m^2 s^{-1}
DTG	Differential thermogravimetric
D_μ	Micropore diffusivity, m^2 s^{-1}
δ_c, δ_s	Characteristic functions
δ_{c,s_M}, δ_{s,s_M}	In-phase and out-of-phase characteristic functions for macro-particle shape factor s_M
δ_{c,s_μ}, δ_{s,s_μ}	In-phase and out-of-phase characteristic functions for micro-particle shape factor s_μ
δ_{in}, δ_{out}	In-phase and out-of-phase components
σ_1, σ_2	Fractional adsorption capacities in the macropore voids and the microparticles
EB	Ethylbenzene
f	Frequency, s^{-1}
FR	Frequency response
FRFs	Frequency response functions
h	Heat transfer coefficient, W m^{-2} K^{-1}
k_{-A}	Rate constant for a surface resistance or surface barrier, s^{-1}
k_a	Adsorption rate constant, s^{-1} Pa^{-1}
k_d	Desorption rate constant, s^{-1}
K	Dimensionless equilibrium constant
K_{iso}	Dimensionless equilibrium constant calculated from adsorption isotherms
K_p	Equilibrium based on the pressure, kmol m^{-3} Pa^{-1}
K_T	Equilibrium based on the temperature, kmol m^{-3} K^{-1}
l	Half thickness of the slab sorbent, m
LHS	Left-hand side
m.	Molecule(s)
MD	Molecular dynamic
MFI	ZSM-5 zeolite structure*
M_t	Amount of sorbate sorbed in a sorbent at time t, mmol g^{-1}
M_∞	Amount of sorbate sorbed in a sorbent at sorption equilibrium, mmol g^{-1}

n	Harmonic number for Fourier transformation
NaX, 13X	Faujusite-type zeolite*
n_m	Coverage of the sorbent, molecules per unit cell
P	Pressure, Pa (1 Torr = 133.33 Pa)
P_B	Relative amplitude of the pressure variation in the absence of sorbent
p-DCB	*p*-dichlorobenzene
PFG NMR	Pulse field gradient nuclear magnetic resonance
P_Z	Relative amplitude of the pressure variation in the presence of sorbent
P_e	Equilibrium pressure of the sorbate, Pa
q	Concentration adsorbed in the sorbent, mmol g^{-1}
QENS	Quasi-elastic neutron scattering
Q_{st}	Heat of adsorption, kJ mol^{-1}
Q_{st}^{iso}	Heat of adsorption calculated from adsorption isotherms, kJ mol^{-1}
R	Gas constant, kJ mol^{-1} K^{-1}
RHS	Right-hand side
R_p	Radii of macro-particles, m
R_μ	Radii of micro-particles, m
S	Dimensionless constant
silicalite-1	Siliceous framework of the MFI zeolite*
s_M	Macro-particle shape factor
s_μ	Micro-particle shape factor
SSFR	Single-step frequency response
t_h	Time constant for heat exchange process, s
t_p	Macropore diffusion time constant, s
T	Temperature, K
theta-1	Zeolite structure*
V_e	Mean volume of sorbate outside the sorbent, m^3
V_g	Volume of the gas phase, m^3
V_s	Volume occupied by the sorbent, m^3
Φ_B	Phase lag of the pressure change in the absence of sorbent, degrees
Φ_Z	Phase lag of the pressure change in the presence of sorbent, degrees
$\Phi_{Z\text{-}B}$	$= \Phi_Z - \Phi_B$
γ	Parameter describing the non-isothermality
ω	Angular frequency of the volume modulation, rad s^{-1}
ξ	Surface resistance effect factor defined in Eq. 19
λ	A measure of the approach to saturation of the Langmuir isotherm
*	cf. Baerlocher C, Meier WM, Olson DH (2001) Atlas of zeolite framework types, 5th edn. Elsevier, Amsterdam.

1 Introduction

The frequency response technique is a quasi-steady state relaxation technique in which a system in equilibrium is perturbed slightly by a rapid, periodic change in a property of the system which disturbs the equilibrium. The adjustment of the system to the new equilibrium is followed and characterised by one or more relaxation times. The response of a parameter characteristic

of the state of the system depends upon the time scale of the dynamic processes affecting the parameter relative to the period of perturbation, the type of perturbation and physical characteristics of the system. The response spectrum of the system to the modulation can, thus, be used to determine the kinetic parameters. This method applies much smaller changes in the system conditions than those typically used for large step change methods, such as gravimetric and volumetric uptake measurements.

By applying an appropriate perturbation to a relevant parameter of a system under equilibrium, various frequency modulation methods have been used to obtain kinetic parameters of chemical reactions, adsorption-desorption constants on surfaces, effective diffusivities and heat transfer within porous solid materials, etc., in continuous flow or batch systems [1–24]. In principle, it is possible to use the FR technique to discriminate between all of the kinetic mechanisms and to estimate the kinetic parameters of the dynamic processes occurring concurrently in heterogeneous catalytic systems as long as a wide enough frequency range of the perturbation can be accessed experimentally and the theoretical descriptions which properly account for the coupling of all of the dynamic processes can be derived.

Diffusional mass transport in microporous materials is of crucial relevance and usually a rate-controlling step for a large number of heterogeneous catalytic and separation processes. The knowledge of the diffusivities is, therefore, of immense importance for obtaining a better understanding of the mechanisms of catalytic and adsorption separation processes. The FR technique has proved to be a very effective and a very powerful method for determining inter- and intracrystalline diffusivities of sorbate molecules in porous materials. An outstanding advantage of the FR method is its ability to distinguish multi-kinetic processes in an FR spectrum, i.e., various rate processes which occur simultaneously can be investigated by this technique [3]. For diffusion measurements in microporous materials, the frequency response method monitors the pressure response of a closed system to a small fluctuation in its volume. This technique was initially applied to study chemisorption kinetics by Polinski and Naphtali [1] and was then used by Yasuda to measure diffusion coefficients in gas-zeolite systems by applying a sinusoidal-wave perturbation to the equilibrium gas phase volume of the system [2–5]. Rees et al. have improved this technique by the use of "pure" square-wave perturbations, by reduction of the response time of the pressure transducer, by automation of the apparatus, and finally, by an expansion of the frequency-range [6–11].

In this chapter the discussion will be mainly focused on the theories and experimental principles of this gaseous batch system subject to square wave volume perturbations and the applications of the method to determine the diffusivities in microporous solid materials. Some other FR techniques, including both theories and apparatus will also be briefly described.

2
Apparatus and Measurement Procedures

The principal features of the FR apparatus developed by Rees et al. are shown in Fig. 1. An accurately known amount of sorbent sample (~50–100 mg) is scattered in a plug of glass wool and outgassed at a pressure of $< 10^{-3}$ Pa and 623 K overnight by rotary and turbo molecular drag pumps (Eq. 6). The temperature was raised to 623 K at 2 K min^{-1} using a programmable tube furnace. A dose of purified sorbate is brought into sorption equilibrium with the sorbent in the sorption chamber (Eq. 8) at the chosen pressure and temperature.

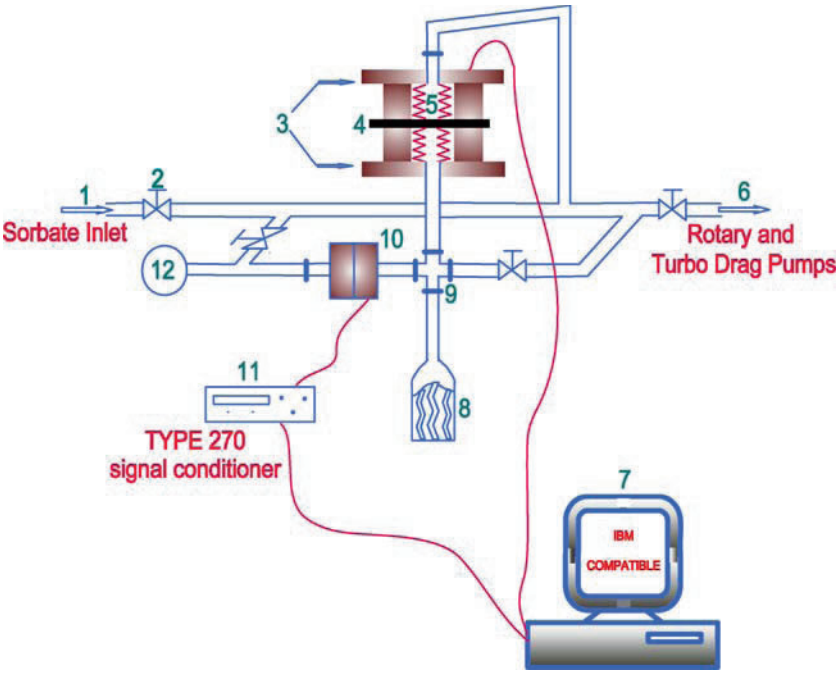

Fig. 1 Schematic diagram of the FR apparatus: *1*: Sorbate inlet *2*: Valve *3*: Electromagnets; *4*: Moving disc *5*: Bellows *6*: Rotary and turbo drag pumps *7*: Computer with A/D and D/A cards *8*: Adsorption vessel with zeolite in glass-wool *9*: Vacuum connectors *10*: Differential Baratron *11*: Signal conditioner *12*: Reference pressure side

A square-wave modulation of ±1% was then applied to the gas phase equilibrium volume, V_e. Such a small perturbation can generally satisfy the assumption of linearity. The modulation was affected by applying a current to each of the two electromagnets (Eq. 3) in turn, which moves the disc (Eq. 4) between the electromagnets rapidly (< 10 ms) and periodically. The brass bellows (Eq. 5) attached to the disc, which is part of the sorption gas

phase volume, was expanded and compressed to produce the ±1% change in volume. A frequency range of 0.001 to 10 Hz was scanned over some 30 increments. The range of diffusivities that can be covered by such an FR apparatus depends on the size and the shape of the adsorbent crystals, as demonstrated in Fig. 2.

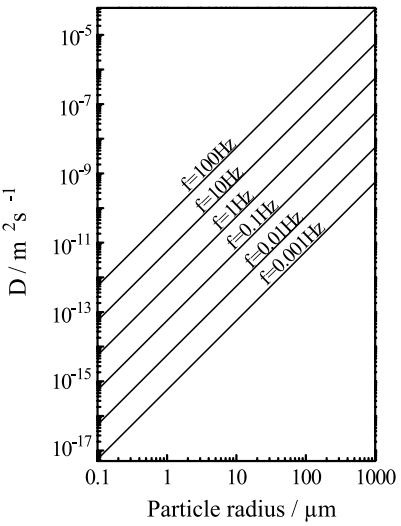

Fig. 2 The relationship of diffusion coefficients, D; frequency, f; and spherical crystal radius, r

The pressure response to the volume perturbation was recorded with a high-accuracy differential Baratron pressure transducer (MKS 698A11TRC) (Eq. 10) at each frequency over three to five square-wave cycles (256 pressure readings per cycle) after the periodic steady-state had been established. The isotherm describing the equilibrium sorption conditions can be linear or curved. However, the horizontal region of a rectangular isotherm cannot be used as there is no sorption/desorption following the square–wave modulation of the equilibrium volume.

The frequency was controlled by an on-line computer (Eq. 7), which was also used for the recording of the pressure data from the Baratron transducer. The conversion rate of the analogue-to-digital converter in the interface unit must be fast enough to cope with the 1 to 4 ms response time of the pressure transducer. The pressure response to the volume change over the whole frequency range was measured in the absence (blank experiment) and presence of sorbent samples to eliminate time constants associated with the apparatus. The FR spectra were derived from the equivalent fundamental sine-wave perturbation by a Fourier transformation of the volume and pressure square-wave forms.

Another batch or closed FR system, similar to the one described above, but applying a sine-wave perturbation to an equilibrium gas phase volume instead of a square-wave is obtained by attaching the bellows to a cam and variable speed motor or to a servomotor [1, 2, 12, 19]. Compared with a sine-wave modulation, a square-wave is easier to create and the system has much better long term reliability. Also, in the case of a square-wave forcing function, the pressure response contains higher harmonics, which makes the study of fast dynamics accessible by using relatively low frequencies of the input perturbations and analysing the higher harmonics in the output signal [9]. This feature redeems a batch FR system from the limitation that the frequencies of the volume modulations in the experimental investigations are restrained to relative low values due to mechanical restrictions.

As can be seen in the subsequent sections, in some circumstances, the dissipation of the heat of adsorption affects the response signal and plays an important role on mass transport processes. A thermal FR apparatus has been built to monitor both pressure and temperature changes resulting from the volume modulations. The temperature is accurately measured by an infrared detector with a standard error on the order of 10^{-4} K [21, 22]. However, the temperature sensing system is quite complex and the components are expensive.

More recently, continuous flow or open FR systems have been developed to measure the adsorption and diffusion properties of sorbate molecules in microporous materials [13–15]. In these systems, either the concentration of the sorbate feed [13] or the pressure within the reactor [14, 15] is oscillated and the resulting changes at the exit stream are measured by using mass spectrometry or a mass flow meter. For a flow FR system, the effect of adsorption heat is reduced as the flowing gases attenuates the temperature change.

Studies of the diffusivities of mixtures of sorbates can be simply carried out and chemical reaction kinetics on porous materials can also be measured using a flow FR system [25]. A flow system is, again, more complex to operate and more expensive to construct than a batch system.

Reyes et al. described their newly designed FR system that combines acoustically coupled moving diaphragms capable of reaching higher forcing frequencies (100 Hz) with two synchronized and identical closed chambers, one containing the sample and the other, an exact equivalent volume, being without sample. They also proposed an idea to use more suitable forcing signals in order to decrease the experimental time required to obtain a response function over a wide range of frequencies by applying signals containing multiple harmonic components. This method can probe the system response over a range of frequencies simultaneously [19, 20].

The apparatus developed by Rees et al. can also be used for single-step FR measurements. In these experiments, the gas phase equilibrium volume, V_e, is only subjected to one half of a square wave perturbation of $\pm 1\%$. Up to 2,048 pressure readings can be recorded by the on-line computer during

one adsorption or desorption half-cycle. The experiments were also carried out in the absence and presence of sorbents to subtract the dead-time of the apparatus. The adsorption and desorption uptake rate curves for each half-cycle were obtained from the difference in the pressure readings of the blank experiment and those when the sorbent was present [8, 26, 27].

3
Theoretical

3.1
Basic Principles for Treatment of Frequency Response Experimental Data

A variety of theoretical models of FR describing different mass transfer mechanisms occurring simultaneously in microporous systems and bidispersed porous systems have been comprehensively developed. A pure, single diffusion process model of an adsorbate in a zeolite sorbent was firstly derived by Yasuda [2, 4], in which the linear FR of an isothermal, batch adsorption system was considered. This work was then extended to multi-independent dynamic processes taking place in the system and to the system where diffusion processes occur coupled with a surface resistance [3]. Sun et al. developed a model for an FR system where the effect of the dissipation of the heat of adsorption on mass transport processes is taken into account [28, 29]. Grenier et al. added the measurement of the temperature response to the pressure response within a batch system to simultaneously determine heat and mass transfer resistances and included the relevant mathematical treatments [21, 22]. Do and co-workers made an in-depth analysis of various mass transport mechanisms in bidisperse adsorbents and provided guidelines for their applicability to different FR systems [24]. The study was then extended to non-isothermal systems including the influence of heat release on adsorption capacity and diffusivities [30]. They also expanded their work to the analysis of non-linear frequency response for both isothermal and non-isothermal systems by using the concept of higher-order frequency response functions (FRFs) [23, 31–33]. They found that the second order FRFs give enough information for the identification of different kinetic mechanisms. Models describing flow FR systems have also been developed by Do et al. and LeVan et al. [14, 31, 34]. Camp recently derived a preliminary theoretical diffusion model of ideal adsorbate molecules diffusing along one-dimensional channels containing random sequences of high- and low-energy barriers [18]. This model will be useful to investigate the kinetic mechanisms occurring in heterogeneous catalytic or separation processes which usually involve porous catalysts or sorbents containing different cationic species or increasing concentrations of internal coke.

In this chapter, we focus only on the theoretical analyses of a linear, batch FR adsorption system in which pressure changes respond to periodic volume perturbations of ±1% as these models have been commonly used and extensively tested experimentally. Details about the other models can be found in the references given above.

The FR data of a linear, closed system can be expressed by the in-phase and out-of-phase equations

$$\text{in-phase:} \quad (P_B/P_Z)\cos\Phi_{Z\text{-}B} - 1 = K\delta_{in} + S \tag{1}$$

$$\text{out-of-phase:} \quad (P_B/P_Z)\sin\Phi_{Z\text{-}B} = K\delta_{out} \tag{2}$$

derived from the solution of Fick's second law for the diffusion of diffusants in a solid subjected to a periodic, sinusoidal surface concentration modulation [4, 35, 36]. K is a constant related to the gradient of the adsorption isotherm, S is a constant that represents a very rapid adsorption/desorption process, which may co-exist with the diffusion processes being measured, δ_{in} and δ_{out} are the respective overall in-phase and out-of-phase characteristic functions.

For the FR system with a closed volume perturbed by a square-wave, the FR parameters of the amplitude ratio P_B/P_Z and the phase lag $\Phi_{Z\text{-}B} = \Phi_Z - \Phi_B$ can be experimentally derived from a Fourier transformation of the volume and the pressure square-wave modulations [9, 36–39]. Φ_Z and Φ_B are the phase lags and P_B and P_Z are the pressure responses to the ±1% volume perturbations in the absence and presence of sorbents, respectively.

Generally, the FR parameters can be derived for the equivalent fundamental sine-wave perturbations from the first harmonic Fourier transformation of the input and the pressure response signals. The higher harmonics can, also, be used to extend the experimental frequency range by a factor of n ($n > 1$, where n is an odd number) when high quality response data are available [9, 37, 39].

The overall in-phase and out-of-phase characteristic functions on the RHS of Eqs. 1 and 2 depend on the theoretical models describing the overall kinetic processes involved in the system. By fitting the experimental data on the LHS with the theoretical models on the RHS of the equations, diffusion coefficients and some other kinetic parameters which are included in the overall FR characteristic functions can be extracted.

3.2 Prediction of Diffusivities

The overall in-phase and out-of-phase characteristic functions rely on the kinetic mechanisms involved in the FR system. As mentioned in Sect. 3.1, various theoretical models have been developed to cover the multi-kinetic processes taking place in the system. Some commonly used models are summarised in the following sections.

3.2.1
Single Diffusion Process Model

When only a single intracrystalline diffusion process occurs in a microporous system, the characteristic functions are [2, 3]

$$\text{in-phase:} \qquad K\delta_{\text{in}} = \frac{RTV_{\text{s}}K_{\text{P}}}{V_{\text{e}}}\delta_{\text{c}} \tag{3}$$

$$\text{out-of-phase:} \quad K\delta_{\text{out}} = \frac{RTV_{\text{s}}K_{\text{P}}}{V_{\text{e}}}\delta_{\text{s}}\,, \tag{4}$$

where R is the gas constant, T is the isotherm temperature, V_{s} is volume occupied by the sorbent, V_{e} the mean volume of sorbate outside the sorbent and K_{p} is the equilibrium constant based on pressure.

For crystals of a slab shape, δ_{c} and δ_{s} are given by [2]

$$\delta_{\text{c}} = \frac{1}{\eta}\left(\frac{\sinh\eta + \sin\eta}{\cosh\eta + \cos\eta}\right) \tag{5}$$

$$\delta_{\text{s}} = \frac{1}{\eta}\left(\frac{\sinh\eta - \sin\eta}{\cosh\eta + \cos\eta}\right)\,. \tag{6}$$

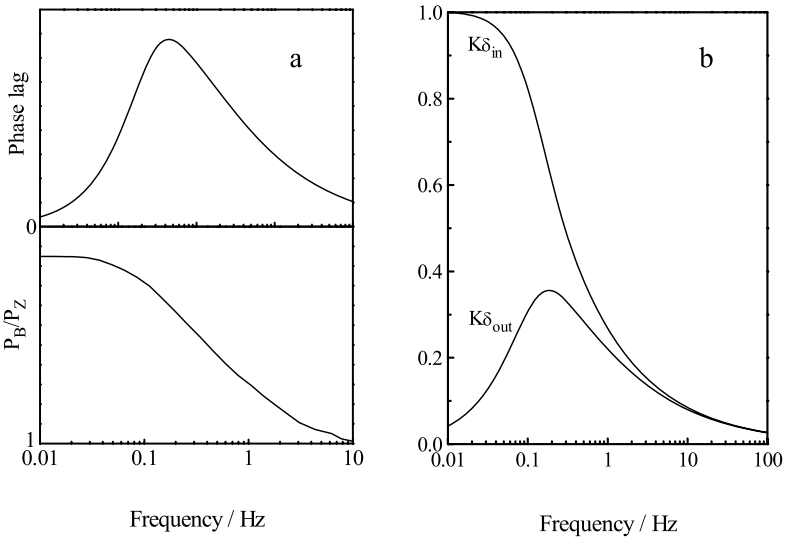

Fig. 3 The ideal shape of the phase lag, $\Phi_{\text{Z-B}}$, and amplitude ratio, $P_{\text{B}}/P_{\text{Z}}$, curves vs. frequency (**a**) and the relevant theoretical characteristic functions, $K\delta_{\text{in}}$ and $K\delta_{\text{out}}$, for a single diffusion process occurring in microporous spherical crystals when $l = 10\,\mu\text{m}$, $K = 1$, and $D = 10^{-11}\ \text{m}^2\,\text{s}^{-1}$

For diffusion in spherical crystals, δ_c and δ_s are given by [2]

$$\delta_c = \frac{3}{\eta}\left(\frac{\sinh\eta - \sin\eta}{\cosh\eta - \cos\eta}\right) \tag{7}$$

$$\delta_s = \frac{3}{\eta}\left(\frac{\sinh\eta + \sin\eta}{\cosh\eta - \cos\eta} - \frac{2}{\eta}\right), \tag{8}$$

where $\eta = (2\omega l^2/D)^{1/2}$, ω is the angular frequency, $f = \omega/2\pi$ = frequency, l is the half thickness of the slab or the radius of the sphere, and D the intracrystalline transport diffusion coefficient. Solutions similar to Eqs. 5–8 have also been carried out for parallelepiped crystals and anisotropic diffusion [40].

The ideal shape and location of the phase lag $\Phi_{Z\text{-}B}$ and amplitude ratio P_B/P_Z curves and the relevant characteristic functions versus frequency are displayed in Fig. 3.

3.2.2 Two Independent Diffusion Processes Model

When two diffusion processes occur simultaneously, provided they are independent of each other, the theoretical treatment can be expanded to give [2, 41, 42]

$$\text{in-phase:} \quad K\delta_{in} = K_1\delta_{c,1} + K_2\delta_{c,2} \tag{9}$$

$$\text{out-of-phase:} \quad K\delta_{out} = K_1\delta_{s,1} + K_2\delta_{s,2}, \tag{10}$$

where subscripts 1 and 2 indicate the two separate kinetic processes. The characteristic functions δ_c and δ_s are also generated by Eqs. 5–8. Figure 4 demonstrates the typical characteristic functions of this bimodal model, where the overall curves can be decomposed into their respective separate components I and II.

3.2.3 Non-Isothermal Diffusion Model

Periodic adsorption and desorption inside adsorbent particles, induced by the volume modulation, may lead to a heat of sorption effect which is dissipated through a heat exchange between the sorbent and the surroundings. When the heat exchange rate is comparable with the diffusion rate, another bimodal form for the frequency response characteristic curves is found [28, 29].

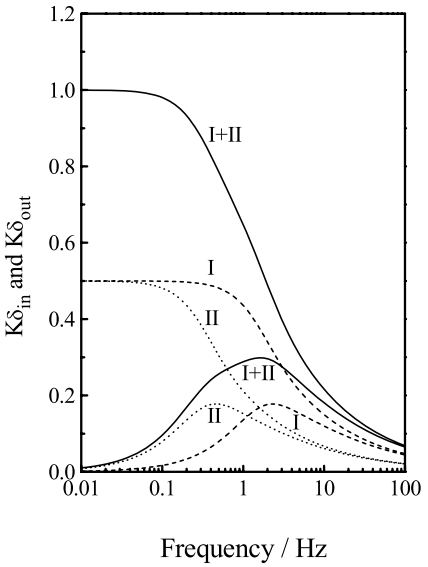

Fig. 4 Typical theoretical characteristic functions, $K\delta_{in}$ and $K\delta_{out}$, for two independent diffusion processes (I + II) when $K_I = K_{II} = 0.5$, $l_I = l_{II} = 20\,\mu m$, and $D_I = 5 \times D_{II} = 5 \times 10^{-10}\ m^2\ s^{-1}$

The overall characteristic functions δ_{in} and δ_{out} for this model are given by

$$\text{in-phase:} \qquad K\delta_{in} = \frac{RTV_s K_P}{V_e}\left(\frac{\delta_c(1+\omega^2 t_h^2) + \gamma(\delta_c^2+\delta_s^2)\omega^2 t_h^2}{(1+\gamma\delta_s\omega t_h)^2 + (1+\gamma\delta_c)^2\omega^2 t_h^2}\right) \tag{11}$$

$$\text{out-of-phase:} \quad K\delta_{out} = \frac{RTV_s K_P}{V_e}\left(\frac{\delta_s(1+\omega^2 t_h^2) + \gamma(\delta_c^2+\delta_s^2)\omega t_h}{(1+\gamma\delta_s\omega t_h)^2 + (1+\gamma\delta_c)^2\omega^2 t_h^2}\right), \tag{12}$$

where t_h is the time constant for heat exchange between the sorbent and its surroundings, and

$$\gamma = K_T Q_{st}/C_s \tag{13}$$

is a measure of the non-isothermality of the system. Q_{st} is the heat of adsorption, C_s is the volumetric heat capacity of the sorbent and K_T is derived from the adsorption isotherm with respect to temperature and defined by

$$K_T = \frac{P_e Q_{st}}{RT^2} K_P\,. \tag{14}$$

δ_c and δ_s are also given by Eqs. 5 and 6, respectively, for slab-shaped crystals and Eqs. 7 and 8, respectively, for spherical crystals.

3.2.4
Diffusion with Surface-Resistance or Surface-Barrier Model

When surface-barriers or a surface-resistance or "skin" effect to sorbate gases occurs, the overall characteristic functions can be indicated by [3, 43, 44]

$$\text{in-phase:} \quad \delta_{\text{in}} = \left(ak_{\text{-A}}/\omega\right)^2 \left(a + c\delta_{\text{c}}\right)/\theta \tag{15}$$

$$\text{out-of-phase:} \quad \delta_{\text{out}} = \left(ak_{\text{-A}}/\omega\right)\left[1 - \left(ak_{\text{-A}}/\omega\right)\left\{\left(ak_{\text{-A}}/\omega\right) + c\delta_{\text{s}}\right\}/\theta\right] \tag{16}$$

where $k_{\text{-A}}$ is the rate constant for the resistance-affected process, δ_{c} and δ_{s} are the same as those in Eqs. 5–8 for slab and spherical crystals respectively, and

$$\theta = \left\{\left(ak_{\text{-A}}/\omega\right) + c\delta_{\text{s}}\right\}^2 + \{a + c\delta_{\text{c}}\}^2 \tag{17}$$

$$c \equiv \left(\mathrm{d}C/\mathrm{d}P\right)_{\text{e}} / \left\{d\left(A + C\right)/\mathrm{d}P\right\}_{\text{e}} = 1 - a \tag{18}$$

Here A is the concentration of adspecies on the external surface, C is the concentration adspecies within the porous adsorbent and P is the pressure and the subscript indicates the equilibrium. The following are the constants: $a \approx 10^{-2}$ and $c \approx 1$ for most zeolites.

The magnitude of the surface resistance can be seen from the area to the right of the intersection between the in-phase and the out-of-phase characteristic function curves as presented in Fig. 5. The surface resistance depends on

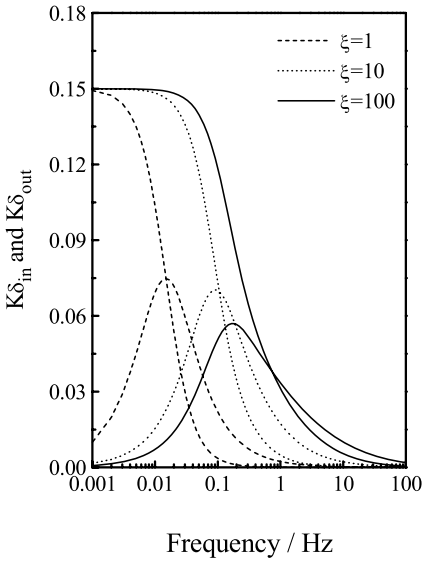

Fig. 5 Theoretical FR spectra for diffusion with surface resistance with ξ as a parameter for spherical crystal geometry when $K = 0.15$ and $D/r^2 = 0.1\ \text{s}^{-1}$

the ratio of ξ defined by

$$\xi = ak_{\text{-A}}/\left(D/l^2\right) \tag{19}$$

suggesting that the "skin" effects depend not only on the ratio of the rate constants of the process related to the surface resistance and of the diffusion processes, but also on the size of crystals. Increasing values of ξ indicates a decreasing "skin" effect as shown in Fig. 5 [44, 45].

For FR spectra, if the experimental range of frequency is wide enough to cover all the rate processes occurring in a system, the asymptotes of the in-phase and out-of-phase characteristic curves should satisfy the following two relations [3]

$$\lim_{\omega\to\infty}\left(P_{\text{B}}/P_{\text{Z}}\right)\cos\Phi_{\text{Z-B}} - 1 = 0 \quad \text{and} \quad \lim_{\omega\to\infty}\left(P_{\text{B}}/P_{\text{Z}}\right)\sin\Phi_{\text{Z-B}} = 0 \tag{20}$$

$$\lim_{\omega\to 0}\left(P_{\text{B}}/P_{\text{Z}}\right)\cos\Phi_{\text{Z-B}} - 1 = K = \frac{RTV_{\text{s}}K_{\text{P}}}{V_{\text{e}}} \quad \text{and} \quad \lim_{\omega\to 0}\left(P_{\text{B}}/P_{\text{Z}}\right)\sin\Phi_{\text{Z-B}} = 0\,. \tag{21}$$

The diffusion coefficients and the other parameters such as $\gamma, \xi, k_{\text{-A}}$, etc. can be obtained by a least-square curve-fitting of the experimental in-phase and out-of-phase FR data with the related theoretical characteristic functions.

3.2.5
Mass Transport in Pellets of Microporous Materials or Membranes

Crystals of microporous materials must be formed into pellets of suitable dimensions, porosity and mechanical strength, or be formed into a membrane on the surface of support materials when used in practice. Such composite pellets or membranes offer a bidispersed porous structure, with macro- or mesopores between the crystals and micropores permeating the crystals. The overall rate of the transport in such systems depends on the interplay of various processes occurring within the pellets or membranes. Jordi and Do [24, 46] have developed a general theoretical model and seven relevant degenerate models to analyse the frequency response spectra of a system containing bidispersed pore structure materials for slab, cylindrical and spherical macro- and micropore geometry. Sun et al. [47] also reported the theoretical models of the FR for non-isothermal adsorption in biporous sorbents.

The overall characteristic functions δ_{in} and δ_{out} for a system involving biporous materials are [24]

$$\text{in-phase:} \qquad \delta_{\text{in}} = \delta_{\text{c},s_{\text{M}}}\left(\sigma_1 + \frac{\sigma_2}{1+\lambda}\delta_{\text{c},s_\mu}\right) - \delta_{\text{s},s_{\text{M}}}\frac{\sigma_2}{1+\lambda}\delta_{\text{s},s_\mu} \tag{22}$$

$$\text{out-of-phase:} \quad \delta_{\text{out}} = \delta_{\text{s},s_{\text{M}}}\left(\sigma_1 + \frac{\sigma_2}{1+\lambda}\delta_{\text{c},s_\mu}\right) + \delta_{\text{c},s_{\text{M}}}\frac{\sigma_2}{1+\lambda}\delta_{\text{s},s_\mu}\,, \tag{23}$$

where $\delta_{\text{c},s_{\text{M}}}$ and $\delta_{\text{s},s_{\text{M}}}$, are the in-phase and out-of-phase characteristic functions for macro-particle shape factor s_{M}, and δ_{c,s_μ} and δ_{s,s_μ} are the in-phase

and out-of-phase characteristic functions for micro-particle shape factor s_μ; σ_1 and σ_2 are the fractional adsorption capacities in the macropore voids and the micro-particles, respectively. For most commercial sorbents, σ_1 is close to zero and σ_2 is close to unity. The parameter λ is a measure of the approach to saturation of the Langmuir isotherm and is defined by

$$\lambda = \frac{k_a}{k_d} C_{Be} , \tag{24}$$

where C_{Be} is a bulk sorbate concentration under equilibrium conditions, k_a and k_d are the rate constants for adsorption and desorption. Small values of λ indicate an equilibrium state in the linear region of the Langmuir isotherm, while saturation is approached as λ increases.

The ratio of the macropore diffusion rate to the micro-pore diffusion rate is defined by

$$\varepsilon = \frac{1}{\sigma_1} \frac{D_\mu R_p^2}{D_p R_\mu^2} , \tag{25}$$

where D_p and D_μ are the macro- and micropore diffusivities, respectively, R_p and R_μ are the radii of the macro- and micro-particles, respectively. If ε is small ($\ll 1$), micropore diffusion controls, while macropore resistance dominates when $\varepsilon \gg 1$.

When the macropore diffusion rate for a system involving biporous sorbents is by far faster than the micropore diffusion rate, i.e., $\varepsilon \ll 1$, the overall kinetic processes for the system can, then, be simply described by the models given in Sects. 3.2.1, 3.2.2 and 3.2.4. Details about the degenerate models describing different situations with various kinetic mechanisms involved in the bidispersed FR systems can be found in the references [24, 38, 46]. Again, the diffusivities involved in these models can be calculated by the curve-fitting of the experimental FR in-phase and out-of-phase characteristic functions.

The diffusivity measured by the FR technique, D, is a transport diffusivity which has to be corrected, by using the Darken Equation (Eq. 26), to obtain the so-called corrected diffusion coefficient where the diffusion is measured at an equilibrium pressure, P_e, which is outside the Henry's law range. This corrected diffusivity is generally taken to be the equivalent of the self-diffusion coefficient D_0:

$$D_0 = D \left(\partial \ln q / \partial \ln P_e \right)_T , \tag{26}$$

where q is the concentration absorbed at the equilibrium pressure, P_e.

3.3 Single-Step Frequency-response Method

In the analysis of the pressure data obtained by the single-step FR (SSFR) technique, where the pressure response of the system following the fast (a)

expansion and (b) compression of the volume in the absence (blank experiment) and in the presence of the microporous solid sample was recorded as shown in Fig. 6, the dead-time is first subtracted from the time scales of the blank experiment and when the sample is present. The subsequent difference in the pressure of the blank experiment and in the presence of sorbent can be considered as the amount sorbed by the solid crystals as a function of time. If M_t denotes the amount of sorbate sorbed at time t and M_∞ the corresponding amount after infinite time, e.g.,, at sorption equilibrium, then the adsorption and desorption rate curves can be obtained by plotting M_t/M_∞ against the square root of time, as shown in Fig. 7.

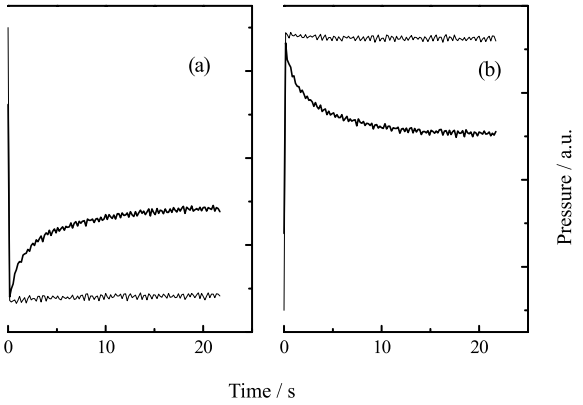

Fig. 6 Pressure changes of benzene response to a volume decrease (**a**) and increase (**b**) in the absence (*horizontal line*) and in the presence (*curve line*) of silicalite-1 (cf. [65]) sample

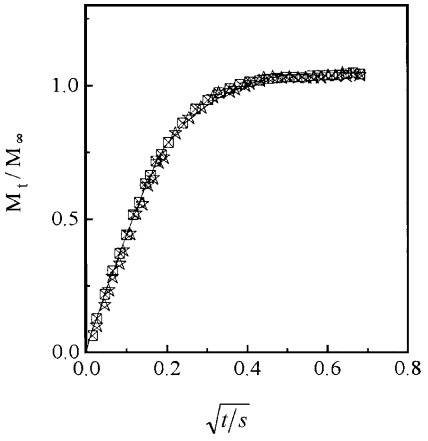

Fig. 7 Sorption uptake-rate curves of benzene in 50 mg of NaX (cf. [65]) at 440 K and 2.0 Torr. □ and ∗ denote adsorption and desorption processes, respectively. The *continuous line* is obtained from Eq. 26 with a fractional uptake of 0.6 and $D = 4.9 \times 10^{-10}$ m^2 s^{-1}. Note: 1 Torr = 133.33 Pa

As the pressure in the gas phase is not constant during the rate measurements, the changing boundary conditions have to be taken into account. Two different representative treatments of the M_t/M_∞ data are given below.

(i) The solution of diffusion controlled uptake from a well stirred solution of limited volume [48] was employed to fit the sorption uptake rate curves. The solution of the diffusion equation for a sphere with radius r is given by

$$\frac{M_t}{M_\infty} = 1 - 6\sum_{n=1}^{\infty} \frac{\alpha(\alpha+1)\exp\left(-Dq_n^2 t/r^2\right)}{9 + 9\alpha + q_n^2\alpha^2}\,, \tag{27}$$

where the values of q_n are the non-zero roots of

$$\tan q_n = \frac{3q_n}{3 + \alpha q_n^2} \tag{28}$$

and α is the ratio of the concentration of sorbate in the gas phase to the concentration in the sorbent after infinite time, i.e., when equilibrium is established.

The corresponding solutions for diffusion in cylindrical and slab crystals can also be obtained [48].

(ii) From the early time linear plots of sorption uptake against $\sqrt{t}$, the $\sqrt{t}$ law [49] for the simultaneous volume and gas-phase concentration changes can be used. The slope, $S(0)$, of a plot of $M_t - M_0$ against $\sqrt{t}$ is given by [49]

$$S(0) = 2A\left(\frac{D}{\pi}\right)^{1/2}\left[\frac{\frac{kV_g(\infty)}{V_g(0)}C_g(\infty)\left(1+\frac{M_\infty - M_0}{\alpha M_\infty}\right)}{1+\frac{KV_g(\infty)}{V_g(0)}C_g(\infty)\left(1+\frac{M_\infty - M_0}{\alpha M_\infty}\right)} - M_0\right]\,, \tag{29}$$

where C_g is the concentration of diffusant in the gas phase and M_0 the concentration of sorbate in the sorbent at time, $t = 0$. V_g denotes the volume of the gas phase, A the total area normal to the direction of the diffusion flux, "0" and "∞" refer to $t = 0$ and ∞, respectively, and it is $k = KM_\infty = M_t/C_g$.

In the SSFR method, the volume change of the gas phase is only $\pm 1\%$ of the total volume, therefore, $V_g(\infty)/V_g(0) \approx 1$. When sorption/desorption follows Henry's law, then Eq. 29 becomes

$$S(0) = \frac{2A}{V_s}\left(\frac{D}{\pi}\right)^{1/2}[M_\infty - M_0]\left(1 + 1/\alpha\right)\,, \tag{30}$$

where V_s is the volume occupied by the sorbent. When the experiment is carried out in the near-saturation region of the sorption isotherm, α becomes large and Eq. 29 approaches that for the infinite volume case

$$S(0) = \frac{2A}{V_s}\left(\frac{D}{\pi}\right)^{1/2}[M_\infty - M_0]\,. \tag{31}$$

By fitting the uptake curve with an appropriate model, the diffusion coefficient can be obtained which can also be corrected by using the Darken

Equation (Eq. 26) to obtain the so-called corrected diffusion, i.e., the self-diffusion coefficient. In these measurements, D is assumed to be constant. In the experiments described here, only very small perturbations from the equilibrium state are involved and, therefore, D is the differential diffusion coefficient for the equilibrium concentration of sorbates and can be safely considered to be constant.

4
Frequency-response Studies of Diffusion in Microporous Materials

An FR spectrum with a broad range of time constants can be applied to characterise multi-kinetic processes occurring in microporous materials, whereas microscopic techniques such as pulse field gradient nuclear magnetic resonance (PFG NMR) [50], quasi-elastic neutron scattering (QENS) [51] and computer simulation calculations [52] were found to be capable of measuring only very fast intracrystalline mobilities. Conventional macroscopic methods such as gravimetric uptake rate measurements can only be carried out with accuracy when longer time constants are involved [53]. The FR method has, therefore, been widely used to measure diffusivities of many different sorbates in various microporous and meso- and/or macroporous materials, e.g.,, Kr-, Xe-, ethane-, and propane-5A [39, 54], *n*-alkanes-silicalite-1 [6, 7, 42, 55–57] and –NaX [58], aromatics-silicalite-1 [10, 59–61], –$AlPO_4$-5 [62] and –NaX [26], CO_2- and propane-theta-1 [45, 63], Xe-, N_2-porous silica [20], and N_2-, O_2-carbon molecular sieves (CMS) [64], etc.(For the abbreviations and names of these zeolites cf. [65]). In this section, some FR measurement results will be presented to demonstrate the potentials and applications of the FR method in diffusion investigations of sorbates in microporous materials.

4.1
Systems Involving a Pure, Single Diffusion Process

The diffusivities can be readily derived from the FR data if only a pure, single diffusion process occurs in a microporous material system where the in-phase and the out-of-phase characteristic curves merge asymptotically at high frequencies as shown in Fig. 3b.

Figure 8 displays some typical FR data of $C_1 - C_6$ *n*-alkanes diffusing in coffin shaped crystals of silicalite-1 ($40 \times 40 \times 260\ \mu m^3$). All the spectra in Fig. 8a–f,1 can be fitted by the theoretical in-phase and out-of-phase characteristic function curves of the single diffusion model described by Eqs. 3–6, implying that only a simple, single diffusion process is involved in these systems. The diffusivities calculated from the best fit are presented in Fig. 9 and Tables 1 and 2. Equations 5 and 6 were applied since the channel framework structure of silicalite-1 is comprised of near circular (0.54×0.56 nm)

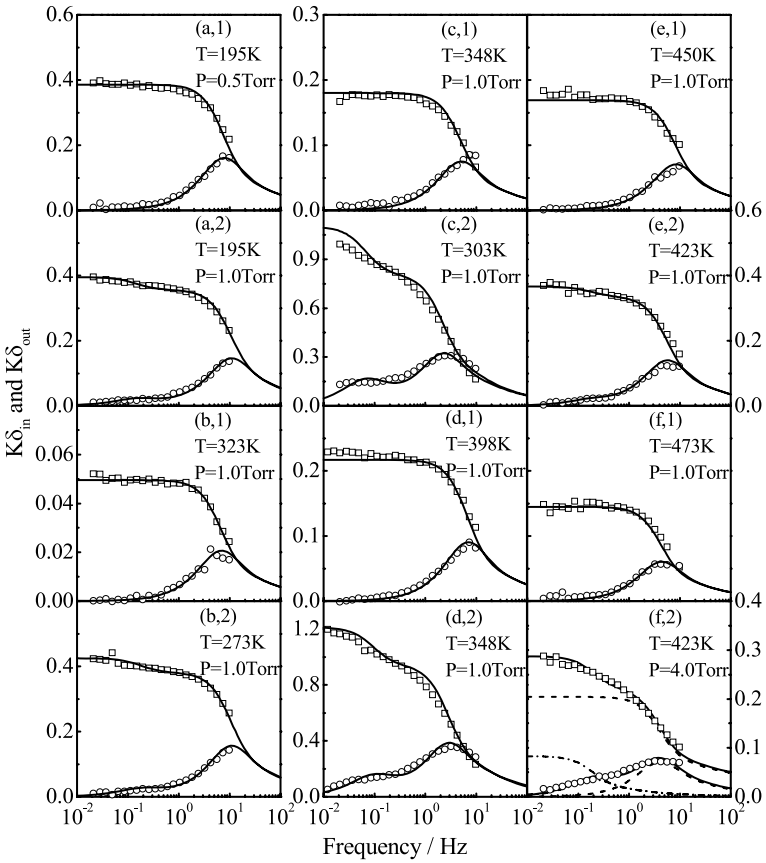

Fig. 8 FR spectra of methane (**a**), ethane (**b**), propane (**c**), *n*-butane (**d**), *n*-pentane (**e**) and *n*-hexane (**f**) in silicalite-1 (cf. [65]). (□, ○) indicate the experimental in-phase $K\delta_{in}$ and out-of-phase $K\delta_{out}$ characteristic functions, respectively. A single diffusion process model was used to fit the data in (1), while the non-isothermal diffusion model was used to fit the data in (2) except (f, 2) which was fitted using the two independent diffusion processes model. *Solid lines* denote the theoretical overall characteristic functions, and *dash* and *dash-dot lines* denote the theoretical diffusion processes occurring in the straight channels (*dash*) and the sinusoidal channels (*dash-dot*). Note: 1 Torr = 133.33 Pa

straight channels running parallel to the *b*-axis [010] which are intersected by elliptical sinusoidal channels (0.51×0.55 nm) running parallel to the *a*-axis [100] (cf. [65]). The single diffusion coefficients measured are the average diffusivities down both the straight and the sinusoidal channel directions for small *n*-alkane molecules or the diffusivity along the straight channel direction for large *n*-alkane molecules such as *n*-hexane [55–57]. The diffusivities obtained from the FR method are in good agreement with the results derived from PFG NMR measurements and other microscopic techniques as shown

Table 1 FR parameters of methane to *n*-pentane in silicalite-1[a] derived from the best theoretical fits using either the single diffusion process model or the non-isothermal diffusion model with comparison of the heat of adsorption obtained from the fits and from the literature

Sorbate	T [K]	P [Torr][b]	n_m [m./u.c.]	K_{iso}	K	$D_0 \times 10^9$ [m^2 s^{-1}]	t_h [s]	h [W m^{-2}] K^{-1}	γ	Q_{st} [kJ mol^{-1}]	Q_{st}^{iso} [kJ mol^{-1}]
Methane	195	0.5	0.20	0.34	0.35	7.7	–	–	–	–	18.4 [66]
		1.0	0.39	0.34	0.35	8.1	0.98	28.4	0.11	17.4	18.4 [66]
		2.0	0.76	0.32	0.27	6.3	1.62	17.3	0.20	18.5	18.4 [66]
		4.0	1.45	0.29	0.25	5.0	1.83	15.3	0.36	18.4	18.4 [66]
Ethane	323	1.0	0.051	0.056	0.056	11.0	–	–	–	–	30.9 [67]
	273	1.0	0.42	0.41	0.42	8.5	0.80	35.0	0.11	29.7	30.9 [67]
		2.0	0.80	0.41	0.40	7.5	1.36	20.6	0.19	29.0	30.5 [67]
		3.0	1.19	0.41	0.38	5.5	1.68	16.0	0.26	32.3	30.5 [67]
Propane	348	1.0	–	–	0.20	6.0	–	–	–	–	–
	303	1.0	1.15	1.10	1.10	1.7	1.76	15.9	0.35	33.7	44.0 [67]
		3.0	2.87	0.76	0.77	1.1	2.70	10.4	0.63	31.9	42.0 [67]
		6.0	4.58	0.48	0.45	1.0	2.79	10.0	0.83	33.8	41.0 [67]
n–butane	398	1.0	0.16	0.17	0.16	6.8	–	–	–	–	–
	373	1.0	0.36	0.32	0.31	5.8	0.46	60.9	0.12	44.0	51.0 [67]
		2.0	0.69	0.29	0.28	3.5	1.41	19.9	0.18	40.5	51.0 [67]
		4.0	1.26	0.24	0.22	4.5	1.22	22.7	0.24	37.3	52.7 [67]
		7.0	1.94	0.18	0.14	2.6	1.64	17.1	0.34	41.5	52.7 [67]
	348	1.0	1.00	0.93	0.96	2.2	1.32	21.2	0.28	37.5	48.2 [67]
n–pentane	450	1.0	0.11	0.12	0.12	8.3	–	–	–	–	–
	423	1.0	0.25	0.20	0.19	5.7	0.25	32.9	0.09	52.8	50.6 [67]
	395	0.5	0.31	0.61	0.64	3.5	0.47	59.6	0.13	49.4	50.6 [67]
		1.0	0.58	0.54	0.54	3.3	0.76	36.8	0.17	45.1	50.6 [67]
		2.0	1.00	0.44	0.40	3.2	1.02	27.5	0.24	43.5	50.6 [67]
		4.0	1.75	0.31	0.26	2.5	1.40	20.0	0.32	45.7	50.6 [67]

[a] cf. [65]
[b] 1 Torr = 133.33 Pa

Table 2 FR parameters of *n*-hexane in silicalite-1[a] derived from the best theoretical fits using the two independent diffusion processes model

T [K]	P [Torr][b]	n_m [m.[c]/u.c.]	K_{iso}	$K = [K_1 + K_2]$	$\frac{K_2}{K_1+K_2}$	$D_{01} \times 10^9$ [m^2 s^{-1}]	$D_{02} \times 10^{10}$ [m^2 s^{-1}]
473	1.0	–	–	0.12	–	4.8	–
423	0.5	0.49	2.0	1.6	0.30	2.9	1.1
	1.0	0.88	1.6	1.2	0.30	2.3	1.1
	2.0	1.45	1.1	0.8	0.33	2.2	0.9
	4.0	2.20	0.63	0.4	0.33	2.1	1.0

[a] cf. [65]
[b] 1 Torr = 133.33 Pa
[c] m.: molecule(s)

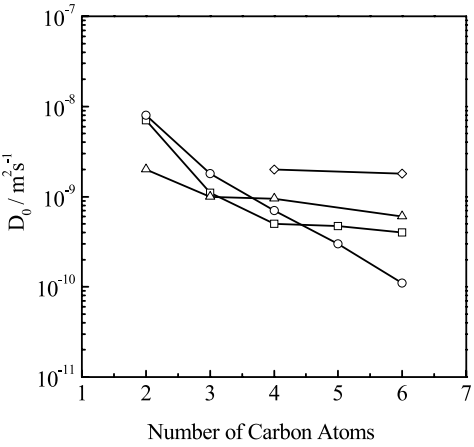

Fig. 9 Chain-length dependence of the self-diffusion coefficients of *n*-alkanes in silicalite-1 (cf. [65]) at 303 K derived from the FR technique (–□–) compared with the results measured by PFG NMR [50] at 298 K (–○–), QENS [51] (–△–) at 300 K and molecular dynamic calculations [52] (–◇–) at 300 K

in Fig. 9. Such agreement is an excellent proof that the FR method is an effective and an accurate technique for determining the diffusivities of sorbate molecules in microporous materials.

Some FR spectra of benzene in silicalite-1 crystals with a cubic shape ($4 \times 3 \times 4\ \mu m^3$) are presented in Fig. 10. Once again, all of the experimental data showed in Fig. 10a–c can be fitted by the single diffusion-model but now Eqs. 7 and 8 are applied instead of Eqs. 5 and 6 because the crystals can be assumed approximately to be spherical. These findings suggest that the mass transport of benzene in silicalite-1 framework is mainly controlled by a pure, single diffusion process at loadings < 4 molecules per unit cell (m./u.c.). The energy minimization simulations [61] of the sorbed benzene molecule in silicalite-1 give an energy barrier for benzene diffusing down the straight channel direction which is in good agreement with the experimental activation energy, implying that the single diffusion process of sorbed benzene takes place mainly along the straight channel direction. A molecular dynamic (MD) simulation run also demonstrated that the diffusion process of the sorbed benzene molecules down the straight channel direction is the dominant process [10, 61, 62].

A single diffusion process was also found by the FR method for *p*-xylene molecules sorbed in silicalite-1 at high temperatures as displayed in Fig. 11c–f. Canonical ensemble Monte Carlo and MD simulations showed that at high temperature, the *p*-xylene molecules sorbed from the external surface of the crystals into the sinusoidal channels will reorient their long axis from the sinusoidal channel direction to the straight channel direction at intersections as they diffuse down the sinusoidal channels. The higher the tempera-

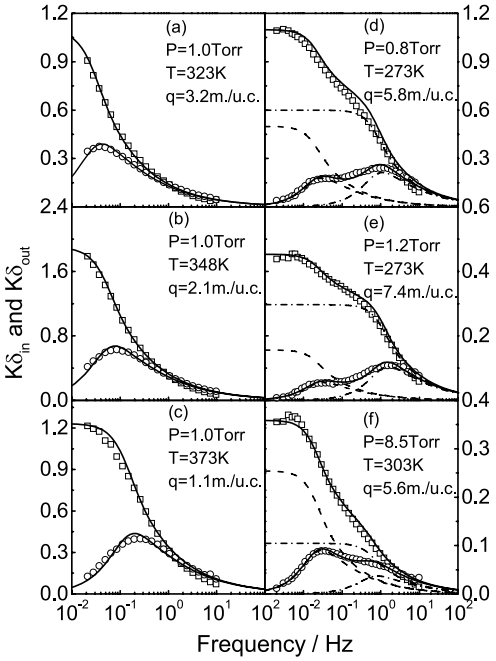

Fig. 10 FR spectra of benzene in silicalite-1 (cf. [65]). Continuous lines are the fits of the theoretical single diffusion process model (**a**–**c**) and the two diffusion processes model (**d**–**f**). The symbols (□, ○) are the experimental in-phase and out-of-phase characteristic function data, respectively. Note: 1 Torr = 133.33 Pa

ture, the easier is this rotation. On the other hand, a *p*-xylene molecule sorbed in a straight channel finds, because of the non-spherical shape of the intersection, it much more difficult to rotate and reorientate its long axis along the sinusoidal channel direction [61, 62], suggesting that the mass transport of the sorbed *p*-xylene in silicalite-1 detected by the FR method results from the single diffusion process of *p*-xylene diffusing down the straight channel direction only.

The above examples demonstrate that for a microporous material system where only a simple, single diffusion process occurs, the diffusion coefficients can be easily obtained by fitting the FR experimental data with the single diffusion process model using the least-square fitting routines. Compared with the PFG NMR and QENS techniques, the FR method is simpler and of low-cost and can follow a much wider range of diffusivities.

The range of measurable diffusivities depends on the size and the shape of the adsorbent crystals as well as the range of frequencies covered by the FR apparatus, as demonstrated in Fig. 2. Appropriate size of the crystals has to be, therefore, chosen in order to be able to detected the diffusivities of the sorbate molecules in the system.

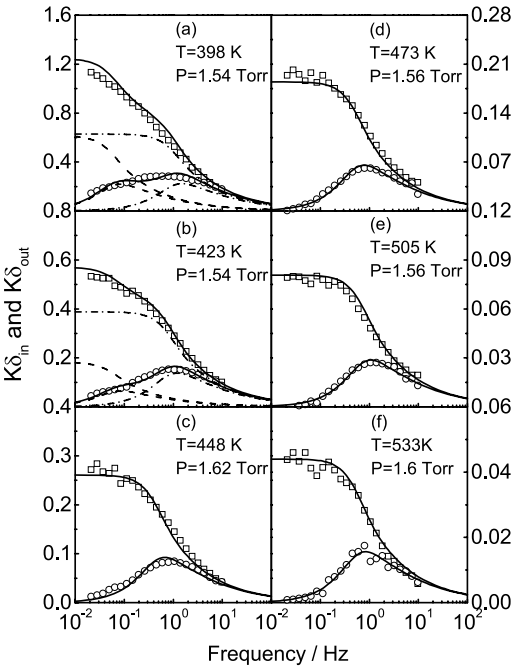

Fig. 11 FR spectra of *p*-xylene in silicalite-1 (cf. [65]). Continuous lines are the fits from the theoretical models of two diffusion processes (*dash* and *dash-dot lines* denote the theoretical characteristic function curves down the sinusoidal and the straight channels, respectively) and the symbols (□, ○) present experimental in-phase and out-of-phase characteristic function data, respectively. Note: 1 Torr = 133.33 Pa

4.2 Identification of Frequency Response Spectra

The FR method has been found to be a very powerful and unique technique for determining the mass transport rates of multi-kinetic processes occurring in various sorbate/sorbent systems. From the shape and the pattern of the spectra, information about the kinetic mechanisms taking place in the system can be obtained, which cannot be achieved from other techniques. It has been found, however, that the rate spectra or the FR spectra are not always uniquely defined and there are generally several combination of parameters, i.e., several theoretical models, which could produce the same FR spectra. Controversial interpretations of one set of experimental data have been reported in the literature [28, 59]. This difficulty can, nevertheless, be tackled by investigating systematically the systems over a wide range of reasonable or possible parameter values, e.g., variation of pressures or temperatures and by testing the validity of theoretical models by analysing the physical parameters derived from the fits.

The FR spectra of $C_1 - C_6$ *n*-alkanes in silicalite-1 shown in Fig. 8a–f,2 cannot be fitted by the single diffusion process model and a bimodal behaviour had to be assumed for these spectra. This bimodal behaviour can be elucidated by three models, i.e., non-isothermal diffusion model (cf. Sect. 3.2.3) [28, 38, 55], two independent diffusion processes model (cf. Sect. 3.2.2) [8, 38, 55, 59], and diffusion-rearrangement model [38, 55, 59, 68], which assumes that for zeolites such as MFI (cf. [65]) the sorbate molecules diffuse only along the transport channels, i.e., the straight channels, but can be stored in the sinusoidal channels, with a finite-rate mass exchange between the two channels. Which process actually operates can be determined by analysing the physical parameters derived from the fits of the theoretical models.

The FR measurements of propane in silicalite-1 (cf. Fig. 8b,2) can be used as an example for the identification of such spectra. Since the channel intersections have a free diameter of ~0.54 nm it seems reasonable to expect that a flexible propane molecule of 0.652 nm length should be able to rotate at the channel intersections. Therefore, it is unlikely that two independent diffusion processes would be observed.

By analysing the parameters obtained from the FR in-phase and out-of-phase curve fits of the non-isothermal diffusion model, it has been found that the pressure and temperature dependence of the heat transfer coefficients, the heat exchange rates, the non-isothermality of the system, the heat of adsorption, and the *K* values derived from the model are all physically rational [38, 55]. One can, therefore, conclude that the low frequency FR spectral data can be attributed to the dissipation of the heats of adsorption between sorbent and the surroundings in the system.

Similar analytical procedures show that for methane to *n*-pentane sorbates, the bimodal FR spectra found at high loadings, i.e., low temperatures and high pressures, result from the dissipation of the heats of adsorption. The mass transport processes of these systems are dominated by the diffusion of the sorbed molecules in both straight and sinusoidal channels of silicalite-1 [57, 67]. The effect of the heat of adsorption on the diffusion process only arises at high loadings. At low loadings, a pure, single diffusion process can be found as shown in Fig. 8a–e,1.

Unlike the fits for methane to *n*-pentane, the parameters obtained from the fits of the non-isothermal diffusion model for *n*-hexane in silicalite-1 are no longer plausible [56, 57, 67]. The sorbed n-hexane molecules are preferentially located in the straight channel segments at very low loadings [67], implying that the single diffusion process measured by the FR technique at these loadings can be attributed to the diffusion of *n*-hexane down the straight channel direction only [52]. When the loading increases, the sorbed molecules will occupy the sinusoidal channels as well as the straight channels due to clustering [67], resulting in two diffusion processes along the two respective channel directions. At this point the loading is still low enough for the molecules

to keep their conformational "memory" and to continue to diffuse in the channel direction where they were originally located [52], i.e., the bimodal behaviour of the FR curves of *n*-hexane in silicalite-1 presented in Fig. 8f,2 results from two independent diffusion processes down the two channel directions.

The bimodal behaviour was also found in the FR spectra of *p*-xylene in silicalite-1 at loadings < 4 m./u.c. and low temperatures as displayed in Fig. 11a,b which can be, again, ascribed to the two independent diffusion processes model. The effect of the dissipation of the heat of adsorption, which can also cause a bimodal FR spectrum as demonstrated above, can be discarded after analysing the data [28, 59–61] because i) the heat of adsorption increases with increasing loading [67], while the low frequency response in the FR spectra disappears with increasing loading; ii) the rate of heat production depends on the rate of adsorption or the diffusivities of sorbate molecules. In the case of *p*-xylene, the latter is much slower than that for the *n*-alkanes/silicalite-1 systems in which the heat effect was observed. The heat of *p*-xylene adsorption will be too slowly produced to be detected in the range of frequencies scanned. This is also true for some other cyclic hydrocarbon molecules adsorbed in silicalite-1 as the diffusivities of the cyclic hydrocarbons are even lower than those of *p*-xylene.

Canonical ensemble Monte Carlo simulations have shown that, when adsorption equilibrium is reached, the adsorbed *p*-xylene molecules will occupy the intersections of the two channels at lower loadings (< 4 m./u.c.) and low temperatures with the orientation of the long molecular axis either along the sinusoidal channel direction or the straight channel direction [61]. It has been well documented that it is difficult for even flexible, long linear hydrocarbon molecules such as *n*-hexane to lose their conformational "memory" quickly inside the host framework channels [52, 54], suggesting that molecules aligned along a particular channel will tend to move along that channel at lower loadings. Thus the bimodal FR behaviour of *p*-xylene in silicalite-1 is, without doubt, due to the sorbed *p*-xylene molecules moving independently down the straight and the sinusoidal channel directions.

As discussed above, the shape and the pattern of the FR spectra give information about the dynamic processes occurring in microporous materials which are not detected by microscopic techniques and by other macroscopic methods. When the adsorption and diffusion properties of benzene in silicalite-1 at loadings > 4 m./u.c. were investigated, two pronounced peaks in the out-of-phase curves of the FR spectra of benzene were unexpectedly found as shown in Fig. 10d–f. In these FR spectra, a new high frequency peak appeared compared with the FR data at loadings < 4 m./u.c. where only a simple, single peak was observed. It is not plausible to assign the high frequency peak to either the dissipation of the heat of adsorption or to a finite-rate mass exchange between the straight and the sinusoidal channels. The FR spectra will give only a simple, single peak if the rate of these two kinetic processes

is faster than that of the diffusion process. It is also inconceivable to associate the two peaks to two independent diffusion processes down the straight and the sinusoidal channel directions, respectively, because only a single diffusion process was detected at low loadings and this appears at low frequencies, i.e., with a slow rate, which has been attributed to diffusion of benzene along the straight channel direction. It is unreasonable to assume that sorbed benzene molecules at high loadings diffuse down the sinusoidal channel direction faster than those at low loadings down the straight channel. The adsorption simulations showed that some of the sorbed benzene molecules are clustered at loadings > 4 m./u.c [10, 69, 70], leading to two different states of the sorbed molecules existing in the framework, i.e., a clustered state and an unclustered state. The differential thermogravimetric (DTG) studies of this system showed that the benzene molecules sorbed above a loading of 4 m./u.c. desorbed more easily than those sorbed at lower loadings [10, 70]. As the molecules at high loadings are sorbed with higher heats of adsorption, mainly because of sorbate-sorbate interactions [10, 70], the ease by which they are desorbed must be due to gains in entropy on desorption as the main driving force. These results imply that the new high frequency peak at high loadings for benzene in silicalite-1 should be related to a diffusion process involving molecules associated with the clustered state while the low frequency peak, which has a time constant similar to that for the single frequency peak at high temperatures and low loadings, must be associated with the diffusion of sorbed molecules located at the intersection sites and not part of clusters. This clustering effect was also found with cyclopentane sorbed in silicalite-1 at high loadings [62]. To the best of our knowledge, this fast diffusion process has not been observed by any other technique.

The effect of a surface resistance or surface barrier on the diffusivities of sorbate molecules in microporous materials can also be observed using the FR technique. From the area to the right of the intersection between the in-phase and the out-of-phase curves the surface-resistance or surface barrier can be easily determined qualitatively. They can also be obtained quantitatively from the theoretical model (cf. Sect. 3.2.4). Such a "skin" effect was found in the FR investigations of the diffusivities of N_2, CO, CO_2 and propane in theta-1 zeolite [45, 63] as illustrated in Figs. 12 and 13, and was attributed to the fact that a single-file diffusion process was occurring in the system [71, 72]. These FR experimental data can be well fitted by the model of diffusion with surface-resistance described in Sect. 3.2.4 with the parameters given in Table 3. The intersection areas indicate the presence of a surface resistance on the external surfaces of theta-1 crystals associated with the diffusion process. This area depends on the ratio of the rate constants of processes related to surface resistance and diffusion processes, which is defined by the parameter ξ in Eq. 19. A large value ξ corresponds to a small "skin" effect.

For both CO_2 and propane sorbed in theta-1 systems, the ξ values increase with increasing temperature and decrease with increasing loading,

Table 3 FR parameters of N_2, CO, CO_2 and propane diffusion in theta-1[a] derived from the fits by using the single-diffusion with surface resistance model

Sorbate	T [K]	P [Torr][b]	$D_0 \times 10^{10}$ [$m^2\ s^{-1}$]	k_{-A} [s^{-1}]	K	ξ
N_2	245	5.0	4.9	471	0.155	11.8
CO	195	2.0	1.5	45	0.56	3.8
CO_2	273	2.0	1.5	60	0.87	5.0
	298	2.0	2.4	150	0.44	7.5
	323	2.0	2.9	450	0.22	19.2
	348	2.0	4.0	626	0.11	18.9
Propane	348	0.27	0.19	3.5	0.48	2.9
	373	0.8	0.26	4.0	0.20	3.2
	398	1.16	0.2	4.0	0.20	2.8
	423	1.16	0.65	23	0.089	5.6
		2.0	0.62	21	0.088	5.4
		4.0	0.51	12	0.082	3.7
		3.1	1.3	92	0.042	11.3

[a] cf. [65]
[b] 1 Torr = 133.33 Pa

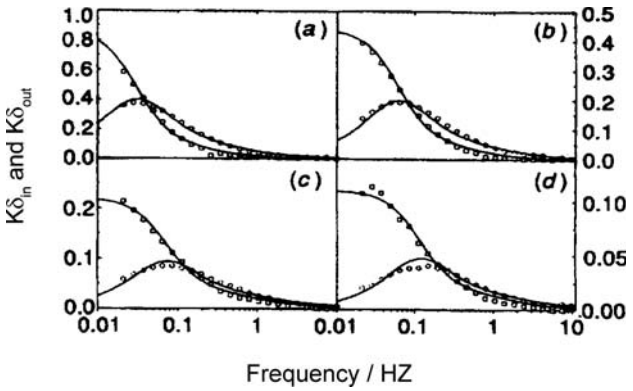

Fig. 12 FR experimental data (□, ○) of CO_2 diffusion in 0.4 g theta-1 (cf. [65]) at 2.0 Torr and temperatures of 273 (**a**), 298 (**b**), 323 (**c**) and 348 K (**d**) fitted by the single diffusion process with surface resistance model. Note: 1 Torr = 133.33 Pa

suggesting that the "skin" effect becomes more significant at low temperatures and high loadings. These findings justify the assumption that the "skin" effect observed in these systems by using the FR technique arises from the single-file diffusion mechanism involved. A surface resistance arising from the structure constraint of sorbate molecules should be very insignificant

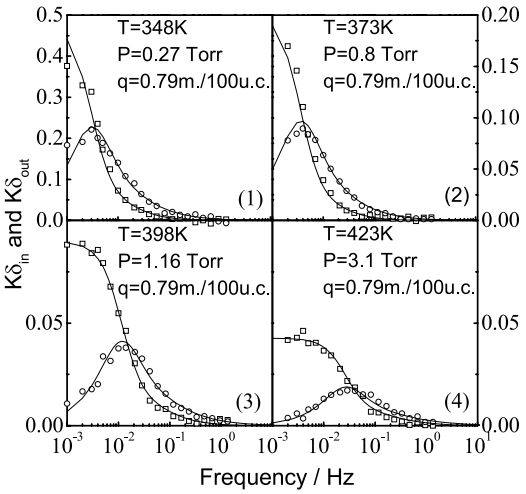

Fig. 13 FR experimental data (□, ○) of propane in theta-1 (cf. [65]) fitted by the single diffusion process with surface resistance model. Note: 1 Torr = 133.33 Pa

for small molecules such as CO_2 and propane. In addition, such surface resistance should be more pronounced at low loadings when the ratio of the external surface adspecies to the adspecies inside the channels of zeolite is at a maximum, which is inconsistent with the above FR results. For single-file diffusion, molecules can propagate only when an empty site is created in the direction of their diffusion. The molecules adsorbed at the entrances of the channels of theta-1 cannot, therefore, move into the channels until the adjacent ones move further down the channels. Similarly, the molecules inside the channels cannot move out of the channels unless the molecules at the entrances escape from the surface of the zeolite, implying that the rate of adsorption and desorption of the molecules at the end of the channels plays a significant role on the single-file diffusion process [71, 72]. The rate of adsorption and desorption of the molecules at the end of the channels becomes higher at high temperatures, which can reduce the surface resistance, whereas high loadings will result in higher occupancies of pore mouth sites, which will increase the surface resistance. It is reasonable to expect that, if the temperature is high enough or the loading low enough (e.g., $\leq$ one molecule per channel section), the surface resistance will vanish and a pure normal diffusion process will be observed. The spectra in Fig. 12 support this conclusion.

The FR measurements of fast kinetic processes require very large crystals or high frequencies. As mentioned above, the higher harmonic ($n > 1$, where n is an odd number) Fourier transformations can be used to extend the experimental frequency range by a factor of n when high quality response data are available.

Figure 14a shows the fundamental frequency response curves of CO_2 diffusion in silicalite-1 at 273 K and 2 Torr equilibrium pressure [45]. It can be seen that the frequency range scanned for this fast diffusion process was not wide enough to define the full range of the response curves. Only the left-hand sides of the response curves were obtained. Higher harmonic Fourier transforms are, therefore, necessary to derive data points above the highest experimental frequency of 10 Hz. Figure 14b presents the third, fifth, seventh and ninth harmonic frequency response spectra of the same raw data superimposed on the fundamental points [45]. It can be seen that these higher harmonic data repeat well the fundamental data at frequencies below 10 Hz and the full range of the response curves can now be covered. Excellent agreement between these higher harmonic data points and the theoretical lines fitted using the single diffusion model can be observed. These higher har-

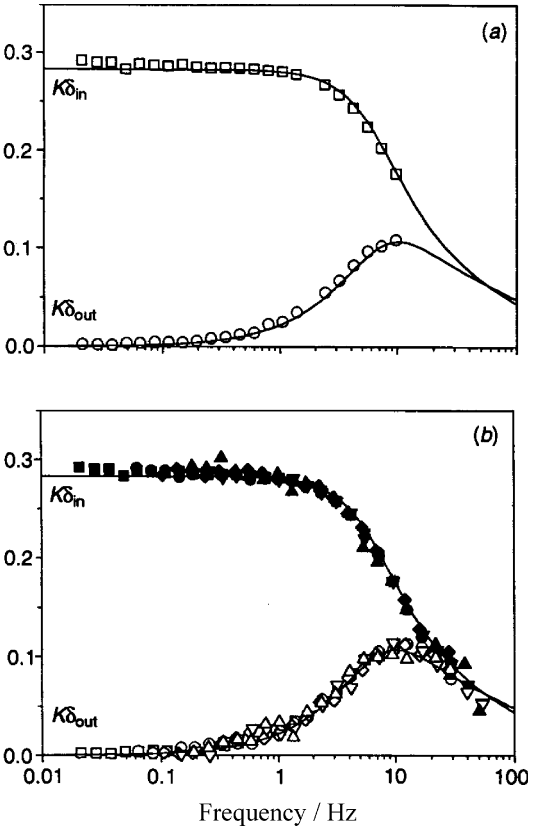

Fig. 14 FR response curves of CO_2 diffusion in silicalite-1 at 273 K and 2.0 Torr. **a** The fundamental frequency response data; **b** the first (■, □), third (●, ○), fifth (♦, ◇), seventh (▼, ▽) and ninth (▲, △) harmonic frequency data fitted by the theoretical model (*lines*) with $D = 2.5 \times 10^{-9}$ m^2 s^{-1} and $K = 0.27$. Note: 1 Torr = 133.33 Pa

monic Fourier transforms widen the dynamic timescales that can be followed by the FR method from 0.1–1000 s to 0.01–1000 s.

To tackle the difficulty of the identification of the FR spectra, Do and co-workers have developed non-linear frequency response models for both isothermal and nonisothermal systems by using the concept of higher-order FRFs [23, 31–33]. By applying the second order FRFs, these theoretical models are able to give unique FR spectra for the multi-kinetic mechanisms occurring in microporous material systems [33]. More parameters have to be measured experimentally, however, which needs a more complex apparatus, and there are no experimental data available yet to test the proposed models.

4.3 Diffusivity Interdependence on Sorbate Properties and Microporous Structures

From the FR spectra, the influence of the subtle differences in molecular shape and size of sorbates and the effect of porous framework structures on the diffusivities of the systems can be readily observed as demonstrated in Figs. 8–18 and Tables 1–4.

The mass transport of benzene in silicalite-1 is mainly controlled by a pure, single diffusion process at loadings < 4 m./u.c. At high loadings, however, a pronounced bimodal FR spectrum was observed with a new peak appearing at a high frequency. This bimodal behaviour has been attributed to diffusion processes associated with two different states of the benzene molecules sorbed in the channels of silicalite-1 as discussed in Sect. 4.2. Analogous to this diffusion behaviour of benzene, two distinct peaks were also found in the FR spectra of cyclopentane in silicalite-1 at loadings higher than 4 m./u.c., and this bimodal behaviour of cyclopentane can be similarly ascribed as that for benzene. The diffusion coefficients of both benzene and cyclopentane in silicalite-1 are of the same order of magnitude.

For *p*-xylene, the sorbed molecules diffuse down the direction of both the straight and sinusoidal channels in silicalite-1 at loadings < 4 m./u.c. and low temperatures. At high temperatures, however, only a pure, single diffusion process can be detected. Surprisingly, the sorbed *p*-xylene molecules diffuse faster down the straight channel direction than benzene, a smaller molecule than *p*-xylene. The diffusivities of the four aromatics illustrated in Fig. 15 show a decrease in the order of *p*-xylene > toluene > benzene > ethylbenzene.

The higher diffusivities of *p*-xylene compared to those of benzene in silicalite-1 can be ascribed to the combination of enthalpy and entropy effects [60–62]. The sorbed benzene molecules have to lose their rotational freedom around their hexagonal axis, C_6, when they move from an intersection to a channel segment, i.e., there is a large decrease in entropy in this jump step. For *p*-xylene, the molecules are, however, orientated with their long molecular axis along either channel direction when they are located at an intersection. The diffusion jump step involves, therefore, only a very small

Table 4 Diffusion coefficients of the cyclic hydrocarbons in silicalite-1[a] measured by the FR method

Sorbate	T [K]	n_m [m.[b]/u.c.]	D_{01}[c] $\times 10^{13}$ [$m^2\ s^{-1}$]	D_{02}[d] $\times 10^{13}$ [$m^2\ s^{-1}$]
Benzene	273	5.8	19.4	0.53
	303	5.6	14.6	0.52
	373	1.1	–	2.58
Toluene	323	4.1	0.35	–
	373	2.0	9.6	0.83
	415	0.5	13.4	–
EB[e]	373	2.9	1.02	–
	415	0.81	7.04	–
p-xylene	323	4.9	7.4	–
	373	3.9	160	15
	473	–	210	–
CP[f]	253	3.8	14.3	0.22
	273	3.6	–	0.83
	373	0.64	9.4	1.5
CH[g]	423	–	0.06	–
cis-DMCH[h]	398	–	< 0.01	–
trans-DMCH[i]	398	–	0.55	–
	448	–	2.9	–

[a] cf. [64]
[b] m.: molecule(s)
[c] Related to the faster diffusion process for benzene and cyclopentane, where two processes exist; for the other sorbates, related to the diffusion process along the straight channel direction
[d] Related to the slower diffusion process where two processes exist or to the single diffusion process for benzene and cyclopentane; for *p*-xylene and toluene, related to the diffusion process down the sinusoidal channel direction
[e] ethylbenzene
[f] cyclopentane
[g] cyclohexane
[h] *cis*-dimethyl cyclohexane
[i] *trans*-dimethyl cyclohexane

entropy decrease compared with benzene. In addition, the energy barriers which have to be overcome are higher for benzene than those for *p*-xylene down the straight channel direction as confirmed by the activation energies listed in Table 5, suggesting that the longer *p*-xylene molecules span across high and low energy sorption sites. This is also true for toluene sorbed in silicalite-1, and that the diffusivity of toluene is faster than that of benzene is mainly due to this enthalpy effect. A large entropy loss will also be required for the sorbed toluene molecules to move from the intersections to the channel segments because the pitching of the asymmetric toluene molecules will

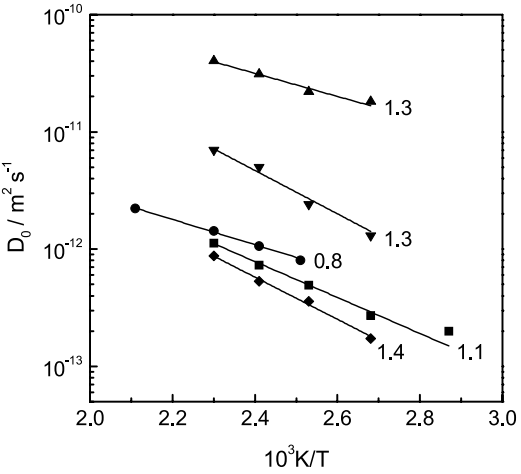

Fig. 15 Arrhenius plots of benzene (■), toluene (●), ethylbenzene (♦) and *p*-xylene in straight channel (▲) and sinusoidal channel (▼) in silicalite-1. The numbers at the *lines* are the number of sorbed molecules per unit cell

Table 5 Activation energies, E_a, of cyclic hydrocarbons diffusing in silicalite-1 [a] channels

Sorbate	E_a [kJ mol^{-1}]
p-xylene	19.0[b], 35.0[c] [60]
Benzene	28.8 [60]
Toluene	20.3 [60]
Cyclohexane	48.1 [73]
cis-DMCH[d]	56.0 [73]
trans-DMCH[e]	38.9 [73]

[a] cf. [64]
[b] related to the straight channels
[c] related to the sinusoidal channels
[d] *cis*-dimethyl cyclohexane
[e] *trans*-dimethyl cyclohexane

be more restricted in the channel segments than in the intersections. The enthalpy effect plays a much more important role in the much slower diffusivity of *p*-xylene in the sinusoidal channels than the entropy effect.

The effect of subtle differences in certain properties of sorbate molecules on the diffusivities can be very intriguingly demonstrated in Fig. 16. With shape and size close to that of *p*-xylene, the long, rigid molecule, *p*-dichlorobenzene (*p*-DCB) displays an FR behaviour in silicalite-1 very similar to that of *p*-xylene. The flexible saturated cyclic hydrocarbons diffuse much more slowly within the channel framework of silicalite-1 than their rigid aromatic

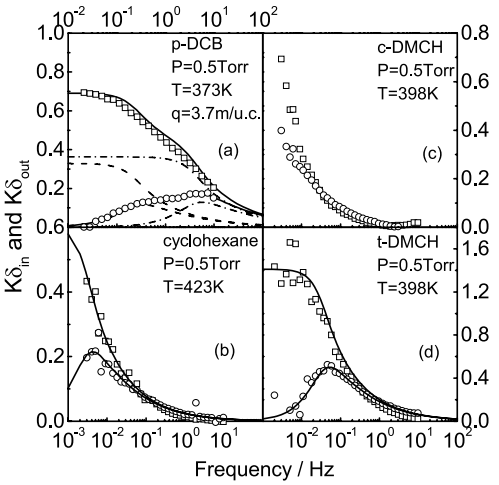

Fig. 16 FR spectra of *p*-DCB (**a**), cyclohexane (**b**), *c*-DMCH (**c**) and *t*-DMCH (**d**) in silicalite-1 (cf. [65]). *Continuous lines* are the fits of the theoretical single diffusion process model (**b** and **d**) and the two diffusion processes model (**a**) in which *dash* and *dash-dot lines* denote the theoretical characteristic function curves for diffusion down the sinusoidal channels and straight channels, respectively, decomposed from the *solid line* overall characteristic functions. The symbols (□, ○) are the experimental in-phase and out-of-phase characteristic function data, respectively. Note: 1 Torr = 133.33 Pa

equivalents and only one single diffusion process can be observed. As found in the case of *p*-xylene and benzene, trans-dimethylcyclohexane (DMCH) diffuses at least one order of magnitude faster than cyclohexane. The *cis*-DMCH, on the other hand, diffuses more slowly than cyclohexane. These findings suggest that molecular dimension and flexibility are crucial factors in determining sorbent/sorbate interactions especially when the size of the sorbate molecule is comparable with the pore size of microporous materials. These results can be ascribed, once again, to entropy and enthalpy effects in the systems.

The influence of microporous framework structures on the diffusivities of the sorbed molecules is illustrated in Fig. 17 where $AlPO_4$-5 was used for the FR measurements of the saturated cyclic hydrocarbons and their equivalent aromatics instead of silicalite-1. Unlike the complex diffusion behaviour in silicalite-1, all sorbate molecules adsorbed in the unidirectional cylindrical channels of $AlPO_4$-5 display a simple FR spectrum but with a surface resistance component. Interestingly, the diffusivities of *cis*- and *trans*-DMCH in $AlPO_4$-5 are now very similar and, also, similar to that for benzene. These results are very different from those above with silicalite-1. The diffusivities of *p*-xylene, cyclohexane and cyclopentane are a little slower than that of benzene whereas in silicalite-1, the diffusivity of *p*-xylene along the straight channel direction is ca. one order of magnitude faster than that of benzene

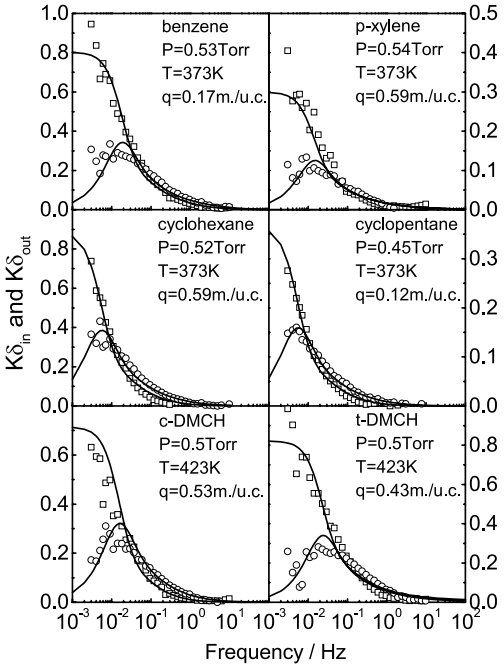

Fig. 17 FR spectra of cyclic hydrocarbons in $AlPO_4$-5 (cf. [65]). Continuous lines are the fits of the theoretical diffusion with surface-resistance or surface-barrier model. The symbols (□, ○) are the experimental in-phase and out-of-phase characteristic function data, respectively. Note: 1 Torr = 133.33 Pa

and the diffusivity of cyclohexane is ca. two order of magnitude slower than that of benzene. The surface resistance is also associated with the single-file diffusion occurring in these systems as discussed for the systems of CO_2 and propane sorbed in silicalite-1 [62].

The pore structure effect can also be seen in Fig. 18 where a comparison of the temperature dependence of propane diffusivities in theta-1 and silicalite-1 measured by the FR method is shown. The diffusion coefficients of propane in theta-1 are about two orders of magnitude smaller than those in silicalite-1, indicating that the diffusion mechanism in these two types of frameworks is different. The sizes of the channels of the two zeolites are quite similar but silicalite-1 possesses a three dimensional channel framework while theta-1 has only unidirectional cylindrical channels running down the *z*-axis [001] direction. The mechanism of single-file diffusion is suggested for the propane/theta-1 system while normal random-walk diffusion is operating in the propane/silicalite-1 system [63]. In single-file diffusion, a displaced molecule is more likely to return to its original position than to proceed further because of the mutual interaction of the diffusant molecules, leading to a negative cross-term correlation effect which reduces the diffusivities

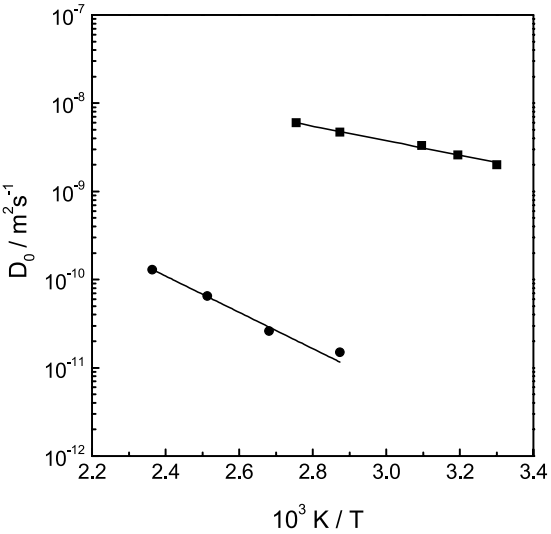

Fig. 18 Comparison of the Arrhenius plots of the diffusion coefficients of propane in theta-1 (cf. [65]) (●) and in silicalite-1 (cf. [65]) (■)

compared with the random walk situation [71, 72]. In the light of the results obtained from molecular dynamic simulations and NMR measurements, it has been established that the mean square displacement in single-file diffusion in an infinite long channel is proportional to the square root of the observation time rather than the observation time [71, 72]. This indicates that the diffusivities of sorbate molecules involved in single-file diffusion are much smaller than those for molecules involved in the normal random-walk diffusion model. This is exactly the case shown in Fig. 18.

The activation energy of the diffusion of propane in theta-1 calculated from the Arrhenius plot is 39 ± 3 kJ mol^{-1} which is much higher than the value of 15.8 ± 0.7 kJ mol^{-1} for silicalite-1. The heat of adsorption of propane in theta-1 (41.7 kJ mol^{-1}) is, however, only slightly higher than that in silicalite-1 (40 kJ mol^{-1}) [74]. According to the framework structures, theta-1 zeolite presents a smoother energy profile than silicalite-1 [74, 75]. Thus, this high activation energy should be ascribed to the consequence of single-file diffusion [45]. It is interesting to note that the activation energy for the diffusion of propane in theta-1 is very close to the heat of adsorption for the system, suggesting that the mass transport process of propane molecules in theta-1 is controlled by the rate of adsorption and desorption of the molecules to or from the zeolite. This finding offers for the first time a remarkable direct experimental evidence of the theoretical assumption for the systems with single-file diffusion behaviour that the adsorption and desorption of the sorbed molecules at pore entrances are considered to be the significant and even the rate-controlling step [71]. At very low sorbate concentrations, single-

file diffusion then occurs at a rate which is close to normal Fickian diffusion rates.

4.4 Diffusivity Measurements in Bidispersed Porous Materials

Studies on mass transport processes of sorbates in bidispersed porous solid materials, exhibiting macro- or mesopores between crystals and micropores inside the crystals, are of considerable importance in obtaining a better understanding of the separation and catalytic processes involved in the systems. Such systems have not, however, been studied in depth. As discussed in Sect. 3.2.5, the FR technique provides a realistic way to investigate the dynamics processes taking place in such biporous systems.

Similar to the FR measurements of sorbates in monodispersed microporous materials, the major difficulty in the application of the FR method is to identify the true kinetic mechanisms occurring in the systems from the rate spectra or the FR spectra as there are generally several combinations of parameters, i.e., several theoretical models, which could produce virtually the same FR curves. This difficulty has been tackled by investigating the systems over a range of reasonable or possible parameter values, e.g., variation of particle size or temperatures.

The FR measurements have been carried out for several systems using bidispersed structured sorbents [64, 76, 77]. All the spectra, however, indicate that either micropore diffusion or macropore diffusion, with or without a surface resistance, was the rate-controlling step for these systems.

Onyestyak et al. investigated the diffusivities of isobutane in 13X (cf. [65]) crystals in both powder and pellet forms using the FR method as displayed in Figs. 19 and 20 [76]. Significant difference in response behaviour can be found. The diffusion of isobutane in X zeolite powders is expected to be very fast, and this is clearly demonstrated by the response signals at high frequencies as presented in Fig. 19a,b which can be ascribed to diffusion within the micropores. The response data for the diffusion of isobutane in commercial 13X pellets under the same conditions as those for the pure crystals are presented in Fig. 19c. The response peak of the out-of-phase characteristic function for this system appears at a frequency more than three orders of magnitude lower than that with the 13X crystals. Further investigations showed that the frequency of the response peak depends on the pellet size as illustrated in Fig. 20, suggesting that the response curves for the 13X pellet system result from macropore diffusion rather than micropore diffusion. The intercrystalline diffusion coefficient, D_p, can be calculated from the slope of the linear plot and found to be ca. 5×10^{-7} m^2 s^{-1}. This value is very close to that estimated assuming Knudsen diffusion [71], i.e., 3.9×10^{-7} m^2 s^{-1}.

FR studies of carbon dioxide, propane and ammonia in 4A, 5A and 13X commercial pellets [77] have, also, been carried out and the results showed

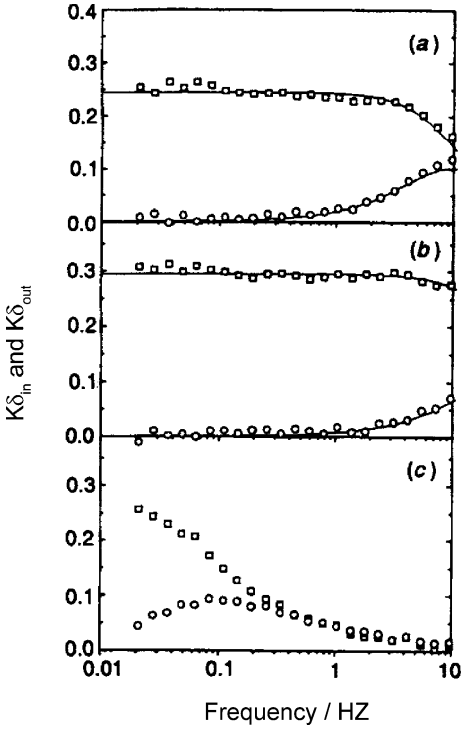

Fig. 19 FR Characteristic functions $K\delta_{\text{in}}$ (□) and $K\delta_{\text{out}}$ (○) of isobutane diffusion in **a** 54 mg of laboratory-synthesized NaX (cf. [65]), **b** 52 mg Lancaster 13X (cf. [65]) and **c** 57 mg Lancaster 13X pellets ($R = 0.30$ mm) at 423 K

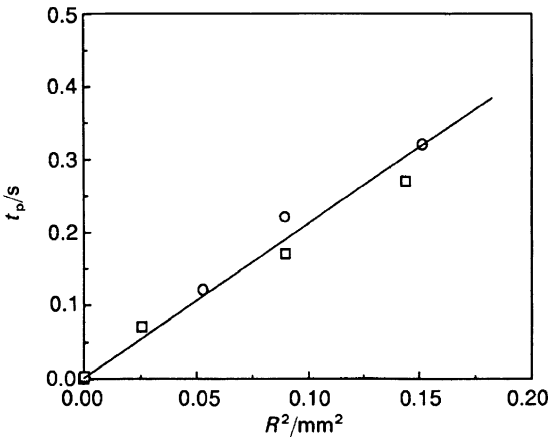

Fig. 20 Pellet size dependence of macropore diffusion time constant for isobutane diffusion in 13X (cf. [65]) pellets (□) and CO_2 diffusion in 5A (cf. [65]) pellets (○) at 423 K obtained using a model discussed in Sect. 3.2.5

that macropore diffusion with a surface resistance is the rate-controlling step for these systems, with the exception that the FR signals of propane in 4A pellets were too small to be detected (cf. Figs. 21 and 22).

Ammonia, which possesses a large dipole moment, has been used extensively as a probe molecule for the characterisation of both Lewis and Brønsted acidic sites. Figure 22 shows the significant difference in the FR data between ammonia in zeolite crystals and in pellets. The FR spectra of ammonia in zeolite crystals demonstrated that the rate of the ammonia adsorption on different acidic sites in the crystals controls the overall dynamics of the processes occurring in the systems. In the case of pellets, the rate-controlling step was found to be macropore diffusion with (Fig. 22a,2,b,2) or without (Fig. 22c,2) surface resistances [77].

Shen et al. measured the FR curves of O_2 and N_2 in different CMS pellets and analysed the data using the above procedures [64]. Micropore diffusion with surface resistance dominates in those CMS samples with a micropore

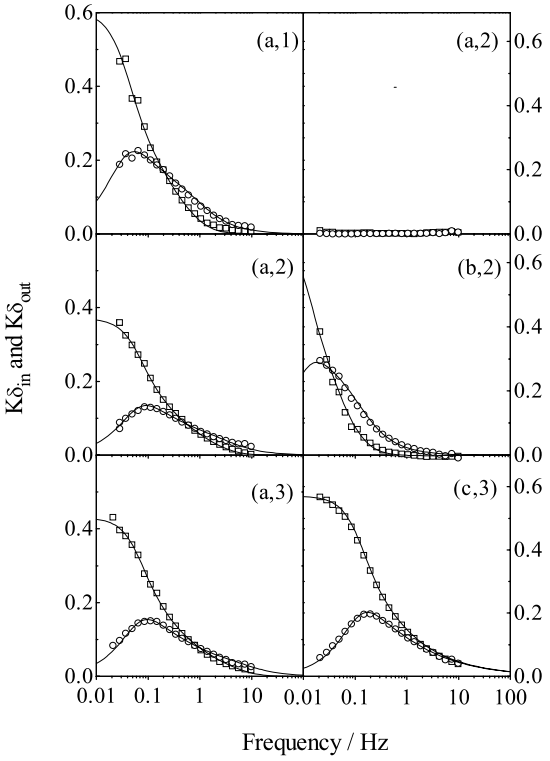

Fig. 21 FR characteristic functions $K\delta_{in}$ (□) and $K\delta_{out}$ (○) for CO_2 (*1*) and propane (*2*) at 373 K and 4 Torr in 4A (cf. [65]) (**a**), 5A (cf. [65]) (**b**) and 13X (cf. [65]) (**c**) zeolite pellets (ca. 100 mg for CO_2 and 200 mg for propane) fitted using a model discussed in Sect. 3.2.5. Note: 1 Torr = 133.33 Pa

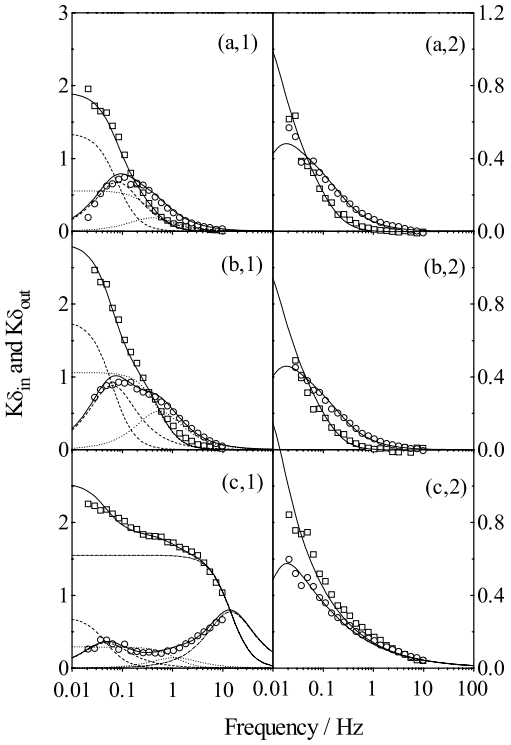

Fig. 22 FR characteristic functions $K\delta_{in}$ (□) and $K\delta_{out}$ (○) for ammonia at 373 K and 1 Torr in ca. 30 mg well-dispersed crystal powder (*1*) and pellets (*2*) of 4A (cf. [65]) (**a**), 5A (cf. [65]) (**b**) and 13X (cf. [65]) (**c**). *Lines* are fits of the theoretical models. Note: 1 Torr = 133.33 Pa

opening of ca. 0.4 nm, while for the sample with a micropore opening of ca. 0.9 nm, the mobility of O_2 and N_2 is mostly controlled by interparticle transport.

The FR spectra when both micro- and macropore diffusion processes are rate-controlling in systems involving dispersed solid materials with biporous structures have not been observed as yet. However it should be possible by adjusting the crystal and pellet sizes, i.e., obtaining an appropriate ε value in Eq. 25.

4.5 Diffusivities of Multi-Component Gas Mixtures in Microporous Materials

The behaviour of a multi-component gas mixture in a microporous adsorbent is important both theoretically and practically in separation and catalytic processes. Detailed theoretical analysis of the frequency response for the diffusion of multiple adsorbates in microporous material crystals have been

reported by Sun et al. [78] for a closed FR apparatus and by Park et al. [79] for an open FR system. Some FR experiments have been carried out for binary gas mixtures, e.g., N_2+O_2 mixture adsorbed in 4A zeolite [80] and *p*-xylene + benzene gas mixtures in silicalite-1 [81], but the studies on gas mixtures have not yet been done in depth because of experimental difficulties.

5
Future Developments

Microscopic techniques are limited to processes involving fast diffusion, while the other macroscopic methods are more reliable for slow diffusing systems. As a macroscopic technique, an outstanding advantage of the FR method is its ability to measure, in an FR spectrum, various rate processes which occur simultaneously in gas-solid systems. The range of the rate constants measured by an FR apparatus depends on the size and the shape of the adsorbent crystals. For fast diffusing species, large crystals are needed to determine the diffusivity. With some zeolites it is, however, very difficult to synthesize large crystals, and until these problems are overcome some very interesting fast diffusion processes cannot be tackled. Although the use of square wave perturbation can take advantage of the higher harmonics contained in the output signal to study fast dynamics, there will be difficulties to obtain very high quality fundamental frequency response data especially for complex systems. An FR apparatus with an experimental high frequency range extended beyond the current mechanical limits will be very welcome. This improvement will allow the measurements of kinetic processes associated with very small industrial crystals ($\sim$1 μm) and provide access to faster kinetic properties of special interest in the study of chemical reactions. An acoustic technique has been proposed to be used to extend the frequency range of the FR measurements, and a primary simplified model has been presented to determine the feasibility of this technique [19, 82].

A non-linear FR approach, e.g., an FR system subject to large amplitude perturbations, would be another possible improvement which would allow one to tackle some of the difficulties of the identification of the FR data discussed above. The theoretical models developed by Do and co-workers [23, 31–33] have laid the foundations for the design and development of this technique.

References

1. Polinski LM, Naphtali LM (1963) J Phys Chem 67:369
2. Yasuda Y (1982) J Phys Chem 86:1913
3. Yasuda Y (1994) Heterog Chem Rev 1:103

4. Yasuda Y (1976) J Phys Chem 80:1867
5. Yasuda Y (1978) J Phys Chem 82:74
6. Van-Den-begin NG, Rees LVC (1989) In: Jacobs PA, van Santen RA (eds) Zeolites: facts, figures, future, Stud Surf Sci Catal. Elsevier, Amsterdam, vol 49B:915
7. Rees LVC (1984) In: Jacobs PA, Jaeger NI, Jírû P, Kazansky VB, Schulz-Ekloff G (eds) Structure and reactivity of modified zeolites. Stud Surf Sci Catal. Elsevier, Amsterdam 18:1
8. Rees LVC, Shen D (1993) Gas Sep Purif 7:83
9. Shen D, Rees LVC (1994) J Chem Soc, Faraday Trans 90:3011
10. Song L, Sun Z-L, Ban H-Y, Dai M, Rees LVC (2004) Phys Chem Chem Phys 6:4722
11. Khodakov AYu, Rees LVC (1997) In: Chon H, Ihm S-K, Uh YS (eds) Progress in zeolite and microporous materials, Stud Surf Sci Catal, Elsevier, Amsterdam 105:1715
12. Turner MD, Capron L, Laurence RL, Conner WmC (2001) Rev Sci Instrum 72:4424
13. Harkness IR, Cavers M, McDougall GS (2003) Phys Chem Chem Phys 5:4708
14. Sward BK, LeVan MD (2003) Adsorption 9:37
15. Wang Y, Sward BK, LeVan MD (2003) Ind Eng Chem Res 42:4213
16. Onyestyak G, Valyon J, Rees LVC (2000) Phys Chem Chem Phys 2:3077
17. Zheng S, Tanaka H, Jentys A, Lercher JA (2004) J Phys Chem B 108:1337
18. Camp PJ (2002) Phys Chem Chem Phys 4:4071
19. Reyes SC, Iglesia E (1994) Catalysis 11:51
20. Reyes SC, Sinfelt JH, DeMartin GJ, Ernst RH (1997) J Phys Chem B 101:614
21. Grenier Ph, Malka-Edery A, Bourdin V (1999) Adsorption 5:135
22. Bourdin V, Gray PG, Grenier Ph, Terrier MF (1998) Rev Sci Instrum 69:2130
23. Petkovska M (2001) Nonlinear Dynam 26:351
24. Jordi RG, Do DD (1993) Chem Eng Sci 48:1103
25. Schrieffer JR, Sinfelt JH (1990) J Phys Chem 90:1047
26. Shen D, Rees LVC (1991) Zeolites 11:666
27. Shen D, Rees LVC (1990) J Chem Soc, Faraday Trans 86:3943
28. Sun LM, Bourdin V (1993) Chem Eng Sci 48:3783
29. Sun LM, Meunier F (1993) Chem Eng Sci 48:715
30. Jordi RG, Do DD (1994) Chem Eng Sci 49:957
31. Petkovska M, Do DD (1998) Chem Eng Sci 53:3081
32. Petkovska M, Do DD (2000) Nonlinear Dynam 21:353
33. Petkovska M, Petkovska LT (2003) Adsorption 9:133
34. Park IS, Petkovska M, Do DD (1998) Chem Eng Sci 53:833
35. Richards RE (1986) PhD thesis, University of London
36. Shen D (1991) PhD thesis, University of London
37. Spiegel MR (1974) Fourier Analysis. McGrew-Hill, New York
38. Rees LVC, Song L (2001) In: Kanellopoulos NK (ed) Recent Advances in Gas Separations by Microporous Membranes, Sect. 1.6. Elsevier, Amsterdam
39. Yasuda Y, Sugasawa G (1984) J Catal 88:530
40. Oprescu D, Rees LVC, Shen D (1992) J Chem Soc, Faraday Trans 88:2955
41. Yasuda Y, Yamda Y, Matsuura I (1986) In: Murakami Y, Iijima A, Ward JW (eds) New Development in Zeolite Science and Technology. Proc. 7th Int Zeolite Conf, Elsevier, Kodansha, p 587
42. Shen D, Rees LVC (1991) Zeolites 11:684
43. Yasuda Y, Suzuki Y, Fukada H (1991) J Phys Chem 95:2486
44. Yasuda Y (1991) Bull Chem Soc Jpan 64:954
45. Shen D, Rees LVC (1994) J Chem Soc, Faraday Trans 90:3017
46. Do DD (1990) Chem Eng Sci 45:1373

47. Sun LM, Meunier F, Grenier Ph, Ruthven DM (1994) Chem Eng Sci 49:373
48. Crank J (1975) The Mathematics of Diffusion. Oxford University Press, Oxford
49. Barrer RM, Craven JB (1990) J Chem Soc, Faraday Trans 1 86:545
50. Heink W, Kärger J, Pfeifer H, Datema KP, Nowak AK (1992) J Chem Soc, Faraday Trans 88:3505
51. Jobic H, Bee M, Kearley GJ (1992) Zeolites 12:146
52. Runnebaum RC, Maginn EJ (1997) J Phys Chem B 101:6394
53. Kärger J, Ruthven DM (1989) Zeolites 9:267
54. Yasuda Y, Yamamoto A (1985) J Catal 93:176
55. Song L, Rees LVC (1996) Microporous Mater 6:363
56. Song L, Rees LVC (1997) J Chem Soc, Faraday Trans 93:649
57. Song L, Rees LVC (1999) In: Treacy MMJ, Marcus BK, Bisher ME, Higgins JB (eds) Proc 12th Int Zeolite Conf, Baltimore 1998, Materials Research Society. Warrendale, Pennsylvania, p 67
58. Giermanska-Kahn J, Cartigny J, De Lara EC, Sun LM (1996) Zeolites 17:365
59. Shen D, Rees LVC (1995) J Chem Soc, Faraday Trans 91:2027
60. Song L, Rees LVC (2000) Microporous Mesoporous Mater 301:35–36
61. Song L, Sun Z-L, Rees LVC (2002) Microporous Mesoporous Mater 55:31
62. Rees LVC, Song L (2006) In: Conner WC, Fraissard J (eds) Fluid Transport in Nanoporous Materials. p 383
63. Song L, Rees LVC (2000) Microporous Mesoporous Mater 41:193
64. Shen D, Bülow M, Lemcoff NO (2003) Adsorption 9:295
65. Baerlocher C, Meier WM, Olson DH (2001) Atlas of zeolite framework types, 5th edn. Elsevier, Amsterdam
66. Rees LVC, Bruckner P, Hampson JA (1991) Gas Sep Purif 5:67
67. Song L (1999) PhD thesis, University of Edinburgh
68. Jordi RG, Do DD (1992) J Chem Soc, Faraday Trans 88:2411
69. Song L, Sun Z-L, Rees LVC (2001) In: Galarneau A, Di Renzo F, Fajula F, Vedrine J (eds) Proceedings of the 13th International Zeolite Conference, Studies in Surface Science and Catalysis. Elsevier, Amsterdam 135:3064
70. Rees LVC, Song L (2006) In: Conner WC, Fraissard J (eds) Fluid Transport in Nanoporous Materials, p 125
71. Kärger J, Ruthven DM (1992) Diffusion in Zeolites and Other Microporous Solids. Wiley, New York
72. Kärger J, Petzold M, Pfeifer H, Ernst S, Weitkamp J (1992) J Catal 136:283
73. Magalhães FD, Laurence RL, Conner WmC (1998) J Phys Chem B 102:2317
74. Hampson JA, Rees LVC (1994) In: Hattori T, Yashima T (eds) Zeolites and Microporous Crystals, Stud Surf Sci Catal, Elsevier, Amsterdam 83:197
75. Barri SAI, Smit GW, White D, Young D (1984) Nature 312:533
76. Onyestyak G, Shen D, Rees LVC (1995) J Chem Soc, Faraday Trans 91:1399
77. Onyestyak G, Rees LVC (1999) J Phys Chem B 103:7469
78. Sun LM, Zhong GM, Gray PG, Meunlier F (1994) J Chem Soc, Faraday Trans 90:369
79. Park I-S, Kwak C, Hwang YG (2000) Korean J Chem Eng 17:704
80. Yasuda Y, Matsumoto K (1989) J Phys Chem 93:3195
81. Shen D, Rees LVC (1993) In: von Ballmoos R, Higgins JB, Treacy MMJ (eds) Proc 9th Int Zeolite Conf, Montreal, Butterworth-Heinemann, Boston USA II:45
82. Nori M, Brandani S (2006) In: Conner WC, Fraissard J (eds) Fluid Transport in Nanoporous Materials

Mol Sieves (2008) 7: 277–328
DOI 10.1007/3829_2007_014
© Springer-Verlag Berlin Heidelberg
Published online: 2 October 2007

Positron Emission Profiling: a Study of Hydrocarbon Diffusivity in MFI Zeolites

E. J. M. Hensen[1] (✉) · A. M. de Jong[2] · R. A. van Santen[1]

[1]Schuit Institute of Catalysis, Faculty of Chemical Engineering and Chemistry, Eindhoven University of Technology, PO Box 513, 5600MB Eindhoven, The Netherlands
e.j.m.hensen@tue.nl

[2]Accelerator Laboratory, Schuit Institute of Catalysis, Faculty of Technical Physics, Eindhoven University of Technology, PO Box 513, 5600MB Eindhoven, The Netherlands

Abstract Zeolites are of prime importance to the petrochemical industry as catalysts for hydrocarbon conversion. In their molecule-sized micropores, hydrocarbon diffusion plays a pivotal role in the final catalytic performance. Here, we present the results of Positron Emission Profiling experiments with labeled hydrocarbons in zeolites with the MFI morphology. Single-component self-diffusion coefficients of hexanes in silicalite-1 and its acidic counterpart H-ZSM-5 are determined. For the first time, self-diffusion co-

efficients of *n*-pentane and *n*-hexane in mixtures are studied. This shows that Positron Emission Profiling is a powerful technique for in situ investigations of the adsorptive and diffusive properties of hydrocarbons in zeolites. The diffusion of hydrocarbons in medium-pore zeolites is determined by a complex interplay of factors such as the loading, the temperature, the preference for certain pore locations, the interactions with other hydrocarbon molecules of the same type or of other types and the presence of acid protons. In the diffusion of mixtures, pore blockage by one of the components might occur, thus strongly decreasing the diffusivity of the faster diffusing hydrocarbon.

Abbreviations

BGO	Bismuth germanium oxide
c	concentration
c^*	Concentration of labeled molecules
c_0	Concentration
c_{gas}	Concentration in gas phase
c_{max}	Maximum concentration
c_x	Concentration inside zeolite crystals
c_z	Concentration along reactor axis z
$c_{z,0-}$	Concentration just in front of column entrance
$c_{z,0+}$	Concentration just after column entrance
CEM	Controlled evaporator and mixer
CBMC	Configurational bias Monte Carlo
D	Diffusion coefficient
D_0	Maxwell–Stefan diffusion coefficient
D_c	Diffusion coefficient inside zeolite crystals
D_{inf}	Diffusion coefficient at infinite temperature
D_t	Transport diffusion coefficient
D_s	Self-diffusion coefficient
D_s^0	Self-diffusion coefficient at infinite dilution
D_{ax}	Axial diffusion coefficient
D_x	Diffusion coefficient
E_{act}	Activation energy
E_{app}	Apparent activation energy
FID	Flame ionization detector
FR	Frequency response
GC	Gas chromatograph
Grav.	Gravimetric
H-ZSM-5	Zeolite structure; cf. [1]
$\overrightarrow{J}$	Flux due to transport diffusion
J	Flux due to transport diffusion in one direction
J_i^*	Flux due to transport diffusion of labeled molecule i
K_a	Adsorption equilibrium constant
K_{ads}	Adsorption equilibrium constant
k_a	Rate constant for adsorption
k_d	Rate constant for desorption
L	Onsager coefficient
LSO	Lutetium oxyorthosilicate

M	Molar mass
MD	Molecular dynamics
MFI	Zeolite structure; cf. [1]
MS	Mass spectrometer
molec.	Molecule(s)
N_c	Mass flux through the boundary of the zeolite crystals
Na-Y	Zeolite structure; cf. [1]
ODE	Ordinary differential equation
p	Partial pressure
PEP	Positron emission profiling
PEPT	Positron emission particle tracking
PET	Positron emission tomography
PFG NMR	Pulsed-field gradient nuclear magnetic resonance
Ps	Positronium
q	Concentration of species adsorbed in pores
R_c	Radius of zeolite crystals
R_g	Ideal gas constant
SEM	Scanning electron microscopy
SCR	Selective catalytic reduction
SCM	Single crystal membrane
t	time
T	Temperature
T_{max}	Maximum kinetic energy of positrons
TAP	Temporal analysis of products
TEOM	tapered element oscillating mass balance
TEX-PEP	tracer-exchange positron emission profiling
uc	unit cell
x	Spatial coordinate
Y	Zeolite structure; cf. [1]
ZLC	Zero length column
z	Coordinate along the reactor axis

Symbols

β	Elementary particle
β^+	Positron
β^-	electron
Γ	Thermodynamic correction factor
ε	Bed porosity
ε_x	Porosity of the zeolite crystals
μ	Chemical potential
μ^0	Chemical potential at standard conditions
Φ_s	Number of collisions between molecules and surface
Θ	Coverage inside the pores of the zeolite
v_{int}	Interstitial velocity
v_{sup}	Superficial velocity

1 Introduction

1.1 Zeolites in Catalysis

Since the 1960s, zeolites have been applied in an increasing number of catalytic processes. Zeolites are crystalline microporous materials close to sand in composition, but with a much wider diversity in structures mainly due to their porous nature and possibilities for functionalization. The silicon-containing oxygen tetrahedra are the basic building blocks to all kinds of structures with pores and cavities of varying dimensions. Up to now, 136 different structures have been reported [1], of which about 40 are naturally occurring. These materials look like sponges, but with a very regular structure and pore sizes, which are typically of molecular dimensions. The topologies of two important medium-pore zeolites are depicted in Fig. 1. The regularly shaped channels in these zeolites can be clearly seen. The different zeolites differ in pore diameter, pore shape and the way these pores are interconnected. Zeolite mordenite has a one-dimensional pore system consisting of channels with a diameter of about 7 Å, while the pores of silicalite-1 form a three-dimensional network of interconnected straight and zigzag channels (shown schematically in Fig. 2) with diameters of about 5.5 Å. While a material like silicalite-1 is neutral and does not contain acid protons, substitution of tetravalent Si by trivalent cations such as Al^{3+} renders these materials Brønsted acidic. As these acid sites are mainly located in the molecularly-

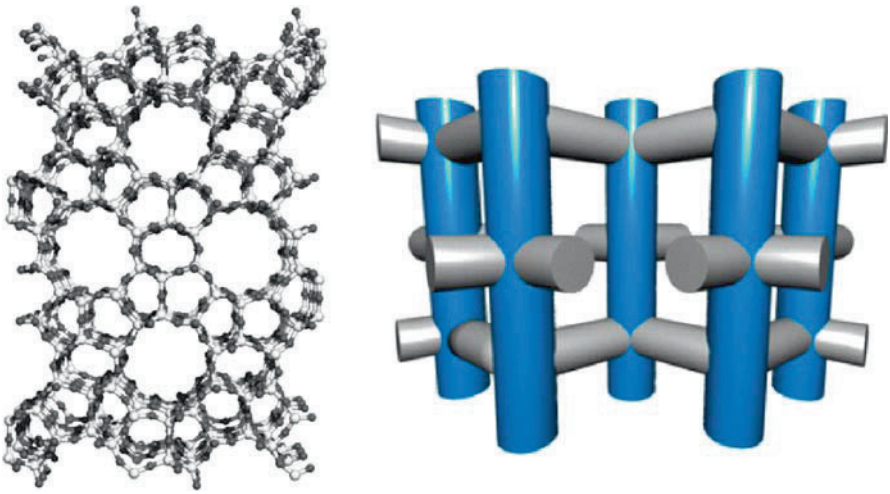

Fig. 1 The structure of the medium-pore zeolite silicalite-1 (*left*) and a schematic representation of the pore system which consists of straight and zigzag channels

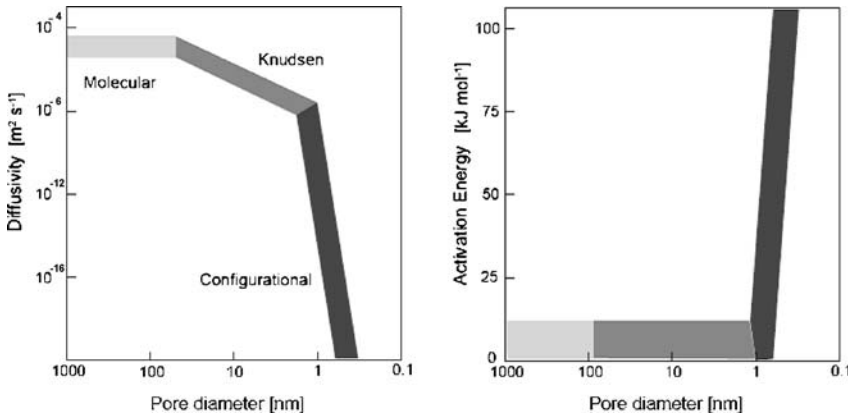

Fig. 2 Effect of pore size on the diffusivity and activation energy of diffusion (taken from Post [7, 8])

sized pore systems, the selectivity of the transformation of molecules such as hydrocarbons can be influenced to a great extent. Different types of selectivity are distinguished, including reactant and product selectivity referring to the sieving properties of the zeolites towards adsorption of reactants and desorption of products and transition-state selectivity referring to the zeolite's pore system to provide limitations to certain transition states. Furthermore, these materials can also act as a support for other catalytic materials (e.g., platinum or palladium), and in this way bifunctional catalysts can be obtained combining acid cracking and hydrogenation-dehydrogenation functionalities.

Among the most important applications of zeolites is the use of these materials to catalyze the conversion of crude oil to more useful products like gasoline, kerosene and other smaller hydrocarbons. A number of different reactions are involved in this conversion, like hydrocracking, hydroisomerization, aromatization and dehydrogenation of cyclohexanes. Catalytic cracking is one of the largest applications of catalysts, with a worldwide production of more than 500 million tons per year. One example of the processes nowadays performed in oil refineries is the so-called Hysomer process, developed by Shell for the hydroisomerization of linear alkanes to branched ones. This process makes use of platinum-loaded acidic mordenite, and is a typical example in which the zeolite acts as a bifunctional catalyst. Pt catalyzes the hydrogenation and dehydrogenation of alkanes, while the acid sites of the zeolites catalyze the conversion of linear alkenes to branched ones. This process is especially useful as it can increase the octane number of the products.

Clearly, the catalytically active sites are not directly accessible to the reacting molecules. The catalytic cycle for zeolite-catalyzed reactions generally encompasses several steps including reactant adsorption, diffusion to the active sites, product formation, diffusion to the surface and product desorption. Because the pores of zeolites have dimensions close to those of the adsorbing

and produced hydrocarbon molecules, the diffusion process is of profound influence on the overall process.

1.2 Diffusion

1.2.1 Introduction

Diffusion in liquids, gases and solids has been studied for more than a century now [2]. The discovery of Brownian motion, which is closely related to diffusion, and the subsequent search for explaining this behavior significantly contributed to the acceptance of the atomic view of matter and kinetic theory of gases and liquids. Diffusion is caused by the thermal motion and subsequent collisions of molecules. Two types of diffusion can be distinguished: transport diffusion resulting from a concentration gradient, and self-diffusion which takes place in a system at equilibrium. The flux due to transport diffusion can be described using Fick's first law of diffusion:

$$\vec{J} = -D \cdot \nabla c \tag{1}$$

in which D is the diffusion constant and c the concentration. Self-diffusion is usually expressed in terms of a self-diffusion constant D_s. In the specific case of tracer diffusion, in which labeled molecules mix with unlabeled molecules with the same chemical properties, the transport and self-diffusivity are identical. Usually, however, although transport and self-diffusion generally occur by essentially the same microscopic principle, the coefficients for transport and self-diffusion are not equal.

Diffusion in zeolites differs from ordinary diffusion in the sense that the molecules have to move through channels of molecular dimensions. As a result, there is a constant interaction between the diffusing molecules and the zeolite framework, and the molecular motion is, thus, also strongly influenced by the exact size and shape of these channels next to parameters such as temperature and concentration. Whereas in the case of gases and liquids the behavior and exact value of the diffusivity can be calculated with relative ease, the exact values of these are much harder to predict for zeolites. The interactions between molecules and the pore wall for example lead to large differences in the diffusivities of different alkane isomers, because bulkier branched isomers have a much larger interaction with the zeolite framework. A special type of diffusion can be observed in one-dimensional zeolites, called *single-file* diffusion. This type of diffusion results from the fact that some types of molecules are unable to pass each other in the narrow pores of the zeolites, leading to a significant reduction of the mobility in these systems. Clearly, these effects are not present in pure liquids and gases.

From an industrial point of view, it is important to be able to predict and describe the mass transfer through the packed-bed reactors used in the chemical industries. A better understanding of this phenomenon will aid in the optimization and development of industrial applications of these materials in separation and catalytic processes. For this purpose, the transport diffusivities are needed. A number of different experimental techniques are nowadays available for determining these values [3]. No reliable theory exists that can easily predict the diffusivity for different components in different zeolites, as it is often hard to relate these values to the underlying microscopic mechanisms [4, 5]. Furthermore, large discrepancies often exist between values obtained from different techniques, and performing these experiments is often not straightforward. It would, thus, be advantageous to have a good understanding of what can happen inside these zeolites, and what kind of influence this will have on a reactor scale.

From a fundamental point of view, the study of diffusion is also interesting as the interactions between molecules and the zeolite can lead to all kinds of unexpected behavior. The dependencies on, for example, the concentration of the diffusing molecules are expected to be completely different, as also the topology of the zeolite pore network plays an important role in this behavior. The diffusion of mixtures of different molecules is also less straightforward. This kind of effects can be readily studied using zeolites, as in a sense, due to their regular structure, they can act as models for more complicated systems like for example amorphous materials. Furthermore, a thorough understanding of the underlying microscopic mechanisms involved will aid in understanding the interaction between transport properties and the reactivity in these materials.

Diffusion of molecules through the pores of a zeolite crystal differs greatly from gaseous diffusion. In gases the diffusion is controlled by the interactions (or collisions) between the different molecules due to their thermal motion. As gases and liquids form an isotropic medium, different properties like the average collision rate, the collision rate and the mean free path can be easily calculated using kinetic theory, based on the laws of classical mechanics [6]. More sophisticated theories, which also account for intermolecular interactions, vibration and rotation of the molecules, and quantum effects are nowadays available and are quite capable of describing the behavior of a variety of systems.

The diffusion of molecules in pores can be classified in a number of different regimes depending on the pore diameter (Fig. 2). For large pore diameters of the order of 1 μm or larger, usually called macropores, collisions between the molecules occurs much more frequently than collisions with the wall, and molecular diffusion is the dominant mechanism. Typically, the diffusion constants of gases are around 10^{-5} m^2 s^{-1}. As the size of the pores decreases, the number of collisions with the wall increases until the diffusion length finally becomes smaller than the mean free path (the average distance traveled

by a molecule between two collisions) of the gas molecules. At this point, Knudsen diffusion takes over, and the mobility starts to depend on the dimensions of the pore [9]. At even smaller pore sizes, in the range of 20 Å and smaller when the pore diameter becomes comparable to the size of the molecules, these will continuously feel the interaction with the walls. Diffusion in the micropores of a zeolite usually takes place in this regime, and is called *configurational* diffusion [10]. The mechanism by which the molecules move through the pores in the configurational regime is comparable to that of surface diffusion of adsorbed molecules on a surface. Due to the small distance between the molecules and the pore wall, the molecules are more or less physically bonded to it. The diffusivity in this regime will depend strongly on the pore diameter, the structure of the pore wall, the interactions between the surface atoms and the diffusing molecules, the shape of the diffusing molecules and the way the channels are connected. As a result, it is very difficult to derive generalized equations relating the aforementioned properties to the diffusion coefficient one finds for these systems. The values of these coefficients, furthermore, span an enormous range from 10^{-8} to as low as 10^{-20} m^2 s^{-1} [4]. Compared to the gas phase, the diffusivity of the molecules inside the zeolite channels is thus greatly reduced and a much stronger temperature dependence is often observed. The fact that the particles have to move through the pore network also introduces correlation effects, which may also greatly enhance the concentration dependence.

1.2.2 Self-Diffusion vs. Transport Diffusion

The foundations of the theory of diffusion were laid by Fick in the 19th century. In one dimension, the flow of a certain species can be related to the gradient of the concentration according to Fick's first law [11]

$$J = - D_t \left(\frac{\partial c}{\partial x} \right) , \tag{2}$$

in which c is the concentration, x is the spatial coordinate, and D_t is the (transport) diffusion coefficient. The diffusion coefficient is, thus, defined as a proportionality constant between the rate of flow and the concentration gradient. Although the above equation is a convenient starting point, it does not reflect the true driving force of diffusion. As diffusion is nothing more than the macroscopic manifestation of the tendency of a system to approach equilibrium, the driving force should be the gradient of the chemical potential μ. Using irreversible thermodynamics, one can derive the Onsager relation:

$$J = - L \left(\frac{\partial \mu}{\partial x} \right) \tag{3}$$

in which L is the phenomenological Onsager coefficient. This equation indeed explicitly identifies the cause for diffusive flow, and will prove to be useful when trying to relate the transport diffusion to self-diffusion.

The pioneering work on zeolitic diffusion, performed by Barrer and Jost [12], was based on the application of Fick's equation. Assuming a concentration-independent diffusion constant, one can transform Eq. 2 into a diffusion equation known as Fick's second law:

$$\frac{\partial c}{\partial t} = - D_{\mathrm{t}} \left(\frac{\partial^2 c}{\partial x^2} \right) . \tag{4}$$

This equation gives the change of concentration in a finite volume element with time. In the approach of Barrer and Jost, the diffusivity is assumed to be isotropic throughout the crystal, as D_{t} is independent of the direction in which the particles diffuse. Assuming spherical particles, Fick's second law can be readily solved in radial coordinates. As a result, all information about the exact shape and connectivity of the pore structure is lost, and only reflected by the value of the diffusion constant.

While for the transport diffusion a gradient in the chemical potential is necessary, self-diffusion is an equilibrium process. This type of diffusion can be monitored by labeling some of the molecules inside the zeolite pores and following how the labeled and unlabeled molecules are mixed. Equation 2 can again be used to describe the flow of the labeled components:

$$J_{\mathrm{i}}^{*} = - D_{\mathrm{s}} \left. \frac{\partial c^{*}}{\partial x} \right|_{c=cons\tan t} \tag{5}$$

in which the asterisk refers to the labeled component, and in this case D_{s} is the self-diffusion constant. Alternatively, the self-diffusion constant can be related to a microscopic quantity called the mean-square displacement, as was shown by Einstein in his study on Brownian motion [13] which is of particular value for evaluation of diffusion coefficient by theoretical methods.

1.2.3 The Darken Relation

As noted earlier, the driving force of diffusion is the gradient of the chemical potential. The chemical potential can be related to the concentration by considering the equilibrium vapor phase:

$$\mu = \mu^{0} + R_{\mathrm{g}} T \ln p , \tag{6}$$

in which p is the partial pressure of the component. Using this equation yields the so-called *Darken equation* – although Darken was not the first to derive it (see in this connection [14]) – which relates the two constants D_{t} and L to

each other:

$$D_t = R_g T L \left(\frac{\partial \ln p}{\partial \ln c} \right) = D_0 \left(\frac{\partial \ln p}{\partial \ln c} \right) = D_0 \Gamma \,. \tag{7}$$

D_0 is generally referred to as the *corrected* or *Maxwell–Stefan* diffusivity, and Γ is called the thermodynamic correction factor, which corrects for the non-linearity between the pressure and the concentration of the adsorbate. Often, the corrected diffusivity is used in experimental studies where the transport diffusion is measured. Although D_0 can still depend on the concentration, in systems near the saturation limit or in the low concentration (Henry's law) regime this dependence has been experimentally shown to be quite small, and the use of the corrected diffusivity helps in directly comparing experimental results under different conditions [3].

A similar expression as Eq. 7 is also used to relate the transport and self-diffusion to each other:

$$D_t(q) = D_s(0) \left(\frac{\partial \ln p}{\partial \ln q} \right) \,, \tag{8}$$

in which q is the concentration of the species adsorbed in the pores. This equation implies that the self- and transport diffusivity coincide at low concentrations. Although the derivation of this relation is rather straightforward [3], the assumption is made that the diffusion process in both completely different experimental situations can be described in a similar fashion. In general this does not have to be the case and deviations from the above expression can be expected [15]. Recently, Paschek and Krishna [14] have suggested that Eq. 7 can indeed be used to relate the transport diffusivity to the Maxwell–Stefan or corrected diffusivity, but that an extra relation is needed to link the corrected and self-diffusivity:

$$D_s = \frac{D_0}{1 + \Theta} \,, \tag{9}$$

in which Θ is the coverage inside the pores of the zeolite.

1.2.4 Factors Influencing Diffusivity

Adsorbate Concentration

In zeolites, the diffusivity of the adsorbates can be strongly dependent on the concentration. As the diffusion of molecules in zeolites takes place in channels where it is difficult or impossible to pass each other, encounters between different molecules will have a much more pronounced influence on the mobility. Barrer [16] explained the concentration dependence of the diffusivity in zeolites using a simple jump model. Assuming that the particle has an elementary diffusion rate D_s^0 at infinite dilution to move from one site to another,

we find that the diffusivity will be proportional to the chance that a neighboring site is empty:

$$D_s(\Theta) = D_s^0(1 - \Theta) . \tag{10}$$

This equation makes use of the fact that, in the mean-field approximation, the average coverage of a site will be equal to Θ. That the actual situation can be rather more complicated has been demonstrated by a number of authors [17–19], who have shown that correlation effects can have a strong impact on the dependence of the diffusivity.

According to Kärger and Pfeifer [20], five different types of concentration dependence of the self-diffusivity (observed with NMR measurements) can be observed, as shown in Fig. 3. These different dependencies can be attributed to differences in the interactions between the framework atoms and the diffusing molecules, like for example interactions with different cations in the zeolite, or the presence of strong and weak adsorption sites. In addition the pore topology can also have a significant influence on the diffusivity, as was shown by Coppens et al. [19]. This is mainly due to the stronger correlations present in systems with lower connectivity. As a result, there is an increased chance that a molecule will move back into its previous location because the chance of finding an empty space at this location is larger. Hence, a larger decrease in mobility with increasing pore loading is observed [3]. The prediction of the concentration dependence for different systems, how-

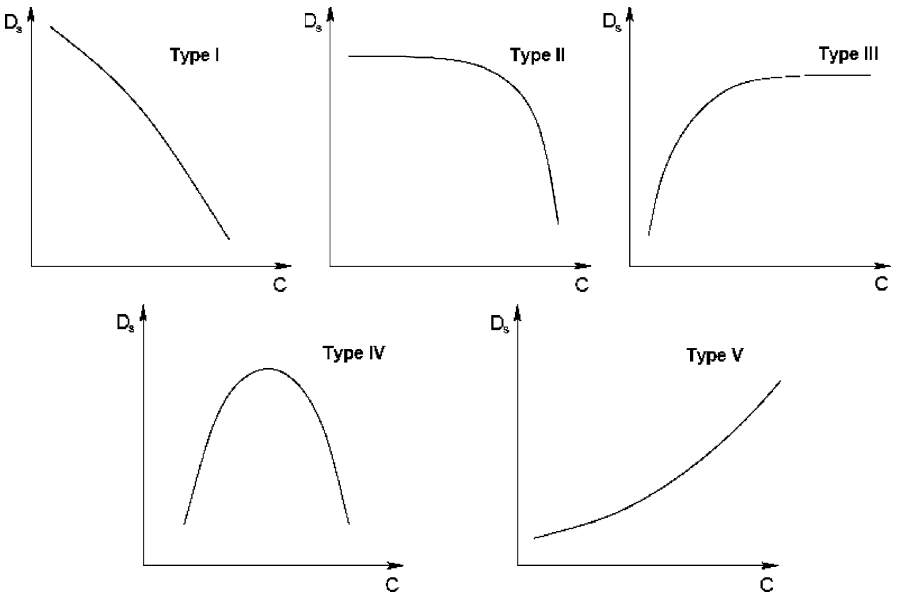

Fig. 3 Types of concentration dependence of the intracrystalline self-diffusion coefficient [20]

ever, remains difficult, and further investigations on this dependence remain of interest.

Temperature

As the molecules are continuously moving in the force field of the zeolite channels, the diffusion process can be described as an activated process, and the temperature dependence can accordingly be described by an Arrhenius-type equation [21]

$$D(T) = D_{\text{inf}} \cdot \exp\left(-\frac{E_{\text{act}}}{R_{\text{g}}T}\right), \tag{11}$$

with D_{inf} the diffusivity at infinite temperature, and E_{act} the activation energy of diffusion. This dependency is usually explained by assuming that diffusion takes place via a sequence of activated hops [22]. The pre-exponential term D_{inf} is related to the elementary rate at which particles attempt to hop to a neighboring adsorption site, while the exponential expresses the chance that the particles are able to overcome the free energy barrier, E_{act}, between these sites. Although this is an oversimplified picture of the true diffusion process, many experimental and theoretical studies have shown that it is capable of accurately describing the temperature dependence in these systems.

Experimentally, the activation energy can thus be determined by measuring the diffusivity at different temperatures. Some care should, however, be taken when interpreting these results. As the concentration of molecules inside the zeolite also depends on the temperature and measurements are often performed at finite loadings, the combined effect of temperature and loading dependence is measured. With increasing temperature, the loading of the zeolite crystals usually decreases. Assuming a type I concentration dependence (cf. [20] and Fig. 3), in addition to the increased mobility of the molecules due to the higher temperatures, we find that this can also lead to an increase of the diffusion rate. As a result, the measured activation energy can in this case be much higher than the real activation energy, and this value will also depend on the gas-phase pressure at which the measurements are performed. This effect has recently been demonstrated for 3-methylpentane in silicalite-1 [23], but the exact influence of the concentration dependence of course depends on the concentration dependence of the system. Ways to circumvent this problem are by measuring at very low coverages, or choosing experimental conditions in such a way that the concentration inside the zeolite remains constant. For systems with a moderate dependence of the diffusivity on the concentration the effect might be small, but this dependence can possibly complicate the comparison of activation energies of diffusion for different experimental conditions, especially when considering that the activation energy itself might also depend on the temperature.

An additional point complicating the comparison of the measured temperature dependence is the different definitions used for the diffusion con-

stant. The above equation is used for both transport as well as self-diffusion, but the temperature dependence of these two quantities do not necessarily have to be the same. In addition, two different definitions are commonly used in literature for the transport diffusivity. The diffusion constant D_t, as encountered before, is defined directly by Fick's first law by considering the gradient of the total adsorbed phase in the crystals. Alternatively, Haynes and Sarma [24] proposed the use of a micropore diffusion constant D_x, assuming that most of the molecules are adsorbed on the pore wall and immobile, and only a small fraction is able to move with a diffusivity equal to this constant. These two diffusion constants can be related to each other via [25]

$$D_x = \varepsilon_x(1 + K_a)D_t \,, \tag{12}$$

in which ε_x is the porosity of the zeolite crystals and K_a is the equilibrium adsorption constant. In most cases $K_a \gg 1$, and D_x thus has an activation energy equal to the sum of the heat of adsorption and the activation energy for diffusion. Some questions, however, remain regarding the use of this diffusion constant, as in the narrow pores of the zeolite there is always a strong interaction between adsorbate and adsorbent, and a gas-phase cannot really exist in this environment. As a result, the distinction between a gas and adsorbed phase seems rather arbitrary, and the use of D_t as de diffusivity of the molecules is more appropriate.

1.3
Positron Emission and Positron-Electron Annihilation

The decay of radioactive isotopes via electron emission, so-called beta decay, is a well-known phenomenon. In this mode unstable nuclei that have an excessive number of neutrons, for example ^{14}C, can emit fast electrons, β^- particles, in order to attain a stable nuclear configuration. Nuclei with insufficient neutrons, such as ^{11}C, can obtain stability by emitting fast positrons, β^+ particles (the anti-matter equivalents of electrons). Both processes are classified as radioactive β decay. In each case, the mass number of the nucleus remains constant but the atomic number changes. There exist several positron emitting isotopes, of which ^{11}C, ^{13}N and ^{15}O in particular are of interest for catalytic reaction studies. Since the half-life time of these isotopes is only 20, 10 and 2 minutes, respectively, they must be produced on-site. Production of such radioactive isotopes is normally done by irradiation of an appropriate target material with protons or deuterons at high energy.

Since the positron is the antiparticle of the electron an encounter between them can lead to the subsequent annihilation of both particles. Their combined rest mass energy then appears as electromagnetic radiation. Annihilation can occur via several mechanisms: direct transformation into one, two, or three photons; or the formation of an intermediate, hydrogen-like bound state between the positron and the electron, called a positronium

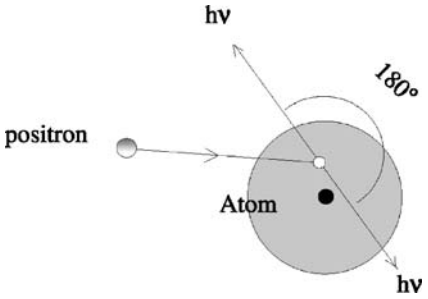

Fig. 4 Schematic drawing of the annihilation event

(Ps). The extent to that each annihilation mechanism contributes depends on the kinetic energy of the positron-electron pair. Positrons emitted during the β^+ decay process, possess a statistical distribution of kinetic energies ranging from zero to a maximum value, T_{max}, dependent on the decaying nucleus (T_{max} = 0.96 MeV for ^{11}C). The average kinetic energy is equal to 0.4 T_{max}. The probability of annihilation is negligibly small at high energies. The emitted positrons must therefore be slowed down by inelastic scattering interactions with the nuclei and the bound electrons within the surrounding medium to near thermal values before annihilation can occur. The lifetime of a positron is of the order of nanoseconds. During its lifetime the positron will travel a distance, known as the stopping distance, which is dependent on the energy of the positron and on the density of the surrounding material. For 0.4 MeV positrons (average kinetic energy of positrons emitted from ^{11}C) in a medium with a density of 0.5 g ml^{-1} (such as a zeolite or metal oxide) this corresponds to circa 3 mm [26]. The predominant annihilation process for thermalized positrons is via the direct production of two photons (Fig. 4). If both the positron and the electron were at rest upon annihilation, conservation of energy dictates that the energy of each emitted photon would be equal to the 511 keV, rest mass energy of the positron or electron. Conservation of momentum implies that the two gamma photons be emitted in opposite directions, since the initial momentum of the positron-electron pair was zero.

1.4 Positron Emission Detection Methods

The emitted gamma photons produced by positron-electron annihilation can be detected using scintillation crystal detectors such as sodium iodide (NaI), bismuth germanium oxide (BGO) and cerium doped lutetium oxyorthosilicate (LSO). The short half-life of most positron emitters leads to high specific activity. Only a very small quantity of radio-labeled molecules is thus required, making positron annihilation detection techniques very non-invasive. In fact, practical catalyst studies can be carried out using less than 37 kBq

of carbon-11, corresponding to less than 6.5×10^7 molecules. The first use of positron-emitting isotopes as tracers in catalysis research was published in 1984 by Ferrieri and Wolf [27, 28] for studying alkyne cyclotrimerization of acetylene and propylene. Baiker and co-workers [29] used ^{13}N-labeled NO to investigate the selective catalytic reduction (SCR) of NO by NH_3 over vanadia/titania at very low reactant concentrations.

For imaging purposes a technique based on the coincident detection of both photons produced via the annihilation event is often applied. This can be achieved by using two scintillation detectors, each placed on opposite sides of the emitting source. In this mode, only pairs of detected events that occur within a preset coincidence window (typically less than 50 ns) are counted. The position of the annihilation event that gave rise to the two detected photons can then be located along a chord joining the two detector elements. The concentration of the radio-labeled isotope at that position can also be determined by integrating the number of events detected during a fixed time. Due to the penetrating power of the emitted 511 keV gamma photons, which can pass through several millimetres of stainless steel, detection is possible from within steel reactors or process vessels. The coincident detection of photons is the principle of techniques such as, the positron emission tomography (PET), positron emission particle tracking (PEPT) and positron emission profiling (PEP).

Positron emission tomography (PET) is now well established as a diagnostic technique in nuclear medicine, providing 3D images of the distribution of radio-labeled molecules within living human organs. The development of a new breed of small self-shielding cyclotrons in the 1980s and significant improvements in computer hardware and software has led to an explosive growth in the number of PET facilities world-wide. Application of PET to problems of industrial interest has occurred only recently [30]. PET has been shown to be capable of monitoring turbulent two-phase (liquid/gas) flows using injected solutions of aqueous $Na^{18}F$ as a radiotracer [31].

Jonkers and co-workers conducted the first study in which PET was applied to chemical reactions in reactors [32, 33]. Since the early 1990s a facility has been developed at the Eindhoven University of Technology (TU/e) dedicated to positron emission imaging of physical and chemical processes in catalytic reactors at practical operating conditions. A positron emission detector has been developed that is specifically tailored to the measurement of activity distributions as a function of time along a single, axial direction, as a measurement of concentration profiles in a single dimension is sufficient under axially-dispersed plug flow conditions (since concentration gradients in the radial direction are negligible). This detector [34] is called a positron emission profiling (PEP) detector to distinguish it from its 3D parent.

The positron emission profiling (PEP) detector is shown in Fig. 5. It has been designed to be flexible, so that it can be used with a variety of different sizes of reactors. Measurements can be carried out on reactors having lengths

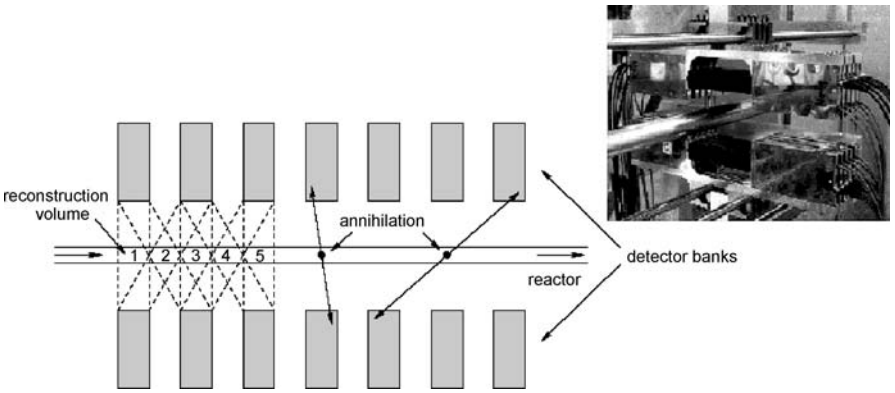

Fig. 5 Schematic drawing of the PEP detector with the two detector banks (not all detector elements are displayed). The first 5 (of 81) reconstruction positions are displayed. The photograph shows the PEP detectors with the stainless steel reactor between the two arrays of detectors

between 4.0 cm and 50 cm and diameters of up to 25 cm. The detector consists of two banks, each containing an array of 16 independent detection elements, and is mounted horizontally, with the reactor and furnace placed between the upper and lower banks. Each detection element is comprised of a bismuth germanium oxide (BGO) scintillation crystal coupled to a photomultiplier. The detection elements are situated in a frame, which allows adjustment of the overall detector dimensions if required.

2 Experimental

2.1 Diffusivity Measurements with PEP

The current PEP setup allows two types of experiments to measure diffusion in microporous materials. In the first type, labeled molecules are injected as a small pulse into a steady-state feed stream of either an inert carrier gas or of unlabeled molecules of the same kind. The propagation of the pulse through the reactor is followed using the PEP detector. Information about the diffusive processes can be obtained from the delay and broadening of the pulse, and quantitative information can be obtained by analysis of the measurements using an appropriate model, as will be discussed in more detail in the next section. This type of experiments is especially suited for diffusion measurements under zero loading conditions. A drawback of this method is that it is limited to the determination of single-component diffusion coeffi-

cients. Since under practical conditions multi-component diffusion occurs, a second method has been developed. In this type of experiments, called tracer-exchange PEP (TEX-PEP) [35], the labeled molecules are constantly "leaked" into the feed stream, instead of being injected as a single pulse. The PEP detector is used to measure the tracer exchange once the injection has started. By switching off the injection of labeled molecules after equilibrium is reached, the subsequent re-exchange can be followed as well. Information on the various processes can be obtained by fitting appropriate models to the time evolution of the tracer exchange at the various positions along the reactor bed. This technique will be applied to the study of binary mixtures. There are several advantages of the PEP technique over more conventional techniques. First of all, it is capable of measuring the concentration inside a packed bed reactor in situ [36]. Furthermore, PEP enables one to observe the evolution of a pulse or step change inside the reactor itself, therefore excluding the influence of reactor exit effects and minimizing the influence of entrance effects. Due to the penetrating power of the γ-photons used in the detection, no special requirements are being put on the experimental system holding the zeolite sample, and standard plugflow reactors can be used under typical conditions also found in the laboratory. Finally, the use of radiochemically labeled molecules makes this method particularly suited to study the diffusion of mixtures, as one of the components can be selectively labeled.

2.2 Experimental Setup

The positron-emitting ^{11}C isotope is produced by irradiation of a nitrogen target with 12 MeV protons from the 30 MeV AVF cyclotron at the Eindhoven University of Technology. The resulting ^{11}C is then transferred as CO/CO_2 to a special setup for the production of labeled hydrocarbons. Details of the homologation process over a Ru/SiO_2 catalyst used for the production of labeled pentanes and hexanes can be found in Cunningham et al. [37]. ^{11}C-labeled C_6 alkanes are synthesized from non-labeled 1-pentene, while non-labeled 1-butene is the starting material for ^{11}C-labeled C_5 alkanes production. After separation of the different products produced in this process, the desired labeled species is collected in a syringe.

Figure 6 shows a schematic diagram of the reactor system used for tracer-exchange positron-emission profiling (TEX-PEP) experiments. During these tracer exchange experiments, a constant flow of unlabeled hydrocarbons in a hydrogen carrier stream is fed into the reactor. The *n*-hexane/2-methylpentane/hydrogen mixture is generated in a dual CEM (controlled evaporator and mixer) system for feeding of *n*-hexane and 2-methylpentane. Each CEM unit consists of a liquid mass flow controller and a thermal gas mass flow controller, giving a controllable, constant flow of a liquid and a gas. The liquid is subsequently evaporated in a controlled manner in the mixing

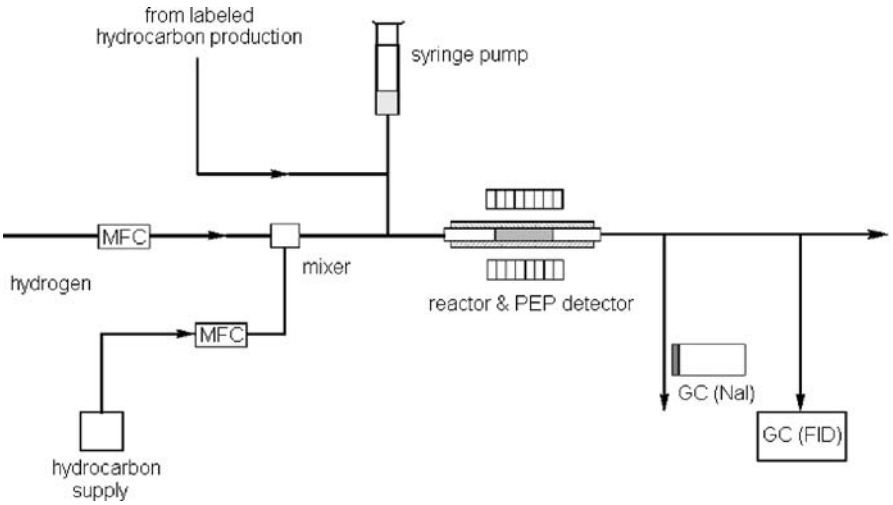

Fig. 6 Schematic layout of the TEX-PEP reactor setup including gas and liquid (unlabeled and labeled hydrocarbons) feed, the reactor and PEP detectors and post-reactor analysis. For diffusion measurements of binary mixtures a second liquid mass flow controller is added (MFC: mass flow controller)

unit of the CEM. We employ a total flow of hydrocarbons and carrier gas of 80.2 ml min^{-1}. In the TEX-PEP experiments, a quantity of labeled molecules of either *n*-hexane or 2-methylpentane is continuously injected into the feed stream using a syringe pump. The tracer exchange and tracer re-exchange processes are monitored by adding the very small tracer flow to the flow containing the non-labeled molecules until an equilibrium is reached and subsequently turning the tracer flow off. Due to switching effects [35], the re-exchange process yields more reliable results, and only this stage of the experiments was used for determining the kinetic parameters.

2.3 Zeolite Samples

All measurements in the present contribution have been performed on large crystals of silicalite-1 and H-ZSM-5 zeolites. Use of large zeolite crystals simplifies significantly the modeling and experimental procedure because it allows one to avoid pelletizing of the crystals. This has the important advantage that no macropore diffusion has to be included in the hydrocarbon transport models and intracrystalline diffusion is the dominating process.

The sample of silicalite-1 has been kindly supplied by Shell Research and Technology Center, Amsterdam. Scanning electron microscopy (SEM) showed that it consisted of regular coffin-shaped crystals with an average size of 150 μm × 50 μm × 30 μm. H-ZSM-5 has been kindly provided by

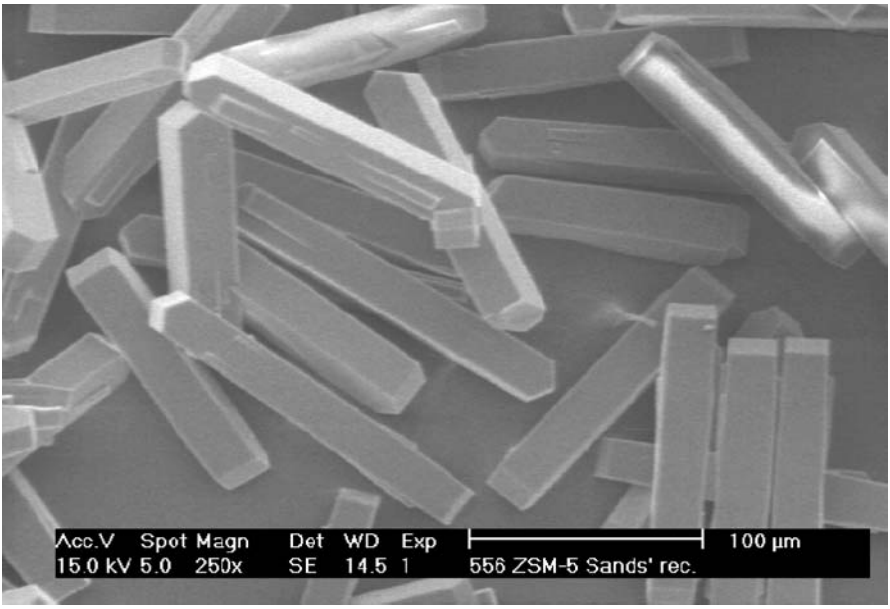

Fig. 7 SEM picture of H-ZSM-5 sample

Dr. L. Gora from Delft University. The average crystal size was determined with scanning electron microscopy and turned out to be 160 µm × 25 µm × 25 µm (Fig. 7). The Si/Al ratio was 40 in the initial gel composition. The concentration of the Brønsted sites equals 7.5×10^{-6} mol g^{-1} as determined by temperature-programmed isopropylamine decomposition. The bed porosity was determined from the pressure drop over the bed. From the Ergun relation a value of $\varepsilon = 0.44$ is calculated. The length of the zeolite bed was equal to 3 cm. Prior to experiments, the zeolite sample was activated for at least one hour at 673 K in a hydrogen stream.

2.4 Modeling the Tracer Exchange Process

In order to derive self-diffusion coefficients from the TEX-PEP experiments, a mathematical model is needed to describe the re-exchange process in the zeolite reactor bed. A common way to describe diffusion in packed beds is to use a set of diffusion equations, describing the mass transport in the zeolite bed and inside the crystals [3, 38, 39]. The model to analyze the TEX-PEP experiment study is basically a modification of the equations by Noordhoek et al. [25]. The process is thought to consist of the transport of molecules via convection and axial diffusion in the space between the crystals, adsorption and desorption at the zeolite crystal surface and diffusion inside the pores

of the crystals. It is assumed that the crystals have a spherical shape. This approximation is commonly made in literature and has been shown to be quite reasonable [3]. This is most probably due to the random orientation of the crystals inside the reactor, making it indeed difficult to explicitly account for the particle shape. As only one component is detected during the experiments, single-component equations can be used to model its behavior. The parameters describing the different processes in the bed will then be effective values for the transport of this component in the mixture.

2.4.1 The Model Equations

Transport in the fluid phase inside the packed bed takes place through convection, axial diffusion and flow to or from the zeolite crystals. A mass balance for a small volume element of the bed results in the following equation for the concentration c_z in the gas phase

$$\frac{\partial c_z}{\partial t} = D_{ax}\frac{\partial^2 c_z}{\partial z^2} - v_{int}\frac{\partial c_z}{\partial z} + \frac{3(1-\varepsilon)}{\varepsilon R_c}N_c \,. \tag{13}$$

In this equation, z is the coordinate along the reactor axis, D_{ax} is the axial diffusion coefficient and v_{int} the interstitial velocity, which can be calculated from the gas flow speed v_{sup} using $v_{int} = v_{sup}/\varepsilon$. The axial diffusivity can be calculated from the molecular diffusion coefficient of the component. For R_c, the radius of the crystals, the equivalent spherical particle radius is taken, defined as the radius of the sphere having the same external surface area to volume ratio [3]. We have estimated a value of 25 μm for the zeolite crystals in the current study.

The boundary conditions used for the bed equation are identical with the ones in Noordhoek et al. [25]. For the column entrance, a mass balance yields (and by neglecting the diffusional term just in front of the column)

$$\frac{\partial c_{z,0^+}}{\partial z} = \frac{v_{int}}{D_{ax}}(c_{z,0^+} - c_{z,0^-}) \tag{14}$$

in which $c_{z,0^-}$ and $c_{z,0^+}$ are the fluid phase concentrations just in front of and just after the column entrance, respectively. For TEX-PEP experiments, the concentration just in front of the packed bed is given by the Heaviside step function

$$c_{z,0^-}(t) = c_0, \quad t > 0 \tag{15a}$$

$$c_{z,0^-}(t) = 0, \quad t \leq 0 \tag{15b}$$

At the column exit, the diffusional term is neglected, turning into a first-order equation which can be used as a boundary condition.

The term N_c equals the mass flux through the boundary of the zeolite and is determined by the rate-limiting step for adsorption/desorption at the crys-

tal boundary. It is assumed that external mass transfer resistance due to the diffusion through the laminar fluid film surrounding the particles can be neglected, because this process is much faster than diffusion inside the zeolite crystals. This has been confirmed by comparing simulations with and without this process included in the model, showing that neglecting the external film mass transfer resistance does not influence the results.

The model of Nijhuis et al. [39] explicitly accounts for adsorption/desorption at the crystal boundary, assuming Langmuir adsorption kinetics. As the TEX-PEP experiments are conducted under steady-state conditions, this mechanism can be replaced by a simple first-order adsorption/desorption process

$$N_c = k_d c_x(R_c, z, t) - k_a c_z(z, t) \tag{16}$$

in which k_a and k_d are the adsorption and desorption rate constants in $[m\,s^{-1}]$. This equation furthermore has the advantage that k_a and k_d have the same dimensions and that there is no need to determine the number of adsorption sites.

Transport inside the zeolite crystals occurs through diffusion inside the zeolite pores. Although it is known that diffusion in zeolites is generally anisotropic [40], the random orientation of the crystals inside the reactor justifies the approximation that micropore diffusion can be described as an isotropic process. A mass balance for the zeolite crystals yields for the adsorbed phase concentration c_x in the crystals

$$\frac{\partial c_x}{\partial t} = D_c \left(\frac{\partial^2 c_x}{\partial x^2} + \frac{2}{x} \frac{\partial c_x}{\partial x} \right) , \tag{17}$$

in which D_c is the intracrystalline diffusivity, and x the radial coordinate of the crystal. In principle, the value of the diffusion constant depends on the concentration of both components. However, as during the experiments the total concentration does not change, D_c can thus be regarded as constant during a single measurement. The boundary condition at the center of the particle is obtained from symmetry considerations

$$\left. \frac{\partial c_x}{\partial x} \right|_{x=0} = 0 . \tag{18}$$

At the crystal boundary, the flow to the surface must be equal to the desorption rate at the crystal boundary at $x = R_c$

$$D_c \left. \frac{\partial c_x}{\partial x} \right|_{x=R_c} = k_a c_z(z, t) - k_d c_x(R_c, z, t) . \tag{19}$$

The initial conditions can be found by realizing that at the start of a tracer re-exchange process, the system is in equilibrium. Assuming that the injected tracer concentration initially is equal to C_0 yields the following initial

conditions

$$c_z(z, t) = c_0 \tag{20a}$$

$$c_x(x, z, t) = K_{ads} \cdot c_0 \,, \tag{20b}$$

in which K_{ads} is the adsorption equilibrium constant and equals $K_{ads} = k_a/k_d$.

2.4.2 Solving the Model

The equations described above have been solved using the numerical method of lines [41]. This procedure has been described for our system in more detail in Noordhoek et al. [36]. In short, this is done by discretizing the spatial coordinates and derivatives, converting the system of partial differential equations into a set of ordinary differential equations (ODEs). These ODEs can then be solved using an ordinary numerical integration routine. Solving the model yields values for the concentration at the each bed and crystal gridpoint. As the PEP detector measures the total concentration of labeled molecules in a certain section of the catalyst bed, volume averaging has to be applied to simulate the response of the PEP detector. The average microparticle concentration at position z inside the reactor bed equals

$$\langle c_x(z, t) \rangle = \frac{3}{R_c^3} \int_0^{R_C} c_x(x, z, t) \cdot x^2 \, dx \,. \tag{21}$$

As the crystal concentration c_x is only known at the gridpoints, this integral has to be evaluated numerically. The total concentration at position z can be calculated by averaging over the bed and crystal concentration

$$\langle c_{tot}(z, t) \rangle = \varepsilon c_z(z, t) + (1 - \varepsilon) \langle c_x(z, t) \rangle \,. \tag{22}$$

Estimation of the different parameters, i.e., the adsorption/desorption and diffusion in the zeolite crystals, is done by fitting the modeled concentration profiles to the measured ones, using the least-squares Levenberg–Marquardt algorithm [42]. All the other parameters were determined experimentally.

2.4.3 Adsorption/Desorption at the Crystal Boundary

If adsorption and desorption at the outer surface of the zeolite crystallites is fast compared to the diffusion inside the pores of the zeolite, adsorption equilibrium can be assumed at the crystal boundary. This seems a reasonable approach, because the diffusion inside the micropores is usually quite slow. An advantage of this approach is that the parameters describing adsorption/desorption at the boundary can be replaced by a single equilibrium ad-

sorption constant K_{ads}. This eliminates the problem that two parameters need to be fitted which are not completely independent, as was already reported by Nijhuis et al. [39]. In order to check whether the adsorption equilibrium assumption is satisfied, results for the model described previously are to be compared to those from a model assuming adsorption equilibrium. Based on the assumption that adsorption/desorption is fast compared to diffusion in the zeolite micropores, the mass flux through the boundary of the zeolite is determined by diffusion to the boundary of the crystal. Equation 15 is then replaced by

$$N_c = - D_c \left. \frac{\partial c_x}{\partial x} \right|_{x=R_c} . \tag{23}$$

The boundary equation at the crystal surface, Eq. 18, can be replaced by a simple equilibrium condition

$$c_x(R_c, z, t) = K_{ads} c_z(z, t) . \tag{24}$$

An estimate of the rate of adsorption can be obtained from kinetic gas theory [43]. The number of collisions between molecules and the surface can be calculated using the following relation

$$\Phi_s = \frac{1}{4} c_{gas} \sqrt{\frac{R_g T}{2\pi M}} , \tag{25}$$

which gives the collision rate per unit surface (in mol m^{-2}), with c_{gas} the concentration of the gas phase, R_g the ideal gas constant, T the temperature and M the molar mass of the molecules. The rate constant for adsorption can be calculated by dividing this expression by the gas phase concentration. It should, however, be realized that the value calculated from Eq. 24 gives an upper bound for the true adsorption rate, because not all collisions with the zeolite crystal surface will result in the adsorption of a molecule inside the micropores (i.e., there exists a "surface barrier" for adsorption, and the sticking coefficient is smaller than 1). Estimation of the sticking coefficient is not straightforward, and it might have values ranging from approximately one to 10^{-3}.

3
Diffusivity Studies of Hexanes in MFI Zeolites

3.1
Self-diffusivity of 2-Methylpentane/*n*-Hexane

The self-diffusivities of 2-methylpentane and *n*-hexane in their binary mixtures have been measured as a function of the ratio of the hydrocarbon in silicalite-1 at a temperature of 433 K. Figure 8 shows the tracer re-exchange

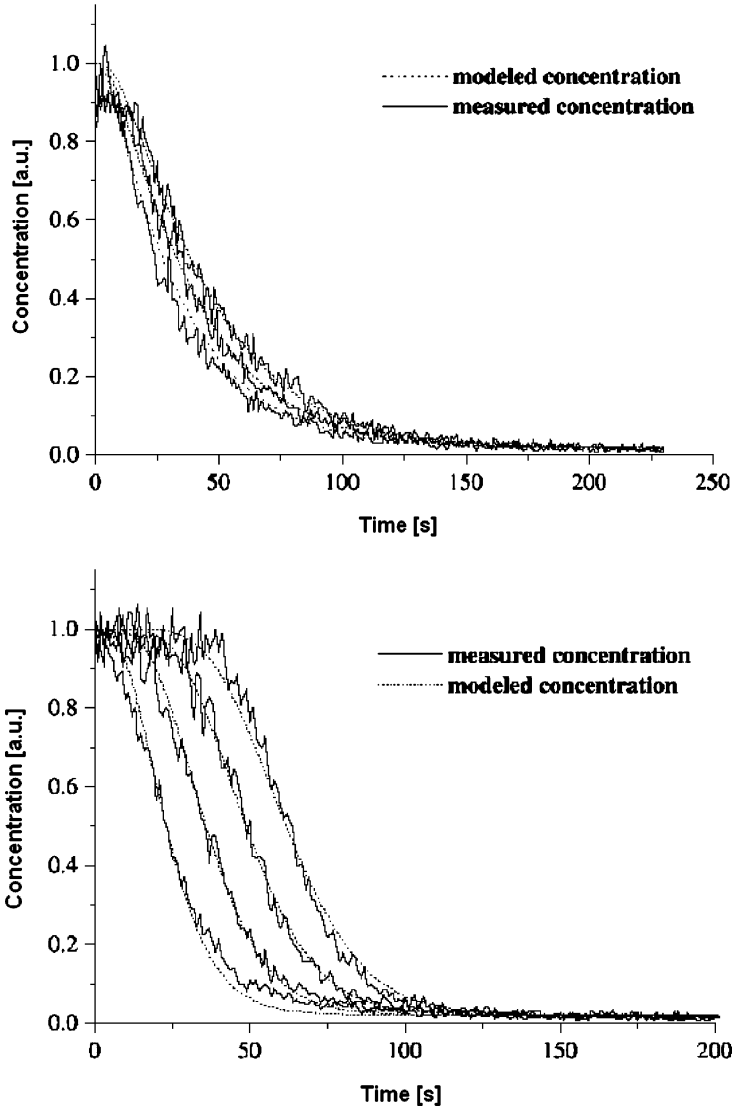

Fig. 8 TEX-PEP profiles for labeled 2-methylpentane (*left*) and *n*-hexane (*right*) at several detection positions in an equimolar mixture of *n*-hexane and 2-methylpentane in silicalite-1 at a total hydrocarbon pressure of 6.6 kPa and a temperature of 433 K (note that these two graphs have been obtained from two different experiments in which one of the two hydrocarbons was labeled)

process at different positions along the reactor axis for 2-methylpentane and *n*-hexane in an equimolar mixture. The results are derived from two different sets of experiments in which either the branched or the linear alkane was isotopically labeled. The data immediately show that the re-exchange process

of the branched molecule is slower than that of the linear hydrocarbon, indicating a correspondingly lower diffusivity for the former. Table 1 gives the hydrocarbon loadings of the two hydrocarbons on silicalite-1 at an adsorption temperature of 433 K.

The slightly lower loading of the branched alkane under equal experimental conditions is in accordance with other studies [44, 45]. Indeed, Zhu et al. [45] measured a higher *n*-hexane loading in silicalite-1 compared to 2-methylpentane even under a significantly higher partial pressure of the iso-alkane. The *n*-hexane loading at a partial pressure of 0.47 kPa and a temperature of 408 K was found to be 2.36 molecules per unit cell, while a value of 2.28 was calculated for 2-methylpentane at a partial pressure of 0.73 kPa. Loadings for both *n*-hexane and 2-methylpentane determined from the independent experiments using a mass spectrometer (MS) are in agreement with those provided by TEX-PEP (see Table 1).

Table 1 Loadings of single components in silicalite at 433 K, 6.6 kPa

Hydrocarbon	Loading [mmol g^{-1}]	Loading [molec. uc^{-1}]	Loading [mmol g^{-1}] (MS)
n-hexane	0.64 ± 0.03	3.6	0.59 ± 0.03
2-methylpentane	0.59 ± 0.03	3.4	0.53 ± 0.03

Theoretically calculated values of the heat of adsorption for *n*-hexane and 2-methylpentane are 70 kJ mol^{-1} and 65 kJ mol^{-1}, respectively [46, 47], which is in agreement with the average values determined by Zhu et al. [48]. As the heats of adsorption of these alkanes are very close, the difference in adsorption is caused by an entropic effect. Indeed, the conformations of the bulkier branched alkanes are much more restricted in the narrow pores of the medium-pore MFI zeolite. For the branched isomer in silicalite-1 there is a large difference in the adsorption entropy between the molecular locations in the intersections and in the channels as shown by Zhu et al. [48]. Therefore, the adsorption of 2-methylpentane from the gas phase leads to a higher reduction in entropy compared to adsorption of *n*-hexane. This makes it entropically less favorable to adsorb the branched isomer [44].

Figure 9 shows the binary adsorption data of *n*-hexane and 2-methylpentane at 433 K as a function of the gas-phase ratio of the hydrocarbons. Obviously, the *n*-hexane loading monotonically decreases upon an increase of the partial pressure and loading of the 2-methylpentane. The total hydrocarbon loading only slightly decreases at high 2-methylpentane fraction in the gas phase. The preference for adsorption of *n*-hexane over the monobranched isomer is in line with the above-mentioned entropic considerations.

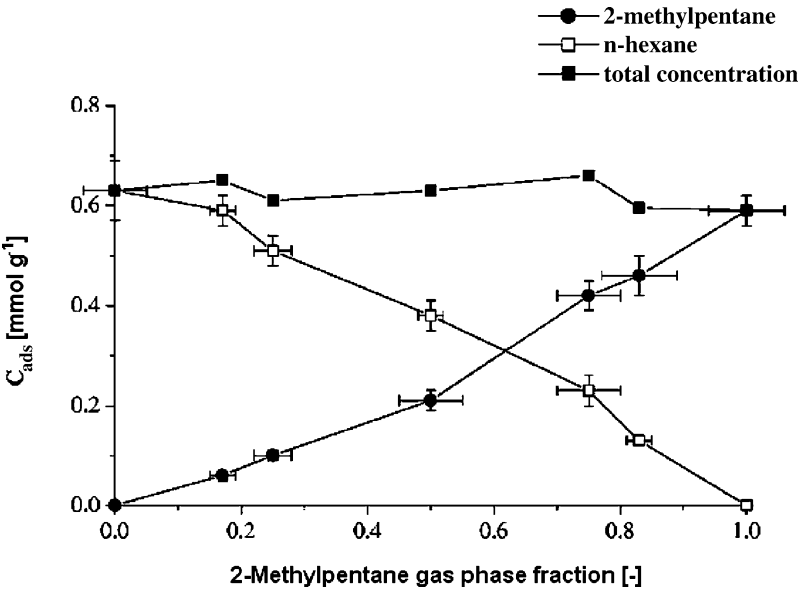

Fig. 9 Loadings of mixture components in silicalite as a function of 2-methylpentane fraction in the gas phase (total hydrocarbon partial pressure 6.6 kPa, $T = 433$ K)

The observations in the present study are supported by results of CBMC simulations performed by Vlugt et al. [44] and Calero et al. [49] on adsorption behavior of linear and branched alkanes and their mixtures. The simulations were performed at a fixed mixture ratio at lower temperatures (300 K and 362 K). It was shown, that at a total loading of approximately 4 molecules per unit cell, the loading of the branched alkanes reaches a maximum value. At lower loadings, both components are adsorbed independently, while at higher loadings the branched alkanes is squeezed out by the linear alkanes. Vlugt et al. [44] showed that this behavior of the component is related to the siting of the molecules in the silicalite pore system. It was found that the *n*-hexane is adsorbed throughout the silicalite-1 pores, whereas 2-methylpentane molecules are located mostly at the intersections between the straight and zigzag channels. Consequently, *n*-hexane displays a higher packing efficiency. Apparently, under the present conditions, the loading of the components were quite high, so that the 2-methylpentane is expelled from the micropores and a preferential adsorption for the linear alkane is observed. This effect can only be counteracted at high partial pressures of 2-methylpentane. This results in substantial nonlinear dependencies of the loadings on the mixture composition. Comparison between our experimental results and those calculated from CBMC simulations [50] performed for 2-methylpentane/*n*-hexane mixtures under almost similar conditions is shown in Fig. 10. The single-component loadings of the single components

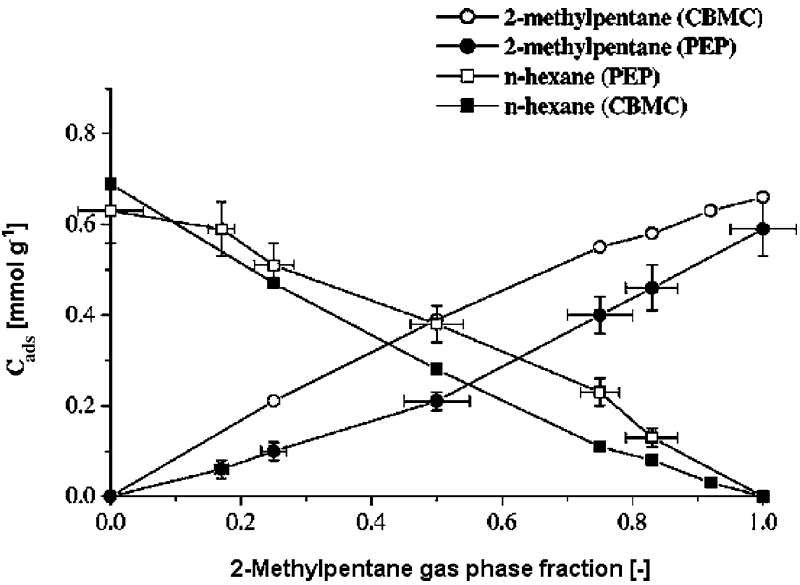

Fig. 10 Loadings of mixture components in silicalite as a function of 2-methylpentane fraction in the gas phase, experiment (total hydrocarbon partial pressure 6.6 kPa, 433 K) and CBMC simulations (total hydrocarbon partial pressure 7.8 kPa, 433 K)

calculated by CBMC simulations are slightly higher than the values obtained from TEX-PEP measurements.

This is more evident for the branched alkane and is related to the higher hydrocarbon partial pressures applied in the CBMC simulations. The slight decrease of the total loading with the branched alkane fraction in the gas phase predicted from the simulations is in agreement with the TEX-PEP data. However, a slight preferential adsorption for the branched alkane is deduced from the simulations, whereas PEP measurements provide lower values for the 2-methylpentane loadings. This disagreement and the tendency shown by Vlugt et al. [44] can probably be attributed to imperfections in the model parameters used in the CBMC simulations.

Figure 11 shows the self-diffusion coefficients obtained from the TEX-PEP experiments for both alkanes as a function of the gas-phase mixture composition. Evidently, we find that the self-diffusivity of *n*-hexane is an order of magnitude higher than that of the 2-methylpentane. Indeed, the kinetic diameter of *n*-hexane (4.3 Å) is smaller than that of isohexane (5.0 Å) [51]. Moreover, we observe a decrease in mobility with increasing fraction of the branched alkane in the gas phase. Analogous behavior was found for CH_4/CF_4 mixtures, where the self-diffusivity of both components decreased as the loading of the slower diffusing tetrafluoromethane increased [52].

The loading dependence of 2-methylpentane is similar to earlier results showing a decrease of 2-methylpentane diffusivity with loading in single-

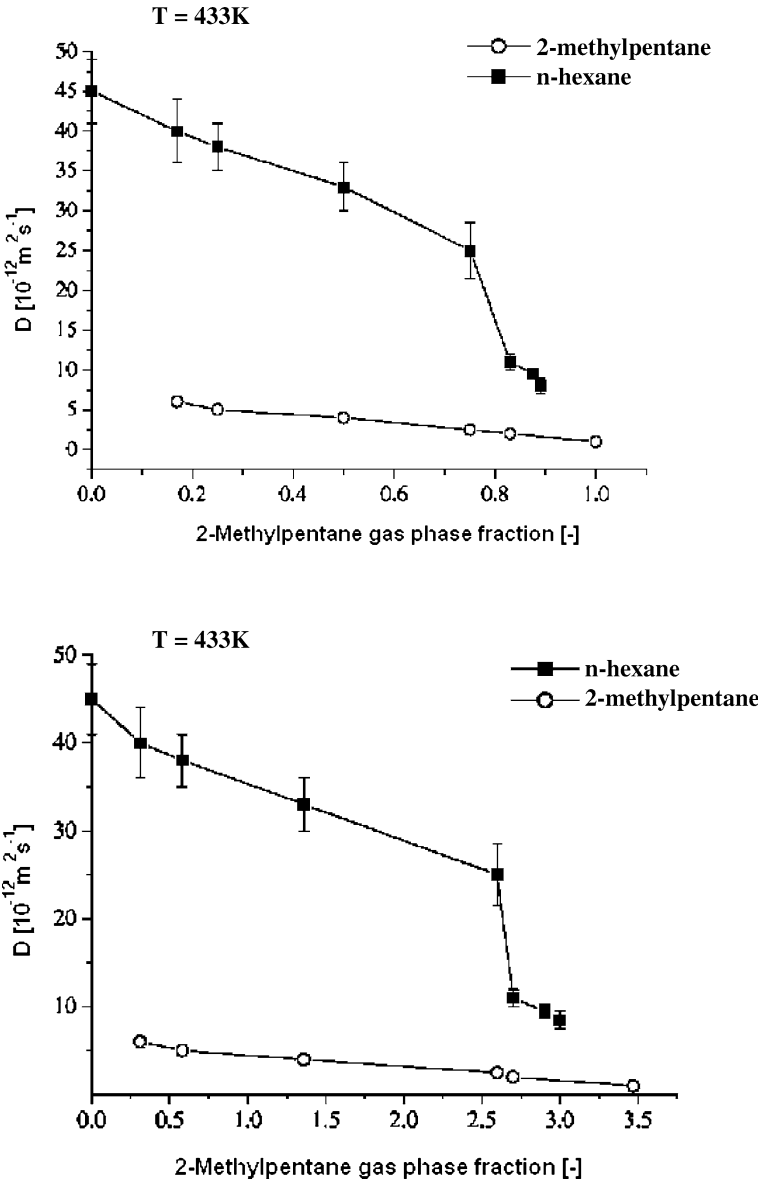

Fig. 11 Self-diffusivities of mixture components in silicalite as a function of the 2-methylpentane fraction in the gas phase (*left*) and as a function of the 2-methylpentane loading (total hydrocarbon pressure 6.6 kPa, 433 K)

component studies [53] and indicating that the mobility of the slower component is not noticeably affected by the presence of a fast one [54–56]. A peculiar observation is found in the dependence of the *n*-hexane self-diffusivity on

the 2-methylpentane fraction. We find a monotonous decrease of the self-diffusivity with an increase of the isohexane fraction up to a value of 0.75. At higher values a strong decrease in the linear alkane diffusivity is observed, and the values for the self-diffusivity of *n*-hexane and 2-methylpentane become close. This sharp drop in mobility results from the hindrance imposed by its branched isomer, because the total loading remains more or less constant. Diffusion in zeolites is considered to proceed via a sequence of activated jumps from one site to the other. A jump is successful if the neighboring site to which the molecule attempts to jump is empty. Isohexane molecules are preferentially adsorbed at the channel intersections that connect the straight and zigzag channels. An increase of the amount of slowly moving molecules (2-methylpentane) will lead to the blockage of these intersections. Thus, the number of successful jumps of the fast component (*n*-hexane) should be determined by the rate at which an empty site is created by a jump of the slow component. Thus, at high loadings of 2-methylpentane, the self-diffusivity of *n*-hexane becomes strongly determined by the self-diffusion rate of its branched isomer. In Fig. 11, the self-diffusion coefficients of both components are shown as a function of the 2-methylpentane loading. One can see that the sudden drop in *n*-hexane diffusivity occurs at a 2-methylpentane loading of approximately 2.75 molecules per unit cell. We surmise that this loading already blocks the three-dimensional pore network of silicalite-1 strongly enough to lead to considerably lower *n*-hexane diffusivities. When all the intersections are occupied by the slowly diffusing branched alkanes, the entire pore system will be blocked. As a consequence of this, the diffusion of hexane will be determined by the diffusion rate of the slow component. Indeed, when the loading of 2-methylpentane increases further, *n*-hexane diffusivity continues to decrease, and one would expect them to become equal at higher loadings. Similar phenomena regarding the blockage of the pore network were observed during the adsorption of methane and benzene in zeolite Na-Y [57] and silicalite [58]. In Na-Y, the benzene molecules block the windows of the supercages and disrupt the mobility of the smaller methane molecules. Förste et al. [58] showed that the decrease of methane diffusivity was also caused by blocking of the channel intersections by benzene in MFI zeolite. For methane/xenon mixtures in silicalite-1, both components are preferentially sited in the interiors of the (straight and zigzag) channels, causing the blocking by the slow components to be less dramatic [54].

For *n*-butane/methane [56] and methane/tetrafluoromethane [52] mixtures in silicalite, a decrease in the diffusivity of both mixture components was observed with an increase of the loading of slower *n*-butane and methane. In the first case, methane shows a preferential adsorption for the intersections, while *n*-butane is approximately equally adsorbed in the straight and zigzag channels [46]. In mixtures of CH_4/CF_4 in silicalite, CF_4 adsorbs preferentially in the straight channels while methane adsorbs in zigzag channels. The decrease in diffusion rates for these components is probably caused

by the decrease of the probability for the molecule to jump to a free neighboring adsorption site. A sharp drop in the diffusivity was indeed observed by Masuda et al. [55], who studied binary diffusion of *n*-heptane and *n*-octane in silicalite. These alkanes do not have any preference for a particular adsorption site. Therefore, both components (the faster and the slower one) will diffuse on a rate similarly decreased upon increased loading. Thus, multicomponent diffusion is not only strongly related to the zeolite topology and adsorption properties of the components, but also by the presence of another adsorbate. The diffusion coefficient of a component will then also depend on the loading of the other component. This makes it crucial to obtain more insight into multicomponent diffusion coefficients because in most practical situations diffusivity will be determined by the mixture components and relative concentrations.

3.2 Influence of Acid Sites on Diffusivity: a Comparison of Silicalite-1 and H-ZSM-5

In the previous section we investigated the diffusivity of *n*-hexane and 2-methylpentane in an all-silica MFI zeolite. To obtain more insight into the role of acidity we compare here results obtained with silicalite-1 and H-ZSM-5. The loadings of both components in silicalite-1 and H-ZSM-5 are displayed in Fig. 12. The adsorbed concentration of *n*-hexane in H-ZSM-5 is higher than in silicalite-1. This result should be expected from the presence of the acid sites, since the enthalpy of *n*-hexane adsorption in H-ZSM-5 (82 kJ mol^{-1}) was reported to be higher than in silicalite-1 (72 kJ mol^{-1}) [59]. For isohexane these values were reported to be lower by 6 kJ mol^{-1}. It was found that in H-ZSM-5 at high *n*-hexane loadings a complex of two hydrocarbon molecules with the bridging hydroxyl group is formed, whereas isoalkane molecules are unable to form such a complex with the acid site. Indeed, in our study 2-methylpentane loadings in mixtures in H-ZSM-5 are very close to those in silicalite-1.

The loading of *n*-hexane in mixtures is somewhat higher than it is expected to be if it were proportional to its partial pressure (Fig. 12). On the contrary, the 2-methylpentane loading is somewhat lower. This points to preferential adsorption of *n*-hexane over isohexane in their mixtures in H-ZSM-5 than in silicalite-1. In earlier experimental [50] and CBMC simulation studies [44] of *n*-hexane/isohexane mixtures in silicalite-1, a slight preferential adsorption of the linear alkane over the branched one has been found. The most prominent explanation for this preference is the molecular siting of these two hydrocarbon molecules. Whereas *n*-hexane exhibits no clear preference for a position in the micropore system of MFI zeolite, the branched isomer is preferentially located at the channel intersections due to entropic reasons [44]. Consequently, 2-methylpentane will be pushed out from silicalite-1 by *n*-hexane. These effects are even stronger for H-ZSM-5, most likely due to the stronger

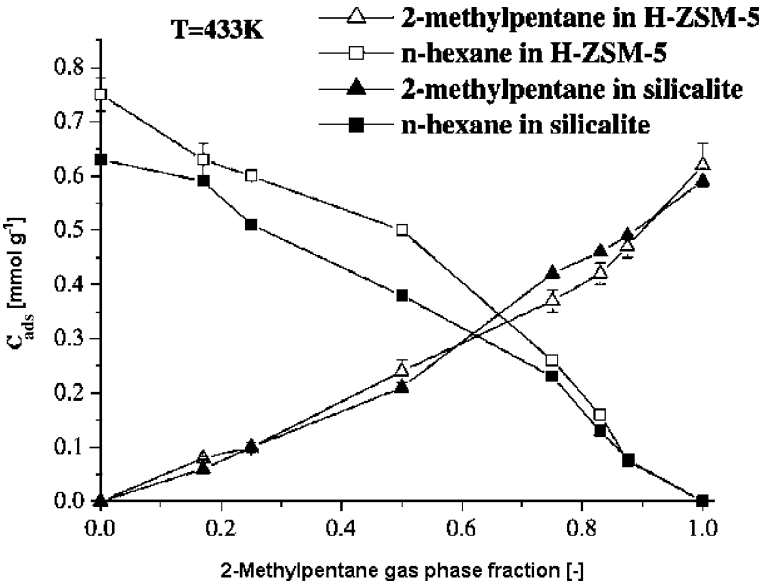

Fig. 12 Loadings of mixture components in both MFI-type zeolites as a function of 2-methylpentane fraction in the gas phase, total hydrocarbon pressure 6.6 kPa, 433 K

interaction of *n*-hexane with acid sites than the branched alkane [59], which results in a higher packing efficiency for the linear alkane (Table 2).

Table 2 shows the adsorbed concentrations of the pure components. At a partial pressure of 6.6 kPa the amount of *n*-hexane is just slightly higher than that of isohexane in silicalite-1, while the linear alkane is obviously adsorbed more strongly than 2-methylpentane in H-ZSM-5 due to the stronger interaction with the acid sites. The maximum loading of each component has been measured by a separate adsorption study. The sorption capacity of *n*-hexane (7 molecules per unit cell), in agreement with earlier studies [48, 59–61] exceeds that of 2-methylpentane (4 molecules per unit cell). The latter value equals the number of channel intersections in the MFI pore system per unit cell. Indeed, the sorption of isohexane molecules at

Table 2 Loadings of single components (mmol g^{-1}) in silicalite-1 and H-ZSM-5 at 433 K (loadings given at a hydrocarbon partial pressure of 6.6 kPa and the maximum loading)

Zeolite	*n*-hexane 6.6 kPa	c_{max}	2-methylpentane 6.6 kPa	c_{max}
H-ZSM-5	0.75	1.1 ± 0.2	0.62	0.74 ± 0.04
silicalite-1	0.63	1.2 ± 0.2	0.59	0.75 ± 0.02

energetically less favorable locations requires high pressures [44]. An experimental study of single-component *n*-butane and isobutane adsorption by the volumetric method in silicalite-1 and H-ZSM-5 leads to similar conclusions [62]. Valyon et al. [62] found that under identical conditions the *n*-butane loading was 1.5 (2.0) times higher than that of isobutane at a temperature of 273 (413) K. For H-ZSM-5 complete saturation with butanes was reached at lower pressures because of the stronger interactions with the acid sites. For *n*-butane the maximum loading was found to be equal to approximately 8 molecules per unit cell, while for isobutane the inflection in the isotherm was observed at a sorbed amount of 4 molecules per unit cell. Our results support the finding that the stronger interaction of linear alkanes with acid protons in H-ZSM-5 compared to branched ones results in a preferential adsorption of linear *n*-hexane over 2-methylpentane.

Figure 13 displays the self-diffusivities of *n*-hexane and 2-methylpentane in silicalite-1 and H-ZSM-5 as a function of the ratio of the hydrocarbons. The self-diffusivities of both hexanes linearly decrease with increasing gas-phase fraction of the branched hexane in the gas phase for the non-acidic and acidic zeolite. In H-ZSM-5, the mobility of alkanes is approximately two times slower than in silicalite-1. Obviously, the presence of acid sites strongly affects the molecular transport due to stronger interactions with the *n*-hexane molecules. A similar effect of Brønsted sites on the single component diffusion of aromatics was observed in MFI zeolites with different concentration of acid sites [63–65]. The *frequency response* (FR) technique provided similar results

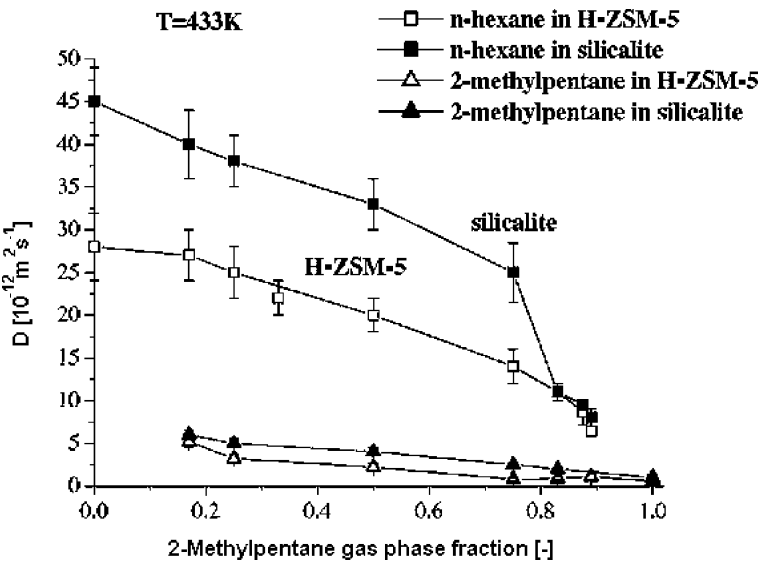

Fig. 13 Self-diffusivities of mixture components in both MFI-type zeolites as a function of 2-methylpentane fraction in the gas phase (total hydrocarbon pressure 6.6 kPa, 433 K)

for *n*-butane and isobutane diffusion in silicalite-1 and H-ZSM-5 [62]: the diffusivity of both components was approximately half in the acidic zeolite sites and the diffusion of isobutane was significantly slower compared to *n*-butane.

In the present study of binary mixtures the self-diffusivity of the faster component (*n*-hexane) in H-ZSM-5 is influenced by two factors: (i) the presence of slower 2-methylpentane molecules and (ii) the strong interaction of the linear alkane with acid sites. As long as the concentration of the branched hexane does not exceed a critical value, the effect of the Brønsted sites is dominating and the diffusion of *n*-hexane in mixtures is roughly two times lower in H-ZSM-5 than in the zeolite without acid sites. A behavior similar to that of *n*-hexane is observed for 2-methylpentane in Fig. 13. Its self-diffusivity decreases in both zeolite-types with increasing loading and analogous to *n*-hexane the self-diffusion coefficient in H-ZSM-5 is half that in silicalite-1, even for the single-component experiment. Thus, the presence of the Brønsted sites noticeably decreases the diffusivities of both hexanes due to the increased hydrocarbon-zeolite interaction in the presence of protonic sites.

Around a value of the gas-phase fraction of 2-methylpentane of about 0.83, the influence of the acid sites on the *n*-hexane diffusivity is not dominant anymore in comparison to the pore occupation of slow-diffusing 2-methylpentane. Figure 14 shows the dependence of the diffusivities of both components versus the concentration of adsorbed 2-methylpentane in terms of molecules per unit cell. The diffusivities of *n*-hexane in silicalite-1 and H-ZSM-5 become nearly equal when the concentration of 2-methylpentane reaches approximately 2.75 molecules per unit cell. For 2-methylpentane we find that the self-diffusivity in silicalite-1 becomes very close to the value in H-ZSM-5 at the same loading.

Earlier we discussed the behavior of binary mixtures of linear and monobranched hexanes in silicalite-1. We found that pore blockage due to preferential adsorption of the branched isomer occurs when its concentration reaches approximately 2.7 molecules per unit cell. From CBMC simulations [44] it is known that monobranched molecules such as 2-methylpentane and 3-methylpentane prefer to occupy the intersections between straight and zigzag channels in MFI-type zeolites. On the other hand, from its crystallographic zeolite structure [1] we know that the MFI unit cell has four intersections. Therefore, the diffusivity of *n*-hexane sharply decreases when more than half of the intersections are occupied by its branched isomer. Figure 14 shows that a further increase of the 2-methylpentane loading up to three molecules per unit cell results in the *n*-hexane diffusivities in silicalite-1 and H-ZSM-5 becoming almost similar. This can be explained by the influence of the co-adsorbed branched isomer. While the acid sites in H-ZSM-5 slow down *n*-hexane diffusivity considerably, this effect is largely absent when 2-methylpentane is present in the micropores. Our observations are confirmed by a recent experimental study of diffusion in silicalite of binary mixtures of alkanes (*n*-heptane, *n*-octane) and aromatics (ortho- and

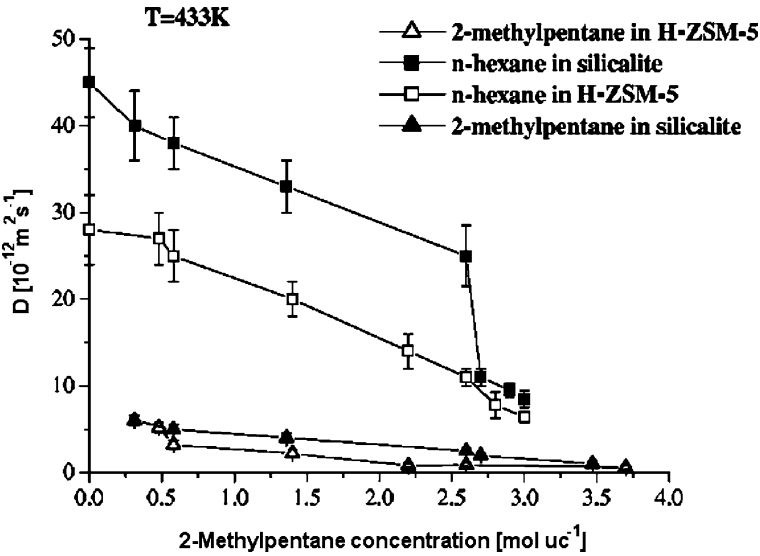

Fig. 14 Self-diffusivities of mixture components in both MFI-type zeolites as a function of 2-methylpentane loading, 433 K

meta-xylene) [55]. These authors found that a component with a low diffusion coefficient can considerably slow down diffusion of a faster one by selective blocking of the zeolite intersections [65]. They also measured that the diffusion of the slow component is not affected by the presence of the fast component, which is in agreement with studies of methane/xenon mixtures [66]. This is also in agreement with our study.

Summarizing, we conclude that for binary mixtures of a linear and branched hexane in H-ZSM-5 and silicalite-1 two factors influence the respective diffusivities: (i) the strong interaction with acid sites preferentially decreases *n*-hexane diffusivity and (ii) the blocking of intersection adsorption sites by 2-methylpentane decreases *n*-hexane diffusivity. At high loadings of the branched isomer the latter effect is dominating, and finally the diffusivity of the linear hexane is totally determined by its branched isomer.

The current work indicates the strong effect of acid sites on the interaction and diffusivity of hydrocarbons. To further study this effect, we determined the single-component diffusion coefficients and specifically the activation energy for diffusion. Activated diffusion is described by the Arrhenius-type Eq. 8. The pre-exponential factor D_{inf} is related to the jump frequency between adsorption sites in the zeolite lattice, while the exponential expresses the chance that the molecules are able to overcome the free energy barrier E_{act} between these sites. The loadings of *n*-hexane and 2-methylpentane in H-ZSM-5 and silicalite-1 have been measured at temperatures between 373 and 533 K at intervals of 20 K. The hydrocarbon pressure was taken identical

to that in the binary mixture experiments (6.6 kPa). The values of the apparent activation energies for diffusion have been obtained. The term *apparent* activation energy of diffusion (E_{app}) is explicitly used to distinguish it from the *true* activation energy of diffusion (E_{act}). The latter activation energy is determined at constant (mostly very low) concentration of the adsorbate. However, in the present experiments a change in temperature not only leads to a change in the diffusion coefficient but also in the adsorbate loading.

Figure 15 displays the loadings of *n*-hexane and 2-methylpentane in both zeolites. Under similar conditions, the adsorbed concentration of *n*-hexane is higher than that of 2-methylpentane, especially at lower temperatures. The interaction with *n*-hexane results in higher loadings for H-ZSM-5 than for silicalite-1. From the temperature dependence of the diffusivity of *n*-hexane in both zeolites, the apparent activation energy has been deduced and the results are collected in Table 3. Corresponding Arrhenius plots are shown

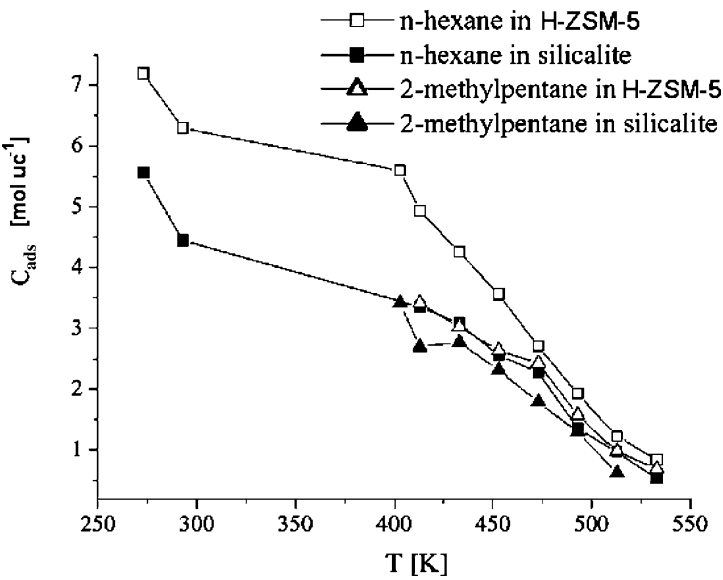

Fig. 15 Loadings of hexanes measured at various temperatures in silicalite-1 and H-ZSM-5

Table 3 Apparent activation energy of diffusion for *n*-hexane in MFI-type zeolites and a comparison with literature

Zeolite	E_{app} [kJ mol^{-1}] TEX-PEP	Refs.
Silicalite-1	18.5 ± 1.5	16–19 [73–75]
H-ZSM-5	22.0 ± 2.0	20–24 [67–69]

in Fig. 16. The apparent activation energy measured with the TEX-PEP is higher for H-ZSM-5 than for silicalite-1, although the difference is small and not totally significant. Experiments earlier performed at 433 K show that

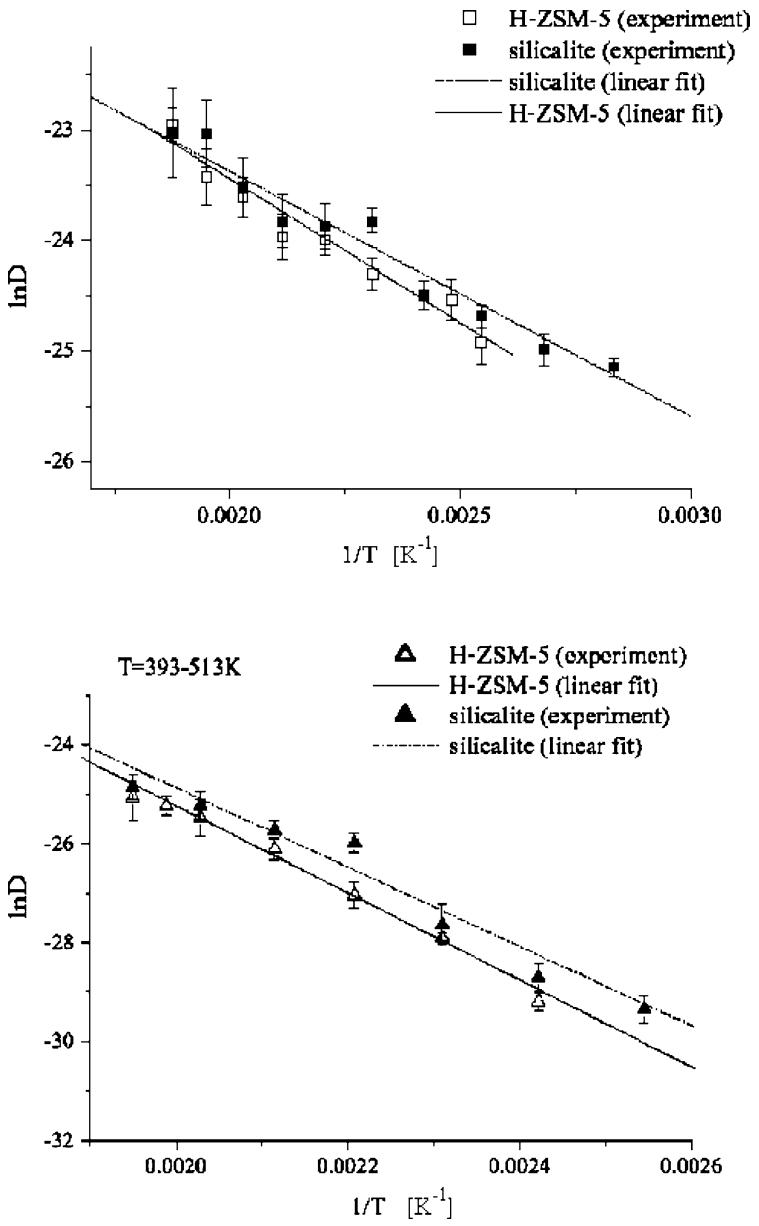

Fig. 16 Arrhenius plots for diffusivities of *n*-hexane (*left*) and of 2-methylpentane (*right*) in silicalite-1 and H-ZSM-5

the diffusivity of *n*-hexane in H-ZSM-5 is by a factor of two lower than in silicalite-1. Valyon et al. [62] have measured the activation energy of diffusion for *n*-butane in silicalite-1 and H-ZSM-5 with the FR method. They found values of 10.7 and 13.1 kJ mol^{-1} respectively, which explained the increase of hydrocarbon diffusivity in the absence of protonic sites. In our case we also find a higher activation energy for the acidic material. The values are in good agreement with values provided by other techniques (Table 3). The activation energy of *n*-hexane diffusion in H-ZSM-5 determined by the FR method [67, 68] is equal to 24 kJ mol^{-1}. The constant volume method provided a value of 20 kJ mol^{-1} [69]. Thus, a value of 22 ± 2 kJ mol^{-1} as measured in this work overlaps very well with these values. On the other hand, Hermann et al. [70–72] found a somewhat lower value of 15.6 kJ mol^{-1} upon measurements of the transport diffusivity of *n*-hexane in H-ZSM-5 at relatively low loading by a micro-FTIR technique.

The value of the apparent activation energy for silicalite-1 is also reproduced by other methods such as the ZLC and the square wave methods [73–75]. Discrepancies, however, occur with techniques such as membrane permeation and TEOM, that provided somewhat higher values of the activation energy for *n*-hexane, i.e., 34.7 kJ mol^{-1} [76] and 38 kJ mol^{-1} [45], respectively. In the membrane permeation technique very high loadings up to eight molecules per unit cell were used, which may explain the discrepancy. The value provided by Zhu et al. [45] is the activation energy deduced from the corrected diffusivities. The diffusivities were measured at different conditions (partial pressures) and the loadings were also up to 5.25 molecules per unit cell.

In principle, one would expect an increase in the activation energy of diffusion in the presence of the acid sites. The interaction of the hydrocarbon with Brønsted sites will increase the barrier to be overcome for hopping of the hydrocarbon from one to the next site. Indeed, this is observed by several authors, although we should note that the effect is generally small compared to the accuracy of the measurements.

Corresponding Arrhenius plots for the diffusion of 2-methylpentane in silicalite-1 and H-ZSM-5 are presented in Fig. 16, and the results are collected in Table 4. The diffusivities have been measured in the temperature interval

Table 4 Apparent activation energy of diffusion for 2-methylpentane in MFI-type zeolites and a comparison to literature data

Zeolite	E_{app} [kJ mol^{-1}] TEX-PEP	Refs.
Silicalite-1	66 ± 6	50 [45]; 46 [77]
H-ZSM-5	72 ± 3	24 [79]; 36 [78]

393–513 K and 413–533 K for silicalite-1 and H-ZSM-5, respectively. An experimental problem is the low concentration of adsorbed 2-methylpentane at higher temperatures which leads to a low signal-to-noise ratio. This prohibits us to measure the diffusivity and the loading of 2-methylpentane in silicalite at 533 K. For the same reason the experimental error was slightly higher than 10% for the other measurements. The apparent activation energies of diffusion found for 2-methylpentane in silicalite-1 and H-ZSM-5 are both significantly higher than those for *n*-hexane. This results in an order of magnitude difference in the diffusion coefficients for these alkanes. This is in agreement with the earlier studies of linear and mono and dibranched alkanes in MFI-type zeolites [77, 78].

The commonly accepted explanation for the higher activation energies of diffusion for isoalkanes in MFI zeolites is that due to its higher critical diameter isoalkanes experience a steric hindrance during diffusion. Similar to *n*-hexane, we find a higher value for the apparent activation energy of 2-methylpentane in H-ZSM-5 than in silicalite-1. This is in agreement with the findings of the FR technique for isobutane diffusion in MFI-type zeolites [62]. The activation energy of isobutane was measured to be 1.2 kJ mol^{-1} higher in H-ZSM-5. TEX-PEP does not allow us to be that precise in this case, but in combination with data on mixture experiments we suggest that the interaction between the alkane and the Brønsted sites results in an increase in the activation energy of diffusion. The values for the activation energy for 2-methylpentane diffusion in both zeolites measured here are significantly higher than those measured by other techniques (Table 4). TEOM [45] and gravimetric measurements [77] provide an activation energy for branched hexane diffusion in silicalite-1 of 50 and 46 kJ mol^{-1}, respectively. This value is even higher than that obtained in H-ZSM-5 as measured by Xiao and Wei with the same method (36 kJ mol^{-1} [78]) and by Keipert and Baerns with a transient technique (24 kJ mol^{-1} [79]).

The discrepancies between the values of the activation energies provided by different authors can be attributed to the different alkane partial pressures. Several theoretical and experimental studies indicate a significant concentration dependence of diffusion in zeolites [4, 19, 77, 78, 80]. Coppens et al. [19] have shown for MFI zeolite with Monte-Carlo simulations that the diffusivity can drop by a factor of ten when the occupancy is close to saturation. In this work we performed our experiments under a hydrocarbon partial pressure of 6.6 kPa, which is higher than the pressures in TEOM, gravimetric and volumetric measurements.

Figure 15 shows the loadings of 2-methylpentane and *n*-hexane in both zeolites in the temperature interval used to determine the activation energy. The loading of 2-methylpentane reaches 3.5 molecules per unit cell with the loadings in H-ZSM-5 being slightly higher than in silicalite-1 at the same temperatures. The maximum loadings of 2-methylpentane in silicalite-1 and H-ZSM-5 were measured to be 0.75 mmol g^{-1}, which corresponds to approxi-

mately 4.2 molecules per unit cell. At a partial pressure of 6.6 kPa, the zeolite loading was up to 80% of the saturation, which is higher than the experimental conditions of other techniques. Indeed, in the transient experiments performed with a TAP reactor [79] a pulse of a very small amount of molecules is admitted to the empty zeolite. In such a case the influence of other hydrocarbons can be excluded. It is also important to note that the experimental conditions (partial pressure) used in the gravimetric experiments [77, 79] were not specified. Nevertheless, diffusion coefficients provided by those techniques are in a fair agreement with the values measured here. The data are collected in Table 5.

Table 5 Diffusion coefficients for 2-methylpentane in MFI-type zeolites and a comparison with literature

Zeolite	D [$m^2 s^{-1}$] (T = 423 K)			
	Grav. [74, 75]	Grav. [76]	TAP [77]	PEP
Silicalite-1	2×10^{-12}			1.1×10^{-12}
H-ZSM-5		9×10^{-13}	1×10^{-12}	4×10^{-13}

Summarizing, we observe that the presence of acid sites causes a decrease in the self-diffusivity of *n*-hexane and 2-methylpentane. In H-ZSM-5, we find that the diffusivity of *n*-hexane in mixtures with its branched isomer is determined by two factors: (i) the interaction with acid sites, strong for the linear alkane, which decreases the diffusivity and (ii) the presence of 2-methylpentane which has an order of magnitude lower diffusivity. At low 2-methylpentane loadings the influence of the acid sites is dominating. However, at a loading of about 2.7 molecules per unit cell, the effect of pore blocking by the preferential location of the branched alkane in the intersections dominates. The diffusivities are then more or less equal in silicalite-1 and H-ZSM-5.

3.3 Self-diffusivity of *n*-Pentane and *n*-Hexane and their Mixtures in Silicalite-1

We have earlier studied the concentration dependence of the self-diffusivity of *n*-hexane in large crystals of silicalite-1 and H-ZSM-5 zeolites [81]. A rather peculiar monotonic increase in the diffusivity was observed with increasing alkane loading for both zeolites up to 4 molecules per unit cell. The diffusion coefficient in H-ZSM-5 was found to be approximately half of that in silicalite-1 due to the interaction of *n*-hexane with the Brønsted acid sites. The increase in the diffusivities with the loading was assumed to be caused by repulsive interactions between the molecules adsorbed in the channel intersections and

the adjacent straight channel. However, we should note that this explanation is rather speculative and has to be supported by theoretical investigations. Here, we will report similar investigations for *n*-pentane and mixtures of *n*-pentane and *n*-hexane. Before discussing in more detail the diffusivities of such mixtures for which PEP is a unique technique, we will focus on the self-diffusivity of *n*-pentane in silicalite-1 as a function of loading at various temperatures. At temperatures of 473 and 453 K the hydrocarbon loading is low, i.e., less than 1.5 molecules per unit cell making accurate determinations of self-diffusion coefficients difficult. At 433 K the loading corresponds to about 3.5 molecules per unit cell. At low temperatures (373 and 393 K) the diffusion coefficient of *n*-pentane increases with its loading. This is in line with previous results for *n*-hexane diffusion in silicalite-1 [81]. In that study, we reported the peculiar phenomenon that an increase of *n*-hexane loading from 0.1 to 4 molecules per unit cell led to a significant increase in self-diffusivity. This unexpected effect is tentatively explained by repulsive interactions between hydrocarbon molecules, leading to an increase in the jump rate between adjacent sites.

Such interactions and their effect on diffusivity have been described by Paschek and Krishna for isobutane in silicalite-1 [82]. We tentatively propose that the concentration dependence of *n*-pentane diffusivity reported here is due to similar effects. In short, this means that repulsive intermolecular interactions lead to increased mobility of *n*-pentane. This tallies with the absence of a siting preference for this hydrocarbon. One would expect slightly weaker repulsions for *n*-pentane compared to the longer *n*-hexane molecules, especially at high temperatures. Indeed, as only one molecule (*n*-pentane or *n*-hexane) fits into a channel or an intersection, the distance between the *n*-pentane molecules adsorbed in the straight channels and the intersections is larger than the corresponding distance for *n*-hexane molecules. One expects that repulsive forces decrease with an increase in the intermolecular distance. At high temperatures, these interactions are weaker as predicted by Paschek and Krishna [82]. This effect is also found in our experiments as the diffusivity of *n*-pentane does not increase with loading at high temperatures ($T > 493$ K).

Besides repulsive interactions between the molecules, other factors influence the diffusion of *n*-pentane in silicalite-1. Theoretical calculations [17–19, 53] have shown a decrease in the diffusivity with loading when repulsive interactions are not taken into account. In this case, pore occupancy plays a dominant role. As the loading increases, the probability for the molecule to jump to the neighboring adsorption site decreases since the chance that the site is already occupied increases. Hence, the molecule will reside longer at its current location. This effectively decreases the jump frequency and thus the self-diffusion coefficient. According to mean-field theory, diffusivity should be proportional to the fraction of the unoccupied sites [2]. For silicalite-1, self-diffusivity was shown to decrease slightly faster with the occupancy due to correlation effects [19]. Krishna and Paschek [84] determined

a jump diffusion at a given occupancy as a jump diffusion at zero occupancy proportional to the vacancy factor and to the repulsion factor, which in turn is also concentration dependent. Therefore, we assume that self-diffusion of *n*-pentane in silicalite is simultaneously affected by the hydrocarbon loading of the zeolite, that causes a decrease in the diffusion, and by repulsive interactions between the molecules, that cause an increase in their mobility. These two effects compete with each other. Experimental conditions determine which of these two dominates. For example, up to a certain partial pressure, molecules such as branched alkanes are preferentially adsorbed in the channel intersections [44, 82, 85]. Under these conditions, there is no repulsion between the molecules, and diffusion decreases with the loading. As soon as the molecules start to appear in the straight channels, diffusion increases [82]. To our opinion, the observation that at relatively high temperatures (433–473 K), the self-diffusion coefficient of *n*-pentane does not change with concentration (Fig. 17) indicates that the pore occupancy effect is compensated by the repulsive interactions between the molecules. At 433 K, the concentration of *n*-pentane in the micropores varied from 0.5 to 3.5 molecules per unit cell. At these pore occupancies, and making the assumption that other interactions are absent, a decrease in the diffusivity is predicted by Coppens et al. [19]. The deviant observation can be tentatively explained by inclusion of repulsive interactions that compensate this decrease of the molecular mobility. On the other hand, at high temperatures diffusion is faster

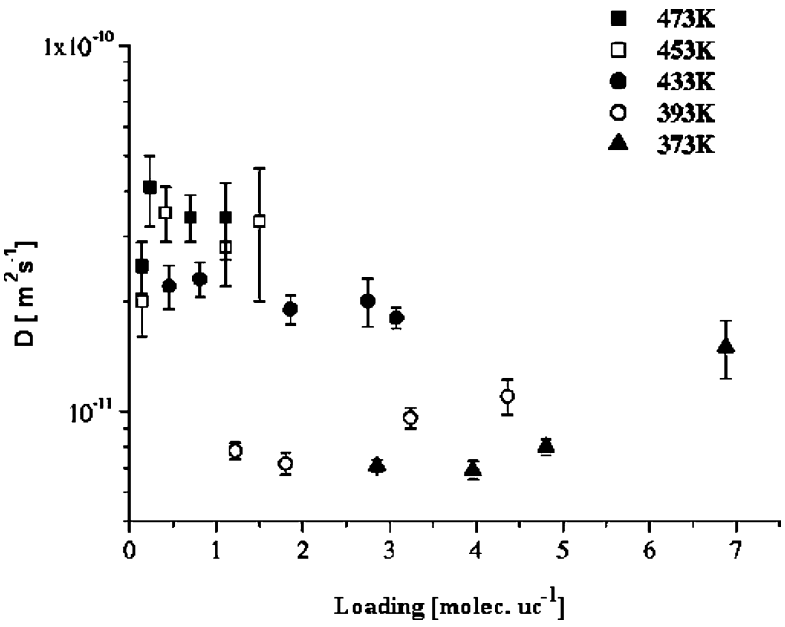

Fig. 17 Self-diffusivity of *n*-pentane in silicalite-1 at various temperatures and loadings

and the repulsive interactions should be weaker. Therefore, such interactions do not dominate over the pore occupancy effect and the diffusion coefficient does not change. At low loadings, both the occupancy and repulsion effects are apparently not of overriding importance, and we find almost constant values for the self-diffusion coefficient within the experimental accuracy limits. At lower temperatures (373–393 K), we observe that diffusion becomes faster at higher loadings. This is similar to our earlier report on *n*-hexane diffusivity [81] and is explained by the dominance of repulsive interactions.

In the work of Heink et al. [86] a decrease in the diffusivity of *n*-pentane in silicalite-1 up to loadings of 0.75 molecules per unit cell and higher than four molecules per unit cell was found with PFG NMR. Despite an apparent disagreement, we note that in their experiments at low concentrations the pore occupancy effect was dominating, resulting in a lowering of the jump frequency with loading. The absence of such an increase in the present study may lie in the lower experimental accuracy. At high loadings (4–12 molecules per unit cell), a decrease of *n*-pentane diffusion was measured [86, 87]. Probably, the occupancy effect is more dominant than the intermolecular repulsive effect in this range. On the other hand, it is known that the maximum sorption capacity of silicalite-1 for *n*-pentane is approximately eight molecules per unit cell, implying that at loadings higher than eight molecules per unit cell the diffusion coefficients do not pertain exclusively to micropore diffusion. Our interpretation is further supported by diffusion measurements of light alkanes in silicalite-1 performed by van de Graaf et al. [91] using a membrane permeation technique. At 303 K, an increase of the intracrystalline diffusivity was observed for C_1-C_3 alkanes. At higher temperatures, the diffusivity did not change with increasing concentration in line with our results. For *n*-propane, the diffusivity had a maximum at pore occupancy of approximately 0.8. Apparently, up to that occupancy diffusivity increases due to the stronger influence of the proposed repulsive interactions. At higher loadings the pore occupancy effect dominates resulting in a decrease of the diffusivity.

Summarizing, we propose the following for *n*-pentane diffusion in silicalite-1. At very low loadings, *n*-pentane diffusion coefficients are constant or slightly decrease with the total pore occupancy. This possible decrease is due to the pore occupancy effect but is too small to be detected by the TEXPEP method. At intermediate loadings, molecules occupy both straight and zigzag channels and start to develop repulsive interactions. The expected decrease in diffusion coefficient with pore occupancy is compensated by an increase in the jump frequency due to such repulsive interactions. At high loadings, the repulsion effect is dominating and the self-diffusion coefficient increases. At even higher loadings, we expect the diffusion to slow down due to strong pore occupancy effects. Note that the repulsive interactions do not have a noticeable impact on the molecular mobility at high temperatures, and consequently the effect of loading on the diffusivity is small at high temperature. In this latter case it is not possible to work at higher loadings because the

Table 6 Comparison of *n*-pentane diffusivities reported in literature with those obtained by TEX-PEP

Method	$D \times 10^{-11}$ [$m^2\ s^{-1}$]	Conditions	Refs.
TEX-PEP	0.7–1.05	373 K, 2.9–7.1 molec.uc^{-1}	
Membrane technique	0.24	334 K, –	[88]
ZLC	0.2	334 K, –	[71, 72]
FR	40	303 K, 7 molec.uc^{-1}	[89]
PFG NMR	40	330 K, 4 molec.uc^{-1}	[86]
PFG NMR	204	334 K, 4–8 molec.uc^{-1}	[87]
SCM	1	300 K, 0.5 kPa	[90]
MD	98.5	333 K, 4 molec.uc^{-1}	[53]

adsorbate has a limited concentration at higher temperatures by the technical design of the feed system.

Table 6 shows a comparison between diffusion coefficients of *n*-pentane in silicalite-1 measured by various macro- and microscopic techniques as well as deduced from molecular dynamics simulations. However, we did not find reports where diffusion coefficients of *n*-pentane in silicalite-1 were measured under conditions similar to this study. TEX-PEP values are in a good agreement with values provided by macroscopic techniques such as the Membrane technique [88], ZLC [71, 72] and the SCM technique [90]. The diffusivity provided by the macroscopic frequency response method is an order of magnitude higher [89]. Tentatively, we explain this to the significantly lower temperature and higher loading which could lead to a dominating influence of the repulsive interactions. Usually, diffusivities measured by microscopic techniques (PFG NMR) or computer simulations are significantly higher than those from macroscopic methods. The authors of a novel macroscopic ultra-high vacuum technique, Multitrack [92], claimed that one of the reasons for the lower values of the diffusivities measured by macroscopic methods is the diffusion resistance caused by the presence of a carrier gas. Comparison with the data found in the literature shows that the diffusivities provided by the TEX-PEP method are in reasonably good agreement with the values supplied by other macroscopic techniques.

Activation Energy of *n*-Pentane Diffusion in Silicalite-1

We have tried to establish whether there is any influence of the proposed repulsive interactions on the apparent activation energy for diffusion. In a theoretical study on isobutane diffusion in silicalite-1 [82], a change in the apparent activation energy was determined. At lower temperatures, the apparent activation energy was lower than at elevated temperatures. This effect was proposed to be caused by repulsive interactions. We determined the ap-

Table 7 Apparent activation energy of diffusion for *n*-pentane in silicalite at various partial pressures

Pressure [kPa]	E_{app} [kJ mol^{-1}]
0.5	18 ± 4
1.0	27 ± 4
3.3	21 ± 3
9.0	13 ± 2

parent activation energy for diffusion of *n*-pentane in silicalite-1 at partial pressures of 0.5, 1.0, 3.3 and 9.0 kPa in the temperature interval 393–473 K. The results are collected in Table 7. At low hydrocarbon partial pressures the accuracy was low which is related to the lower accuracy in the determination of the self-diffusivities. Nevertheless, the values are in the range of literature data, varying from 8.3 kJ mol^{-1} (PFG NMR [86]) to 21 kJ mol^{-1} (FR, [89]). Evidently, the apparent activation energy does change with the partial pressure. We explain this by the competing influence of two factors, i.e., the pore occupancy and the repulsive interactions. Which of these two effects is dominant depends on the temperature and adsorbate concentration. The *n*-pentane loadings in silicalite-1 are depicted in Fig. 18.

Earlier, we have reported that the apparent activation energy for diffusion of 3-methylpentane in silicalite-1 increases with the partial pressure. This was explained by the pore occupancy effect influencing the pre-exponential fac-

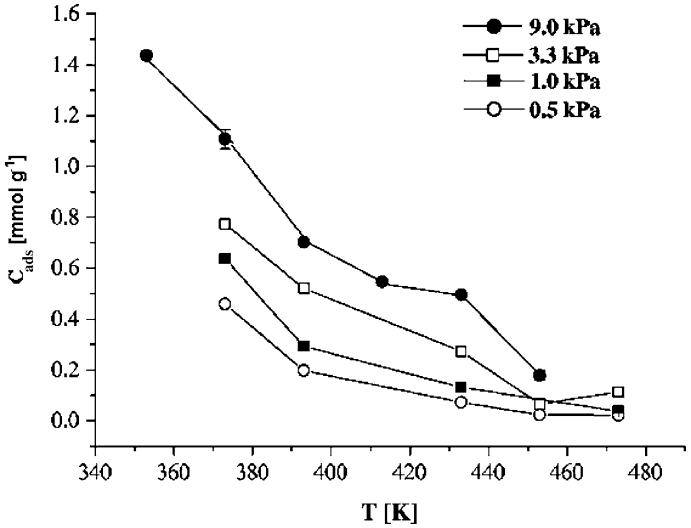

Fig. 18 *n*-Pentane loadings at various temperatures and partial pressures in silicalite-1

tor of diffusion which is proportional to the jump frequency, D_{inf}. This is explained by the fact that under fixed partial pressure conditions the zeolite loading will vary as a function of temperature.

On the other hand, the apparent activation energy for *n*-pentane diffusion in silicalite-1 might decrease due to the repulsive interactions as shown earlier. The lower apparent activation energy at a partial pressure of 0.5 kPa is due to the compensation of the pore occupancy and repulsive effects. We speculate that the apparent activation energy is close to the one at zero loading. At higher partial pressures the pore occupancy starts to play a more significant role, leading to an increase in the apparent activation energy. At high partial pressure (9.0 kPa), the apparent activation energy has the lowest value, which is attributed to the strong increase in diffusivity due to the dominating repulsive interactions.

The current trends identified for *n*-pentane are strikingly similar to those for *n*-hexane. TEX-PEP provides the unique possibility to study diffusion of two linear hydrocarbon in two separate sets of experiments. In a first set, *n*-pentane is labeled and its diffusion coefficients are determined in a mixture with non-labeled *n*-hexane, while the reverse is done in a second set. The experiments have been performed at a temperature of 433 K and the total hydrocarbon pressure was kept constant at 6.6 kPa by varying the ratio between *n*-hexane and *n*-pentane in the gas phase. Figure 19 shows the loadings of both components in the mixture as a function of the *n*-hexane fraction in

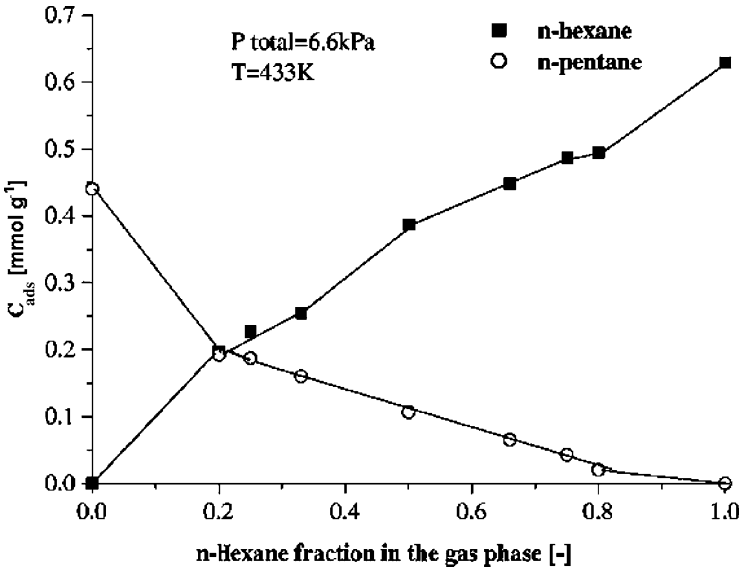

Fig. 19 Loadings of mixture components in silicalite as a function of *n*-hexane fraction in the gas phase (total hydrocarbon pressure 6.6 kPa, 433 K)

the gas phase. Obviously, *n*-hexane is preferentially adsorbed over *n*-pentane. In the equimolar gas mixture, the *n*-hexane loading was approximately three times higher compared to that of *n*-pentane (0.39 and 0.13 mmol g^{-1}, respectively). This corresponds to the larger heat of adsorption of *n*-hexane in silicalite-1 than that of *n*-pentane, 71 and 42 kJ mol^{-1} [93], respectively. Since both alkanes are likely to be situated throughout the micropore space [85] under the applied conditions, the stronger adsorption is due to enthalpic and not entropic reasons. Clearly, this corresponds to the higher single-component loading for *n*-hexane (0.63 mmol g^{-1}) than that for *n*-pentane (0.45 mmol g^{-1}).

Figure 20 shows the self-diffusivities of *n*-pentane and *n*-hexane as a function of gas mixture composition. The loadings of both components depend on the gas phase composition fraction. Note that in these experiments the total hydrocarbon pressure is kept constant (6.6 kPa). The loading of a feed of pure *n*-hexane under these conditions (433 K, 6.6 kPa) is 3.6 molecules per unit cell. Unexpectedly, we observe a lower diffusion coefficient for pure *n*-pentane than for *n*-pentane in a mixture with *n*-hexane. Tentatively, we ascribe this to the more drastic increase in *n*-hexane diffusivity with loading than for *n*-pentane. As discussed earlier, this can be ascribed to stronger repulsive interactions for the longer hexane hydrocarbons. It is clear from Fig. 20 that at low *n*-hexane concentrations, its diffusion is slower than of *n*-pentane. The diffusivity of hexane increases with *n*-hexane loading, while the diffusivity of pure *n*-pentane was found to be independent on the concentration at this temperature. Repulsion between *n*-pentane

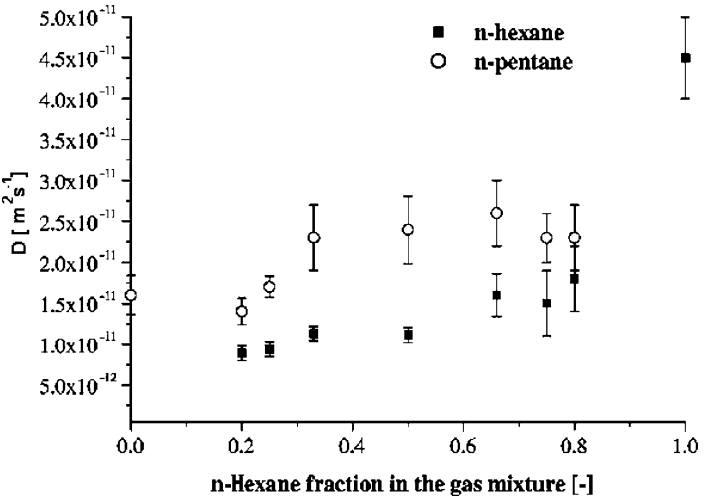

Fig. 20 Self-diffusivities of mixture components in silicalite at various gas mixture compositions (total hydrocarbon pressure 6.6 kPa, 433 K). Gas mixture composition is determined by the ratios between the components in the gas phase

molecules should be weaker than between *n*-hexane molecules. In mixtures, *n*-pentane and *n*-hexane molecules are randomly distributed in the zeolite. We argue that also repulsive interactions are present between *n*-pentane/*n*-hexane molecules. In our crude estimation, the distance between *n*-hexane/*n*-pentane is shorter than that between npentane/*n*-pentane molecules. Thus, increasing the *n*-hexane loading effectively replaces neighboring *n*-pentane by *n*-hexane molecules. This leads to stronger intermolecular repulsive interactions and a consequent increase in the self-diffusion coefficient of the shorter alkane. From Fig. 20, it is clear that *n*-hexane diffusion in mixtures with *n*-pentane is slower compared to its single-component diffusion. Our simple model can explain this by a decrease of intermolecular repulsive interactions in the order of *n*-hexane/*n*-hexane > *n*-hexane/*n*-pentane > *n*-pentane/*n*-pentane. This also indicates that in the absence of such interactions *n*-hexane is slower than *n*-pentane, which is a reasonable behavior to expect. As the concentration of *n*-hexane in the silicalite pores increases further, diffusion of *n*-hexane slightly increases due to increased repulsions.

At first sight, these results are somewhat different from those obtained by Masuda et al. [55] for *n*-heptane/*n*-octane mixtures in silicalite-1. A decrease in the diffusivity of the faster-diffusing *n*-heptane was observed as the loading of slower *n*-octane increased, while the octane diffusivity did not change in the presence of *n*-heptane. This difference may be attributed to different experimental conditions, since the temperature was higher (448–498 K) and the total pressure significantly lower (13 Pa). In this case, a relatively small pore occupancy is expected and repulsive interactions should be minimal. This leads to similarly low mobility of the faster hydrocarbon as of the slow one.

In conclusion, TEX-PEP allowed us to study the concentration dependence of self-diffusion of *n*-pentane and its diffusion in mixtures with *n*-hexane in silicalite-1. Diffusion of *n*-pentane was found to be independent on the loading at high temperatures, while at lower temperatures a slow increase in the self-diffusion coefficient was observed. In a tentative simple model, we attribute this to intermolecular repulsive interactions between the molecules located in the intersections of the straight and zigzag channels and those sited in the adjacent straight channels. This may result in an increase in the hydrocarbon mobility of the molecules [82]. However, *n*-pentane diffusivity is also affected by the pore occupancy, which causes a decrease in the diffusivity. Although these two factors are competing, it appears that they more or less compensate each other at high temperatures. As a result diffusion is independent of the concentration. At low temperatures, repulsive interactions are stronger, and the diffusivity tends to increase with increasing loading. The complex effects also influence the apparent activation energy for diffusion.

In mixtures with *n*-hexane for which the influence of intermolecular repulsive forces appear to be stronger, we find that *n*-pentane diffusivity is enhanced. This is most likely due to higher repulsive forces between *n*-pentane/*n*-hexane molecules residing in adjacent pore positions than between

n-pentane/*n*-pentane pairs. Thus, at high loading of *n*-hexane, the mobility of *n*-pentane molecules becomes very close to that of *n*-hexane. Molecularly, this can be interpreted that the diffusivity of the shorter alkane is totally determined by the longer one. On the contrary, *n*-hexane diffuses slower in mixtures with *n*-pentane compared to pure *n*-hexane under similar conditions. With increasing fraction of *n*-pentane the repulsive forces become weaker and the diffusivity of *n*-hexane becomes even slower than that of *n*-pentane. It appears that the presence of another hydrocarbon with a slightly different diffusion coefficient results in a complex behavior depending on the temperature and the total and fractional micropore occupancy. These experimental data cannot yet be described by molecular models in detail and call for further refinement of molecular simulations. A crucial point will be to develop methods to determine self-diffusion coefficients at realistic hydrocarbon loadings.

4 Conclusions

Zeolites are widely used in the petrochemical industry as catalysts and adsorbents. In order to enhance the understanding of the complex interplay of reaction and diffusion, there is a large interest in understanding of diffusion processes of alkanes in medium-pore zeolites. Much attention has been paid to study diffusivity of alkanes in MFI zeolite, mostly of the all-silica type (silicalite-1). In the present contribution, we have studied single-component self-diffusion coefficients of hexanes in silicalite-1 and its acidic counterpart, H-ZSM-5 by tracer exchange positron emission profiling (TEX-PEP). Moreover, we investigated the diffusivity of mixtures of alkanes. For the first time, the diffusion of *n*-pentane and *n*-hexane in mixtures was studied in detail. This shows that positron emission profiling is a powerful technique for in situ investigations of the adsorption and diffusive properties of hydrocarbons in zeolites. As the technique is based on the labeling of a small portion of the hydrocarbons, one can perform tracer exchange experiments under chemical steady-state conditions. This allows one to extract self-diffusion coefficients of hydrocarbons at finite loadings, even in the presence of another unlabeled alkane.

We have discussed the adsorption and diffusion of binary mixtures of linear (*n*-hexane) and branched (2-methylpentane) alkanes in silicalite-1. It turned out that not only the size but also the siting of the molecules in the particular zeolite plays an important role in the behavior of the mixture components. A slight preference for the adsorption of *n*-hexane over 2-methylpentane was observed because of the higher packing efficiency of the linear alkane. This is due to the preferential location of the branched alkane in the zeolite intersections. A consequence of this is that the diffusivity of *n*-hexane

is strongly influenced by that of the slower branched component. A drastic decrease in the diffusivity of *n*-hexane is observed at a 2-methylpentane loading of about 2.75 molecules per unit cell. This is explained by blocking of the channel intersections. The loading roughly corresponds to the situation where three out of four channel intersections are occupied by the isohexane.

A comparison between silicalite-1 and H-ZSM-5 teaches that acid sites have a profound influence on the self-diffusivity of alkanes. The self-diffusivities of both components decrease strongly, and we observe a significant preferential adsorption of the linear over the branched hexane. This is caused by the relatively stronger interaction of the linear hexane with the acid sites. On the contrary, 2-methylpentane loadings in mixtures in silicalite-1 and H-ZSM-5 are very close. In H-ZSM-5, the diffusivity of the linear alkane in mixtures with the branched alkane is influenced by two factors (i) interaction with the acid sites, which decreases the diffusivity by approximately a factor of two and (ii) the presence of 2-methylpentane, which has a ten-times lower diffusivity. At low loadings of the branched alkane, the interactions with the acid sites is prevailing. As soon as the loading of isohexane exceeds approximately 2.7 molecules per unit cell, the effect of the Brønsted sites on the diffusion becomes negligible compared to the blockage of the pore network connection by the branched alkane.

Our earlier studies confirmed that diffusion of 3-methylpentane in silicalite-1 decreases with increasing loadings. This simple behavior points to the absence of intermolecular interactions, which tallies with the notion that this branched alkane is preferentially located in the zeolite's intersections. Similar measurements with *n*-hexane showed that its self-diffusivity increases with increasing loading. This is tentatively attributed to intermolecular repulsive interactions which are more pronounced between *n*-hexane molecules located in the intersections and the channels. Here, we investigated the diffusivity of *n*-pentane as a single component and in mixtures with *n*-hexane in silicalite-1. From the single-component *n*-pentane measurements, we derived that the increase of diffusivity with loading was less dramatic than for *n*-hexane. This is in line with the smaller dimensions of the C_5 alkane which should reduce the repulsive interactions. Interestingly, we found that *n*-pentane diffuses faster in a mixture with *n*-hexane than in a single-component experiment at the same total hydrocarbons partial pressure. This is believed to be caused by stronger repulsive interactions with *n*-hexane than between *n*-pentane molecules. Consequently, we can explain that at high loadings of *n*-hexane, the mobility of *n*-pentane molecules becomes very close to that of *n*-hexane. On the contrary, *n*-hexane diffuses slower in mixtures with *n*-pentane compared to the single-component diffusivity under similar conditions. Upon increasing the fraction of *n*-pentane, repulsive interactions become weaker and the diffusivity of *n*-hexane becomes even slower than that of *n*-pentane.

Summarizing, the diffusion of hydrocarbon molecules in medium-pore zeolites is determined by a complex interplay of factors, such as the loading,

the temperature, the preference for certain pore locations, the interactions with other hydrocarbons of the same type or others and the presence of acid protons. In diffusion of mixtures, pore blockage by one of the components might occur, thus strongly decreasing the diffusivity of the fast hydrocarbon.

References

1. Baerlocher C, Meier WM, Olson DH (2001) Atlas of zeolite framework types, 5th ed. Elsevier, Amsterdam, The Netherlands
2. Jost W (1960) Diffusion in solids, liquids and gases. Academic Press, New York
3. Kärger J, Ruthven DM (1992) Diffusion in zeolites and other microporous solids. John Wiley & Sons, Inc, New York
4. Chen NY, Degnan TF Jr, Smith CM (1994) Molecular transport and reaction in zeolites design and application of shape selective catalysis. VCH Publishers, New York
5. Benes NE, Verweij H (1999) Langmuir 15:8292
6. Kauzmann W (1966) Kinetic theory of gases. Addison-Wesley, Reading
7. Post MFM (1991) In: Van Bekkum H, Flanigen EM, Jansen JC (eds) Introduction to zeolite science and practice. Elsevier, Amsterdam, pp 391–443
8. Post MFM (1991) Stud Surf Sci Catal 58:391
9. Wakao N, Kaguei S (1982) Heat and mass transfer in packed beds. Gordon and Breach Science, London
10. Weisz PB (1973) Chem Tech 3:498
11. Fick A (1855) Ann Phys 94:59
12. Barrer RM, Jost W (1949) Trans Faraday Soc 45:928
13. Einstein A (1905) Ann Phys 17:549
14. Paschek D, Krishna R (2001) Chem Phys Lett 333:278
15. Skoulidas AI, Sholl DS (2001) J Phys Chem B 105:3151
16. Barrer RM (1941) Trans Faraday Soc 37:590
17. Theodorou DN, Wei J (1983) J Catal 83:205
18. Tsikoyiannis J, Wei J (1991) Chem Eng Sci 46:233
19. Coppens MO, Bell AT, Chakraborty AK (1998) Chem Eng Sci 53:2053
20. Kärger J, Pfeifer H (1987) Zeolites 7:90
21. Xiao J, Wei J (1992) Chem Eng Sci 47:1123
22. Riekert L (1970) Adv Catal 21:281
23. Koriabkina AO, De Jong AM, Schuring D, Van Santen RA (2002) J Phys Chem B 106:9559
24. Haynes HW, Sarma PN (1973) AIChE J 19:1043
25. Noordhoek NJ, Van Ijzendoorn NJ, Anderson BG, De Gauw FJ, Van Santen RA, De Voigt MJA (1998) Ind Eng Chem Res 37:825
26. Mangnus AVG (2000) A detection system for Positron Emission Profiling, Ph.D. thesis. Eindhoven University of Technology, Eindhoven, The Netherlands
27. Ferrieri RA, Wolf AP (1984) J Phys Chem 88:2256
28. Ferrieri RA, Wolf AP (1984) J Phys Chem 88:5456
29. Baltensperger U, Ammann M, Bochert UK, Eichler B, Gäggeler HW, Jost DT, Kovacs JA, Türler A, Sherer UW, Baiker A (1993) J Phys Chem 97:12325
30. Hawkesworth MR, Parker DJ, Fowles P, Crilly JF, Jefferies NL, Jonkers G (1991) Nucl Instrum Methods A310:423
31. Hensel F (1996) Institut Sicherheitsforschung, Forschungszentrum Rossendorf, Dresden D-01314, Germany. FZR, FZR-152, p 12

32. Jonkers G, Vonkeman KA, Van der Wal SWA, Van Santen RA (1992) Nature 355:63
33. Jonkers G, Vonkeman KA, Van der Waal SWA (1993) In: Weijnen MPC, Drinkenburg AAH (eds) Precision Process Technology. Kluwer Academic Publishers, The Netherlands, p 533
34. Mangnus AVG, Van Ijzendoorn LJ, De Goeij JJM, Cunningham RH, Van Santen RA, De Voigt MJA (1995) Nucl Instrum Methods B99:649
35. Schumacher RR, Anderson BG, Noordhoek NJ, De Gauw FJMM, De Jong AM, De Voigt MJA, Van Santen RA (2001) Microporous Mesoporous Mater 35–36:315
36. Noordhoek NJ, Schuring D, De Gauw FJMM, Anderson BG, De Jong AM, De Voigt MJA, Van Santen RA (2002) Ind Eng Chem Res 41:1973
37. Cunningham RH, Mangnus AVG, Van Grondelle J, Van Santen RA (1996) J Mol Catal A 107:153
38. Rosen JB (1952) J Chem Phys 20:387
39. Nijhuis TA, Van den Broeke LJP, Linders MJG, Van de Graaf JM, Kapteijn F, Makkee M, Moulijn JA (1999) Chem Eng Sci 54:4423
40. Hong U, Kärger J, Kramer R, Pfeifer H, Seiffert G, Müller U, Unger KK, Lück HB, Ito T (1991) Zeolites 11:816
41. Schiesser WE (1991) The Numerical Method of Lines: Integration of Partial Differential Equations. Academic Press, San Diego
42. Marquardt D (1963) J Appl Math 11:431
43. Atkins PW, De Paula J (2002) Physical Chemistry, 7th ed. Oxford University Press, Oxford, United Kingdom, pp 822–824
44. Vlugt TJH, Krishna R, Smit B (1999) J Phys Chem B 103:1102
45. Zhu W, Kapteijn F, Moulijn JA (2001) Microporous Mesoporous Mater 47:157
46. June RL, Bell AT, Theodorou DN (1992) J Phys Chem B 96:1051
47. June RL, Bell AT, Theodorou DN (1990) J Phys Chem B 94:1508
48. Zhu W, Kapteijn F, Van der Linden B, Moulijn JA (2001) Phys Chem Chem Phys 3:1755
49. Calero S, Smit B, Krishna R (2001) J Catal 202:395
50. Schuring D, Koriabkina AO, De Jong AM, Smit B, Santen RA (2001) J Phys Chem B 105:7690
51. Breck DW (1974) Zeolite Molecular Sieves. John Wiley, New York
52. Snurr RQ, Kärger J (1997) J Phys Chem B 101:64
53. Schuring D, Jansen APJ, Van Santen RA (2000) J Phys Chem B 104:941
54. Jost S, Bar NK, Fritzsche S, Haberlandt R, Kärger J (1998) J Phys Chem B 102:6375
55. Masuda T, Fujikata Y, Ikeda H, Hashimoto K (2000) Microporous Mesoporous Mater 38:323
56. Gergidis LN, Theodorou DN (1999) J Phys Chem B 103:3380
57. Nivarthi SS, Davis HT, McCormick AV (1995) Chem Eng Sci 50:3217
58. Förste C, Germanus A, Kärger J, Pfeifer H, Caro J, Pilz W, Zikánová A (1987) J Chem Soc Faraday Trans 83:2301
59. Eder F (1996) Thermodynamics and siting of alkane sorption in molecular sieves, Ph.D.Thesis. University of Twente, The Netherlands
60. Wu P, Debebe A, Ma Y (1983) Zeolites 3:118
61. Anderson J, Foger K, Mole T, Rajadhyaksha R, Sanders J (1979) J Catal 58:114
62. Valyon J, Onyestyak G, Rees LVC (2000) In: Proc of 2nd Pac Basin Conf, p 482
63. Zikanova A, Bülow M, Schlodder H (1987) Zeolites 7:11
64. Shen D, Rees LVC (1991) Zeolites 11:666
65. Masuda T, Fujikata Y, Nishida T, Hashimoto K (1998) Microporous Mesoporous Mater 23:157

66. Jost S, Bar NK, Fritzshe S, Haberlandt R, Kärger J (1999) In: Treacy MMC, Marcus BK, Bisher ME, Higgins JB (eds) Proc 12th Int Zeolite Conf, Baltimore, USA, July 5–10, 1998. Materials Research Society, Warrendale PA, USA, p 149
67. Bülow M, Schodder H, Rees LVC, Caro J, Richards R (1986) In: Murakami Y, Iijima A, Ward JW (eds) New developments in zeolite science and technology; Proc. 7th Int Zeolite Conf, Tokyo, Japan, 1986. Elsevier, Amsterdam, pp 579–586
68. Bülow M, Schodder H, Rees LVC, Caro J, Richards R (1986) Stud Surf Sci Catal 28:579
69. Hashimoto K, Masuda T, Murakami N (1991) In: Jacobs PA, Jäger NI, Kubelkova L, Wichterlova B (eds) Zeolite Chemistry and Catalysis; Proc Int Symp, Prague, Czechoslovakia, September 8–13, 1991. Elsevier, Amsterdam, p 477
70. Hermann M, Niessen W, Karge HG (1996) In: LeVan MD (ed) Fundamentals of adsorption; Proc 5th Int Conf Fundamentals of adsorption, Asilomar Pacific Grove, California, USA, May 13–18, 1995. Kluwer Acad Publ Norwell, Mas, pp 377–384
71. Hermann M, Niessen W, Karge HG (1995) In: Beyer HK, Karge HG, Kiricsi I, Nagy JB (eds) Proc Int Symp Catalysis by Microporous Materials, Elsevier, Amsterdam, pp 131–138
72. Hermann M, Niessen W, Karge HG (1995) Stud Surf Sci Catal 94:131
73. Van-Den-Begin N, Rees LVC, Caro J, Bülow M (1989) Zeolites 9:287
74. Eic M, Ruthven DM (1989) In: Jacobs PA, Van Santen RA (eds) Zeolites: Facts, figures, future; Proc. 8th Int Zeolite Conf, Amsterdam, The Netherlands, 1989. Elsevier, Amsterdam, p 897
75. Eic M, Ruthven DM (1989) Stud Surf Sci Catal 49:897
76. Millot B, Methivier A, Jobic H, Moueddeb H, Dalmon JA (2000) Microporous Mesoporous Mater 38:85
77. Cavalcante CL, Ruthven DM (1995) Ind Eng Chem Res 34:185
78. Xiao J, Wei J (1992) Chem Eng Sci 47:1143
79. Keipert OP, Baerns M (1998) Chem Eng Sci 53:3623
80. Coppens MO, Bell AT, Chakraborty AK (1999) Chem Eng Sci 54:3455
81. Koriabkina AO, De Jong AM, Hensen EJM, Van Santen RA (2004) Microporous Mesoporous Mat 77:119
82. Paschek D, Krishna R (2001) Chem Phys Lett 342:148
83. Trout BL, Chakraborty AK, Bell AT (1997) Chem Eng Sci 52:2265
84. Krishna R, Paschek D (2002) Chem Eng J 85:715
85. Smit B, Maesen T (1995) Nature 374:42
86. Heink W, Kärger J, Pfeifer H, Datema KP, Nowak AK (1992) J Chem Soc Faraday Trans 88:3505
87. Datema KP, Den Ouden CJJ, Ylstra WD, Kuipers HPCE, Post MFM, Kärger J (1991) J Chem Soc Faraday Trans 87:1935
88. Hayhurst DT, Paravar A (1988) Zeolites 8:27
89. Song L, Rees LVC (1999) In: Treacy MMC, Marcus BK, Bisher ME, Higgins JB (eds) Proc 12th Int Zeolite Conf, Baltimore, USA, July 5–10, 1998. Materials Research Society, Warrendale PA, USA, p 67
90. Talu O, Sun MS, Shah DB (1998) AIChE J 44:681
91. Van de Graaf JM, Kapteijn F, Moulijn JA (2000) Microporous Mesoporous Mater 35–36:267
92. Nijhuis TA, Van den Broeke LJP, Van de Graaf JM, Kapteijn F, Makkee M, Moulijn JA (1997) Chem Eng Sci 52:3401
93. Sun MS, Talu O, Shah DB (1996) J Phys Chem B 100:17276

Mol Sieves (2008) 7: 329–366
DOI 10.1007/3829_2007_018
© Springer-Verlag Berlin Heidelberg
Published online: 25 January 2008

Single-File Diffusion in Zeolites

Jörg Kärger

Fakultät für Physik und Geowissenschaften, Universität Leipzig, Linnéstraße 5, 04103 Leipzig, Germany
kaerger@physik.uni-leipzig.de

Abstract The exclusion of the mutual passage of diffusants in zeolites with one-dimensional channels leads to patterns of molecular transportation which are unknown in amorphous materials or from zeolites with multi-dimensional pore networks. In particular, there is no possibility to describe molecular transport by the well-known Fick's equations of molecular diffusion. Molecular transport in such systems has been termed single-file diffusion. It is characterized by the molecular mean square displacements, which in infinitely extended single-file diffusion is found to increase in proportion with the square root of the observation time rather than with the observation time itself. For finite single-file systems, the rate of molecular exchange between the crystals and their surroundings, representing one of the key parameters for their practical application in heterogeneous catalysis and mass separation, decreases with the third rather than with the second power of the crystal size.

As a consequence of the correlation of the movement of the individual diffusants and the thus-mediated long-range influence of boundaries, the treatment of single-file systems of finite length is particularly complicated. Present attempts of analytical treatment of such systems and the quantification of the boundary conditions do not provide anything more than first approaches. Monte-Carlo simulations supported by analytical approaches reveal striking peculiarities of zeolitic single-file systems. These peculiarities include an

enhanced dependence of the intracrystalline mean lifetime, and hence of the effectiveness factor, on the size of the catalyst particle, and the possibility of an enhancement of the apparent activation energy of catalytic reactions under transport control. Though there is still some controversy concerning the evidence obtained by the different methods applied, indications of single-file diffusion in zeolites have been observed by various experimental techniques including pulsed field gradient NMR, quasi-elastic neutron scattering and tracer exchange measurements.

Keywords Anomalous diffusion · Confinement · Diffusion-limited reaction · Dynamic Monte Carlo simulation · Molecular traffic control · Random walk · Single-file diffusion

Abbreviations

$AlPO_4$-5 (-8,-11)	Zeolite structure types with one-dimensional channels ("Aluminum Phosphate")
DMC	Dynamic Monte Carlo simulation
MD	Molecular dynamics
NMR	Nuclear magnetic resonance
PFG NMR	Pulsed field gradient NMR
QENS	Quasielastic neutron scattering
VPI-5	Zeolite structure type ("Virginia Polytechnic Institute")
ZSM-5	Zeolite structure type ("Zeolite Socony Mobil")
ZSM-12 (-22,-23,-48)	Zeolite structure types with one-dimensional channels

Symbols

a	Mean distance between two adjacent molecules
D	Coefficient of self-diffusion (self-diffusivity)
D_{eff}	Effective diffusivity
D_{sim}	Modified (center-of-mass) diffusivity in a single-file system
F	Mobility factor of single-file diffusion as defined by Eq. 2
k	Intrinsic reactivity
k^*	Effective reactivity
L	Channel length
l	Mean free distance between adjacent molecules
N	Total number of sites in a single-file system
N^*	Modified site number in a single-file system
n	Particle number ($= \theta N$)
$P(\Delta z, t)$	Probability density that during time t a molecule is shifted over a distance Δz (= propagator)
s	Space coordinate of an isolated (sole) molecule
t	Time
x	Site number in file-direction
z	Space coordinate in file direction
$\gamma(t)$	Tracer exchange curve
Δs, Δz	Particle displacement
η	Effectiveness factor
η_{i}	Reactant concentration profile
θ	Relative loading, site occupancy ($= n/N$)
θ_{i}	Relative loading of site i

κ	Probability of reaction between two diffusion steps
λ	Step length
σ	Particle diameter
σ_i	Parameter indicating whether a site is vacant ($\sigma_i = 0$) or occupied ($\sigma_i = 1$)
τ	Mean time between two jump attempts, residence time
τ_{ex}	Mean exchange time between two adjacent molecules
τ_i	Average time that a particle which is found at site i, has already spent in the single-file system
τ_{intra}	Intracrystalline mean life time (residence time in a single-file system)
ϕ	Thiele modulus
$\varphi_{(i)}(\tau)$	Residence time distribution function (of a particle at site i in the single-file system)
ω	Particle-particle interaction parameter

1 Introduction

Studying molecular diffusion in zeolite crystallites is complicated by the small size of the objects of investigation. Inevitable deviations of the real structure of a sample from the ideal one lead to an additional complication of the situation. It is not unexpected, therefore, that in spite of considerable progress in the experimental techniques, there is still some controversy in the understanding of intracrystalline zeolitic diffusion (cf. the preceding chapters of this volume).

The situation is far more complicated if the zeolite framework compels the diffusants to remain in one and the same order, i.e., if the zeolite pore system consists of non-intersecting channels with diameters small enough so that a mutual passage of adjacent sorbate molecules is prohibited. Zeolites offering such a possibility include the structure types ZSM-12, -22, -23, -48; $AlPO_4$-5, -8, -11 and many more. The situation may be compared to that of a string of pearls, where one pearl may only be shifted in a given direction if there is sufficient free space, i.e., if all pearls originally situated in this range have also been shifted in the same direction [1]. Since the concentration of molecules in front of those shifted tends to exceed the concentration behind the considered diffusant, subsequent displacements are more likely to be directed backward than forward. This correlation between subsequent displacements increases with increasing molecular shifts. In normal diffusion, in striking contrast to this situation, subsequent displacements eventually become independent from each other. It is this condition which allows description of molecular transport on the basis of the well-known Fick's equations. By contrast, the highly correlated motion in single-file systems excludes the application not only of Fick's laws but presumably of any type of differential equation.

It should be noted that in the literature the term single-file diffusion has sometimes been used to indicate only the mutual steric hindrance of the molecules in zeolite channels and not the additional constraint of an absolute exclusion of their mutual passage. Such terminology is clearly misleading since in this case molecular propagation would also be subjected to Fick's laws.

When investigating single-file diffusion in zeolites, one must face not only the general experimental problems of diffusion studies with zeolites, but also additional aggravations. These are due to possible transitions between the regimes of single-file and normal diffusion and the influence of the real structure on these transitions. There is also substantial need for a satisfactory and handy theoretical description of the expected processes. Sects. 2 and 3 of this chapter are devoted to this problem, while Sect. 4 provides a survey of the available experimental data in this rather new field of research.

2
Single-File Systems of Infinite Extension

2.1
Random Walk Considerations

Long before the term single-file diffusion was introduced into the zeolite community [2], it had been coined as a quite general description of any type of one-dimensional transport of hard-core particles, including such diverse phenomena as transport in the ion channels of biological membranes and along dislocation lines in crystals [3, 4]. The abundance of intriguing questions associated with such systems has fascinated mathematicians and theoretical physicists for many years [5, 6]. In the most simple model, molecular transportation in single-file systems has repeatedly been assumed to proceed by steps of equal spacing between adjacent adsorption sites. In this case, the mean square displacement in the file direction is given by the relation [5–13]

$$\left\langle (\Delta z)^2 \right\rangle = \lambda^2 \frac{1-\theta}{\theta} \sqrt{\frac{2}{\pi}} \sqrt{\frac{t}{\tau}}, \tag{1}$$

where λ stands for the step length and θ denotes the occupancy of the adsorption sites. τ is the mean time between subsequent jump attempts. Jump attempts are only considered to be successful if the site to which they are directed is unoccupied. Following the notation of the Einstein equation of normal one-dimensional diffusion [14]

$$\left\langle (\Delta z)^2 \right\rangle = 2Dt, \tag{2}$$

Eq. 1 may be transferred into

$$\left\langle (\Delta z)^2 \right\rangle = 2F\sqrt{t}\,, \tag{3}$$

with the so-called mobility factor of single-file diffusion [1]

$$F = \lambda^2 \frac{1-\theta}{\theta} \frac{1}{\sqrt{2\pi\tau}}\,, \tag{4}$$

with the essential difference that the mean square displacement increases in proportion to the square root of the observation time rather than to the observation time itself. Eq.1 has been derived in different ways [5–11], all of which are far from being straightforward as a consequence of the correlated motion in a single-file system. In [12], this complication is circumvented by considering the particle shift as a consequence of the movement of the vacancies within single-file systems. This movement can be considered to be uncorrelated, so that a derivation of Eq. 1 by elementary arguments becomes possible. Moreover, in this way all higher moments $\langle (\Delta z)^\nu \rangle$ of molecular displacements may also be calculated. This knowledge permits the determination of the probability distribution functions of molecular displacement, the so-called propagator. As in the case of normal diffusion ([14], Eq. 5), the propagator is found to be a Gaussian [13]

$$P(\Delta z, \mathrm{t}) = \left(2\pi \left\langle (\Delta z)^2 \right\rangle\right)^{-1/2} \exp\left[-(\Delta z)^2 / 2\left\langle (\Delta z)^2 \right\rangle\right], \tag{5}$$

where now, clearly, the mean square displacement follows Eq. 3 rather than Eq. 2.

The mean square displacement in single-file systems may quite generally be shown to be related to the movement of a sole molecule by the expression [8, 10]

$$\left\langle (\Delta z)^2 \right\rangle = l \langle |\Delta s| \rangle\,, \tag{6}$$

where $\langle |\Delta s| \rangle$ denotes the mean value of molecular displacement of a sole particle (i.e. of a diffusant without any interaction with other particles), and l stands for the mean free distance (clearance) between adjacent molecules. Under the supposition that an isolated diffusant in the single-file system is subjected to normal diffusion, Eq. 5 with Eq. 2 may be used to determine the mean value of molecular displacement of this particle, yielding

$$\langle |\Delta s| \rangle = \sqrt{\frac{4D}{\pi}}\sqrt{t}\,. \tag{7}$$

Combining Eqs. 3, 6 and 7, the mobility factor F of a single-file system and the diffusivity of a sole molecule in this system may be shown to be related to

each other by the expression

$$D = \pi F^2 / l^2 \,. \tag{8}$$

Eq. 1 results as a special case of Eq. 6 by using Eq. 7 with the well-known expression [15, 16]

$$D = \frac{\lambda^2}{2\tau} \tag{9}$$

for the self-diffusivity of an isolated particle and by using the relation

$$l = \lambda \frac{1-\theta}{\theta} \,, \tag{10}$$

where the step length λ has been set equal to the particle diameter σ.

The single-file expressions Eq. 1 and Eq. 6 are only valid for sufficiently large observation times. In the limit of short observation times, i.e. in a time regime where the individual molecules have not yet become "aware" of their neighbors, molecular displacement may be described by a diffusion-like motion with a diffusivity

$$D = \frac{\lambda^2}{2\tau}(1-\theta) \,. \tag{11}$$

In comparison with Eq. 9 for the isolated molecule, the additional factor $(1-\theta)$ takes into account that a jump attempt is only successful with the probability $1-\theta$. Equating the mean square displacements following from Eq. 2 with D as given by Eq. 11 and from Eq. 3 with F as given by Eq. 4 yields

$$t = \frac{2\tau}{\pi\theta^2} \tag{12}$$

for the time of crossover between the regimes of normal diffusion and of single-file diffusion.

The analytical expression

$$\left\langle \left(\Delta z\right)^2 \right\rangle = \frac{\lambda^2(1-\theta)t/\tau}{1+\theta\sqrt{\pi/2}\sqrt{t/\tau}} \tag{13}$$

has been shown to comprise both cases with satisfactory accuracy [17]. One should be aware of the fact that there is also the possibility of a direct transition from the "ballistic" behavior of the particle (i.e. from the regime of proportionality between displacement and time for sufficiently short observation times) to single-file behavior. Clearly, in this case an establishment of a time regime of normal diffusion could not be observed. It may be shown by molecular dynamics simulations that this tendency becomes more and more dominant with increasing concentration [18].

Since normal and single-file diffusion are described by the same propagator, Eq. 5, due to the analogy of Eq. 2 and Eq. 3 the propagation pattern of a given particle in a single-file system coincides with that of normal diffusion

if the self-diffusivity D is substituted by F and the time t by $\sqrt{t}$. This analogy, however, is of only limited value for the treatment of practical problems, since in the case of normal diffusion there is no counterpart for the correlation in the movement of distant particles as is typical of single-file systems. This correlation prohibits extending the analogy between Eq. 2 and Eq. 3 to the treatment of single-file diffusion (as attempted, e.g., in [19]) if it is subjected to certain initial and boundary conditions [20, 21]. The treatment of finite single-file systems in Sect. 3 will demonstrate that we are still far from the development of an adequate analytical tool for handling this correlation.

2.2 Molecular Dynamics

Molecular dynamics (MD) simulations in single-file systems are additionally complicated by the requirement that in the absence of external forces the center of mass must be preserved. This complication results from the fact that, as a consequence of the correlated motion in a single-file system, the shift of a particular molecule must be accompanied by shifts of other molecules in the same direction. Depending on the total amount of molecules under consideration, the conservation of the center of mass therefore prohibits arbitrarily large molecular shifts. The maximum mean square displacement may be shown to obey the relation [22]

$$\left\langle \left(\Delta z\right)^2 \right\rangle_\infty = \frac{1}{6}\left(1-\theta\right)^2 \frac{n\sigma^2}{\theta^2} = \frac{1}{6}\frac{\left(1-\theta\right)^2}{\theta} L\sigma \,, \tag{14}$$

where n denotes the number of particles considered and $L \equiv n\sigma/\theta$ stands for the length of the single-file system (channel length). MD simulations as illustrated by Fig. 1 are in excellent agreement with Eq. 14 [22]. It turns out that one has to consider as many as 10 000 particles in order to avoid the unwanted limitation effects during the time interval considered in Fig. 1. Such particle numbers are much larger than generally considered in MD simulations. It is not unexpected, therefore, that first MD simulations with the zeolites ferrierite [23, 24] and mordenite [25], which contain one-dimensional or quasi-one-dimensional channel systems, did not reveal any indication of the $\sqrt{t}$ behavior, as expected on the basis of Eq. 3 for single-file systems. This type of restriction does not exist in the case of normal diffusion, where the molecules are able to change their positions relative to each other. Obviously, in such a situation arbitrarily large molecular displacements are possible, without the necessity of a shift of the center of mass.

The great expense in calculation time due to the inevitably large particle numbers in single-file systems calls for the application of simplified potentials. Figure 1 shows the results obtained for spherical molecules diffusing in an unstructured tube [22]. Particle-particle and particle-wall interactions have been simulated by a shifted-force Lennard-Jones potential [26] and an

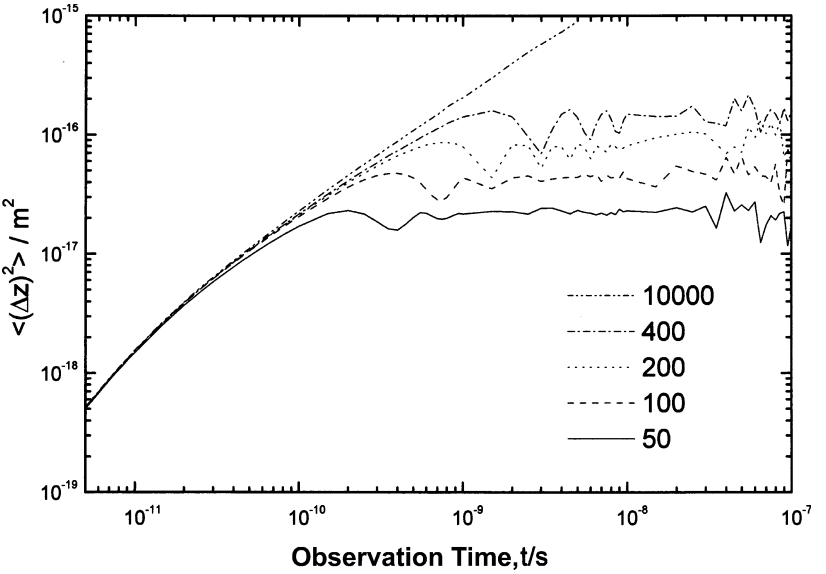

Fig. 1 Time dependence of the mean square displacement $\langle(\Delta z)^2\rangle$ for simulations with various small numbers of particles (as indicated in the *insert*). $\langle z^2\rangle$ tends to a limiting value $\langle(\Delta z)^2\rangle_\infty$. For comparison, the result for 10 000 particles is also given. From [22] with permission

inverse Lennard–Jones potential, respectively. The particle and tube diameters were chosen in such a way that any mutual passage of the particles was definitively excluded. Hence, at first glance, the proportionality between $\langle(\Delta z)^2\rangle$ and the observation time t appears to be in striking contrast to the $\sqrt{t}$ behavior expected on the basis of Eq. 3 for single-file systems. This apparent conflict may be resolved, however, on the basis of the more general Eq. 6. In fact, a sole particle in an unstructured tube behaves completely deterministically with a displacement $\langle|\Delta s|\rangle$ increasing in proportion to the observation time. Therefore, according to Eq. 6, the mean square displacement $\langle(\Delta z)^2\rangle$ in the single-file system also has to increase linearly with t. Moreover, by determining $\langle|\Delta s|\rangle$ via the mean absolute velocity, the results of the MD simulations may even be shown to be in quantitative agreement with the prediction of Eq. 6 [22].

According to Eq. 6, proportionality between the mean square displacement in single-file systems and the square root of the observation time can only be expected if the movement of the isolated molecule is a random walk. In [22] this condition was fulfilled by either introducing an additional force, stochastically acting on the individual molecules, or by considering tubes with periodically varying diameters. In both cases, molecular displacements in single-file systems were found to follow Eq. 3 over observation times covering two orders of magnitude. In this way, for the first time the $\sqrt{t}$ behavior

of single-file diffusion as resulting from random walk considerations was confirmed by MD simulations. Moreover, the MD simulations were found to satisfactorily reflect even the concentration dependence that follows from Eq. 1 if the occupancy θ is defined with respect to a chain-like arrangement of the molecules along the tube axis.

The exclusion of a mutual passage of the molecules within the zeolite channels is crucial for the occurrence of single-file diffusion. First attempts to perform such discriminations by MD simulations with methane and ethane in $AlPO_4$-5 have been presented in [27–29]. In these studies both the methane and ethane molecules are found to be readily able to pass each other. Since such simulations are extremely sensitive to the potentials used [30–34], the evidence of such results is still under discussion.

Figure 2 displays the results of MD simulations which have been carried out to provide an overview of the different time regimes of molecular propagation possible in single-file systems [35]. After the initial ballistic period with $(\Delta z)^2 \propto t^2$, the mean square displacement is soon found to follow the typical single-file dependence $(\Delta z)^2 \propto \sqrt{t}$. As already mentioned with reference to Eq. 13 [17], there is only a very faint indication, if at all, of a time regime $(\Delta z)^2 \propto t$ reflecting normal diffusion. The simulations have been carried out with various channel diameters. The probability of mutual passages between adjacent particles clearly increases with increasing channel

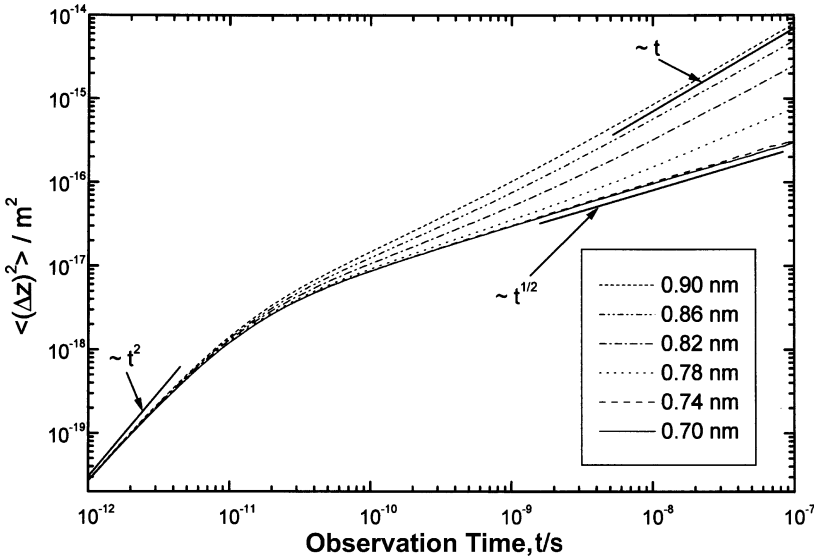

Fig. 2 Various time regimes of molecular propagation in single-file systems as resulting from MD simulations. The inset indicates the channel diameters considered in the different simulations. In all cases, the diameter of the diffusants was assumed to be equal to 0.383 nm. From [35] with permission

diameters. Correspondingly, with increasing channel diameters deviations from single-file diffusion become notable for shorter and shorter observation times. For sufficiently large observation times, the molecular displacements are completely determined by these passages. By simple random walk arguments the mean square displacement may then be shown to obey the relation

$$\left\langle (\Delta z)^2 \right\rangle = a^2 t/\tau_{ex}\,, \tag{15}$$

with τ_{ex} and a $(= l + \sigma)$ denoting, respectively, the mean exchange time between two adjacent molecules and their mean distance. Following the time dependence of ordinary diffusion, $\langle (\Delta z)^2 \rangle$ is now increasing in proportion to the observation time. The mean square displacements calculated on the basis of Eq. 15 are found to be in satisfactory agreement with the simulated displacements. Since the calculation of $\langle (\Delta z)^2 \rangle$ requires much larger simulation times than τ_{ex}, Eq. 15 may significantly help to save simulation times for the consideration of the long-time regime in zeolite channels when mutual passages between adjacent molecules eventually become dominant.

The concept of single-file diffusion has most successfully been applied for MD simulations in carbon nanotubes [36–39], yielding both the square-root time dependence of the molecular mean square displacement and a remarkably high mobility of the individual, isolated diffusants. In [40–42], the astonishingly high single-particle mobilities in single-file systems have been attributed by MD simulations to a concerted motion of clusters of the adsorbed molecules.

3
Finite Single-File Systems

3.1
The Mean Square Displacement

Proportionality between the mean square displacement and the square root of the observation time as reflected by Eq. 3 only strictly results for single-file systems of infinite extension. As soon as the boundary conditions at the ends of the single-file system become relevant, substantial deviations may occur. In single-file systems with closed ends the mean square displacement will obviously deviate from this dependence, approaching a constant value for sufficiently large observation times [5]. Such a behavior has been repeatedly verified by Monte Carlo simulations [43, 44]. Under the assumption that with the exception of the preserved particle sequence there is no correlation between the positions of the diffusants at the beginning and at the end of the experiment, the limiting value of the mean square displacement may be

shown to be [35]

$$\left\langle (\Delta z)^2 \right\rangle_\infty = \frac{1}{3} \frac{(1-\theta)^2}{\theta} L\sigma \,. \tag{16}$$

As to be expected, this value is much smaller than the corresponding value for restricted normal diffusion in one direction [45],

$$\left\langle (\Delta z)^2 \right\rangle_\infty = L^2/6 \,, \tag{17}$$

since normal diffusion enables maximum molecular displacement up to the extension L of the confinement, while a single-file particle is already confined by its two neighbors.

In contrast to finite single-file systems with closed ends, single-file systems with open ends lead to an enhancement of the mean square displacements in comparison with the pure single-file case. Eventually, molecular displacements are even found to follow the laws of normal diffusion. This behavior may intuitively be understood by realizing that in an appropriately selected time interval, a molecule may enter the single-file system on one side while another molecule may leave the single-file system on the other side. Such a coincidence of events shifts the total chain of molecules and hence any particle by one position. This type of molecular shift, however, is uncorrelated with the next one, caused by the same sequence of events. We have, therefore, a Markovian process, leading to normal diffusion. Considering the elementary steps quantitatively [2, 3], the mean square displacement of this process may be shown to obey the relation [35, 46–48]

$$\left\langle (\Delta z)^2 \right\rangle = 2D \frac{1-\theta}{n} t = 2D \frac{1-\theta}{\theta} \frac{\lambda}{L} t \,, \tag{18}$$

where $D = \lambda^2/2\tau$ is the diffusivity of an isolated particle in the single-file system. It is interesting to note that the effective diffusivity,

$$D_{\text{eff}} = D \frac{1-\theta}{n} = D \frac{1-\theta}{\theta} \frac{\lambda}{L} \,, \tag{19}$$

following from this relation via Eq. 2, coincides with the diffusivity under the condition of normal diffusion as given by Eq. 11, divided by the total number n of molecules in the single-file system. This effective diffusivity is sometimes referred to as the "center-of-mass" diffusivity. Irrespective of the small diffusivity, the proportionality with t determines that the mean square displacement in finite single-file systems with open ends is eventually governed by a diffusion-type equation Eq. 2, rather than by Eq. 3. Equating Eq. 18 and Eq. 1, the crossover time from single-file diffusion to normal diffusion in finite single-file systems with open ends may be determined to be equal to

$$t = L^2/\pi D \,, \tag{20}$$

with $D = \lambda^2/2\tau$.

Experiments with single-file systems of finite extension are thus found to be easily affected by the influence of the boundary conditions. Therefore, one should be aware of the fact that the observed displacements are sufficiently below the limiting values for which the boundary conditions start to become relevant.

Since the two limiting cases of open and closed ends have been shown to lead, respectively, to an enhancement and a reduction of the mean square displacement in comparison to an infinite single-file system, it may be anticipated that, under the influence of boundary conditions intermediate between these two limiting cases, molecular propagation in a finite single-file system may even proceed as in a single-file system of infinite extension.

3.2 Tracer Exchange

Before the introduction of measuring techniques such as pulsed field gradient (PFG) NMR ([14, 16, 45], pp. 168–206) and quasielastic neutron scattering (QENS) [49, 50], which are able to trace the diffusion path of the individual molecules, molecular diffusion in adsorbate-adsorbent systems has mainly been studied by adsorption/desorption techniques [16]. In the case of single-file systems, adsorption/desorption techniques cannot be expected to provide new features in comparison to the case of normal diffusion [51, 52]. In adsorption/desorption measurements it is irrelevant whether or not two adjacent molecules have exchanged their positions. But it is this effect which makes the difference between normal and single-file diffusion.

The situation is completely different, however, if one is considering the mutual replacement of particles which may be distinguished from each other. The classical experiment of this type is the tracer exchange measurement where the two species A and B are assumed to be distinguishable but identical in their microdynamic properties. For these measurements, in general, the adsorbate-adsorbent system which had been equilibrated with an atmosphere of species A is brought into an atmosphere of species B of the same pressure. Under the assumption that the process of molecular migration is subject to the laws of normal diffusion, the exchange curve may be predicted analytically. If the process is controlled by one-dimensional diffusion, which is the case for a parallel-sided slab, e.g., the exchange curve may be shown to follow the relation (cf. [16], p.239)

$$\gamma(t) = 1 - \frac{8}{\pi^2} \sum_{\substack{i=1 \\ \text{odd}}}^{\infty} \frac{1}{\mathrm{i}^2} \exp\left(- \frac{\pi^2}{12} \mathrm{i}^2 \frac{t}{\tau_{\text{intra}}} \right) , \tag{21}$$

where $\gamma(t)$ denotes the ratio between the amount of species B within the adsorbate-adsorbent system at time t divided by the final amount of species B (which in the considered case of tracer exchange clearly coincides with the

initial amount of species A). For simplicity, it has additionally been assumed that the species B is in abundance, i.e., that there is no re-entrance of species A into the system. τ_{intra} denotes the intracrystalline mean lifetime of a molecule in the system, defined by the relation [53, 54]

$$\tau_{\text{intra}} = \int_0^\infty \big(1 - \gamma(t)\big)\,\mathrm{d}t\,. \tag{22}$$

It is related to the length of the system (slab thickness L) and the diffusivity by the equation

$$\tau_{\text{intra}} = L^2/(12D)\,. \tag{23}$$

Eq. 21 with Eq. 23 results as the solution of the corresponding differential equation of normal diffusion with the appropriate initial and boundary conditions. These relations hold with the adequate interpretation of D as a self-diffusivity or a transport diffusivity, respectively, for both tracer exchange between the initially adsorbed species A by species B and the relative uptake in an adsorption experiment. It should be noted that Eq. 21 also describes the molecular uptake by single-file systems, since with respect to adsorption/desorption there are no differences between single-file systems and systems which permit normal diffusion.

As soon as the movements of different species have to be distinguished from each other, however, the mutual correlation of the molecules in single-file systems makes it impossible to predict the evolution of the particle distributions by differential equations. For this reason, the time dependence of the tracer exchange in single-file systems has thus far only been investigated by Monte Carlo simulations [1, 55–57].

As an example, Fig. 3 shows the initial stages of tracer exchange for the total site numbers $N = 150$, 300 and 600 and the site occupancies $\Theta = 0.25$, 0.50. 0.75 and 0.90 [56, 57]. For comparison, the slopes expected for diffusion-limited exchange (broken line) and for exchange limited by single-file confinement (full line) are also indicated. For the very first steps of the particles leaving the single-file system, single-file confinement is obviously not yet relevant, so that the time dependence is that of a diffusion-limited process. This initial part is followed by dependencies which may be shown analytically to result from tracer exchange under single-file confinement [57]. As a strong argument that under these conditions the above-described diffusion-like mechanism of displacement does not work, one has to consider the fact that for any given loading the product of the tracer exchange curve and the total number of sites is independent of the file length. Since this product is nothing else than the total number of exchanged molecules, the total file length is obviously not of any influence on the observed behavior up to the given time.

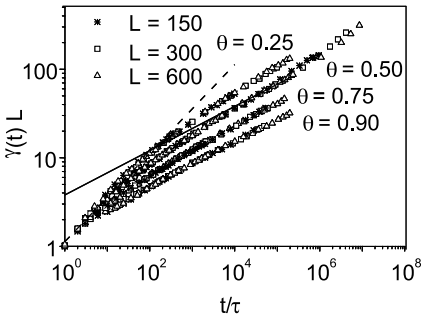

Fig. 3 The normalized tracer exchange curves in single-file systems obtained by dynamic Monte Carlo (DMC) simulations for various file lengths (=L in the figure) and loadings (Θ) (*points*). The *dashed* and *solid lines* show the best fit lines for $\Theta = 0.5$ with the slope of 1/2 and 1/4 expected for the mechanism of normal and single-file diffusion, respectively, in the limit of short times. From [57] with permission

Only in the case of $\Theta = 0.50$, with $L = 300$ and 600, Fig. 3 indicates the beginning of the transition to the diffusion-controlled regime of tracer exchange. It is demonstrated by Fig. 4 that over the largest part of the file, the concentration profiles during the exchange process are astonishingly well represented by the corresponding solutions of the classic diffusion equation, i.e. of Fick's second law. In the approach taken, a certain part of the file at the two openings has been assumed to attain the equilibrium concentration instantaneously, so that the exchange had to be followed over N^* rather than over N sites. Table 1 indicates the values of the ratio N^*/N and of the ratio $D_{\mathrm{sim}}/D_{\mathrm{eff}}$ between the diffusivity used in the analytical simulations and the effective file diffusivity, as given by Eq. 19, which have led to the best agree-

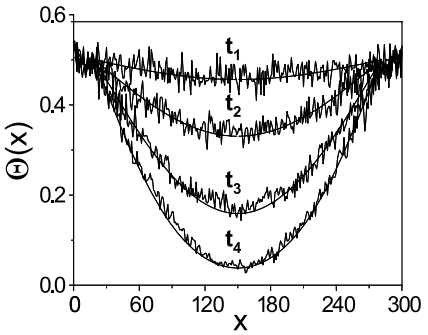

Fig. 4 Comparison of the concentration profiles of tagged particles obtained by DMC simulations for tracer exchange in single-file systems of length L (*oscillating solid lines*) with the concentration profiles for normal diffusion, with D_{sim} and N^* given in Table 1 (*solid lines*) at times $t_1 = 0.93 \times 10^6\tau$, $t_2 = 2.1 \times 10^6\tau$, $t_3 = 3.7 \times 10^6$, and $t_4 = 7.6 \times 10^6\tau$ (τ is the duration of the elementary diffusion step). From [57] with permission

Table 1 Results of the best fit D_{sim} and N^* and the center-of-mass diffusivity D_{eff} and site number N in the final time domain of tracer exchange (controlled by center-of-mass diffusion) [57]

N	D_{sim}/D_{eff}	N^*/N
150	1.51	0.83
300	1.49	0.87
600	1.80	0.92

ment with the simulation data. Not unexpectedly, the site number N^* relevant for the simulations approaches the total number with increasing file length. It is interesting to note that D_{sim}, though on the order of D_{eff}, does not seem to approach this value.

Most importantly, combining the expressions for the intracrystalline mean life time Eq. 23 and the effective self-diffusivity (Eq. 19), in the case of single-file diffusion the mean time of molecular exchange is found to scale with L^3, rather than with the L^2 dependence typical of normal diffusion. Therefore, under the conditions of single-file diffusion, the exchange rate with zeolite crystallites decreases even more pronounced with increasing crystal sizes as in the case of normal diffusion.

3.3 Theory of Catalytic Reactions

The combined influence of molecular transport and catalytic reaction in adsorbate-adsorbent systems has so far been exclusively described by supplementing Fick's differential equations of mass transfer with a reaction term and solving them under the relevant initial and boundary conditions [16, 58, 59]. Due to the correlated movement of the individual particles, this approach fails in the case of single-file diffusion. Transport inhibition may intuitively be anticipated to be much more stringent in single-file systems than in systems subject to normal diffusion, since a product molecule can only get out of the file – i.e. in our case the zeolite channel – if all the other molecules in front of it have been shifted in the same direction. Since the probability of such a combined process is very low, the rate of exchange of the product molecules with the surrounding atmosphere must be dramatically smaller than in the case of ordinary diffusion, where the product molecules may get to the crystallite surface without any correlation to the movement of the other molecules. This situation is reflected by the different scaling patterns of the molecular exchange time with increasing crystal sizes in the cases of normal and single-file diffusion as discussed at the end of the previous section.

As in the case of tracer exchange, quantitative information about the correlated effect of transport and catalytic reactions in single-file systems has

so far only been attained by Monte Carlo simulations. Figure 5 illustrates the situation due to the combined effect of diffusion and catalytic reaction in a single-file system for the case of a monomolecular reaction A → B [1]. For the sake of simplicity it is assumed that the molecular species A and B are completely equivalent in their microdynamic properties. Moreover, it is assumed that in the gas phase A is in abundance and that, therefore, only molecules of type A are captured by the marginal sites of the file. Figure 5 shows the concentration profile of the reaction product B within the single-file system under stationary conditions. A parameter of the representation is the probability κ that during the mean time between two jump attempts (τ), a molecule of type A is converted to B. It is related to the intrinsic reactivity k by the equation

$$\kappa = k \cdot \tau \,. \tag{24}$$

In the case of normal diffusion, the corresponding concentration profile may be calculated analytically [2, 16, 58, 59] yielding

$$\frac{\theta_B}{\theta} = 1 - \frac{\cosh\left(z\sqrt{k/D}\right)}{\cosh\left(L/2\sqrt{k/D}\right)} \equiv 1 - \frac{\cosh\left(2z/L\phi\right)}{\cosh\phi}\,, \tag{25}$$

with

$$\phi = \frac{L}{2}\sqrt{\frac{k}{D}}\,, \tag{26}$$

denoting the Thiele modulus.

For comparison, Fig. 5 also displays the concentration profile of species B for the case of normal diffusion as given by Eq. 25, with the particular choice of the parameter $\phi = 2.77$.

In complete agreement with the fact that the product molecules in a single-file system are prevented from leaving the system by their file neighbors, the concentration profiles in the single-file cases show a much more pronounced tendency of accumulation of the reaction products in the file center than in the case of normal diffusion. Under stationary conditions, the effective reactivity k^* is related to the intrinsic reactivity k by the equation

$$k^* = \frac{\bar{\theta}_A}{\theta} k\,, \tag{27}$$

where $\bar{\theta}_A$ denotes the mean value of the site occupancy of molecules A. The ratio

$$\eta = \frac{k^*}{k} = \frac{\bar{\theta}_A}{\theta} \tag{28}$$

represents the effectiveness factor, which may be easily determined by integrating over the concentration profile. Obviously, by integrating over Eq. 25,

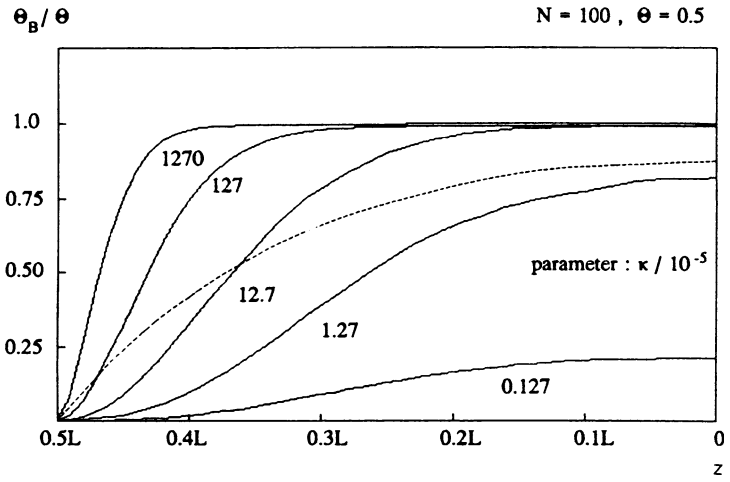

Fig. 5 Concentration profiles of the molecules of species B within the single-file system under stationary conditions and comparison with the dependence to be expected for ordinary diffusion (*broken line*, Eq. 29). The quantity $2L(k/D)^{1/2}$ (the Thiele modulus ϕ) in Eq. 29 has been chosen to coincide with the generalized Thiele modulus (cf. Eq. 30) of the single-file reaction for $\kappa = 1.27 \times 10^{-5}$ ($\phi = 2.77$). z denotes the distance from the middle of the file and $L = N\lambda$ its length. From [1] with permission

the effectiveness factor under the conditions of normal diffusion is thus found to be a sole function of the Thiele modulus

$$\eta = \frac{\tanh\phi}{\phi} \,. \tag{29}$$

This dependence is represented by the dotted line in Fig. 6. In a first attempt to systematize the simulation results of molecular reaction and diffusion in single-file systems, a generalized Thiele modulus has been introduced [1]. Combining Eq. 25 and Eq. 23, the Thiele modulus may be expressed in the alternative notation

$$\phi = \sqrt{3k\tau_{\text{intra}}} \,, \tag{30}$$

which, in contrast to Eq. 26, is not restricted to a particular transport model and also includes the case of single-file diffusion. In this way, reactivities under the conditions of normal and single-file diffusion may be directly related to each other. The Thiele modulus of the example of normal diffusion in Fig. 5 was thus chosen to coincide with the generalized one in the single-file case with $\kappa = 1.27 \times 10^{-5}$. It is demonstrated by Fig. 6 that the dependence of the effectiveness factor in single-file systems on the generalized Thiele modulus is at least qualitatively reflected by the classical dependence of the Thiele concept, as provided by Eq. 29. One should not be confused by the slightly larger values in the case of single-file systems for comparable generalized

Thiele moduli. These also appear in the smaller area below the single-file profile curve for $\kappa = 1.27 \times 10^{-5}$ in Fig. 5, in comparison to the area under the profile resulting from the conditions of normal diffusion with the same Thiele modulus. By comparing single-file diffusion with ordinary diffusion the prevailing effect is clearly the dramatic enhancement of τ_{intra} and hence of the Thiele modulus, leading to a correspondingly dramatic reduction of the effectiveness factor.

Since tanh ϕ approaches the value of 1 for sufficiently large Thiele moduli, it follows from Eq. 29 that the effectiveness factor approaches the reciprocal value of the Thiele modulus. In the classical Thiele concept, this leads to the well-known reduction in the apparent activation energy for transport-controlled reactions, since the effective reactivity is now proportional to $\sqrt{k}$ rather than to k, as in the absence of any transport limitation.

It should be noted that in the case of single-file diffusion the situation might be different. This is because the temperature dependence of τ_{intra}, which is the second relevant quantity in Eq. 30 and in the case of normal diffusion is generally assumed to be inferior to that of the intrinsic reactivity, may become significant. Since the occupancy of the single-file system may substantially decrease with increasing temperature, the enhanced temperature dependence of τ_{intra} may be a simple consequence of its concentration dependence, as given by Eq. 19. A quantitative estimate of this effect is given in [55].

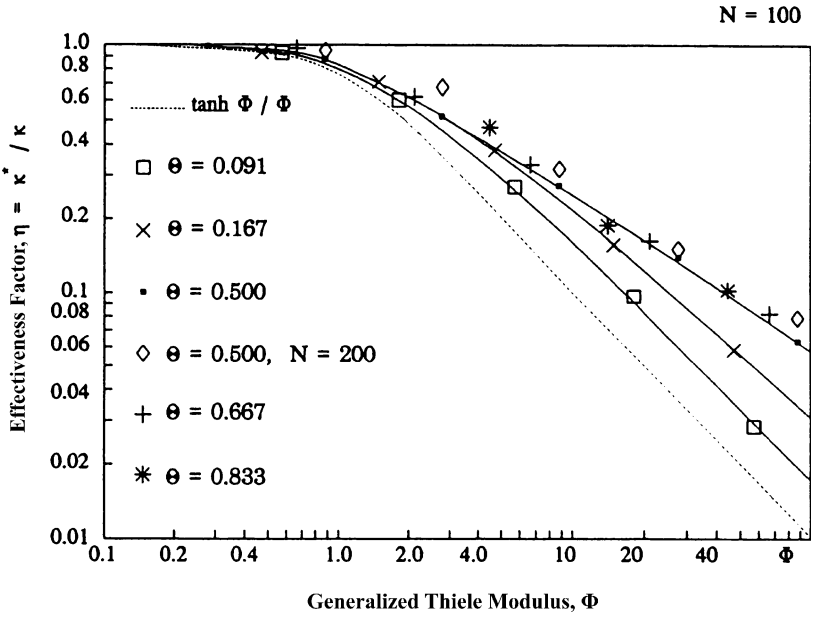

Fig. 6 Effectiveness factor $\eta = \kappa^*/\kappa$ of single-file reaction plotted as a function of the generalized Thiele modulus. From [1] with permission

Networks of interconnecting single-file systems with different accommodation probabilities for molecules participating in chemical reactions [56, 60–63] have recently been introduced as model systems for the quantification of the effect of Molecular Traffic Control (MTC) [64, 65], i.e. for the enhancement of the effective reactivity by an optimization of the intracrystalline transport of the molecules involved in the reaction. In the given case, this reactivity enhancement is caused by a preferential adsorption of the reactant and product molecules along different diffusion paths (channels) in the interior of the zeolite crystallites and a corresponding reduction of their mutual interference. MD simulations [66, 67] have confirmed the feasibility of such situations. MTC reactivity enhancement is found to become particularly pronounced with increasing file lengths between subsequent intersections.

This tendency can be understood by realizing that the mean lifetime in single-file systems (Eq. 23 with Eq. 19) scales with the third power of the file length L. We use this proportionality to estimate the mean lifetime required for the reactant and product molecules to diffuse from one channel intersection to an adjacent one, with L being proportional to the number of sites between the intersections. This type of reasoning clearly only applies for a system of uniform overall concentration, i.e. if the sum of the reactant and product concentrations is constant throughout the system. Without the difference in the adsorption preferences of the reactant and product molecules considered above, this would also be the case in the single-file network considered. Since the components are attributed to the individual channels with different probabilities, however, the concentration gradients of the individual components inherent to chemical reactions (i.e., falling concentrations from outside to inside for the reactant molecules and increasing concentrations for the product molecules) would to some extent appear in the channels as well. Under the influence of such concentration gradients, molecular transport in single-file systems proceeds under the conditions of normal diffusion, with the mean lifetime scaling with L^2 rather than L^3. Hence, for sufficiently large distances L between the channel intersections, the MTC conditions will ensure a smaller degree of transport inhibition and thus a higher effective reactivity.

3.4 Analytical Treatment

Our understanding of diffusion and reaction in single-file systems is impaired by the lack of a comprehensive analytical theory. The traditional way of analytically treating the evolution of particle distributions by differential equations is prevented by the correlation of the movement of distant particles. One may respond to this restriction by considering joint probabilities covering the occupancy and further suitable quantities with respect to each individual site. These joint probabilities may be shown to be subject to master equations,

i.e. to equations correlating the populations of the different states by considering the mutual transition probabilities. These equations may be solved with a much smaller expense of computation time than necessary for Monte-Carlo simulation. Moreover, the master equations may also easily account for the possibility of mutual passages of adjacent particles and particle-particle interaction. Examples of such studies including chemical reactions and comparison with mean-field approaches may be found in [68–73]. In [72], this concept has been developed and successfully applied using three different sets of probabilities:

The configuration probability $\theta^{\sigma_1\sigma_2\cdots\sigma_N}$ (with $\sigma_i = 0$ or 1) denoting the probability of a particular occupation pattern, where $\sigma_i = 0$ (1) means that the i-th site is vacant (occupied).

The residence time distribution function $\varphi_i^{\sigma_1\cdots\sigma_{i-1}*\sigma_{i+1}\cdots\sigma_N}(\tau)$ providing the probability (density) that the particle configuration is given by the parameter set $\sigma_1\cdots\sigma_{i-1}1\sigma_{i+1}\cdots\sigma_N$, and that the particle on site i has entered the file a time interval τ ago.

The reactant concentration profile $\eta_i^{\sigma_1\cdots\sigma_{i-1}*\sigma_{i+1}\cdots\sigma_N}$ representing the probability that site i is occupied by a reactant molecule and that the occupation of the other sites (either by reactant or product molecules) is described by the set of parameters $\sigma_1\cdots\sigma_{i-1}, \sigma_{i+1}\cdots\sigma_N$.

One of the most important features of all these probabilities is that they are time-invariant under stationary conditions. In particular, this means that the probability distribution for the residence time of a particle at a given site (and for a given configuration) remains unchanged for any time. In the considered simple case of a first-order reaction, after residing over a time τ within the single-file system, a reactant molecule A will not have been converted into a product molecule B with the probability $\exp(-k\tau)$. Therefore, the reactant concentration profile follows easily by multiplying the residence time distribution function with the probability that for a particular residence time there was no conversion, and integration over all residence times τ yields

$$\eta_i^{\sigma_1\cdots\sigma_{i-1}*\sigma_{i+1}\cdots\sigma_N} = \int_0^\infty e^{-k\tau}\varphi_i^{\sigma_1\cdots\sigma_{i-1}*\sigma_{i+1}\cdots\sigma_N}(\tau)\,d\tau\,. \tag{31}$$

Thus the reactant concentration profile is found to be nothing else than the Laplace transform of the residence time distribution.

The probability functions can be calculated by solving the adequate master equations and transferred into experimentally relevant quantities by summing over the two possible states (vacant and occupied) of all sites of the system. For the relative occupancy of site i one thus obtains

$$\theta_i = \sum_{\sigma_1=0}^{1}\cdots\sum_{\sigma_{i-1}=0}^{1}\sum_{\sigma_{i+1}=0}^{1}\cdots\sum_{\sigma_N=0}^{1}\theta^{\sigma_1\cdots\sigma_{i-1}1\sigma_{i+1}\cdots\sigma_N}\,. \tag{32}$$

In a completely equivalent way one may determine the residence time distribution $\varphi_i(\tau)$ of site i and the probability η_i that site i is occupied by a reactant molecule.

Though the master equations clearly represent analytical expressions for the intrinsic dynamics in single-file systems, the calculations become rather time consuming with increasing file lengths. As a reasonable compromise between needed computation time and gained information, in [72] single-file systems with 8 sites have been considered. As an example, Fig. 7 shows the concentration profile of a single-file system for different particle-particle interaction parameters ω [72]. The parameter ω describes the reduction in the hopping rates if a jump starts from a position adjacent to another molecule as compared to the jump rate of an isolated molecule (with $\omega = 1$ denoting totally missing interaction). As is to be expected, the attractive interaction leads to an accumulation of the particles in the center of the single-file system. Figure 8 shows the average intracrystalline residence time profile for the same cases as considered in Fig. 7. The intracrystalline residence time τ_i is determined by the residence time distribution function $\varphi_i(\tau)$ via the relation Eq. 33

$$\tau_i = \int_0^\infty \tau \varphi_i(\tau)\, \mathrm{d}t\,, \tag{33}$$

and denotes the average time that a particle found at site i has already spent in the channel. The mean lifetime τ_{intra} of an arbitrarily selected particle clearly follows as a mean over all values τ_i. Note that Fig. 8 does not give the average time the particles have spent at the individual sites, but the average total time they have already spent in the channel.

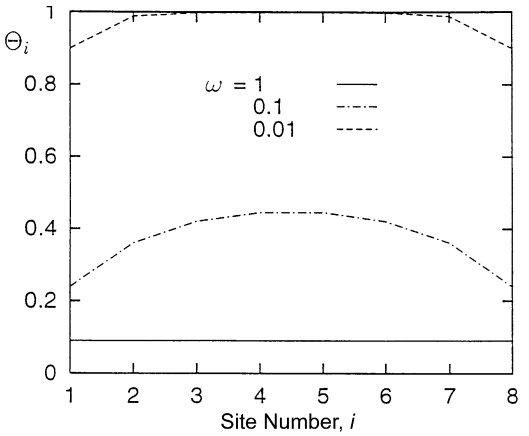

Fig. 7 Concentration profile θ_i over the site number i for different values of the particle-particle interaction parameter ω as resulting from the solution of the master equations. From [72] with permission

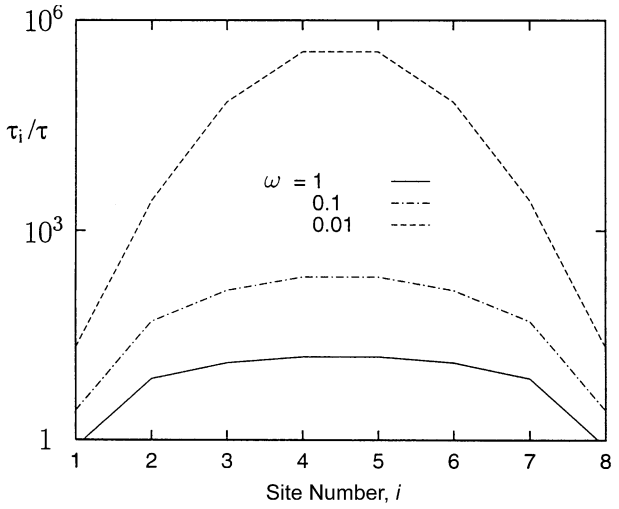

Fig. 8 Average residence time profile (in units of the time τ between two jump attempts) of the particles in the single-file systems considered in Fig. 7. From [72] with permission

The benefit of the analytical treatment presented thus far for the calculation of the characteristic functions of the single-file system is only limited by the increasing complexity of the joint probabilities and the related master equations. This treatment, however, has suggested a most informative access to the treatment of systems subjected to particle exchange with the surroundings and to internal transport and reaction mechanisms [74, 75]. Summing over all values $\sigma_i = 0$ and 1 and, subsequently, over all sites i, Eq. 31 may be transferred to the relation Eq. 34

$$\eta(k) = \int_0^\infty e^{-k\tau} \varphi(\tau)\, d\tau\,, \tag{34}$$

where $\varphi(\tau)$ denotes the residence time distribution function of the molecules in the system and $\eta(k)$ is the effectiveness factor as introduced by Eq. 28. Adopting the reasoning leading to Eq. 31, Eq. 34 is found to hold quite generally for any system with an intrinsic reactivity k and a stationary residence time distribution. The residence time distribution curve is not only a function of theoretical relevance. It is also experimentally accessible precisely as the response curve of a tracer ZLC experiment [76–82].

It is interesting to note that the residence time distribution may also be used as a generating function for the tracer exchange curve as introduced in Sect. 3.2. The relative amount of tracer exchange at a certain time t is simply the sum over all molecules which have entered and remained in the system between time zero and the present instant, or, in other words, the residence

times of which are between zero and t. Thus, one has

$$\gamma(t) = \int_0^t \varphi(\tau)\,\mathrm{d}\tau\,, \tag{35}$$

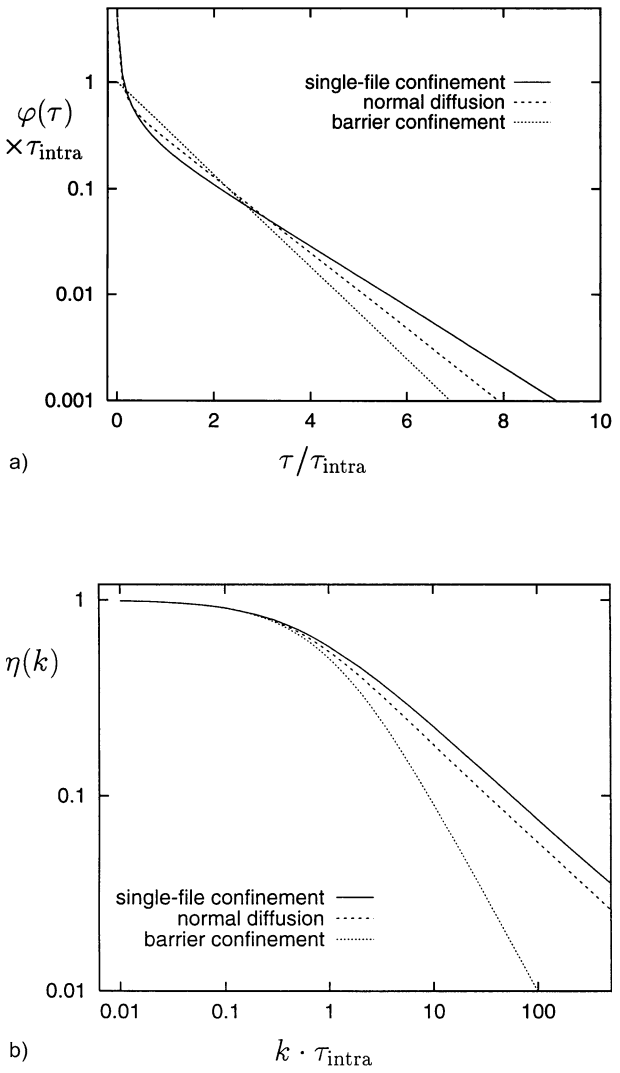

Fig. 9 Probability distribution function $\varphi(\tau)$ (**a**) and effectiveness factor $\eta(k)$ (**b**) corresponding to the tracer exchange curves in the limiting cases of dominating single-file diffusion, normal diffusion and surface barriers as a function of the quotient of τ and τ_{intra}. From [74] with permission

with the inversion

$$\varphi(\tau) = \frac{\mathrm{d}}{\mathrm{d}t}\gamma(t)\,|_{t=\tau} \quad . \tag{36}$$

Like Eq. 34, Eqs. 35 and 36 hold quite generally for systems containing particles, the residence times of which are subjected to a stationary probability distribution. The interrelation of the "characterizing" functions $\eta(k)$, $\gamma(t)$ and $\phi(\tau)$ and their wide field of application for stationary population are described in great detail in [83, 84].

Figure 9 displays the probability distribution function $\varphi(\tau)$ and the effectiveness factor $\eta(k)$, which have been calculated via Eqs. 36 and 34 from the tracer exchange curves in the limiting cases of single-file diffusion, normal diffusion and barrier confinement. The fact that in all cases the residence time distribution function is found to decrease monotonically may be easily rationalized as a quite general property. Due to the assumed stationarity of the residence time distribution function, the number of molecules with a residence time τ is clearly the same at any instant of time. The number of molecules with a residence time $\tau + \Delta\tau$ may therefore be considered as the number of molecules with a residence time τ minus the number of molecules which will leave the system in the subsequent time interval $\Delta\tau$. Therefore, $\varphi(\tau)$ must quite generally be a monotonically decaying function.

It is reflected by Fig. 9a that in the long-time range all curves are simple exponentials. It is impossible, therefore, to determine the dominating transport mechanism from this part of the distribution curve. Thus, for a given value of $k\tau_{\mathrm{intra}}$, the analytically determined effectiveness factors for the typical single-file case (i.e., for large concentrations) as shown in Fig. 9b are slightly larger than in the case of diffusion limitation and are therefore in complete agreement with the simulation results given in Fig. 6. In addition, the effectiveness factor in the case of barrier limitation is found to be even smaller. It is interesting to note that this sequence also appears in the concentration profiles, which are most pronounced in the case of single-file diffusion (cf. Figure 5) and which degenerate to a horizontal line reflecting uniform concentration over the whole sample in the case of transport limitation by surface barriers.

4
Experimental Results

4.1
Pulsed Field Gradient NMR

As a non-invasive technique being able to monitor directly molecular displacements of the order of micrometers [14, 16, 45], the pulsed field gradient

(PFG) NMR technique is the most efficient technique for directly probing single-file diffusion. By varying the observation time (from typically milliseconds up to hundreds of milliseconds), it should be possible to easily decide whether the mean square displacement increases linearly, as required for normal diffusion (Eq. 2), or only in proportion to the square root of the observation time (Eq. 3), indicating the occurrence of single-file diffusion. PFG NMR studies with zeolites containing one-dimensional channels, however, are subjected to a number of additional difficulties. (i) The fraction of the intracrystalline void volume is generally smaller than in zeolites with more-dimensional pore networks, correspondingly the sorbate concentrations and hence the signal intensities are also smaller. (ii) The molecular confinement within the one-dimensional channels leads to smaller transverse nuclear magnetic relaxation times which may dramatically impair the measuring conditions. (iii) The reduced translational mobility leads to much smaller displacements than are generally observed in more-dimensional networks which are more difficult to observe. In addition, one must keep in mind that molecular transport in one-dimensional channels is much more affected by inevitable deviations from an ideal structure than in a more-dimensional pore network.

Owing to these difficulties, PFG NMR studies with CF_4 and CH_4 in the one-dimensional channel system of VPI-5 only allowed one to estimate an upper limit of 0.5 μm for the molecular displacements during the observation time of 2 ms [52]. Using Eq. 2, from these data the diffusivity of CF_4 and CH_4 in VPI-5 may be estimated to be smaller than 5×10^{-11} m^2 s^{-1}. Already, this upper limit is by at least one order of magnitude smaller than the corresponding value in ZSM-5. The channel diameters in ZSM-5 (0.51–0.56 nm) are much smaller than in VPI-5 (1.21 nm), so that at a first glance, the smaller diffusivities in VPI-5 are astonishing. However, since in VPI-5 the channels are parallel, without mutual intersections as in ZSM-5, the low diffusivities may be considered as an indication of the mutual confinement typical of single-file systems [52].

The first direct evidence for the occurrence of single-file diffusion in zeolites was provided for ethane in $AlPO_4$-5 [27, 85] and for methane and CF_4 in $AlPO_4$-5 and zeolite Theta [75, 86–88]. In Fig. 10, the mean square displacements for ethane in $AlPO_4$-5 are shown to be, in fact, much better approached by a square-root dependence on the observation time than by a linear dependence [85]. Owing to the double-logarithmic scale, in Fig. 11, an even larger range of mean square displacements and observation times is covered [75]. The measurements have been carried out with CF_4 on $AlPO_4$-5, and again the typical single-file dependence is observed. Moreover, the data are also found to be in reasonably good agreement with the concentration dependence predicted by Eq. 1. Table 2 summarizes the single-file mobility factors resulting from the experimental data on the basis of Eq. 3 as well as the dif-

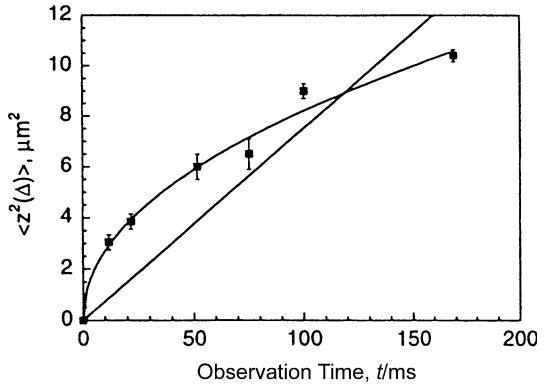

Fig. 10 Ethane mean square displacements in $AlPO_4$-5 plotted as a function of observation time. Linear and power-law best fits to the data are also shown. The linear fit is made to pass through the origin. From [85] with permission

fusivities, which one has to attribute to an isolated molecule on the basis of Eq. 8 [75, 88].

It should be noted that the thus estimated diffusivity is by two orders of magnitude larger than the highest diffusivities thus far measured for CF_4 in zeolites with more-dimensional pore networks [89, 90]. For methane in $AlPO_4$-5, the single-particle diffusivities at infinite dilution are, in this way, estimated to amount to even 10^{-4} m^2 s^{-1} [87]. This large molecular mobility may be rationalized as the effect of molecular guidance by the channels. It may be shown by MD simulations of molecular diffusion in a periodic potential of rotational symmetry [88] that such high values may in fact result for a sufficiently small difference between the minima and maxima of the potential energy. It is likely that this supermobility is reflected in the large

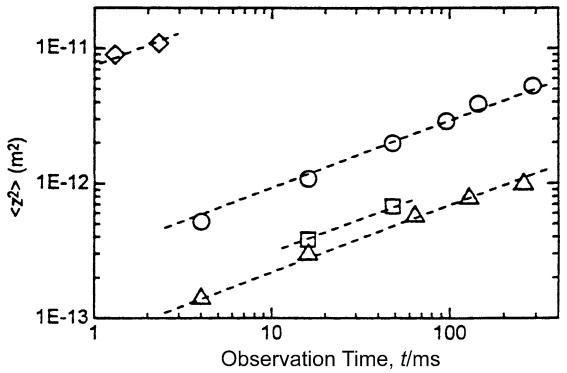

Fig. 11 Molecular mean square displacement of CF_4 in $AlPO_4$-5 at 180 K as a function of the observation time at a sorbate concentration of 0.005 (◇), 0.05 (O), 0.2 (□), and 0.4 (△) molecules per unit cell. From [88] with permission

Table 2 Results of the PFG NMR self-diffusion studies with CF_4 adsorbed in $AlPO_4$-5 at 180 K, represented in terms of the single-file mobility factor F [cf. Eq. 3] and the single-particle diffusivity D [cf. Eq. 8]. The mean free distance l is calculated according to Eq. 10. The errors of the experimental values are about 50% [47]

c/molecules/unit cell	L/nm	F/m^2 s$^{-1/2}$	D/m^2 s^{-1}
0.4	1.63	0.7×10^{-12}	0.6×10^{-6}
0.2	3.73	1.5×10^{-12}	0.5×10^{-6}
0.05	16.3	4.5×10^{-12}	0.3×10^{-6}
0.005	167	1.0×10^{-10}	1.1×10^{-6}

permeabilities observed for n-heptane in $AlPO_4$-5 membranes in comparison with ZSM-5 [91]. More recent MD simulations of molecular propagation in confining channels ("nano-tubes") [36–39] confirm the possibility of the existence of such states of "super-mobility".

An appreciation of the PFG NMR studies of zeolite $AlPO_4$-5 performed to date, however, has to take at least two critical issues into account:

(i) Recent investigations by interference microscopy of molecular uptake on zeolites that are generally accepted to be of single-file type [92–95] revealed dramatic deviations from the ideal text book structure. In [14], such deviations have already been discussed as one of the possible explanations for the large differences in the diffusivities determined by different techniques. One has to be rather skeptical, therefore, as to whether the real structure of available zeolite specimens may really be perfect enough to yield all features to be expected for ideal systems.

(ii) The mean square distance $\langle z^2(t)\rangle_c$ covered by the molecules in the transition ranging from the time regimes of single-file diffusion to normal diffusion may be easily determined from the crossover time given by Eq. 20. Even for crystals of ideal single-file structure and with sizes of more than 100 μm, the resulting value of $\langle z^2\rangle_c = (2/\pi)\cdot(1-\theta)/\theta\, L\lambda$ would yield crossover distances of less than 1 μm which are at the limit of accessibility by PFG NMR. Moreover, in addition to internal defects, deviations from the ideal crystal structure are, in particular, expected to affect the boundary conditions with the options of both a reduction (via Eq. 16) or an enhancement (via Eq. 18) of the mean square displacement in comparison with single-file diffusion in an unlimitedly large system. These deviations would obviously lead to opposite tendencies in the time dependence of single-file diffusion and might, therefore, serve as a possible explanation of differences in the findings in [96] and [75, 86–88]. Thus, a substantial demand for the continuation of the PFG NMR measurements of zeolitic single-file diffusion exists.

4.2 Quasielastic Neutron Scattering

In contrast to PFG NMR, which is able to trace molecular displacements over micrometers, quasi-elastic neutron scattering (QENS) is particularly sensitive to the elementary steps of diffusion [49, 50, 97–100]. The range of displacements accessible by QENS is therefore not larger than a few nanometers. This, however, is exactly the order of magnitude of the typical distance between adjacent molecules in zeolitic single-file systems. QENS should, therefore, provide the unique possibility to trace both the ballistic phase (i.e., free particle movement) and/or normal diffusion (when considering sufficiently small displacements) and single-file diffusion for sufficiently large displacements. The differences between these two types of movement should appear in a different broadening of the quasi-elastic peak in the representation of the differential scattering cross sections versus the energy exchange [101]. The messages of first QENS studies [102] with potential candidates for zeolitic single-file systems are slightly controversial. Both for methane and ethane in $AlPO_4$-5, the QENS data could be fitted much better to a model based on unidirectional normal diffusion than to single-file diffusion. The resulting diffusivities are, respectively, 1.6×10^{-9} m^2/s and 1.2×10^{-9} m^2/s for methane concentrations of 0.7 and 1 molecule/u.c. at 155, and 1.4×10^{-9} m^2/s, 1.1×10^{-9} m^2/s and 0.9×10^{-9} m^2/s for ethane concentrations of 0.7, 1.4 and 1.6 molecules/u.c. These measurements are in conflict with the PFG NMR results with respect to both the absolute values of the diffusivities and the predicted diffusion mechanism. Since the minimum scattering vectors of the QENS studies correspond to maximum displacements of the order of 3 nm, it appears that both the methane and ethane molecules should be able to pass each other in the channels. With respect to methane, such a conclusion would be in agreement with [96], but in conflict with [75, 86–88]. For ethane, the messages of QENS were in contrast with [85].

In the case of cyclopropane in $AlPO_4$-5 and methane in ZSM-48, however, the QENS data also show the typical scattering pattern of single-file diffusion [101, 102]. It is interesting to note that for methane in ZSM-48, a transition from normal diffusion (at low concentrations, $D \approx 2.5 \times 10^{-9}$ m^2 s^{-1}) to single-file diffusion (at higher concentrations, $F \approx 2 \times 10^{-12}$ m^2 s$^{-1/2}$, data for 155 K) may be observed. Such behavior is in complete agreement with intuition. A quantitative treatment on the basis of Eq. 8, however, fails to confirm this agreement. The single-file mobility factors F measured at high concentrations would correspond to much larger single-particle diffusivities than measured for low concentration. This inconsistency within one and the same set of experiments illustrates the difficulties of QENS experiments, which must be based on model assumptions. The above-mentioned values of D and F have been determined on the basis of the asymptotic laws of normal diffusion (Eq. 2) and single-file diffusion (Eq. 3)

which are clearly not valid in the transition range between these two regimes of diffusion. Moreover, the ballistic phase which may be shown to be of much greater influence in one-dimensional than in multidimensional channel systems has been completely neglected in the model considerations. It cannot be excluded, therefore, that by choosing other more auspicious model parameters, satisfactory agreement between both the QENS data themselves and the QENS and PFG NMR data may be obtained. Since QENS provides the fourfold Fourier transform of the propagator [97] rather than the propagator itself, the present question is a typical example of an inverse problem. Theory and application of reciprocal problems is a most attractive problem of current research [103].

4.3
Macroscopic Measurements

Molecular adsorption, desorption and permeation do not distinguish between different molecules and are therefore insensitive to the possibility or impossibility of the mutual passage of adjacent molecules. All techniques like uptake, ZLC, frequency response and permeation measurements which are exclusively based on these phenomena do not allow, therefore, one to decide about the occurrence of single-file diffusion. This, by no way, means that these techniques are unable to trace differences between multidimensional and one-dimensional diffusion since the latter process may be easily affected by transport resistances on the channel openings and by self-sticking of the diffusants. Hence, in particular, various FR-studies have been performed with zeolitic adsorbate-adsorbent systems including possible hosts of single-file systems [104, 105]. Restriction to one-dimensional diffusion, however, does not determine whether unidirectional molecular propagation is subjected to the constraint of single-file diffusion. In order to get such information, the macroscopic measurements must involve at least two distinguishable components. Typical representatives of this kind of investigation are the counter-diffusion measurements [106] which have become an attractive application of in-situ IR measurements [107–112], though, also other spectroscopic methods like NMR or mass spectroscopy are applicable. Thus far, however, such studies have not been carried out with single-file systems. As a second possibility, two different groups of molecules may be created by isotope labeling. Their distinction may be based on the same techniques as in counter-diffusion measurements. The theoretical treatment of such studies, e.g., in the case of tracer exchange experiments, is facilitated by the fact that the mobility of the two components is essentially identical. Experiments of this type have been carried out by the tracer ZLC technique and by monitoring the ^{1}H NMR signal intensity during the exchange of a hydrogen-containing species with its deuterated isotope and shall be presented in this section. A third type of macro-

scopic measurement, the observation of catalytic reactions, will be considered in Sect. 4.4.

Figure 12 displays the results of a tracer exchange experiment with propane in $AlPO_4$-5 at a loading of about 0.7 molecules per unit cell at room temperature [75]. With the definition provided by Eq. 22, from Fig. 12 the intracrystalline mean life time of propane in the $AlPO_4$-5 crystals under study is found to be equal to 1.3×10^4 s. Molecular uptake was observed to proceed with a time constant of less than 100 s [75]. This time constant has to be considered as an upper limit of the mean life time of an isolated molecule without single-file interaction (Eq. 23 with Eq. 9) in the channels since, in addition to this effect of diffusion, the uptake time constant includes the influence of adsorption heat release immanent to transient adsorption phenomena [16]. Since tracer exchange and molecular uptake have been studied with the identical host, according to Eq. 23, the differences in the observed time constants may be attributed to the corresponding (effective) diffusivities, namely to Eqs. 9 and 19. Hence, the difference of more than two orders of magnitude between the time constants can be taken as an indication that the mean number n of molecules in each of the individual channels of the zeolites $AlPO_4$-5 under study amounts to more than 100. This realistic estimate does in fact suggest the occurrence of single-file diffusion.

First tracer ZLC measurements [113], however, are in contrast to this finding. In these studies, tracer exchange is found to be rather fast, so that there is no indication of single-file behavior. Moreover, it appears that the (transport) diffusivities resulting from ZLC measurements are in complete agreement with the concentration dependence of the (self-) diffusivities resulting from

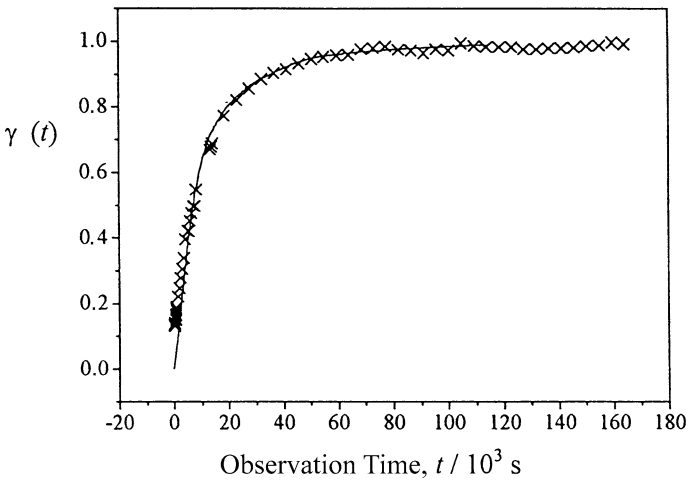

Fig. 12 Tracer exchange curve of propane in $AlPO_4$-5 at 293 K and a loading of 0.7 molecules per unit cell. From [75] with permission

the correspondingly interpreted tracer ZLC response curves. In the case of single-file diffusion, clearly substantial differences are to be expected. As a possible explanation of the difference to the PFG NMR measurements and to the NMR tracer exchange studies, one has to realize that the sorbate concentrations considered in the tracer ZLC studies are much smaller than those in the PFG NMR measurements. It cannot be excluded, therefore, that the molecular transport monitored in the tracer ZLC studies only referred to a fraction of the channels where imperfections facilitated molecular exchange with the surroundings.

4.4 Catalysis

It has been theoretically demonstrated in Sect. 3.3 that the effectiveness factor of catalytic reactions in zeolites is reduced much more by molecular transport under single-file conditions than by normal diffusion. This is a consequence of the dramatic enhancement of the intracrystalline mean lifetime and, hence, of the generalized Thiele modulus via Eq. 30. In view of the significant effect predicted by theory, it is remarkable that for many years this peculiarity of molecular transport did not play any role in the treatment of zeolite catalysis [59]. It should be noted, however, that in fact in many systems which can be considered as good candidates for the occurrence of single-file phenomena, such as aromatics in mordenite, molecular transport could be shown to be of negligible influence for the observed reactions [114–116]. This is not necessarily in contrast to the above considerations, since catalytic reactions are generally considered at higher temperatures with correspondingly low sorbate concentrations. Since, moreover, the single-particle diffusivity in single-file systems has been found to be larger than expected from studies with multidimensional pore networks, Eqs. 8, 19 and 23 show that the relevant single-file mobility factors and, hence, the molecular exchange rates tend to be larger than expected at first glance. In addition, zeolite catalysts are generally applied as very small crystallites. It follows from Eq. 23 with Eq. 19 that for single-file systems this is far more relevant than for the case of ordinary diffusion for ensuring short intracrystalline lifetimes. Finally, one should be aware of the fact that the real structure of zeolites may substantially differ from the ideal one of a given zeolite type. It is rather likely, therefore, that due to structural defects in zeolite catalysts with one-dimensional channel systems, the mutual passage of the reactant and product molecules becomes possible.

The first studies of catalytic processes which confirm the relevance of single-file diffusion in zeolite catalysis were carried out by Sachtler and co-workers. During investigation of palladium-catalyzed conversion of neopentane in supports of different topologies, characteristic differences were observed [117]. With zeolite HY, the process was found to proceed at substantially lower

apparent activation energies than in SiO_2-supported catalysts. By contrast, equivalent experiments with zeolite L did yield an enhancement of the activation energies. The Pd/HY data are obviously in complete agreement with the Thiele–Wheeler theory, which predicts a reduction of the apparent activation energy under diffusion control. Transport inhibition of single-file type as is expected in the unidirectional channels of zeolite L, however, is even found to lead to an enhancement of the apparent activation energy. It has been shown in Sect. 3.3 that the possibility of this tendency may in fact be a predominant feature of catalytic reactions in single-file systems. Extensive model calculations on the basis of the formalism presented in Sect. 3.3 [118, 119] support this supposition. In [120] this effect was confirmed by extensive comparative studies of neopentane reactions over Pt/H-mordenite and Pt/SiO_2 catalysts including H/D exchange, isomerization and hydrogenolysis. At 150 °C the Arrhenius plot of neopentane conversion over Pt/H-mordenite shows a break, indicating the crossover from the single-file controlled to the chemically controlled regime. In [121], the transport inhibition in single-file systems was demonstrated by a characteristic change in the probability distribution of the number of exchanged atoms during the H/D exchange of cyclopentane on Pd/mordenites. When there is no transport resistance, most likely zero, five or ten hydrogen atoms are exchanged. This is an immediate consequence of the elementary step of exchange which will with high probability involve all five hydrogen atoms on the side of the molecule that is in contact with the metal. Such a distribution has been observed for transition metals on amorphous supports and in zeolite Y [122]. As a consequence of the large residence time under single-file conditions, however, before desorbing into the gas phase the molecules have reacted many times so that the initial "double-U-shaped" probability distribution of the number of exchanged hydrogen atoms gets lost. Following these pioneering studies, in [123] the hydroisomerization of *n*-hexane over Pt/H-mordenites was successfully described by model equations, including the loading dependence of the effective diffusivities as given by the single-file expression, Eq. 19.

Upon studying the alkane isomerization over two different types of solid acid catalysts, Pt/H-mordenite and Pt/ZrO_2-SO_4, the special features of the single-file system appeared even in two peculiar cases [124]. Again, as in [117] and [120], the activation energy in the single-file system was substantially larger than in the amorphous catalyst. Additionally, Pt/*H*-mordenite turned out to be virtually inactive for n-butane isomerization. This may be attributed to the geometrical constraints of the one-dimensional channels in mordenite which suppress the dimerization step. By contrast, Pt/ZrO_2-SO_4 with acid sites of comparable strength but without the single-file constraint was found to be a highly active and stable catalyst.

Surprisingly, in [125] the catalytic activity for the heptane conversion over platinum supported by *H*-mordenites was found to increase with increasing platinum particles, corresponding to a decreasing total surface. It

could be shown, however, that this phenomenon may be easily rationalized by the peculiarities of the single-file systems, while under the conditions of high platinum dispersion corresponding to small particles, the channel structure is preserved and the generation of the larger platinum particles necessarily leads to a local destruction of the zeolite framework. This removes the transport restrictions of single-file diffusion. The reduction of the surface of the catalytically active platinum particles is obviously overcompensated by the transport promotion due to the transition from single-file to normal diffusion. In the absence of the latter process, clearly any reduction of the surface of the platinum particles should necessarily lead to a reduction in catalytic activity. Such behavior is in fact well-known for platinum on amorphous supports and zeolites with three-dimensional pore systems [126].

5 Concluding Remarks

The exclusion of a mutual passage of the diffusants in zeolites with one-dimensional channels leads to patterns of molecular transportation which are unknown from amorphous materials or from zeolites with more-dimensional pore networks. In particular, no comprehensive methods exist of describing molecular transport by the well-known Fick's equations of molecular diffusion. Molecular transport in such systems has been termed single-file diffusion. As a most characteristic feature, the molecular mean square displacements in infinitely extended single-file diffusion is found to increase in proportion with the square root of the observation time rather than with the observation time itself. For finite single-file systems, the rate of molecular exchange between the crystals and their surroundings, representing one of the key parameters for their practical application in heterogeneous catalysis and mass separation, decreases with the third rather than with the second power of the crystal size.

As a consequence of the correlation of the movement of the individual diffusants and the thus-mediated long-range influence of boundaries, the treatment of single-file systems of finite length is particularly complicated. Present attempts of analytical treatment of such systems and the quantification of the boundary conditions do not provide anything more than first approaches. Monte-Carlo simulations supported by analytical approaches reveal striking peculiarities of zeolitic single-file systems. These peculiarities include an enhanced dependence of the intracrystalline mean life time, and hence of the effectiveness factor, on the size of the catalyst particle, and the possibility of an enhancement of the apparent activation energy of catalytic reactions under transport control. Though there is still some controversy on the evidence obtained by the different methods applied, indications of

single-file diffusion in zeolites have been observed by various experimental techniques including pulsed field gradient NMR, quasi-elastic neutron scattering and tracer exchange measurements.

It should be emphasized, however, that likely in none of these studies was the zeolite material of such an ideal structure as implied in data analysis. In this respect, experimental studies with artificially created single-file systems [127–129] may provide a much higher reliability of the pre-supposed structural features. A treatise on the substantial deviations of the real structure, with particular emphasis on the consequences for ideal host systems for single-file diffusion as evidenced by optical techniques, is given in [95]. Irrespective of these limitations, however, a number of peculiarities of catalytic reactions in zeolites with one-dimensional channel systems are most likely to be attributed to the special conditions of molecular transport and molecular arrangement under single-file conditions.

Since single-file diffusion is found to lead to a dramatic increase in the intracrystalline mean life times, it may be of crucial importance for zeolite-based technical processes like separation, purification and catalysis [130–132]. Since essentially any technical application has to deal with multi-component systems, for the development of the different strategies to technically exploit single-file diffusion, the concept of dual-mode diffusion [133–135] deserves special recognition. This concept takes the various options of how different types of molecules may propagate in channel systems into consideration, including the option that smaller molecules are "slaved" by the larger ones, compelling them to a joint single-file type motion. Most interestingly, the large differences in two-component permeation through zeolite membranes from the behavior expected from their single-component properties may be referred to this exact slaving pattern [136]. In [132], this phenomenon is considered as an option of hydrocarbon trapping, including such important technical applications as the reduction of cold-short hydrocarbon emissions from automotive exhaust. Hence, in addition to the multitude of intriguing theoretical questions of correlated molecular transport in one dimension, a substantial practical demand for a better understanding of single-file diffusion in zeolites and the corresponding experimental studies exists. Our present knowledge cannot be considered to be much more than an exciting starting point.

Acknowledgements I am deeply obliged to Lothar Riekert, who has drawn my attention to the fascinating field of single-file diffusion in zeolites and to Jens Weitkamp, who has highly motivated me to stick to this problem. I thank Hervé Jobic, Douglas M. Ruthven, Wolfgang M.H. Sachtler and Gunter Schütz for numerous stimulating discussions and my co-workers and students, in particular Peter Bräuer, Andreas Brzank, Karsten Hahn, Volker Kukla, Christian Rödenbeck and Sergey Vasenkov for their important contributions. Financial support by DFG, CNRS, EPSRC and NWO within the frame of national and international research networks is also gratefully acknowledged.

References

1. Kärger J, Petzold M, Pfeifer H, Ernst S, Weitkamp J (1992) J Catal 136:283
2. Riekert L (1970) Adv Catal 21:281
3. Rickert H (1964) Z Phys Chem NF 34:129
4. Hodkin AL, Keynes RD (1955) J Physiol 128:61
5. van Bejeren H, Kehr KW, Kutner R (1983) Phys Rev B 28:5711
6. Kehr KW, Mussawisade K, Wichmann T (1997) In: Kärger J, Heitjans P, Haberlandt R (eds) Diffusion in Condensed Matter. Vieweg, Wiesbaden, p 265
7. Fedders PA (1978) Phys Rev B 17:40
8. Levitt DG (1973) Phys Rev A 8:3050
9. Kehr KW, Binder K (1987) In: Binder K (ed) Applications of the Monte Carlo Method in Statistical Physics. Springer, Berlin, p 181
10. Hahn K, Kärger J (1995) J Phys A-Math General 28:3061
11. Kehr KW, Mussawisade K, Schütz GM, Wichmann T (2005) In: Heitjans P, Kärger J (eds) Diffusion in Condensed Matter – Methods, Materials, Models. Springer, Berlin, p 975
12. Kärger J (1992) Phys Rev A 45:4173
13. Kärger J (1993) Phys Rev E 47:1427
14. Kärger J (2008) Diffusion Measurements by NMR Techniques, in this volume
15. Allnatt AR, Lidiard AB (1993) Atomic Transport in Solids. University Press, Cambridge, p 572
16. Kärger J, Ruthven DM (1992) Diffusion in Zeolites and Other Microporous Solids. Wiley & Sons, New York
17. Brandani S (1996) J Catal 160:326
18. Kärger J, Hahn K (1996) J Catal 160:328
19. Roque-Malherbe RM (2002) Microporous Mesoporous Mater 56:322
20. Roque-Malherbe R, Ivanov V (2001) Microporous Mesoporous Mater 47:25
21. Kärger J (2002) Microporous Mesoporous Mater 56:321
22. Hahn K, Kärger J (1996) J Phys Chem 100:316
23. Leherte L, Vercauteren DP, Derouane EG, Lie GC, Clementi E, André JM (1989) In: Jacobs PA, van Santen RA (eds) Proc 8th Int Zeolite Conf, Amsterdam, The Netherlands, July 10–14, 1989. Elsevier, Amsterdam, 1989, p 773
24. Leherte L, Vercauteren DP, Derouane EG, Lie GC, Clementi E, André JM (1989) Stud Surf Sci Catal 49:773
25. Nowak AK, Denouden CJJ, Pickett SD, Smit B, Cheetham AK, Post MFM, Thomas JM (1991) J Phys Chem 95:848
26. Haberlandt R, Fritzsche S, Peinel G, Heinzinger K (1995) Molekulardynamik – Grundlagen und Anwendungen. Vieweg, Braunschweig, p 252
27. Keffer D, McCormick AV, Davis HT (1996) Molec Phys 87:367
28. Bhide SY, Yashonath S (2002) J Phys Chem A 106:7130
29. Demontis P, Gonzalez JG, Suffritti GB, Tilocca A (2001) J Am Chem Soc 123:5069
30. Demontis P, Suffritti GB, Bordiga S, Buzzoni R (1995) J Chem Soc, Faraday Trans 91:525
31. Fritzsche S, Haberlandt R, Pfeifer H, Heinzinger K (1993) Chem Phys 174:229
32. Fritzsche S, Haberlandt R, Hofmann G, Kärger J, Heinzinger K, Wolfsberg M (1997) Chem Phys Lett 265:253
33. Fan JF, Xia QY, Gong XD, Xiao HM (2001) Chinese J Chem 19:251
34. Haberlandt R, Fritzsche S, Vörtler HL (2001) In: Nalwa HS (eds) Handbook of Surfaces and Interfaces of Materials. Academic Press, New York, p 357

35. Hahn K, Kärger J (1998) J Phys Chem 102:5766
36. MacElroy JMD, Suh SH (2001) Microporous Mesoporous Mater 48:195
37. Mon KK, Percus JK (2002) J Chem Phys 117:2289
38. Mao ZG, Sinnott SB (2000) J Phys Chem B 104:4618
39. Jakobtorweihen S, Verbeek MG, Lowe CP, Keil FJ, Smit B (2005) Phys Rev Lett 95:044501
40. Sholl DS, Fichthorn KA (1997) Phys Rev A 55:7753
41. Sholl DS, Fichthorn KA (1997) Phys Rev Lett 79:3569
42. Sholl DS, Lee CK (2000) J Chem Phys 112:817
43. Pitale KK, Rajadhyaksha RA (1988) Curr Sci 57:172
44. Palekar MG, Rajadhyaksha RA (1995) Chem Eng Sci 40:1085
45. Kärger J, Pfeifer H, Heink W (1988) Adv Magn Res 12:2
46. Nelson PH, Auerbach SM (1999) J Chem Phys 110:9235
47. Nelson PH, Auerbach SM (1999) Chem Eng J 74:43
48. Rödenbeck C, Kärger J (1999) J Chem Phys 110:3970
49. Jobic H (1994) In: Imelik B, Vedrine JC (eds) Catalyst Characterization: Physical Techniques for Solid Materials. Plenum Press, New York, p 347
50. Jobic H, Theodorou DN (2007) Microporous Mesoporous Mater 21:50
51. Kutner R (1981) Phys Lett 81A:239
52. Kärger J, Keller W, Pfeifer H, Ernst S, Weitkamp J (1995) Microporous Mater 3:401
53. Kocirik M, Zikanova A (1972) Z Phys Chem Leipzig 250:250
54. Barrer RM (1978) Zeolites and Clay Minerals as Sorbents and Molecular Sieves. Academic Press, London, p 497
55. Rödenbeck C, Kärger J, Hahn K (1995) J Catal 157:656
56. Bräuer P, Fritzsche S, Kärger J, Schütz GM, Vasenkov S (2004) In: Haberlandt R, Michel D, Pöppl A, Stannarius R (eds) Molecules in Interaction with Surfaces and Interfaces. Springer, Berlin, p 511
57. Vasenkov S, Kärger J (2002) Phys Rev E 66:052601
58. Wheeler A (1951) Adv Catal 3:249
59. Chen NY, Degnan TF, Smith CM (1994) Molecular Transport and Reaction in Zeolites. VCH, New York, p 309
60. Bräuer P, Kärger J, Neugebauer N (2001) Europhys Lett 53:8
61. Neugebauer N, Bräuer P, Kärger J (2000) J Catal 194:1
62. Brzank A, Schutz GM, Brauer P, Kärger J (2004) Phys Rev E 69
63. Brzank A, Schütz GM (2005) Appl Catal A: General 288:194
64. Derouane EG, Gabelica Z (1980) J Catal 65:486
65. Weitkamp J, Puppe L (1999) Catalysis and Zeolites. Springer, Berlin Heidelberg, p 564
66. Snurr RQ, Kärger J (1997) J Phys Chem B 101:6469
67. Clark LA, Ye GT, Snurr RQ (2000) Phys Rev Lett 84:2893
68. Nedea SV, Jansen APJ, Lukkien JJ, Hilbers PAJ (2002) Phys Rev E 6506:6701
69. Nedea SV, Jansen APJ, Lukkien JJ, Hilbers PAJ (2002) Phys Rev E 66:066705
70. Nedea SV, Jansen APJ, Lukkien JJ, Hilbers PAJ (2003) Phys Rev E 67:046707
71. Jansen APJ, Nedea SV, Lukkien JJ (2003) Phys Rev E 67:036104
72. Rödenbeck C, Kärger J, Hahn K (1997) Phys Rev 55:5697
73. Rödenbeck C, Kärger J, Hahn K (1998) Phys Rev E 57:4382
74. Rödenbeck C (1997) PhD Thesis, University of Leipzig, Leipzig
75. Kukla V (1997) PhD Thesis, University of Leipzig, Leipzig
76. Rödenbeck C, Kärger J, Hahn K (1997) Collect Czechoslovak Chem Commun 62:995
77. Brandani S, Hufton J, Ruthven D (1995) Zeolites 15:624

78. Hufton JR, Brandani S, Ruthven DM (1994) In: Weitkamp J, Karge HG, Pfeifer H, Hölderich W (eds) Zeolites and Related Microporous Materials: State of the Art 1994, Proc 10th Int Zeolite Conf, Garmisch-Patenkirchen, Germany, July 17–22, 1994. Elsevier, Amsterdam, p 1323
79. Hufton JR, Brandani S, Ruthven DM (1994) Stud Surf Sci Catal 84:1323
80. Ruthven DM, Post MFM (2001) In: van Bekkum H, Flanigen EM, Jacobs PA, Jansen JC (eds) Introduction to Zeolite Science and Practice, 2nd edn. Elsevier, Amsterdam, p 525
81. Ruthven DM, Post MFM (2001) Stud Surf Sci Catal 137:525
82. Ruthven DM, Brandani S (2000) In: Kanellopoulos NK (ed) Recent Advances in Gas Separation by Microporous Ceramic Membranes. Elsevier, Amsterdam, p 187
83. Rödenbeck C, Kärger J, Hahn K (1998) Ber Bunsen-Ges, Phys Chem Chem Phys 102:929
84. Rödenbeck C, Kärger J, Schmidt H, Rother T, Rödenbeck M (1999) Phys Rev E 60:2737
85. Gupta V, Nivarthi SS, McCormick AV, Davis HT (1995) Chem Phys Lett 247:596
86. Kukla V, Hahn K, Kärger J, Kornatowksi JJ, Pfeifer H (1995) In: Rozwadowski M (ed) Proc 2nd Polish-German Zeolite Colloquium, Torun. Nicholas Copernicus Univ Press, Torun, p 110
87. Kukla V, Kornatowski J, Demuth D, Gimus I, Pfeifer H, Rees LVC, Schunk S, Unger KK, Kärger J (1996) Science 272:702
88. Hahn K, Kärger J, Kukla V (1996) Phys Rev Lett 76:2762
89. Kärger J, Pfeifer H, Rudtsch S, Heink W, Gross U (1988) J Fluorine Chem 39:349
90. Fenzke D, Kärger J (1993) Z Phys D 25:345
91. Kölsch P, Venzke D, Noack M, Toussaint P, Caro J (1994) J Chem Soc Chem Commun, p 2491
92. Kärger J, Vasenkov S (2003) In: Laeri F, Schüth F, Simon U, Wark M (eds) Host-Guest Systems Based on Nanoporous Crystals. Wiley-VCH, Weinheim, p 255
93. Lehmann E, Chmelik C, Scheidt H, Vasenkov S, Staudte B, Kärger J, Kremer F, Zadrozna G, Kornatowski J (2002) J Am Chem Soc 124:8690
94. Lehmann E, Vasenkov S, Kärger J, Zadrozna G, Kornatowski J, Weiss Ö, Schüth F (2003) J Phys Chem B 107:4685
95. Karge HG, Kärger J (2008) Application of IR Spectroscopy, IR Microscopy and Optical Interference Microscopy on Diffusion Zeolites
96. Nivarthi SS, McCormick AV, Davis HT (1994) Chem Phys Lett 229:297
97. Jobic H, Bee M, Kearley GJ (1989) Zeolites 9:312
98. Jobic H (2000) In: Kanellopoulos NK (ed) Recent Advances in Gas Separation by Microporous Ceramic Membranes. Elsevier, Amsterdam, p 109
99. Jobic H, Kärger J, Bee M (1999) Phys Rev Lett 82:4260
100. Jobic H, Methivier A, Ehlers G, Farago B, Haeussler W (2004) Angew Chem Int Ed 43:364
101. Hahn K, Jobic H, Kärger J (1999) Phys Rev E 59:6662
102. Jobic H, Hahn K, Kärger J, Bée M, Noack M, Grinus I, Tuel A, Kearley GJ (1997) J Phys Chem 101:5834
103. Schäfer H, Sternin E (1997) Phys Canada 77
104. Song LJ, Rees LVC (2000) Microporous Mesoporous Mater 41:193
105. Onyestyak G, Valyon J, Rees LVC (2001) Solid State Ion 141:93
106. Kärger J (1997) In: Ertl G, Knözinger H, Weitkamp J (eds) Handbook of Heterogeneous Catalysis. Wiley-VCH, Weinheim, p 1252
107. Karge HG, Niessen W (1991) Catal Today 8:451

108. Hermann M, Niessen W, Karge HG (1995) In: Beyer HK, Karge HG, Kiricsi I, Nagy JB (eds) Catalysis by Microporous Materials, Proc ZEOCAT '95, Szombathely, Hungary, July 9–13, 1995. Elsevier, Amsterdam, p 131
109. Hermann M, Niessen W, Karge HG (1995) Stud Surf Sci Catal 94:131
110. Karge HG (1998) In: Rozwadowski M (eds) Proc Third Polish-German Zeolite Colloquium. Nicolas Copernicus Univ Press, Torun, p 11
111. Karge HG, Niessen W, Bludau H (1996) Appl Catal A General 146:339
112. Niessen W, Karge HG (1993) Microporous Mater 1:1
113. Brandani S, Ruthven DM, Kärger J (1997) Microporous Mater 8:193
114. Karge HG, Ladebeck J, Sarbak Z, Hatada K (1982) Zeolites 2:94
115. Karge HG, Weitkamp J (1986) Chem Ing Tech 58:946
116. Weitkamp J, Ernst S (1994) Catal Today 19:107
117. Kapinski Z, Ghandi SN, Sachtler WMH (1993) J Catal 141:337
118. Rödenbeck C, Kärger J, Hahn K (1998) J Catal 176:513
119. Rödenbeck C, Kärger J, Hahn K, Sachtler W (1999) J Catal 183:409
120. Lei GD, Carvill BT, Sachtler WMH (1996) Appl Catal A General 142:347
121. Lei GD, Sachtler WMH (1993) J Catal 140:601
122. Vanbroekhoven EH, Schoonhoven J, Ponec V (1985) Surf Sci 156:899
123. de Gauw FJMM, van Grondelle J, van Santen RA (2001) J Catal 204:53
124. Liu H, Lei GD, Sachtler WMH (1996) Appl Catal A General 137:167
125. Carvill BT, Lerner BA, Adelman BJ, Tomczak DC, Sachtler WMH (1993) J Catal 144:1
126. Ribeiro F, Marcilly C, Guisnet M (1982) J Catal 78:275
127. Lutz C, Kollmann M, Leiderer P, Bechinger C (2004) J Phys Condens Matter 16:S4075
128. Wei QH, Bechinger C, Leiderer P (2000) Science 287:625
129. Lutz C, Kollmann M, Bechinger C (2004) Phys Rev Lett 93:026001
130. Adhangale P, Keffer D (2003) Separation Sci Technol 38:977
131. Sheintuch M, Efremenko I (2004) Chem Eng Sci 59:4739
132. Czaplewski KF, Reitz TL, Kim YJ, Snurr RQ (2002) Microporous Mesoporous Mater 56:55
133. Sholl DS, Fichthorn KA (1997) J Chem Phys 107:4384
134. Sholl DS, Fichthorn KA (1998) J Chem Phys 109:5693
135. Hahn K, Kärger J (1997) J Chem Phys 109:5691
136. Caro J, Noack M, Kölsch P, Schäfer R (2000) Microporous Mesoporous Mater 38:3
137. Vasenkov S, Kärger J (2002) Phys Rev E 66:052601

Subject Index